Orbit Simulation and Design and Verification of the Electrical Power System of the Delfi-C3 Nanosatellite

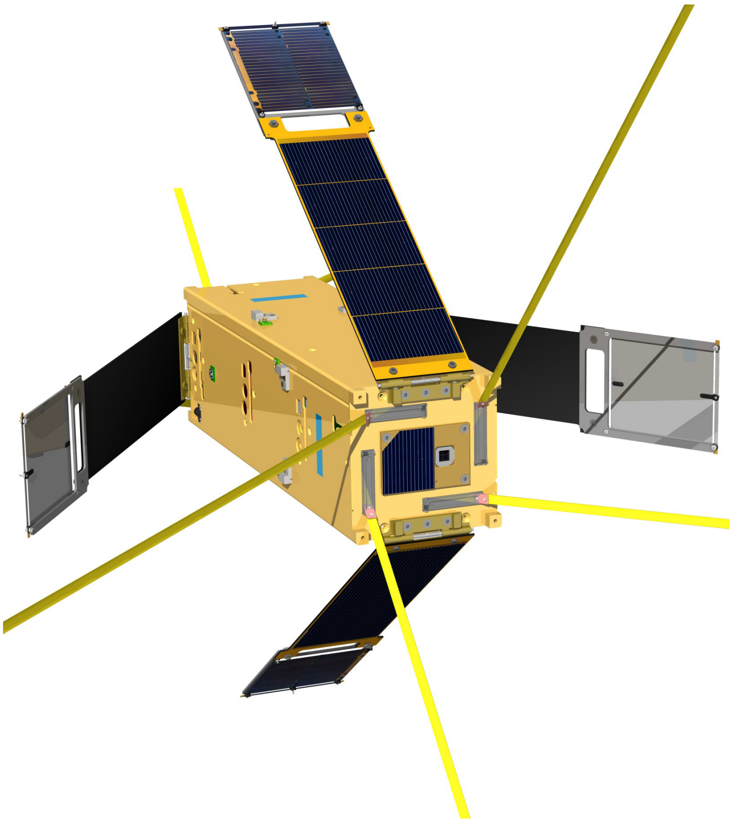

F. te Hennepe

Chair of Space Systems Integration
Faculty of Aerospace Engineering
Delft University of Technology

June, 2007

[DELFI.C3.TW.025]

Orbit simulation and design and verification of the electrical power system of the Delfi-C3 nanosatellite

Master of Science Thesis in Aerospace Engineering

Chair of Space Systems Integration
Department of Earth Observation and Space Systems
Faculty of Aerospace Engineering
Delft University of Technology

F. te Hennepe

Delft, 13 June 2007

The Earth is the cradle of the mind, but one cannot eternally live in a cradle.

Konstantin E. Tsiolkowsky

Preface

Because I always had a special interest in aerospace and spaceflight, I decided to study aerospace engineering after graduation from high school. Although I enjoyed the studies during my Bachelor's education, I missed a special incentive. However during the design synthesis exercise, I came into contact with electrical and electronical systems in space. This occurence seemed to have awakened a dormant gene, which is running in the family. Enthusiastically, I decided to concentrate my Master's education on the school of electrical power engineering, effectively resulting in a crossbreed studies in aerospace and electrical engineering. After enjoying my internship at the spacecraft power division at ESA-ESTEC, I came to regret choosing aerospace engineering over electrical engineering at the start of my studies.

Performing my Master thesis in the Delfi-C3 project eliminated this feeling of regret completely by showing that aerospace engineering had been a wise choice after all. Participating in the design, manufacturing and verification process of a spacecraft, which will be launched in real-life, is a unique opportunity for anyone interested in spaceflight. The combination of knowledge in the fields of aerospace engineering and electrical engineering helped fulfill the role of electrical systems engineer and simulation engineer.

Although the road to success is not always an easy one, I really enjoyed working in this project. I cannot deny the fact that working in a hands-on environment has substantially enhanced my engineering skills. Knowledge and supervision of others cannot be missed in this respect, which leads to a great word of thanks to Bert Monna, Adil Bahrouch, Harm-Jan de Graaf, Chris Verhoeven and Thijmen Hamoen. Furthermore, I want to thank Rob Hamann, Barry Zandbergen, Abe Bonnema and Wouter-Jan Ubbels for their supervision. I cannot thank enough my colleagues of the Delfi-C3 team, which have enabled the blooming of the Delfi-C3 project. In special, I would like to thank Bram Vaartjes, Jasper Bouwmeester, and Gerard Aalbers for the great times filled with cynical humor in the project room. Last but certainly not least, I want to thank my parents, siblings, and friends for their unconditional support during my studies.

Frank te Hennepe

Abstract

Delfi-C3 is a nanosatellite developed by MSc students of the Faculties of Aerospace Engineering and Electrical Engineering, Mathematics and Computer Science at the Delft University of Technology. It will serve as an in-orbit test bed for three innovative technologies. Delfi-C3 is scheduled for launch in August 2007 by an Indian PSLV launcher.

This report focuses on the design process of the electrical power system. Because Delfi-C3 applies a constant voltage power bus, a power conversion system is introduced to transport power from the solar arrays to the power bus. Additional conversion systems are designed for power supply to the various electronics boards. Furthermore, designs are made for interfaces between the electrical power system and the other subsystems. These designs will be presented and discussed in this report. Because electrical power is a scarce resource in spaceflight, a power budget has been generated and maintained throughout the complete Delfi-C3 project. Interface control is applied to ensure efficient cooperation between the various subsystems. In this report, the power budget and interface control process will be presented.

A second focus in this report is the simulation and verification process of the electrical systems of Delfi-C3. To generate an adequate impression of the behaviour of the Delfi-C3 spacecraft in orbit, several orbit simulations are performed. As simulation output, the orbital position is calculated. In addition, the control and disturbance torques are used to reconstruct the attitude profile of the spacecraft. These parameters are subsequently used to calculate the incoming solar power. It will be shown that the incoming solar power is sufficient to supply Delfi-C3 with electrical power. Electrical system verification is part of the spacecraft's testing process. It has to be verified whether the electrical power system is successful in converting solar array power to bus power. The power distribution system has to be tested to guarantee that power arrives at every subsystem in the correct conditions. It will be shown that the electrical power system performs in accordance with requirements and is qualified for spaceflight.

Contents

Preface iii

Abstract v

I THESIS AND MISSION INTRODUCTION 1

1 Introduction 3
- 1.1 Thesis Assignment 3
- 1.2 Body Fixed Reference Frame 3
- 1.3 Document Structure 4

2 Delfi-C3 Mission Overview 5
- 2.1 Mission Background 5
- 2.2 Mission Characteristics 5
  - 2.2.1 Payload Summary 6
  - 2.2.2 Launch and Orbit 7
- 2.3 Mission Objectives 7

II ELECTRICAL SYSTEM DESIGN 9

3 Introduction 11

4 Design of centralized part of electrical power system 13
- 4.1 Introduction 13
- 4.2 Topology of energy flow 13
- 4.3 Solar arrays 14
- 4.4 Step-up converters 17

5 Design of decentralized part of electrical power system 21
- 5.1 Introduction 21
- 5.2 Description of decentralized EPS topology 21
- 5.3 Local EPS PIC supply circuitry 21
- 5.4 Subsystem power switching 22
- 5.5 Step-down DC/DC converters 23
- 5.6 Current measurement circuitry 24

6 Interface design between electrical power system and other subsystems 25
- 6.1 Introduction 25
- 6.2 I2C repeater circuitry design 25
- 6.3 Appendage resistor burn circuitry design 25
- 6.4 ICD2 programmer power supply 26

III SYSTEMS ENGINEERING 29

7 Introduction 31

8 Power budget 33
8.1 Introduction 33
8.2 Power budget description 33
8.2.1 Evaluation of required power 33
8.2.2 Evaluation of generated power 37
8.2.3 Margins 38
8.2.4 Version management 38
8.2.5 Change implementation 38
8.3 Latest version 39

9 Interface control 41
9.1 Introduction 41
9.2 System bus 41
9.3 Board voltages 41
9.4 EPS PIC pin assignment 42
9.5 Measurement reference voltages 43

IV ORBIT SIMULATIONS 45

10 Introduction 47

11 Implementation of Delfi-C3 geometry into EuroSim 49
11.1 Introduction 49
11.2 Satellite fixed reference frame 49
11.3 Definition of Delfi-C3 geometric surfaces 50
11.4 Calculation of center of mass 52
11.5 Evaluation of inertia tensor 52

12 Modeling of magnetic control torque 55
12.1 Introduction 55
12.2 Orientation of magnetic material 55
12.3 Evaluation of control torque 56

13 Modeling of disturbance torques 59
13.1 Introduction 59
13.2 Types of disturbance torques 59
13.3 Gravity gradient torque 60
13.4 Aerodynamic torque 60
13.5 Solar radiation torque 61
13.6 Magnetic disturbance torque 62
13.7 Magnitude comparison 62

14 Estimation of solar array temperature 63
14.1 Introduction 63
14.2 Description of solar panel thermal model 63
14.3 Solar panel temperature evaluation 64

15 Evaluation of solar array incoming power 65
15.1 Introduction 65
15.2 Solar flux 65
15.3 Albedo flux 67
15.4 Evaluation of solar array power 67
15.5 Final notes 68

16 Initial operational timeline 69
16.1 Introduction 69
16.2 Simulation conditions 69
16.3 Simulation results 70

V ELECTRICAL SYSTEM VERIFICATION 71

17 Introduction 73

18 Requirements for the electrical power system 75
18.1 Introduction 75
18.2 List of requirements 75

19 Test procedure for the centralized part of the electrical power system 77
19.1 Introduction 77
19.2 Test plan 77
19.3 Test procedure 78

20 Test results for the centralized part of the electrical power system 79
20.1 Introduction 79
20.2 Test results 79

21 Test procedure for the decentralized part of the electrical power system 83
21.1 Introduction 83
21.2 Test plan 83
21.3 Test procedure 83

22 Test results for the decentralized part of the electrical power system 85
22.1 Introduction 85
22.2 Test results 85

VI CONCLUSIONS AND RECOMMENDATIONS 87

23 Conclusions and recommendations 89
23.1 Main conclusion 89
23.2 Electrical system design 89
23.3 Systems engineering 90
23.4 Orbit simulations 91
23.5 Testing and verification 92
23.6 Miscellaneous 93

VII APPENDICES 97

A Appendant CD 99

B Original thesis assignment 101

C PIC Topology Selection 103
C.1 Introduction 103
C.2 PIC Topology Selection 103
  C.2.1 Trade-off criteria 103
  C.2.2 Definition of scenarios 103
  C.2.3 PIC allocation in stack 105
  C.2.4 Surface area 106
  C.2.5 Power consumption 107
  C.2.6 Software implementation 109
  C.2.7 Final words 109
C.3 Conclusions and recommendations 109

D Oscillator switch of local EPS PIC 111
D.1 Introduction 111
D.2 Oscillator switch of local EPS PIC 111
D.3 Conclusions and recommendations 113

E Simultaneous energizing of two burning resistors 115
E.1 Introduction 115
E.2 Simultaneous energizing of two burning resistors 115
E.3 Conclusions and recommendations 117

F External power supply for ICD2 programmer 119
F.1 Introduction 119
F.2 External power supply for ICD2 programmer 119
F.3 Conclusions and recommendations 122

G Step-Down DC/DC Converter Operations 125
G.1 Introduction 125
G.2 Operational characteristics of step-down DC/DC converter 125
  G.2.1 Electronic topology of step-down DC/DC converter 125
  G.2.2 Lossless continuous operation 126
  G.2.3 Lossless discontinuous operation 128
  G.2.4 Incorporation of dissipation losses 131
  G.2.5 Output voltage ripple 132
G.3 Conclusions and Recommendations 133

H Ripple in current measurement circuitry output 135
H.1 Introduction 135
H.2 Ripple in current measurement circuitry output 135
  H.2.1 Definition of current measurement problem 135
  H.2.2 Statement of possible solutions 136
  H.2.3 Postulation of maximum value tracking design solution 137
  H.2.4 Postulation of low pass post-filtering solution 139
  H.2.5 Preliminary measurement on low pass filter application 143
H.3 Conclusions and recommendations 143

I PIC induced collapse of I2C bus 145
I.1 Introduction 145
I.2 PIC induced collapse of I2C bus 145
  I.2.1 Definition of the problem of I2C pull-down 145
  I.2.2 Brief desciption of original topology 146
  I.2.3 Postulation of FET transfer design proposal 146
  I.2.4 Postulation of I2C repeater design proposal 147
  I.2.5 Design option trade-off 149
I.3 Conclusions and recommendations 150

J Latest version of power budget 151
J.1 Summary of latest version of power budget 152
J.2 Example of application of power budget: measurement board 153

K EuroSim - Geometrical properties 155
K.1 Introduction 155
K.2 Geometrical properties 155
  K.2.1 Determination of center of mass 155
  K.2.2 Calculation of inertia tensor 158
K.3 Conclusions and recommendations 168

L EuroSim - Determination of magnetic control torque 169
L.1 Introduction 169
L.2 Determination of magnetic control torque 169
  L.2.1 Description of Earth magnetic field 169
  L.2.2 Medium transition of magnetic field lines 170
  L.2.3 Characteristics of applied magnetic material 172
  L.2.4 Calculation of magnetic control torque 174
L.3 Conclusions and recommendations 177

M EuroSim - Determination of gravity gradient torque 179
M.1 Introduction 179
M.2 Determination of gravity gradient disturbance torque 179
M.2.1 Derivation of governing equations 179
M.2.2 Construction of rotational matrix 181
M.2.3 Analytical evaluation of gravity gradient torque 182
M.3 Conclusions and recommendations 183

N EuroSim - Determination of aerodynamic torques 185
N.1 Introduction 185
N.2 Determination of aerodynamic torque 185
N.2.1 Nature of aerodynamic forces 185
N.2.2 Generation of aerodynamic torques 189
N.2.3 Calculation of aerodynamic torque due to a single deployed solar panel 190
N.3 Conclusions and recommendations 192

O EuroSim - Determination of antennae induced torques 193
O.1 Introduction 193
O.2 Determination of antennae induced torques 193
O.2.1 General remarks 193
O.2.2 Disturbance torque about y-axis 193
O.2.3 Disturbance torque about x-axis 198
O.2.4 Disturbance torque about z-axis 199
O.2.5 Torque magnitude estimation 201
O.2.6 Shortcomings 202
O.3 Conclusions and recommendations 203

P EuroSim - Area shadowing algorithm 205
P.1 Introduction 205
P.2 Determination of area shadowing algorithm 205
P.2.1 General remarks 205
P.2.2 Longitudinal shadowing 205
P.2.3 Lateral exposure 207
P.2.4 Centers of pressure 211
P.2.5 Shortcomings 211
P.3 Conclusions and recommendations 212

Q EuroSim - Determination of solar radiation torques 213
Q.1 Introduction 213
Q.2 Determination of solar radiation torques 213
Q.2.1 Derivation of solar radiation force 213
Q.2.2 Generation of solar radiation torque 216
Q.2.3 Calculation of solar radiation torque due to a single deployed solar panel 217
Q.3 Conclusions and recommendations 218

R EuroSim - Assessment of magnetic disturbance torques 219
R.1 Introduction 219
R.2 Assessment of magnetic disturbance torques 219
R.2.1 Derivation of Lorentz torque 219
R.2.2 Evaluation of Lorentz torque 220
R.2.3 Derivation of induction torque 222
R.2.4 Evaluation of induction torque 226
R.3 Conclusions and recommendations 226

S Thermal inputs for solar array performance simulation 227
S.1 Introduction 227
S.2 Delfi-C3 solar panel thermal analysis 227
S.2.1 Influence of temperature on solar cell characteristics 227
S.2.2 Brief recapitulation of thermal analysis 227
S.2.3 Construction of a complete stratic thermal model 228
S.2.4 Addition of solar radiation dynamics 236
S.2.5 Influence of spacecraft body 238

S.2.6 Modeling of illumination sources 240
S.2.7 Flow of electrical power 242
S.2.8 Simulation results 242
S.2.9 Compliance with complete spacecraft thermal model results 245
S.3 Conclusions and recommendations 246

T Production drawings of solar panel components 247
T.1 TEC Structure 248
T.2 TFSC Structure 249

U Initial operations timeline 251
U.1 Scenario #1: Successful deployment - No initial rotational rate 251
U.1.1 Array power 251
U.1.2 Rotational velocity 253
U.1.3 Rotational speed 255
U.2 Scenario #2: Successful deployment - Maximal initial rotational rate 256
U.2.1 Array power 256
U.2.2 Rotational velocity 258
U.2.3 Rotational speed 260
U.3 Scenario #3: Single deployment failure - No initial rotational rate 261
U.3.1 Array power 261
U.3.2 Rotational velocity 263
U.3.3 Rotational speed 265
U.4 Scenario #4: Single deployment failure - Maximal initial rotational rate 266
U.4.1 Array power 266
U.4.2 Rotational velocity 268
U.4.3 Rotational speed 270

V Dummy load board verification 271
V.1 Introduction 271
V.2 Dummy load board verification 271
V.3 Conclusions and recommendations 273

W Electrical power subsystem requirements 275

X Test procedure for the centralized electrical power system 277

Y Example test procedure for the decentralized electrical power system 279

Acronyms

AC	Alternating Current
ACS	Attitude Control System
ADC	Analog-to-Digital Converter
ADCS	Attitude Determination and Control Subsystem
ADS	Attitude Determination Subsystem
AE	Aerospace Engineering
AIT	Assembly, Integration and Test
AIV	Assembly, Integration and Verification
AoR	Axis of Roatation
ATRX	Advanced Transceiver
AWG	American Wire Gauge
AWSS	Autonomous Wireless Sun Sensor
ACS	Attitude Control Subsystem
BEng	Bachelor of Engineering
BJT	Bipolar Junction Transistor
BPSK	Binary Phase Shift Keying
CBE	Current Best Estimate
CDHS	Command and Data Handling Subsystem
CFRP	Carbon Fiber Reinforced Plastic
CoM	Center of Mass
COMBO	Combination Board
COTS	Commercial Off The Shelf
CPU	Central Processing Unit
DAC	Digital-to-Analog Converter
DC	Direct Current
DCGS	Delfi Central Ground Station
EEMCS	Electrical Engineering, Mathematics and Computer Science
EGSE	Electrical Ground Support Equipment
EMC	Electromagnetic Compatibility
EP	Electrical Power
EPS	Electrical Power Subsystem
ESD	Electro Static Discharge
FET	Field Effect Transistor
GSE	Ground Support Equipment
GSN	Ground Station Network
LDO	Low Drop-Out Regulator
LED	Light Emitting Diode
LEO	Low Earth Orbit
LO	Local Oscillator
LTAN	Local Time Ascending Node
I2C	Inter Integrated Circuit
IC	Integrated Circuit
ICB	InterConnect Board
ICD	Interface Control Document
ICE	I2C Checkout Equipment
IF	Intermediate Frequency
MAB	Modular Antenna Box
MAIV	Manufacturing, Assembly, Integration and Verification
MEBO	Measurement Board
MechS	Mechanism Subsytems
MGSE	Mechanical Ground Support Equipment
MoI	Moment of Inertia
MOSFET	Metal Oxide Semiconductor Field Effect Transistor
MPP	Maximum Power Point
MSc	Master of Science
OBC	On-Board Computer
OBM	OnBoard MORON (Malfunctioning OBC Recovery OptioN)
OC	Open Circuit
OPAMP	Operational Amplifier
P-POD	Poly-Picosatellite Orbital Deployer
PCB	Printed Circuit Board
PIC	Peripheral Interface Controller
PM	Project Management
PMAS	Passive Magnetic Attitude Stabilization (System)
PSLV	Polar Satellite Launch Vehicle
PV	Photo-Voltaic
PWM	Pulse Width Modulation
RAP	Radio Amateur Platform
RF	Radio Frequency
RMS	Root Mean Square
ROBO	Rod Board
RX	Receiver
SA	Solar Array
SC	Short Circuit
SCL	Serial Clock Line
SDA	Serial Data Line
SE	Systems Engineering
SPF	Single Point Failure
SIS	Systems Integration of Spacecraft
SLR	Standard List of References

SMD Surface Mounted Device

SP Solar Panel

STS Structural Subsystem

TBC To Be Confirmed

TBD To Be Determined

TBW To Be Written

TCS Thermal Control Subsystem

TFSC Thin Film Solar Cells

TM TeleMetry

TN Technical Note

TP Test Plan

TR Test Results

TRIAC Triode for Alternating Current

TTS Titanium Temperature Strip

TX Transmitter

USB Universal Serial Bus

VCO Voltage Controlled Oscillator

VLASS Very Large Area Solar Simulation

List of Figures

1.1 Delfi-C3 body fixed reference frame 4

2.1 Delfi-C3 mission's history overview 5
2.2 AWSS housing display model with circuit board mock-up 7
2.3 Toronto's X-POD and the PSLV Launch Vehicle 8

4.1 Global schematic of Delfi-C3 energy flow 13
4.2 General IV characteristic including relevant quantities 14
4.3 Equivalent circuit of a single junction solar cell 15
4.4 Equivalent circuit of a Delfi-C3 triple junction solar cell 16
4.5 IV characteristic of the a single Delfi-C3 solar array 17
4.6 Equivalent circuit of a general step-up converter 18
4.7 Equivalent circuit of a single array converter in the Delfi-C3 electrical power system . . . 19

5.1 Schematic representation of the decentralized part of the electrical power system 22
5.2 Equivalent electrical circuit of the power supply circuitry of the decentralized EPS PIC . 23
5.3 Equivalent electrical circuit of the MOSFET switch in the subsystem power line 23
5.4 Equivalent electrical circuit of the step-down DC/DC converter 24
5.5 Equivalent electrical circuit of the current measurement circuitry 24

6.1 Application of the I2C repeater to a PIC microcontroller. 26
6.2 Equivalent electrical circuit of appendage resistor burn circuitry 27
6.3 Equivalent electrical circuit of the ICD2 programmer power supply 27

11.1 Illustration of the satellite fixed reference frame 49
11.2 Surface definition of the Delfi-C3 spacecraft 50

12.1 Configuration of magnetic material rods in Delfi-C3 spacecraft 55
12.2 BH-curve of AlNiCo 5 cast magnetic material 56
12.3 Simplified BH-curve of PermeNorm 5000H2 hysteresis material 57

13.1 Substitution of an offset force by a force and a torque 59

14.1 Complete static thermal model of solar panel 64

15.1 Position of the Delfi-C3 spacecraft in the Earth-Sun system 66
15.2 Situational sketch of solar flux incident on body surface i 67

20.1 Test results for a Delfi-C3 solar array illuminated by a theatre spot 80
20.2 Simulation model for a inhomogeneous illuminated solar array of the Delfi-C3 spacecraft . 81
20.3 Simulation results for a inhomogeneous illuminated solar array of the Delfi-C3 spacecraft . 82

C.1 Analysis of influence of ICD2 current on PIC input voltage 104
C.2 Example of a Zener diode characteristic 105
C.3 Schematic representation of the single PIC concept 106
C.4 Schematic representation of the dual PIC concept 106

D.1 Equivalent electrical circuit for measurement of PIC current consumption 112

E.1 PIC supply voltage as a function of system bus voltage 117

F.1 Analysis of influence of ICD2 current on PIC input voltage 120
F.2 Solution #1: Connecting a 3.3V power supply to the ICD2 power line 121
F.3 Solution #2: Connecting a 12V power supply to the ICD2 power line 122
F.4 Customized connector for providing power to the ICD2 programmer 123

G.1 Equivalent electrical circuit of a step-down DC/DC converter 126
G.2 Inductor voltage in continuous operation 128
G.3 Inductor current in continuous operation 129
G.4 Input current in continuous operation 129
G.5 Inductor voltage in discontinuous operation 131
G.6 Inductor current in discontinuous operation 131
G.7 Input current in discontinuous operation 132
G.8 Capacitor current in continuous operation 133
G.9 Capacitor charge ripple in continuous operation 134

H.1 Pulse current waveform at input of step-down DC/DC converter 136
H.2 Switching frequency vs. input voltage of the MAX1836 step-down converter 139
H.3 Output voltage of low pass filter - cut-off frequency 1000 Hz 140
H.4 Output voltage of low pass filter - cut-off frequency 100 Hz 140
H.5 Output voltage of low pass filter - cut-off frequency 10 Hz 141
H.6 Output voltage of low pass filter - final design 142
H.7 Output voltage of low pass filter - final design (close-up) 142
H.8 Bode diagram of low pass filter - final design; R = 10 kΩ; C = 1 μF 143
H.9 Measurement of input voltage of low pass filter 144
H.10 Measurement of input voltage of low pass filter 144

I.1 Electrical schematic of an I2C port on a PIC microcontroller 146
I.2 Schematic representation of original dual PIC concept 147
I.3 Schematic representation of dual PIC concept with transfer of MOSFET switch 148
I.4 Equivalent electrical circuit of an I2C repeater 148
I.5 Schematic representation of dual PIC concept with I2C repeater application 149

K.1 Sketch of Delfi-C3 spacecraft model in xz-plane of satellite fixed reference frame 156
K.2 Sketch of standard geometric objects with relevant dimensions 159
K.3 Sketch of an arbitrary body having its axis of rotation displaced with respect to its center of mass 159
K.4 Sketch of Delfi-C3 spacecraft model in yz-plane of satellite fixed reference frame 162
K.5 Sketch of Delfi-C3 spacecraft model in xy-plane of satellite fixed reference frame 164

L.1 Sketch of Delfi-C3 spacecraft model in xy-plane of satellite fixed reference frame 171
L.2 Situational sketch for evaluating magnetic flux density behaviour at medium transition . . 171
L.3 Illustration of fringing of magnetic flux density due to presence of magnetic material . . . 172
L.4 Simplified BH-curve of PermeNorm 5000H2 hysteresis material 173
L.5 BH-curve of AlNiCo 5 cast magnetic material 174
L.6 Situational sketch of a rotating rod of magnetic material in a stationary magnetic field . . 175
L.7 Magnetic control torque generated by a permanent magnet as function of incidence angle 176
L.8 Magnetic control torque generated by a hysteresis material rod as function of incidence angle 177

M.1 Rigid body in a circular orbit 180

N.1 Illustration of the generation of aerodynamic torques 186
N.2 Atmospheric temperature as a function of altitude [13] 188
N.3 Situational sketch for determining aerodynamic torque on a deployed solar panel 190
N.4 Illustration of Earth Inertial reference frame 191

O.1 Illustrational sketch for calculation of downlink antennae induced torques about y-axis . . 194
O.2 Illustrational sketch for antenna view factor determination 194
O.3 Sketch of Delfi-C3 spacecraft model in xz-plane of satellite fixed reference frame 195
O.4 Illustrational sketch for calculation of uplink antennae induced torques about y-axis . . . 196
O.5 Analysis of normalized disturbance torque about y-axis as a function of incidence angle . 199
O.6 Illustrational sketch for calculation of downlink antennae induced torques about x-axis . . 199
O.7 Analysis of normalized disturbance torque about x-axis as a function of incidence angle . 200

O.8 Sketch of Delfi-C3 spacecraft model in xy-plane of satellite fixed reference frame 200
O.9 Analysis of normalized disturbance torque due to a single antenna about z-axis as a function of incidence angle 201
O.10 Analysis of normalized disturbance torque about z-axis as a function of two incidence angles 202

P.1 Sketch of shadowing principle 206
P.2 Sketch of shadowing principle 206
P.3 Situational sketch of exposure principle in lateral direction 208
P.4 Illustration of lateral exposure in case $\beta < \epsilon$ 208
P.5 Illustration of lateral exposure in case $\beta > \epsilon$, $y < w$ 210
P.6 Illustration of lateral exposure in case $\beta > \epsilon$, $y > w$ 210

Q.1 Illustration of exchange of momentum between incident photon and spacecraft 215
Q.2 Illustration of optical properties of an illuminated body panel 216
Q.3 Situational sketch for determining solar radiation torque on a deployed solar panel 217

R.1 Situational sketch of current loop in a solar array 220
R.2 Situational sketch of rotating short-circuited coil in an external magnetic field 222
R.3 Equivalent circuit of a short-circuited coil rotating in a stationary magnetic field 224
R.4 Phasor diagram of a short-circuited coil rotating in a stationary magnetic field 225
R.5 Induction torque generated on single solar array 226

S.1 Example solar cell IV characteristics for three different temperatures 228
S.2 Example solar cell IV characteristics for three different temperatures 229
S.3 Representation of thermal nodes on solar panel front side 229
S.4 Representation of thermal nodes on solar panel back side 229
S.5 Complete static thermal model of solar panel 230
S.6 Complete static thermal model of solar panel 234
S.7 Sketch of mutual heat exchange between back side of solar panel and spacecraft body . . 239
S.8 Sketch of Delfi-C3 attitude in Sun Earth system 241
S.9 Sketch of Delfi-C3 attitude in Sun Earth system 241
S.10 Thermal profile of TEC photovoltaic cells - rotational velocity 0.2 deg.s^{-1} 243
S.11 Thermal profile of TEC photovoltaic cells - rotational velocity 10 deg.s^{-1} 244
S.12 Close-up of thermal profile of TEC photovoltaic cells - rotational velocity 10 deg.s^{-1} . . . 244
S.13 Thermal profile of TEC photovoltaic cells - constant maximum solar flux 245
S.14 Thermal profile of TEC photovoltaic cells - no solar flux 246

U.1 Scenario 1 - Orbit 1 - Array power 251
U.2 Scenario 1 - Orbit 2 - Array power 252
U.3 Scenario 1 - Orbit 3 - Array power 252
U.4 Scenario 1 - Orbit 1 - Rotational velocity 253
U.5 Scenario 1 - Orbit 2 - Rotational velocity 253
U.6 Scenario 1 - Orbit 3 - Rotational velocity 254
U.7 Scenario 1 - Rotational speed 255
U.8 Scenario 2 - Orbit 1 - Array power 256
U.9 Scenario 2 - Orbit 2 - Array power 256
U.10 Scenario 2 - Orbit 3 - Array power 257
U.11 Scenario 2 - Orbit 1 - Rotational velocity 258
U.12 Scenario 2 - Orbit 2 - Rotational velocity 258
U.13 Scenario 2 - Orbit 3 - Rotational velocity 259
U.14 Scenario 2 - Rotational speed 260
U.15 Scenario 3 - Orbit 1 - Array power 261
U.16 Scenario 3 - Orbit 2 - Array power 261
U.17 Scenario 3 - Orbit 3 - Array power 262
U.18 Scenario 3 - Orbit 1 - Rotational velocity 263
U.19 Scenario 3 - Orbit 2 - Rotational velocity 263
U.20 Scenario 3 - Orbit 3 - Rotational velocity 264
U.21 Scenario 3 - Rotational speed 265
U.22 Scenario 4 - Orbit 1 - Array power 266
U.23 Scenario 4 - Orbit 2 - Array power 266
U.24 Scenario 4 - Orbit 3 - Array power 267

U.25 Scenario 4 - Orbit 1 - Rotational velocity 268
U.26 Scenario 4 - Orbit 2 - Rotational velocity 268
U.27 Scenario 4 - Orbit 3 - Rotational velocity 269
U.28 Scenario 4 - Rotational speed 270

List of Tables

4.1 Structural characteristics of Delfi-C3 photovoltaic cells 15
4.2 Electrical characteristics of Delfi-C3 photovoltaic cells 16
4.3 Parameter values used for solar array composition of Delfi-C3 16

8.1 Board voltages per PCB 34
8.2 Allocation of values to the relevant variables in generated power calculation 37
8.3 Indication of uncertainties to budgeted power values 38

9.1 Pin allocation on system bus 42
9.2 Summary of the applied board voltages per printed circuit board 42
9.3 Allocation of pins of the local EPS PIC microcontroller 43

12.1 Maximum and minimum values of magnetic control torques 57

13.1 Comparison of magnitudes of the various torques acting on the Delfi-C3 spacecraft 62

14.1 Results of solar panel thermal analysis 64

15.1 Properties of InGaP/GaAs/Ge Triple-Junction photovoltaic cells on-board Delfi-C3 67

16.1 Initial conditions used for performing orbit simulations 69

20.1 Test results of the centralized EPS 82

22.1 Test results of the decentralized EPS on measurement board Z- 85
22.2 Test results of the decentralized EPS on combination board 86
22.3 Test results of the decentralized EPS on electrical power subsystem board 86

C.1 Allocation and clock frequency of PICs in single PIC concept 107
C.2 Allocation and clock frequency of PICs in dual PIC concept 107
C.3 Input currents for the Microchip PIC18F4680 at various input voltages and clock frequencies 107
C.4 Combined PIC power consumption in single PIC concept 108
C.5 Combined PIC power consumption in single PIC concept 109

D.1 PIC current (including adjacent circuitry) consumption at various oscillator configurations 112

E.1 On-resistance values of applied semiconductor components 115
E.2 Power consumption of energized subsystems in deployment mode 116

F.1 List of electronic components supplied with power by the PIC power supply 120

I.1 Trade-off table of major design options 150
I.2 Trade-off table of I2C repeater enable pin connection 150

K.1 Relevant geometrical characteristics of the Delfi-C3 spacecraft model 157
K.2 Relevant geometrical characteristics of the Delfi-C3 spacecraft model 158
K.3 Determination of moment of inertia about y-axis in nominal case 161
K.4 Determination of moment of inertia about x-axis in nominal case 164
K.5 Determination of moment of inertia about z-axis in nominal case 166

L.1 Important characteristics of PermeNorm 5000H2 hysteresis material 172

L.2 Important characteristics of AlNiCo 5 cast hard magnetic material 174
L.3 Maximum and minimum values of magnetic control torques 176

O.1 Relevant characteristics of the Delfi-C3 spacecraft model 198
O.2 Summary of maximum estimated induced antenna torques 202

Q.1 Relevant parameters for solar flux calculation 218

R.1 Geometrical parameters relevant for solar array Lorentz torque analysis 221
R.2 Generated Lorentz torques due to response of a single solar array to various magnetic field vectors 222
R.3 Relevant parameters for induction torque analysis on single solar array 226

S.1 Summary of thermal node representation of solar panel 229
S.2 Geometrical characteristics of TEC photovoltaic cells 230
S.3 Geometrical characteristics of TEC support structure 231
S.4 Geometrical characteristics of TFSC support structure 231
S.5 Geometrical characteristics of TFSC photovoltaic cells 231
S.6 Summary of volumes and surface areas of the various components on solar panel 232
S.7 Summary of applied solar panel materials with corresponding specific thermal capacities . 232
S.8 Summary of thermal capacities of various thermal nodes 233
S.9 Summary of applied solar panel materials with corresponding thermal conductivities . . . 234
S.10 Summary of thermal resistances between involved nodes in solar panel thermal model . . 236
S.11 Summary of optical characteristics of various nodes in solar panel thermal model 237
S.12 Summary of additional parameters for determining dynamic behaviour of solar panel thermal model 237
S.13 Summary of characteristics of solar panel hinge 238
S.14 Relevant geometrical parameters of spacecraft body 239
S.15 Summary of parameters for determination of solar flux 242
S.16 Extreme values of TEC photovoltaic cell temperature - rotational velocity 0.2 deg.s^{-1} . . 243
S.17 Extreme values of TEC photovoltaic cell temperature - rotational velocity 10 deg.s^{-1} . . . 245
S.18 Extreme values of TEC photovoltaic cell temperature - rotational velocity 10 deg.s^{-1} . . . 245

V.1 Impedance values of various load batches 272
V.2 Load batch allocation to the various switches on the dummy load board 272
V.3 Measured and calculated resistance of the various dummy load batches 272
V.4 Inspected capacitance of the various dummy load batches 272

Part I

THESIS AND MISSION INTRODUCTION

Chapter 1

Introduction

Delfi-C3 is the first nanosatellite student project of the Delft University of Technology in Delft, the Netherlands. The satellite is based on the CubeSat concept and a number of novel technologies will be tested on board the satellite:

- TFSC experiment;
- AWSS experiment;
- ATRX experiment.

This thesis report serves to show a description of the work performed by the author during his affiliation with the Delfi-C3 project. Furthermore, it can function as a reference document for the current project and for future spacecraft projects.

In this chapter, the main action items relating to the author's thesis are presented. Furthermore, the structuring of this document will be described.

1.1 Thesis Assignment

At the initiation of the author into the Delfi-C3 project, the project was already running for over one-and-a-half years. The first group of involved students, which had done the preliminary design of the Delfi-C3 spacecraft, had graduated. This resulted in the need for reinforcements on the project. At the start of the author's thesis assignment in August 2006, he was requested to take part in the Delfi-C3 project and continue the work of his predecessors.

Due to the affinity of the author with power electronics, he was asked to take responsibility of the electical power system. This action item included the generation and management of the power budget and the electrical interfaces. Furthermore, the author was asked to implement an orbital simulator of the Delfi-C3 spacceraft into the OpSim simulator. As the project progressed, and arrived in the testing and verification phase, it became clear that the author was required to control the testing of the electrical power system. Hence, the thesis assignment of the author can be divided into the following parts:

- Design of electrical power system
- Systems engineering
- Orbital simulations
- Testing and verification

In appendix B, the original thesis assignment of the author is presented.

1.2 Body Fixed Reference Frame

In this report there will be referencing to surfaces on the satellite to indicate a certain feature or component. A body fixed reference frame has been defined to make it clear to which side is referred.

The body fixed reference frame is attached to the geometric center of the satellite body. The Z_{BF}-axis is defined parallel to the long side of the satellite body. The X_{BF}-axis and Y_{BF}-axis are defined as shown in figure 1.1. Two angles are defined in the Body Fixed Reference Frame, θ which is defined as a rotation along the Y_{BF}-axis and φ which is a rotation along the X_{BF}-axis. The positive Z_{BF}-axis directed to the top panel of the satellite and the negative Y_{BF}-axis is towards the side with external access ports. The solar panels that are on the $X_{BF}+$ and X_{BF}- side of the satellite are attached to the $Z_{BF}+$ body panel, while the $Y_{BF}+$ and Y_{BF}- solar panels are attached to the Z_{BF}- body panel.

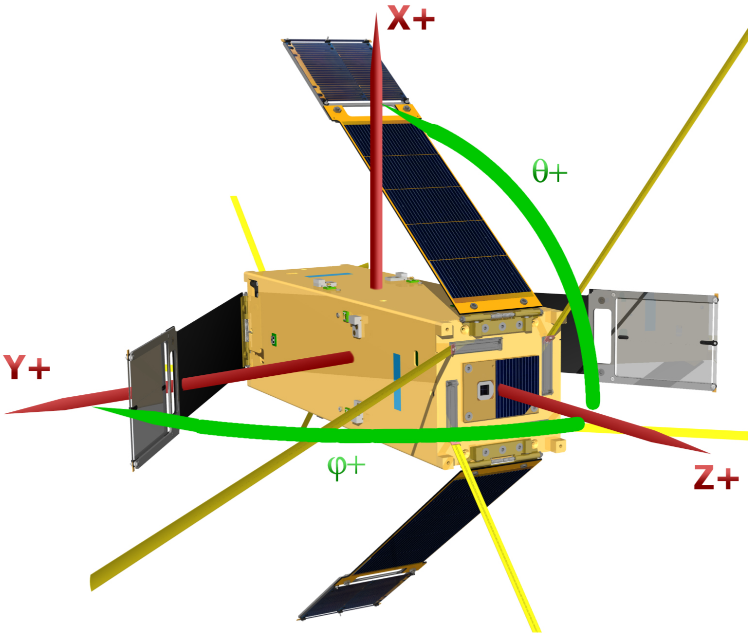

Figure 1.1: Delfi-C3 body fixed reference frame

1.3 Document Structure

Most of the performed work of the author has already been documented previously for internal communication in so-called technical notes. These documents are mainly used for transfer of knowledge, and therefore they contain an excellent description of the performed work of the author. As most information is already is documented, the author has chosen to create a supporting skeletal structure for the main body of his report. In this main body a concise description of the work is given with a treatise of results and conclusions. For detailed information, the report depends heavily on references to technical notes, which are attached as annexes.

The main structure of the report is divided into six parts, with each representing one of the main actions in the thesis assignment. Part I introduces the author's work and the Delfi-C3 mission. In Part II, a presentation is shown of the design of the electrical power system. This largely refers to the design of the so-called local EPS and the interfaces between the EPS and other subsystems. Part III is a description of the performed systems engineering work, which includes the power budget and interface identification. Part IV gives a treatise of the orbital simulations in EuroSim, with a derivation of the used algorithms and an evaluation of the simulation results. Testing and verification is treated in Part V, which includes test procedures and test results for the subsystems under responsibility of the author. Finally in Part VI, several conclusions and recommendations with respect to the author's work and the project in general are postulated. Relevant documentation is attached to the report in the forms of appendices. Additional information is included on the appendant CD in appendix A.

Chapter 2

Delfi-C3 Mission Overview

2.1 Mission Background

Delfi-C3 saw its first light in October of 2004, when the Technical University of Delft together with Dutch Space and TNO Science & Industry agreed upon the development of a nanosatellite that would carry a payload from both industrials. Further fruition of the mission came with the introduction of the CubeSat concept through ir. Zandbergen, whom learned about it at the International Aerospace Conference (IAC) 2004 held in Vancouver, Canada. The CubeSat concept would serve as the basis for the design of the nanosatellite, as its envelope and external layout were more or less fixed. With two payloads already on-board, a very preliminary conceptual layout identified and a preliminary financial budget more or less agreed upon, the decision to at least initiate the project could be taken within just a few weeks.
Another aspect that added to this rapid decision is the fact that both the Faculty of Aerospace Engineering and the Faculty of Electrical Engineering, Mathematics and Computer Science of Delft University of Technology can provide a part of the required mission support with their in-house facilities. Figure 2.1 summarizes the history of Delfi-C3.

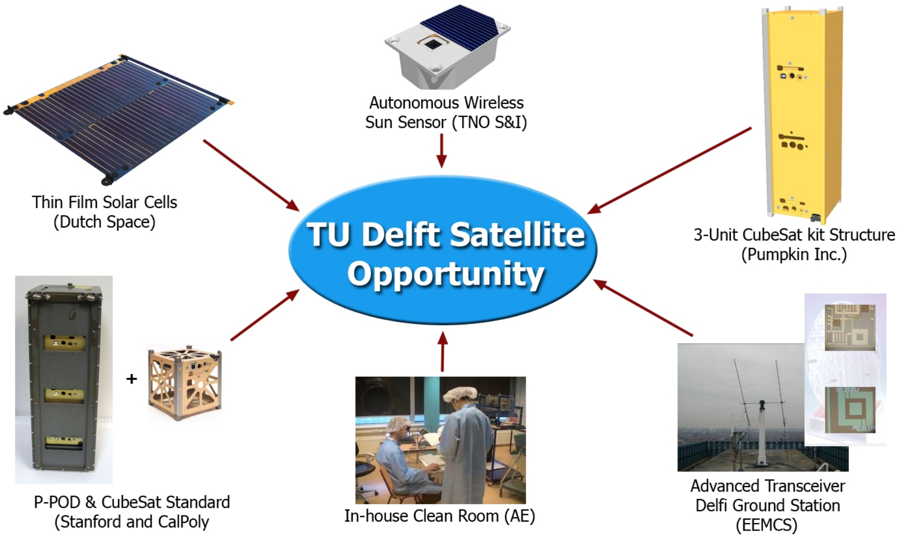
Autonomous Wireless
Sun Sensor (TNO S&I)
Thin Film Solar Cells
(Dutch Space)
TU Delft Satellite
Opportunity
3-Unit CubeSat kit Structure
(Pumpkin Inc.)
+
P-POD & CubeSat Standard
(Stanford and CalPoly
In-house Clean Room (AE)
Advanced Transceiver
Delfi Ground Station
(EEMCS)

Figure 2.1: Delfi-C3 mission's history overview

The project was kicked-off on November 1st 2004 as a Master of Science thesis project at the Faculty of Aerospace Engineering (AE) and the Faculty of Electrical Engineering, Mathematics and Computer Science (EEMCS) of Delft University of Techonology.

2.2 Mission Characteristics

The mission characteristics can be summarized as follows: Being a thesis project, all activities, both technical and non-technical, required for the design, development and realization of Delfi-C3 will be performed by students that dedicate their thesis work to the project. An exception to these activities are cost control and the manufacturing of parts and components. Students are supervised and supported by the AE professors and by other faculty employees and industry contacts.

The time frame for Delfi-C3 is rather ambitious. The goal is to design, develop and realize Delfi-C3 from scratch in just three years. However, as students will be performing all the work, the project should not have a development time that is much longer, as that would require multiple replacements of students working on a single subsystem during the course of the project. Not only will this most likely be harmful for the team's efficiency, it might also have adverse consequences for the team's morale.

Another important characteristic is that the project is based on a low financial budget. This budget concerns cost for procurement, production and use of hardware, software and support equipment, since most students are unpaid for the design and development work.

2.2.1 Payload Summary

The following three payloads will be flown on Delfi-C3:

Thin film Solar cells flown for Dutch Space:

- First flight opportunity
- High power to mass ratio
- Efficiency $>$ 12 % (BOL)
- Mass $<$ 600 g/m^2
- Max. operating Temperature $\sim$ 375 K
- Body Mounting not possible

Testing involves:
- IV-curve Measurement
- Operating Temp. Measurement
- Reference for Solar Flux required

Four pairs of two Thin Film Solar Cells (TFSC) will be flown. The TFSCs are made up of CIGS (copper indium gallium selenide) Solar cells on a 50 μm thick titanium foil. A TFSC has an area of 80×40 mm, with eight 2 mm diameter connection holes. Each pair is interconnected by two plastic pressure contacts requiring an overlap of 5 mm and four pressure contacts on the corners are used to mount each set.

Autonomous wireless Sun sensor flown for TNO Science & Industry:

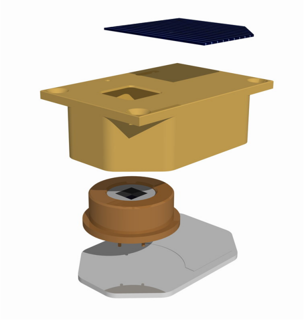

- Based on analog Sun sensor (flight spare)
- Custom designed read-out electronics
- Integrated wireless communication (RF)
- 'Plug & Play' design

Testing involves:
- Autonomy verification
- Wireless communication verification
- Temperature ranges

Two Autonomous Wireless Sun Sensors (AWSS) combined with one single RF-receiver are to be flown on Delfi-C3. The AWSS is a precursor to the micro digital Sun sensor (μDSS) from TNO Science & Industry.

The AWSS has an envelope of 60×40.5×17.8 mm and a total mass of 75 grams. The AWSS housing is the first hardware component that is completely finished and ready for assembly; it was manufactured by the work shop at the faculty of AE. The final product can be seen in figure 2.2; this is the display model, three others will serve as flight units and a spare.

The circuit board for the read-out and communication electronics fits inside a recess on the bottom of the housing and will be 1.6 mm thick. The circuit board will be glued to the housing with a conductive adhesive to make a Faraday cage.

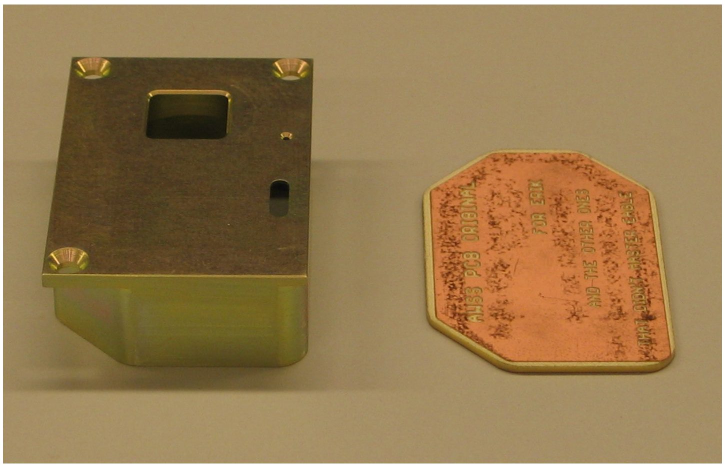

Figure 2.2: AWSS housing display model with circuit board mock-up

Advanced Transceiver flown for the Faculty of EEMCS:

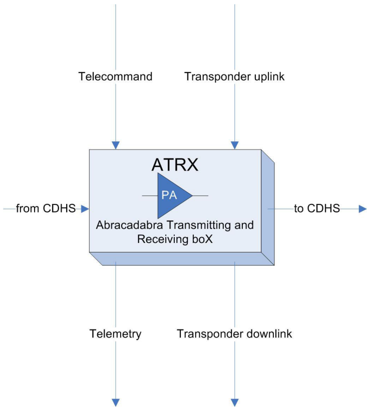

- Custom transceiver design
- High efficiency linear Power Amplifier
- Integrated linear transponder

Testing involves:
- Functionality verification
- Power Amplifier efficiency verification

The Advanced Transceiver will be the primary communication device for Space-Ground and Ground-Space communication. It is however backed up by another transceiver: the Radio Amateur Platform, which is designed by BEng students from TH Rijswijk. However it will not be possible to finish the development for the entire ATRX on time and therefore it is decided to fly a less advanced Advanced Transceiver. The fully developed ATRX will therefore be scheduled to fly (if this is decided upon) on a second mission, the Delfi-C3 Mk2. The currently used "ATRX" will therefore have many similarities with the Radio Amateur Platform.

2.2.2 Launch and Orbit

The Delfi-C3 spacecraft is scheduled for launch in the fourth quarter of 2007 aboard the X-POD canister provided by the University of Toronto's Space Flight Laboratory with whom the Launch Service Agreement is signed. Together with the Antrix Cooperation which is responsible for the commercial launch activities with the launch vehicles of the Indian Space and Research Organization (ISRO). Delfi-C3 will be launched from the Indian launch site Sriharikota onboard the Polar Satellite Launch Vehicle (PSLV). Delfi-C3, will be launched as a secondary payload to a Sun synchronous orbit, with an altitude of 635 kilometers and an inclination of 97.91 degrees. Note that this is compliant with the requirement, which states that a minimum launch inclination of 60 degrees is necessary, in order to obtain good coverage over the Delft ground station which is situated at 52 degrees latitude.

2.3 Mission Objectives

Delfi-C3's mission objectives are separated into technical objectives and educational objectives. The basic technical mission objectives are related to the payloads mentioned above and are to:

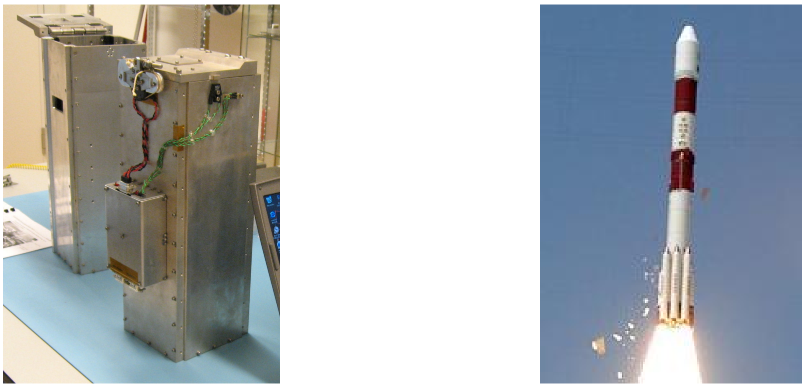

Figure 2.3: Toronto's X-POD and the PSLV Launch Vehicle

- In-orbit test the performance of a new type of Thin Film Solar Cells for Dutch Space by measuring their IV-curves, the accompanying temperature ranges and sun incidence angles.
- In-orbit test the full autonomy of an analog Sun Sensor in orbit, using a wireless RF-interface.
- In-orbit test the performance of a transceiver that is advanced in its high efficiency and miniaturization.
- Set up a ground station network distributed over the Earth for use for Delfi-C3 and future missions.

The setup of a distributed ground station network is added as the interface between Delfi-C3 and the Radio Amateur Community, as they will form the majority of that ground station network.
Since Delfi-C3 is a university project to be run by students, these technical mission objectives are accompanied by the following educational objectives, which are to:

- Provide students with an opportunity to gain interdisciplinary hands-on engineering experience by providing a real-world application.
- Prepare students for careers in aerospace and related industries by encouraging development of their teamwork, leadership and communication skills.
- Be a motivation for students to participate in satellite projects and to choose the aerospace engineering discipline as a field of study in general and be a challenge for students to be innovative and efficient at the same time.
- Interface with the Master of Science programs of the Faculties of Aerospace Engineering, and Electrical Engineering, Mathematics and Computer Science of the TU Delft.
- Enable other educational programs at a variety of educational organizations to participate in the project.

Part II

ELECTRICAL SYSTEM DESIGN

Chapter 3

Introduction

In order to operate the various subsystems on-board the Delfi-C3 spacecraft successfully, they have to be supplied by electrical power. In case of Delfi-C3, this electrical power is generated on solar arrays. Solar arrays convert incoming solar power into electrical power, and are therefore a convenient method in spaceflight for generating electricity. In addition, Delfi-C3 makes use of several electrical circuits for distribution and conditioning of the electrical power. This complete set of electrical circuits is defined as the electrical power system (EPS).

For transport of electrical power within the Delfi-C3 spacecraft, a power bus is introduced. This bus operates on a constant voltage. However, the solar arrays are not capable of generating a constant voltage of 12V. After all, the voltage and current of the arrays is highly dependent on the illumination conditions and the load impedance. For this reason, a power conversion system is inserted, which converts solar array power to bus power.

As not every subsystem in the Delfi-C3 spacecraft operates on the bus voltage, it is necessary to apply additional conversion systems. These systems convert the bus power to board power, which is conditioned to a specific board voltage. Every subsystem has distinct operating voltages, and therefore dedicated converters are required on every board.

In addition to the independent operation of the EPS, several interfaces are present between the electrical power system and other subsystems in the spacecraft. For successful operation of these interfaces, additional circuitry is designed.

The most striking characteristic of the Delfi-C3 electrical power system, is the absence of a battery. This feature has been decided due to the fact that every payload requires solar radiation to operate. Therefore, operation of the spacecraft in eclipse is not needed and power storage is not required.

In this part, the design issues relating to the electrical power system are discussed. Chapter 4 presents the design process for the centralized part of the electrical power system. A similar presentation is done for the decentralized part of the electrical power system in chapter 5. In chapter 6, the designs of the interfaces between the electrical power systems and other subsystems are shown and discussed.

Chapter 4

Design of centralized part of electrical power system

4.1 Introduction

Every subsystem in Delfi-C3 requires electrical power to operate successfully. In order to generate electrical power, the Delfi-C3 spacecraft makes use of solar arrays. These devices are capable of converting solar light into electricity. However, the electrical power produced at the solar arrays is not suitable for directly powering the various subsystems. Therefore, Delfi-C3 incorporates a centeralized electrical power system. This subsystem is responsible for converting the raw array power into conditioned bus power. More accurately, this means that the input power at a variable array voltage is transformed into output power with a constant bus voltage.

In this chapter, the centralized part of the Delfi-C3 electrical power system will be described. In section 4.2, the energy flow resulting in powering of the Delfi-C3 spacecraft is explained. A treatise of the applied solar arrays is presented in section 4.3. In section 4.4, a description of the step-up converters used for conditioning the power bus is shown.

4.2 Topology of energy flow

On-board the Delfi-C3 spacecraft, electrical power is generated at the solar arrays. These arrays consist of solar cells, which convert solar light into electricity. This solar light is available from two sources:

- Solar flux - solar radiation directly transmitted by the sun;
- Albedo flux - solar radiation reflected by the Earth atmosphere.

The electrical power generated at the solar arrays is variable in nature. Although illumination conditions are the same, it is possible for the array voltage and array current to change. It is not advisable to offer this variable electrical power to electronic equipment. Therefore, the raw array power is conditioned by a centralized (or global) electrical power system. As output of this subsystem, a power bus is created, which has a constant voltage of 12V DC.

In figure 4.1, a schematic is depicted, which shows this flow of energy.

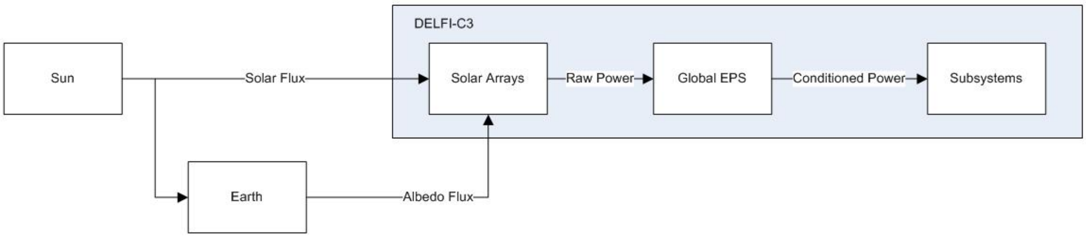

Figure 4.1: Global schematic of Delfi-C3 energy flow

It has to be noted that it is questionable to what extent the albedo flux contributes to the generation of array power. As albedo flux is generated by the reflection of solar radiation of the Earth's atmosphere, it will likely experience a change in electromagnetic spectrum with respect to the original solar flux.

The solar cells applied to the Delfi-C3 arrays are susceptible to a particular range in the electromagnetic spectrum. Therefore, the possibility exists that albedo flux is not radiated in this particular range in the spectrum, and will therefore not affect the solar cells.

4.3 Solar arrays

A general solar cell (or photovoltaic cell) cannot be represented as an infinite power supply. This implies that it is not capable of generating a current without affecting the voltage, in constrast to e.g. a public power grid. The performance of a general solar cell is described by its so-called IV characteristic. In this characteristic, the current produced by the cell is plotted as function of the voltage of the cell.

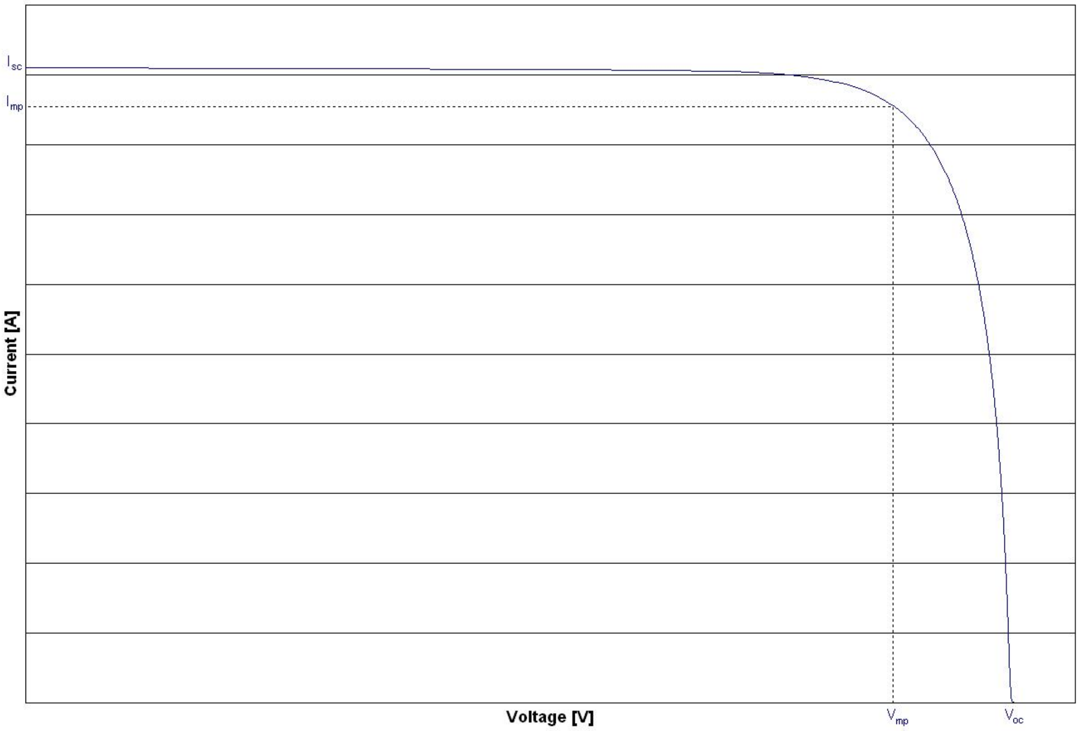

Figure 4.2: General IV characteristic including relevant quantities

In figure 4.2, a general solar cell IV characteristic is shown. Quantities defining the performance of the solar cell are also mentioned. These are:

- Current at maximum power point I_{mp}
- Voltage at maximum power point V_{mp}
  The maximum power point is defined as the point on the IV-curve at which:

$$\frac{\mathrm{d}P}{\mathrm{d}V} = \frac{\mathrm{d}P}{\mathrm{d}I} = 0 \tag{4.1}$$

- Short circuit current I_{sc}
  The short circuit current is the current generated by the solar cell at which:

$$V|_{I=I_{sc}} = 0 \tag{4.2}$$

- Open circuit voltage V_{oc}
  The open circuit voltage is the voltage over the cell terminals at which:

$$I|_{V=V_{oc}} = 0 \tag{4.3}$$

A general solar cell consists of a semi-conductor junction, which generates an electrical current under conditions of irradiation. The structure can be compared to that of a diode, due to the presence of a junction between the p- and n-layers. This pn-junction can be ideally modelled as a current source with a diode in parallel. Every junction is subject to a small amount of current loss, which is modelled by a shunt resistance R_p in parallel with the diode and current source. Moreover, the bulk semiconductor layers possess an electrical resistance R_s, which is in series with the model of the pn-junction. A model of a general single junction solar cell is shown in figure 4.3.

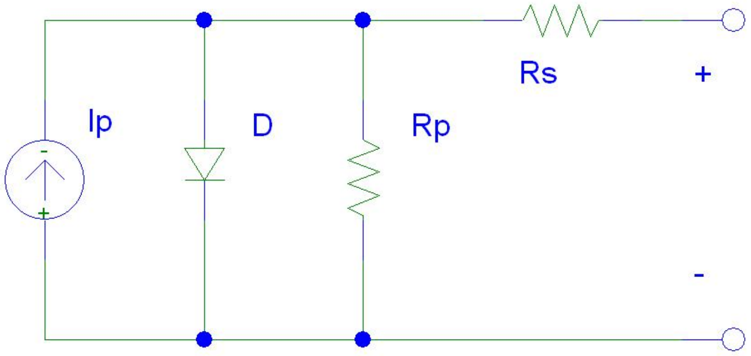

Figure 4.3: Equivalent circuit of a single junction solar cell

However, the Delfi-C3 spacecraft does not use single junction solar cells to generate power, but applies triple junction cells. This means effectively that instead of one pn-junction, three pn-junctions are present in a cell. In addition, a by-pass diode D_p is incorporated in the design. This diode has the function to provide a substitute current path in case a cell fails in open circuit. The equivalent circuit for a Delfi-C3 triple junction photovoltaic cell is shown in figure 4.4.

The magnitude of the current source representing the current producing junction is highly dependent on the amount of irradiation captured by this junction. In the aforementioned IV characteristics, it is common practice to use one solar constant at a 90 ° incidence angle. In a general situation, the incidence angle will be smaller than 90 °, which will have an impact on the IV characteristic of the solar cell.

As a general rule of thumb, the magnitude of the current source will diminish using the cosine rule. Therefore, the following equation can be written:

$$I_p = \bar{I}_p \cdot \cos\alpha \tag{4.4}$$

where $\bar{I}_p$ is the magnitude of the junction current at 90 ° incidence angle, and α is the incidence angle.

In addition, the temperature plays a large part in the performance of the solar cell. In general, a high temperature will lead to a decrease in cell performance. A detailed treatise of this effect is shown in chapter 14.

In table 4.1, the structural characteristics of the Delfi-C3 photovoltaic cells are shown.

Table 4.1: Structural characteristics of Delfi-C3 photovoltaic cells

Parameter	Variable	Value	
Length	l	63.22	mm
Width	w	38.46	mm
Mass	m	2	g

The electrical characteristics of the Delfi-C3 photovoltaic cells are presented in table 4.2.

A general solar array is composed out of m parallel strings, which each consist of n photovoltaic cells in series. Therefore, the following relations hold:

$$V_{array} = m \cdot V_{cell} \tag{4.5}$$

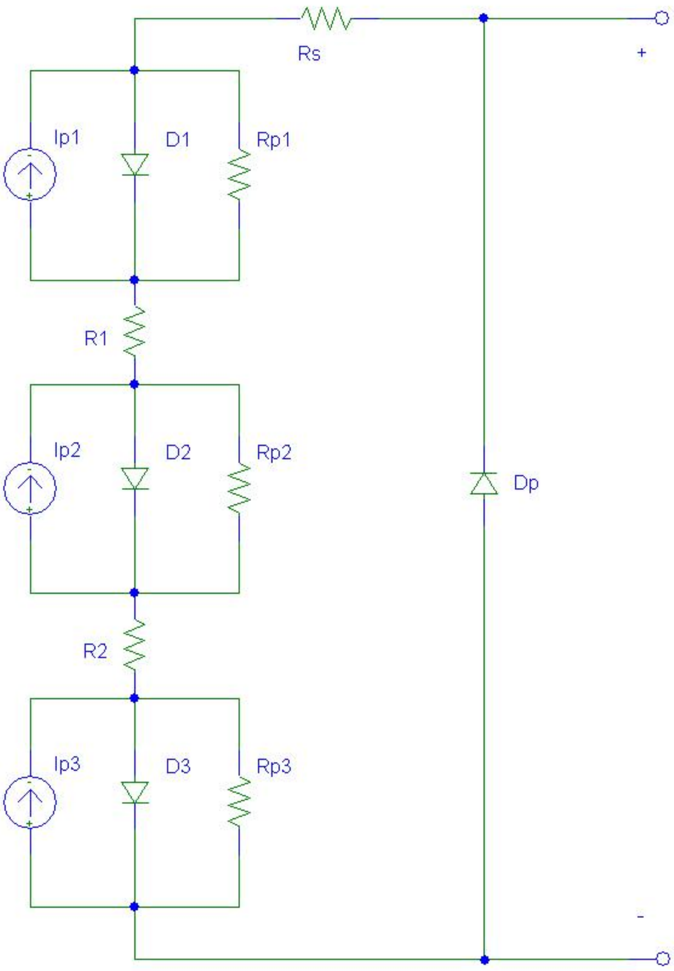

Figure 4.4: Equivalent circuit of a Delfi-C3 triple junction solar cell

Table 4.2: Electrical characteristics of Delfi-C3 photovoltaic cells

Parameter	Variable	Value	
Short circuit current @ 28 °C	I_{sc}	0.389	A
Open circuit voltage @ 28 °C	V_{oc}	2.47	V
Maximum power point current @ 28 °C	I_{mp}	0.366	A
Maximum power point voltage @ 28 °C	V_{mp}	2.13	V
Short circuit current temperature gradient	$\frac{\mathrm{d}I_{sc}}{\mathrm{d}T}$	0.146	mA.K^{-1}
Open circuit voltage temperature gradient	$\frac{\mathrm{d}V_{oc}}{\mathrm{d}T}$	-5.5	mV.K^{-1}
Maximum power point current temperature gradient	$\frac{\mathrm{d}I_{mp}}{\mathrm{d}T}$	0.141	mA.K^{-1}
Maximum power point voltage temperature gradient	$\frac{\mathrm{d}V_{mp}}{\mathrm{d}T}$	-5.1	mV.K^{-1}

$$I_{array} = n \cdot I_{cell} \tag{4.6}$$

In table 4.3, the parameters defining the composition of a single solar array of the Delfi-C3 spacecraft are presented.

Table 4.3: Parameter values used for solar array composition of Delfi-C3

Parameter	Variable	Value
Cells per string	n	5
Strings per array	m	1

Delfi-C3 applies TEC1D GaAs photovoltaic cells, which are provided by Dutch Space. In figure 4.5, the

IV characteristic corresponding to a single Delfi-C3 solar array is shown.

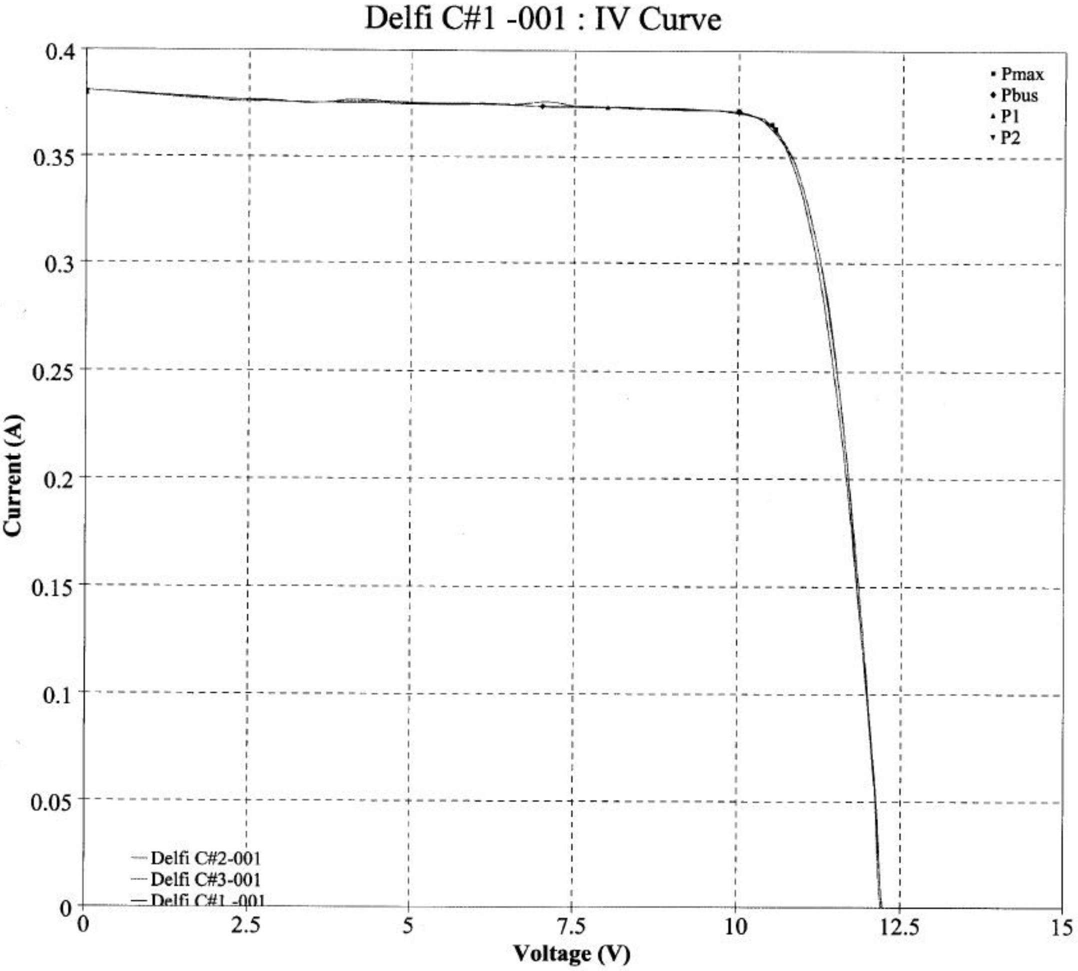

Figure 4.5: IV characteristic of the a single Delfi-C3 solar array

4.4 Step-up converters

For conditioning of the raw power supplied by the solar arrays, step-up converters are used in the electrical power system. Every array is equipped with a dedicated converter. Therefore, every combination of array and converter is a modular part in the design.

Every array is connected to a step-up converter (or boost converter). This device converts the array power at a varying voltage to bus power at a constant voltage.

In figure 4.6, the equivalent circuit of a general step-up converter is depicted.

By investigating figure 4.6, the operational characteristics of a step-up converter can be determined. In fact, the main parameter determining the operational characteristics of the converter is the status of MOSFET switch M_1. During the analysis of the operational characteristic, it is assumed that all involved components are ideal.

In the situation, during which switch M_1 is closed, the voltage over inductor L_1 equals the input voltage V_{in}. In other words, V_L equals V_{in}.

In case switch M_1 is open, the voltage over inductor L_1 is equal to the difference between the output voltage and the input voltage. Voltage V_L is equal to $V_{in} - V_{out}$.

For steady-state operation, the integrated inductor voltage over a single switching period of MOSFET switch M_1 should be equal to zero. Therefore:

$$\int_{\tau=t}^{t+T} V_L \cdot \mathrm{d}\tau = 0 \tag{4.7}$$

where T is the time of a single switching period, and is defined by:

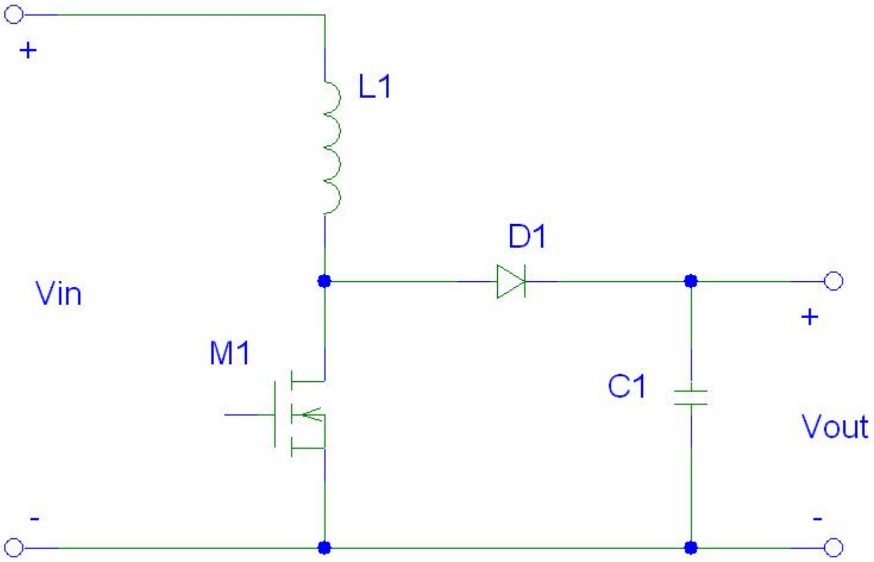

Figure 4.6: Equivalent circuit of a general step-up converter

$$T = \frac{1}{f} \tag{4.8}$$

where f is the switching frequency of switch M_1.
Evaluating this expression for a step-up converter in continuous operation results in:

$$V_{in} \cdot T_{on} + (V_{in} - V_{out}) \cdot T_{off} = V_{out} \cdot T_{on} + (V_{in} - V_{out}) \cdot T = 0 \tag{4.9}$$

where V_{in} is the converter input voltage, V_{out} is the converter output voltage, T_{on} is the time in a single switching period, during which switch M_1 is closed, and T_{off} is the time in a single switching period, during which M_1 is open.
The duty cycle of the MOSFET switch M_1 is defined as:

$$\delta = \frac{T_{on}}{T_{off}} \tag{4.10}$$

Substituting this expression into equation 4.9 leads to:

$$V_{out} \cdot \delta + (V_{in} - V_{out}) \cdot T = 0 \tag{4.11}$$

Solving for the duty cycle δ yields:

$$\delta = 1 - \frac{V_{in}}{V_{out}} \tag{4.12}$$

Note that in case of a step-up converter output voltage V_{out} is larger in magnitude than the input voltage V_{in}. Hence, $0 < \delta < 1$.
Assuming that the converter is ideal, the power balance can be written:

$$P_{in} = P_{out} \tag{4.13}$$

Introducing equation 4.12 into the power balance and solving for the required input current yields:

$$I_{in} = \frac{I_{out}}{1 - \delta} \tag{4.14}$$

In figure 4.7, the equivalent circuit of a single array converter as applied in the Delfi-C3 spacecraft is shown. This design is produced by A. Bahrouch of SystematIC Design B.V.
In the design of the converter, two major operational modes can be distinguished:

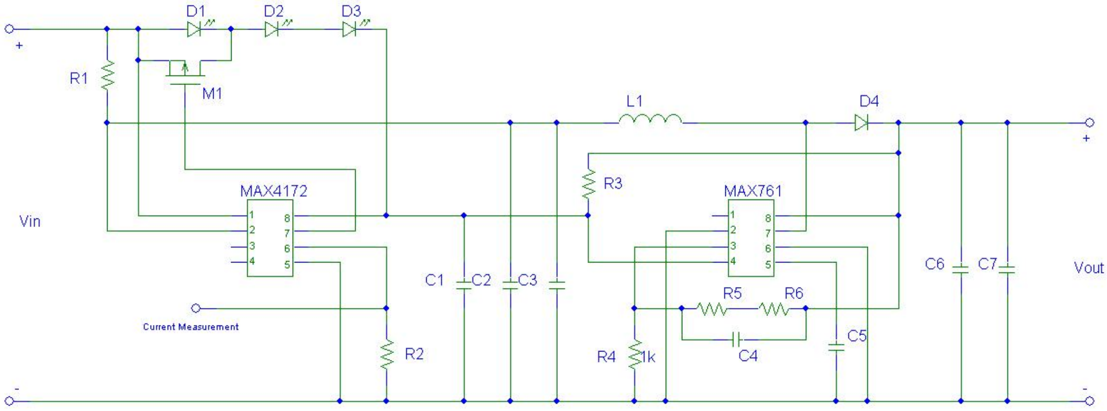

Figure 4.7: Equivalent circuit of a single array converter in the Delfi-C3 electrical power system

- Start-up behaviour
- Steady-state behaviour

Investigating figure 4.7, the start-up behaviour is governed by the MAX4172 integrated circuit. The MAX4172 chip has a special function, which is capable of determining whether the supply power to this PIC is sufficient.
This function is represented by a $\bar{P}G$, or "Not Power Good", signal. This signal is set to a digital high if the supply voltage of the MAX4172 drops below a particular threshold voltage. In case the supply voltage is above this threshold, the signal is equal to a digital low. According to the MAX4172 data sheet, the value of the supply voltage threshold is equal to approximately 2.7V.
The supply voltage pin of the MAX4172 chip is connected to the array via three light emitting diodes (LEDs). Therefore, the input voltage of the MAX4172 chip is equal to the array voltage minus the voltage drop due to three LEDs. As the voltage drop over a single red emitting LED is relatively constant at 1.6V, the array voltage, at which the chip input voltage reaches the threshold for $\bar{P}G$ output, equals approximately 7.5V.
The $\bar{P}G$ signal line is connected to the shutdown pin of the MAX761 chip. In case this pin is at a digital high, the MAX761 is not in operation, and the step-up converter is not functioning. When this pin is at a digital low, the MAX761 is funtioning according to nominal converter operations.
This combination ensures that the converter will be switched on in case the photovoltaic array is capable of generating sufficient power. After all, in case the array voltage is below 7.5V, the $\bar{P}G$ signal is high, and the converter is turned off. As soon as the array voltage is above 7.5V, the $\bar{P}G$ signal will become low, and the MAX761 converter is switched on.

In steady-state behaviour, the converter reaches nominal step-up converter operation as has been previously explained. The MAX761 integrated circuit is the heart of the step-up converter. This chip takes the role of the converter switch. It incorporates a feedback mechanism, which automatically adjusts the duty cycle δ of the switch. In this way, the output voltage is kept constant at the desired value of 12V DC. A small offset is possible to exist, which is found to be at maximum ±0.48V.

Chapter 5

Design of decentralized part of electrical power system

5.1 Introduction

In addition to the centralized converter required for conditioning the array power produced by the photovoltaic cells, the electrical power system consists of a decentralized part. Its function is to supply every printed circuit board in the Delfi-C3 spacecraft with electrical power in the required conditions. Furthermore, this part is responsible for determining the current flow to every individual subsystem.
In this chapter, a description is presented of the decentralized part of the electrical power system. In section 5.2, a general description is shown of the topology of the decentralized EPS. The supply circuitry required for powering the local EPS PIC microcontroller is highlighted in section 5.3. Section 5.4 shows a treatise of the solid-state switches applied for power switching to the various subsystems. A description of the step-down DC/DC converters is shown in section 5.5. Section 5.6 presents an explanation of the current measurement circuitry is presented.

5.2 Description of decentralized EPS topology

The heart of the decentralized (or local) part of the EPS is formed by a PIC microcontroller. This PIC is supplied by a dedicated power supply of 3.3V. This supply is generated out of the 12V bus by applying a resistor bridge between the 12V power bus and the 3.3V input line. For stabilizing the 3.3V supply voltage, a voltage reference is used.
Switching power to the main subsystem circuitry is the primary task of the local EPS PIC microcontroller. This switching sequence is introduced for having a smooth boot-up sequence without collapse of the power bus. By steering the gate of a MOSFET in series with the main supply line to the main subsystem, the microcontroller is capable of directing the power status of the subsystem.
By turning on the MOSFET switches, power is consequently supplied to the step-down DC/DC converters. These will generate the various board voltages required for operating the subsystem. After perfoming this action, the subsystem is supplied with electrical power and will function in nominal mode.
A secondary task of the local EPS PIC is measurement of the current flowing into the subsystem. This is performed by a placing a sensing resistor in series with the main power supply line to the subsystem. A MAX4172 chip is capable of measuring the voltage drop over the resistor, and will consequently convert the voltage drop into a corresponding current. Shunting this current into a resistor generates a voltage, which can be measured by the PIC microcontroller. Post-processing of this measurement data will result in the value of the current through the power line.
In figure 5.1, the topology of the decentralized part of the electrical power system is shown.

5.3 Local EPS PIC supply circuitry

Every local EPS PIC is operating on a 3.3V supply voltage. As the supply power for every printed circuit board arrives at a voltage of 12V, a conversion mechanism has to be designed to generate a steady 3.3V voltage. This mechanism consists of a resistor between the 12V power bus and the 3.3V input, and a voltage reference of 3.3V. This voltage reference ensures that the 3.3V remains at a constant value, while the resistor accomodates the voltage drop from 12V to 3.3V.

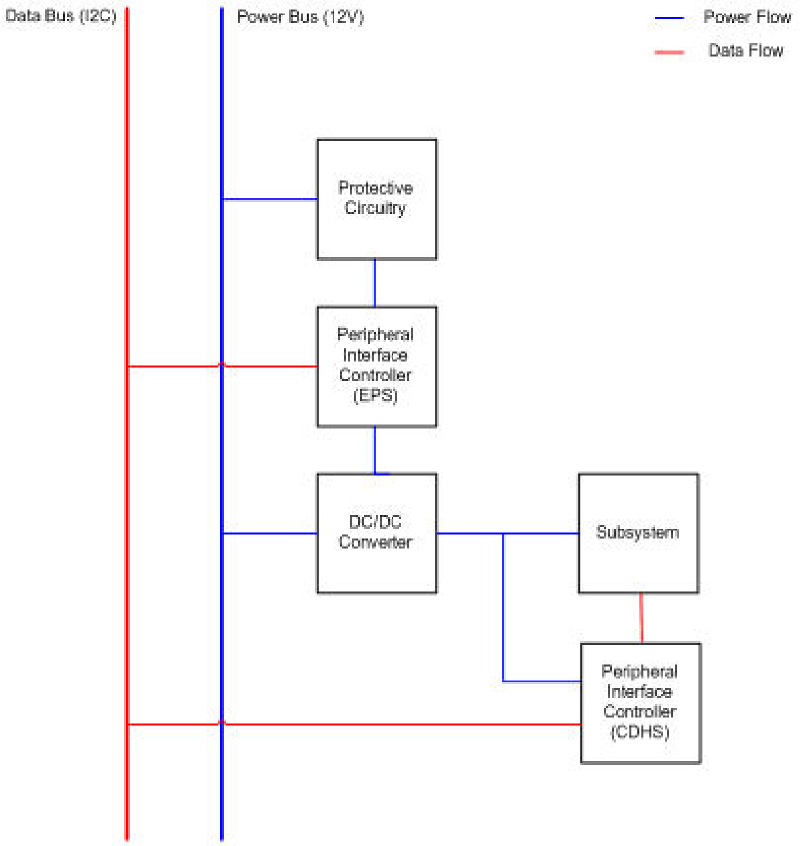

Figure 5.1: Schematic representation of the decentralized part of the electrical power system

For redundancy purposes, the resistor is replaced by a series-parallel circuit, which is composed of 4 resistors. This topology offers protection to the voltage bus for both short circuit failures and open cirucit failures in the resistors. Furthermore, the voltage reference is implemented double redundant.

In appendix C, a detailed explanation of the supply circuitry for the local EPS PIC microcontroller is shown.

In figure 5.2, the equivalent electrical circuit of the local EPS PIC supply circuitry is shown.

During preliminary testing, it was noticed that the INTRC oscillator on the PIC microcontrollers was not sufficiently accurate. Therefore, a change in oscillator was realized, and the INTRC oscillator was substitued by the INTOSC oscillator. However, in the new configuration, the PIC microcontrollers were consuming more current as in the original situation. Therefore, the resistors in the supply circuitry had to be adapted. In appendix D, a detailed description of this design change is presented.

5.4 Subsystem power switching

In order to prevent premature collapse of the power bus during boot-up of the spacecraft, every power line to a subsystem is equipped with MOSFET switches. These switches enable sequential switching of the various subsystems. This will prevent the appearance of very low load impedances to the power bus, which could lead to excessive current consumption and collapse of the power bus.

Every switch is steered by the decentralized PIC microcontroller. Normally, the switches are turned off leading to a cut-off in supply current to the subsystem. As soon as the PIC microcontroller steers the input signal to the switches high, the MOSFET switches will be turned on, and current is allowed to flow into the subsystem. Consequently, the subsystem will start to operate in nominal mode.

The MOSFET switches in the power line are applied double redundant. This will prevent direct connection of the subsystem to the power bus in case a single switch fails in short circuit.

In figure 5.3, the equivalent electrical circuit of the MOSFET switches in the power line of every subsystem is shown.

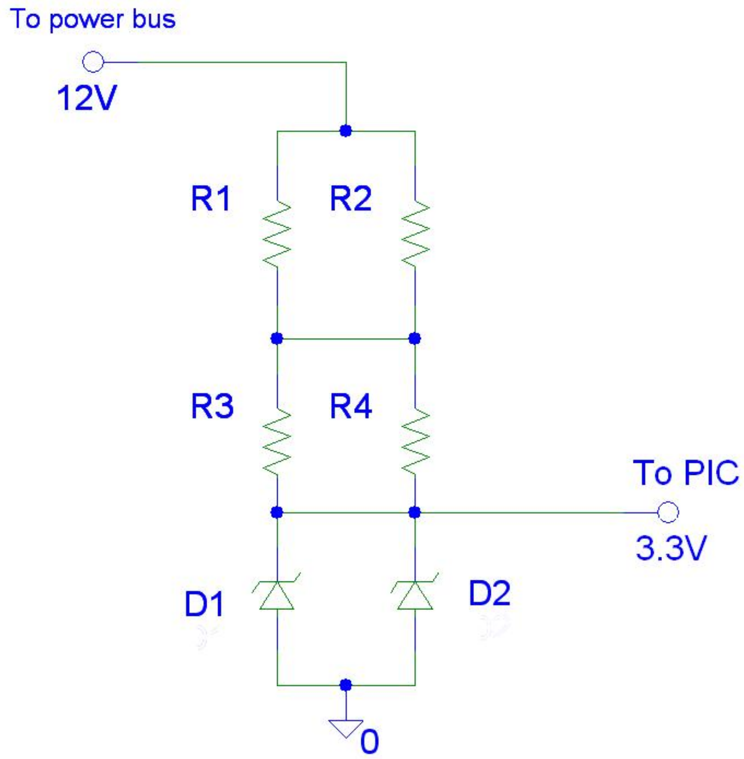

Figure 5.2: Equivalent electrical circuit of the power supply circuitry of the decentralized EPS PIC

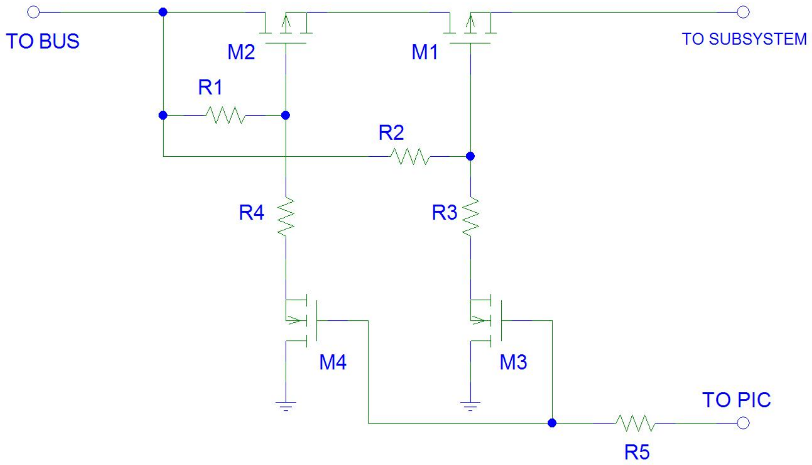

Figure 5.3: Equivalent electrical circuit of the MOSFET switch in the subsystem power line

5.5 Step-down DC/DC converters

Every subsystem makes use of individual supply voltages to operate successfully. These voltages are produced on the respective printed circuit board. This is done by using a step-down DC/DC converter, which converts bus power at the bus voltage to board power at a subsystem voltage. As it is possible for a subsystem to require multiple supply voltage, multiple step-down DC/DC converters can exist on a single printed circuit board.

At the core of the step-down DC/DC converter is the MAX1836 integrated circuit. This chip is capable of producing a constant output voltage by applying a feedback loop into the conversion cycle. Therefore, the output voltage can experience a minor offset of $/pm0.192$V.

The equivalent electrical circuit of a single step-down DC/DC converter is shown in figure 5.4.

A more detalied treatise of the operational behaviour of the step-down DC/DC converters is shown in appendix G.

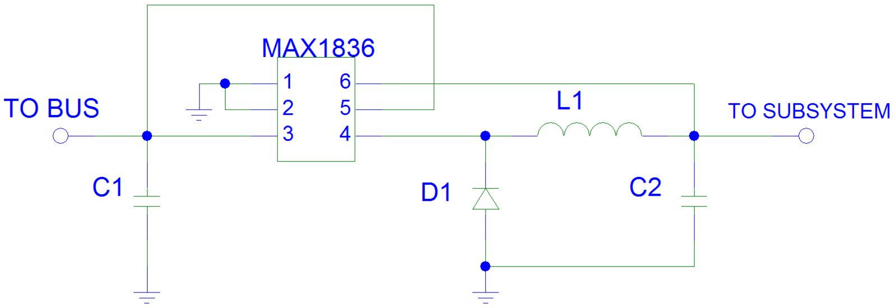

Figure 5.4: Equivalent electrical circuit of the step-down DC/DC converter

5.6 Current measurement circuitry

Assessment of the status of the various subsystems in the Delfi-C3 spacecraft is an important task in mission operations. In order to obtain a rough indication of the health of a subsystem, the respective power supply lines are equipped with a current measurement circuit. In figure 5.5, the equivalent circuit of this current measurement circuitry is shown.

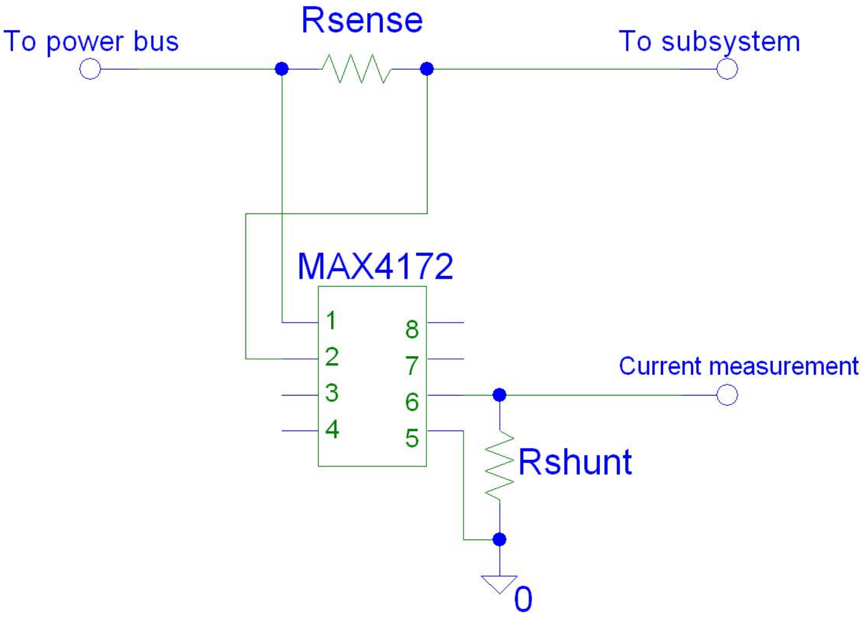

Figure 5.5: Equivalent electrical circuit of the current measurement circuitry

The current measurement circuitry is composed of an integrated circuit, which measures the voltage drop over a sensing resistor. This voltage drop is linearly related to the current flowing through this resistor. The integrated circuit outputs a small current, which is linearly related to the voltage drop over the sensing resistor. By shunting this current through a resistor, an output voltage is generated, which can be sampled by the PIC microcontroller. Post-processing of this measurement sample results in the corresponding value of the current through the power line.

During preliminary testing, it was found that the output of the current measurement circuitry showed large variations. These were the result of the switching DC/DC converters used for converting the bus voltage to the board voltages. Stabilization of the current measurement chip output could be achieved by a small redesign in the circuitry. In appendix H, the design procedure for this redesign is presented.

Chapter 6

Interface design between electrical power system and other subsystems

6.1 Introduction

In the Delfi-C3 spacecraft, several interfaces exist between the electrical power system and other subsystems. These interfaces include the maintenance of the I2C data bus, the burn circuitry for deploying the appendages, and the power supply for the ICD2 microcontroller programmer. In order for these interfaces to work properly, additional circuitry had to be designed.

A description of these designs is shown in this chapter. In section 6.2, the design of the I2C repeater circuitry is treated. The burn circuitry for the appendages is illustrated in section 6.3. In section 6.4, a description is given of the power supply for the ICD2 programmer.

6.2 I2C repeater circuitry design

During initial testing of the I2C data bus, it was discovered that a unpowered PIC was capable of pulling down the I2C bus. This caused the I2C bus to collapse, disabling communication between the various spacecraft subsystems.

The cause of the pull-down of the I2C data bus was tracked to the presence of a clamping diode in the I2C ports on the PIC microcontroller. In switched-off state of a PIC microcontroller, this diode would start to draw current. This current flow consequently leads to the collapse of the I2C bus.

A solution to this problem was found in the implementation of an I2C repeater. This device is capable of disconnecting the central I2C bus from the disabled PIC microcontroller. As soon as the PIC is coming online, the I2C repeater will be switched on. This results in the central I2C bus being connected to the PIC microcontroller, causing communication between the PIC and the rest of data system to be enabled.

It has to be mentioned that I2C repeaters have to be applied to the data PICs and the bitshaper PICs. After all, those PICs are the only microcontrollers in a possible switched-off state in case the I2C data bus is powered. As the decentralized EPS PICs are all powered directly after boot-up of the spacecraft, pull-down of the I2C bus by these PICs is not an issue.

In figure 6.1, the equivalent electrical circuit of the application of the I2C repeater is shown.

A detailed description of the I2C repeater design procedure is shown in appendix I.

6.3 Appendage resistor burn circuitry design

For controlling the burn sequence of the Delfi-C3 deployables, a dedicated burn circuit is designed. This circuitry consists of a MOSFET switch in series with a burn resistor required for deploying one of Delfi-C3's appendages. It was decided to put two MOSFETs in series with the resistor to have a degree of redundancy. In this situation, a short circuit failure of one of the MOSFETs does not lead to direct connection of the burn resistor to the power bus. Therefore, a dramatic increase in power consumption leading to failure of the power bus is not possible. Control of the MOSFET switches is accomplished by a PIC microcontroller. As the switches are normally off, an input signal sent by the PIC is used to initiate deployment.

Electrical power required for burning the resistors is provided by a dedicated power bus. This power bus is only powered during the deployment sequence. In order to achieve power on this bus, a PIC

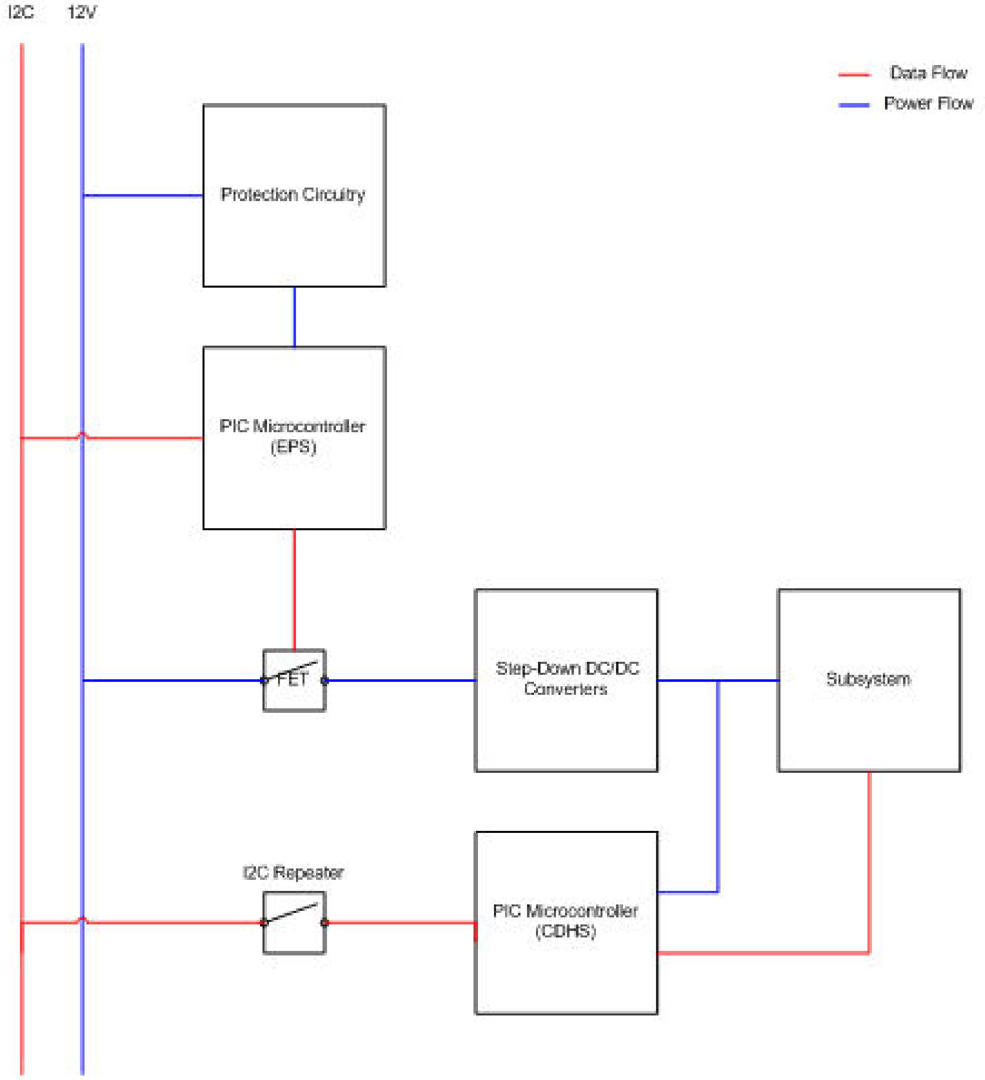
I2C
12V
Data Flow
Power Flow
Protection Circuitry
PIC Microcontroller (EPS)
FET
Step-Down DC/DC Converters
Subsystem
I2C Repeater
PIC Microcontroller (CDHS)

Figure 6.1: Application of the I2C repeater to a PIC microcontroller.

microcontroller has to send a signal to a switch. By closing this switch the "deployment" bus is short circuited to the main power bus, and is therefore capable of providing power at 12V DC.
Every appendage is equipped with two burn circuits in parallel. Therefore, two parallel strings of MOSFET switches have to be incorporated for every appendage to serve the needs of the double redundant burn resistors. As every interconnect board is equipped with two PIC microcontrollers, every parallel string is controlled by a dedicated PIC microcontroller. In this way, the redundancy concept is fully taken advantage of.
In addition to the burn resistors, every deployable is equipped with a tact switch. This switch is used to provide information about the deployment status of the corresponding appendage. By applying a voltage divider, a signal is generated, which is serving as input for the PIC microcontroller. As the tact switch is "normally open", this deployment signal will be a digital high, in case the appendage is in stowed configuration. A digital low will be generated, if the appendage is in deployed configuration.
A schmamtic showing the the equivalent electrical circuit of the burn circuitry for a single deployable is shown in figure 6.2.
It has to be noted that it is not advisable to deploy multiple appendages simultaneously. This would result in an excessive current flow, which consequently leads to collapse of the power bus. In appendix E, a detailed description of the consequences of energizing two burning resistors simultaneously is shown.

6.4 ICD2 programmer power supply

Programming of every PIC microcontroller in the Delfi-C3 spacecraft is accomplished by using the ICD2 programmer. This programmer provides the interface between the programming equipment and the

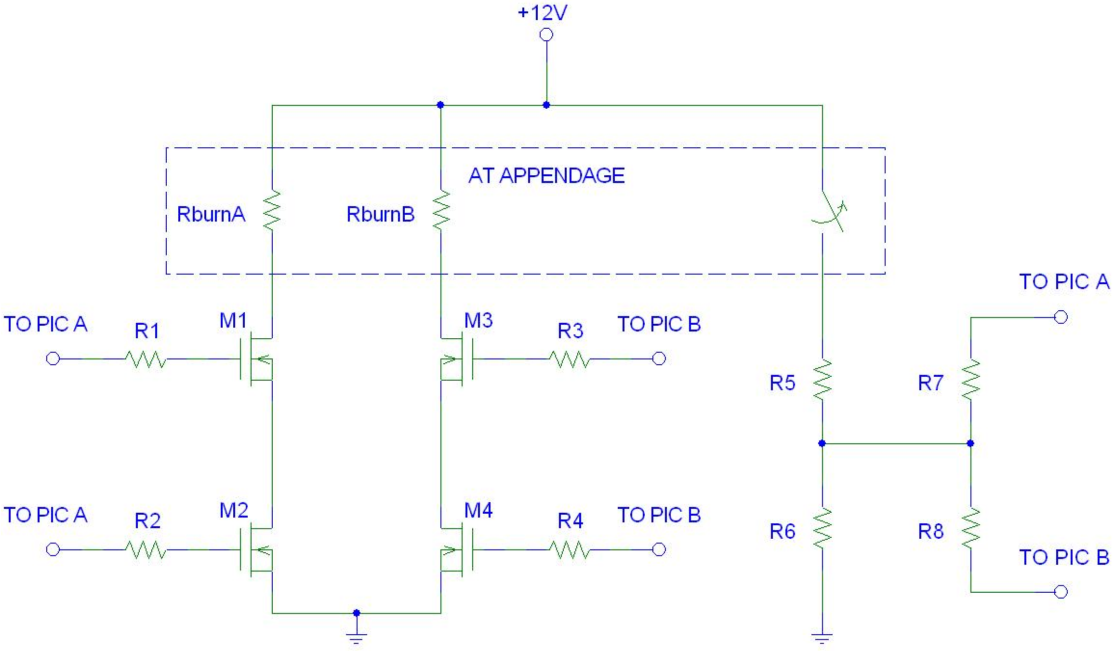
+12V
AT APPENDAGE
RburnA
RburnB
TO PIC A
R1
M1
M3
R3
TO PIC B
TO PIC A
R5
R7
TO PIC A
R2
M2
M4
R4
TO PIC B
R6
R8
TO PIC B

Figure 6.2: Equivalent electrical circuit of appendage resistor burn circuitry

programmable memory of the PIC microcontrollers. During initial measurements, it was found that the programmer is powered by drawing current from the target circuitry.
In case of the local EPS PICs, the total amount of current is limited by the supply circuitry. Direct connection of the ICD2 programmer to the power supply of the PIC would lead to a drop in supply voltage. A solution has been found by inserting an additional current path from the 12V power supply to the 3.3V input. This path is in parallel with the original supply line.
In figure 6.3, the equivalent electrical circuit of the power supply for the ICD2 programmer is shown.

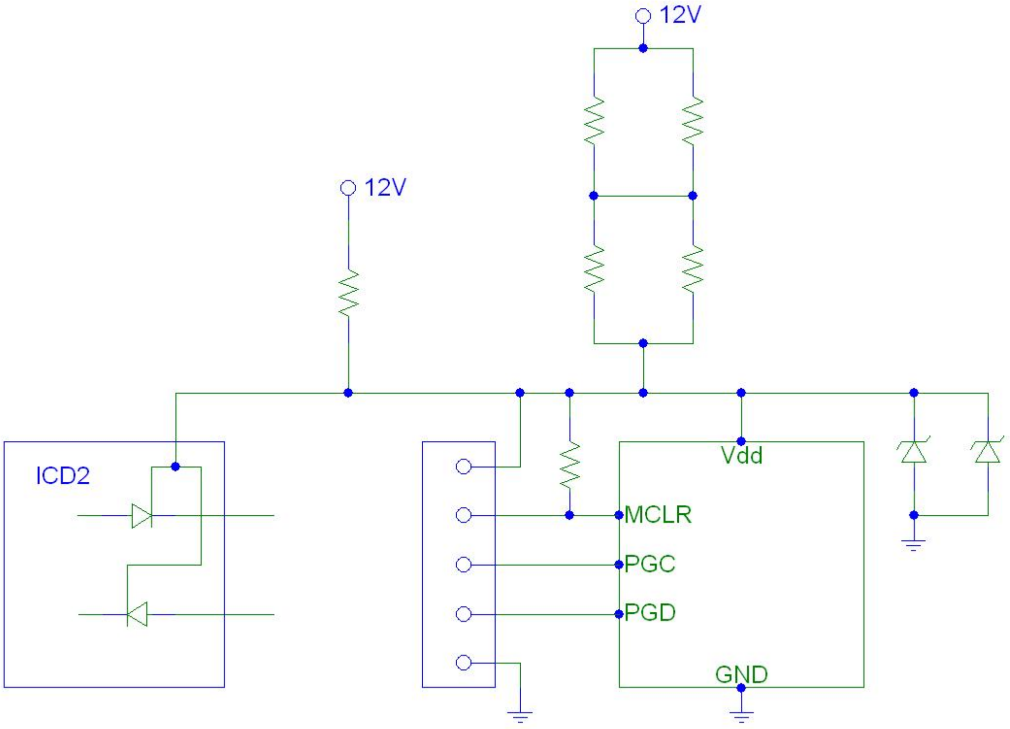
12V
12V
ICD2
Vdd
MCLR
PGC
PGD
GND

Figure 6.3: Equivalent electrical circuit of the ICD2 programmer power supply

Note that this additional power supply is only needed for a programming session of the local EPS PIC. For programming of a CDHS PIC or a bitshaper PIC, this supply line is not required.

A detailed description of the design and manufacturing of the ICD2 programmer power supply is presented in appendix F.

Part III

SYSTEMS ENGINEERING

Chapter 7

Introduction

Systems engineering is a branch of engineering, in which generation of a design is taking place in view of a complete system. Its main task is monitoring the interfaces between the various subsystems to ensure compatibility. Furthermore, generation and maintenance of various resource budgets is an important tasks in system engineering. Although these tasks involve the complete system, they can be often designated to a particular subsystem.

Several systems engineering tasks are assigned to the electrical power system due to their direct relation with electrical systems. The most important tasks is generation and maintenance of the power budget. A power budget is produced with the notion that electrical power is a scarce resource in spaceflight. Therefore, the power consumption of every subsystem has to be controlled to ensure that sufficient power is available to energize the complete spacecraft. Another systems engineering task is interface control. As the electrical power system possesses various interfaces with other spacecraft subsystems, it is necessary to define and monitor these interfaces.

In this part, the systems engineering tasks accompanying the design of the electrical power system are illustrated. In chapter 8, the generation and management of the power budget is highlighted. Chapter 9 described the procedure of interface control.

Chapter 8

Power budget

8.1 Introduction

A power budget summarizes the power consumption of the various components in a spacecraft. In this way, the total power consumption can be monitored to ensure that sufficient electrical power is available for powering all subsystems. Throughout the entire design process, the power budget has to be maintained and updated.

This chapter will give a brief description of the power budget. The various components treated in the power budget will be briefly described, as well as the management aspects of the power budget. In section 8.2.1, an evaluation of the power needed to operate the spacecraft will be described. An evaluation of the minimum generated power will be treated in section 8.2.2. A treatise of contingency management is given in section 8.2.3. The methodology of managing various versions of the power budget will be described in section 8.2.4. In section 8.2.5, the course of action to be taken to implement changes in the power budget is treated. Finally, the latest version of the power budget is presented in section 8.3.

8.2 Power budget description

8.2.1 Evaluation of required power

In the power budget, the power consumption of every individual board will be evaluated. In order to have an orderly budgeting method, every board in its turn is broken down into its components. For every component, the input voltage and the operating modes are determined.

Operational modes

For every component in the spacecraft, it is evaluated in which modes this particular component is operational. In the power budget, this is indicated by a boolean. The operational modes of the spacecraft are:

- Boot-Up
- Deployment
- RAP Science Mode
- RAP Transponder Mode
- ATRX Science Mode
- ATRX Transponder Mode
- Degraded Mode (On-Board MORON)

Board voltages

On board of the Delfi-C3 spacecraft the bus voltage will be converted to other voltages. The amount of different voltages and the values are dependent on the type of PCB. In general, the following voltages are produced aboard the spacecraft:

- 12V
- 5V
- -1.25V
- 3.3V

In table 8.1, it is shown, which voltages are locally produced on every printed circuit board in the stack of the Delfi-C3 spacecraft.

Table 8.1: Board voltages per PCB

PCB	12V	5V	-1.25V	3.3V
Inter Connect Board Z+	×			×
Measurement Board Z+		×	×	×
Combination Board				×
Flight Board FM/430		×		
Radio Amateur Platform	×	×		×
Advanced Transceiver	×	×		×
Electrical Power Subsystem Board				×
Measurement Board Z-		×	×	×
Inter Connect Board Z-	×			×

Electronic components

On every PCB, the power consuming components are split into the following divisions. Every division is evaluated separately in the power budget.

- EPS PIC
  This component indicates the microcontroller, which sends the switching signal to the MOSFETs in control of the power supply of the respective PCB. Moreover, the protective circuitry, which ensures that the PIC input voltage equals 3.3V, is included. As the substitute resistance is equal to 13k, the power consumption is calculated to be:

$$P = V \cdot I = V \cdot \frac{V_R}{R} = 12 \cdot \frac{12 - 3.3}{13 \cdot 10^3} = \approx 8.071 \cdot 10^{-3} = 8.071 \text{ mW} \tag{8.1}$$

- CDHS PIC
  This component indicates the microcontroller, which controls the communication of the PCB electronics with the I2C data bus. In addition to the current consumption of the PIC, the peripherals will also draw current. Applying a least-squares analysis, the following peak current consumptions can be found at a PIC input voltage of 3.3V:

• Peripheral Interface Controller @ 32 kHz	0.0714 mA
• Peripheral Interface Controller @ 1 MHz	1.2885 mA
• Watchdog timer	0.0129 mA
• Brownout reset	0.0503 mA
• Oscillator	0.008365 mA

  In case the clock frequency of the PIC is equal to 32 kHz, the power consumption can be calculated to be equal:

$$\begin{aligned} P = V \cdot ((I_{PIC})_{32kHz} + I_{WT} + I_{BR} + I_{osc}) = \\ + 3.3 \cdot (7.14 + 1.29 + 5.03 + 0.8365) \cdot 10^{-2} \approx 0.472 \text{ mW} \end{aligned} \tag{8.2}$$

  And the power consumption of the PIC at a clock frequency of 1 MHz is equal to:

$$\begin{aligned} P = V \cdot ((I_{PIC})_{1MHz} + I_{WT} + I_{BR} + I_{osc}) = \\ + 3.3 \cdot (128.85 + 1.29 + 5.03 + 0.8365) \cdot 10^{-2} \approx 4.488 \text{ mW} \end{aligned} \tag{8.3}$$

- DC/DC Converter

  DC/DC converters are used to transform the bus voltage to local board voltages used for input of board electronics. These electronic devise will not operate with ideal efficiency and will incur dissipation losses during the conversion. Therefore, use is made of the following expression [11]:

  $$P_{out} = \eta \cdot P_{in} = \eta \cdot (P_{out} + P_{diss}) \tag{8.4}$$

  where P_{in} is the converter input power, P_{out} is the converter output power, P_{diss} is the power in the converter, and η is the converter efficiency. This equation can be rewritten to solve for P_{diss}:

  $$P_{diss} = \frac{1-\eta}{\eta} \cdot P_{out} \tag{8.5}$$

  The output power P_{out} can be simply calculated by:

  $$P_{out} = V_{out} \cdot I_{out} \tag{8.6}$$

  where V_{out} is the converter output voltage, i.e. the board voltage, and I_{out} is the load current supplied by the converter.

  In general, the converter efficiency η can be expressed as:

  $$\eta = P_{conv} + K_1 \cdot I_{out} + K_2 \cdot I_{out}^2 \tag{8.7}$$

  with:

  $$P_{conv} = a_1 + a_2 \cdot V_{in} \tag{8.8}$$

  $$K_1 = b_1 + b_2 \cdot V_{in} \tag{8.9}$$

  $$K_2 = c_1 + c_2 \cdot V_{in} \tag{8.10}$$

  Because the converter input voltage V_{in} is always equal to the bus voltage, the coefficients a_1, a_2, b_1, b_2, c_1, and c_2 can be determined by performing a least-squares analysis by inserting the efficiency curve given in the data sheet.

- Current measurement circuitry

  This component indicates the measurement circuitry used on every printed circuit board for measuring the supply current. In fact, it consists of a sensing resistor and a measurement chip. A biasing current is needed to operate the chip in addition to a sourcing current needed to generate a signal. The power consumption of the measuring circuit is then:

  $$P = V_{load} \cdot (I_{bias} + I_s) \tag{8.11}$$

  In nominal operations, the biasing current of the circuit I_{bias} is 0.8 mA.

  As the sourcing current is a linear relation of the voltage drop caused by the sensing resistor, the following expression can be written:

  $$I_s = \gamma \cdot V_s = \gamma \cdot I_{out} \cdot R_s \tag{8.12}$$

where I_{out} is the current through the sensing resistor, which equals the current needed by the printed circuit board from the bus, R_s is the value of the sensing resistor and γ is the transconductance of the measurement chip.

In principle, the sourcing current is drawn from the low-voltage side. Therefore, the equivalent current needed from the high-voltage side is equal to:

$$\hat{I}_s = \frac{1}{\eta} \cdot \frac{V_{load}}{V_{bus}} \cdot I_s = \frac{1}{\eta} \cdot \frac{V_{load}}{V_{bus}} \cdot \gamma \cdot I_{out} \cdot R_s \tag{8.13}$$

Furthermore, it is known that:

$$I_{out} = \hat{I}_s + I_{load} \tag{8.14}$$

Then:

$$\eta \cdot \frac{\hat{I}_s}{\gamma \cdot R_s} \cdot \frac{V_{bus}}{V_{load}} = \hat{I}_s + I_{load} \tag{8.15}$$

And solving for $\hat{I}_s$ yields:

$$\hat{I}_s = \frac{I_{load}}{\frac{\eta}{\gamma \cdot R_s} \cdot \frac{V_{bus}}{V_{load}} - 1} \tag{8.16}$$

Finally, the sourcing current at the low voltage side becomes:

$$I_s = \frac{I_{load}}{\frac{1}{\gamma \cdot R_s} - \frac{1}{\eta} \cdot \frac{V_{load}}{V_{bus}}} \tag{8.17}$$

The value of every sensing resistor R_s is set at 0.68 Ω. For the transconductance of the measuring chip γ, a nominal magnitude is found in the datasheet of 10.

- I2C Repeater

  An I2C repeater is applied to prevent collapse of the I2C data bus in case a disabled PIC is connected to the bus. It is only necessary to apply a repeater on the printed circuit board, for which the CDHS PIC is disabled during boot-up of the spacecraft. These boards are:

  - Measurement Board Z+
  - Combination Board
  - Radio Amateur Platform
  - Advanced Transceiver
  - Measurement Board Z-

  Consulting the data sheet of the I2C repeater, it is found that the maximum current consumption is 5.0 mA. As the current is delivered by the same bus, to which the CDHS PIC is connected, the power consumption of a single I2C repeater will be equal to:

$$P = V_{PIC} \cdot I_{rep} = 3.3 \cdot 5.0 = 16.5 \text{ mW} \tag{8.18}$$

- Board components

  For the board electronics, the input voltage and current consumption can be found in corresponding data sheets or by performing tests.

8.2.2 Evaluation of generated power

In addition to the required power, it is useful to make an estimation of the produced power. In order to do this, the worst case is evaluated. This worst case is attained at a specific spacecraft attitude and at the highest temperature of the solar cells. The minimum available power can be written as:

$$P_{min} = P_{\perp} \cdot \cos\left(\frac{\pi}{2} - \phi\right) \tag{8.19}$$

where $P_{\perp}$ is the power generated by a single solar panel in case the solar radiation vector is parallel to the panel normal vector, and ϕ is the angle with which the solar panel is inclined to the body. Evaluating $P_{\perp}$, the following expression can be written:

$$P_{\perp} = n \cdot m \cdot V_{mp}(T) \cdot I_{mp}(T) \tag{8.20}$$

where n is the number of cells placed in series in a single string, m is the number of strings in a single solar array, $V_{mp}(T)$ is the voltage at the terminals of a single cell in the maximum power point as a function of temperature, and $I_{mp}(T)$ is the current produced by a single string in the maximum power point as a function of temperature.
The temperature dependent electrical characteristics are expressed by:

$$V_{mp}(T) = \left(V_{mp}\right)_{ref} + \lambda \cdot \left(T - T_{ref}\right) \tag{8.21}$$

$$I_{mp}(T) = \left(I_{mp}\right)_{ref} + \mu \cdot \left(T - T_{ref}\right) \tag{8.22}$$

where $\left(V_{mp}\right)_{ref}$ and $\left(I_{mp}\right)_{ref}$ are respectively the voltage and the current at the maximum power point at the reference temperature, λ and μ are the temperature derivatives of respectively the voltage and current, and T_{ref} is the reference temperature.
Evaluating the temperature derivatives of the voltage and the current, it is noticed that the net temperature derivative of the power is negative. Therefore, the minimum power will be generated at the maximum attainable temperature of the solar cells.
In table 8.2, values for the relevant variables in the calculation of generated power are shown.

Table 8.2: Allocation of values to the relevant variables in generated power calculation

Variable	Value	
ϕ	$\frac{7}{36}\pi$	rad
n	5	
m	1	
$\left(V_{mp}\right)_{ref}$	2.1118	V
$\left(I_{mp}\right)_{ref}$	0.3624	A
λ	$-5.1 \cdot 10^{-3}$	V.K^{-1}
μ	$1.41 \cdot 10^{-4}$	A.K^{-1}
T_{ref}	301.15	K

The only unknown remaining in the calculation is the actual maximum cell temperature T. From preliminary thermal analyses, it is estimated that the maximum cell temperature is deviating between 55 °C and 80 °C. Therefore, for both 55 °C and 80 °C, the available solar power is calculated:

$$T = 55\,^{\circ}\mathrm{C} \longrightarrow \left(P_{SA}\right)_{min} = 2.782 \text{ W} \tag{8.23}$$

$$T = 80\,^{\circ}\mathrm{C} \longrightarrow \left(P_{SA}\right)_{min} = 2.628 \text{ W} \tag{8.24}$$

In addition to the efficiency losses on the solar array, the electrical power will experience dissipation losses in electronic components. These losses are caused by:

- Wiring losses

- Conversion losses
- Diode losses

Wiring losses are caused by the finite conductivity of the go-return wires from the DC/DC converters on the EPS board to the solar arrays. These are very difficult to estimate accurately. As a very rough estimation however, a loss of 5% can be incorporated.

Conversion losses are caused by inefficiencies in the step-up converters, which convert the variable input voltage, which equals the array voltage, to the bus voltage of 12V. The efficiency of these converters is dependent on the input voltage and is therefore variable as the input voltage is variable. However, after consulting the data sheet, it can be safely assumed that the efficiency will stay above 90%. Therefore, the efficiency of the converters can be set at the worst case of 90%.

Diode losses are caused by the blocking diodes in every power line to the bus. These can be estimated rather accurately using the data sheet. In the worst-case, the minimum available power is produced by a single solar array and the complete current will flow through a single diode. Using a current of 200 mA, which coincides with 2.4 W of bus power, an efficiency loss can be calculated:

$$\eta_{diode} = 1 - \frac{V_d}{V_{bus}} = 1 - \frac{0.36666}{12} \approx 0.97 \tag{8.25}$$

Therefore, an efficiency of 97% is taken.

Taking all efficiencies into account, the following bus powers can be generated:

$$T = 55\,^{\circ}\mathrm{C} \longrightarrow (P_{bus})_{min} = 2.306 \text{ W} \tag{8.26}$$

$$T = 80\,^{\circ}\mathrm{C} \longrightarrow (P_{bus})_{min} = 2.178 \text{ W} \tag{8.27}$$

8.2.3 Margins

In order to take into account uncertainties in the values of estimated power, a margin will be allocated to every power value. This margin is dependent on the maturity of the design. In general, the margin will be relatively large in an early stage of the project and will decrease during maturation of the design. In table 8.3, the various possibilities for indicating uncertainties to estimated values are given.

Table 8.3: Indication of uncertainties to budgeted power values

Indication	Uncertainty	Description
E	18 %	Early estimated power
L	12 %	Estimated power at time of long lead procurement
P	8 %	Estimated power at Preliminary Design Review
C	4 %	Estimated power at Critical Design Review
X	2 %	Actual power at Unit Assembly, Integration and Test
A	0 %	Certified power prior to flight

8.2.4 Version management

On regular intervals, an update will be made of the power budget. During such an update, the power consumption of every component will be corrected to the value, which is representative at the respective time. Moreover, the contingencies have to be evaluated anew during an update, because the design has matured during the interval between updates.

Every month, the most up-to-date version of the power budget will be published. To keep track of the budget evolution, every published budget will be assigned an individual version.

8.2.5 Change implementation

Any subsystem engineer is allowed to check whether any changes in the design comply with the requirements as laid down by the power budget, by inserting updating numbers into an off-the-record version of the power budget. Any official changes to the power budget have to be implemented by the power engineer with approval of the systems engineer. In absence of the power engineer, the systems engineer is allowed to implement changes by himself. In absence of the systems engineer, the power engineer is allowed to implement changes by himself only if approved by the project manager.

8.3 Latest version

A partition of the latest version of the power budget is shown in appendix J. This latest version is version 5.0, which was last changed at 16 February 2007.

In the appendix, two workbooks of the power budget are shown. In appendix J.1, a summary of the latest power budget is shown. For every subsystem, the amount of required power is listed. Furthermore, the total amount of required power is shown. In appendix J.2, an example of the application of the power budget per subsystem is given. In this example, the measurement board Z- is budgeted. Power consumption per involved component is listed. Every component is classified according to required input voltage.

Concludingly, it is noticed that the Delfi-C3 spacecraft requires 2580 mW on the power bus to operate successfully.

Chapter 9

Interface control

9.1 Introduction

Successful operation of the Delfi-C3 spacecraft is highly dependent on the cooperation between the various subsystems. This cooperation is defined by the interfaces existing between these subsystems. As the interfaces involve multiple subsystems, a system engineer is tasked to monitor their quality. This so-called interface control is applied to ensure compatibility between the various subsystems in the spacecraft.
In this chapter, the interface control for the electrical interfaces in the Delfi-C3 spacecraft is described. In section 9.2, the interfaces running via the system bus are treated. A description of the voltages used for powering the various boards is shown in section 9.3. In section 9.4, the allocation of functions to the pins on the local EPS PIC microcontrollers is presented. A treatise of the reference voltages used for the definition of measurements is given in section 9.5.

9.2 System bus

The system bus is a bundle of electrical wiring running through the complete spacecraft. It plays a very important role in interfacing between the various subsystems. After all, it ensures that every printed circuit board in the Delfi-C3 spacecraft is supplied with electrical power and command data. The system bus is produced out of a cable with 34 individual wires. In table 9.1, the allocation of functions to all wires in the system bus is shown.
Important lines in the system bus for the electrical power system are:

- Pin 3 + 4: Power SP(Z+X+)
- Pin 5 + 6: Power SP(Z+X-)
- Pin 7 + 8: Power SP(Z-Y+)
- Pin 9 + 10: Power SP(Z-Y-)
- Pin 13 + 14: V_bus_high
- Pin 15 + 16: V_bus_high_ABF_SYS_C
- Pin 17 + 18: V_bus_high_ABF_SYS_C_ABF_DEP_C
- Pin 19 + 20: V_bus_high_ABF_SYS_C_ABF_DEP_C_LS_C
- All GND pins

9.3 Board voltages

Every printed circuit board makes use of individual board voltages for powering its electrical circuitry. Although the power is delivered to the board using the bus voltage of 12V, this power is converted to the required voltages on-board every printed circuit board. In fact, four different voltage levels are used for powering the electronics in the spacecraft. These are:

- 12V
- 5V

Table 9.1: Pin allocation on system bus

Pin #	Name	S/S	Function
1			
2			
3	GO power SP(Z+X+)	EPS	Connect solar arrays to EPS
4	RETURN power SP(Z+X+)	EPS	Connect solar arrays to EPS
5	GO power SP(Z+X-)	EPS	Connect solar arrays to EPS
6	RETURN power SP(Z+X-)	EPS	Connect solar arrays to EPS
7	GO power SP(Z-Y+)	EPS	Connect solar arrays to EPS
8	RETURN power SP(Z-Y+)	EPS	Connect solar arrays to EPS
9	GO power SP(Z-Y-)	EPS	Connect solar arrays to EPS
10	RETURN power SP(Z-Y-)	EPS	Connect solar arrays to EPS
11	GND1	EPS	Ground
12	GND2	EPS	Ground
13	V_bus_high	EPS	Deliver electrical power to ABF connector on ComBo
14	V_bus_high	EPS	Deliver electrical power to ABF connector on ComBo
15	V_bus_high_ABF_SYS_C	EPS	Deliver electrical power to subsystems except deployment systems
16	V_bus_high_ABF_SYS_C	EPS	Deliver electrical power to subsystems except deployment systems
17	V_bus_high_ABF_SYS_C_ABF_DEP_C	EPS	Intermediate power bus
18	V_bus_high_ABF_SYS_C_ABF_DEP_C	EPS	Intermediate power bus
19	V_bus_high_ABF_SYS_C_ABF_DEP_C_LS_C	EPS	Deliver electrical power to deployment systems
20	V_bus_high_ABF_SYS_C_ABF_DEP_C_LS_C	EPS	Deliver electrical power to deployment systems
21	GND3	EPS	Ground
22	GND4	EPS	Ground
23	I2C SDA	CDHS	Serial data bus
24	I2C SCL	CDHS	Serial data bus
25	I2C SDA	CDHS	Serial data bus
26	I2C SCL	CDHS	Serial data bus
27	GND5	EPS	Ground
28	GND6	EPS	Ground
29	TC_RAP	CDHS	Dedicated Telecommand channel from RAP
30	GND7	EPS	Ground
31	TC_ATRX	CDHS	Dedicated Telecommand channel from ATRX
32	GND8	EPS	Ground
33	VCO channel	OBM	VCO signal from MeBos to RAP
34			

- 3.3V
- -1.25V

In table 9.2 a summary is given of the board voltages for every printed circuit board in the Delfi-C3 spacecraft.

Table 9.2: Summary of the applied board voltages per printed circuit board

PCB	12V	5V	-1.25V	3.3V
Inter Connect Board Z+	×			×
Measurement Board Z+		×	×	×
Combination Board				×
Flight Board FM/430		×		
Radio Amateur Platform	×	×		×
Advanced Transceiver	×	×		×
Electrical Power Subsystem Board				×
Measurement Board Z-		×	×	×
Inter Connect Board Z-	×			×

9.4 EPS PIC pin assignment

Every printed circuit board in the Delfi-C3 spacecraft is equipped with a so-called local EPS PIC microcontroller. In general, this microcontroller is in charge of connecting the supply line of the respective subsystem to the power bus. Furthermore, it is taking measurements of the amount of current flowing into the respective subsystem.

In the situation of the interconnect boards, the PIC microcontroller supervises the deployment sequence of the spacecraft appendages. It steers the MOSFET switches used for energizing the burning resistors. Furthermore, it reads the output of the appendage tact switches used for illustrating the deployment status of the appendages.

Every controlling function of the PIC microcontroller has to be assigned to an output pin. Allocation of an input pin has to be used for assigning a measurement function to the PIC microcontroller. A matrix showing the allocation of the various pins of the local EPS PIC microcontroller per printed circuit board is shown in table 9.3.

Table 9.3: Allocation of pins of the local EPS PIC microcontroller

Pin #	Name	Function	MB	CB	RAP	ATRX	ICB
1	RC7	Digital I/O for MAB Z- X- / Z+ Y- FET H switching control					×
2	RD4	Digital I/O for MAB Z- X- / Z+ Y- optocoupler switching control					×
3	RD5	Digital I/O for SP Y- / X- FET H switching control					×
4	RD6	Digital I/O for MAB Z- Y+ / Z+ X- FET H switching control					×
5	RD7	Digital I/O for MAB Z- X- / Z+ Y- FET L switching control					×
6	Vss	Ground reference	×	×	×	×	×
7	Vdd	Positive supply	×	×	×	×	×
8		Spare interrupt pin (INT0) / spare analog input (AN10)					
9		Spare interrupt pin (INT1) / spare analog input (AN8)					
10		Spare interrupt pin (INT2)					
11	RB3	Digital I/O for SP Y+ / X+ FET L switching control					×
12	NC	No connect					
13	NC	No connect					
14		Spare analog input (AN9)					
15	RB5	Digital I/O for SP Y- / X- FET L switching control					×
16	PGC	ICSP programming clock pin	×	×	×	×	×
17	PGD	ICSP programming data pin	×	×	×	×	×
18	MCLR	Master Clear (Reset) input	×	×	×	×	×
19	AN0	Analog input for primary line current measurement	×	×	×	×	
20	AN1	Analog input for secondary line current measurement		×	×	×	
21	AN2	Analog input for determining SP Y+ / X+ tact switch signal					×
22	AN3	Analog input for determining SP Y- / X- tact switch signal					×
23	RA4	Digital I/O for power switching control	×	×	×	×	×
24	AN4	Analog input for determining MAB Z- X- / Z+ Y- optocoupler signal					×
25	AN5	Analog input for determining MAB Z- Y- / Z+ X+ optocoupler signal					×
26	AN6	Analog input for determining MAB Z- X+ / Z+ Y+ optocoupler signal					×
27	AN7	Analog input for determining MAB Z- Y+ / Z+ X- optocoupler signal					×
28	Vdd	Positive supply	×	×	×	×	×
29	Vss	Ground reference	×	×	×	×	×
30		Not used (OSC1)					
31		Not used (OSC2)					
32	RC0	Digital I/O for MAB Z- Y- / Z+ X+ FET L switching control					×
33	NC	No connect					
34	NC	No connect					
35	RC1	Digital I/O for MAB Z- X+ / Z+ Y+ FET L switching control					×
36	RC2	Digital I/O for MAB Z- Y- / Z+ X+ optocoupler switching control					×
37	SCL	Synchronous serial clock I/O for I2C	×	×	×	×	×
38	RD0	Digital I/O for MAB Z- Y- / Z+ X+ FET H switching control					×
39	RD1	Digital I/O for MAB Z- X+ / Z+ Y+ FET H switching control					×
40	RD2	Digital I/O for MAB Z- X+ / Z+ Y+ optocoupler switching control					×
41	RD3	Digital I/O for SP Y+ / X+ FET H switching control					×
42	SDA	I2C data I/O	×	×	×	×	×
43	RC5	Digital I/O for MAB Z- Y+ / Z+ X- optocoupler switching control					×
44	RC6	Digital I/O for MAB Z- Y+ / Z+ X- FET L switching control					×

9.5 Measurement reference voltages

For processing of the measurement values taken on board the Delfi-C3 spacecraft, the analog outputs of every measurement circuitry is connected to an input pin on a PIC microcontroller situated on the respective printed circuit board. This PIC microcontroller makes use of an analog-to-digital converter to take a sample of the analog input signal. This sample is consequently transformed into a 10-bit data word, which will be sent over the I2C data bus to the on-board computer for further processing.

Conversion of the analog signal to a digital data word is accomplished by comparing the magnitude of the analog signal to a voltage reference. Consequently, a data word is produced, which is dependent on the linear relation between the signal and the reference. This means that in case the signal is equal to ground level, the data word equals 10 binary zeroes. Similarly, if the signal equals the reference value, the data word is composed out of 10 binary ones. Values in between are produced by a linear interpolation between these two extreme values.

In the case of a 10-bit output, the analog step required for changing the data word by 1 is equal to:

$$\Delta = \frac{V_{ref}}{2^{10}} = \frac{V_{ref}}{1024} \tag{9.1}$$

This relation can be used during data processing for obtaining the analog value of the measurement.
All PIC microcontrollers use their supply voltage as measurement reference. Therefore, the maximum value of the output data will be equal to 3.3V. An exception is the PIC microcontroller on the measurement board. For the reference diode measurement, the IV curve measurement, and the temperature strip measurement, it uses a dedicated measurement reference of 2.048V.

Part IV

ORBIT SIMULATIONS

Chapter 10

Introduction

As part of the verification procedure of the Delfi-C3 spacecraft, the feasibility of the design for meeting its requirements has to be assessed. An initial method of establishing this assessment is performing orbit simulations. In such a simulation, the orbit of a spacecraft is simulated on a computer. At every instance, the position of the spacecraft can be determined. Other physical quantities, which relate to the spacecraft, can also be easily evaluated.

For performing the orbit simulations of the Delfi-C3 spacecraft, the EuroSim simulation environment is used. EuroSim is a computational programme developed by Dutch Space. It uses a powerful numerical integration routine to calculate the orbital behaviour of a spacecraft. It allows for a large degree of flexibility as it enables users to insert additional algorithms for calculation of physical quantities relating to the spacecraft's orbit.

The EuroSim environment has been in use at the Delft University of Technology in the incarnation of the OpSim programme. In OpSim, the concept projects of Delfi-0 and Delfi-1 were implemented for simulation. Therefore, a large part of the required algorithm was already developed by Lex Meijer, Paul van Gelder, Bastiaan Naber and Robin Raus.

To obtain adequate simulation results for Delfi-C3, several changes had to be made to the existing OpSim software. Being the most delicate resource in Delfi-C3, the value of available electrical power had to be accurately determined. Therefore, the incoming solar power is the most important output of the OpSim programme. For determining this parameter, the rather unusual geometry of Delfi-C3 has to be inserted. Furthermore, the attitude behaviour has to be known, which leads to the necessity of modeling the control and disturbance torques [16].

In this part, the process of designing the various customized algorithms is explained. Furthermore, simulations results for different operational scenarios are presented. In chapter 11, the procedure of implementing the geometry of Delfi-C3 into OpSim is elaborated. An explanation of modeling of the control torque is given in chapter 12 , while a similar explanation is shown for the disturbance torques in chapter 13. An estimation of the solar array temperature is shown in 14. Chapter 15 illustrates the procedure of determining the incoming solar power. Finally, several simulation results are discussed in chapter 16.

Chapter 11

Implementation of Delfi-C3 geometry into EuroSim

11.1 Introduction

For the orbit simulations of the Delfi-C3 spacecraft to be successful, the geometry of Delfi-C3 has to be inserted into the EuroSim simulator. After all, the incoming power is dependent on the orientation of the solar panels in the heliocentric reference frame. Disturbance torques are dependent on the orientation and the surface area of the various body surfaces. Furthermore, the position of the center of mass and the moments of inertia play important roles in the determination of the spacecraft attitude.
In this chapter, it will be shown, in which way the geometry of the Delfi-C3 spacecraft is implemented in the EuroSim simulator. In section 11.2, a treatise is given of the satellite fixed reference frame. A description of the implementation of the body surfaces is given in section 11.3. Calculation of the position of the center of mass is presented in section 11.4. Section 11.5 explains the determination of the moments of inertia.

11.2 Satellite fixed reference frame

In figure 11.1, a sketch is shown of the satellite fixed reference frame.

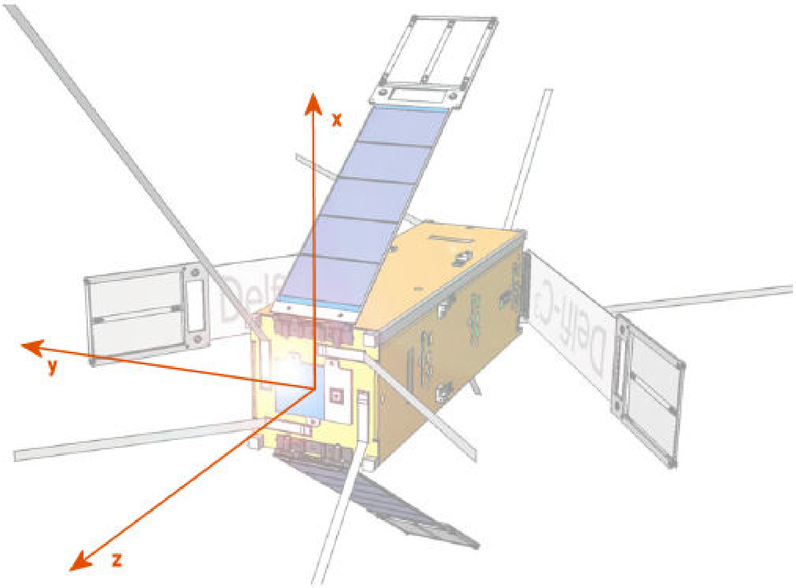

Figure 11.1: Illustration of the satellite fixed reference frame

Investigating figure 11.1, it can be noticed that the origin of the Delfi-C3 coordinate system is situated in the centre of the square surface of the main body, to which the long downlink antennae are connected (designated as "top panel"). The z-axis is going parallel to the long dimension of the main body. The x-axis is going perpendicular to the z-axis, pointing in the direction of one of the solar panel hinges situated

in the plane perpendicular to the z-axis. The y-axis completes the right-hand coordinate system.
Note that the body fixed reference frame (see section 1.2) is constructed by shifting the origin of the satellite reference frame to the center of mass of the spacecraft. Alignment of the coordinate axes does not change. // // The central body of Delfi-C3 is shaped like a beam. This means that two of its three dimensions are of equal value. The third dimension has a larger value than the other two. The longer dimension, going parallel to the z-axis of the coordinate system, is hereby designated as the length and is referenced to as l. The shorter two dimensions are designated as width and depth, with the width going parallel to the y-axis and the depth going parallel to the x-axis. These are respectively referred to as w and d. As nominal values for the dimensions are given:

$$l = 326.5 \text{ mm} \tag{11.1}$$

$$w = 100.0 \text{ mm} \tag{11.2}$$

$$d = 100.0 \text{ mm} \tag{11.3}$$

As nominal value for the mass of the Delfi-C3 spacecraft, the maximum allowed value is taken. Checking the requirements, this is found to be:

$$m = 3.0 \text{ kg} \tag{11.4}$$

11.3 Definition of Delfi-C3 geometric surfaces

The geometry of Delfi-C3 can be globally described as a beam-shaped central body with four flat plate appendages, serving as solar panels, attached to it. This configuration can be seen in figure 11.2.

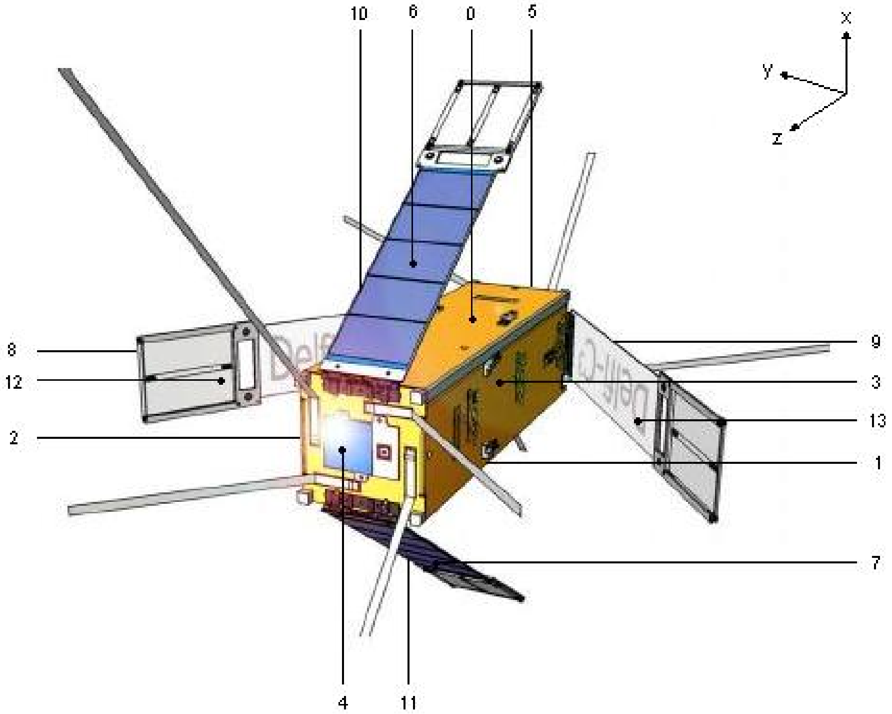

Figure 11.2: Surface definition of the Delfi-C3 spacecraft

For simulating purposes, the complete spacecraft geometry is defined by 14 surfaces: 6 sides of the beam-shaped main body, 4 "front" sides of the appendages pointing away from the main body, and 4 "back" sides of the appendages pointing towards the main body. Every panel is assigned a number for easy referencing. Figure 11.2 shows a sketch of Delfi-C3 with the assigned panel numbers.

Surface 4 is the designation of the body plate, in which the origin of the coordinate system is located. Surface 5 is at the opposite end of the body, with the negative z-axis going perpendicular in the outward direction. The positive x-axis is going in outward direction perpendicular to surface 0, while the same occurs for the negative x-axis for surface 1. Surface 2 has the positive y-axis going perpendicular outward of it, and surface 3 has the negative y-axis perpendicular to it. The designation of the solar panels is done with respect to the main body surface positioned directly underneath the appendages, or coinciding with them in stowed mode. The designations of the "front", or outward facing, sides of the panels can be found by adding "6" to the corresponding main body surface designation. The "back", or inward facing, sides of the solar panels can be found by adding "4" to the respective "front" side designation.

In stowed configuration, the solar panels are collapsed onto the body, resulting in a solar panel angle of $0\,^\circ$ for all panels. In operating configuration, these panels are deployed with a nominal solar panel angle of $35\,^\circ$. However, to ensure flexibility in the simulation, e.g. for simulating situations with one of the panels failing to be deployed, the solar panel angles are written in a vector with four variables. This vector is given in equation 11.5.

$$\vec{\theta} = \begin{pmatrix} \theta_{06} \\ \theta_{17} \\ \theta_{28} \\ \theta_{39} \end{pmatrix} \tag{11.5}$$

Here, θ_{ij} denotes the angle between surfaces i and j. In stowed and nominal operating situations, $\vec{\theta}$ is written as equation 11.6 and equation 11.7 respectively.

$$\vec{\theta}_{stowed} = \begin{pmatrix} 0\,^\circ \\ 0\,^\circ \\ 0\,^\circ \\ 0\,^\circ \end{pmatrix} \tag{11.6}$$

$$\vec{\theta}_{nom} = \begin{pmatrix} 35\,^\circ \\ 35\,^\circ \\ 35\,^\circ \\ 35\,^\circ \end{pmatrix} = \begin{pmatrix} 0.611 \\ 0.611 \\ 0.611 \\ 0.611 \end{pmatrix} \text{rad} \tag{11.7}$$

In the EuroSim simulation programme, the spacecraft is in stowed condition directly after launch. It remains in this condition until a preset time interval has passed. Thereafter, the spacecraft appendages will be in deployed configuration.

The surface areas of the body panels of the Delfi-C3 spacecraft can be dtermined by using the geometrical dimensions mentioned in equations 11.1, 11.2, and 11.3. By investigating figure 11.2, the following vector can be constructed:

$$\vec{A} = \begin{pmatrix} A_0 \\ A_1 \\ A_2 \\ A_3 \\ A_4 \\ A_5 \\ A_6 \\ A_7 \\ A_8 \\ A_9 \\ A_{10} \\ A_{11} \\ A_{12} \\ A_{13} \end{pmatrix} = \begin{pmatrix} l \cdot w \\ l \cdot w \\ l \cdot d \\ l \cdot d \\ d \cdot w \\ d \cdot w \\ l \cdot w \\ l \cdot w \\ l \cdot d \\ l \cdot d \\ l \cdot w \\ l \cdot w \\ l \cdot d \\ l \cdot d \end{pmatrix} = \begin{pmatrix} 32650 \\ 32650 \\ 32650 \\ 32650 \\ 10000 \\ 10000 \\ 32650 \\ 32650 \\ 32650 \\ 32650 \\ 32650 \\ 32650 \\ 32650 \\ 32650 \end{pmatrix} \text{mm}^2 \tag{11.8}$$

The normal vector of a body panel is defined as the unit vector pointing perpendicularly to the panel in the outward direction. In equation 11.9, a matrix is written down containing the normal vectors of every panel. These normal vectors are given in the satellite fixed reference frame as given in figure 11.1.

$$\mathbf{n} = \begin{pmatrix} \vec{n}_0 & \vec{n}_1 & \vec{n}_2 & \vec{n}_3 & \vec{n}_4 & \vec{n}_5 & \vec{n}_6 & \vec{n}_7 & \vec{n}_8 \vec{n}_9 & \vec{n}_{10} & \vec{n}_{11} & \vec{n}_{12} & \vec{n}_{13} \end{pmatrix} =$$

$$\begin{pmatrix} 1 & -1 & 0 & 0 & 0 & 0 & \cos\theta_{06} & -\cos\theta_{17} & 0 & 0 & -\cos\theta_{06} & \cos\theta_{17} & 0 & 0 \\ 0 & 0 & 1 & -1 & 0 & 0 & 0 & 0 & \cos\theta_{28} & -\cos\theta_{39} & 0 & 0 & -\cos\theta_{28} & \cos\theta_{39} \\ 0 & 0 & 0 & 0 & 1 & -1 & \sin\theta_{06} & \sin\theta_{17} & -\sin\theta_{28} & -\sin\theta_{39} & -\sin\theta_{06} & -\sin\theta_{17} & \sin\theta_{28} & \sin\theta_{39} \end{pmatrix} \tag{11.9}$$

In equation 11.10, a matrix is given containing all vectors pointing to the surface centers of the body panels. These vectors are given in the satellite fixed reference frame as shown in figure 11.1.

$$\mathbf{r} = \left(\vec{r}_0 \quad \vec{r}_1 \quad \vec{r}_2 \quad \vec{r}_3 \quad \vec{r}_4 \quad \vec{r}_5 \quad \vec{r}_6 \quad \vec{r}_7 \quad \vec{r}_8\vec{r}_9 \quad \vec{r}_{10} \quad \vec{r}_{11} \quad \vec{r}_{12} \quad \vec{r}_{13} \right) =$$

$$\left(\begin{array}{cccccccccc} \frac{d}{2} & -\frac{d}{2} & 0 & 0 & 0 & 0 & \frac{d}{2}\left(1+\sin\theta_{06}\right) & -\frac{d}{2}\left(1+\sin\theta_{17}\right) & \ldots \\ 0 & 0 & \frac{w}{2} & -\frac{w}{2} & 0 & 0 & 0 & 0 & \ldots \\ -\frac{l}{2} & -\frac{l}{2} & -\frac{l}{2} & -\frac{l}{2} & 0 & -l & -\frac{l}{2}\cos\theta_{06} & -\frac{l}{2}\cos\theta_{17} & \ldots \end{array} \right.$$

$$\left. \begin{array}{ccccccc} \ldots & 0 & 0 & \frac{d}{2}\left(1+\sin\theta_{06}\right) & -\frac{d}{2}\left(1+\sin\theta_{17}\right) & 0 & 0 \\ \ldots & \frac{w}{2}\left(\sin\theta_{28}\right) & -\frac{w}{2}\left(1+\sin\theta_{39}\right) & 0 & 0 & \frac{w}{2}\left(\sin\theta_{28}\right) & -\frac{w}{2}\left(1+\sin\theta_{39}\right) \\ \ldots & -\frac{l}{2}\left(2-\cos\theta_{28}\right) & -\frac{l}{2}\left(2-\cos\theta_{39}\right) & -\frac{l}{2}\cos\theta_{06} & -\frac{l}{2}\cos\theta_{17} & -\frac{l}{2}\left(2-\cos\theta_{28}\right) & -\frac{l}{2}\left(2-\cos\theta_{39}\right) \end{array} \right) \tag{11.10}$$

11.4 Calculation of center of mass

In order to calculate the center of mass of Delfi-C3, the following expression is applied, which governs the determination of the center of mass of a geometric object:

$$q_{Com} = \frac{M_q}{m_{S/C}} \tag{11.11}$$

where q_{CoM} is the coordinate on the q-axis of the projection of the center of mass onto the q-axis, $m_{S/C}$ is the mass of the complete spacecraft, and M_q is the so-called first moment of mass about the q-axis. The first moment of mass about the q-axis is defined as:

$$M_q = \int \sqrt{r^2 + s^2} \cdot \mathrm{d}m \tag{11.12}$$

where dm is the mass of an infinitesimally small element, and r and s are the coordinates of the respective projections of the mass element onto the r- and s-axis, where the r- and s-axis are the two axes, which are orthogonal to the q-axis in the qrs-reference frame.
Applying and evaluating these expressions to the Delfi-C3 spacecraft results in the following position of the center of mass:

$$\vec{x}_{CoM} = \begin{pmatrix} 0 \\ 0 \\ -162.2 \end{pmatrix} \text{mm} \tag{11.13}$$

Note that this vector is taken with respect to the center of the top panel of Delfi-C3 (surface 4). The orientation of the axes is similar to the orientation of the satellite fixed reference frame.
In appendix K.2.1, a calculation is shown for the determination of the center of mass of the Delfi-C3 spacecraft.

11.5 Evaluation of inertia tensor

For calculating the moment of inertia about the q-axis, the following expression is used:

$$I_{qq} = \int \left(r^2 + s^2\right) \cdot \mathrm{d}m \tag{11.14}$$

where dm is the mass of an infinitesimally small element, and r and s are the coordinates of the respective projections of the mass element onto the r- and s-axis, where the r- and s-axis are the two axes, which are orthogonal to the q-axis in the qrs-reference frame.
Similarly, the product of inertia is governed by:

$$I_{qr} = \int q \cdot r \cdot \mathrm{d}m \tag{11.15}$$

Applying these equations to the geometry of the Delfi-C3 spacecraft results in the following inertia tensor. Note that this tensor is taken with respect to the satellite fixed reference frame.

$$\mathbf{I} = \begin{pmatrix} 3.494 \cdot 10^{-2} & 0 & 0 \\ 0 & 3.494 \cdot 10^{-2} & 0 \\ 0 & 0 & 1.505 \cdot 10^{-2} \end{pmatrix} \mathrm{kg.m}^{-2} \tag{11.16}$$

In appendix K.2.2, a detailed description of the evaluation of the inertia tensor of the Delfi-C3 spacecraft is given.

Chapter 12

Modeling of magnetic control torque

12.1 Introduction

For controlling its attitude behaviour, Delfi-C3 makes use of rods of magnetic material. These rods react to the magnetic field of the Earth by generating a torque. In this way, the attitude of Delfi-C3 can be roughly controlled. Furthermore, the rotational rate of the spacecraft will be limited in magnitude. As the magnetic control torque influences the attitude behaviour of the Delfi-C3 spacecraft heavily, inclusion of this torque in the EuroSim simulation is necessary for accurate reconstruction of the attitude profile.

In this chapter, the modeling procedure of the magnetic control torque is presented. In section 12.2, a description of the applied magnetic material is given. An evaluation of the magnitude of the control torque is shown in section 12.3.

12.2 Orientation of magnetic material

Two types of magnetic material are applied for attitude control in the Delfi-C3 spacecraft. In 12.1, the orientation of the rods of magnetic material in the spacecraft is shown.

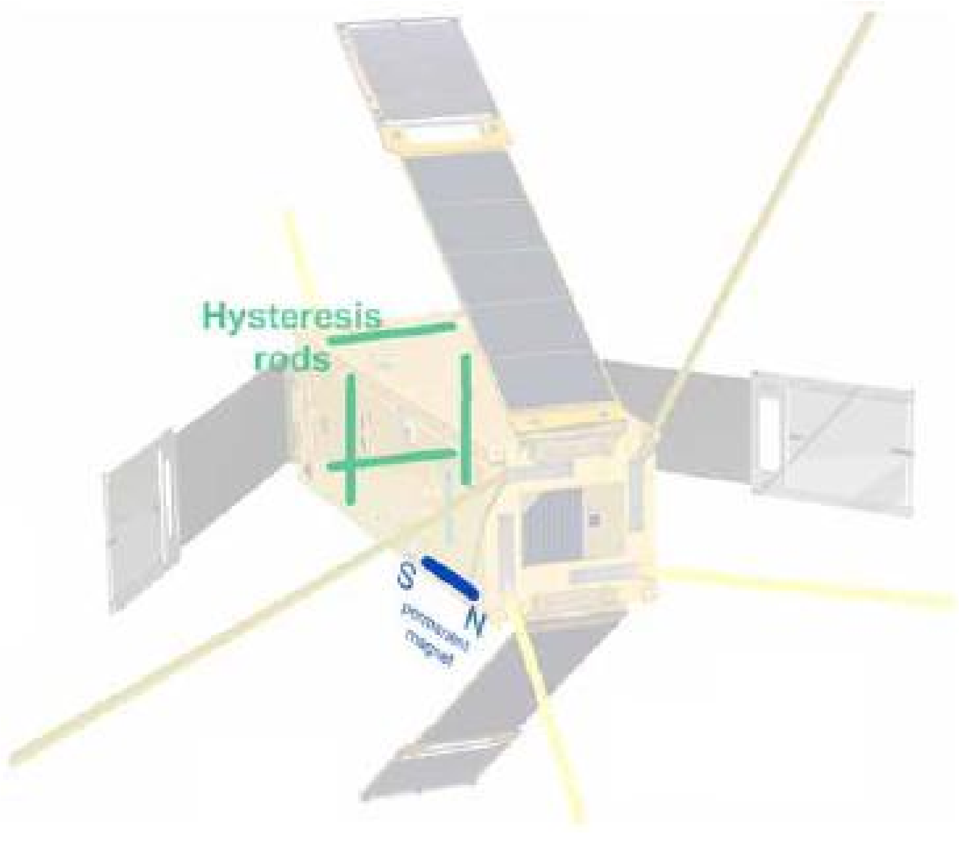

Figure 12.1: Configuration of magnetic material rods in Delfi-C3 spacecraft

It is noticed that parallel to the z-axis a permanent magnet is placed. This is illustrated in figure 12.1 by the blue rod. This magnet is manufactured out of AlNiCo 5 cast hard magnetic material. Its primary function is to align the z-axis of the spacecraft with the Earth magnetic field vector, resulting in a rough control of the spacecraft attitude.
The BH-curve corresponding to AlNiCo 5 cast hard magnetic material is shown in figure 12.2.

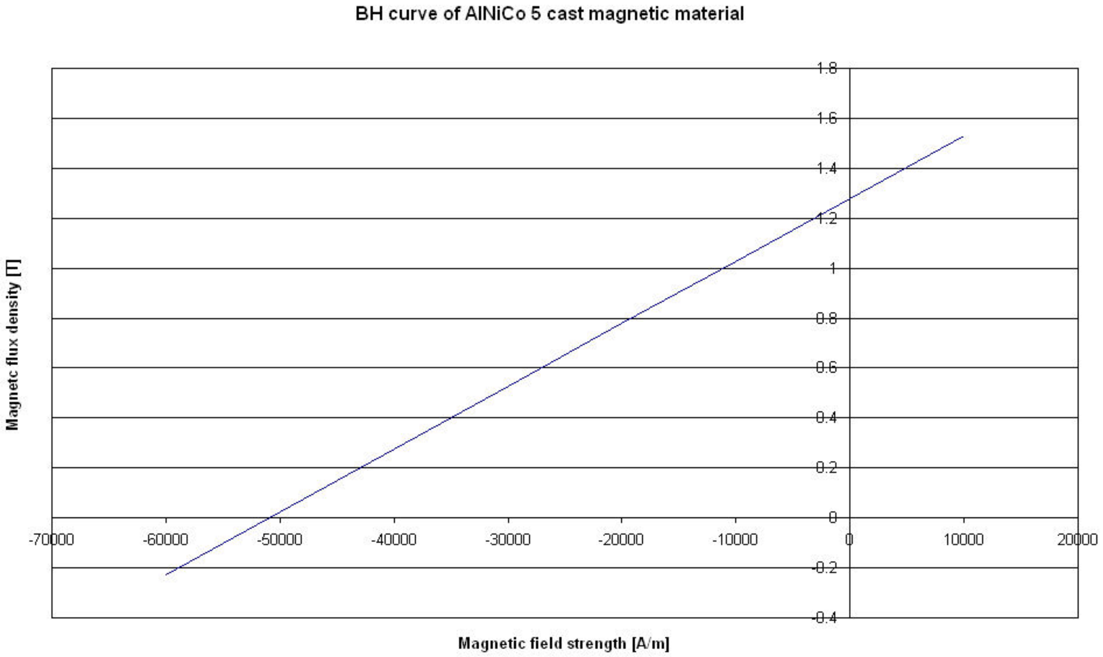

Figure 12.2: BH-curve of AlNiCo 5 cast magnetic material

Returning to figure 12.1, it can be seen that parallel to the x- and y axes rods of hysteresis material are placed. This is illustrated in figure 12.1 by the green rods. These hysteresis rods are manufactured out of PermeNorm 5000H2 hysteresis material. This material has the characteristic that during a single loop over the BH-curve, more energy is required for magnetizing the material than is gained by demagnetizing the material. Therefore, energy is dissipated during a magnetizing cycle. This characteristic makes hysteresis material ideal for dampening the rotational rate about the x- and y-axes.
The simplified BH-curve corresponding to PermeNorm 5000H2 hysteresis material is shown in figure 12.3.

12.3 Evaluation of control torque

For calculating the torque produced by a rod of magnetic material, the dipole moment corresponding to this rod has to be determined. The magnetic dipole moment is calculated with:

$$\vec{m} = \vec{B} - \frac{\vec{H}}{\mu 0} \cdot V \tag{12.1}$$

where $\vec{B}$ is the magnetic flux density of the magnetic material, $\vec{H}$ is the magnetic field strength of the magnetic material, μ_0 is the magnetic permeability of vacuum, and V is the volume of the involved rod of magnetic material.
With the dipole moment known, it is possible to calculate the generated torque with:

$$\vec{T}_{mag} = \vec{m} \times \vec{B}_{ext} \tag{12.2}$$

where m is the magnetic dipole moment generated by the involved rod of magnetic material, and B_{ext} is the Earth magnetic flux density at the position of the spacecraft.
Performing these calculations for the material in the Delfi-C3 spacecraft leads to the results shown in table 12.1. For the volume of a hysteresis material rod about a single axis, a value of $500 \cdot 10^{-9}$ m^3 is taken. As value for the volume of the permanent magnet a value of $250 \cdot 10^{-9}$ m^3 is taken. These values are chosen after a careful attitude analysis performed by F.P. Poppenk.
In appendix L, a detailed analysis of the magnetic control torque is presented.

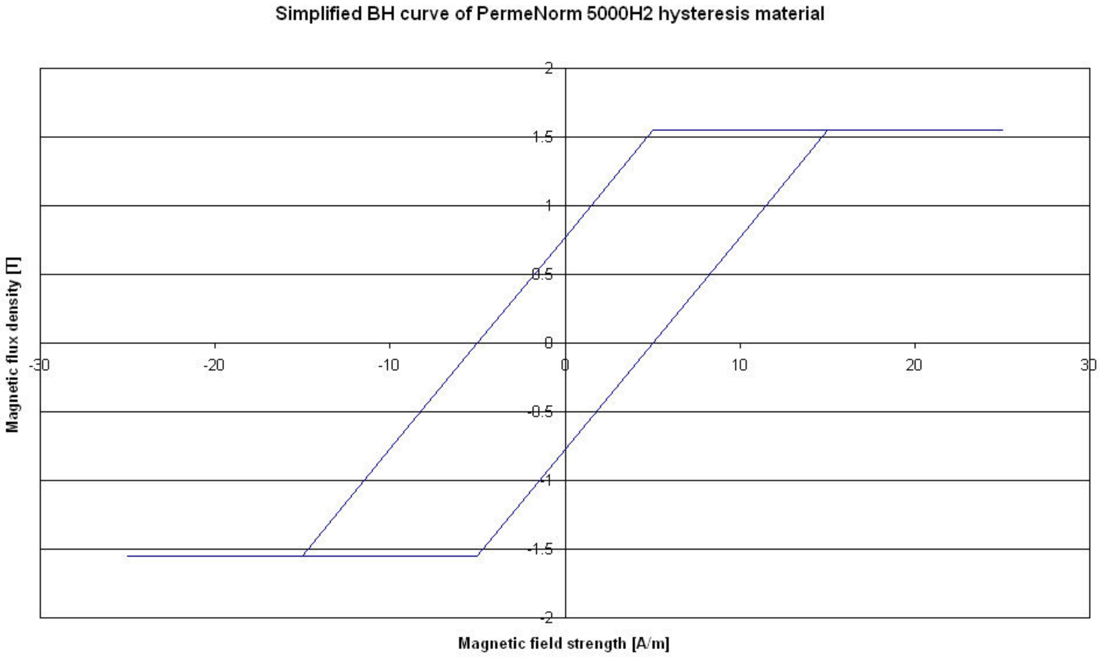

Figure 12.3: Simplified BH-curve of PermeNorm 5000H2 hysteresis material

Table 12.1: Maximum and minimum values of magnetic control torques

Type of magnetic material	Maximum torque (N.m)	Minimum torque (N.m)
Permanent magnet	$1.189 \cdot 10^{-5}$	$-1.189 \cdot 10^{-5}$
Hysteresis material	$2.632 \cdot 10^{-5}$	$-2.852 \cdot 10^{-5}$

Chapter 13

Modeling of disturbance torques

13.1 Introduction

In addition to the magnetic control torque, Delfi-C3 will experience so-called disturbance torques in orbit. Disturbance torques will lead to a deviation of a spacecraft's attitude from its desired value. In fact, they are the reason for inclusion of a control principle in spacecraft. Therefore, to reconstruct the attitude profile of Delfi-C3 it is necessary to model the disturbance torques.
In this chapter, a description is given of the modeling of the various disturbance torques. In section 13.2, a small summary is given of the types of disturbance torques in existence. In section 13.3, the modeling principle of the gravity gradient torque is presented, while a similar description is given in section 13.4 for the aerodynamic torque. An explanation of the modeling principle of the solar radiation torque is shown in section 13.5. In section 13.6, a treatise of the magnetic disturbance torque is presented. A summary of the magnitudes of the various disturbance torques is given in section 13.7.

13.2 Types of disturbance torques

In orbit, several types of disturbance torques are acting on the Delfi-C3 spacecraft. These disturbance torques can be categorized into:

- Gravity gradient torque
- Aerodynamic torque
- Solar radiation torque
- Magnetic disturbance torque

In principle, every disturbance torque is created by a disturbance force, which is at an offset distance from the center of mass of the spacecraft. This situation is well known in classical mechanics, and is illustrated in figure 13.1.

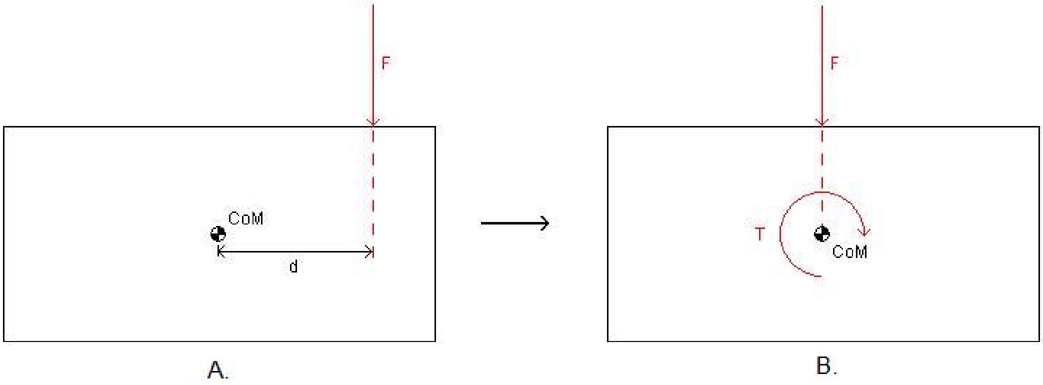

Figure 13.1: Substitution of an offset force by a force and a torque

In situation A. of figure 13.1, a force F is acting on a geometrical object. This force is at a working line, which is at an offset distance d form the center of mass. This situation can be substituted by situation B. The working line of force F has been shifted to run exactly through the center of mass. A torque T has been included to take into account the original offset distance. Torque T can be expressed by:

$$\vec{T} = \vec{F} \times \vec{d} \tag{13.1}$$

Note that in the EuroSim simulations, the disturbance forces are neglected. On the other hand, the torques resulting from these forces are taken into account.

13.3 Gravity gradient torque

Gravity gradient torques are generated in case the center of mass of a spacecraft does not coincide with the geometrical center of the spacecraft. Inhomogenities in the gravitional field of the Earth can result in a small torque.
Gravity gradient torques are expressed by:

$$\begin{pmatrix} M_x \\ M_y \\ M_z \end{pmatrix} = 3n^2 \begin{pmatrix} 0 & -c_1c_2 & s_1 \\ c_1c_2 & 0 & c_1s_2 \\ -s_1 & -c_1s_2 & 0 \end{pmatrix} \begin{pmatrix} J_{xx} & 0 & 0 \\ 0 & J_{yy} & 0 \\ 0 & 0 & J_{zz} \end{pmatrix} \tag{13.2}$$

where $s_i \equiv \sin\theta_i$, and $c_i \equiv \cos\theta_i$.
Furthermore, n equals the orbital rotation rate of the spacecraft, θ_i is the Euler angle about the i-axis, an J_{ii} is the moment of inertia of the spacecraft about the i-axis.
Note that the governing expression yields the torque in the satellite fixed reference frame.
Performing the analysis on the Delfi-C3 spacecraft results in the maximum value of the graviy gradient torque being equal to:

$$\begin{pmatrix} (M_x)_{max} \\ (M_y)_{max} \\ (M_z)_{max} \end{pmatrix} = \begin{pmatrix} 3.448 \cdot 10^{-8} \\ 3.448 \cdot 10^{-8} \\ 0 \end{pmatrix} \text{ N.m} \tag{13.3}$$

In appendix M, a detailed description of the modeling procedure of the gravity gradient torque is shown.

13.4 Aerodynamic torque

Aerodynamic forces are created by collision of the spacecraft external surface with resident air particles in the orbital track. Due to the unusual geometry of the Delfi-C3 spacecraft, these forces will produce aerodynamic torques.
The aerodynamic force generated on an exposed surface is governed by:

$$D = \frac{1}{2} \cdot C_D \cdot \rho \cdot V^2 \cdot S \tag{13.4}$$

where C_D is the so-called drag coefficient of the exposed surface, ρ is the mass density of the resident air particles, V is the relative speed of the spacecraft with respect to the surrounding air, and S is the area of the exposed surface.
The resultant aerodynamic torque, which is created by a single exposed surface, is calculated by taking the cross-product of the respective aerodynamic force and the distance between the center of aerodynamic pressure of the surface and the center of mass of the spacecraft. For the complete spacecraft, the aerodynamic torque can be found by integrating the aerodynamic torques over all exposed surfaces. Therefore, the following expression can be written:

$$\vec{T}_a = \sum_{i=0}^{n} \left(\vec{T}_a\right)_i = \sum_{i=0}^{n} \left(\left(\vec{F}_a\right)_i \times \left(\vec{x}_{CoP/CoM}\right)_i\right) \tag{13.5}$$

where $\left(\vec{F}_a\right)_i$ is the aerodynamic force acting on surface i, and $\left(\vec{x}_{CoP/CoM}\right)_i$ is the distance between the center of aerodynamic pressure of surface i and the center of mass of the spacecraft.

Note that the corresponding torque is given in the satellite fixed reference frame.
Performing the analysis of the aerodynamic torque for the Delfi-C3 spacecraft yields for the torque created by a single solar array:

$$|T_a|_{max} = 7.651 \cdot 10^{-8} \text{ N.m} \tag{13.6}$$

A detailed analysis of the aerodynamic torque is given in appendix N
Because the aerodynamic torque is directly dependent on the amount of exposed surface, the uplink and downlink antennas will produce a torque as well. This torque will amount to:

$$(|T_a|_{max})_{ant} = 2.56 \cdot 10^{-8} \text{ N.m} \tag{13.7}$$

In appendix O, a description is given of the aerodynamic torques produced by the antennas.
Furthermore, the amount of exposed aurface area is dependent can be affected by the solar panels. After all, the solar panels can effectively shadow part of the body surface resulting in changes in exposed area and position of the center of aerodynamic pressure.
An explanation of the algorithm used to evaluate the effect of shadowing of the solar panels is shown in appendix P.

13.5 Solar radiation torque

Solar radiation forces are generated by the absorption and reflection of solar radiation on the spacecraft external surface. Due to the unusual geometry of the Delfi-C3 spacecraft, these forces will produce aerodynamic torques.
The solar radiation force generated on an exposed surface is governed by:

$$F_s = (\alpha + 2 \cdot \rho) \cdot \frac{S}{c} \cdot A \tag{13.8}$$

where α is the absorption coefficient of the exposed surface, ρ is the reflection coefficient of the exposed surface, S is the solar flux at the position of the spacecraft, c is the speed of light in vacuo, and A is the area of the exposed surface.
The resultant solar radiation torque, which is generated by a single exposed surface, is calculated by taking the cross-product of the respective solar radiation force and the distance between the center of solar pressure of the surface and the center of mass of the spacecraft. For the complete spacecraft, the solar radiation torque can be found by integrating the solar radiation torques over all exposed surfaces. Therefore, the following expression can be written:

$$\vec{T}_s = \sum_{i=0}^{n} \left(\vec{T}_s\right)_i = \sum_{i=0}^{n} \left(\left(\vec{F}_s\right)_i \times \left(\vec{x}_{CoP/CoM}\right)_i\right) \tag{13.9}$$

where $\left(\vec{F}_s\right)_i$ is the aerodynamic force acting on surface i, and $\left(\vec{x}_{CoP/CoM}\right)_i$ is the distance between the center of solar pressure of surface i and the center of mass of the spacecraft.
Note that the corresponding torque is given in the satellite fixed reference frame.
Performing the analysis of the solar radiation torque for the Delfi-C3 spacecraft yields for the torque created by a single solar array:

$$|T_s|_{max} = 1.403 \cdot 10^{-8} \text{ N.m} \tag{13.10}$$

A detailed analysis of the solar radiation torque is given in appendix Q
Because the solar radiation torque is directly dependent on the amount of exposed surface, the uplink and downlink antennas will produce a torque as well. This torque will amount to:

$$(|T_s|_{max})_{ant} = 4.19 \cdot 10^{-9} \text{ N.m} \tag{13.11}$$

In appendix O, a description is given of the solar radiation torques produced by the antennas.
Furthermore, the amount of exposed aurface area is dependent can be affected by the solar panels. After all, the solar panels can effectively shadow part of the body surface resulting in changes in exposed area and position of the center of solar pressure.
An explanation of the algorithm used to evaluate the effect of shadowing of the solar panels is shown in appendix P.

13.6 Magnetic disturbance torque

Magnetic disturbance torque are the result of the interaction between electrical currents in the spacecraft and the magnetic field of the Earth. Two types of magnetic disturbance torques have been identified:

- Lorentz torque
- Induction torque

Lorentz forces are the result of an interaction between the steady-state currents flowing in the spacecraft and the magnetic field of the Earth. This force can be expressed by:

$$\vec{F}_L = \vec{B} \times \vec{I} \cdot l \tag{13.12}$$

where $\vec{B}$ is the Earth magnetic field vector, $\vec{I}$ is the electrical current flow, and l is the length of the current carrying wire.
As the spacecraft has to be electrically powered to function successfully, electrical current will always flow and Lorentz forces will be present. After performing a calculation on the Lorentz force generated due to a single current generating solar panel, the magnitude of this force is found to be:

$$\left|\vec{F}_L\right|_{max} = 6.0748 \cdot 10^{-9} \text{ N.m} \tag{13.13}$$

Induction torques are produced due to the rotational motion of the spacecraft. As the spacecraft rotates in a steady-state magnetic field, voltages will be induced in wiring loops in the spacceraft. Consequently, these voltages will lead to a flow of current. This current flow will react on the magnetic field by generating a torque.
Performing a calculation on the generated induction torque by a single solar panel on the Delfi-C3 spacecraft yields:

$$\left|\vec{F}_i\right|_{max} = 4.3 \cdot 10^{-16} \text{ N.m} \tag{13.14}$$

In appendix R, a detailed analysis is given of the derivation of the Lorentz torque and the induction torque.
Both kinds of torque are relatively small in magnitude, and are therefore neglected in the EuroSim simulations.

13.7 Magnitude comparison

In table 13.1, a summary is shown of all the torques acting on the Delfi-C3 spacecraft. Note that in the EuroSim orbit simulations, all types of torque are taken into account except the magnetic disturbance torque.

Table 13.1: Comparison of magnitudes of the various torques acting on the Delfi-C3 spacecraft

Type of torque	Order of magnitude (N.m)
Magnetic control torque	10^{-5}
Gravity gradient torque	10^{-8}
Aerodynamic torque	10^{-7}
Solar radiation torque	10^{-8}
Magnetic disturbance torque	10^{-9}

Chapter 14

Estimation of solar array temperature

14.1 Introduction

The temperature of a solar array has a large influence on its performance. In general, a hot solar array will experience a decrease in performance. For assessing the minimum available power on the solar arrays, it is therefore necessary to have an indication of the extreme values of the Delfi-C3 solar arrays.
In section 14.2, the thermal model used for assessing the temperature of the solar panels is described. Results of the thermal simulation are presented in 14.3.

14.2 Description of solar panel thermal model

For assessing the thermal behaviour of the solar panels during illumination, a thermal analysis is performed. This analysis is done in the electrical circuit simulation programme PSpice.
A thermal model is constructed consisting out of four nodes:

- TEC array front structure - body side
- TEC array front structure - TFSC side
- TEC photovoltaic cells
- TEC array back structure
- TFSC photovoltaic cells + structure

Every node is connected to the others by a thermal resistance. Furthermore, every node possesses a distinct thermal capacitance. The resulting static thermal model is depicted in figure 14.1.
Radiation dynamics are incorporated for every node. These dyanmics are composed out of several components.
Radiation absorption by a particular object can be expressed by:

$$P_{abs} = \alpha \cdot A \cdot S \tag{14.1}$$

where A is the exposed surface area of the component, S is the solar flux at the position of the spacecraft, and α is the so-called absorptivity of the object, which relates to the ratio of radiation absorbed by the object to the total amount of incoming radiation.
Emission of radiation by a particular object is written as:

$$P_{em} = \epsilon \cdot \sigma \cdot A \left(T^4 - {T_s}^4\right) \tag{14.2}$$

where ϵ is the so-called emissivity of the object, σ is the Stefan-Boltzmann constant, A is the exposed surface area of the component, and T is the temperature of the object, and T_s is the temperature of cold space.
Albedo radiation is governed by the following expression:

$$P_{alb} = \alpha \cdot a \cdot A \cdot S \cdot (\sin\rho)^2 \tag{14.3}$$

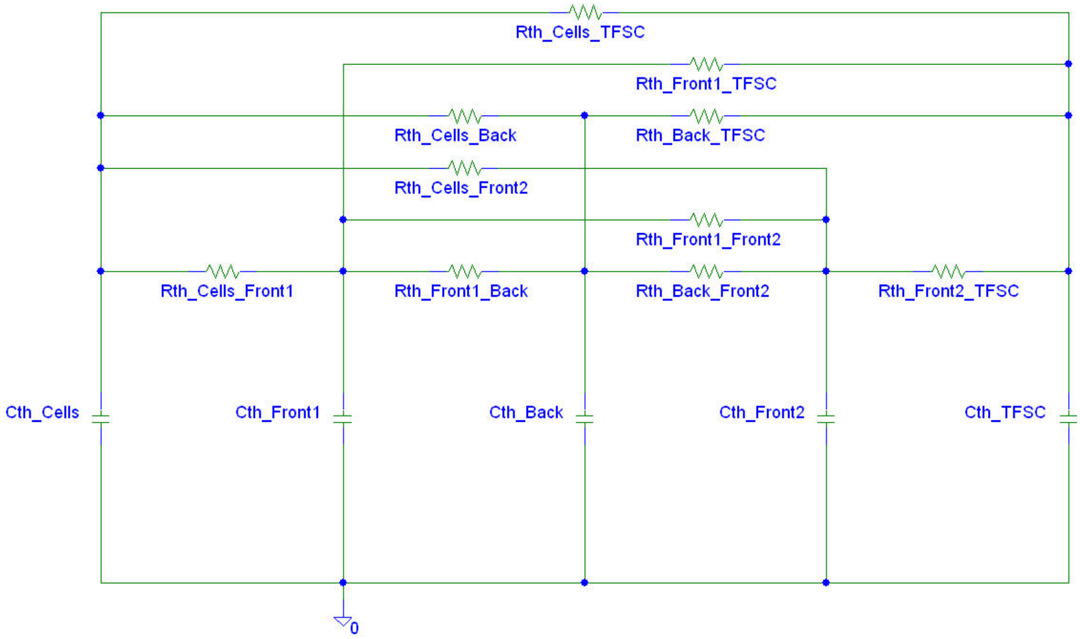
Rth_Cells_TFSC
Rth_Front1_TFSC
Rth_Cells_Back
Rth_Back_TFSC
Rth_Cells_Front2
Rth_Front1_Front2
Rth_Cells_Front1
Rth_Front1_Back
Rth_Back_Front2
Rth_Front2_TFSC
Cth_Cells
Cth_Front1
Cth_Back
Cth_Front2
Cth_TFSC
0

Figure 14.1: Complete static thermal model of solar panel

where a is the albedo factor, and ρ is Earth angular radius.
Infrared radiation is represented by:

$$P_{ir} = \epsilon \cdot \sigma \cdot A \cdot \left(T^4 - {T_E}^4\right) \cdot (\sin\rho)^2 \tag{14.4}$$

where T_E is the mean temperature of the Earth.
In addition to the static model and the radiation dynamics, the influence of the body and the flow of electrical power are taken into account in the thermal model.
A detailed description of the construction of the solar panel thermal model is shown in appendix S.

14.3 Solar panel temperature evaluation

After construction of the thermal model, several simulations have been performed. The thermal profile of the solar panel for a scenario, in which the spacecraft is rotating with 0.2 $^\circ$.s^{-1}, has been investigated. A similar analysis has been performed for a situation, in which the spacecraft is rotating with 10 $^\circ$.s^{-1}. Furthermore, the absolute maximum and minimum temperature have been determined.
In table 14.1, the results of the thermal analysis are summarized.

Table 14.1: Results of solar panel thermal analysis

Simulation scenario	Maximum temperature (°C)	Minimum temperature (°C)
$\omega = 0.2\,^\circ.\text{s}^{-1}$	74.1	-23.3
$\omega = 10\,^\circ.\text{s}^{-1}$	36.6	-18.2
$\omega = 0\,^\circ.\text{s}^{-1}$; full illumination	87.6	–
$\omega = 0\,^\circ.\text{s}^{-1}$; no illumination	–	-35.2

Chapter 15

Evaluation of solar array incoming power

15.1 Introduction

In order to accurately calculate the available electrical power in the Delfi-C3 spacecraft, it is necessary to determine the amount of solar flux incident on the solar panels of Delfi-C3. This solar flux will be converted to electrical power by the solar panels. This array power is consequently used by the electrical power system to be converted to bus power.

In this chapter, a description is given of the procedure of determining the amount of electrical power produced by the solar panels of Delfi-C3. In section 15.2, an explanation of the calculation of the available solar flux is given. A description of the determination of albedo flux is shown in section 15.3. The algorithm used to model the conversion of solar flux to electrical power is presented in section 15.4.

15.2 Solar flux

For determining the received solar flux on every body surface of Delfi-C3, an inertial reference frame A is attached to the center of the Sun. With respect to the inertial reference frame A, the Earth's position can be expressed by a vector $\vec{r}_{S-E}$. This situation is shown in figure 15.1.

Now, a reference frame B will be constructed at the center of the Earth, with all of its axes aligned parallel to the respective axes of inertial reference frame A. This is equivalent to a purely translational motion, in case reference frame A is transformed to reference frame B, i.e. no rotational transformation is involved. At any instance, the position of Delfi-C3 can be expressed by a vector $\vec{r}_{E-D}$ in reference frame B.

Note, that reference frame B is an Earth Inertial reference frame, not an Earth fixed reference frame.

The position of Delfi-C3 in reference frame A can now easily be determined at any moment, due to the fact that reference frame B is an Earth Inertial reference frame. Therefore, the position of the Delfi-C3 satellite with respect to the Sun is equal to:

$$\vec{r}_{S-D} = \vec{r}_{S-E} + \vec{r}_{E-D} \tag{15.1}$$

Noting that:

$$\vec{r}_{S-E} = -\vec{r}_{E-S} \tag{15.2}$$

Subsituting this result in equation 15.1 results in:

$$\vec{r}_{S-D} = \vec{r}_{E-D} - \vec{r}_{E-S} \tag{15.3}$$

This last equation leads to the conclusion that reference frame A has become superfluous in the calculation of $\vec{r}_{S-D}$, which can be performed solely in reference frame B.

For modeling purposes, the Sun is depicted as an infinitely small sphere. Then, the radiated solar flux density at a particular distance from the Sun is expressed by:

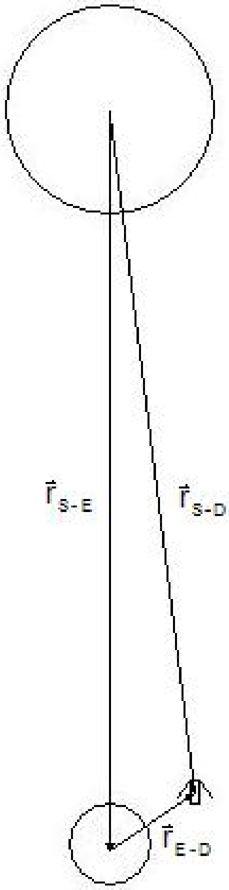

Figure 15.1: Position of the Delfi-C3 spacecraft in the Earth-Sun system

$$Q_S = \frac{S}{4\pi r^2} \tag{15.4}$$

where S equals the total radiated power of the Sun, and r is the distance from the Sun to the point of consideration.

Wiht this information, it is possible to construct a solar flux vector at the position of the Delfi-C3 satellite. This vector denotes the magnitude and direction of solar energy, which is radiated in a direction radially outward from the Sun.

$$\vec{q}_S = \frac{S}{4\pi r_{S-D}^2}\hat{r}_{S-D} = \frac{S}{4\pi r_{S-D}^3}\vec{r}_{S-D} \tag{15.5}$$

where r_{S-D} equals $|\vec{r}_{S-D}|$.

The solar flux, which is received by a particular body surface of the Delfi-C3 spacecraft can be expressed as:

$$\left(q_S\right)_i = \left(\vec{q}_S \cdot \vec{n}_i\right) A_i = -A_i \cdot \frac{S}{4\pi r_{S-D}^2}\cos\alpha_i \tag{15.6}$$

where $\vec{n}_i$ is the outward normal vector of body panel i in the Earth Inertial reference frame, A_i is the area of body panel i, and α_i is the angle between the outward normal vector of body panel i and the solar flux vector at the position of Delfi-C3.

In figure 15.2, a sketch of this situation is shown.

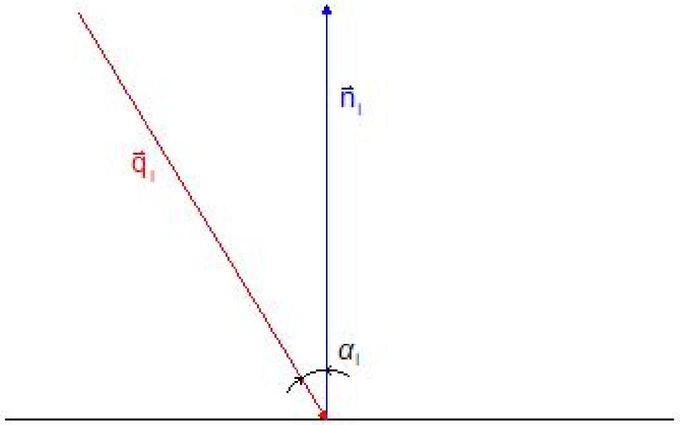

Figure 15.2: Situational sketch of solar flux incident on body surface i

15.3 Albedo flux

In addition to direct solar flux, albedo flux will also play a role in the generation of electrical power. In general, albedo is solar flux reflected by Earth's atmosphere and surface.

Direct modeling of the incident albedo flux is a rather cumbersome process, due to the multitude of variables involved. In the program, albedo flux is modeled by dividing the hemisphere of the Earth directed to the Delfi-C3 spacecraft's position into 180 different parts. For every part the incident albedo flux on the various body panels of Delfi-C3 is then calculated. The total incident albedo flux on surface i is then expressed by:

$$(q_A)_i = \sum_{j=1}^{180} \left(-\left(\vec{q}_A\right)_j \cdot \vec{n}_i \right) A_i = \sum_{j=1}^{180} \frac{k_j C \cos \alpha_{ij}}{4\pi \left(\left(r_{EP-D}\right)_j \right)^2} A_i \tag{15.7}$$

where $\vec{n}_i$ is the outward normal vector of body panel i in the Earth Inertial reference frame, A_i is the area of body panel i, α_{ij} is the angle between the outward normal vector of body panel i and the albedo flux vector of part j of the Earth hemisphere at the position of Delfi-C3, k_j is a scaling factor with respect to the total reflected solar flux of part j of the Earth hemisphere, and $\left(r_{EP-D}\right)_j$ is the distance between Delfi-C3 and part j of the Earth hemisphere.

15.4 Evaluation of solar array power

In table 15.1, the properties of the Delfi-C3 photovoltaic cells are summarized.

Table 15.1: Properties of InGaP/GaAs/Ge Triple-Junction photovoltaic cells on-board Delfi-C3

Parameter	Value	
Length of a single cell	63.22	mm
Width of a single cell	38.46	mm
Number of cells per array	5	
Efficiency @ 28 °C	0.23	
Relative temperature coefficient	-0.00060	K^{-1}
Yearly degradation	0.0275	

Both the incident solar flux and the incident albedo flux will be converted into electrical power. Because the photovoltaic cells are only susceptible to a specific band in the electromagnetic spectrum of the solar flux, an efficiency has to be incorporated. This value can be expressed by:

$$\eta = \left(\eta_{REF} + \gamma \cdot \left(T - T_{REF}\right)\right) \left(1 - \lambda\right)^{\left(t - t_{BOL}\right)} \tag{15.8}$$

where η_{REF} denotes the solar cell efficiency at reference temperature T_{REF}, γ is the relative temperature coefficient, λ is the solar cell annual degradation, and t_{BOL} is the time at beginning-of-life of the satellite.

Note that time t is expressed in years.
The temperature of the solar cells has to be modelled by a complete thermal model. A description of this model has been shown in chapter 14.
It has to be noted that the solar panels of Delfi-C3 are not completely covered by solar cells. In other words, not every part of the solar panel surface area is capable of converting solar flux into electrical power. To take this into account, use is made of an area efficiency. This parameter is calculated with:

$$\eta_{area} = \frac{A_{SC}}{A} \tag{15.9}$$

where A_{SC} is the surface area of the combined photovoltaic cells on a single panel, and A is the total surface area of a single solar panel.
Now, the total generated electrical power in the Delfi-C3 satellite can be calculated by using equation 15.10:

$$P_E = \sum_{i=0}^{13} \eta \cdot \eta_{area} \cdot \left((q_S)_i + (q_A)_i \right) \tag{15.10}$$

15.5 Final notes

It has to be mentioned that in the EuroSim simulation, a best case scenario is sketched. This can be explained by the following reasons.
First of all, the albedo flux is fully taken into account in the simulations. However, the susceptibility of the solar cells to albedo radiation is unknown. After all, the solar cells are susceptible to a specific spectral band in the electromagnetic spectrum. It is not well known, in which spectral band albedo radiation is situated.
Secondly, the simulations assume that the solar cells are always operating in their maximum power point. This is not the case in reality, because the solar arrays are clamped to the input of the electrical power system. Therefore, the operating point of the cells is fully determined by the operational principle of the elctrical power system.

Chapter 16

Initial operational timeline

16.1 Introduction

After generation of the entire orbit simulator, it is possible to perform simulations on the Delfi-C3 spacecraft. Simulations of a nominal operating spacecraft is of main interest. However, to yield a complete image of the in-orbit operations of the spacecraft, simulations of a spacecraft failing to deploy a solar panel have to run additionaly. Therefore, severla simulation scenarios are defined.

In this chapter, the initial operational timeline obtained as output of the EuroSim simulator is presented. In section 16.2, the input conditions for the simulations are presented. The results of the various performed simulations are highlighted in section 16.3.

16.2 Simulation conditions

For performing the scenarios, several initial conditions had to be inserted. Those are chosen to be equal to the initial conditions for the real-life scheduled orbit of the Delfi-C3 spacecraft. Therefore, the initial position corresponds with a position exactly above the launch site, Sriharikota in India.

The used parameters are summarized in table 16.1.

Table 16.1: Initial conditions used for performing orbit simulations

Parameter	Value	
Orbit altitude	635000	m
Orbit inclination	97.91	°
Orbit eccentricity	0	
Initial latitude	13.576 N	°
Initial longitude	80.293 E	°

Four scenarios have been tested:

- Successful deployment - No initial rotational rate
- Successful deployment - Maximum initial rotational rate
- Single solar panel deployment failure - No initial rotational rate
- Single solar panel deployment failure - Maximum initial rotational rate

For the maximum rotational rate, a value of 10 degrees per second is taken. This rotation is performed about the x-axis in the satellite fixed reference frame. This value has been obtained after an analysis by G. van Ekris investigating the rotational rate resulting from the separation of the spacecraft out of the X-POD .

It has to be noted that directly after launch, the spacecraft will be in stowed configuration. After 1800 seconds, the deployment sequence is initiated. This is modelled in the EuroSim simulation as an instanteneous action. In the following period, the spacecraft is in deployed configuration.

16.3 Simulation results

As output of the EuroSim simulator, several quantities are presented. These are:

- Total array power
- Rotational velocity (vector)
- Rotational speed (scalar)

In appendix U, the resulting timelines of the various simulation scenarios are presented.
Several conclusions can be drawn from the simulations:

- In stowed configuration, it is possible for the solar arrays to experience a blind spot, i.e. values of 0W array power are possible.
- In case the deployment sequence is successfully performed, the minimum amount of power produced by the solar arrays will never drop beneath 3W.
- In case the deployment sequence is successfully performed, the maximum amount of power produced by the solar arrays will never exceed 4W.
- In case of a solar panel deployment failure, the minimum amount of power produced by the solar array will never drop beneath 1.75W.
- In the situation that the spacecraft has an initial rotation of 10 deg.s^{-1}, the rotational rate will be dampened by the attitude control system to a steady-state value of approximately 1.5 deg.s^{-1}
- In the situation that the spacecraft has an initial rotation of 10 deg.s^{-1}, the rotational rate will decrease to 20% of its original value after a single orbit.
- In case the spacecraft has no initial rotation, the spacecraft will experience a spin-up, i.e. the rotational rate will increase to approximately 0.5 deg.s^{-1}.
- At the deployment of the appendages, the spacecraft will experience a sudden increase in rotational velocity.

Part V

ELECTRICAL SYSTEM VERIFICATION

Chapter 17

Introduction

An important phase in the development process of a spacecraft is assembly, integration and testing. In this period, all individual spacecraft subsystems will be tested. This is a very important milestone in the design, because the test results define whether the prodcued designed comply with the requirements. After all, failure to meet these requirements implies a return to the drawing board as the spacecraft is not qualified for its mission.

The verification procedure can be divided into two phases. In the first phase, every subsystem is tested individually. A check will be performed whether the functional requirements of this subsystem are met. Furthermore, the performance of the various payloads has to be determined. In the second phase, all subsystems will be integrated to represent a complete spacecraft. Tests in this phase will be performed to verify the interfaces and compatibility between the various subsystems.

In this part, the test procedures and test results relating to the electrical power system are described. A list of requirements rleevant for the electrical power system is shown in chapter 18. In chapter 19, a description the test plan and test procedure for the centralized part of the electrical power system is shown. Chapter 20 displays the verification results for the centralized part of the electrical power system. The test plan and test procedure for the decentralized part of the electrical power system are presented in chapter 21. In chapter 22, the test results for the decentralized part of the electrical power system are shown.

Chapter 18

Requirements for the electrical power system

18.1 Introduction

In the initial phase of the design of the Delfi-C3 spacecraft, several requirements for the various subsystems have been generated. At the core of these requirements are the demands laid down by the primary customers of the spacecraft. A flow down of additional requirements followed from this core, leading to a complete collection of requirements. This collection is partitioned into separate sets appiclable to individual subsystems. Hence, for the design of the electrical power system, several requirements have been derived.

In this chapter, the requirements for the electrical power system are postulated. In section 18.2, a list of requirements, which is of importance to the design of the electrical power system, is displayed.

18.2 List of requirements

Several requirements are in existence for the electrical power system. A list of the most important requirements for the electrical power system can be found in appendix W. An exhaustive list of requirements can be found in the Delfi-C3 SPEC file.

Chapter 19

Test procedure for the centralized part of the electrical power system

19.1 Introduction

Verification of the centralized power system is performed according to a test preparation document. This test preparation document can be globally divided into a test plan and a test procedure. A test plan describes the test conditions and lists the tests scheduled to be performed. A test procedure shows a step-by-step procedure for performing all scheduled tests.
In this chapter, the test procedure for the centralized power system is presented. In section 19.2, the test plan for the centralized electrical power system is shown. A treatise of the test procedure for the centralized electrical power system is shown in section 19.3.

19.2 Test plan

As the centralized electrical power system is situated on a dedicated printed circuit board, the test plan has to involve all tests relating to this board. Hence in addition to the functional tests, several structural tests and environmental tests have to be described as well.
Two methods exist for performing the functional verification of the centralized electrical power system.

In the first method, the input of the electrical power system is connected to a real-life solar array. By iluminating this solar array, input power will be provided to the electrical power system. By determining the input and output conditions of this system, the performance of the electrical power system can be assessed.
An advantage is that the solar arrays provide the authentic electrical characteristics of the in-orbit Delfi-C3 solar arrays. This means that no additional electronics are needed to simulate the IV characteristic or the array impedance. On the other hand, an installation has to be constructed, which is able to provide representative illumination of the solar arrays. Moreover, the attitude behaviour of the solar arrays is very difficult to simulate.

In the second method, a solar array simulator is connected to the input of the electrical power system. The design and manufacturing of this solar cell simulator is accredited to P. Beckers. This simulator is capable of mimicking the characteristic behaviour of the solar arrays by using an intricate electronic circuit. Features included in this simulator are simulation of the IV characteristic and the thermal behaviour of the photovoltaic arrays. However, imitation of the array impedance is not included in the simulator.
An advantage of using the solar cell simulator is that it offers a large degree of flexibility. It is able to simulate every possible illumination condition resulting in a thorough verification of the electrical power system's performance. However, the accuracy of the simulator is not as good as the accuracy provided by real solar arrays.
In both methods, the output of the electrical power system is connected to a dummy load board. This dummy load board is capable of simulating the load impedance, which the electrical power system will experience in spacecraft operation. A primary feature of this dummy load board is the possibility to connect or deconnect loads to the output. In this way, the dummy load board can simulate the varying load during the boot-up sequence of the Delfi-C3 spacecraft.

In appendix V, the verification results of the dummy load board are presented.

In the following list, all tests on the centralized electrical power subsystem are summarized.

- General tests
  - Mass measurement
  - Board envelope determining
- Functional tests
  - Static conversion efficiency test (solar arrays)
  - Static conversion efficiency test (simulator)
  - Start-up behaviour test
  - Dynamic conversion efficiency test (solar arrays)
  - Dynamic conversion efficiency test (simulator)
- Performance tests
  - PIC supply voltage test
  - Current measurement test
  - I2C interface test
- Environmental tests
  - Elevated temperature test
  - Reduced temperature test
  - Electromagnetic susceptibility test
  - Electromagnetic radiation test

19.3 Test procedure

For every involved test for the centralized electrical power system, a test procedure has been generated. In appendix X, this test procedure is shown.

Chapter 20

Test results for the centralized part of the electrical power system

20.1 Introduction

After generation of the test procedure, the verification of the centralized power system was performed. In this chapter, the test results for the centralized part of the electrical power system are presented.

20.2 Test results

During inital testing of the centralized electrical power system, a theatre spot was used as an illumination source. This set-up allowed verification of the electrical power system board in the clean room at the faculty of Aerospace Engineering.
Two solar arrays were avaliable to act as test power source for the electrical power system. These arrays were at 90 ° angle from each other. The complete assembly of arrays could be rotated to vary the incidence angle of the illumination. At the output of the electrical power system board, the dummy load board was connected.
The theatre spot was placed at an exact distance from the solar arrays, such that it would represent a single solar constant. This distance was found by measuring the short circuit current of a single solar panel. By varying the position of the theatre spot, the light intensity would change leading to a variation in short circuit current. In case the value of the short circuit current was exactly equal to the value generated with a single solar constant illumination, the correct position of the spot was determined.

It was found during initial testing that the input power of the electrical power system board was not sufficient to maintain a steady bus voltage of 12V. This situation was found at full load. Changing the incidence angles of the solar array would lead to a slight improvement, but the power would never reach a sufficient level. In the best case scenario, in which both panels were illuminated at a 45 ° incidence angle, the bus voltage would be equal to 9.66V.

Initially, it was hypothesized that the solar arrays would become very hot during the test. By attaching thermocouples to the solar panel, this hypothesis was verified. At full illumination, the temperature of the panel would raise to an assymptotoic level of 102 °C. A solution was found by applying a fan, which would cool the solar panel by blowing air at room temperature over the panel. After application of the fan, the temperature would rise to 65 °C, which was within reasonable bounds. Nevertheless, the problem of insufficient array power remained in existence.
At a further stage in the verification phase, a test was performed on the solar arrays. It was decided to determine the IV characteristic of the array under illumination of the theatre spot. This analysis was performed by connecting a resistor to the output of the array. By measuring the voltage and applying Ohm's law, a point on the IV characteristic could be found. Starting out with a very high resistance and decreasing this resistance step by step, the IV characteristic would be passed from the open circuit point to the short circuit point.
Performing the test on the solar array lead to a peculiar IV characteristic. This IV characteristic showed a step wise graph with four constant-current "plateaus". In figure 20.1, a plot of the discovered IV characteristic is shown.
A new hypothesis for the cause of the problems was formulated. It was realized that the Delfi-C3 solar cells were manufactured as triple junction cells. Failure to boost any of the three junctions would lead

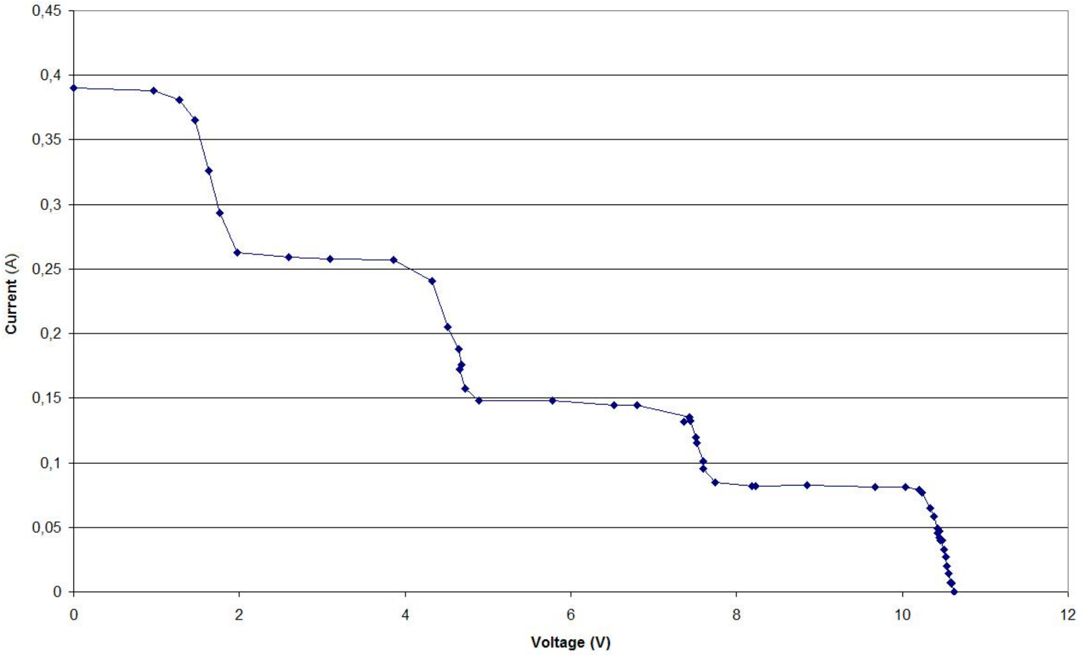

Figure 20.1: Test results for a Delfi-C3 solar array illuminated by a theatre spot

to a severe drop in performance of the cells. These junctions were all optimized to be susceptible to the electromagnetic spectrum of solar illumination. However, the applied theatre spot used a lamp, which produced another spectrum. Further analysis showed that the theatre spot was radiating mainly in the infrared spectrum. However, the sun radiates for a large part in the green band. Therefore, the theatre spot was a bad representative of the sun.

A closing answer was given by M. Kroon of Dutch Space. The applied theatre spot was not capable of producing a homogeneous parallel beam of light. On the contrary, it generated a divergent beam, which had a higher intensity in its center than on the sides. Therefore, particular cells in the array string were illuminated more intensely than others.

In this scenario, the least illuminated cell in the string would limit the array current. This can be noticed by the horizontal part of a plateau. This situation continued until the voltage reached the value, at which the cell's by-pass diode entered forward bias mode. This would lead to an addditional current path, and the current limited cell could be circumvented allowing free flow of current. This would continue until the next cell would impose an additional constriction to the array current. In the IV characteristic, this situation is noticed as the vertical part of a plateau.

This scenario was simulated in the electrical network modelling programme PSpice. In this simulation, the equivalent circuit for a solar cell has been used as has been treated in chapter 4. However, parasitic resistances in the cell have been negelected. In figure 20.2, the used network model is displayed.

Note that the difference in value of the involved current sources is the result of the difference in illumination intensity for the various cells.

In figure 20.3, the results of the simulation are shown. As can be noticed, the simulation results closely resemble the IV characteristic found during the tests.

After disconvering that the use of the theatre spot for representation of the sun was flawed, an appointment was made with Dutch Space B.V. to test the electrical power system with help of the Very Large Area Solar Simulation (VLASS). The VLASS is a professional test facility capable of prodcuing a homogeneous light bundle with a large diameter. The intensity of this light bundle is configurable. During the inital tests on the electrical power system, a light bundle has been used with intenaity of 1 solar constant.

A similar set-up was used as in the tests with the theatre spot. Only a singel solar array was used as input for the electrical power system. During these tests, the output load could attain two values:

- Light load: 223 Ω
- Heavy load: 56 Ω

During the tests, the initial load was the light load. After the output voltage was settled at a steady-state value, an additional impedance was switched parallel to this load resulting in the heavy load.

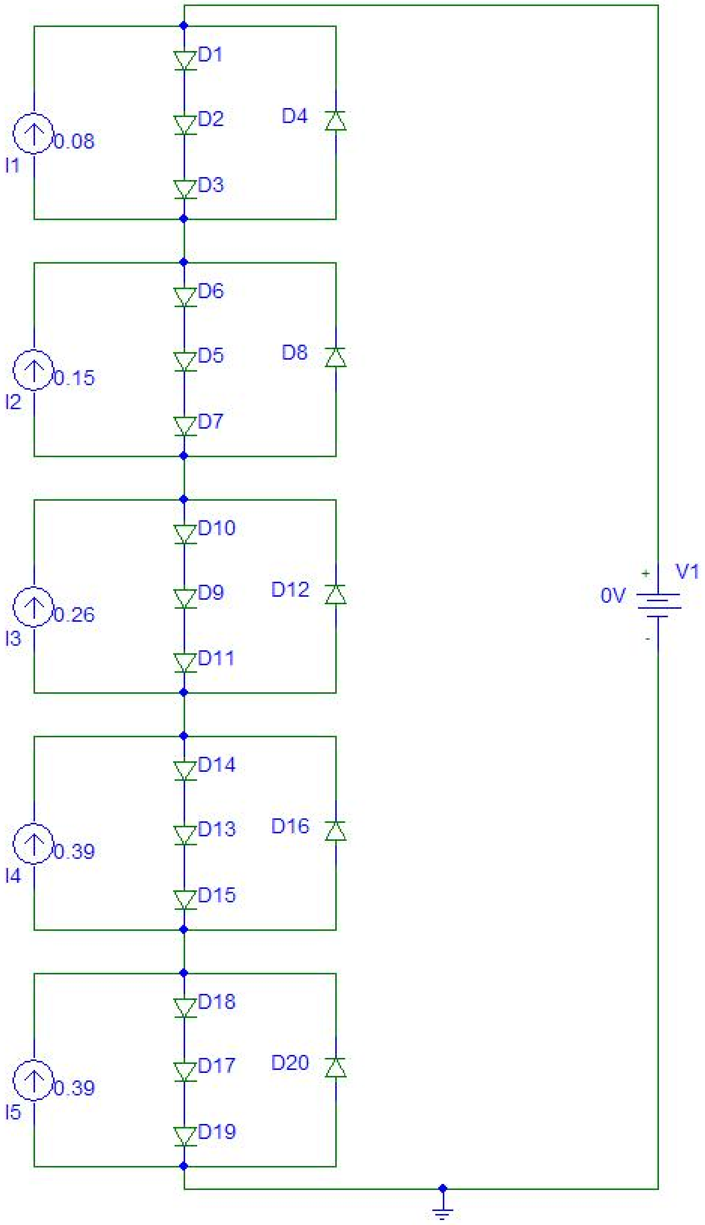

Figure 20.2: Simulation model for a inhomogeneous illuminated solar array of the Delfi-C3 spacecraft

Several tests were performed with the independent variable being the incidence angle of the light onto the solar array. This has been implemented during the tests by varying the solar flux to correspond with the solar flux perpendicular to the solar array in case the array was at the respective incidence angle. This can be expressed as:

$$S = \hat{S} \cdot \cos\alpha \tag{20.1}$$

where $\hat{S}$ is the original solar flux at 1 solar constant, and α is the incidence angle of the solar flux on the solar array.

In table 20.1, the results of the tests performed at Dutch Space are summarized.

It can be concluded that the electrical power system is capable of generating a stable bus voltage of 12V up to incidence angles of 35 °.

It has to be mentioned that additional tests are scheduled for verification of the centralized electrical power system. The most important of these tests is the behaviour during flux transition from one solar array to the other.

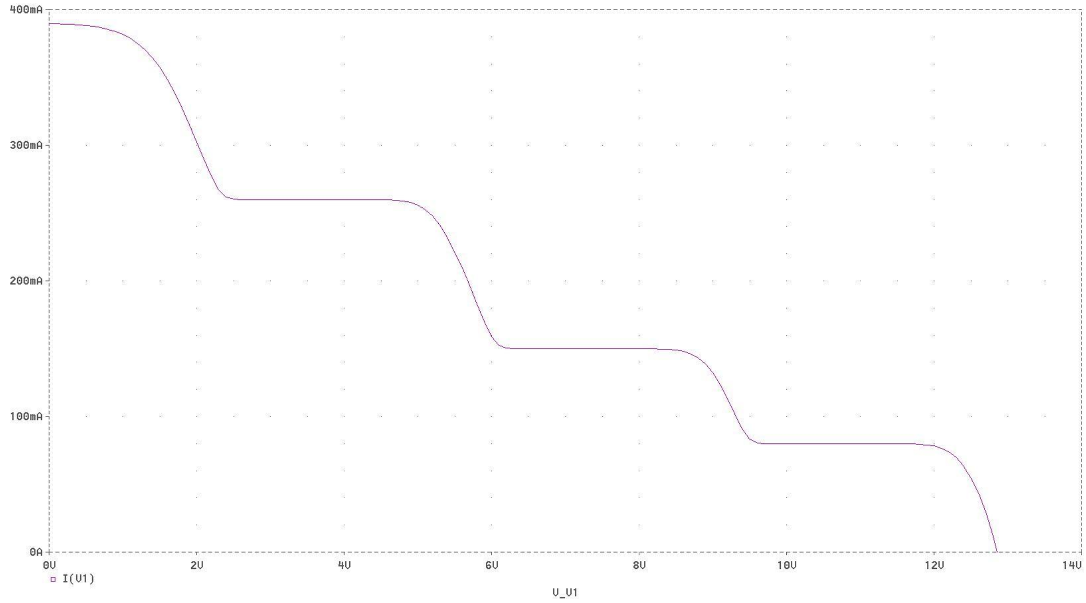

Figure 20.3: Simulation results for a inhomogeneous illuminated solar array of the Delfi-C3 spacecraft

Table 20.1: Test results of the centralized EPS

Incidence angle α	Solar flux ($W.m^{-2}$)	Light load		Heavy load	
		V_{in} (V)	V_{out} (V)	V_{in} (V)	V_{out} (V)
0	1367	12.33	12.21	11.53	12.22
5	1361	12.33	12.21	11.55	12.22
10	1346	12.31	12.21	11.52	12.22
15	1320	12.29	12.21	11.46	12.22
20	1284	12.28	12.21	11.38	12.22
25	1239	12.25	12.21	11.32	12.22
30	1184	12.22	12.21	11.19	12.22
35	1120	12.19	12.21	10.93	12.20
40	1047	12.15	12.21	6.74	9.37

Chapter 21

Test procedure for the decentralized part of the electrical power system

21.1 Introduction

Verification of the decentralized power system is performed according to a test preparation document. In a similar situation as for the centralized power system, the test preparation document is divided into a test plan and a test procedure.
In this chapter, the test procedure for the centralized power system is presented. The test plan for the decentralized electrical power system is treated in section 21.2. In section 21.3, the test procedure for the centralized electrical power system is elaborated.

21.2 Test plan

Verification of the decentralized subsystem is performed on every printed circuit board, on which a decentralized part of the electrical power system is situated. These tests are listed in the test procedure of the corresponding subsystem.
Nevertheless, all tests have a similar tendency. The main goal of the verification of the decentralized power system is to check the produced voltage levels generated on every printed circuit boards. These voltages will be produced by the various DC/DC converters, or by a resistor – voltage reference combination for supplying the decentralized EPS PIC. An additional test is performed for checking the current measurements performed by the MAX4172 chip.

- PIC supply voltage test
- 3.3V voltage conversion test (I/A)
- 5.0V voltage conversion test (I/A)
- -1.25V voltage conversion test (I/A)
- Current measurement test

21.3 Test procedure

For every individual subsystem, a separate part of the test procedure is reserved for the decentralized electrical power system. Therefore, the verification of the decentralized electrical power system is performed on the basis of multiple test procedure. As these procedures are all similar in build-up, it is sufficient to show one of these procedures as a leading example. In appendix Y, the part of the test procedure of the combination board dealing with the corresponding decentralized power system is shown.

Chapter 22

Test results for the decentralized part of the electrical power system

22.1 Introduction

After generation of the test procedure, the verification of the decentralized power system was performed. In this chapter, the test results for the decentralized part of the electrical power system are summarized.

22.2 Test results

Verification results of the decentralized electrical power system are shown in several tables.

In table 22.1, the test results for the electrical power system situated on the measurement board are shown.
In this table, the independent variable V_{bus} denotes the voltage of the main power bus, I_{bus} is the current drawn from the main power bus, V_{PIC} is the supply voltage for the decentralized EPS PIC, $V_{3.3}$ is the output voltage of the DC/DC converter with nominal output of 3.3V, $V_{5.0}$ is the output voltage of the DC/DC converter with nominal output of 5.0V, and $V_{-1.25}$ is the output voltage of the DC/DC converter with nominal output of -1.25V.

Table 22.1: Test results of the decentralized EPS on measurement board Z-

V_{bus} (V)	I_{bus} (mA)	V_{PIC} (V)	$V_{3.3}$ (V)	$V_{5.0}$ (V)	$V_{-1.25}$ (V)
8.00	8.64	3.31	3.33	4.99	-1.26
8.50	8.12	3.31	3.33	4.98	-1.26
9.00	7.69	3.31	3.33	4.98	-1.26
9.50	7.29	3.31	3.33	4.99	-1.26
10.00	6.94	3.31	3.33	4.99	-1.26
10.50	6.64	3.31	3.33	4.99	-1.26
11.00	6.38	3.31	3.33	4.99	-1.26
11.50	6.10	3.31	3.33	4.99	-1.26
12.00	5.89	3.31	3.32	4.99	-1.26
12.50	5.71	3.31	3.33	4.99	-1.26
13.00	5.52	3.31	3.33	4.99	-1.26

The test results for the electrical power system situated on the combination board are shown in table 22.2.
In this table, V_{bus} equals the voltage of the main power bus, I_{bus} is the current drawn from the main power bus, V_{PIC} is equal to the supply voltage for the decentralized EPS PIC, V_{FM430} denotes the output voltage of the DC/DC converter, which is sevring the FM/430 circuitry at nominal voltage of 5.0V, and V_{AWSS} is the output voltage of the DC/DC converter, which is serving the AWSS circuitry at nominal voltgae of 3.3V.
In table 22.3, The test results for the electrical power system situated on the combination board are shown.
In this table, V_{bus} is the voltage of the main power bus, I_{bus} denotes the current drawn from the main power bus, V_{PIC} is equal to the supply voltage for the PIC performing the array current measurements.

Table 22.2: Test results of the decentralized EPS on combination board

V_{bus} (V)	I_{bus} (mA)	V_{PIC} (V)	V_{FM430} (V)	V_{AWSS} (V)
8.00	5.39	3.32	4.95	3.32
8.50	5.12	3.32	4.95	3.32
9.00	4.90	3.32	4.95	3.32
9.50	4.73	3.32	4.95	3.32
10.00	4.58	3.32	4.94	3.32
10.50	4.46	3.32	4.94	3.32
11.00	4.33	3.32	4.94	3.32
11.50	4.22	3.32	4.94	3.32
12.00	4.12	3.32	4.94	3.32
12.50	4.03	3.32	4.94	3.32
13.00	3.95	3.32	4.94	3.32

Table 22.3: Test results of the decentralized EPS on electrical power subsystem board

V_{bus} (V)	I_{bus} (mA)	V_{PIC} (V)
8.00	0.40	2.94
8.50	0.42	3.15
9.00	0.45	3.31
9.50	0.48	3.31
10.00	0.53	3.31
10.50	0.57	3.31
11.00	0.60	3.31
11.50	0.64	3.31
12.00	0.68	3.31
12.50	0.72	3.31
13.00	0.76	3.31

With respect to these results, the folowing conclusions can be drawn:

- Over a wide range of input voltages, the output voltage of the DC/DC converter with nominal output of 3.3V remains very stable;
- Over a wide range of input voltages, the output voltage of the DC/DC converter with nominal output of 5.0V remains very stable;
- Over a wide range of input voltages, the output voltage of the DC/DC converter with nominal output of -1.25V remains very stable;
- The supply voltage for the decentralized PIC remains stable over a large range of input voltages. Only at very low input voltages, a slight deviation occurs;
- Current consumption of the various subsystems decreases with increasing bus voltage. Although this seems illogical, it can be attributed to the high efficiency of the DC/DC converters at high input voltages.

Part VI

CONCLUSIONS AND RECOMMENDATIONS

Chapter 23

Conclusions and recommendations

23.1 Main conclusion

Investigating the initial operations timeline, the available array power is equal to 3000 mW in nominal operations. Consulting the data sheet of the MAX761 step-up converter, which makes up the centralized electrical power system, an efficiency is found of 0.9. However, additional transmission losses have to be incorporated. A generally accepted value of the total efficiency from array to load is 0.8 [16]. This is in the situation, when a maximum power point tracker is used for power conditioning of the solar arrays. As in the Delfi-C3, a step-up converter is used instead of a maximum power point tracker, additional losses have to be introduced. In the power budget, an initial approximation of the available power is made:

$$P_{av} = 2300 \text{ mW}$$

Consulting the power budget, a value for the total required power in the Delfi-C3 spacecraft is found. Hence:

$$P_{req} = 2580 \text{ mW}$$

An initial conclusion can be drawn that the available power is not sufficient to serve all the spacecraft loads in nominal operations, as the required power exceeds the available power. However, it has to be noted that the discrepancy is small. By making slight improvements to the electrical circuitry, a smaller power consumption of the spacecraft load can be achieved. Furthermore, a last ditch effort can be made by reducing the amount of power for the transceiver. Although this is not advisable, as it reduces the quality of the transmission signal, it can be used to remove the discrepancy between required and available power.

In fact, improvements in the power consumption of the spacecraft load have been noticed during initial testing of the various subsystems. Measurements showing a current consumption of only 60% of the budgeted value have been observed leading to a conclusion that a reduction in power consumption of Delfi-C3 is certainly possible.

Therefore, a firm believe is established that the Delfi-C3 spacecraft is capable of producing sufficient power in-orbit to supply all its loads with electrical power. Consequently, the electrical power system performs in accordance with requirements and is qualified for spaceflight.

23.2 Electrical system design

Conclusions

Design of centralized EPS A printed circuit board containing the centralized electrical power system has been successfully designed by SystematIC B.V. Lay-out and manufacturing of the board has succeeded.

Dual PIC concept Control of every subsystem is divided among two PIC microcontrollers. One microcontroller oversees the electrical functioning of the subsystem. The other microcontroller controls the processing and transmission of data.

Power switching of subsystems Every subsystem is equipped with MOSFET switches in the power line, enabling specific powering of the subsystem. A signal sent by the relevant local EPS microcontroller enables powering of the subsystem.

Step-down DC/DC converters Dedicated step-down DC/DC converters are implemented on every printed circuit baord. Their task is to generate relevant board voltages for use by the electronics on the printed circuit board.

Current measurement In order to assess the status of every subsystem, a current measurement circuit has been implemented in the power line. This circuit is capable of determining the current flowing through the supply line. The corresponding measurement value is read by the relevant local EPS microcontroller.

Burn circuitry for deployables Circuitry has been designed for controlling the burning sequence of the Delfi-C3 deployables. As every deployable is equipped with two redundant resistor, the control circuitry is implemented in twofold.

Implementation of I2C repeater For protecting the I2C data bus from collapse, a circuit is design for implementing an I2C repeater. Every data PIC is equipped with a dedicated I2C repeater.

Recommendations

Investigation of power conditioning topologies Although the current design of the centralized electrical power system is functioning well, it may be worthwhile to investigate other power conditioning topologies. The current design applies step-up DC/DC converters, which have a limited efficiency. Other topologies (e.g. a maximum power point tracker) may result in a higher efficiency leading to higher amount of available power.

Absolute power of the Data Sheet During the design of an electrical system, component data sheets are a primary source of information for determining the suitability of a component for a particular function. However, the data sheet does not grant absolute certainty, as subtle changes in operating conditions can have a major impact on the performance of a component. It is advisable to take the information in a data sheet with a grain of salt.

Documentation of design choices Documentation of the complete design procedure is very important to transfer the rationale of the design to other people. Therefore, not only the chosen design has to be documented, but the discarded design options too. Writing down rationale and reasoning for rejecting a particular design is imperative for avoiding return of a previously discarded option in amlater stage of the design.

Operational conditions of components In case a change is introduced in a design, the compatibility of the original components with the new conditions has to be checked. E.g. a newly introduced voltage level could result in saturation of an operational amplifier rendering the functioning of the amplifier useless. Errors found during the verification phase can often be traced to an unnoticed incompatibility issue.

23.3 Systems engineering

Conclusions

Power budget generation and maintenance A power budget has been generated for Delfi-C3 power budget. It has been maintained throughout the entire project. For the complete spacecraft to function successfully, 2580 mW of electrical power on the 12V bus is required.

System bus definition A definition of the system bus has been generated. Every line in the system bus is assigned a dedicated function.

Allocation of pins of local EPS microcontroller For every function of the local EPS microcontroller a pin has been assigned. An allocation table has been generated.

Recommendations

Update of the power budget An up-to-date representation of the power budget is indispensable for the success of a spacecraft development process. However, not every subsystem specialist will inform the systems engineer voluntarily about (minor) design changes. A systems engineer has to develop a zeal for keeping the power budget updated by constantly asking the subsystem specialists about a change in the power budget.

Documentation of interfaces Every interface in the Delfi-C3 spacecraft has to be accurately defined. Any change in the definition of an interface has to be unambiguously communicated to the involved subsystem engineers.

23.4 Orbit simulations

Conclusions

Implementation of Delfi-C3 geometry into EuroSim simulator The geometry of the Delfi-C3 spacecraft has been incorporated in the EuroSim simulator. Both the main body and the solar panels are implemented.

Evaluation of magnetic control torque in EuroSim simulator An algorithm has been developed for determining the torque produced by the magnetic control rods. Both the permanent magnet and the hysteresis rods have been taken into account. Evaluation of this torque shows $2.852 \cdot 10^{-5}$ N.m for a single hysteresis rod with a volume of $500 \cdot 10^{-9}$ m^3, and $1.189 \cdot 10^{-5}$ N.m for a permanent magnet with a volume of $250 \cdot 10^{-9}$ m^3.

Implementation of disturbance torques into EuroSim simulator An algorithm has been developed for evaluating the disturbance torques acting on the Delfi-C3 spacecraft. Subroutines for the gravity gradient, aerodynamic, and solar radiation torques are implemented in the EuroSim simulator. Evaluation of the complete set of disturbance torques yields a magnitude in the order 10^{-7} N.m.

Assessment of array power in EuroSim simulator An algorithm has been developed for evaluating the electrical power produced on the Delfi-C3 solar arrays. Both the solar flux and albedo flux are taken into account. The magnitude of the array power is dependent on the incidence angle of the solar flux and the albedo flux, and the array temperature. A thermal model of the solar panel has been developed to assess the temperature of the solar cells.

Simulation of operational timeline in successful deployment scenario An initial timeline has been produced with help of the EuroSim simulator for the Delfi-C3 spacecraft in a succesful deployment scenario. After deployment, the minimum array power is approximately equal to 3000 mW. Applying an initial rotational velocity of $10\,^{\circ}.\mathrm{s}^{-1}$ would lead to a steady-state rotational velocity of $1.5\,^{\circ}.\mathrm{s}^{-1}$. On the other hand, starting with no initial rotational velocity results in a steady-state rotational velocity of $0.5\,^{\circ}.\mathrm{s}^{-1}$.

Simulation of operational timeline in single deployment failure scenario An initial timeline has been produced with help of the EuroSim simulator for the Delfi-C3 spacecraft in a single deployment failure scenario. After deployment, the minimum array power is approximately equal to 1750 mW. Applying an initial rotational velocity of $10\,^{\circ}.\mathrm{s}^{-1}$ would lead to a steady-state rotational velocity of $1.5\,^{\circ}.\mathrm{s}^{-1}$. On the other hand, starting with no initial rotational velocity results in a steady-state rotational velocity of $0.5\,^{\circ}.\mathrm{s}^{-1}$.

Recommendations

Improvement of shadowing algorithm In the current simulation model, the shadowing of the solar panels onto the main body is taken into account for determining the aerodyanmic and solar radiation disturbance torques. Furthermore, the shadowing of the main body onto the back side of the solar panels is implemented. However, the shadowing of one solar panel onto the back side of another panel is not inserted in the model. Shadowing caused by antennae and shadowing onto antennae is not taken into account either. A very accurate model would be produced if these omitted parameters were implemented. However, this would require a very ingeneous algorithm or the implementation of vector algebra into the EuroSim simulator.

Susceptibility of photovoltaic cells to albedo flux In the current evaluation of the electrical power produced by the solar arrays, the albedo flux is taken into account. It is not unambiguous, to which extent the albedo flux contributes to the generation of electrical power. Investigation in this matter would result in a more accurate prediction of the generated array power.

Inclusion of solar panel thermal model in simulator As the temperature of the solar cells have a high influence on the performance of the solar arrays, assessment of the cell temperature is an important action for determining the minimum amount of array power. In the current simulator, a worst-case temperature is assumed. However, a more accurate prediction would be outputted by including a complete thermal model of a solar panel in the EuroSim simulator.

Evaluation of array voltage and array current Although the power on the solar arrays is assessed in the EuroSim simulator, an improvement can be made by determining the array voltage and the array current. This would lead to better understanding of the electrical behaviour of the array, resulting in a more accurate prediction of the operation of the electrical power system. One method for separating the array power into array voltage and array current is the Mottet model [12].

23.5 Testing and verification

Conclusions

Generation of EPS requirements A complete set of requirements for the electrical powwer system has been produced.

Production of centralized EPS test procedure A test procedure for the centralized EPS has been produced. Both a test plan and a detailed test procedure describing all involved tests have been generated.

Test results of centralized EPS test procedure The centralized electrical power system has been tested in the VLASS facility at Dutch Space. A single solar array has been used as input source. This single array is capable of supplying the spacecraft with electrical power up to an incidence angle of 35 °.

Production of decentralized EPS test procedure A test procedure for the decentralized EPS has been produced. Both a test plan and a detailed test procedure describing all involved tests have been generated. This test procedure is integrated in veery subsystem test procedure as a testing block for the decentralized EPS.

Test results of decentralized EPS test procedure The decentralized EPS for the combination board, measurement board, and electrical power system board has been tested. The supply voltage for the PIC microcontrollers is very constant. Furthermore, the board voltages generated by the step-down DC/DC converters is extremely stable.

Recommendations

Measurement equipment Before commencing verification, check all applied measurement equipment. Measurement units of the same series can show differences in their output. Calibration of the results to take this difference into account is necessary.

Validity of connectors Before commencing verification, check all applied connectors. It has to be ensured that all connector lines are inserted in the correct connector pins.

Validity of stimulating equipment Before commencing verification, check all applied stimulating equipment. As styimulating equipment is used for simulating an external stimulation source, it has to be ensured that the equipment represents this external source in a sufficient way.

Creation of solar cell stimulator Up to present date, all tests on the centralized electrical power system have been performed with Delfi-C3 solar arrays. For verifying the dynamic behaviour of the centralized EPS, it is more convenient to use an electronic contraption capable of simulating the Delfi-C3 solar cells. At the moment, this device is being manufactured by P. Beckers.

Performing additional tests on centralized EPS All tests performed on the centralized electrical power system involved steady-state illumination tests. Additional verification is required to qualify the electrical power system. The most important tests involve dynamic behaviour by investgating the transition of input power from one array to another.

23.6 Miscellaneous

Conclusions

Hands-on experience The Delfi-C3 project offers an excellent educational opportunity for prospective space industry students. Students will receive hands-on experience in working in a spacecraft design project.

Scheduled launch A main attraction of Delfi-C3 is the fact that the conclusion of the project will be launched into space. A tangible end result will produced, which is a major motivation for every person involved in the project. At the moment, Delfi-C3 is scheduled for launch in September 2007.

Recommendations

Knowledge in other fields of engineering In a development programme of a spacecraft, it is unavoidable for any involved engineer to come in contact with other fields of engineering. In general, the knowledge of these engineers about these unfamiliar fields is very small. Enhancement of the knowledge of electrical engineering and computer engineering for aerospace engineers will result in a smoother and faster design trajectory.

Drive for out-of-the-box engineering Every engineer involved in a spacecraft design project should learn to apply out-of-the-box engineering. Many interfaces are in existence in a spacecraft, yielding high interdepecies bewteen the various subsystems. Therefore, design of a subsystem should not occur with only this respective subsystem in mind, but by keeping track of the complete set of related subsystems as well. Therefore, knowledge of the operational principle of these related subsystems and of the existing interfaces is imperative for a successful design.

Management of personnel Certainty of the availability of team members is indispensable for the success of a project. Generation of an availability schedule will help with the planning of project activities. Compliance of the schedule is not open to discussion.

Compliance to deadlines A deadline is not a joke! As a chain is vulnerable at its weakest link, failure of a subsystem to meet a design deadline will lead to schedule slip for the complete project. Therefore, subsystem engineers have to do their utmost to adhere to a deadline.

Maintain good relation with industry For successful verification of the centralized electrical power system, the VLASS facility at Dutch Space was a great help. The availability of this facility for use on Delfi-C3 was enabled by good relations with Dutch Space. Good relations and contacts with industry will open up possibilities to make spacecraft development easier.

Bibliography

[1] M.R. Brozel, editor. Properties of Gallium Arsenide. Institute of Engineering and Technology, London, United Kingdom, third edition, 1996.

[2] Engineers Edge. Engineers Edge - Design, Engineering and Manufacturing Solutions. Online database, 2007. http://www.engineersedge.com.

[3] eFunda Incorporated. eFunda, the Ultimate Online Reference for Engineers. Online database, 2007. http://www.efunda.com.

[4] D.J. Griffiths. Introduction to Electrodynamics. Prentice-Hall Inc., Upper Saddle River, New Jersey, United States of America, third edition, 1999.

[5] M.J. Hoeijmakers. Elektrische Omzettingen. Delft University Press, Delft, the Netherlands, third edition, 2003.

[6] N. Mohan, T.M. Undeland, and W.P. Robbins. Power Electronics: Converters, Applications, and Design. John Wiley & Sons, Inc., third edition, 2003.

[7] R. Noomen, Q.P. Chu, and A. Kamp. Space Engineering and Technology III. Delft University of Technology, Delft, the Netherlands, July 2005. Lecture notes.

[8] J. Rotteveel. Providing a customizable control framework for the Delfi-C3 mission by means of flexible systems engineering and thermal control tools. Master's thesis, Delft University of Technology, Delft, the Netherlands, April 2006.

[9] P.C. Sen. Principles of Electric Machines and Power Electronics. John Wiley and Sons, second edition, 1997.

[10] G. Simonelli, D. Richard, W. Veith, and F. Tonicello. PSpice thermo-electrical model of the Aeolus electrical power system. In Proceedings of Seventh European Space Conference, Stresa, Italy, 2005.

[11] F. te Hennepe. Implementation and validation of a electrical/thermal model of a Sony 18650HC Li-ion cell in PSpice. Technical report, ESA ESTEC - TEC-EP Division, Noordwijk, the Netherlands, May 2006.

[12] E. van den Berg and M. Kroon. Algorithms and performance of a space dedicated solar array modelling tool. In Proceedings of Sixth European Space Conference, Porto, Portugal, 2002.

[13] F. van der Laan. Het natuurlijk ruimtemilieu en de schade die het kan veroorzaken aan ruimtevoertuigen. Master's thesis, Delft University of Technology, Delft, the Netherlands, 1986.

[14] E.N. van der Linden. Delfi-C3: Detailed design of the structure, solar panel, and deployment mechanism. Master's thesis, Delft University of Technology, Delft, the Netherlands, 2005.

[15] K.F. Wakker. Astrodynamics I. Delft University of Technology, Delft, the Netherlands, June 2002. Lecture notes.

[16] J.R. Wertz and W.J. Larson, editors. Space Mission Analysis and Design. Microcosm Press, El Segundo, California, United States of America, third edition, 1999.

[17] Bong Wie. Space Vehicle Dynamics and Control. AIAA Education Series, 1998.

Part VII

APPENDICES

Appendix A

Appendant CD

This CD contains:

- System bus pin out
- PIC pin out
- Electrical and board design guidelines
- Complete initial timelines in Excel
- Data sheets of involved components
- Power budget
- Electrical schematics
- Technical notes
- Minutes of meetings

Appendix B

Original thesis assignment

Thesis assignment F. te Hennepe

Electrical Power Subsystem Delfi-C3

Customer: Delfi-C3 / R.J. Hamann, W.J. Ubbels
Project supervisor: B.T.C. Zandbergen
Starting date: 14 August 2006
Final date: approx. 30 June 2007

List of actions

- OPSIM
  - Perform EuroSim simulation to produce:
    - Output electrical power profile (P_{sa} and/or P_{bus})
    - Output gravity gradient torque (I/F DH (CoM, inertia tensor))
    - Output aerodynamic torque (I/F DH (CoM, inertia tensor))
    - Output solar radiation torque (I/F DH (CoM, inertia tensor))
    - Output magnetic element torque (I/F FP (magnetic element data); DH (CoM, inertia tensor))
    - Output attitude profile (Euler angles; angles w.r.t. fixed orbital directions (angle in XZ-plane w.r.t. nadir, angle out of XZ-plane w.r.t. nadir, angle TBD))
    - Attitude/operations timeline from separation through SA deployment, ANT deployment, rate damping/rate acceleration (two cases)
  - Constraints:
    - Delfi-C3 orbit as defined by PSLV (h = 635 km, i = 97.91 °, e = 0, LTAN = 10.30)
    - Launch date: 30 June 2007
    - Modes: deployed SA, stowed SA and single deployed SA failure
    - Mission duration: 3 months
    - Delfi-C3 geometry
    - Delfi-C3 center of mass position
    - Temperature SA -> worst case
    - Separation conditions
- Systems Engineering
  - Oversee detailed design of electrical power system done by SystematIC Design BV
    - Output design schedule
  - Keep track of and update power budget
    - Generate detailed description of power budget model
    - Output updated power budget

  - Keep track of and design EPS - subsystem interfaces
    - Keep track of EPS design and implementation
    - Output updated interface document
  - Investigate validity of current EPS requirements
    - Output updated EPS requirements document

- Testing
  - Write test plans for EPS (consult GB, CV, WU, AB, BM)
    - Output test plans and procedures for board level tests
    - Output test plans and procedures for system level tests
  - Operate solar array s(t)imulator as built and designed by P. Beckers during EPS tests
  - Oversee preliminary tests on EPS performed by SystematIC Design BV
    - Output test evaluation report

- Post-launch operations
  - Perform post-launch operations / take care of training of successor
    - Write part of mission operations plan involving EPS
    - Output Delfi-C3 operations manual

- Progress meetings
  - Every 2 weeks on Tuesday an internal progress team meeting is organized
  - Every week a concise individual progress update will be given to the customers
  - TBD (day-month) an individual mid-term review will be organized

Appendix C

DC3-TN-609-061
PIC Topology Selection

C.1 Introduction

Peripheral Interface Controllers (PICs) are microcontrollers used onboard the Delfi-C3 spacecraft for performing calculations at a local level. With exception of the FM/430 flight board, every printed circuit board in the stack of Delfi-C3 is outfitted with one or more PICs. Major functions of a PIC include connecting the subsystem on the relevant printed circuit board to the power bus, and processing of data received from the on-board computer or the relevant subsystem. Other functions are also possible and are often defined by the nature of the local environment of the relevant PIC.

During meetings for the electrical power system and command and data handling system, several concerns were sounded whether a single PIC was able to perform all assigned tasks in a fail-safe way with an acceptable performance. Therefore, a proposal was made to implement an additional PIC on every PCB. In this document, the issue under investigation is whether 2 separate PICs or 1 only PIC have to be applied on every PCB for controlling the various functions on the relevant PCB. First of all, several trade-off criteria will be put down in section C.2.1. Next in section C.2.2, the two scenarios will be described by defining their topologies. Section C.2.3 will treat the allocation of PICs in the stack. In sections C.2.4 to C.2.6, for both scenarios, the trade-off criteria, being respectively surface area, power consumption and software implementation, will be further evaluated. Finally, in section C.2.7, the trade-off between both concepts will be performed.

C.2 PIC Topology Selection

In this section, the concept implementing only one PIC per PCB (hereafter known as "single PIC scenario") will be compared with the concept applying two PICs per PCB (hereafter known as "dual PIC scenario").

C.2.1 Trade-off criteria

The PIC implementation concepts will both be evaluated with respect to three trade-off criteria. These criteria are listed below:

- Power consumption

  The amount of electrical power, which is needed to enable the PIC concept to operate successfully;

- Surface area

  The area needed on the printed circuit board to accommodate the PIC concept;

- Software implementation

  The complexity and modularity of PIC software needed for the PIC concept to operate successfully.

C.2.2 Definition of scenarios

Description of protective circuitry

To provide power to the subsystem at the required input voltage, use is made of a DC/DC converter, which converts power coming from the power bus at 12V to input power for the subsystem at 3.3V. To avoid single point failures in the design of the electrical power system, the DC/DC converter has to be able to be switched on and off. This switching function is controlled by a PIC, which controls the power input of the subsystem (known as EPS PIC, or PIC 1). The required input voltage for this PIC is 3.3V at its nominal value. However, it is not possible to place the PIC controlling the switching of the DC/DC converter behind this converter, as this would lead to a situation in which the PIC would never receive power.

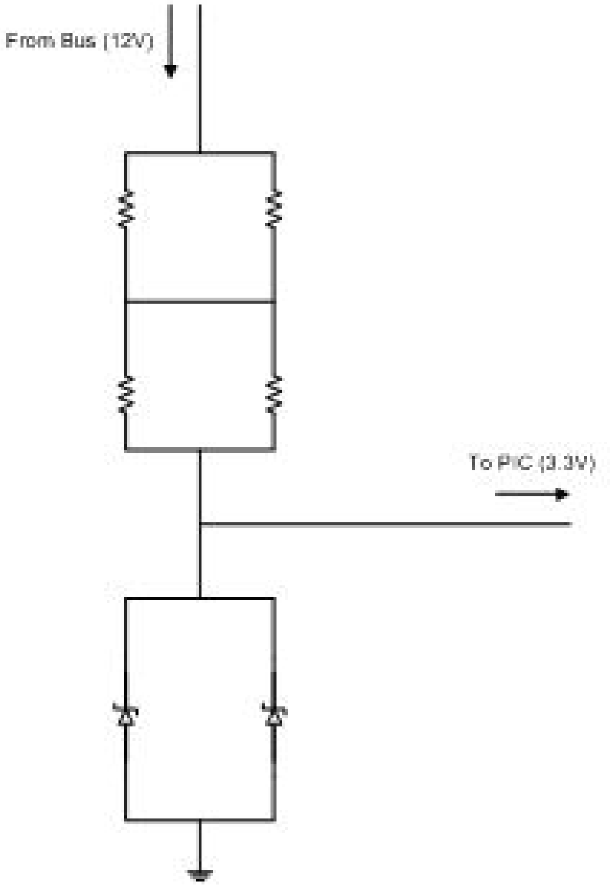

Figure C.1: Analysis of influence of ICD2 current on PIC input voltage

Therefore, the PIC is placed behind a special protective circuitry, which is shown in figure C.1. Investigating figure C.1, it is noticed that a voltage reference is present in the form of a Zener diode. A Zener diode is a special sort of diode, which is able to make use of a so-called controlled breakdown. An ideal ordinary diode has the characteristic to block any current is a reverse bias voltage is applied to this diode. In case of a Zener diode however, at a certain reverse bias voltage the diode experiences a breakdown, which leads to a high conductivity of the diode. Moreover, in breakdown, the differential resistance of the diode is very high, i.e. the value of the voltage derivative of the current $\frac{\mathrm{d}I}{\mathrm{d}V}$ is very high. An example of a Zener diode characteristic is shown in figure C.2.

The characteristics of a Zener diode make it extremely attractive to use as a voltage reference. Returning to figure C.1, it is noticed that the presence of the Zener diode have to result in a voltage reference equal to the PIC input voltage (3.3V). Putting two Zener diodes in parallel ensures redundancy of the voltage reference in case one of the diodes fails in open. Note, however that in case one of the diodes fails in short, the voltage reference and as a result the complete subsystem fails completely.

The resistors in the circuit function as a voltage absorption mechanisms from the 12V bus voltage to the 3.3V PIC input voltage. The difference in voltage will be dissipated in the resistors. Note that the use of four resistors in an H-bridge will leads to redundancy for both an open-circuit failure and a short-circuit failure of one of the resistors.

The usefulness of this protective circuitry lies in the fact that it is passive, i.e. no switching mechanisms are used, and that it provides over-current protection. This last characteristic is explained by the fact that the current coming from the bus in case the PIC or one of the Zeners fails in short is limited by the resistors. A large disadvantage is the large amount of dissipation in the resistors, which will lead to a high power consumption and in possible thermal issues.

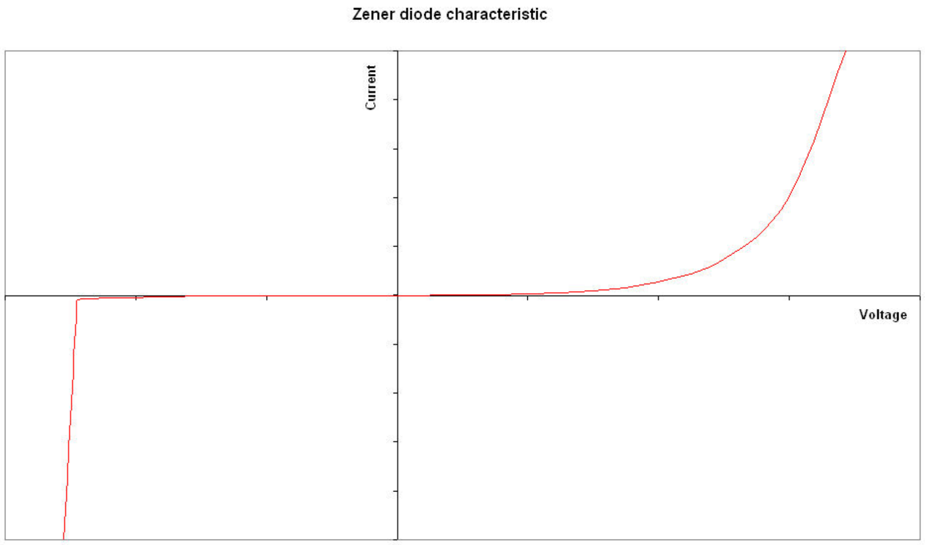

Figure C.2: Example of a Zener diode characteristic

In addition to a PIC, which controls the electrical power input of the subsystem, there is also a PIC needed to process the data coming from the OBC and correspondingly sending data to the subsystem, and for processing data coming form the subsystem and correspondingly sending data down the I2C bus to the onboard computer. In the implementation of this last PIC (known as CDHS PIC or PIC 2) lies the difference between the single PIC and dual PIC concepts.

Description of single PIC concept

In the single PIC concept, the involved PIC provides the interfaces of the subsystem with both the electrical power system (EPS) and the command and data handling system (CDHS). This effectively leads to the combination of PIC 1 and PIC 2 into one single PIC. As the PIC still has to drive the DC/DC converter and therefore needs to be connected to the power bus, the protective circuitry described in the previous sub-subsection is still needed to provide the PIC with the required input voltage. This leads to the situation shown in figure C.3.

Description of dual PIC concept

In the dual PIC concept, one PIC is used to provide control over the electrical power input to the subsystem. As this PIC has to be connected at all time to the power bus, this PIC is placed behind the protective circuitry described in the first sub-subsection of this subsection. An additional PIC is used to provide an interface with the data bus. As this PIC only needs to function in case the subsystem is powered (i.e. the DC/DC converter is switched on), this PIC is placed behind the DC/DC converter. This effectively leads to a division of tasks over two PICs; one PIC doing all EPS related tasks, and one PIC doing all CDHS related tasks. This leads to the situation shown in figure C.4.

C.2.3 PIC allocation in stack

On several PCBs in the stack, a single control PIC is not sufficient to provide all the needed functions on the PCB. Both communications PCBs (i.e. RAP and ATRX) are outfitted with two CDHS PICs, being a bit shaping PIC and a control PIC. Both ICBs have for redundancy reasons two PICs controlling the deployment of the antennas and solar panels, which are hot redundant, i.e. both PICs are on in nominal situation. Furthermore, it has to be mentioned that the flight board (FM/430) does not possess a PIC (the on-board computer is not counted as a PIC in this discussion).

For selecting the clock frequencies of the PICs, a choice can be made between two possible frequencies: 32 kHz and 1 MHz. The PICs with the high clock frequency are used on PCBs requiring many calculations, which are evaluated to be the measurement boards and both communication platform. For performing the control of the electrical power input, a PIC clocked at 32 kHz can be used. This will lead to the frequencies given in table C.1 for the single PIC concept and table C.2 for the dual PIC concept.

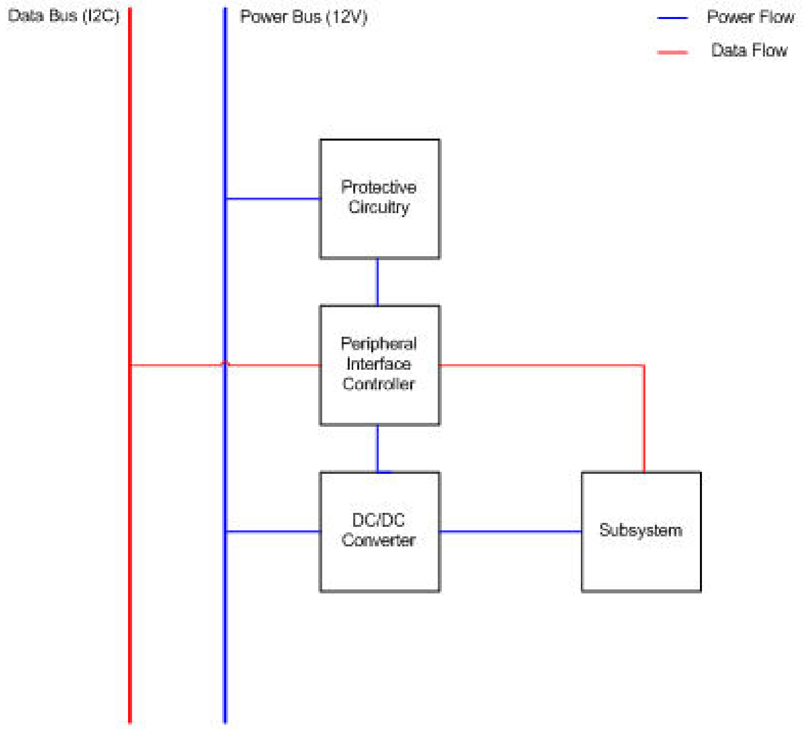
Data Bus (I2C)
Power Bus (12V)
Power Flow
Data Flow
Protective Circuitry
Peripheral Interface Controller
DC/DC Converter
Subsystem

Figure C.3: Schematic representation of the single PIC concept

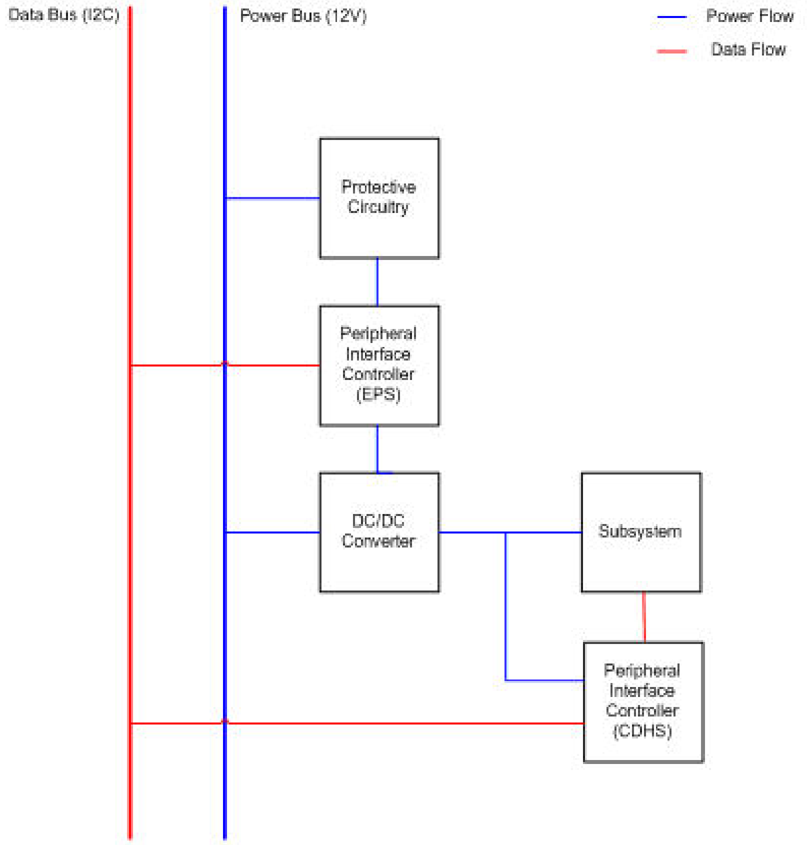
Data Bus (I2C)
Power Bus (12V)
Power Flow
Data Flow
Protective Circuitry
Peripheral Interface Controller (EPS)
DC/DC Converter
Subsystem
Peripheral Interface Controller (CDHS)

Figure C.4: Schematic representation of the dual PIC concept

C.2.4 Surface area

For the evaluation of surface area, it has to be noticed that the dual PIC concept requires more surface area on all PCBs than the single PIC concept. After investigation of the available surface area on every PCB, it was decided that surface area is not a serious driver for determining the concept to be chosen.

Table C.1: Allocation and clock frequency of PICs in single PIC concept

Board reference	Frequency of PIC
Inter Connect Board Z+	32 kHz (2)
Measurement Board Z+	1 MHz
FM/430	-
Combination Board 32	kHz
Radio Amateur Platform	1 MHz (2)
Advanced Transceiver	1 MHz (2)
Electrical Power System Board	32 kHz
Measurement Board Z-	1 MHz
Inter Connect Board Z-	32 kHz (2)

Table C.2: Allocation and clock frequency of PICs in dual PIC concept

Board reference	Frequency of PIC 1	Frequency of PIC 2
Inter Connect Board Z+	32 kHz (2)	32 kHz (2)
Measurement Board Z+	32 kHz	1 MHz
FM/430	-	-
Combination Board	32 kHz	32 kHz
Radio Amateur Platform	32 kHz	1 MHz (2)
Advanced Transceiver	32 kHz	1 MHz (2)
Electrical Power System Board	32 kHz	32 kHz
Measurement Board Z-	32 kHz	1 MHz
Inter Connect Board Z-	32 kHz (2)	32 kHz (2)

C.2.5 Power consumption

Before evaluating the power consumption of the two PIC concepts, it has to be recalled that the power consumption of a PIC is dependent on its clock frequency. Furthermore, the input current of a PIC is dependent on its input voltage. The values of these input currents at various voltages and clock frequencies can be found in the data sheet of the PICs. It is known that the PICs applied in the design are of the type Microchip PIC18F4680. In table C.3, values of the input current for the applied PIC are given at various input voltages and PIC clock frequencies.

Table C.3: Input currents for the Microchip PIC18F4680 at various input voltages and clock frequencies

	Clock frequency = 32 kHz		Clock frequency = 1 MHz	
Input voltage	Typical current	Peak current	Typical current	Peak current
2.0 V	0.02 mA	0.035 mA	0.55 mA	1.1 mA
3.0 V	0.047 mA	0.06 mA	0.9 mA	1.2 mA
5.0 V	0.12 mA	0.17 mA	1.7 mA	2.3 mA

Both peak currents and typical currents are shown in table C.3. For the evaluation of the power consumption, the power consumption at peak current is considered, so only the peak currents are relevant in this discussion.

As can be noticed in table C.3, the nominal input voltage of 3.3V is not shown. To this end, a least squared analysis is performed, which results in a quadratic function of the input current with respect to the input voltage. Evaluating this function at the nominal input voltage of 3.3V leads to the following values of input current (at peak):

$$f_{PIC} = 32\ \text{kHz} \longrightarrow (I_{PIC})_{peak} = 0.0714\ \text{mA} \tag{C.1}$$

$$f_{PIC} = 1\ \text{MHz} \longrightarrow (I_{PIC})_{peak} = 1.2885\ \text{mA} \tag{C.2}$$

In the single PIC concept, the power consumption of the PIC including protective circuitry is calculated by considering the power consumption of the PIC, the Zener diodes, and the resistor bridge. Electrical power is expressed by the simple expression:

$$P = V \cdot I \tag{C.3}$$

Therefore, the complete power usage of the PIC including protective circuitry can be calculated by:

$$P = P_{PIC} + P_{Zener} + P_R = V_{PIC} \cdot I_{PIC} + V_{Zener} \cdot I_{Zener} + V_R \cdot I_R \tag{C.4}$$

In the EPS/CDHS meeting of 15 September 2006, it was mentioned that a single component acting as a Zener consumes 20 μA in current to maintain a voltage of 3.3V. Moreover, it is known that:

$$I_R = I_{PIC} + I_{Zener} \tag{C.5}$$

and:

$$V_R = V_{bus} - V_{PIC} \tag{C.6}$$

Therefore, evaluating the PIC power consumption yields equation C.7 in the case the clock frequency is 32 kHz, and equation C.8 for a clock frequency of 1 MHz.

$$P = 3.3 \cdot 0.0714 + 3.3 \cdot 2 \cdot 0.02 + (12 - 3.3) \cdot (0.0714 + 2 \cdot 0.02) = 1.3368 \text{ mW} \tag{C.7}$$

$$P = 3.3 \cdot 1.2885 + 3.3 \cdot 2 \cdot 0.02 + (12 - 3.3) \cdot (1.2885 + 2 \cdot 0.02) = 15.942 \text{ mW} \tag{C.8}$$

Evaluating the power consumption of all PICs in the system then yields for the single PIC concept, using table C.1:

Table C.4: Combined PIC power consumption in single PIC concept

Board	Power (mW)	Bus current (mA)
ICB Z+	2.6736	0.2228
MeBo Z+	15.942	1.3285
ComBO	1.3368	0.1114
FM 430	0	0
RAP	31.884	2.657
ATRX	31.884	2.657
EPS	1.3368	0.1114
MeBo Z-	15.942	1.3285
ICB Z-	2.6736	0.2228

In the dual PIC concept, all boards are equipped with a PIC clocked at 32 kHz behind the protective circuitry. A PIC having 32 kHz or 1 MHz as clock frequency is placed behind a DC/DC converter. This DC/DC converter has a finite efficiency. This efficiency is a function of the total load current, which is not relevant in this discussion. Therefore, an estimated value of 0.82 is taken as converter efficiency.

$$P_{f_2} = P_{f_1} = 32 \text{ kHz} + \frac{I_{PIC_2} \cdot V_{PIC}}{\eta} \tag{C.9}$$

Implementing these values in the power consumption evaluation leads to a power consumption described by equation C.10 in case the second PIC is clocked at 32 kHz, and equation C.11 for a second PIC clock frequency of 1 MHz.

$$P_{f_2 = 32\text{ kHz}} = 1.3368 + \frac{0.0714 \cdot 3.3}{0.82} = 1.6241 \text{ mW} \tag{C.10}$$

$$P_{f_2 = 1\text{ MHz}} = 1.3368 + \frac{1.2885 \cdot 3.3}{0.82} = 6.5222 \text{ mW} \tag{C.11}$$

Table C.5: Combined PIC power consumption in single PIC concept

Board	Power (mW)	Bus current (mA)
ICB Z+	3.2483	0.2707
MeBo Z+	6.5222	0.5435
ComBO	1.6241	0.1353
FM 430	0	0
RAP	11.708	0.9756
ATRX	11.708	0.9756
EPS	1.6241	0.1353
MeBo Z-	6.5222	0.5435
ICB Z-	3.2483	0.2707

Combining the power consumptions of all PICs in the system yields the situation given in table C.5.

Update

At the time of trade-off, the clock frequency of the bitshaping PICs in both communication platforms was estimated at 1 MHz. After an additional discussion about the actual value, the clock frequency was set to 4.9152 MHz. Rounding this value to 5 MHz, and performing a least squares analysis with the assumption that power increases linearly with clock frequency, yields as power consumption:

$$P_{f_2=5\ \mathrm{MHz}} = \frac{I_{PIC_2} \cdot V_{PIC}}{\eta} = \frac{4.577367 \cdot 3.3}{0.82} = 18.4211\ \mathrm{mW} \tag{C.12}$$

Evaluating the combined power consumption of all PICs in the system, yields for the single PIC concept:

$$P = 182.6\ \mathrm{mW} \tag{C.13}$$

and for the dual PIC concept:

$$P = 72.7\ \mathrm{mW} \tag{C.14}$$

As can be noticed the difference in power consumption between the two concepts becomes even more distinct by using a bitshaping PIC with a higher clock frequency.

C.2.6 Software implementation

In general, two software packages are of relevance for the PICs under discussion. One package is used for the control of the electrical power input of the subsystem, while the other package is used for data processing and interaction with the data bus.

In principle, it is possible to combine the two software packages into one package and to plug this package into one PIC. It would probably involve several additional lines of code, but this should pose no problem. An advantage of having one PIC controlling all operations on a board is that only one address is needed. However, having two PICs with two separate addresses does not involve any problems either.

C.2.7 Final words

As no real distinction between the two concepts can be made with respect to the criteria of surface area and software implementation, the only criterion remaining is power consumption. Taking a quick glance at tables C.4 and C.5, it is easily seen that the dual PIC concept is preferred over the single PIC concept in terms of power. Therefore, it is decided to implement the dual PIC concept on every printed circuit board.

C.3 Conclusions and recommendations

After performing a trade-off between the single PIC concept and the dual PIC concept, the dual PIC concept is chosen to be implemented on all printed circuit board in the stack. The deciding criterion in this trade-off is the power consumption, which amounted to a factor two difference.

Appendix D

DC3-TN-703-104
Oscillator switch of local EPS PIC

D.1 Introduction

For a successful deployment sequence, the clock frequencies of the various deployment PICs have to run synchronously. Furthermore, synchronous internal clocks are important to all PICs for a successful OBM mode. During preliminary tests, it was noticed that a discrepancy was present in the clock frequencies of the deployment PICs. This deviation was contributed to use of the inaccurate INTRC oscillator. A switch to the INTOSC oscillator was inevitable in order to synchronize the PIC microcontrollers. This switch in oscillator configuration would also result in a design change in the power supply circuitry in order to have the PICs operating properly.

In this document, the analysis of the problem with the non-synchronicity in the PIC clock frequencies is described. Firstly, the problem is laid down and the implemented solution of switching to the INTOSC oscillator is presented. Furthermore, the additional current consumption is mentioned and the needed design change in the power supply circuitry is illustrated.

D.2 Oscillator switch of local EPS PIC

During initial tests on the interconnect board, it was perceived that the clock frequencies of the two deployment PICs were not running synchronous. This was noticed due to the fact that the burning sequence controlled by one PIC was not occurring simultaneously with the sequence controlled by the other PIC. This phenomenon was considered odd, because the software programmed in the two microcontrollers was exactly equal. Investigation of the clock frequencies has exposed a serious deviation.

Measurements showed that the clocks of the two PICs were both running faster than the specified value. The measured frequencies are:

- U_1: 35.7 kHz
- U_2: 34.2 kHz

However, the nominal value is equal to 31.25 kHz.

The clock frequencies on both PICs are controlled by an RC circuit, which acts as oscillator (INTRC). After several attempts on tuning this oscillator, it was found that tuning the INTRC oscillator is impossible. Therefore, the decision was made to switch the oscillator on all local EPS PICs (including deployment PICs and the EPS measurement PIC) to the INTOSC oscillator, which is an on-chip unidentified oscillating object.

Preliminary measurements on the deployment PICs operating on 31.25 kHz with the INTOSC oscillator shows excellent behaviour of the clock frequency. However, the current consumption of the PIC microcontroller increased and resulted in a drop in supply voltage. In order to prevent this voltage drop from occurring, the supply circuitry has to be adapted. To be able to produce a proper design, the actual increase in current consumption has to be measured.

Current measurements are performed by building a set-up, which represents the equivalent circuit displayed in figure D.1. Tests were performed on the test version of the combination board.

In the set-up of figure D.1, a 3.3V power source is directly connected to the supply line to the PIC. A current meter is placed in series to measure the amount of current flowing into the circuit. Careful

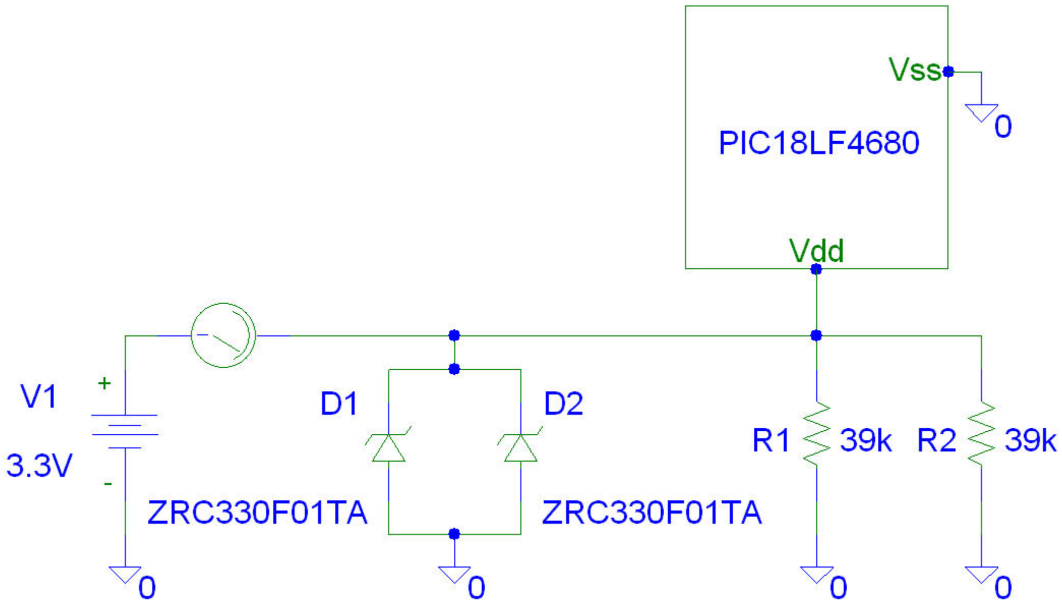

Figure D.1: Equivalent electrical circuit for measurement of PIC current consumption

attention had to be paid to avoid exceeding 3.3V, because the voltage references on the circuit consume a gigantic amount of current in that situation.

In table D.1, the current consumption of the PIC and its surrounding circuitry at various oscillator oscillations is shown.

Table D.1: PIC current (including adjacent circuitry) consumption at various oscillator configurations

Oscillator type	Nominal clock frequency	Current consumption (μA)
INTRC	31.25 kHz	417
INTOSC	31.25 kHz	594
INTOSC	125 kHz	638

Looking at table D.1, it is noticed that three configurations were investigated. Use of the INTRC oscillator at 31.25 kHz nominal clock frequency is the current configuration, which resulted in the synchronizing problems. With the INTOSC oscillator applied at 31.25 kHz, the synchronizing problems disappeared, leading to the conclusion that this configuration is most desirable. As the CDHS department wanted the possibility of having the INTOSC oscillator at 125 kHz investigated, this configuration is included for purposes of completeness.

Comparing the various test cases, it is noticed that the only variable is the oscillator configuration. As the deviation in current consumption has to originate from the change in oscillator settings, the extra parallel resistance required to supply the additional current for the INTOSC oscillator can be calculated. Calculation of this extra resistance can be performed by using the following expression:

$$R_2 = \frac{V_{bus} - V_{PIC}}{I_{INTOSC} - I_{INTRC}} = \frac{12 - 3.3}{594 \cdot 10^{-6} - 417 \cdot 10^{-6}} = 49152.5\ \Omega \tag{D.1}$$

For determining the substitute resistance needed for supplying the PIC microcontroller sufficient current to operate on the INTOSC oscillator, the following expression will be applied:

$$R_{sub} = \frac{R_1 \cdot R_2}{R_1 + R_2} \tag{D.2}$$

Substituting values yields:

$$R_{sub} = \frac{18000 \cdot 49152.5}{18000 + 49152.5} = 13175.2\ \Omega \tag{D.3}$$

This calculated value has to be rounded to the nearest value in the E96 series. After all, resistor components are only available in particular values. Therefore, the value of the substitute resistance will be set to 13 kΩ.

As a final issue, the power consumption of the PIC microcontroller will be discussed. Firstly, calculate the power consumption of the PIC in case it uses the INTRC oscillator using the following expression:

$$P_{INTRC} = \frac{V_{bus} - V_{PIC}}{R_1} \cdot V_{bus} = \frac{12 - 3.3}{18000} \cdot 12 = 5.8 \cdot 10^{-3} \text{ W} \tag{D.4}$$

In comparison, the power consumption of the PIC in the situation it is operating with the INTOSC oscillator is equal to:

$$P_{INTOSC} = \frac{V_{bus} - V_{PIC}}{R_{sub}} \cdot V_{bus} = \frac{12 - 3.3}{13000} \cdot 12 = 8.03 \cdot 10^{-3} \text{ W} \tag{D.5}$$

Next, the additional power needed to facilitate the use of the INTOSC oscillator can be calculated. As the number of PICs needing a swap in oscillator amount to 10, the following expression can be written:

$$\Delta P = n \cdot (P_{INTOSC} - P_{INTRC}) = 10 \cdot 8.03 \cdot 10^{-3} - 5.8 \cdot 10^{-3} = 22.3 \cdot 10^{-3} \text{ W} \tag{D.6}$$

This additional power consumption of 22.3 mW has to be incorporated in the power budget.

D.3 Conclusions and recommendations

In order to have the clock frequencies of the various local EPS PICs running synchronously, the oscillator on the PICs have to be changed from INTRC to INTOSC mode. Changing oscillators resulted in a more accurate clock frequency of the PIC microcontrollers. However, current consumption of the PICs increased, forcing a change in the resistor bridge in the supply circuitry.

After measurement, it was found that the current consumption increased by 177 μA per PIC microcontroller. Analysis leads to the event of changing the resistors in the supply circuitry from 18 kΩ to 13 kΩ. An overall increase in power consumption of 22.3 mW is expected.

Appendix E

DC3-TN-701-087
Simultaneous energizing of two burning resistors

E.1 Introduction

In order to deploy the various appendages on the Delfi-C3 spacecraft, resistors are applied to burn the wires holding the appendages in a stowed position. In nominal operations, the switch-on of these resistors is governed by the on-board computer. However, in degraded operations (OBC or I2C data bus is malfunctioning), the PIC microcontrollers present on every interconnection board have to decide for themselves at what moment a particular resistor has to commence burning. Timers are implemented in order to determine these moments. As the managing of the complete set of resistors is divided over four PIC microcontrollers, several issues are possible to occur.

The foremost of these issues is an asynchronicity in timers on the various PICs. After all, such asynchronicity could lead to an overlap in burn sequences, which leads to simultaneous burning of resistors. The current baseline is that the PIC microcontrollers incorporate an extra time in their timing sequence to take the asynchronicity into account. However, this is highly ineffective and will lead to long times, during which Delfi-C3 is inoperable.

In this document, an investigation is presented of the effect of simultaneous burning of two resistors on the system bus voltage. Furthermore, an evaluation is given whether this effect will lead to a complete black-out of the spacecraft.

E.2 Simultaneous energizing of two burning resistors

In order to determine the performance of the electrical system in case two resistors are burning simultaneously, the resistance value of a single branch of the burning circuitry has to be calculated. A single branch consists of two FDN360P FETs, two IRF7503PBF FETs and a single 75 Ω resistor in series. The on-resistance of the semiconductor components is shown in table E.1.

Table E.1: On-resistance values of applied semiconductor components

Component	On-resistance (Ω)
FDN360P	0.08
IRF7503PBF	0.222

For the 75 Ω resistor, a tolerance is demanded of 1%. Furthermore, the temperature coefficient of the resistor is found to be equal to 50 ppm.K^{-1}. The temperature envelope of the resistor is set equal to −45 °C to 80 °C . In this case, the minimum possible resistance is found to be:

$$R_{min} = (1-\lambda\cdot(T_{nom}-T_{min}))\cdot(1-\delta)\cdot R_{nom} = \left(1-50\cdot10^{-6}\cdot(28+45)\right)\cdot(1-0.01)\cdot 75 = 73.98\ \Omega \quad (E.1)$$

In this situation, the substitute resistance of the complete branch is expressed by:

$$R_{sub} = 2\cdot R_{FDN360} + 2\cdot R_{IRF7503} + R_{min} = 2\cdot 0.08 + 2\cdot 0.222 + 73.98 = 74.6\ \Omega \quad (E.2)$$

During deployment, several subsystems in the spacecraft are active. These are the communications receivers, the on-board computer and all local EPS microcontrollers. The power consumption of these components can be retrieved from the power budget and is shown in table E.2.

Table E.2: Power consumption of energized subsystems in deployment mode

Component	Power (mW)
Local EPS PICs (#10)	27.3
FM/430	118.2
RAP Rx	118.55
ATRX Rx	118.55
Total	382.6

Furthermore, after investigating the power budget it is noticed that the minimum incoming power at the solar arrays is equal to 3.0 W. This will lead to 2580 mW on the system power bus after taking EPS conversion efficiency, diode voltage drops, and wiring losses into account.

For use on resistors, the remaining power is then equal to:

$$P_R = P_{gen} - \sum P_{fix} = 2580 - 382.6 = 2197.4 \text{ mW} \tag{E.3}$$

In general, the electrical power needed to energize a single branch of burning resistors is calculated by:

$$P = \frac{V_{bus}^2}{R_{sub}} \tag{E.4}$$

For two simultaneous energized branches in parallel, this becomes:

$$P = 2 \cdot \frac{V_{bus}^2}{R_{sub}} \tag{E.5}$$

Substituting values and solving for the bus voltage then results in:

$$V_{bus} = \sqrt{\frac{P \cdot R_{sub}}{2}} = \sqrt{\frac{2.1974 \cdot 74.6}{2}} \approx 9.05 \text{ V} \tag{E.6}$$

With this value of the bus voltage, the power at the resistor is equal to:

$$P_R = I^2 \cdot R_{min} = \left(\frac{V_{bus}}{R_{sub}}\right)^2 \cdot R_{min} = \left(\frac{9.05}{74.6}\right)^2 \cdot 73.98 \approx 1.089 \text{ W} \tag{E.7}$$

Previously, FH conducted an analysis of the PIC supply voltage for varying values of the system bus voltage. In figure E.1, the results of this analysis are shown.

After consulting with GA, it is determined that every local EPS PIC is equipped with a so-called brown-out voltage. This peripheral is used to protect the PIC from under-voltages. In general, this will lead to the situation that a PIC will not function until the supply voltage is equal to or higher than the brown-out voltage. The value of this brown-out voltage is equal to 2.6V.

Identifying the accompanying bus voltage in figure E.1, it is noticed that the critical bus voltage in order to let all the local EPS PICs function is approximately 8.0V. Recalling that the bus voltage in case of simultaneous burning of two resistors is equal to 9.05V, it is seen that this value is higher than the critical value. Therefore, the local EPS PICs will not shut down in case the bus voltage drops down to 9.05V.

Shutdown of the on-board computer or communications receivers is not an issue, as these are supplied by local DC/DC converters, which convert the bus voltage down to the required board voltage. These converters are capable of operating at a bus voltage of 8.0V.

Note that the power consumption of the PICs will change due to a drop in supply voltage. Furthermore, the efficiency of the DC/DC converters will rise due to the smaller input voltage. Therefore, additional power is available for powering the burning resistors. This will lead to a slightly higher value of the bus voltage with respect to the calculated value.

Power consumption of a single resistor is decreased significantly in case of simultaneous burning. Therefore, it is not recommended to incorporate simultaneous burning on purpose, as it is highly probable that the power consumption is too low to attain the required resistor temperature.

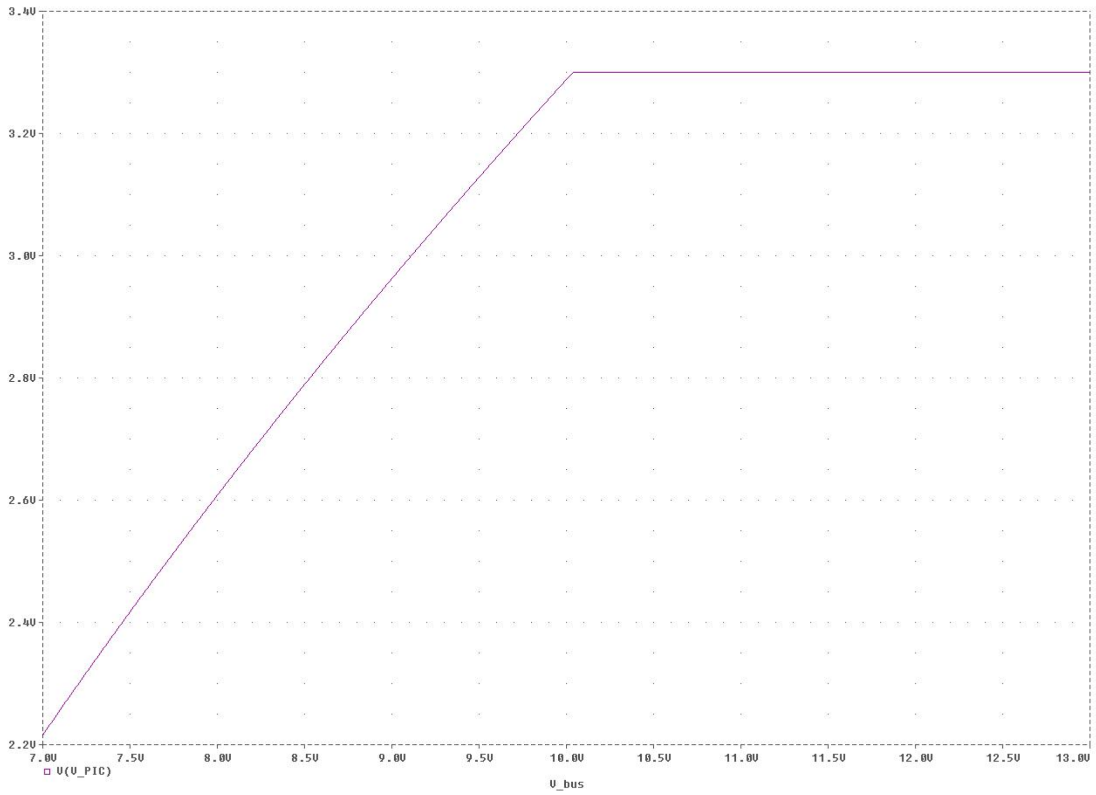

Figure E.1: PIC supply voltage as a function of system bus voltage

E.3 Conclusions and recommendations

In the previous section, an analysis is performed in order to evaluate the behaviour of the system power bus in case two burning resistors are energized simultaneously. It is found that this situation will not lead to shut-down of the system. Therefore, simultaneous burning of two resistors will not lead to a collapse of the system.

Appendix F

DC3-TN-702-095
External power supply for ICD2 programmer

F.1 Introduction

For various tasks in the Delfi-C3 spacecraft, PIC microcontrollers are applied. These microcontrollers are dependent on dedicated software, which has to be programmed in the relevant PICs. In order to program the PIC microcontrollers on the various printed circuit boards, an ICD2 programmer is applied.
In general, the required power for the ICD2 programmer is sourced by the target circuitry. In case of the local EPS PICs and the deployment PICs, it is found that the required current cannot be provided by the power supply of the PIC microcontroller. Therefore, an additional power supply has to be used to energize the ICD2 programmer.
In this document, the power deficiency problem during programming of the local EPS PICs and the deployment PICs is identified. Furthermore, various possible solutions are presented, and the final solution is briefly explained.

F.2 External power supply for ICD2 programmer

On the various printed circuit boards, a dedicated power supply is present to energize the local EPS PICs. This power supply is also applied for the deployment PICs on the ICB boards. With help of this power supply, the 12V bus voltage is converted down to the 3.3V PIC supply voltage. This transition is accomplished with help of resistors. However due to these resistors, the provided current is limited in magnitude. The maximum value for the magnitude of this current delivered by the PIC power supply is calculated with:

$$I_{del} = \frac{V_{bus} - V_{PIC}}{R} = \frac{12 - 3.3}{39 \cdot 10^3} \approx 0.223077 \text{ mA} \tag{F.1}$$

Several components on the printed circuit boards are supplied with power with help of this power supply. After all, the primary function of this power supply is to provide current to these components. In table F.1, a list of the supplied components is given alongside their respective current consumptions.
Therefore, the magnitude of the unassigned current is equal to:

$$\Delta I = I_{del} - I_{req} = 0.223077 - 0.184954 = 0.038123 \text{ mA} \tag{F.2}$$

In nominal operations, this does not pose a problem as the residual current is sunk in the voltage references. However, during programming of the local EPS PICs and deployment PICs, additional current is needed. This is caused by the fact that the ICD2 programmer, which is used for programming the PICs, is energized from the target circuitry. During preliminary measurements of this current consumption performed by MF, it was found that at maximum 0.2 mA is required by the ICD2 programmer.
As the required current is larger than the maximum excess current, it can be concluded that an external power supply is needed to energize the ICD2 programmer successfully. After all, a brief analysis performed by FH yielded the result that in case no additional measures are taken, the PIC supply voltage would

Table F.1: List of electronic components supplied with power by the PIC power supply

Component	Required current (mA)
PIC Microcontroller @ 32 kHz	0.0714
Watchdog timer	0.012889
Brownout reset	0.0503
Oscillator	0.008365
Analog-to-digital converter	0.002
Voltage reference #1	0.02
Voltage reference #2	0.02
Total I_{req}	0.184954

drop to 0.53V in contrast to the nominal value of 3.3V. This is no option to consider as the brownout voltage of the PICs is equal to 2.6V, which would lead to powering down of the PICs if the supply voltage would only amount to 0.53V.
A plot of this analysis is shown in figure F.1.

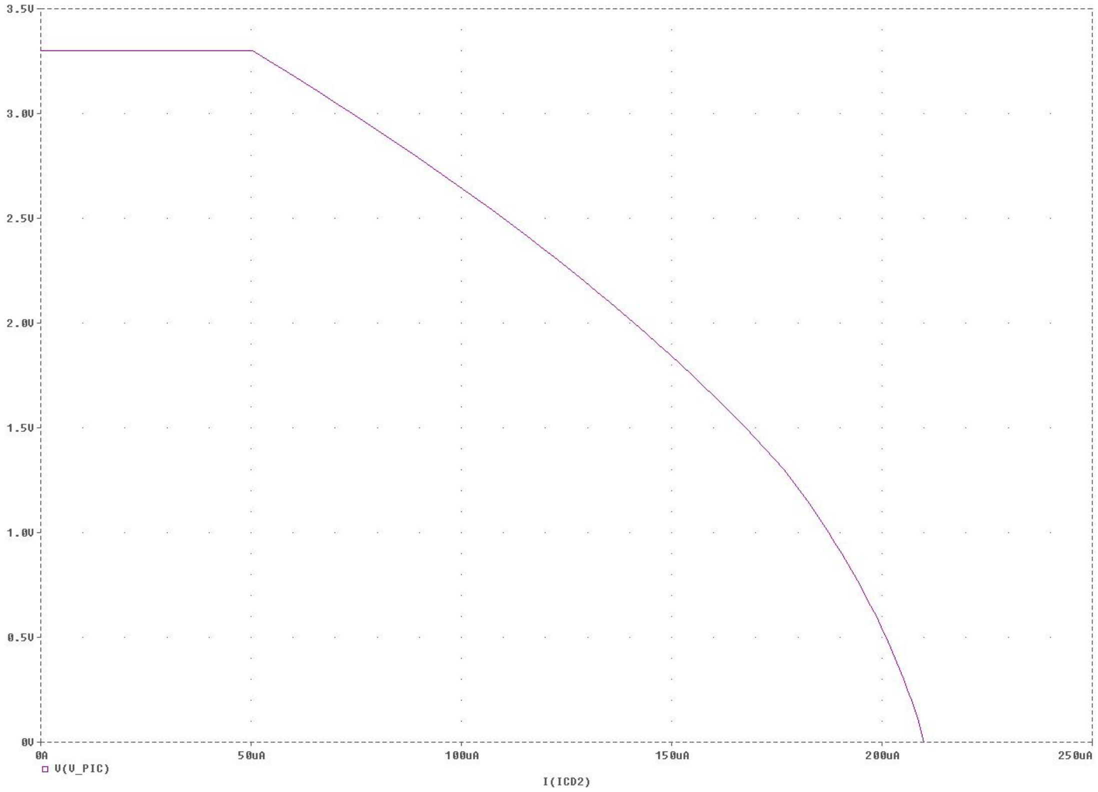

Figure F.1: Analysis of influence of ICD2 current on PIC input voltage

To counteract this power deficiency problem, two main solutions exist.

- Connect a 3.3V external power supply directly to the supply line of the local EPS PIC

  In this configuration, an external power supply is connected to the supply line of the local EPS PIC. This power supply is set to deliver electrical power at a voltage of 3.3V. This means that the additional current is sourced by this external power supply, during which the input voltage of the EPS PIC remains at a constant value of 3.3V.

  However, a major disadvantage accompanies this solution. As the PIC supply voltage is clamped by the 3.3V power supply, in case this voltage is set slightly higher than 3.3V the voltage references will start to consume tremendous amounts of power. Therefore, this magnitude of 3.3V has to be set very accurately. Furthermore, an additional power supply is needed as the 12V bus power and the 3.3V external programming power cannot be simultaneously by a single power supply.

  A sketch of this solution is shown in figure F.2.

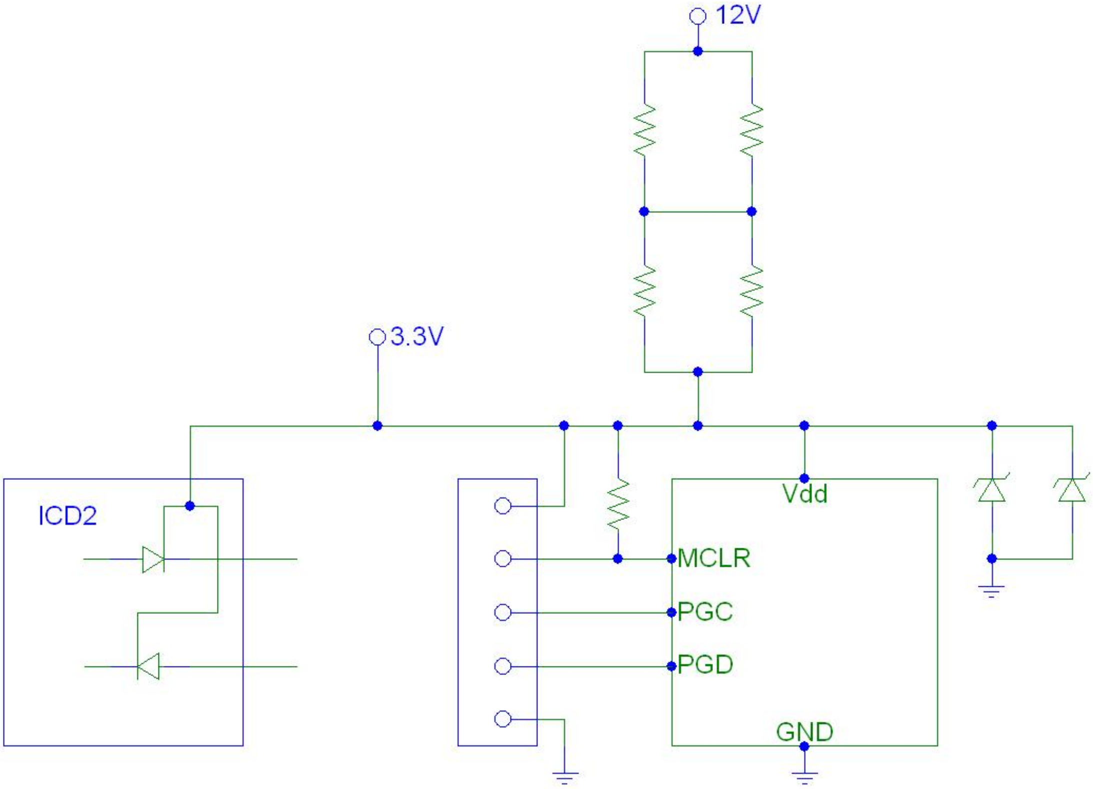

Figure F.2: Solution #1: Connecting a 3.3V power supply to the ICD2 power line

- Connect a 12V external power supply via a resistor to the supply line of the local EPS PIC

  In this configuration, an additional 12V power supply is attached to the ICD2 power line with help of a resistor. As the ICD2 power line is at the same voltage as the voltage references, the value of the PIC supply voltage is 3.3V. The additional required current for the ICD2 programmer is provided by the extra power supply, while the current for the PIC, its peripherals and the voltage references is supplied by the original power supply.

  A resistor ensures that the 12V output voltage of the extra power supply is converted down to the PIC supply voltage of 3.3V. The resistance value can be expressed by:

$$R_{conn} = \frac{V_{bus} - V_{PIC}}{I_{ICD2}} = \frac{12 - 3.3}{200 \cdot 10^{-6}} = 43.5 \cdot 10^3\ \Omega \tag{F.3}$$

  Due to availability of resistors, this value is decreased to 43 kΩ. This poses no problem, as the additional flowing current is sunk in the voltage references. The same scenario applies in case the external power supply is connected and no programming takes place: all additional current is sunk in the voltage references.

  An advantage of this solution is that the input voltage is directly determined by the on-board voltage references instead of the external power supply. Furthermore, a slight fluctuation in the voltage of the external power supply will not lead to a gigantic current consumption of the voltage references. It is even possible to connect the input node of the external power supply and the input node of the power bus in parallel to the positive terminal of a single power supply. After all, both nodes are set at 12V.

  A sketch of this configuration is shown in figure F.3.

A dedicated connector has been manufactured by FH and BV, which is to be used during programming of the local EPS PICs and the deployment PICs. This connector has three terminals:

- Connection to the printed circuit board;

- Connection to the ICD2 programmer;

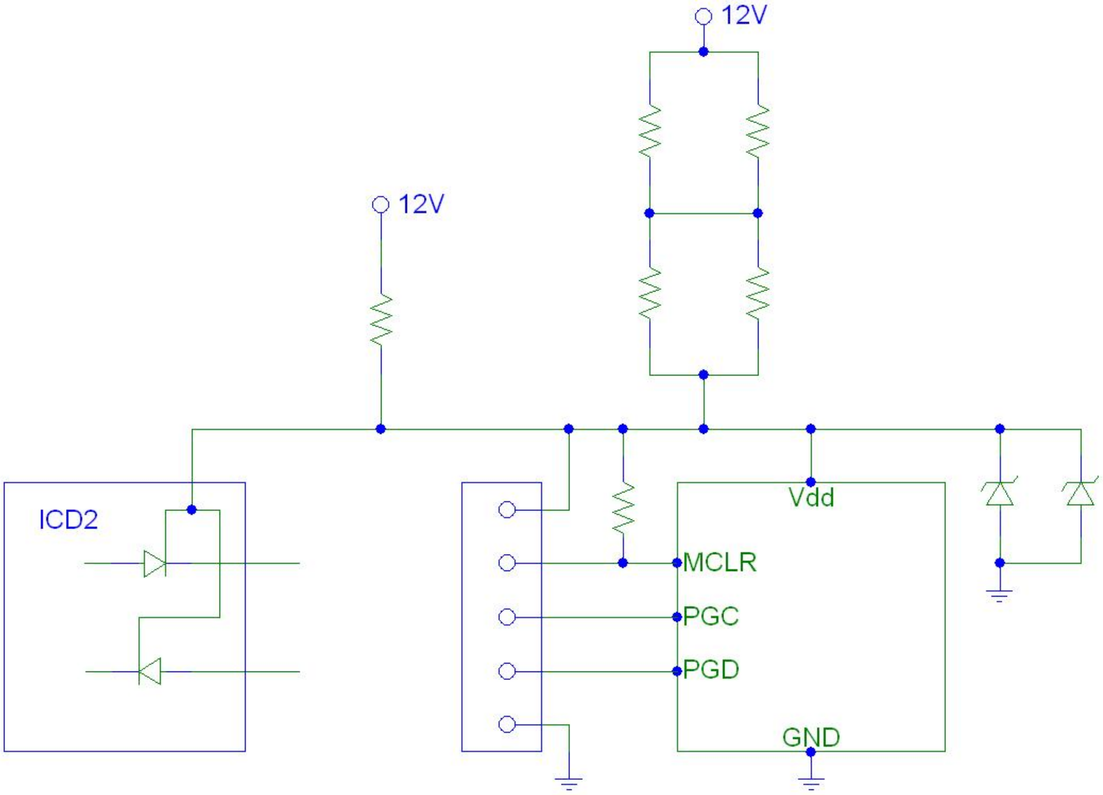

Figure F.3: Solution #2: Connecting a 12V power supply to the ICD2 power line

- Connection to the 12V DC power supply.

In order to evade possible failure to insert the resistor in the ICD2 powering circuitry, this resistor has been integrated in the connector. Therefore, no additional resistor is required for providing power to the ICD2 programmer.
In figure F.4, a picture of the customized connector is shown.

F.3 Conclusions and recommendations

In order to provide sufficient power to the ICD2 programmer during programming of the local EPS PICs and the deployment PICs an additional power supply is applied. This power supply is set to output 12V DC. Furthermore, a customized connector is manufactured which has to be inserted between the relevant printed circuit board and the ICD2 programmer. The third terminal is connected to the positive terminal of the extra 12V DC power supply.
Note that this set-up is only necessary for the local EPS PICs and the deployment PICs. For the various data PICs and the bitshaping PICs no extra precautions have to be taken.

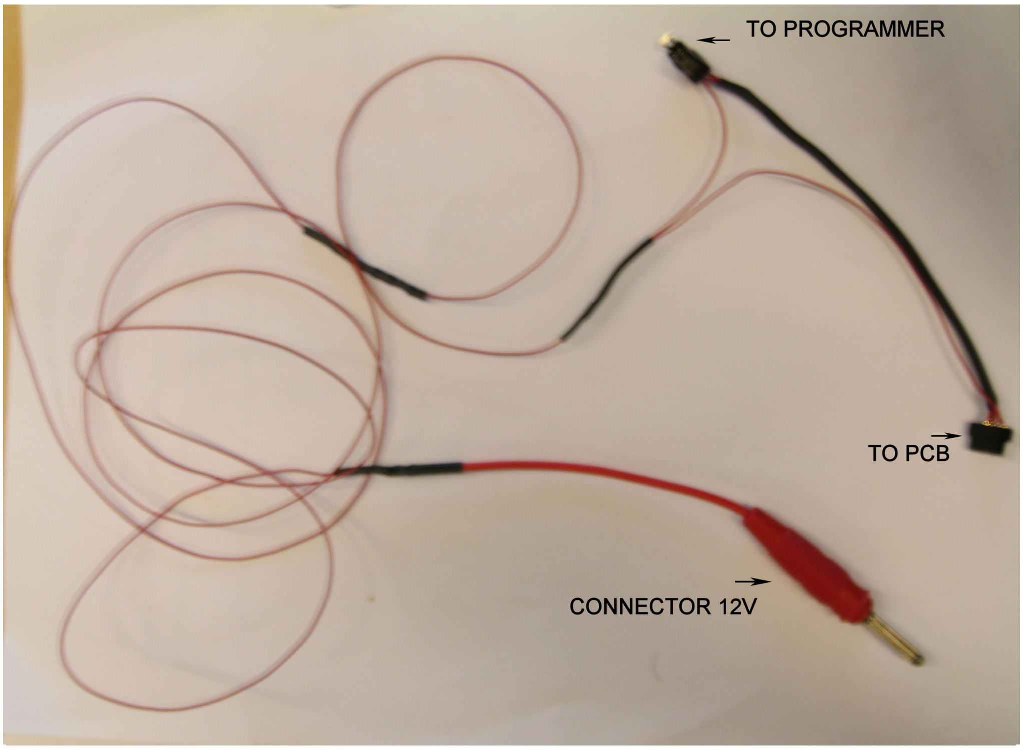
TO PROGRAMMER
TO PCB
CONNECTOR 12V

Figure F.4: Customized connector for providing power to the ICD2 programmer

Appendix G

DC3-TN-703-103 Step-Down DC/DC Converter Operations

G.1 Introduction

In a general electronic system, the involved components are operating on several different voltages. As the power supply is operating on a single input voltage, it is necessary to apply voltage regulators for producing the various voltages. An efficient way of converting a high DC voltage down to a lower DC voltage is a so-called step-down DC/DC converter or buck converter. This converter is part of the switching shunt regulator family, by applying an electronic switch to transfer power from the high voltage side to the low voltage side. In fact, this type of converter has a higher conversion efficiency with respect to dissipative converters, e.g. LDOs.

In the Delfi-C3 spacecraft, several step-down DC/DC converters are implemented. After all, the power bus operates on 12V DC, while the various printed circuit boards require voltages of 3.3V DC, 5V DC and -1.25V DC. In order to create some insight into the electrical behaviour of the electrical power system in the spacecraft, the operational characteristics of the step-down DC/DC converter have to be analyzed [6] [5].

In this document, the characteristics of a step-down DC/DC converter are explained. In section G.2.1, the electrical circuit of a step-down converter is briefly described. Operational characteristics for a converter in continuous operation are shown in section G.2.2, while the characteristics for a converter in discontinuous operation are given in section G.2.3. In section G.2.4, dissipation losses due to non-ideality of components are treated. The ripple on the converter output voltage is treated in section G.2.5.

G.2 Operational characteristics of step-down DC/DC converter

G.2.1 Electronic topology of step-down DC/DC converter

To commence the analysis of the operational characteristics of a step-down DC/DC converter, the electrical circuit of this converter has to be known. In figure G.1, the equivalent electrical circuit of a general step-down DC/DC converter is shown. By investigating figure G.1, two situations can be distinguished in the converter, which have to do with the state of the MOSFET switch M_1. After all, the converter will act differently whether M_1 is closed or open. During the initial analysis of the converter, all components are assumed ideal, i.e. no parasitic dissipation losses are generated.

In case the switch M_1 is closed, the inductor voltage V_L is equal to V_{in} minus the output voltage V_{out}. More accurately, the voltage drop over M_1 has to be taken into account, too. This latter quantity is set to zero, as M_1 is assumed ideal. Hence with M_1 closed, V_L equals $V_{in} - V_{out}$.

In this situation, the current is supplied by the power supply connected to V_{in}. It is flowing through M_1 and L_1 into capacitor C_1 and the load connected to V_{out}. Connecting the negative terminals of V_{in} and V_{out} ensures completion of the electrical circuit.

When the switch M_1 is opened, the inductor voltage V_L is equal to $-V_{out}$. In principle, the voltage drop over the freewheeling diode D_1 has to be subtracted. This latter quantity equals to zero, as D_1 is assumed ideal. Hence with M_1 opened, V_L equals $-V_{out}$.

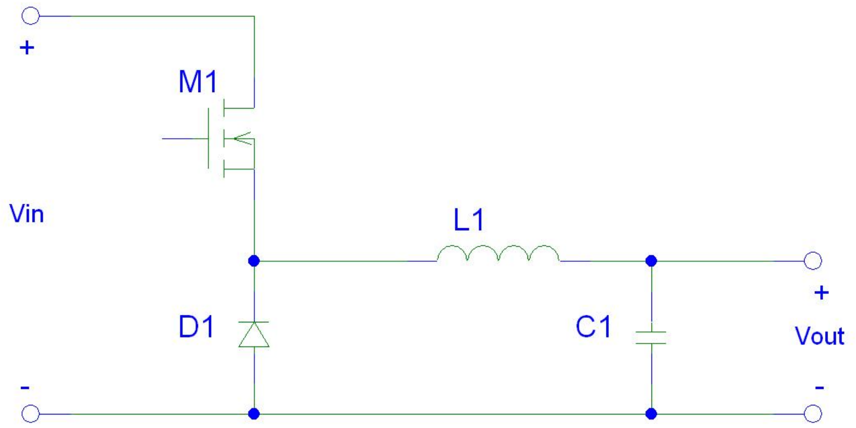

Figure G.1: Equivalent electrical circuit of a step-down DC/DC converter

As a result of the switched-on state of M_1, current is flowing through L_1, which cannot be interrupted instantaneously due to the nature of the inductor. Therefore, the current has to be supplied by C_1 and flows into the load connected to V_{out}. Furthermore, another current flow goes through L_1 with the current loop completed by the freewheeling diode D_1.

For steady-state operation, the integrated inductor voltage over a single switching period of MOSFET switch M_1 should be equal to zero. Therefore:

$$\int_{\tau=t}^{t+T} V_L \cdot \mathrm{d}\tau = 0 \tag{G.1}$$

where T is the time of a single switching period, and is defined by

$$T = \frac{1}{f} \tag{G.2}$$

where f is the switching frequency of switch M_1.

A step-down DC/DC converter can function in two different modes of operandi. These can be described as:

- Continuous operation
- Discontinuous operation

In continuous operation, the inductor current is always positive in magnitude. This means that current is continuously flowing through the inductor.

This is in contrast to discontinuous operation, in which the inductor current will be equal to zero during part of a single switching period. This means that the current is interrupted during converter operation. In the following sections, these two distinct operational modes will be described.

G.2.2 Lossless continuous operation

In continuous operation, the current through inductor L_1 always has a positive value. In steady-state conditions, inductor L_1 has to comply with equation G.1, which can be written for a converter in continuous operation as:

$$(V_{in} - V_{out}) \cdot T_{on} - V_{out} \cdot T_{off} = 0 \tag{G.3}$$

where V_{in} is the converter input voltage, V_{out} is the converter output voltage, T_{on} is the time in a single switching period, during which switch M_1 is closed, and T_{off} is the time in a single switching period, during which M_1 is open.

The duty cycle of the MOSFET switch M_1 is defined as:

$$\delta = \frac{T_{on}}{T_{off}} \tag{G.4}$$

Substituting this expression into equation G.3 leads to:

$$(V_{in} - V_{out}) \cdot \delta - V_{out} \cdot (1 - \delta) = 0 \tag{G.5}$$

Cleaning up this equation results in:

$$V_{in} \cdot \delta = V_{out} \tag{G.6}$$

Solving for duty cycle δ leads to:

$$\delta = \frac{V_{in}}{V_{out}} \tag{G.7}$$

As an additional expression, the power balance of the DC/DC converter can be investigated. Because an ideal converter is considered, which does not introduce any dissipation losses, the input power has to be equal to the output power. Therefore, the power balance is written as:

$$P_{in} = P_{out} \tag{G.8}$$

By introducing the definition of the effective value of power, the following equation, which is representative of equation G.8, can be written:

$$\frac{1}{T} \cdot \int_{\tau=t}^{t+T} v_{in} i_{in} \cdot \mathrm{d}\tau = \frac{1}{T} \cdot \int_{\tau=t}^{t+T} v_{out} i_{out} \cdot \mathrm{d}\tau \tag{G.9}$$

where v_{in} is the instantaneous input voltage, i_{in} is the instantaneous input current, v_{out} is the instantaneous output voltage, and i_{out} is the instantaneous output current of the converter. The instantaneous input voltage v_{in} is constant and can be extracted form the integral. Furthermore, the load is constant, which results in a constant output power.

Therefore:

$$V_{in} \cdot \frac{1}{T} \cdot \int_{\tau=t}^{t+T} i_{in} \cdot \mathrm{d}\tau = V_{out} \cdot I_{out} \tag{G.10}$$

By dividing the integral into two parts, with one part representing the on-state of switch M_1 and the other the off-state of M_1, equation G.10 becomes:

$$V_{in} \cdot \frac{1}{T} \cdot \left(\int_{\tau=t}^{t+T_{on}} \left(I_{min} + (I_{max} - I_{min}) \cdot \frac{\tau - t}{T_{on}} \right) \mathrm{d}\tau + \int_{\tau=t+T_{on}}^{t+T} 0 \cdot \mathrm{d}\tau \right) = V_{out} \cdot I_{out} \tag{G.11}$$

where I_{max} is the maximum attainable inductor current, and I_{min} is the minimum attainable inductor current in a single switching period of switch M_1.

Evaluating the integral leads to:

$$V_{in} \cdot \frac{1}{T} \cdot \left(I_{min} + \frac{1}{2} \cdot (I_{max} - I_{min}) \cdot T_{on} \right) = V_{out} \cdot I_{out} \tag{G.12}$$

Substituting duty cycle δ and cleaning up the expression yields:

$$V_{in} \cdot \delta \cdot \frac{1}{2} \cdot (I_{max} + I_{min}) = V_{out} \cdot I_{out} \tag{G.13}$$

Applying the definition of δ given in equation G.7 yields:

$$V_{in} \cdot \frac{V_{out}}{V_{in}} \cdot \frac{1}{2} \cdot (I_{max} + I_{min}) = V_{out} \cdot I_{out} \tag{G.14}$$

Solving for output current I_{out} yields:

$$I_{out} = \frac{1}{2} \cdot (I_{max} + I_{min}) \tag{G.15}$$

For evaluating the maximum current flowing through the inductor, use is made of the general expression governing inductor voltage and inductor current:

$$v_L = L \cdot \frac{\mathrm{d}i_L}{\mathrm{d}t} \tag{G.16}$$

Evaluating this expression during the period that switch M_1 is in on-state yields:

$$I_{max} = I_{min} + \frac{(V_L)_{on}}{L} \cdot T_{on} \tag{G.17}$$

Rewriting and introducing the duty cycle δ results in:

$$I_{max} = I_{min} + \frac{(V_L)_{on}}{L} \cdot \frac{T_{on}}{T} \cdot T = I_{min} + \frac{V_{in} - V_{out}}{L} \cdot \frac{\delta}{f} \tag{G.18}$$

Substituting the definition of δ:

$$I_{max} = I_{min} + \frac{V_{in} - V_{out}}{L} \cdot \frac{1}{f} \cdot \frac{V_{out}}{V_{in}} \tag{G.19}$$

Substituting this expression into equation G.14 yields:

$$V_{in} \cdot \delta \cdot \left(I_{min} + \frac{1}{2} \cdot \frac{V_{in} - V_{out}}{L} \cdot \frac{1}{f} \cdot \delta \right) = V_{out} \cdot I_{out} \tag{G.20}$$

In figure G.2, the waveform showing the inductor voltage for an example converter in steady-state continuous operation is given. The magnitude of the input voltage is taken to be equal to 12V, while the value of the output voltage equals 3.3V. Switching frequency f is set to 10 kHz.

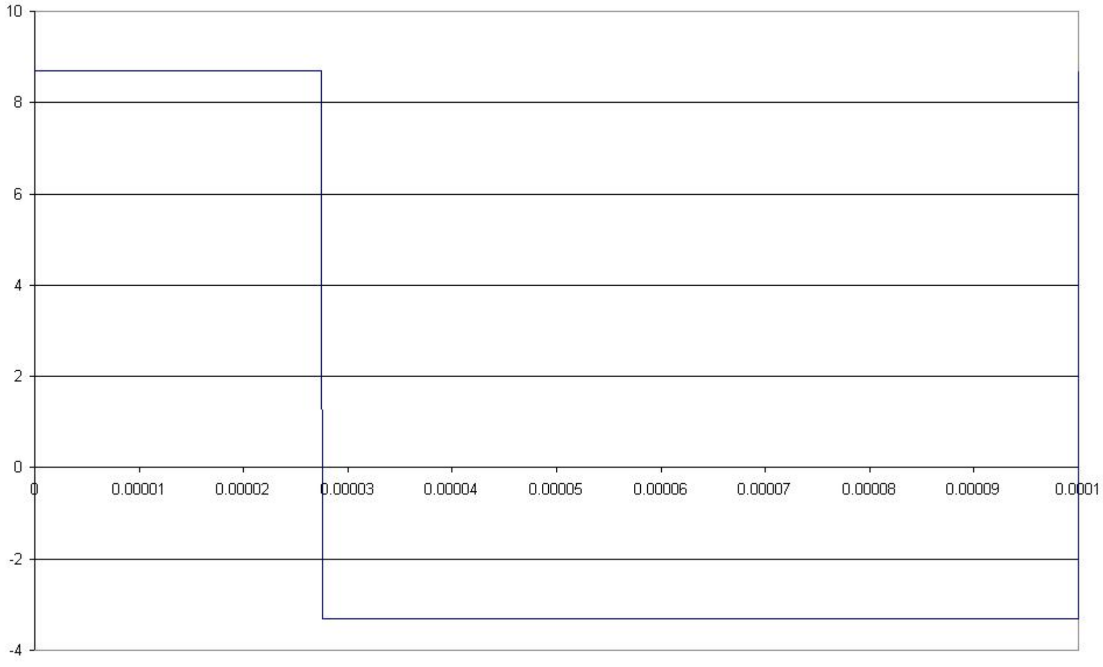

Figure G.2: Inductor voltage in continuous operation

By assuming a minimum current of 1A flowing through the inductor, the waveform for the inductor current can be created as shown in figure G.3. In the corresponding calculation, the value of the inductor L_1 was set to 500 μH.
As during the period switch M_1 is closed, the inductor current has to be generated by the power supply, the input current is represented by the waveform shown in figure G.4.

G.2.3 Lossless discontinuous operation

In discontinuous mode, the current flowing through the inductor is not non-zero for a complete single switching period, i.e. during part of the switching period, the current will be equal to zero. Therefore,

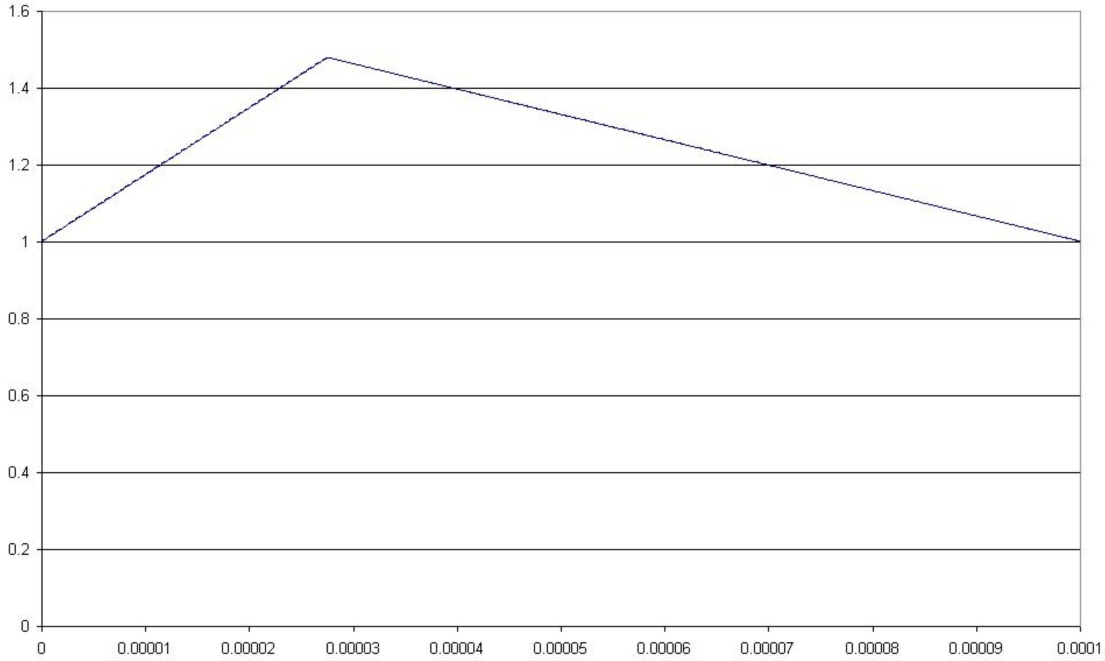

Figure G.3: Inductor current in continuous operation

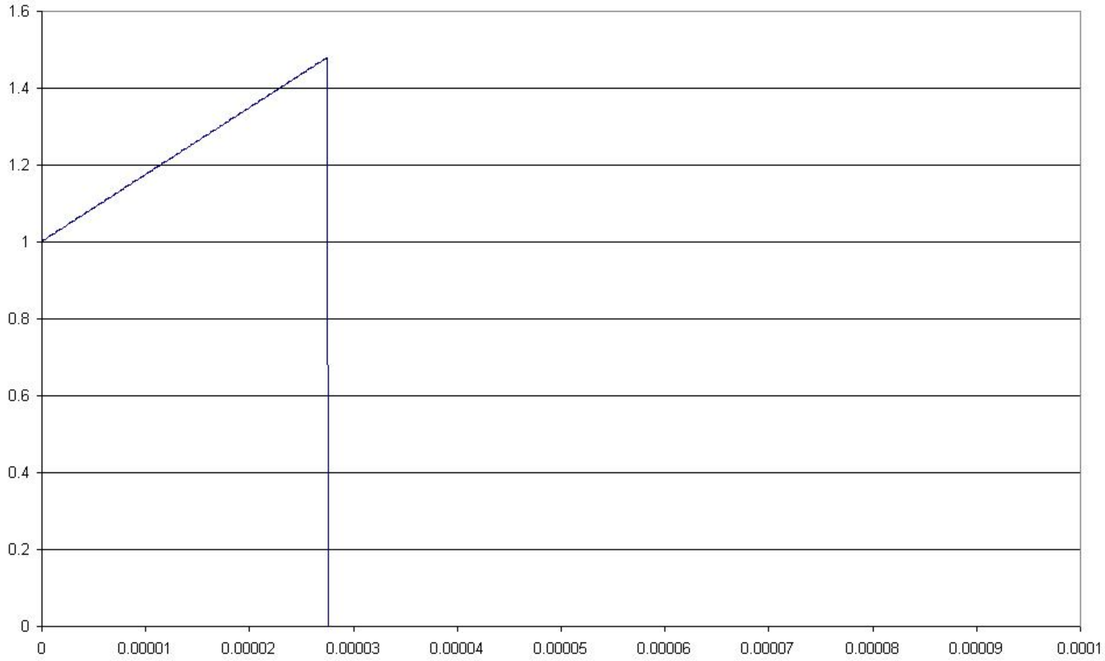

Figure G.4: Input current in continuous operation

the inductor voltage waveform can be divided into three distinct parts. Incorporating this waveform behaviour into equation G.1, leads to the following integral equation for the inductor voltage:

$$(V_{in} - V_{out}) \cdot T_{on} - V_{out} \cdot T_1 + 0 \cdot T_2 = 0 \tag{G.21}$$

where T_{on} is the time in a single switching period, during which switch M_1 is closed, and T_1 is the time in a single switching period, during which M_1 is open and current is flowing through the inductor, and T_2 is the time in a single switching period, during which M_1 is open and no current is flowing through the inductor. Note that the following equation holds:

$$T_1 + T_2 = T_off \tag{G.22}$$

where T_off is the time in a single switching period, during which switch M_1 is open.
Reordering terms in equation G.23 leads to:

$$(V_{in} - V_{out}) \cdot T_{on} = V_{out} \cdot (T_{on} + T_1) \tag{G.23}$$

Note that in contrast to continuous operation, the duty cycle of switch M_1 is not unambiguously defined by considering solely the input and output voltage. To evaluate the duty cycle, additional parameters are needed.
For analyzing additional characteristics of the step-down converter in discontinuous mode, the power balance shown in equation G.8 is introduced:

$$V_{in} \cdot \frac{1}{T} \cdot \left(\int_{\tau=t}^{t+T_{on}} \left(I_{max} \cdot \frac{\tau - t}{T_{on}} \right) \mathrm{d}\tau + \int_{\tau=t+T_{on}}^{t+T} 0 \cdot \mathrm{d}\tau \right) = V_{out} \cdot I_{out} \tag{G.24}$$

Evaluating this integral leads to:

$$V_{in} \cdot \frac{1}{T} \cdot I_{max} \cdot \left(\frac{1}{2} \cdot \frac{\tau^2}{T_{on}} - \frac{t}{T_{on}} \cdot \tau \right) \Bigg|_{\tau=t}^{t+T_{on}} = V_{out} \cdot I_{out} \tag{G.25}$$

Substituting the boundary values results in:

$$V_{in} \cdot \frac{1}{T} \cdot I_{max} \cdot \left(\frac{1}{2} \cdot \frac{(t + T_{on})^2 - t^2}{T_{on}} - \frac{t}{T_{on}} \cdot ((t + T_{on}) + t) \right) = V_{out} \cdot I_{out} \tag{G.26}$$

Expanding the quadratic term:

$$V_{in} \cdot \frac{1}{T} \cdot I_{max} \cdot \left(\frac{1}{2} \cdot \frac{2 \cdot t \cdot T_{on} - T_{on}^2}{T_{on}} - \frac{t}{T_{on}} \cdot T_{on} \right) = V_{out} \cdot I_{out} \tag{G.27}$$

Cleaning up the expression yields:

$$V_{in} \cdot \frac{1}{T} \cdot I_{max} \cdot \left(\frac{1}{2} \cdot T_{on} \right) = V_{out} \cdot I_{out} \tag{G.28}$$

Finally, by introducing the duty cycle δ:

$$\frac{1}{2} \cdot V_{in} \cdot I_{max} \cdot \delta = V_{out} \cdot I_{out} \tag{G.29}$$

Next, the general relation between inductor current and inductor voltage as given in equation G.16 is introduced. Evaluating this expression for the on-state period of switch M_1 yields:

$$I_{max} = \frac{(V_L)_{on}}{L} \cdot T_{on} = \frac{V_{in} - V_{out}}{L} \cdot T_{on} \tag{G.30}$$

Introducing the duty cycle:

$$I_{max} = \frac{V_{in} - V_{out}}{L} \cdot \frac{T_{on}}{T} \cdot T = \frac{V_{in} - V_{out}}{L} \cdot \frac{\delta}{f} \tag{G.31}$$

Substituting the previous expression into equation G.29 results in:

$$\frac{1}{2} \cdot V_{in} \cdot \frac{V_{in} - V_{out}}{L} \cdot \frac{\delta^2}{f} = V_{out} \cdot I_{out} \tag{G.32}$$

Note that this expression is similar to equation G.20, with zero substituted as value for I_{min}.
In Figure G.5, the waveform showing the inductor voltage for an example converter in steady-state discontinuous operation is given. The magnitude of the input voltage is taken to be equal to 12V, while the value of the output voltage equals 3.3V. Duty cycle δ is taken to be equal to 0.25, and switching frequency f is set to 10 kHz.
The waveform for the inductor current is shown in figure G.6. In the corresponding calculation, the value of the inductor L_1 was set to 500 μH.
As during the period switch M_1 is closed, the inductor current has to be generated by the power supply, the input current is represented by the waveform shown in figure G.7.

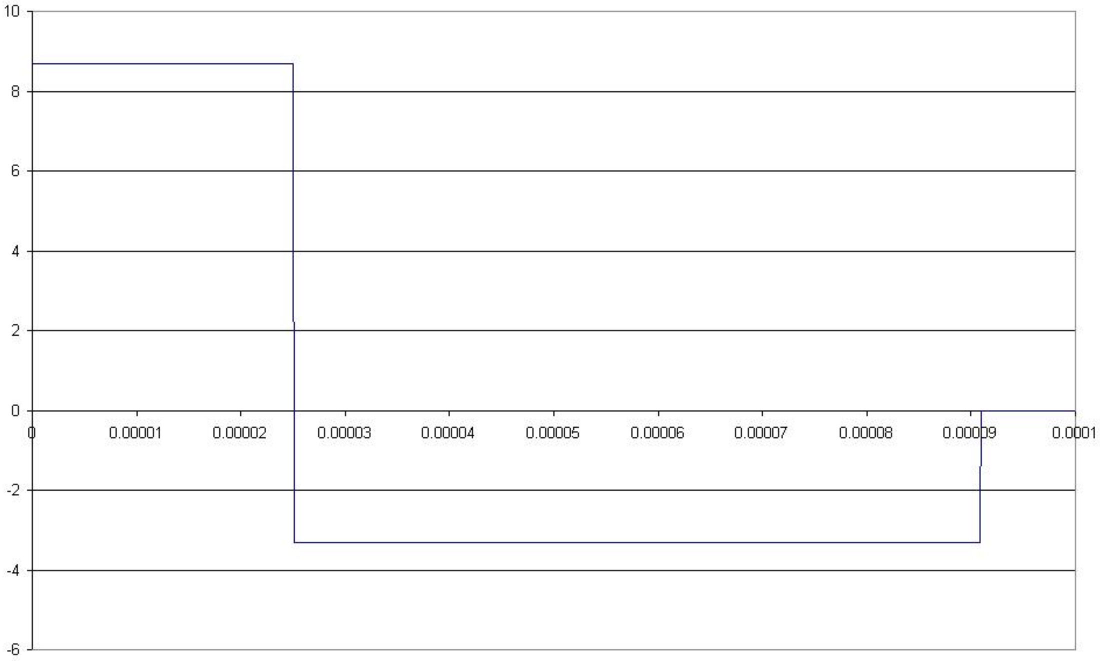

Figure G.5: Inductor voltage in discontinuous operation

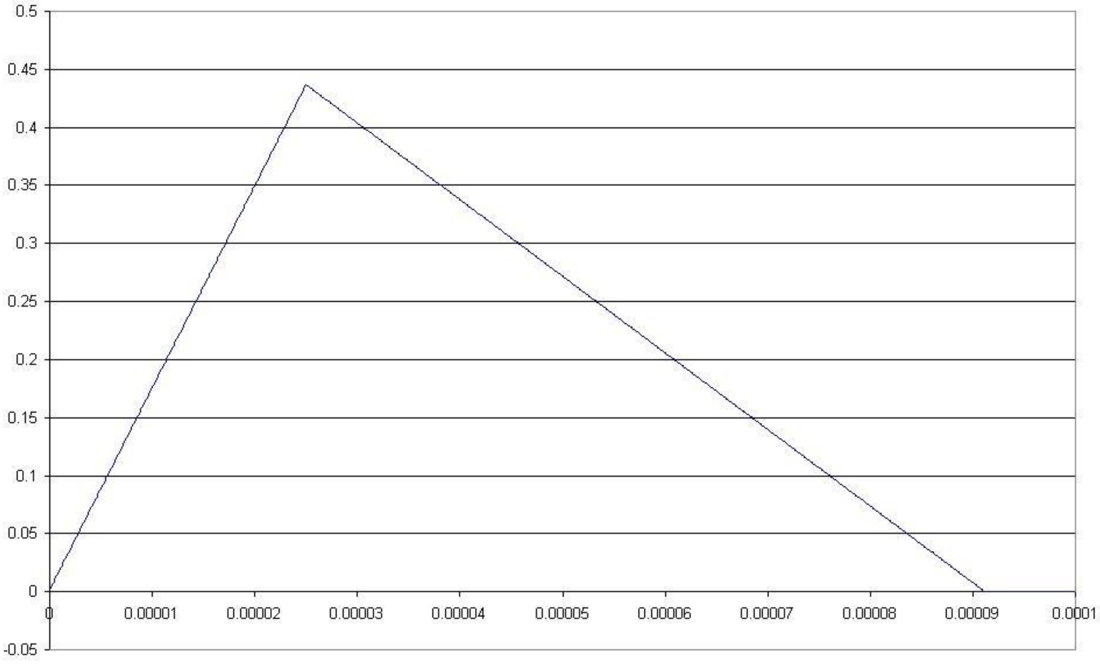

Figure G.6: Inductor current in discontinuous operation

G.2.4 Incorporation of dissipation losses

In the previous discussion, the step-down DC/DC converter was assumed to be composed of ideal components. Therefore, parasitic dissipation losses were not taken into account. However, a real-life converter experiences non-idealities in their components. Therefore, voltage drops will be generated by components assumed ideal in the previous discussion.
As an example, equation G.3 is rewritten taking parasitic voltage drops into account:

$$(V_{in} - V_{out} - V_M) \cdot T_{on} - (V_{out} - V_D) \cdot T_{off} = 0 \tag{G.33}$$

where V_M is the voltage drop over the MOSFET switch M_1 in on-state, and V_D is the voltage drop over

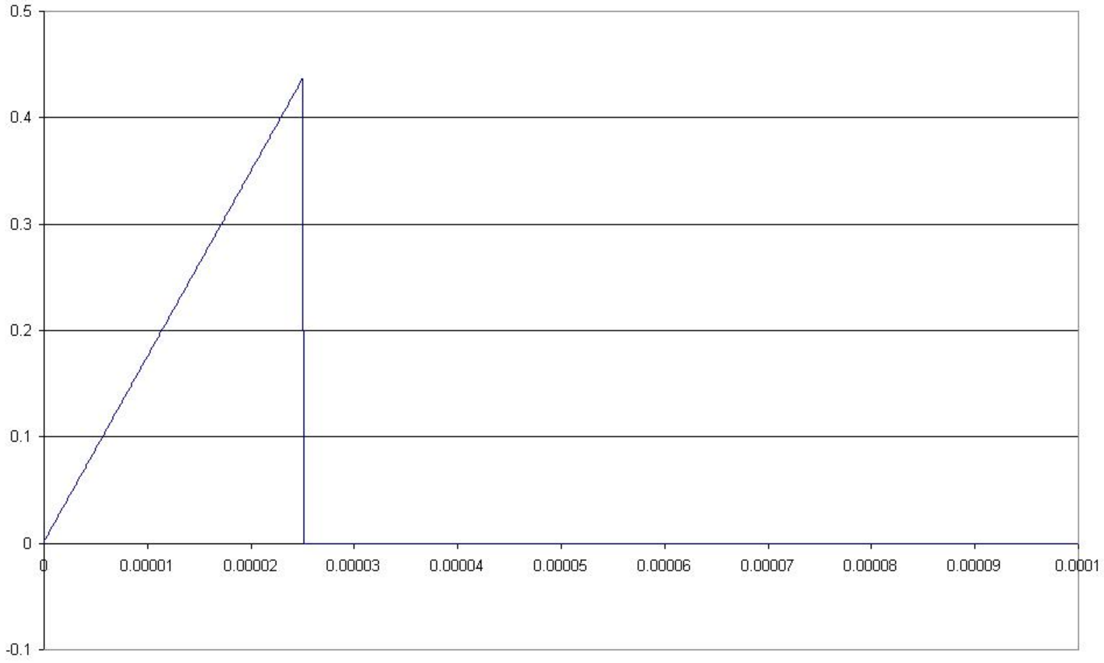

Figure G.7: Input current in discontinuous operation

the freewheeling diode D_1 in forward bias. Note that wiring losses and connection losses are not taken into account.
As can be noticed from equation G.33, parasitic dissipation losses impact the characteristics of the step-down converter. A general method to take these losses into account is by introducing an efficiency factor into the power balance. Therefore, equation G.8 is rewritten to:

$$P_{in} = \frac{1}{\eta} \cdot P_{out} \tag{G.34}$$

where η is the efficiency of the step-down DC/DC converter. Introducing the efficiency into expression G.32 finally yields:

$$\frac{1}{2} \cdot \eta \cdot V_{in} \cdot \frac{V_{in} - V_{out}}{L} \cdot \frac{\delta}{f} \cdot \delta = V_{out} \cdot I_{out} \tag{G.35}$$

G.2.5 Output voltage ripple

In order to fully describe the operational characteristics of a step-down DC/DC converter, the voltage ripple at the converter output has to be evaluated. In this discussion, a converter in continuous operation is considered.
In steady-state operation, the current flowing into the capacitor integrated over a single switching period has to equal zero. Therefore:

$$i_C = C \cdot \frac{\mathrm{d}v_C}{\mathrm{d}t} \tag{G.36}$$

Integrating this expression over a single switching period results in:

$$\int_{\tau=t}^{t+T} i_C \cdot \mathrm{d}\tau = \int_{\tau=t}^{t+T} C \cdot \frac{\mathrm{d}v_C}{\mathrm{d}t} \cdot \mathrm{d}\tau = 0 \tag{G.37}$$

By recalling the converter is in continuous operation, the operation of the capacitor can be analyzed. It has to be noticed that during switch-on of M_1 the capacitor will be charge by the difference between the incoming current and the output current. During switch-off of M_1, the capacitor is discharged with the output current. Writing the integral expression for a capacitor during the on-state yields:

$$\frac{1}{2} \cdot (I_{max} - I_{out}) \cdot \frac{T}{2} = C \cdot \Delta (V_C)_{tt} \tag{G.38}$$

Substituting equation G.15, which is governing output current I_out:

$$\frac{1}{2} \cdot \left(I_{max} - \frac{1}{2} \cdot (I_{max} + I_{min}) \right) \cdot \frac{1}{f} \cdot \frac{1}{2} = C \cdot \Delta (V_C)_{tt} \tag{G.39}$$

Cleaning up this expression results in:

$$\frac{1}{8} \cdot (I_{max} - I_{min}) \cdot \frac{1}{f} = C \cdot \Delta (V_C)_{tt} \tag{G.40}$$

Finally, solving for the voltage ripple yields:

$$\Delta (V_C)_{tt} = \frac{1}{8} \cdot (I_{max} - I_{min}) \cdot \frac{1}{f} \cdot \frac{1}{C} \tag{G.41}$$

In figure G.8, the incoming capacitor current is shown for the situation corresponding to the converter described by figure G.2, figure G.3, and figure G.4. For the capacitance, a value of 100 μF is chosen.

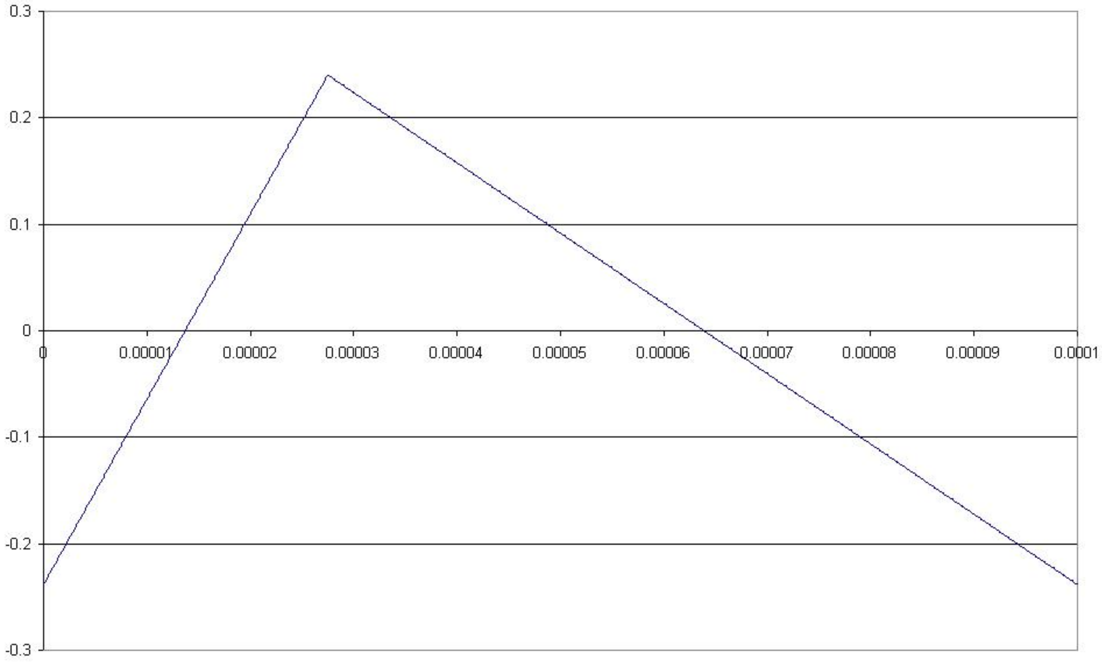

Figure G.8: Capacitor current in continuous operation

The charge ripple corresponding to the current shown in figure G.8 is given in figure G.9. Note that the voltage ripple is directly related to the charge ripple by the expression:

$$C = \frac{Q}{V_C} \tag{G.42}$$

G.3 Conclusions and Recommendations

In this document, the operational characteristics of a step-down DC/DC converter were shown. The equivalent electrical circuit is given, and the main principle of operation is explained. A strep-down DC/DC converter can function in two operational modes. In continuous mode, the current through the inductor is always positive. In discontinuous mode, the current will drop to zero during a particular part of a switching period. Both operational modes have been analyzed. Furthermore, attention is paid to non-idealities in the converter components and to the output voltage ripple.

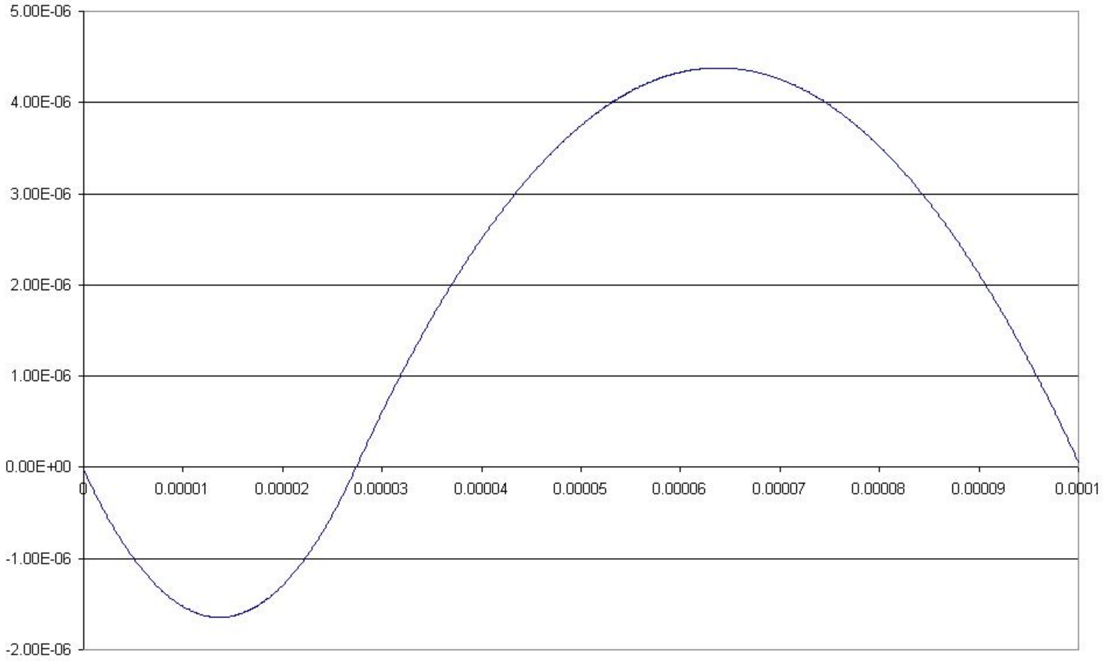

Figure G.9: Capacitor charge ripple in continuous operation

Appendix H

DC3-TN-702-097
Ripple in current measurement circuitry output

H.1 Introduction

Initial testing of the combination board revealed that the current measurements performed by the PIC microcontroller showed large deviations in magnitude. It was found that this behaviour was caused by the switching behaviour of the step-down DC/DC converter applied on the combination board. This behaviour would cause the creation of a current pulse in the supply line. As the MAX4172 current measurement chip is sensing the current flowing through this supply line, the output would also display a pulsating waveform too. This resulted in the large deviations in the output of the PIC microcontroller.

In order to remove the effects of the current pulse on the output of the PIC microcontroller, provisions have to be taken with respect to the design of the current measurement circuitry. Several design solutions are available, which can be globally divided into software solutions and hardware solutions.

In this document, the various design solutions will be presented and a decision will be taken on which solution will be implemented. In subsection H.2.1, the revealed problem with the current measurement circuitry will be briefly described. The various available design solutions will be presented in subsection H.2.2. In subsection H.2.3, the design solution using maximum value tracking is described, while the design solution applying a low pass post-filtering is outlined in subsection H.2.4. Initial measurement results due to application of a low pass filter in the MAX4172 output are shown in subsection H.2.5.

H.2 Ripple in current measurement circuitry output

H.2.1 Definition of current measurement problem

During functional testing of the current measurement circuitry on the combination board, it was found that the PIC microcontroller in charge of sampling the magnitude of the current will output an unforeseen value. Although measurement with a multimeter yields an acceptable value for the output of the MAX4172 circuitry, the PIC microcontroller will give an output deviating largely from this value. This can be explained by realizing that a multimeter output the RMS value of the measured quantity. On the other hand, the PIC microcontroller outputs the value at the exact moment of sampling.

It has been noticed that the PIC output does not yield a constant value but instead has a value between zero and a value larger than the expected RMS value. Measuring the output voltage of the MAX4172 circuitry with an oscilloscope yields a pulsating waveform. This phenomenon can be explained by realizing that the applied DC/DC converters are of the switching type.

In figure H.1, the current waveform as measured at input of the MAX4172 current measurement circuitry of the combination board is shown. Note that this pulsating current will also appear at the input of the DC/DC converter.

With this pulsating waveform, the magnitude of the current will be equal to zero during a large part of the switching period. Therefore, the PIC microcontroller will output wrong values of the current in case these are interpreted as RMS values.

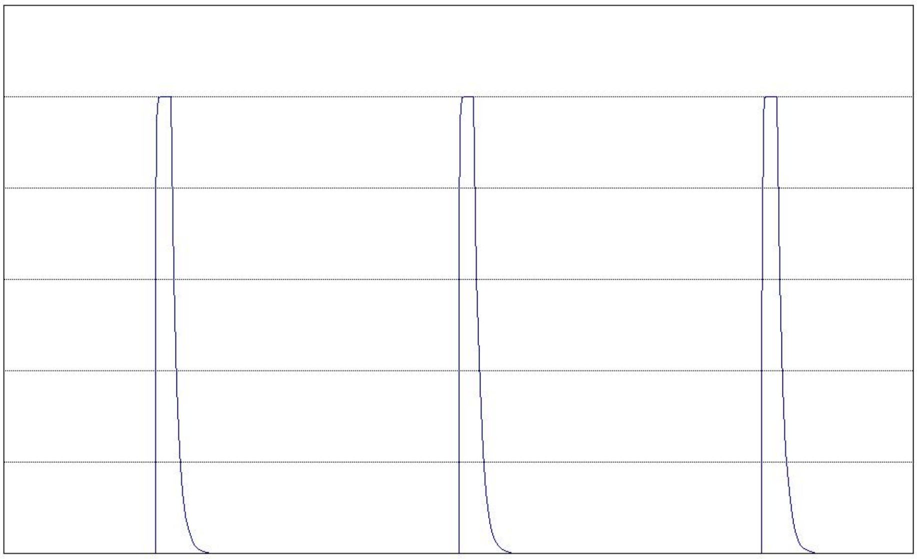

Figure H.1: Pulse current waveform at input of step-down DC/DC converter

H.2.2 Statement of possible solutions

In order to overcome the problem of having the MAX4172 measuring a non-constant pulsating current waveform and thereby outputting a wrong corresponding value, several design solutions were invented by FH and GA. In general the solutions can be divided into software solutions and hardware solutions. Software solutions will result in adjustment of the programming code in the PIC processing the MAX4172 measurement results. Implementation of hardware solutions will require addition or change of electronical components on the printed circuit board. All possible solutions will be listed and shortly explained in the following:

Software solutions

- Software buffering
  This solution implements a buffer in the PIC processing the MAX4172 measurement outputs. By applying this buffer, the possibility is enabled to calculate the RMS value of the current. This can be done by raising the amount of samples taken and integrating the current over time by applying the expression for RMS quantities on the taken set of samples. A major drawback is that one set of samples has to be taken in a single switching period of the converter. A failure to meet this requirement will lead to inaccurate results. An advantage is that very accurate results could be obtained when this design solution is correctly implemented. Nevertheless, large variations of the switching frequency with output current and board temperature will lead to large headaches when incorporating this solution.

- Increase sampling time of ADC
  This solution implements an increase in sample time of the analog-to-digital converter. By increasing this time, it is possible to have an overlap of one or multiple switching periods of the converter in the sample. By using this increased sampling time, the current waveform is integrated over one or multiple switching periods. Calculating the mean will thereafter yield the average current flowing through the supply line to the subsystem. An advantage of this solution is that no extra components have to be added to the design. Furthermore, the average current can be measured accurately by tweaking the sampling time. Disadvantages are that the amount of switching periods sampled has to be equal to an integer in order to have accurate results. Moreover, it is questionable whether the sampling capacitor is capable of sampling current for the required prolonged periods.

- Maximum value tracking
  This solution implements tracking in the measurement processing PIC of the maximum value in the set of measurement inputs. In order to have a sufficiently large set to filter out a representative value for the maximum current flowing through the supply line, the amount of samples taken have to be increased. Every measurement is read by the digital-to-analog converter in the relevant PIC, and is compared to the current maximum value in the buffer of the PIC. In case the measured value is higher than the buffered value, the current measurement will replace the buffered value.

In case the measured value is lower than the buffered value, the measurement will be discarded. After a complete set of measurement, the maximum value, which is in the buffer of the PIC, will be outputted. By having a relation between the maximum and the RMS value of the current flowing through the supply line, this RMS current can be determined. No extra components have to be implemented for this solution. Furthermore, a complete measurement set does not have to be an exact number of switching periods. However, creating a relation between maximum and RMS value of the current can be bothersome.

Hardware solutions

- Low pass pre-filtering
  This solution implements a low-pass filter in the 12V supply line. A low pass filter is used to dampen out the AC components of a signal with a higher frequency than the characteristic frequency of the filter. By applying such a low-pass filter, the current pulses will be suppressed and a smoother current waveform will appear. In this solution a low-pass filter is applied in the 12V supply line. A general low-pass filter consists of a series resistance and a shunt capacitance. Therefore, usage of a low-pass filter will result in the insertion of a series resistance in the 12V supply line. A major disadvantage of this solution will be large dissipation losses in this series resistance. Furthermore, addition of the extra resistance and capacitance will lead to redesign or rework of the printed circuit boards. An advantage is that the current waveform will become smoother and therefore peak currents will be removed. This will avoid possible stalling of the MAX4172 integrated circuit due to excessively high input voltages.

- Low pass post-filtering
  This solution implements a low-pass filter in the output line of the MAX4172 integrated circuit. Therefore, a series resistor and a shunt capacitance are placed between the output of the MAX4172 and the measurement pin of the PIC microcontroller. This will ensure that the output signal of the MAX 4172 integrated circuit is smooth and does not experience high current peaks. An advantage is that no extra dissipation losses are introduced and that rework or redesign of the printed circuit boards is relatively simple. However, one has to carefully keep in mind the input impedance of the measurement pin on the PIC microcontroller as this can influence measurements.

- Measurement circuitry transfer
  This solution implements a positional transfer of the current measurement circuitry to the low voltage side of the DC/DC converter. Because the current at the low voltage side of the converter has a smoother waveform than the current on the high voltage side, the measurements will be more cohesive. Therefore, the measurements will contain more reliable information. However, the complete circuitry has to be transferred to the low-voltage side leading to major redesign of the various printed circuit boards. Furthermore, due to the higher currents and the lower voltages, the impact of the series sensing resistor on the supply voltage will be higher than on the high voltage side.

- Measurement circuitry removal
  This solution will remove the current measurement circuitry all together. As this rigorous action will remove the ability to measure the current flowing through the supply line, it is not desired to be performed. However, if no viable solution can be found for counteracting the measurement problems it may be the only remaining choice.

After a short discussion, it was decided that maximum value tacking and low pass post-filtering are the most viable design solutions. These will be illustrated in the following sections.

H.2.3 Postulation of maximum value tracking design solution

One of the design solutions, which is deemed viable, is maximum value tracking. In this solution, the maximum in a particular set of measurements is identified and outputted by the PIC microcontroller to the housekeeping data package. During post-processing the RMS current value can be calculated by a relation between the RMS current and the maximum current. However, in order to obtain a relation between maximum and RMS current, it has to be identified whether the DC/DC converter is in continuous or discontinuous operation.

It will be verified whether the converter is in continuous or discontinuous operation by looking at the switching frequency. For this reason, the minimum needed switching frequency for continuous operation will be calculated. In appendix G, the expression for maximum current flowing into the DC/DC converter during continuous operation can be found to be equal to:

$$I_{max} = \frac{V_{in} - V_{out}}{L} \cdot \frac{1}{f} \cdot \frac{V_{out}}{V_{in}} \tag{H.1}$$

Furthermore, the output current during continuous operation is expressed by:

$$I_{out} = \frac{1}{2} \cdot (I_{min} + I_{max}) \tag{H.2}$$

After realizing that the minimum switching frequency for continuous operation will be attained when the minimum current I_{min} equals zero, substituting equation H.2 into equation H.1 yields:

$$I_{out} = \frac{1}{2} \cdot \frac{V_{in} - V_{out}}{L} \cdot \frac{1}{f} \cdot \frac{V_{out}}{V_{in}} \tag{H.3}$$

Rewriting this expression and solving for the minimum switching frequency required for continuous operation results in:

$$f_{min} = \frac{1}{2} \cdot \frac{V_{in} - V_{out}}{L} \cdot \frac{1}{I_{out}} \cdot \frac{V_{out}}{V_{in}} \tag{H.4}$$

Substituting values gives:

$$f_{min} = \frac{1}{2} \cdot \frac{12 - 3.3}{22 \cdot 10^{-6}} \cdot \frac{1}{17.9 \cdot 10^{-3}} \cdot \frac{3.3}{12} \approx 3.0 \cdot 10^{6} \text{ Hz} \tag{H.5}$$

This frequency will never be attained, and therefore the converter will never go into continuous operation. Preliminary measurements show a switching frequency of approximately 10 kHz, but this frequency can change between 2 kHz and 50 kHz depending on the output current. As the converter is in discontinuous operation, an additional expression has to be obtained in order to relate the maximum current value to the RMS value. In appendix G, the expression for the maximum current flowing through the DC/DC converter in discontinuous operation is found to be:

$$\frac{1}{2} \cdot V_{in} \cdot I_{max} \cdot \delta = V_{out} \cdot I_{out} \tag{H.6}$$

Investigating this equation and realizing that the input voltage is constant yields for the RMS current:

$$I_{RMS} = \frac{1}{2} \cdot I_{max} \cdot \delta \tag{H.7}$$

An additional expression can be written for the maximum current I_{max}:

$$I_{max} = \frac{V_L}{L} \cdot \frac{T_{on}}{T} \cdot T = \frac{V_L}{L} \cdot \frac{\delta}{f} \tag{H.8}$$

Substituting this equation into equation H.7 results in:

$$I_{RMS} = \frac{1}{2} \cdot \frac{I_{max}^2}{V_{in} - V_{out}} \cdot L \cdot f \tag{H.9}$$

Investigating this expression, it is noticed that next to the measured quantity I_{max} an additional unknown is present in the form of the switching frequency f. Although this switching frequency is a highly nonlinear function of the output current, a graph in the data sheet of the converter can yield a solution. This graph is shown in figure H.2.

However, in order to use the graph in figure H.2, the output current has to be known. This is the primary variable for which the measurement was to be taken and is in fact unknown! A bothersome numerical integration procedure would be unavoidable in this case. Furthermore, implementing the graph would be a real pain as this has to be done very accurately.

Another point of interest is the fact that although many samples will be taken per switching period of the converter, the chances are high that the exact maximum is not measured. Due to the steep slope of the current pulse waveform a small offset from the maximum would mean a significantly lower measurement value. Therefore, it is questionable whether this solution would yield an accurate result.

All taken together, this solution would pose many problems and is therefore dismissed in favor of the hardware solution.

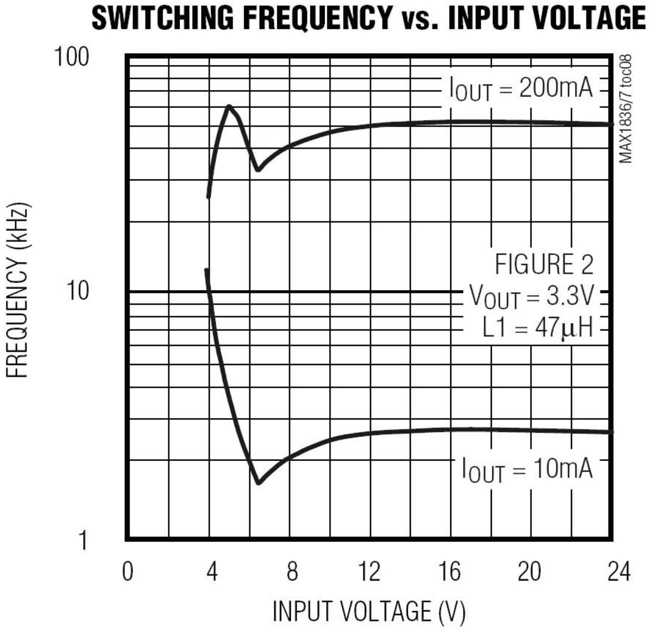

Figure H.2: Switching frequency vs. input voltage of the MAX1836 step-down converter

H.2.4 Postulation of low pass post-filtering solution

Another design solution is the implementation of a low pass filter in the output line of the MAX4172 integrated circuit. The filter is implemented by inserting a resistor between the output pin of the MAX4172 component and the measurement pin on the PIC microcontroller. Furthermore, a shunt capacitor has to be placed at the measurement pin.

This low pass filter has to comply with two requirements. First of all the ripple in the output has to be suppressed sufficiently in order to have a representative measurement. Secondly, the low pass filter has to have a fast response to low frequency changes in current. In principle, these two requirements are contradictory as fast response calls for a small filter while ripple suppression needs a large filter. Therefore, the filter has to be designed that both requirements are met in a satisfactory way.

A design of a low pass filter is performed by tuning its characteristic frequency. The characteristic or cut-off frequency of a low pass filter is expressed by:

$$f = \frac{1}{2\pi \cdot R \cdot C} \tag{H.10}$$

In general, all frequencies in the input signal to the low pass filter, which are higher than the cut-off frequency, are suppressed, while all frequencies lower than the cut-off frequency are unaffected by the filter. As the switching frequency of the DC/DC converter is found to be approximately 10 kHz, the cut-off frequency has to be lower than this value. For various values of the cut-off frequency, a simulation is performed by FH in the PSpice simulation environment.

In figures H.3, H.4, and H.5, the results of the PSpice simulations are shown for respectively a cut-off frequency 1000 Hz, 100 Hz, and 10 Hz. The test case for these simulations is the Radio Amateur Platform, which experiences after all the largest current in its supply line of all printed circuit boards. Furthermore, it is assumed that the step-down DC/DC converter switches with a frequency of 10 kHz.

Investigating figures H.3, H.4, and H.5, it is noticed that for higher cut-off the transient behaviour has a much faster response. As a consequence however, the voltage ripple is larger too. In order to choose correct component values for the design of the low-pass filter, an assessment has to be made of the resolution of the analog-to-digital converter in the PIC microcontroller. By recalling that this AD converter output a 10-bit data word at a reference voltage of 3.3V, the resolution equals:

$$\Delta V = \frac{V_{max}}{n} = \frac{3.3}{1024} = 3.223 \cdot 10^{-3} \text{ V} \tag{H.11}$$

In principle, the design of the low pass filter has to result in a ripple in the output voltage, which is approximately equal or smaller in magnitude than the resolution of the AD converter. By investigating the previous figures, it can be concluded that the cut-off frequency has to be smaller than 100 Hz.

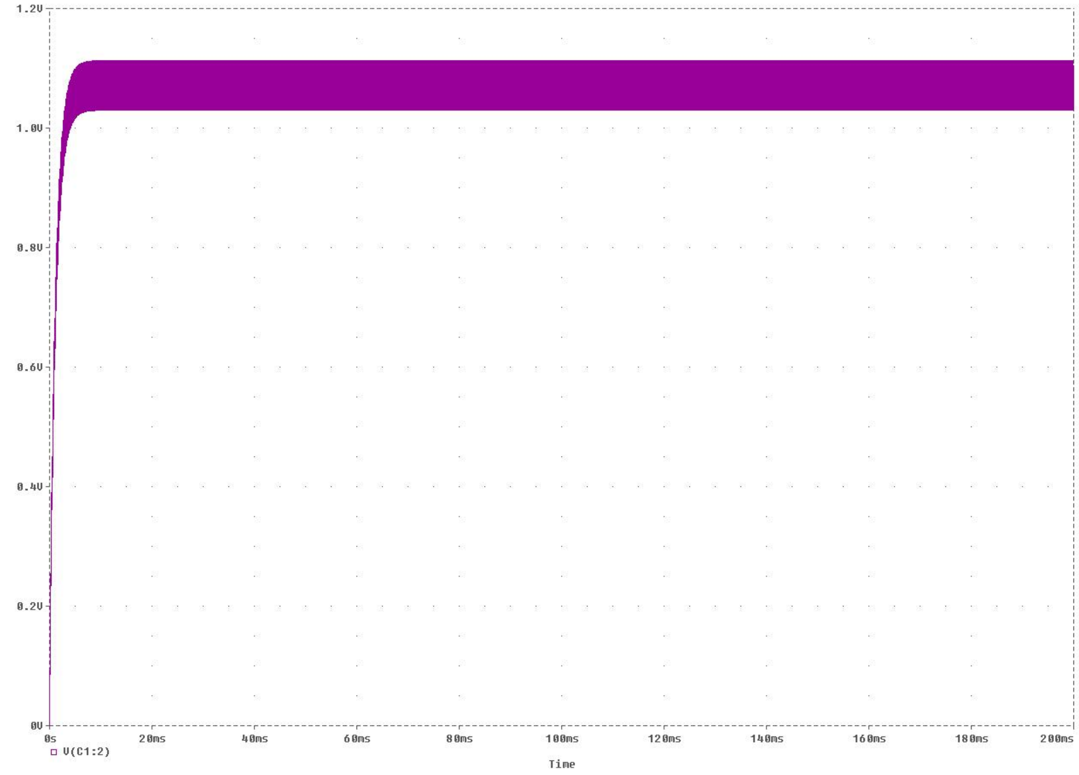

Figure H.3: Output voltage of low pass filter - cut-off frequency 1000 Hz

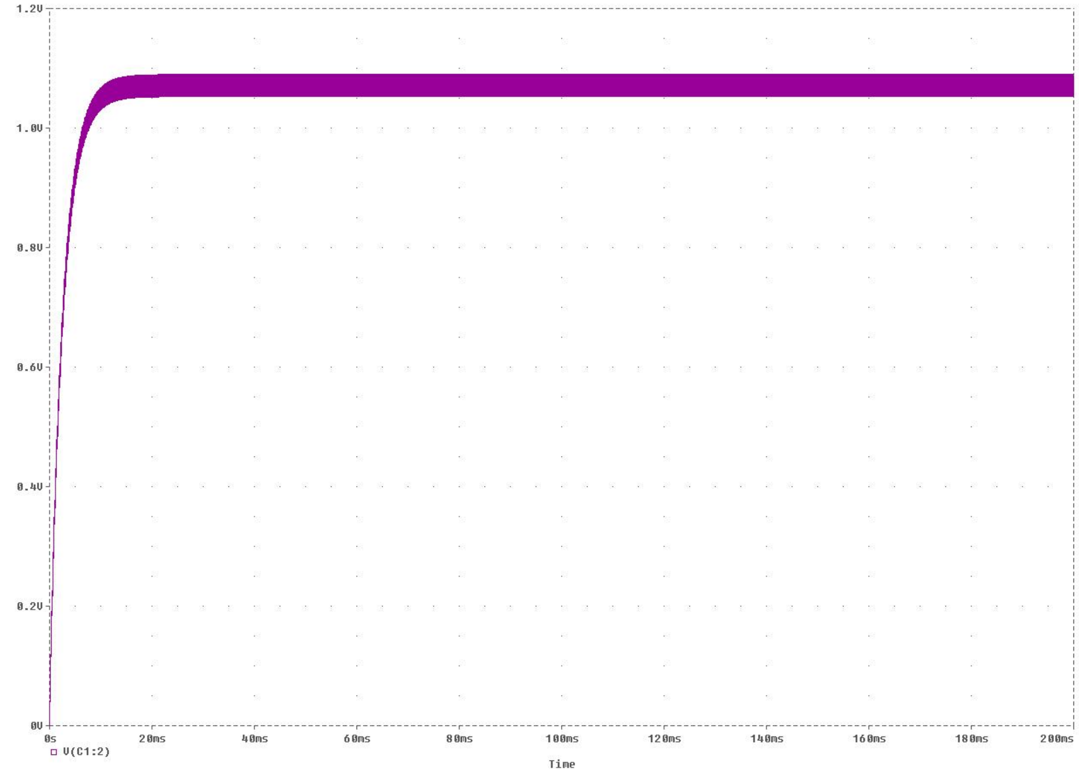

Figure H.4: Output voltage of low pass filter - cut-off frequency 100 Hz

Although the requirement with respect to voltage ripple is that it has to be approximately equal in magnitude as the resolution of the AD converter, a restrictive requirement to the value of this ripple is not present. Therefore, the filter is chosen to be designed with components, which have convenient values for their electrical characteristics.

With consultation of WU and TH, the components for the low pass filter are chosen to be:

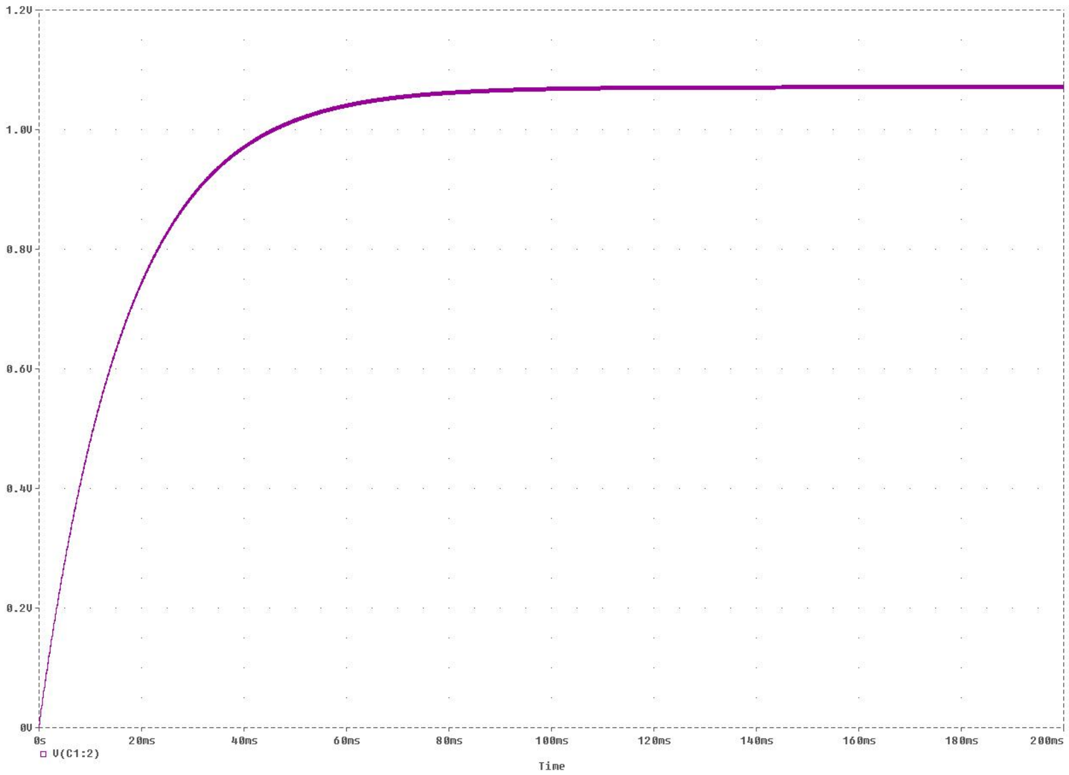

Figure H.5: Output voltage of low pass filter - cut-off frequency 10 Hz

- Resistor: 10 kΩ
- Capacitor: 1 μF

Using these values, the cut-off frequency of the filter will be:

$$f = \frac{1}{2\pi \cdot 10 \cdot 10^3 \cdot 1 \cdot 10^{-6}} \approx 15.9 \text{ Hz} \tag{H.12}$$

In figure H.6, the behaviour of the output voltage of the designed low pass filter is shown. A close-up on the steady-state voltage ripple is shown in figure H.7. Investigating figure H.7, it is noticed that the voltage ripple equals 8.73 mV. This value is approximately thrice the resolution of the AD converter, and was deemed acceptable.

In figure H.8, the frequency behaviour of the low pass filter is shown. It can be noticed that components with a frequency larger than 100 Hz are suppressed, while components with a frequency smaller than 10 Hz are largely unaffected.

In order to derive the RMS value of the current flowing through the supply line from the voltage measured at the output of the low pass filter, the unfiltered voltage, which represents the instantaneous supply current, is written as a Fourier series:

$$V = V_0 + \sum_{n=1}^{\infty} V_n \cdot \sin\left(2\pi \cdot n \cdot \frac{t}{T}\right) \tag{H.13}$$

Calculating the mean of the unfiltered voltage coincides with:

$$\frac{1}{T}\int_{t=0}^{T} V \mathrm{d}t = \frac{1}{T}\int_{t=0}^{T} \left(V_0 + \sum_{n=1}^{\infty} V_n \cdot \sin\left(2\pi \cdot n \cdot \frac{t}{T}\right)\right) \mathrm{d}t \tag{H.14}$$

Evaluating the integral of the term in the summation leads to:

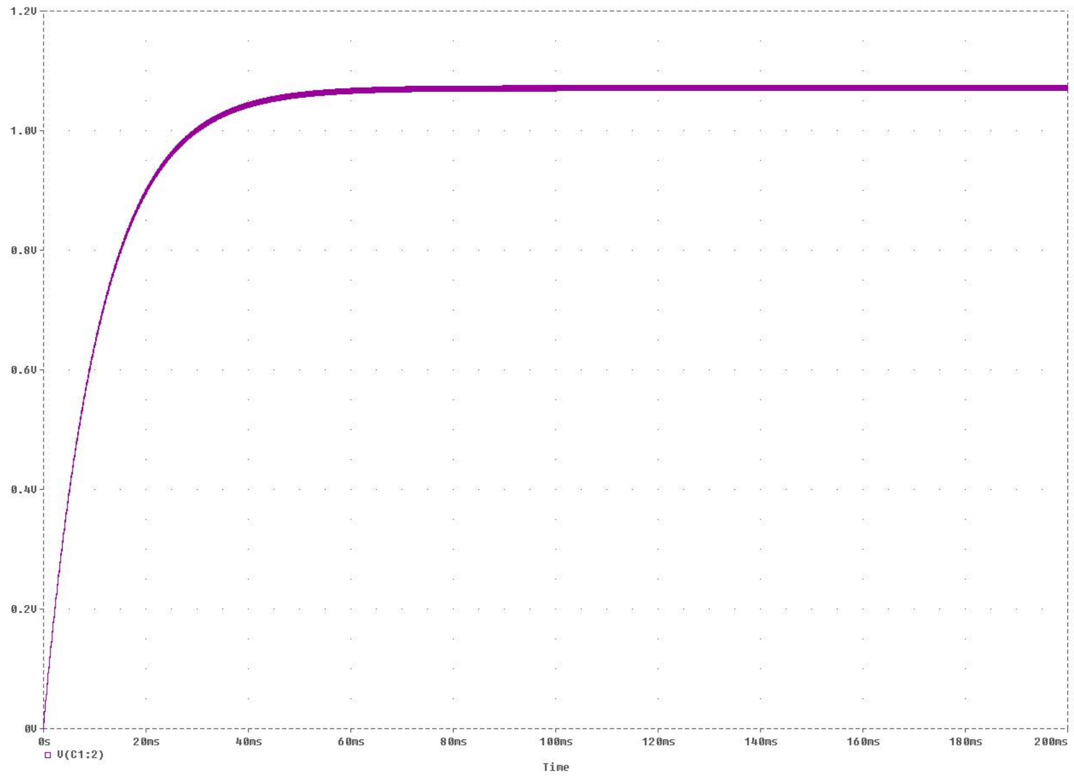

Figure H.6: Output voltage of low pass filter - final design

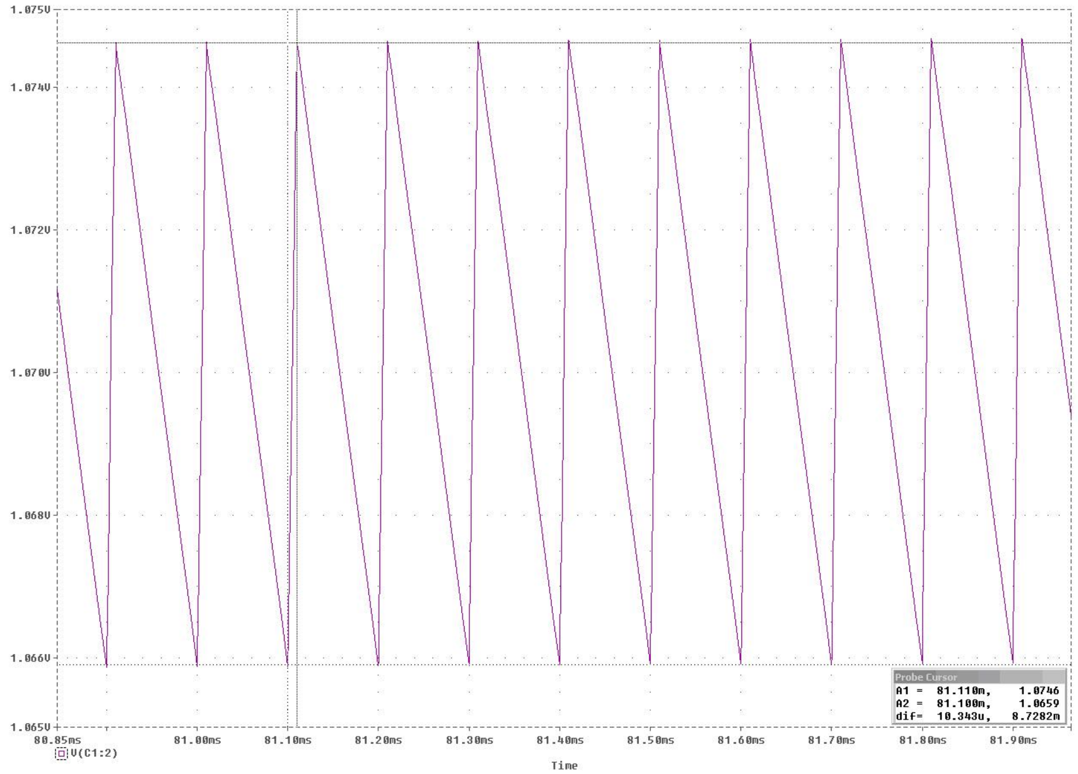

Figure H.7: Output voltage of low pass filter - final design (close-up)

$$
\begin{aligned}
&\int_{t=0}^{T} V_n \cdot \sin\left(2\pi \cdot n \cdot \frac{t}{T}\right) \mathrm{d}t = -\frac{T}{2\pi \cdot n} \cdot V_n \cdot \cos\left(2\pi \cdot n \cdot \frac{t}{T}\right) \Bigg|_{t=0}^{t=T} = \\
&-\frac{T}{2\pi \cdot n} \cdot V_n \cdot \left(\cos\left(2\pi \cdot n \cdot \frac{0}{T}\right) - \cos\left(2\pi \cdot n \cdot \frac{T}{T}\right)\right) = \\
&\hfill -\frac{T}{2\pi \cdot n} \cdot V_n \cdot (1 - 1) = 0 \qquad \text{(H.15)}
\end{aligned}
$$

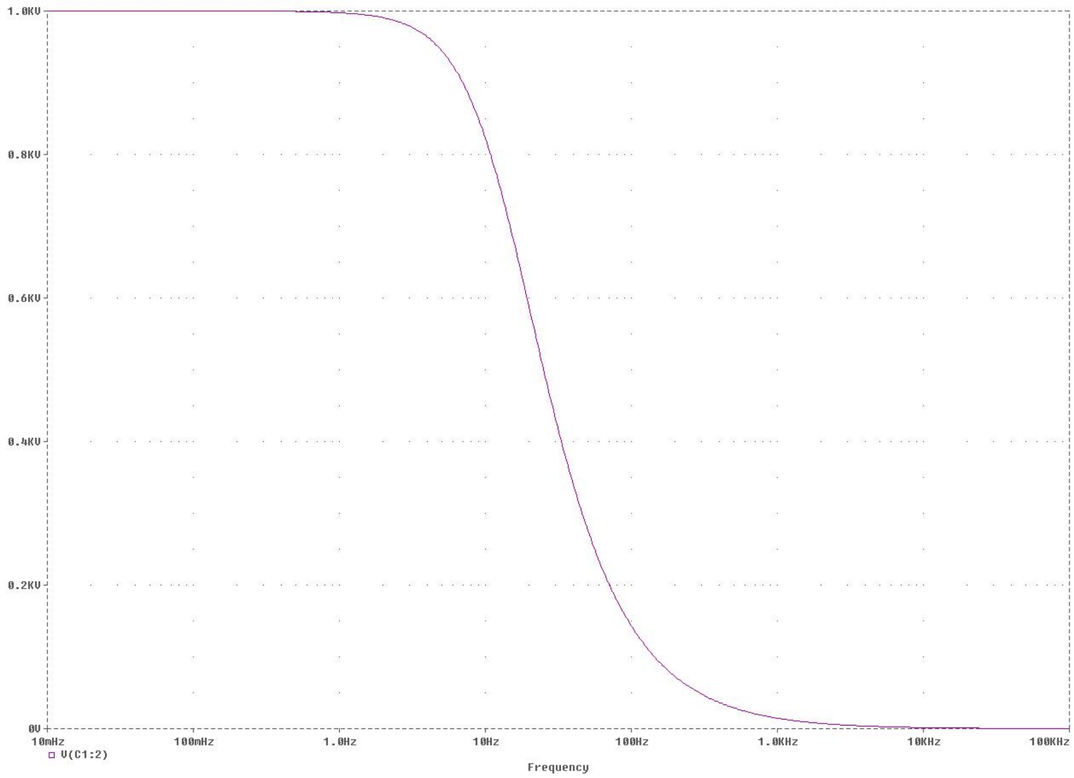

Figure H.8: Bode diagram of low pass filter - final design; R = 10 kΩ; C = 1 μF

Substituting this result in the original integral then leads to:

$$\frac{1}{T}\int_{t=0}^{T} V\mathrm{d}t = \frac{1}{T}\int_{t=0}^{T} V_0\mathrm{d}t \tag{H.16}$$

By investigating this result, it can be perceived that the average output voltage has to be equal to the DC component of the unfiltered voltage. This is expressed with:

$$V_{avg} = V_0 \tag{H.17}$$

It can be concluded that sufficient suppression of AC components in the input voltage will lead to the production of the mean voltage at the output of the low pass filter. Therefore, the measured voltage will be equal to the mean of the unfiltered voltage as created by the MAX4172 component. Direct transformation of the quantity outputted by the PIC microcontroller will yield the mean current flowing through the supply line.

H.2.5 Preliminary measurement on low pass filter application

The low pass filter has been assembled on the combination board for testing purposes. Using a digital oscilloscope Tektronic TDS 20148, the input and output of the filter have been measured. The corresponding waveforms are shown in figures H.9 and H.10, respectively.
Investigating figures H.9 and H.10, it is perceived that the input voltage consists of a pulse with a frequency of approximately 3000 Hz. The height of the pulse is approximately 8.0 mV. At the output of the filter, the voltage waveform approaches DC behaviour. In contrast to the input of the filter, no distinctive pulse can be observed. A clear voltage ripple is not noticeable, because it disappears in the background noise of the measurement probe.

H.3 Conclusions and recommendations

During preliminary testing of the combination board, it was noticed that the output of the MAX4172 current measurement circuitry shows a pulsating behaviour. This behaviour affected the capacity of the

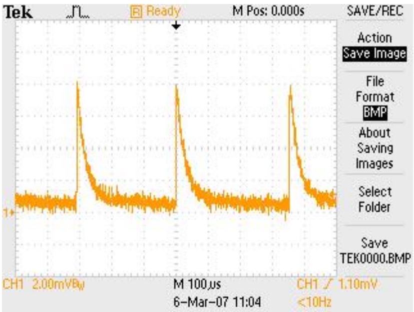

Figure H.9: Measurement of input voltage of low pass filter

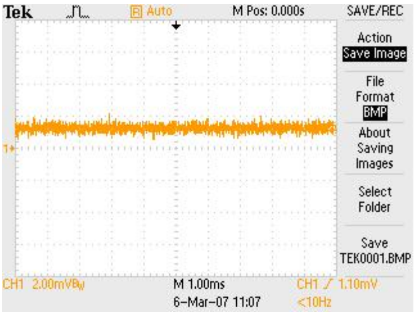

Figure H.10: Measurement of input voltage of low pass filter

PIC microcontroller for measuring the current through the supply line to the relevant subsystem. As average currents are of real interest, measures have to be taken to have the PIC microcontroller output an average current without the effects of the current pulse. Several design options have been produced, of which only two were deemed viable.
Maximum value tracking is a software solution, which requires an increase in the sampling frequency and having the PIC microcontroller output the maximum value.
Implementation of a low pass filter would filter out the high frequency components out of the signal. This would lead to a smooth quasi-constant signal, which would be easily measured. This design solution was chosen for implementation, with a resistor of 10 kΩ and a capacitor of 1 μF.
Initial tests show excellent filtering behaviour of the designed low pass filter.

Appendix I

DC3-TN-702-096
PIC induced collapse of I2C bus

I.1 Introduction

Internal communication in the Delfi-C3 spacecraft is accomplished by the I2C data bus. This bus consists of two lines, being a SCL clock line and a SDA data line. Data transfer is performed by using binary encoding, i.e. using 1s and 0s. This so-called I2C protocol depicts a 0 as a block voltage of 0V. On the other hand, a 1 is illustrated by using a voltage block of 3.3V. A large deviation from these two voltages is prohibited, as one of the data devices connected to the I2C bus may not recognize a 1 or 0 if the voltage level does not correspond to the respective nominal value.

In order to enable successful communication, the pull-up of the I2C bus to 3.3V has to be performed without any problems. However, preliminary testing of the combination board has shown that a disabled PIC microcontroller connected to the I2C bus is able to induce a collapse of the bus. In this situation, successful communication in the spacecraft is not possible. Therefore, a design change has to be implemented to counteract pull-down of the I2C bus by a disabled PIC.

In this document, several design options are presented to prevent collapse of the I2C bus. In section I.2.1, the problem of I2C bus pull-down is defined. A brief description of the original topology leading to the collapse of the I2C bus is shown in section I.2.2. In section I.2.3, the design option involving a positional transfer of the MOSFET switch is presented, while in section I.2.4 the design option with application of I2C repeaters is illustrated. Finally, in section I.2.5 a trade-off is accomplished and one of the options is chosen to be implemented.

I.2 PIC induced collapse of I2C bus

I.2.1 Definition of the problem of I2C pull-down

During testing of the I2C data bus on the combination board, it was found that the data bus is unable to attain a sufficiently high voltage. In nominal conditions, both the SCL and SDA line have to be at 3.3V. However, in case of a powered down AWSS PIC, these lines were only at a voltage of 1.56V. Powering up of the AWSS PIC solved the problem: both the SCL and SDA line remained constant at 3.3V.

Detailed investigation learned that this drop in voltage was caused by the presence of clamping diodes in the I2C ports of the PIC. These diodes were inserted in order to protect the PIC from electro-static discharge, but they will cause a problem when the PIC is not powered. This problem was already identified at an earlier stage in the project, but decisive action to counteract it has not been taken since. Nevertheless, the problem is caused due to the fact that the supply voltage line to a disabled PIC is at 0V, while the I2C lines are at a nominal 3V3. As the I2C lines are clamped to the supply line via the diodes, the I2C lines will be pulled down, resulting in a lower voltage.

In figure I.1, an electrical schematic is shown of the circuitry of a single PIC port incorporating clamping diodes.

With the schematic shown in figure I.1, the problem caused by the clamping diodes is easily identified. In case the PIC is powered, the I2C bus and the 3V3 bus are at an equal potential. In this case, diode D_1 is not conducting and no current will flow through D_1 leading to a stable I2C bus. Diode D_2 is in reverse bias as its anode is connected to the I2C bus, which is at a higher potential than its cathode which is connected to ground.

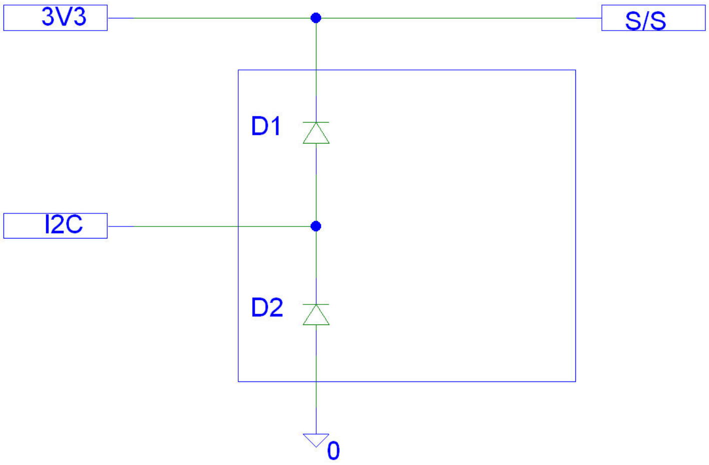

Figure I.1: Electrical schematic of an I2C port on a PIC microcontroller

In the situation of a powered down PIC, the I2C bus is at a nominal voltage of 3.3V and the 3.3V bus is at 0V. Diode D_2 remains in reverse bias, as the I2C bus is at a higher potential than ground. However, diode D_1 is in forward bias as the cathode of D_1 is connected to the I2C bus, while its anode is connected to the 3.3V bus, which has a potential equal to ground. As the potential difference between the terminals of D_1 is rather high in a nominal situation, a very large current will flow. Stabilization of the situation will occur when the I2C is pulled down, thereby reducing the potential difference between the cathode and anode of D_1.

I.2.2 Brief desciption of original topology

With the problem identified, WU, GA, and FH concocted several design options to counteract the problem of a powered down PIC being able to pull the I2C bus down. However to understand the problem in detail, the original topology has to be illustrated.

In the original concept, a single PIC microcontroller is used for switching power to the relevant subsystem. This microcontroller was supplied by applying a protective circuitry consisting of a series-parallel network of resistors and voltage references. Switching occurred by applying MOSFET solid state switches in the supply power branch to the subsystem. Consequently, after the MOSFET switches are turned on, the step-down DC/DC converters are energized and the relevant subsystem will be provided with power.

Data collection and processing was accomplished by another single PIC microcontroller. This PIC was burdened with data acquisition from the subsystem and transferring it to the I2C bus. Its power supply was connected to the branch behind the step-down DC/DC converters, which also serves as power supply for the rest of the subsystem. This topology is in fact the reason why the I2C bus can be pulled down. After all, energizing of the CDHS PIC will occur at exactly the same moment as energizing of the subsystem. Therefore, when the subsystem is switched off, the CDHS PIC is also switched off leading to the wake up of the clamping circuitry as the I2C bus is in any case energized even when the subsystem is switched off.

In figure I.2, a schematic representation of the original topology incorporating the local EPS PIC and the CDHS PIC is shown.

I.2.3 Postulation of FET transfer design proposal

One solution of counteracting the problem of an I2C bus pull-down is the transfer of the MOSFET switch to a position behind the DC/DC converter. Furthermore, the power supply of the CDHS PIC has to be connected to the 3.3V supply line regulated by the step-down converter. However, this connecting node has to be placed in front of the MOSFET switch to avoid turning off of the PIC. The subsystem itself is placed behind the MOSFET switch and can be turned on and off by sending a signal to the FET. In this topology, the CDHS PIC is always energized whenever a voltage is present on the power bus. This prevents a powering down of the CDHS PIC, thereby avoiding a pull-down of the I2C bus. With respect to the original topology, the subsystem does not undergo any changes; it is switched on or off with help of the MOSFET switch.

Nevertheless, several disadvantages accompany this topology. Because the CDHS PIC is always on, additional power will be consumed during the boot-up sequence. Moreover, the DC/DC converters are

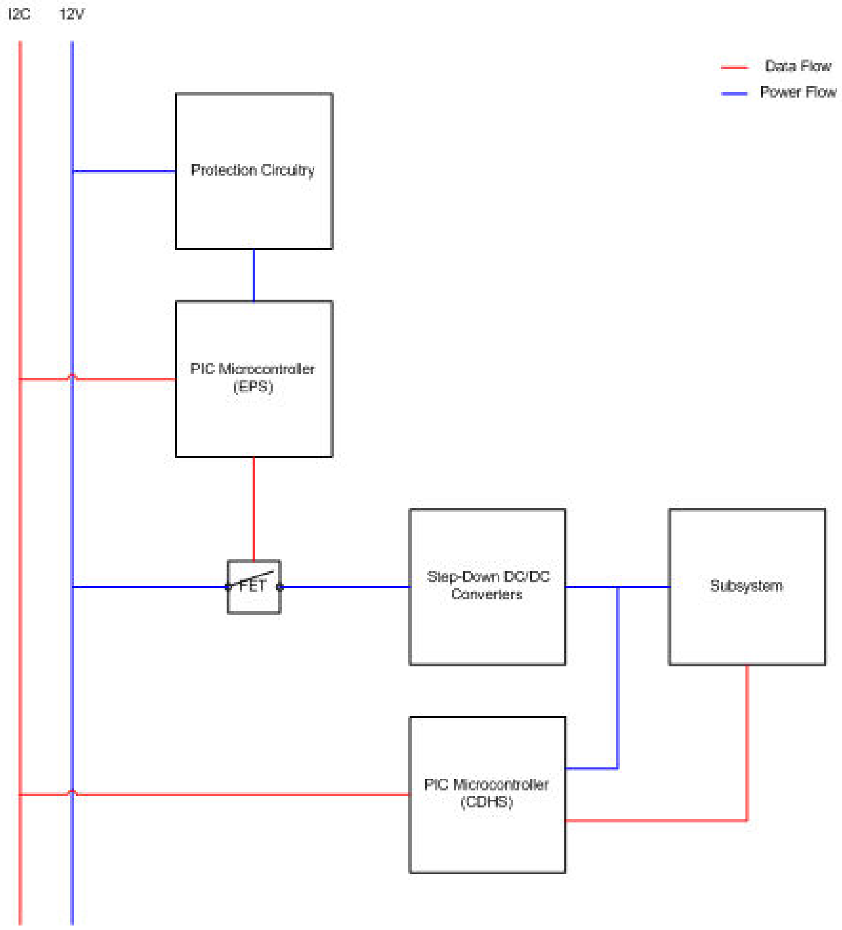
I2C
12V
Data Flow
Power Flow
Protection Circuitry
PIC Microcontroller (EPS)
FET
Step-Down DC/DC Converters
Subsystem
PIC Microcontroller (CDHS)

Figure I.2: Schematic representation of original dual PIC concept

always energized, too. Although their efficiency is reasonably high, losses will occur in the conversion process leading to additional power consumption. Though this power consumption is a disadvantage, it is minor one. After all, the magnitude of this extra power is low.
An additional disadvantage is major redesign or rework of the printed circuit board in order to incorporate the new topology. This disadvantage yields especially in situations, in which multiple supply voltages are produced on-board. Furthermore, additional components have to be implemented.
A schematic representation of the concept incorporating a positional transfer of the MOSFET switch is shown in figure I.3.

I.2.4 Postulation of I2C repeater design proposal

An other solution of preventing the CDHS PIC of pulling the I2C bus down is the addition of an I2C repeater in the design. An I2C repeater is an electronic device, which is inserted in series between the I2C bus and the I2C input pins on the PIC. It is in fact a switch, which is opened in case no enable signal is sent to the repeater. Application of an enable signal will close the switch, thereby enabling communication between the I2C bus and the PIC.
An equivalent electrical circuit of an I2C repeater is shown in figure I.4.
Investigating figure I.4, the general behaviour of an I2C repeater can be determined. Firstly, it has to be noticed that a repeater is inserted in an I2C SCL branch and an I2C SDA branch. One terminal of the SCL branch is connected to the SCL bus, the other terminal to the SCL input pin of the PIC microcontroller. The same build-up yields for the SDA line. In principle, an I2C repeater mimics the behaviour of a triac in the SCL branch and a triac in the SDA branch. After all by having a high input signal on the enable pin, both triac structures will enter conducting modes and communication between the buses and the PIC microcontroller is enabled. However, a difference with a triac structure is that in case of a low signal on the enable pin, communication between the buses and the PIC microcontroller is immediately disabled. This makes the I2C repeater an effective switch between the I2C buses and the PIC microcontroller.
Application of an I2C repeater in the original design prevents the I2C bus from pull-down by a disabled

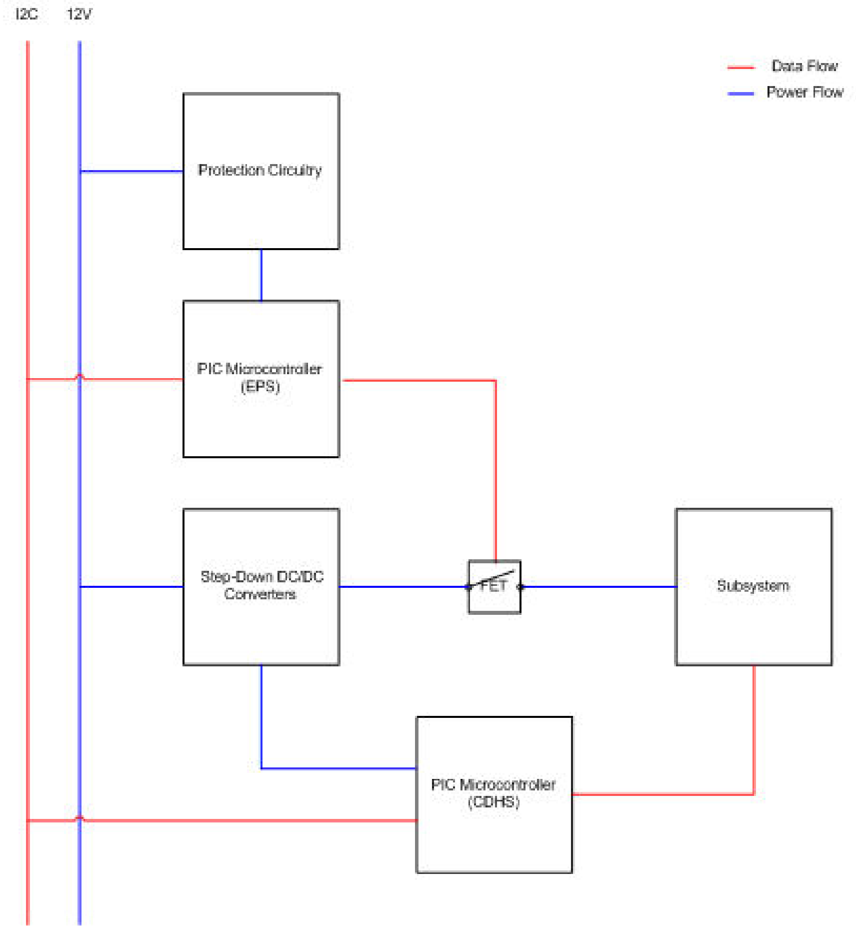
I2C
12V
Data Flow
Power Flow
Protection Circuitry
PIC Microcontroller (EPS)
Step-Down DC/DC Converters
FET
Subsystem
PIC Microcontroller (CDHS)

Figure I.3: Schematic representation of dual PIC concept with transfer of MOSFET switch

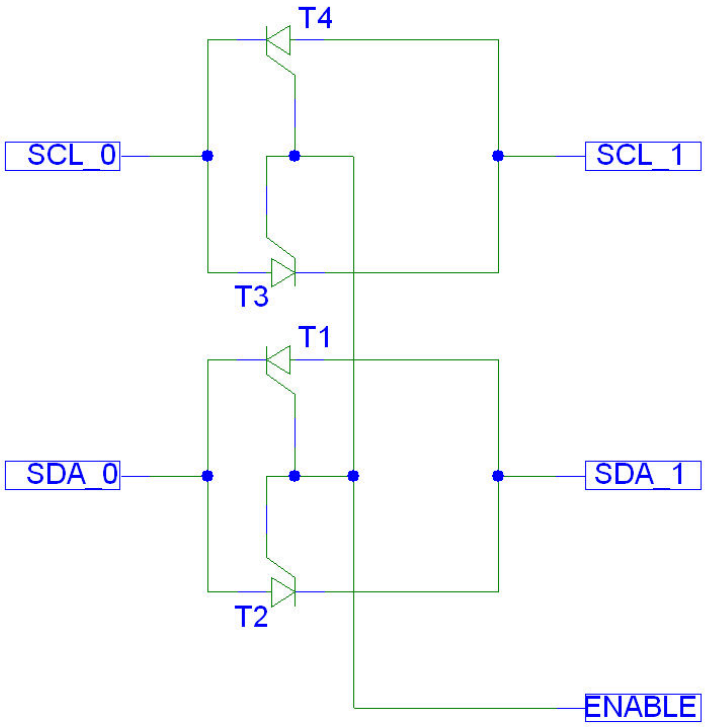
T4
SCL_0
SCL_1
T3
T1
SDA_0
SDA_1
T2
ENABLE

Figure I.4: Equivalent electrical circuit of an I2C repeater

PIC microcontroller. After all in case of a disabled PIC, the respective I2C repeater will be switched off

making communication between the I2C bus and the PIC impossible. The problematic clamping diodes are not connected and collapse of the I2C bus is avoided.
In figure I.5, a schematic representation of the design applying an I2C repeater is shown.

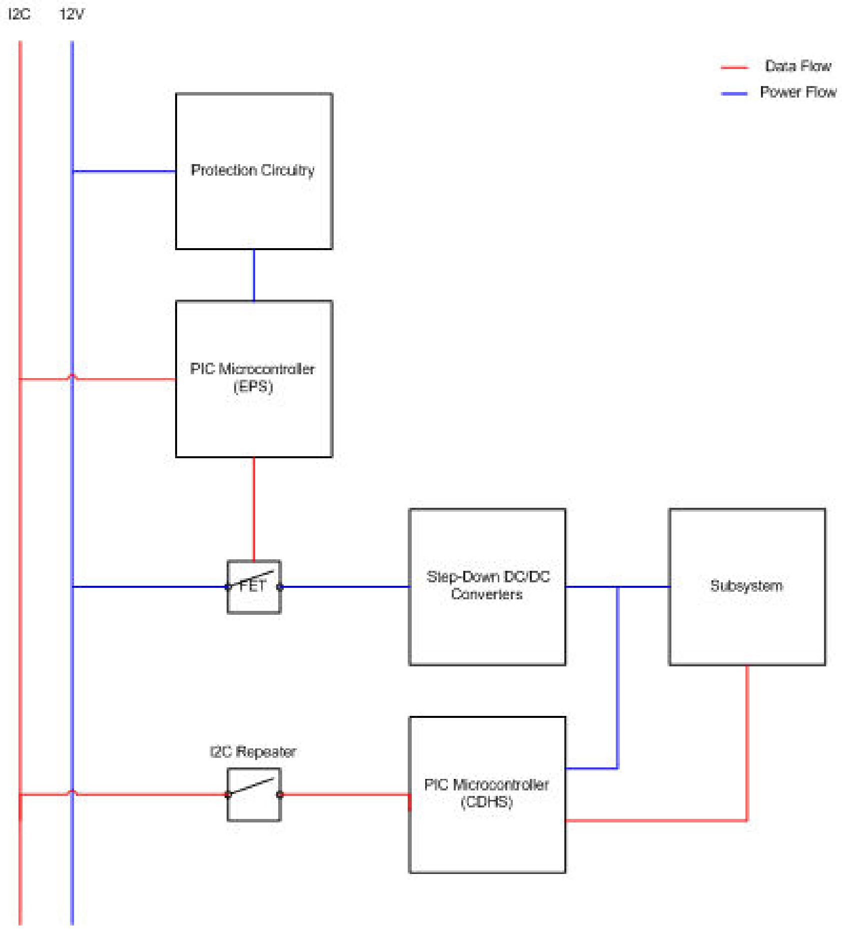
I2C
12V
Data Flow
Power Flow
Protection Circuitry
PIC Microcontroller (EPS)
FET
Step-Down DC/DC Converters
Subsystem
I2C Repeater
PIC Microcontroller (CDHS)

Figure I.5: Schematic representation of dual PIC concept with I2C repeater application

A point of interest in the application of the I2C repeater is the connection of the enable pin. In general, two options can be distinguished.
One option has the enable pin connected to an output port of the CDHS PIC microcontroller. With an additional subroutine in the program of the PIC, the enable pin can be set high as soon as the CDHS PIC is powered up. Another option is connecting the enable pin of the repeater directly to the 3.3V supply bus behind the step-down DC/DC converter. In this case, the repeater will be switched on whenever the MOSFET switch in front of the converter is closed.
One disadvantage of this topology is that an additional component has to be integrated in the design. This will result in a small amount of redesign or rework of the printed circuit boards.
Furthermore, the I2C repeater needs a small amount of power to operate. Investigating the data sheet of the I2C repeater, it is found that maximum current usage will amount to 5 mA at a 3.3V supply voltage for every applied I2C repeater.

I.2.5 Design option trade-off

In order to arrive at design solution, a trade-off between the various design solutions has to be performed. In the previous sections, the main design solutions were presented.
In table I.1, a trade-off table is presented of all major design options. The array of design possibilities consists of three options. As a first option, the positional transfer of the switching MOSFET is presented. With respect to the application of I2C repeaters, two options can be distinguished. Therefore, the second option refers to the application of repeaters to all PICs in the spacecraft. In the third option, only the CDHS PICs will be equipped with repeaters; the data lines of the local EPS PICs and deployment PICs are directly connected to the relevant buses.
Performing the trade-off, it was decided by GA and FH that the application of I2C repeaters to the CDHS PICs is the most viable design option. It combines the advantages of I2C repeater usage with a

Table I.1: Trade-off table of major design options

Design option	Pros	Cons
Positional transfer of MOSFET switches	– Low additional power usage	– Major redesign of printed circuit boards – Additional I/O ports needed on local EPS PIC – Large amount of additional complexity
Application of I2C repeaters on all PICs	– Protection of I2C bus in case of PIC failure – Small amount of additional complexity	– Very high additional power usage – Moderate redesign of printed circuit boards
Application of I2C repeaters on CDHS PICs	– Limited protection of I2C bus in case of PIC failure – Minor redesign of printed circuit boards – Small amount of additional complexity	– Moderately high additional power usage

moderate impact on the design.

A second design decision has to be taken on the connection of the enable pin of the I2C repeaters. A first option is to connect the enable pin to an output pin of the CDHS PIC. With an additional subroutine in the PIC software, the I2C repeater can be switched on as soon as the CDHS PIC is turned on. In this configuration, the I2C repeater can be switched off on command yielding a flexible design. As a second option the enable pin can be connected directly to the 3.3V supply; in this case the enable pin is switched in parallel with the supply pin of the repeater. This design is a more rigid design with respect to the former option, but it does not need additional software. A trade-off table of these two options is shown in table I.2.

Table I.2: Trade-off table of I2C repeater enable pin connection

Design option	Pros	Cons
Enable pin of I2C repeater connected to I/O pin of PIC	– Switchable connection of PIC to I2C bus	– Additional software needed in CDHS PIC
Enable pin of I2C repeater connected to 3.3V supply	– Only a single line needed to control I2C repeater operation	– No active switching

After performing a trade-off, GA and FH concluded that the latter option is the most viable one.

Summarizing, the design change involves application of I2C repeaters to the CDHS PICs exclusively, with their enable pins connected to the 3.3V supply line.

I.3 Conclusions and recommendations

Disabled PIC microcontrollers are able to pull-down the I2C bus due to the presence of clamping diodes in the I2C input ports. In order to avoid unwanted collapse of the I2C bus, precautions have to be taken in the design of the printed circuit boards.

Three design options are available for counteracting pull-down of the I2C bus. As a first option, a positional transfer of the MOSFET switch is presented. Application of I2C repeaters to all PICs in the spacecraft is illustrated as a second option. A third option is application of I2C repeaters to CDHS PICs exclusively. After performing a trade-off, this latter option is chosen to be the most viable.

A second design decision is taken on the connection of the enable pins of the I2C repeaters. Two design options are available. As a first option, the enable pin can be connected to an output pin of the CDHS PIC. A second option is connecting the pin to the 3V3 supply. A small trade-off is accomplished resulting in the choice of the latter option.

Appendix J

Latest version of power budget

J.1 Summary of latest version of power budget

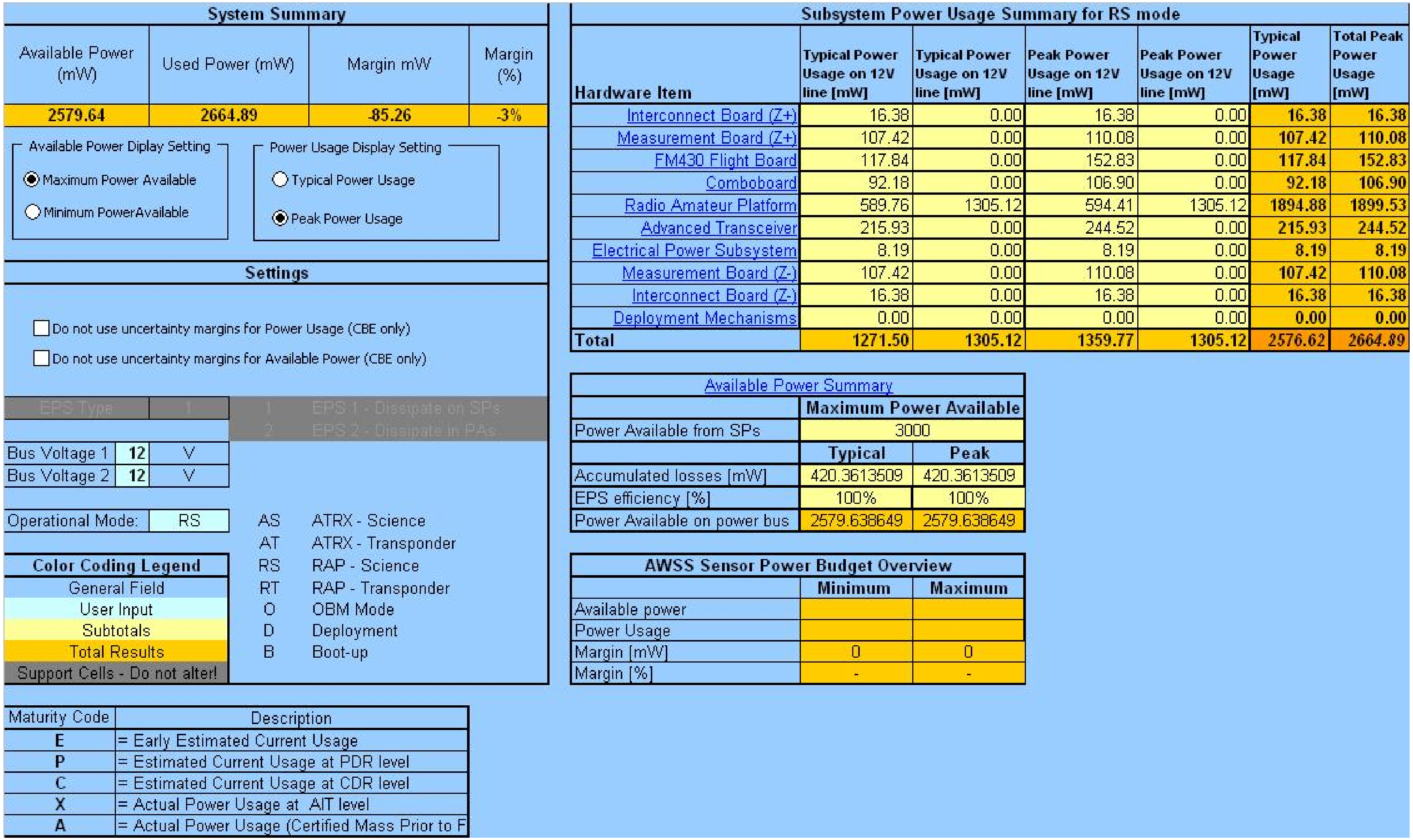

System Summary

Available Power (mW)	Used Power (mW)	Margin mW	Margin (%)
2579.64	2664.89	-85.26	-3%

Available Power Diplay Setting
● Maximum Power Available
○ Minimum PowerAvailable

Power Usage Display Setting
○ Typical Power Usage
● Peak Power Usage

Settings

☐ Do not use uncertainty margins for Power Usage (CBE only)
☐ Do not use uncertainty margins for Available Power (CBE only)

EPS Type	1	1	EPS 1 - Dissipate on SPs
		2	EPS 2 - Dissipate in PAs

Bus Voltage 1	12	V
Bus Voltage 2	12	V

Operational Mode: RS

AS	ATRX - Science
AT	ATRX - Transponder
RS	RAP - Science
RT	RAP - Transponder
O	OBM Mode
D	Deployment
B	Boot-up

Color Coding Legend
General Field
User Input
Subtotals
Total Results
Support Cells - Do not alter!

Maturity Code	Description
E	= Early Estimated Current Usage
P	= Estimated Current Usage at PDR level
C	= Estimated Current Usage at CDR level
X	= Actual Power Usage at AIT level
A	= Actual Power Usage (Certified Mass Prior to F

Subsystem Power Usage Summary for RS mode

Hardware Item	Typical Power Usage on 12V line [mW]	Typical Power Usage on 12V line [mW]	Peak Power Usage on 12V line [mW]	Peak Power Usage on 12V line [mW]	Typical Power Usage [mW]	Total Peak Power Usage [mW]
Interconnect Board (Z+)	16.38	0.00	16.38	0.00	**16.38**	**16.38**
Measurement Board (Z+)	107.42	0.00	110.08	0.00	**107.42**	**110.08**
FM430 Flight Board	117.84	0.00	152.83	0.00	**117.84**	**152.83**
Comboboard	92.18	0.00	106.90	0.00	**92.18**	**106.90**
Radio Amateur Platform	589.76	1305.12	594.41	1305.12	**1894.88**	**1899.53**
Advanced Transceiver	215.93	0.00	244.52	0.00	**215.93**	**244.52**
Electrical Power Subsystem	8.19	0.00	8.19	0.00	**8.19**	**8.19**
Measurement Board (Z-)	107.42	0.00	110.08	0.00	**107.42**	**110.08**
Interconnect Board (Z-)	16.38	0.00	16.38	0.00	**16.38**	**16.38**
Deployment Mechanisms	0.00	0.00	0.00	0.00	**0.00**	**0.00**
Total	**1271.50**	**1305.12**	**1359.77**	**1305.12**	***2576.62***	***2664.89***

Available Power Summary

	Maximum Power Available	
Power Available from SPs	3000	
	Typical	**Peak**
Accumulated losses [mW]	420.3613509	420.3613509
EPS efficiency [%]	100%	100%
Power Available on power bus	2579.638649	2579.638649

AWSS Sensor Power Budget Overview

	Minimum	Maximum
Available power		
Power Usage		
Margin [mW]	0	0
Margin [%]	-	-

J.2 Example of application of power budget: measurement board

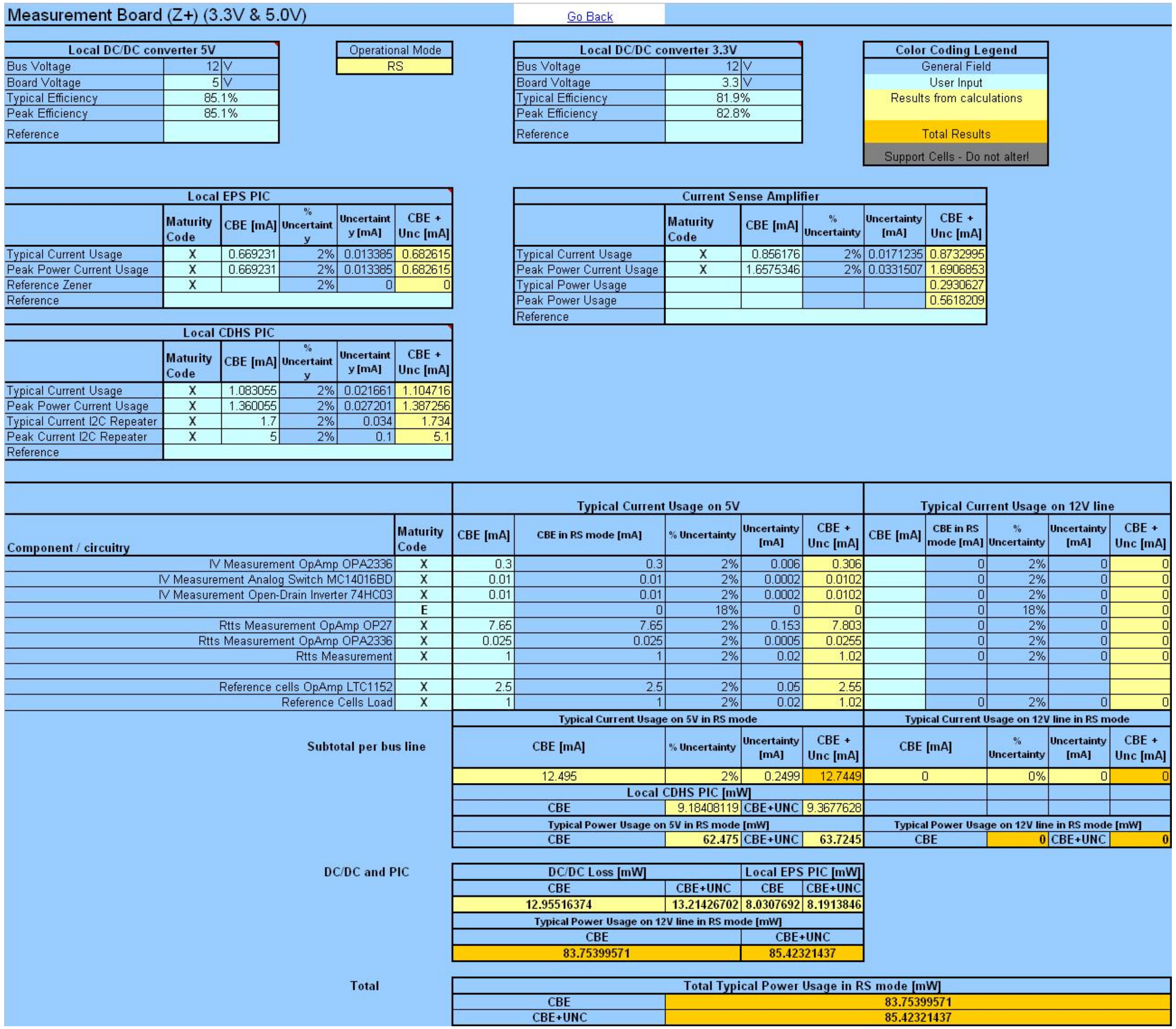

Measurement Board (Z+) (3.3V & 5.0V)

Go Back

Local DC/DC converter 5V		
Bus Voltage	12	V
Board Voltage	5	V
Typical Efficiency	85.1%	
Peak Efficiency	85.1%	
Reference		

Operational Mode
RS

Local DC/DC converter 3.3V		
Bus Voltage	12	V
Board Voltage	3.3	V
Typical Efficiency	81.9%	
Peak Efficiency	82.8%	
Reference		

Color Coding Legend
General Field
User Input
Results from calculations
Total Results
Support Cells - Do not alter!

Local EPS PIC	Maturity Code	CBE [mA]	% Uncertainty	Uncertainty [mA]	CBE + Unc [mA]
Typical Current Usage	X	0.669231	2%	0.013385	0.682615
Peak Power Current Usage	X	0.669231	2%	0.013385	0.682615
Reference Zener	X		2%	0	0
Reference					

Current Sense Amplifier	Maturity Code	CBE [mA]	% Uncertainty	Uncertainty [mA]	CBE + Unc [mA]
Typical Current Usage	X	0.856176	2%	0.0171235	0.8732995
Peak Power Current Usage	X	1.6575346	2%	0.0331507	1.6906853
Typical Power Usage					0.2930627
Peak Power Usage					0.5618209
Reference					

Local CDHS PIC	Maturity Code	CBE [mA]	% Uncertainty	Uncertainty [mA]	CBE + Unc [mA]
Typical Current Usage	X	1.083055	2%	0.021661	1.104716
Peak Power Current Usage	X	1.360055	2%	0.027201	1.387256
Typical Current I2C Repeater	X	1.7	2%	0.034	1.734
Peak Current I2C Repeater	X	5	2%	0.1	5.1
Reference					

		Typical Current Usage on 5V					Typical Current Usage on 12V line				
Component / circuitry	Maturity Code	CBE [mA]	CBE in RS mode [mA]	% Uncertainty	Uncertainty [mA]	CBE + Unc [mA]	CBE [mA]	CBE in RS mode [mA]	% Uncertainty	Uncertainty [mA]	CBE + Unc [mA]
IV Measurement OpAmp OPA2336	X	0.3	0.3	2%	0.006	0.306		0	2%	0	0
IV Measurement Analog Switch MC14016BD	X	0.01	0.01	2%	0.0002	0.0102		0	2%	0	0
IV Measurement Open-Drain Inverter 74HC03	X	0.01	0.01	2%	0.0002	0.0102		0	2%	0	0
	E		0	18%	0	0		0	18%	0	0
Rtts Measurement OpAmp OP27	X	7.65	7.65	2%	0.153	7.803		0	2%	0	0
Rtts Measurement OpAmp OPA2336	X	0.025	0.025	2%	0.0005	0.0255		0	2%	0	0
Rtts Measurement	X	1	1	2%	0.02	1.02		0	2%	0	0
Reference cells OpAmp LTC1152	X	2.5	2.5	2%	0.05	2.55					
Reference Cells Load	X	1	1	2%	0.02	1.02		0	2%	0	0

Subtotal per bus line

Typical Current Usage on 5V in RS mode				Typical Current Usage on 12V line in RS mode			
CBE [mA]	% Uncertainty	Uncertainty [mA]	CBE + Unc [mA]	CBE [mA]	% Uncertainty	Uncertainty [mA]	CBE + Unc [mA]
12.495	2%	0.2499	12.7449	0	0%	0	0

Local CDHS PIC [mW]			
CBE	9.18408119	CBE+UNC	9.3677628

Typical Power Usage on 5V in RS mode [mW]				Typical Power Usage on 12V line in RS mode [mW]			
CBE	62.475	CBE+UNC	63.7245	CBE	0	CBE+UNC	0

DC/DC and PIC

DC/DC Loss [mW]		Local EPS PIC [mW]	
CBE	CBE+UNC	CBE	CBE+UNC
12.95516374	13.21426702	8.0307692	8.1913846

Typical Power Usage on 12V line in RS mode [mW]	
CBE	CBE+UNC
83.75399571	85.42321437

Total

Total Typical Power Usage in RS mode [mW]	
CBE	83.75399571
CBE+UNC	85.42321437

Appendix K

DC3-TN-609-062 EuroSim - Geometrical properties

K.1 Introduction

EuroSim is a simulation platform, in which the orbit of the Delfi-C3 spacecraft will be simulated. Interesting quantities, which can be determined from this simulation, are power generation and attitude reconstruction. For attitude reconstruction, it is important to determine the geometrical properties of the spacecraft.
In this report, the process of determining the mechanical properties of the Delfi-C3 spacecraft will be outlined. It has to be mentioned that the involved calculations are basic, and therefore the results are not extremely accurate. However, for simulation purposes the results are sufficient.
First of all, the center of mass of the Delfi-C3 spacecraft will be determined. The second calculation involves the determination of the inertia tensor of the Delfi-C3 spacecraft.

K.2 Geometrical properties

K.2.1 Determination of center of mass

The coordinates of the center of mass of the Delfi-C3 spacecraft can be easily calculated using the following expression:

$$q_{Com} = \frac{M_q}{m_{S/C}} \tag{K.1}$$

where q_{CoM} is the coordinate on the q-axis of the projection of the center of mass onto the q-axis, $m_{S/C}$ is the mass of the complete spacecraft, and M_q is the so-called first moment of mass about the q-axis. Note that in the previous and following expressions, the variable q has been used to denote an axis reference. In a Cartesian coordinate system, q can be set as x, y, or z.
The first moment of mass about the q-axis is defined as:

$$M_q = \int \sqrt{r^2 + s^2} \cdot \mathrm{d}m \tag{K.2}$$

where dm is the mass of an infinitesimally small element, and r and s are the coordinates of the respective projections of the mass element onto the r- and s-axis, where the r- and s-axis are the two axes, which are orthogonal to the q-axis in the qrs-reference frame (e.g. if x equals q, then y equals r and z equals s).
Unfortunately, equation K.2 can be extremely bothersome to use for calculating the first mass moment of an object. However, for an object consisting of n discrete elements, this expression can be simplified to:

$$M_q = \sum_{i=1}^{n} (M_q)_i = \sum_{i=1}^{n} m_i \cdot (q_{CoM})_i \tag{K.3}$$

where m_i is the mass of the i-th element, and $(q_{CoM})_i$ is the coordinate of the projection of the center of mass of the i-th element onto the q-axis.

The Delfi-C3 spacecraft is modeled as a collection of discrete elements. The main body is modeled as a box with dimensions $l \times w \times d$. Attached to this box are the solar panels, which are modeled as flat plates with dimension $l \times w$ or $l \times d$, dependent on the panel under consideration. All solar panels are nominally at an offset angle θ with respect to the underlying body panel. Furthermore, two sets of four antennae are attached to the front and back end of the satellite. At the front end are the long downlink antennae with dimension l_{DLA}, while the short uplink antennae with dimension l_{ULA} are at the back end. Both sets of antennae are at an angle ϕ with respect to the xy-plane. A sketch of this model in the xz-plane is shown in figure K.1.

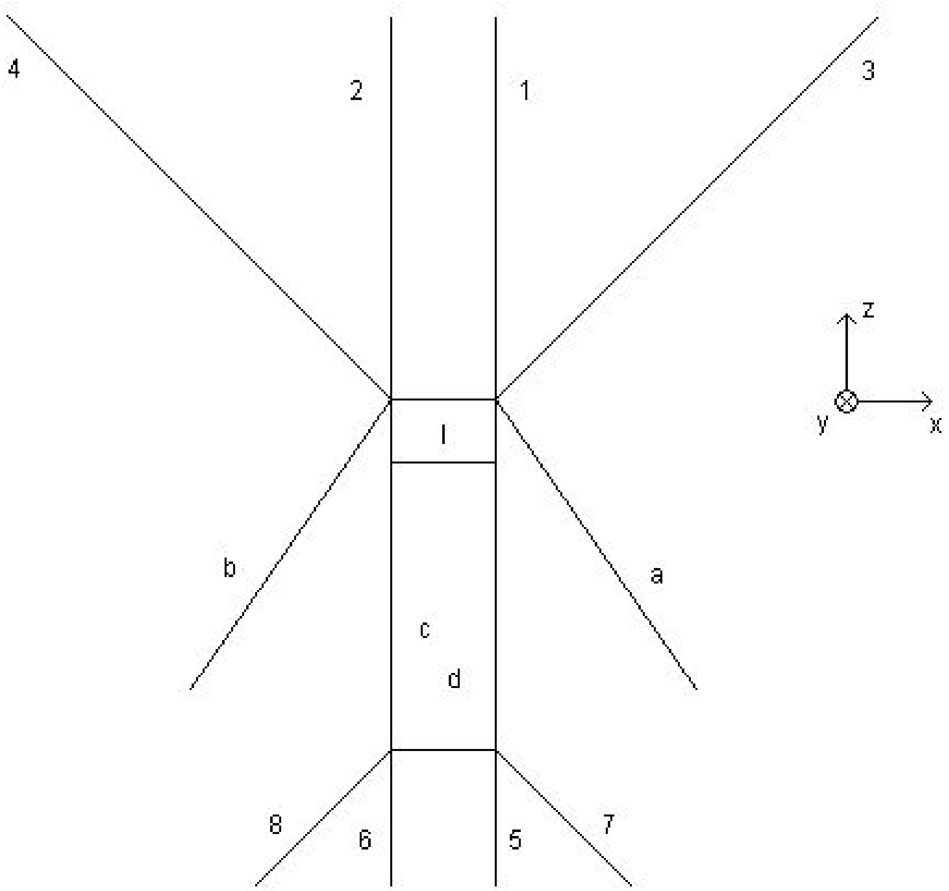

Figure K.1: Sketch of Delfi-C3 spacecraft model in xz-plane of satellite fixed reference frame

In table K.1, several relevant characteristics of the model of the Delfi-C3 spacecraft are given.
Please note that SF refers to satellite fixed reference frame. The value for the total spacecraft mass has been calculated by adding the masses of all individual elements, leading to the following expression:

$$m_{S/C} = m_{mb} + 4 \cdot m_{sp} + 4 \cdot m_{DLA} + 4 \cdot m_{ULA} \tag{K.4}$$

It has to be noted that the Delfi-C3 spacecraft is mass symmetrical around the z-axis, when all angles are at their nominal value. Therefore, the x- and y-coordinate of the center of mass of the spacecraft are assumed to correspond to the respective coordinates of the geometrical center of the spacecraft. However, in case of a deployment failure of one solar panel or antenna the mass symmetry will be disturbed and an offset with respect to the geometrical center will be created for the center of mass in the x- and y-direction. However, it is assumed that these offsets are sufficiently small to be neglected.
Returning to figure K.1, it is noticed that the Delfi-C3 spacecraft consists of multiple elements, which all have been given a reference. In the following paragraph, the formulae used for calculating the $(M_z)_i$ for these elements will be given. Note that these first moments of mass are calculated with respect to the origin of the satellite fixed reference frame, which is situated in the center of the front plate.

Table K.1: Relevant geometrical characteristics of the Delfi-C3 spacecraft model

Parameter	Variable	Value		Remark
Length	l	326.5	mm	z-dimension SF
Width	w	100.0	mm	x-dimension SF
Depth	d	100.0	mm	y-dimension SF
Downlink antenna length	l_{DLA}	500.0	mm	
Uplink antenna length	l_{ULA}	180.0	mm	
Nominal solar panel angle	θ	35.0	°	w.r.t. underlying body panel
Nominal antenna angle	ϕ	40.0	°	w.r.t. xy-plane SF
Main body mass	m_{mb}	2573.0	g	
Solar panel mass	m_{sp}	102.5	g	
Downlink antenna mass	m_{DLA}	3.125	g	
Uplink antenna mass	m_{ULA}	1.125	g	
Total spacecraft mass	$m_{S/C}$	3000.0	g	

The first moment of mass of the main body (reference I) is calculated with:

$$(M_z)_I = -\frac{1}{2} \cdot l \cdot m_{mb} \tag{K.5}$$

Similarly, for the solar panels, which are perpendicular to the yz-plane (reference a, b)

$$(M_z)_a = (M_z)_b = -\frac{1}{2} \cdot l \cdot \cos\theta_i \cdot m_{sp} \tag{K.6}$$

where θ_i denotes the actual angle, which the solar panel describes with the underlying body panel. Note that in the nominal case, θ_i equals θ.

For the first moment of mass of the solar panels perpendicular to the xz-plane (reference c, d), the following expression applies:

$$(M_z)_c = (M_z)_d = -\left(l - \frac{1}{2} \cdot l \cdot \cos\theta_i\right) \cdot m_{sp} \tag{K.7}$$

Using the same principle for the downlink antennae (reference 1, 2, 3, 4), the following expression applies:

$$(M_z)_1 = (M_z)_2 = (M_z)_3 = (M_z)_4 = l_{DLA} \cdot \sin\theta_i \cdot m_{DLA} \tag{K.8}$$

In a similar way for the uplink antennae (reference 5, 6, 7, 8):

$$(M_z)_5 = (M_z)_6 = (M_z)_7 = (M_z)_8 = -\left(l + l_{ULA} \cdot \sin\theta_i\right) \cdot m_{ULA} \tag{K.9}$$

Applying equation K.3 to the Delfi-C3 spacecraft yields the following:

$$(M_z)_{S/C} = \sum_{i=1}^{n} (M_z)_i = (M_z)_I + \sum_{j=a}^{d} (M_z)_j + \sum_{k=1}^{8} (M_z)_k \tag{K.10}$$

Finally, equation K.1 can be used to determine the z-coordinate of the center of mass.

Filling out the values corresponding to every involved variable leads to the results given in table K.2, in which the nominal case is considered. The values in table K.2 are generated using the formulae in equation K.1 and equations K.5 to K.10.

Concluding, the position vector of the center of mass can be determined in the satellite fixed reference frame. This position vector is generated with:

$$\vec{x}_{CoM} = \begin{pmatrix} x_{CoM} \\ y_{CoM} \\ z_{CoM} \end{pmatrix} \tag{K.11}$$

Table K.2: Relevant geometrical characteristics of the Delfi-C3 spacecraft model

Part	Reference	M_z (kg.m)
Main body	I	-0.42004225
Solar panel	a	-0.01370697
Solar panel	b	-0.01370697
Solar panel	c	-0.01975928
Solar panel	d	-0.01975928
Downlink antenna	1	0.000502178
Downlink antenna	2	0.000502178
Downlink antenna	3	0.000502178
Downlink antenna	4	0.000502178
Uplink antenna	5	-0.00043239
Uplink antenna	6	-0.00043239
Uplink antenna	7	-0.00043239
Uplink antenna	8	-0.00043239
Total		-0.48669562
z_{CoM} (m)		-0.16223187

which becomes in the nominal case:

$$\vec{x}_{CoM} = \begin{pmatrix} 0 \\ 0 \\ -162.2 \end{pmatrix} \text{mm} \tag{K.12}$$

K.2.2 Calculation of inertia tensor

For determining the rotational dynamics of the Delfi-C3 spacecraft, it is essential to make an accurate calculation of its inertia tensor. The inertia tensor is written as:

$$\mathbf{I} = \begin{pmatrix} I_{xx} & I_{xy} & I_{xz} \\ I_{yx} & I_{yy} & I_{yz} \\ I_{zx} & I_{zy} & I_{zz} \end{pmatrix} \tag{K.13}$$

where I_{ij} is known as the moment of inertia about axis i, if i equals j, or as the ij-product of inertia, if i is not equal to j. Both i and j are chosen from the set $\{x, y, z\}$.
The moment of inertia about axis q is defined as:

$$I_{qq} = \int \left(r^2 + s^2\right) \cdot \mathrm{d}m \tag{K.14}$$

where dm is the mass of an infinitesimally small element, and r and s are the coordinates of the respective projections of the mass element onto the r- and s-axis, where the r- and s-axis are the two axes, which are orthogonal to the q-axis in the qrs-reference frame (e.g. if x equals q, then y equals r and z equals s).
Fortunately, for simple geometries, it is not necessary to evaluate the integral every time as standard formulae have been produced. As the geometry of the Delfi-C3 spacecraft can be broken up into a collection of beams and flat plates in every plane, the knowledge of the standard moment of inertia values for beams and plates is sufficient to determine the total moment of inertia of the spacecraft.
In figure K.2, sketches are shown of both a flat plate and a beam. Dimensions, which are relevant for the calculation of the moment of inertia, are included.
Using figure K.2a, the moment of inertia of a flat plate about an axis parallel to the z-axis running through its center of mass is defined as:

$$\left(I_{zz}\right)_{CoM} = \frac{1}{12} \cdot m \cdot \left(x^2 + y^2\right) \tag{K.15}$$

where x is the length of the plate, y is the width of the plate, and m is the mass of the plate. The moment of inertia of a one-dimensional beam is found by setting one dimension in equation K.15 to zero. This

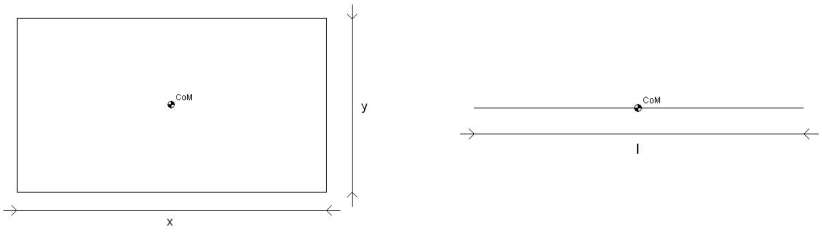

a.

b.

Figure K.2: Sketch of standard geometric objects with relevant dimensions; a. flat plate; b. beam

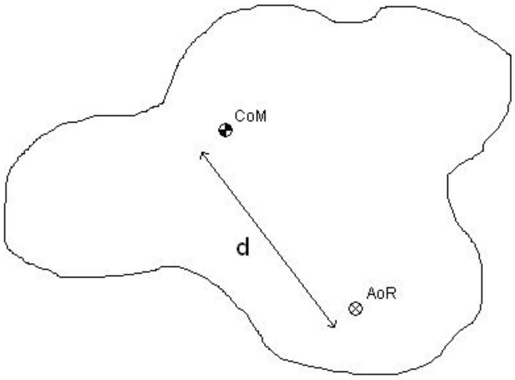

Figure K.3: Sketch of an arbitrary body having its axis of rotation displaced with respect to its center of mass

yields as an expression for the moment of inertia of a beam about an axis parallel to the z-axis running through its center of mass, using figure K.2b:

$$(I_{zz})_{CoM} = \frac{1}{12} \cdot m \cdot l^2 \tag{K.16}$$

where l is the length of the beam, and m is the mass of the beam.
However, the principal axis of rotation will likely not go through the center of mass of the geometrical object, but goes through the center of mass of the complete spacecraft. Therefore, a translation of the rotational axis must take place for every element considered. This brings a change in moment of inertia with it, which is known as Steiner's rule.
Steiner's rule dictates that the moment of inertia will be larger when the axis of rotation is displaced from the center of gravity of the body. Therefore, the following equation applies, using figure K.3:

$$\Delta I_{zz} = m \cdot d^2 \tag{K.17}$$

where m is the mass of the geometrical element, and d is the distance between the axis of rotation and the center of mass of the element under consideration. Note that the axis of rotation runs through the center of mass of the complete spacecraft. The total moment of inertia of the geometrical element can be found by adding the two contributions:

$$I_{zz} = (I_{zz})_{Com} + \Delta I_{zz} \tag{K.18}$$

Recall that in equations K.15 to K.18, the index z can be replaced by x or y if relevant.
In the following sections, the moments of inertia around the various axes will be evaluated. As an initial reference point, the geometrical center of the satellite will be taken, i.e. the point in the center of the

main body. Note that this point does not coincide with center of mass. This will corrected at a later stage, however.

Calculation of I_{yy}

First, the moment of inertia about the y-axis is considered. Returning to figure K.1, a helpful sketch is given for calculating the value of this moment of inertia. Evaluating the moment of inertia of the main body (reference I) yields the following expression:

$$\left((I_{yy})_{CoM}\right)_I = \frac{1}{12} \cdot m_{mb} \cdot \left(l^2 + w^2\right) \tag{K.19}$$

$$(\Delta I_{yy})_I = 0 \tag{K.20}$$

For the solar panels, which are perpendicular to the xz-plane (reference a, b), the following expression applies:

$$\left((I_{yy})_{CoM}\right)_a = \left((I_{yy})_{CoM}\right)_b = \frac{1}{12} \cdot m_{sp} \cdot l^2 \tag{K.21}$$

$$(\Delta I_{yy})_a = (\Delta I_{yy})_b = m_{sp} \cdot \left(\left(\frac{l}{2} - \frac{l}{2} \cdot \cos\theta_i\right)^2 + \left(\frac{w}{2} + \frac{l}{2} \cdot \sin\theta_i\right)^2\right) \tag{K.22}$$

In these equations, θ_i is the actual angle the solar panel describes with the underlying body panel. In a similar way, the moments of inertia of the solar panels perpendicular to the yz-plane (reference c, d) can be calculated:

$$\left((I_{yy})_{CoM}\right)_c = \left((I_{yy})_{CoM}\right)_d = \frac{1}{12} \cdot m_{sp} \cdot \left((l \cdot \cos\theta_i)^2 + w^2\right) \tag{K.23}$$

$$(\Delta I_{yy})_c = (\Delta I_{yy})_d = m_{sp} \cdot \left(\frac{l}{2} - \frac{l}{2} \cdot \cos\theta_i\right)^2 \tag{K.24}$$

For the downlink antennae in the yz-plane (reference 1, 2) the following applies:

$$\left((I_{yy})_{CoM}\right)_1 = \left((I_{yy})_{CoM}\right)_2 = \frac{1}{12} \cdot m_{DLA} \cdot (l_{DLA} \cdot \sin\phi)^2 \tag{K.25}$$

$$(\Delta I_{yy})_1 = (\Delta I_{yy})_2 = m_{DLA} \cdot \left(\left(\frac{l}{2} + \frac{l_{DLA}}{2} \cdot \sin\phi\right)^2 + \left(\frac{w}{2}\right)^2\right) \tag{K.26}$$

Evaluating the moments of inertia for the downlink antennae in the xz-plane (reference 3, 4) yields:

$$\left((I_{yy})_{CoM}\right)_3 = \left((I_{yy})_{CoM}\right)_4 = \frac{1}{12} \cdot m_{DLA} \cdot l_{DLA}^2 \tag{K.27}$$

$$(\Delta I_{yy})_3 = (\Delta I_{yy})_4 = m_{DLA} \cdot \left(\left(\frac{l}{2} + \frac{l_{DLA}}{2} \cdot \sin\phi\right)^2 + \left(\frac{w}{2} + \frac{l_{DLA}}{2} \cdot \cos\phi\right)^2\right) \tag{K.28}$$

The same procedure can be employed for the uplink antennae. Therefore, for the uplink antennae in the yz-plane (reference 5, 6) the following is valid:

$$\left((I_{yy})_{CoM}\right)_5 = \left((I_{yy})_{CoM}\right)_6 = \frac{1}{12} \cdot m_{ULA} \cdot (l_{ULA} \cdot \sin\phi)^2 \tag{K.29}$$

$$(\Delta I_{yy})_5 = (\Delta I_{yy})_6 = m_{ULA} \cdot \left(\left(\frac{l}{2} + \frac{l_{ULA}}{2} \cdot \sin\phi \right)^2 + \left(\frac{w}{2} \right)^2 \right) \tag{K.30}$$

For the uplink antennae in the xz-plane (reference 7, 8) applies:

$$\left((I_{yy})_{CoM} \right)_7 = \left((I_{yy})_{CoM} \right)_8 = \frac{1}{12} \cdot m_{ULA} \cdot l_{ULA}^2 \tag{K.31}$$

$$(\Delta I_{yy})_7 = (\Delta I_{yy})_8 = m_{ULA} \cdot \left(\left(\frac{l}{2} + \frac{l_{ULA}}{2} \cdot \sin\phi \right)^2 + \left(\frac{w}{2} + \frac{l_{ULA}}{2} \cdot \cos\phi \right)^2 \right) \tag{K.32}$$

Now, the total moment of inertia of the complete satellite about its geometrical center can be generated by adding all individual contributions. Hence, this value becomes:

$$(I_{yy})_{S/C} = (I_{yy})_I + \sum_{j=a}^{d} (I_{yy})_j + \sum_{k=1}^{8} (I_{yy})_k \tag{K.33}$$

However, the moment of inertia about the center of mass is the quantity of interest. Therefore, a small correction has to be made, because the center of mass does not exactly coincide with the geometrical center of the spacecraft body. Recalling equations K.17 and K.18, the following expression can be produced:

$$(I_{yy})_{CoM} = I_{yy} - \Delta I_{yy} = I_{yy} - m \cdot d^2 \tag{K.34}$$

where d denotes in this situation the distance between the geometrical center and the center of mass. Evaluating this expression for the complete Delfi-C3 spacecraft yields:

$$\left((I_{yy})_{CoM} \right)_{S/C} = I_{yy} - \Delta I_{yy} = (I_{yy})_{S/C} - m_{S/C} \cdot d^2 = (I_{yy})_{S/C} - m_{S/C} \cdot \left(\frac{l}{2} - z_{CoM} \right)^2 \tag{K.35}$$

Filling out the relevant values for every involved variable leads to a value for the moment of inertia about the y-axis calculated in table K.3. For the calculations of these values, equations K.18 to K.35 are used.

Table K.3: Determination of moment of inertia about y-axis in nominal case

Part	Reference	I_{yy} (CoM)	I_{yy} (Steiner)	I_{yy} (total)
Main body	I	0.025001466	0	0.025001466
Solar panel //	a	0.000910561	0.02204061	0.003114622
Solar panel //	b	0.000910561	0.02204061	0.003114622
Solar panel ⊥	c	0.000696412	8.93424E-05	0.000785755
Solar panel ⊥	d	0.000696412	8.93424E-05	0.000785755
Downlink antenna //	1	2.68995E-05	0.000335755	0.000362654
Downlink antenna //	2	2.68995E-05	0.000335755	0.000362654
Downlink antenna ⊥	3	6.51042E-05	0.000510216	0.00057532
Downlink antenna ⊥	4	6.51042E-05	0.000510216	0.00057532
Uplink antenna //	5	1.25502E-06	5.78088E-05	5.90638E-05
Uplink antenna //	6	1.25502E-06	5.78088E-05	5.90638E-05
Uplink antenna ⊥	7	3.0375E-06	7.09124E-05	7.39499E-05
Uplink antenna ⊥	8	3.0375E-06	7.09124E-05	7.39499E-05
Total				0.034944196
z_{CoM} (m)				-0.16223187
Corrected				0.034941086

Calculation of I_{xx}

In the following, the moment of inertia about the x-axis will be determined. The geometry of the Delfi-C3 spacecraft projected onto the xz-plane does not differ much from it projection onto the yz-plane. Therefore, the calculation of I_{xx} coincides to the calculation of I_{yy} for a large part. In figure K.4, a sketch of the projection of the Delfi-C3 spacecraft onto the yz-plane is shown.

In the following paragraphs, the equations governing the calculation of the moment of inertia of the involved individual elements will be given. The moments of inertia are taken about the geometrical center of the spacecraft.

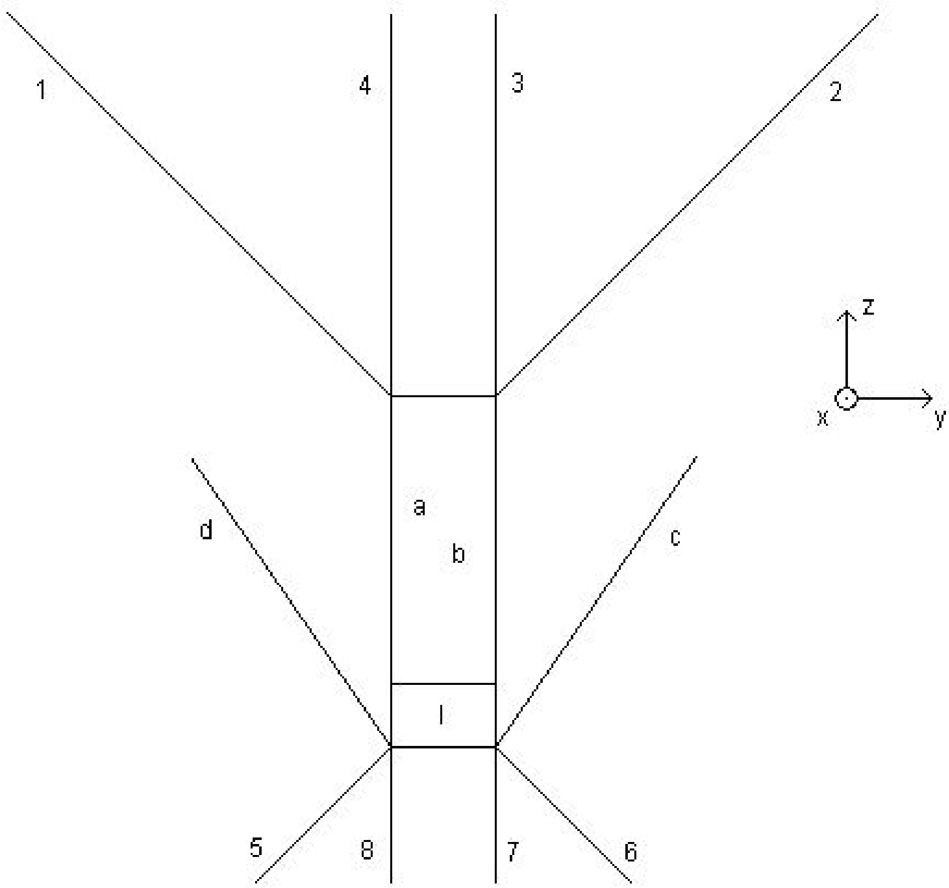

Figure K.4: Sketch of Delfi-C3 spacecraft model in yz-plane of satellite fixed reference frame

Firstly, the moment of inertia of the main body (reference I) will be considered, yielding the following expression:

$$((I_{xx})_{CoM})_I = \frac{1}{12} \cdot m_{mb} \cdot \left(l^2 + d^2\right) \tag{K.36}$$

$$(\Delta I_{xx})_I = 0 \tag{K.37}$$

After evaluating the moments of inertia of the solar panels, which are perpendicular to the xz-plane (reference a, b), the following expression can be written:

$$((I_{xx})_{CoM})_a = ((I_{xx})_{CoM})_b = \frac{1}{12} \cdot m_{sp} \cdot \left((l \cdot \cos\theta_i)^2 + d^2\right) \tag{K.38}$$

$$(\Delta I_{xx})_a = (\Delta I_{xx})_b = m_{sp} \cdot \left(\frac{l}{2} - \frac{l}{2} \cdot \cos\theta_i\right)^2 \tag{K.39}$$

For the moments of inertia of the solar panels perpendicular to the yz-plane (reference c, d), the following expression applies:

$$((I_{xx})_{CoM})_c = ((I_{xx})_{CoM})_d = \frac{1}{12} \cdot m_{sp} \cdot l^2 \tag{K.40}$$

$$(\Delta I_{xx})_c = (\Delta I_{xx})_d = m_{sp} \cdot \left(\left(\frac{l}{2} - \frac{l}{2} \cdot \cos\theta_i\right)^2 + \left(\frac{d}{2} + \frac{l}{2} \cdot \sin\theta_i\right)^2\right) \tag{K.41}$$

Writing the relevant expression for the downlink antennae in the yz-plane (reference 1, 2) yields:

$$((I_{xx})_{CoM})_1 = ((I_{xx})_{CoM})_2 = \frac{1}{12} \cdot m_{DLA} \cdot l_{DLA}^2 \tag{K.42}$$

$$(\Delta I_{xx})_1 = (\Delta I_{xx})_2 = m_{DLA} \cdot \left(\left(\frac{l}{2} + \frac{l_{DLA}}{2} \cdot \sin\phi\right)^2 + \left(\frac{d}{2} + \frac{l_{DLA}}{2} \cdot \cos\phi\right)^2\right) \tag{K.43}$$

Considering the moments of inertia for the downlink antennae in the xz-plane (reference 3, 4) results in the following expression:

$$((I_{xx})_{CoM})_3 = ((I_{xx})_{CoM})_4 = \frac{1}{12} \cdot m_{DLA} \cdot (l_{DLA} \cdot \sin\phi)^2 \tag{K.44}$$

$$(\Delta I_{xx})_3 = (\Delta I_{xx})_4 = m_{DLA} \cdot \left(\left(\frac{l}{2} + \frac{l_{DLA}}{2} \cdot \sin\phi\right)^2 + \left(\frac{d}{2}\right)^2\right) \tag{K.45}$$

For the uplink antennae in the yz-plane (reference 5, 6) the following expression applies:

$$((I_{xx})_{CoM})_5 = ((I_{xx})_{CoM})_6 = \frac{1}{12} \cdot m_{ULA} \cdot l_{ULA}^2 \tag{K.46}$$

$$(\Delta I_{xx})_5 = (\Delta I_{xx})_6 = m_{ULA} \cdot \left(\left(\frac{l}{2} + \frac{l_{ULA}}{2} \cdot \sin\phi\right)^2 + \left(\frac{d}{2} + \frac{l_{ULA}}{2} \cdot \cos\phi\right)^2\right) \tag{K.47}$$

Evaluating the moments of inertia of the uplink antennae in the xz-plane (reference 7, 8) leads to:

$$((I_{xx})_{CoM})_7 = ((I_{xx})_{CoM})_8 = \frac{1}{12} \cdot m_{ULA} \cdot (l_{ULA} \cdot \sin\phi)^2 \tag{K.48}$$

$$(\Delta I_{xx})_7 = (\Delta I_{xx})_8 = m_{ULA} \cdot \left(\left(\frac{l}{2} + \frac{l_{ULA}}{2} \cdot \sin\phi\right)^2 + \left(\frac{d}{2}\right)^2\right) \tag{K.49}$$

In a similar way as in the case of the moment of inertia about the y-axis, the moment of inertia of the complete spacecraft about the x-axis can be determined by adding all individual components. Another point of action to be taken is correcting this value by shifting the axis of rotation to the center of mass. This operation is governed by:

$$((I_{xx})_{CoM})_{S/C} = (I_{xx})_{S/C} - m_{S/C} \cdot d^2 = (I_{xx})_{S/C} - m_{S/C} \cdot \left(\frac{l}{2} - z_{CoM}\right)^2 \tag{K.50}$$

After performing the aforementioned operations, the moment of inertia about the x-axis can be found to be equal to the value shown in table K.4 in the nominal case.

Table K.4: Determination of moment of inertia about x-axis in nominal case

Part	Reference	I_{xx} (CoM)	I_{xx} (Steiner)	I_{xx} (total)
Main body	I	0.025001466	0	0.025001466
Solar panel ⊥	a	0.000696412	8.93424E-05	0.000785755
Solar panel ⊥	b	0.000696412	8.93424E-05	0.000785755
Solar panel //	c	0.000910561	0.02204061	0.003114622
Solar panel //	d	0.000910561	0.02204061	0.003114622
Downlink antenna ⊥	1	6.51042E-05	0.000510216	0.00057532
Downlink antenna ⊥	2	6.51042E-05	0.000510216	0.00057532
Downlink antenna //	3	2.68995E-05	0.000335755	0.000362654
Downlink antenna //	4	2.68995E-05	0.000335755	0.000362654
Uplink antenna ⊥	5	3.0375E-06	7.09124E-05	7.39499E-05
Uplink antenna ⊥	6	3.0375E-06	7.09124E-05	7.39499E-05
Uplink antenna //	7	1.25502E-06	5.78088E-05	5.90638E-05
Uplink antenna //	8	1.25502E-06	5.78088E-05	5.90638E-05
Total				0.034944196
z_{CoM} (m)				-0.16223187
Corrected				0.034941086

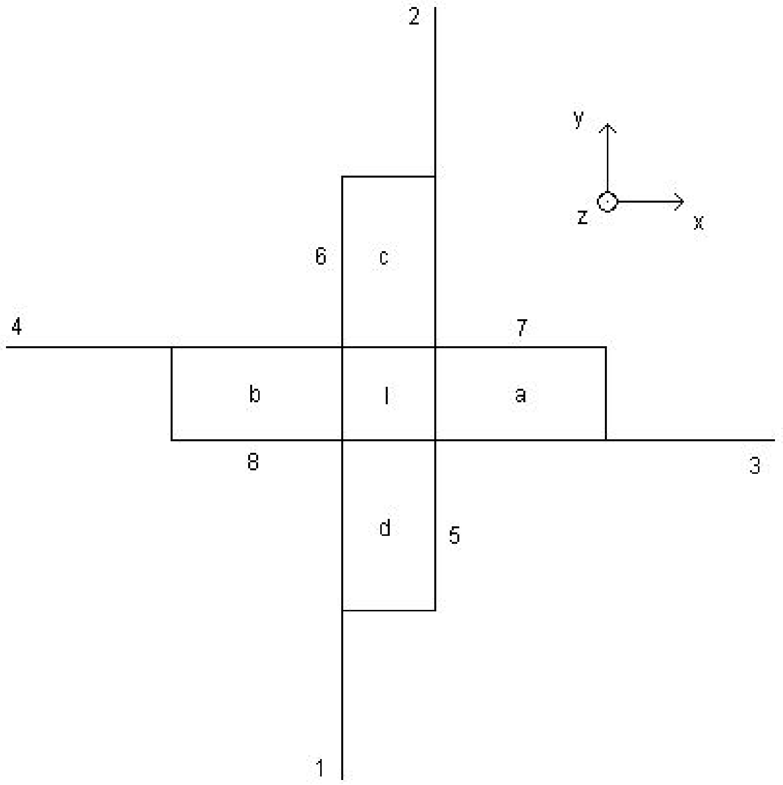

Figure K.5: Sketch of Delfi-C3 spacecraft model in xy-plane of satellite fixed reference frame

Calculation of I_{zz}

In this section, the moment of inertia about the z-axis will be calculated. In figure K.5, a sketch of the projection of the Delfi-C3 spacecraft onto the xy-plane is shown.

In the following paragraphs, the moments of inertia about the z-axis will be determined for every individual element. This moment of inertia is taken about the geometrical center of the complete Delfi-C3 spacecraft. In the projection of the spacecraft onto the xy-plane, this point coincides with the center of

mass.
The moment of inertia about the z-axis of the main body (reference I) is expressed by:

$$((I_{zz})_{CoM})_I = \frac{1}{12} \cdot m_{mb} \cdot \left(w^2 + d^2\right) \tag{K.51}$$

$$(\Delta I_{zz})_I = 0 \tag{K.52}$$

For the moments of inertia of the solar panels perpendicular to the xz-plane (reference a, b), the following expression can be written:

$$((I_{zz})_{CoM})_a = ((I_{zz})_{CoM})_b = \frac{1}{12} \cdot m_{sp} \cdot \left((l \cdot \sin\theta_i)^2 + w^2\right) \tag{K.53}$$

$$(\Delta I_{zz})_a = (\Delta I_{zz})_b = m_{sp} \cdot \left(\frac{w}{2} + \frac{l}{2} \cdot \sin\theta_i\right)^2 \tag{K.54}$$

Similarly, for the moments of inertia of the solar panels perpendicular to the yz-plane (reference c, d) applies:

$$((I_{zz})_{CoM})_c = ((I_{zz})_{CoM})_d = \frac{1}{12} \cdot m_{sp} \cdot \left((l \cdot \sin\theta_i)^2 + d^2\right) \tag{K.55}$$

$$(\Delta I_{zz})_c = (\Delta I_{zz})_d = m_{sp} \cdot \left(\frac{d}{2} + \frac{l}{2} \cdot \sin\theta_i\right)^2 \tag{K.56}$$

The following expression governs the calculation of the moments of inertia about the z-axis for the downlink antennae in the yz-plane (reference 1, 2):

$$((I_{zz})_{CoM})_1 = ((I_{zz})_{CoM})_2 = \frac{1}{12} \cdot m_{DLA} \cdot (l_{DLA} \cdot \cos\phi)^2 \tag{K.57}$$

$$(\Delta I_{zz})_1 = (\Delta I_{zz})_2 = m_{DLA} \cdot \left(\left(\frac{w}{2}\right)^2 + \left(\frac{d}{2} + \frac{l_{DLA}}{2} \cdot \cos\phi\right)^2\right) \tag{K.58}$$

For the moments of inertia about the z-axis for the downlink antennae in the xz-plane (reference 3, 4), the following expression applies:

$$((I_{zz})_{CoM})_3 = ((I_{zz})_{CoM})_4 = \frac{1}{12} \cdot m_{DLA} \cdot (l_{DLA} \cdot \cos\phi)^2 \tag{K.59}$$

$$(\Delta I_{zz})_3 = (\Delta I_{zz})_4 = m_{DLA} \cdot \left(\left(\frac{d}{2}\right)^2 + \left(\frac{w}{2} + \frac{l_{DLA}}{2} \cdot \cos\phi\right)^2\right) \tag{K.60}$$

The moments of inertia about the z-axis of the uplink antenna perpendicular in the yz-plane (reference 5, 6) comply with:

$$((I_{zz})_{CoM})_5 = ((I_{zz})_{CoM})_6 = \frac{1}{12} \cdot m_{ULA} \cdot (l_{ULA} \cdot \cos\phi)^2 \tag{K.61}$$

$$(\Delta I_{zz})_5 = (\Delta I_{zz})_6 = m_{ULA} \cdot \left(\left(\frac{w}{2}\right)^2 + \left(\frac{d}{2} + \frac{l_{ULA}}{2} \cdot \cos\phi\right)^2\right) \tag{K.62}$$

Writing an expression that described the calculation of the moments of inertia about the z-axis of the uplink antennae in the xz-plane (reference 7, 8) results in:

$$((I_{zz})_{CoM})_7 = ((I_{zz})_{CoM})_8 = \frac{1}{12} \cdot m_{ULA} \cdot (l_{ULA} \cdot \cos\phi)^2 \tag{K.63}$$

$$(\Delta I_{zz})_7 = (\Delta I_{zz})_8 = m_{ULA} \cdot \left(\left(\frac{d}{2}\right)^2 + \left(\frac{w}{2} + \frac{l_{ULA}}{2} \cdot \cos\phi\right)^2 \right) \tag{K.64}$$

In a similar fashion as in the cases of the moments of inertia about the x- and y-axis, the moment of inertia about the z-axis of the total spacecraft can be found by adding the contributions of all individual elements. However, no offset of the geometrical center with the center of mass is present in this case, so no correction has to be applied.

Adding all individual moments of inertia in the nominal case results for the moment of inertia about the z-axis in the value shown in table K.5.

Table K.5: Determination of moment of inertia about z-axis in nominal case

Part	Reference	I_{zz} (CoM)	I_{zz} (Steiner)	I_{zz} (total)
Main body	I	0.004288333	0	0.004288333
Solar panel	a	0.000384982	0.002114719	0.002499701
Solar panel	b	0.000384982	0.002114719	0.002499701
Solar panel	c	0.000384982	0.002114719	0.002499701
Solar panel	d	0.000384982	0.002114719	0.002499701
Downlink antenna	1	2.68995E-05	0.000146541	0.000173441
Downlink antenna	2	2.68995E-05	0.000146541	0.000173441
Downlink antenna	3	2.68995E-05	0.000146541	0.000173441
Downlink antenna	4	2.68995E-05	0.000146541	0.000173441
Uplink antenna	5	1.25502E-06	1.58983E-05	1.71533E-05
Uplink antenna	6	1.25502E-06	1.58983E-05	1.71533E-05
Uplink antenna	7	1.25502E-06	1.58983E-05	1.71533E-05
Uplink antenna	8	1.25502E-06	1.58983E-05	1.71533E-05
Total				0.015049512

Treatise of the products of inertia

A product of inertia of a specific body is written as:

$$I_{qr} = \int q \cdot r \cdot \mathrm{d}m \tag{K.65}$$

where dm is the mass of an infinitesimally small element, and q and r are the coordinates of the respective projections of the mass element onto the q- and r-axis. Note that both q and r can be chosen from the set x, y, z, although they cannot denote the same axis at the same time.

Investigating equation K.65, it is noticed that the product of inertia Iqr equals zero in the case when the body shows symmetry in the qr-plane.

Returning to figure K.1, it is seen that the Delfi-C3 spacecraft has a measure of symmetry in the xz-plane about the z-axis. Investigating figure K.4 in a similar way, it can be seen that Delfi-C3 is symmetric in the yz-plane about the z-axis, too. Therefore, the conclusion can be drawn that I_{xz}, I_{zx}, I_{yz}, and I_{zy} all equal zero.

It has to be noted, however, that in the case of a deployment failure of one of the solar panels, the symmetry will be lost and two of the products of inertia will be unequal to zero.

On the other hand, after paying attention to figure K.5, it is noticed that no symmetric tendencies can be observed in the xy-plane. Therefore, the products of inertia I_{xy} and I_{yx} have to be evaluated. This will be done using the following expression:

$$I_{xy} = I_{yx} = \int x \cdot y \cdot \mathrm{d}m \tag{K.66}$$

The asymmetric properties of Delfi-C3 are contributed to the antennae, because the main body is in fact symmetric. Therefore, the products of inertia of the antennae have to be determined. Using:

$$\mathrm{d}m = \frac{M}{l} \cdot \mathrm{d}l \tag{K.67}$$

where M is the mass of a single antenna, l is the length of the antenna, and $\mathrm{d}l$ is an infinitesimal small distance in the dimension along the length of the antenna.
Evaluating the product of inertia for antenna with reference 1:

$$\left(I_{xy}\right)_1 = \left(I_{yx}\right)_1 = \int\limits_{\frac{w}{2}}^{l_{DLA}+\frac{w}{2}} x \cdot y \frac{m_{DLA}}{l_{DLA}} \cdot \mathrm{d}l \tag{K.68}$$

As m_{DLA}, l_{DLA}, and the y-coordinate of the antenna with reference 1 are constant, this equation can be simplified to:

$$\left(I_{xy}\right)_1 = \left(I_{yx}\right)_1 = -\frac{m_{DLA}}{l_{DLA}} \cdot \frac{d}{2} \cdot \int\limits_{\frac{w}{2}}^{l_{DLA}+\frac{w}{2}} y \cdot \mathrm{d}l \tag{K.69}$$

However, as the antenna is at an angle ϕ with the main body, the position coordinate x relates to the variable l with the expression:

$$y = -l \cdot \cos\phi \tag{K.70}$$

Substituting this expression results in:

$$\left(I_{xy}\right)_1 = \left(I_{yx}\right)_1 = \frac{m_{DLA}}{l_{DLA}} \cdot \cos\phi \cdot \frac{d}{2} \cdot \int\limits_{\frac{w}{2}}^{l_{DLA}+\frac{w}{2}} l \cdot \mathrm{d}l \tag{K.71}$$

Evaluating the integral leads to:

$$\begin{aligned}\left(I_{xy}\right)_1 = \left(I_{yx}\right)_1 = \frac{m_{DLA}}{l_{DLA}} \cdot \cos\phi \cdot \frac{d}{2} \cdot \frac{1}{2} \cdot \left(\left(l_{DLA} + \frac{w}{2}\right)^2 - \left(\frac{w}{2}\right)^2\right) = \\ \frac{m_{DLA}}{l_{DLA}} \cdot \cos\phi \cdot \frac{d}{4} \cdot \left(l_{DLA}^2 + w \cdot l_{DLA}\right)\end{aligned} \tag{K.72}$$

It can be shown, that the products of inertia for the antenna with reference 2 has equal values as the product of inertia for the antenna with reference 1. For the antennae with references 3 and 4, the expression given in equation K.72 can be written too as d and w are equal in value. However, the sign of this expressed value is opposite of the value obtained with equation K.72.
For the uplink antennae (reference 5, 6, 7, 8), it can be shown that the product of inertia of a single antenna can be written as:

$$\left(I_{xy}\right)_{5,6} = \left(I_{yx}\right)_{5,6} = -\left(I_{xy}\right)_{7,8} = -\left(I_{yx}\right)_{7,8} = -\frac{m_{ULA}}{l_{ULA}} \cdot \cos\phi \cdot \frac{d}{4} \cdot \left(l_{ULA}^2 + w \cdot l_{ULA}\right) \tag{K.73}$$

The complete product of inertia is attained by adding the contributions of all individual elements. As the product of inertia for every antenna has an equal but opposite counterpart all contributions cancel out in the summation. This leads to the following expression:

$$I_{xy} = I_{yx} = \sum_{i=1}^{8} \left(I_{xy}\right)_i = 0 \tag{K.74}$$

Construction of inertia tensor

As all values in the inertia tensor are now determined, the inertia tensor can be constructed. Applying equation K.13 in the nominal case results in:

$$\mathbf{I} = \begin{pmatrix} 3.494 \cdot 10^{-2} & 0 & 0 \\ 0 & 3.494 \cdot 10^{-2} & 0 \\ 0 & 0 & 1.505 \cdot 10^{-2} \end{pmatrix} \text{kg.m}^{-2} \tag{K.75}$$

Comparison with CATIA results

In view of validation of the obtained results, a comparison will be made between the inertia tensor obtained in section K.2.2 and numerical results obtained by using the software package CATIA. In May 2006, a last numerical evaluation of the moments of inertia of the Delfi-C3 spacecraft was performed by E. van der Linden. This evaluation led to the following outputs by CATIA:

$$\mathbf{I} = \begin{pmatrix} 3.5 \cdot 10^{-2} & -2.227 \cdot 10^{-5} & -8.829 \cdot 10^{-6} \\ -2.227 \cdot 10^{-5} & 3.4 \cdot 10^{-2} & -3.659 \cdot 10^{-5} \\ -8.829 \cdot 10^{-6} & -3.659 \cdot 10^{-5} & 1.1 \cdot 10^{-2} \end{pmatrix} \text{kg.m}^{-2} \tag{K.76}$$

Comparing equation K.75 with equation K.76, it can be seen that the products of inertia about the x- $(_{xx})$ and y-axes (I_{yy}) coincide in a respectable way. However, the calculated moment of inertia about the z-axis (I_{zz}) deviates slightly from the corresponding CATIA output.

K.3 Conclusions and recommendations

In this document, the geometrical properties were determined. A simplified model of the Delfi-C3 spacecraft has been used for calculating the center of mass and inertia properties. The distance vector from the center of mass to the front body panel of the Delfi-C3 spacecraft equals:

$$\vec{x}_{CoM} = \begin{pmatrix} 0 \\ 0 \\ -162.2 \end{pmatrix} \text{mm}$$

The inertia tensor is found to be equal to:

$$\mathbf{I} = \begin{pmatrix} 3.494 \cdot 10^{-2} & 0 & 0 \\ 0 & 3.494 \cdot 10^{-2} & 0 \\ 0 & 0 & 1.505 \cdot 10^{-2} \end{pmatrix} \text{kg.m}^{-2}$$

Appendix L

DC3-TN-610-078 EuroSim - Determination of magnetic control torque

L.1 Introduction

EuroSim is a simulation platform, in which the orbit of the Delfi-C3 spacecraft will be simulated. Interesting quantities, which can be determined from this simulation, are power generation and attitude reconstruction. For accurate attitude reconstruction, it is important to determine the magnetic control torques acting on the spacecraft.
Magnetic control torques are torques generated on purpose in order to stabilize the attitude of the spacecraft. In order to create magnetic control torques, magnetic material will be used, which will produce a torque under influence of Earth magnetic field. Two kinds of magnetic material are applied, being hysteresis material and permanent magnet, which both have different magnetic characteristics. Therefore, the behaviours of these magnetic materials have to be described in order to determine the generated magnetic torque.
In this report, a treatise will be given of the magnetic control torque on the Delfi-C3 spacecraft. A description of Earth magnetic field is given in subsection L.2.1. In subsection L.2.2, a derivation is shown of the governing equations of a medium transition for magnetic field lines. The characteristics of the applied magnetic material are described in subsection L.2.3. Finally in subsection L.2.4, a calculation is accomplished to estimate the value of the generated magnetic torques.

L.2 Determination of magnetic control torque

L.2.1 Description of Earth magnetic field

For determining the magnetic torque produced by the hysteresis elements and the permanent magnet, firstly the behaviour of the magnetic field of the Earth in vacuum has to be evaluated. As a first approximation, the Earth's magnetic field can be described by a simple dipole model. In this case, the magnetic field potential equals [7]:

$$V = \frac{\vec{M} \cdot \vec{r}}{r} = -\frac{M \cdot \sin\Phi}{r^2} \tag{L.1}$$

where M represents the moment of the magnetic dipole, with a value of $8.05 \cdot 10^{19}$ gauss.m^3, which is equal to $8.05 \cdot 10^{15}$ T.m^3. Furthermore, the previous expression describes the potential in a point in space with spherical coordinates (r, Φ, Λ).
Note however that the dipole model is a simplification of the actual magnetic field. A more accurate, but more complex model of the true field can be given by a harmonic expansion model:

$$V(r, \Phi, \Lambda) = \frac{R_e}{\mu_0} \sum_{n=0}^{\infty} \sum_{m=0}^{n} \left(\frac{R_e}{r}^{n+1} P_{n,m} \cdot sin\Phi \cdot (g_{n,m} \cdot \cos m\Lambda + h_{n,m} \cdot \sin m\Lambda) \right) \tag{L.2}$$

In both the simple dipole model and the complex harmonic expansion model, the magnetic flux density, or magnetic induction, at a particular point in space can be found by partial differentiation of the magnetic potential with respect to direction of interest. Therefore, the flux density in radial direction equals:

$$B_r = -\frac{\partial V}{\partial r} = -\frac{2M \cdot \sin \Phi}{r^3} \tag{L.3}$$

and the flux density in tangential direction is equal to:

$$B_\Phi = -\frac{1}{r}\frac{\partial V}{\partial \Phi} = -\frac{M \cdot \cos \Phi}{r^3} \tag{L.4}$$

Expressing the value of the magnetic flux density as a scalar quantity leads to:

$$B = \sqrt{B_r^2 + B_\Phi^2} = \frac{M}{r^3} \cdot \left(1 + 3 \cdot \sin^2 \Phi\right)^{\frac{1}{2}} \tag{L.5}$$

L.2.2 Medium transition of magnetic field lines

The magnetic field strength in a particular medium is coupled to magnetic flux density via the equation [9]:

$$\vec{B} = \mu \cdot \vec{H} = \mu_0 \cdot \mu_r \cdot \vec{H} \tag{L.6}$$

where $\vec{B}$ is the magnetic flux density vector, $\vec{H}$ is the magnetic field strength vector, μ is the magnetic permeability of the medium, μ_0 is the magnetic permeability in vacuum, and μ_r is the relative magnetic permeability of the medium. Note that this equation is only valid for linear mediums.

In vacuum, the relative permeability μ_r is equal to unity. After rewriting expression L.6, the value of the magnetic field strength can be derived.

$$\vec{H} = \frac{\vec{B}}{\mu_0} \tag{L.7}$$

General electromagnetic theory learns that a change in medium can impose a change in behaviour of electromagnetic quantities. Therefore, the magnetic field at the border between vacuum and the magnetic material has to be investigated. Firstly, write down the following Maxwell equation in integral form:

$$\oint\limits_C \vec{H} \cdot \mathrm{d}\vec{l} = \iint\limits_S \vec{J} \cdot \vec{A} + \iint\limits_S \frac{\mathrm{d}}{\mathrm{d}t}\vec{D} \cdot \vec{A} \tag{L.8}$$

where $\vec{H}$ is the magnetic field strength, $\vec{J}$ is the free current density, and $\vec{D}$ is the electric flux density. At the left hand side, the integral term denotes that the magnetic field strength has to be evaluated in tangential direction when traversing the closed loop C. The integral terms at the right hand side of the equation denote that the free current density and the time derivative of the electric flux density have to be evaluated in normal direction of the surface area A, which is encompassed by loop C.

In many cases, the time derivative of the electric flux density is equal to zero. Incorporating this observation leads to the following expression, known as Ampère's law:

$$\oint\limits_C \vec{H} \cdot \mathrm{d}\vec{l} = \iint\limits_S \vec{J} \cdot \vec{A} \tag{L.9}$$

Now, this expression can be evaluated at the transition from vacuum to magnetic material. A situational sketch is shown in figure L.1.

It is known that the electrical current in this region has to be equal to zero. After expanding the integral term at the left hand side, expression L.9 can be rewritten to:

$$(H_1 + H_3) \cdot x + (H_2 + H_4) \cdot \mathrm{d}y = 0 \tag{L.10}$$

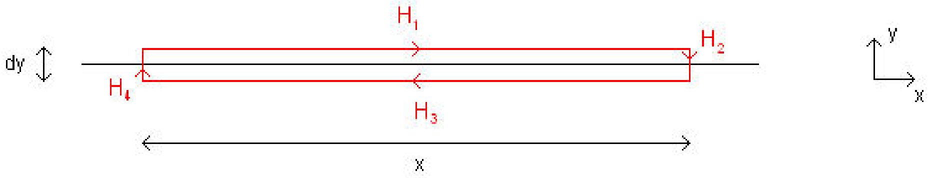

Figure L.1: Sketch of Delfi-C3 spacecraft model in xy-plane of satellite fixed reference frame

Furthermore, it is known that the y-dimension of the loop is much smaller than its x-dimension. Hence:

$$\mathrm{d}y \ll x \tag{L.11}$$

Then, the only solution to equation L.10 is:

$$H_1 = -H_3 \tag{L.12}$$

which implicates that the contributions of the magnetic field strength, which are tangential to the border, remain the same in value and direction after a transition in mediums.
During derivation of the previous values of magnetic field strength, a potential conflict with another physical law arose. Writing Gauss' law for magnetization:

$$\iint_S \vec{B} \cdot \mathrm{d}\vec{A} = 0 \tag{L.13}$$

Recall that equation L.13 denotes a physical constraint that sources or sinks of magnetic flux density are non-existent. In figure L.2, a sketch is shown, which depicts a medium transition between the magnetic material and vacuum. On the transition, a small box is drawn, with dimension x parallel to the transition, dimension dy perpendicular to the transition and dimension z perpendicular to the paper.

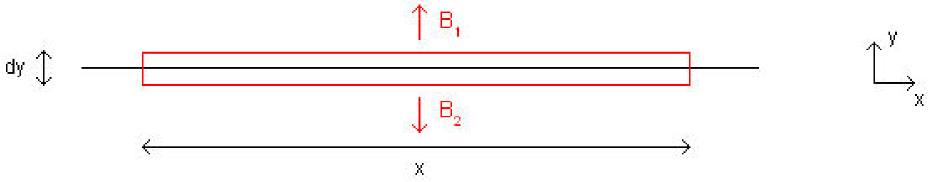

Figure L.2: Situational sketch for evaluating magnetic flux density behaviour at medium transition

Evaluating the area integral for the box in figure L.2 yields:

$$(B_1 + B_2) \cdot x \cdot z + \sum_{n=3}^{6} B_i \cdot \mathrm{d}y \cdot q_i = 0 \tag{L.14}$$

where B_i equals the magnetic flux density perpendicular to side i of the box, and q_i is the dimension of side i perpendicular to dy, being either x or z.
It is also known that the y-dimension is much smaller than the z-dimension, i.e.:

$$\mathrm{d}y \ll z \tag{L.15}$$

Applying equations L.11 and L.15 to equation L.14, then yields:

$$B_1 = -B_2 \tag{L.16}$$

In this equation, B_1 is the magnetic flux density in vacuum, and B_2 is the magnetic flux density in the magnetic material. It is known that the magnetic flux density and the magnetic field strength are related to each other by the magnetic permeability μ. Furthermore, it is known that the magnetic permeabilities for vacuum and the magnetic material are significantly different, i.e. they differ a factor 1000. Realizing that the magnetic field strengths in vacuum and the magnetic material are equal, the result would be that the magnetic flux densities would be unequal. However, this is in contradiction with equation L.16. A possible explanation is fringing ("uitbloezen") of the magnetic flux density. This phenomenon means that the flux lines contract at the interface of vacuum and the magnetic material, resulting in a higher flux density at the interface. In this way, the situation can comply with equation L.16, because the magnetic flux density directly in front of the medium transition is not equal to the value in undisturbed vacuum. An illustration of the fringing phenomenon is shown in figure L.3.

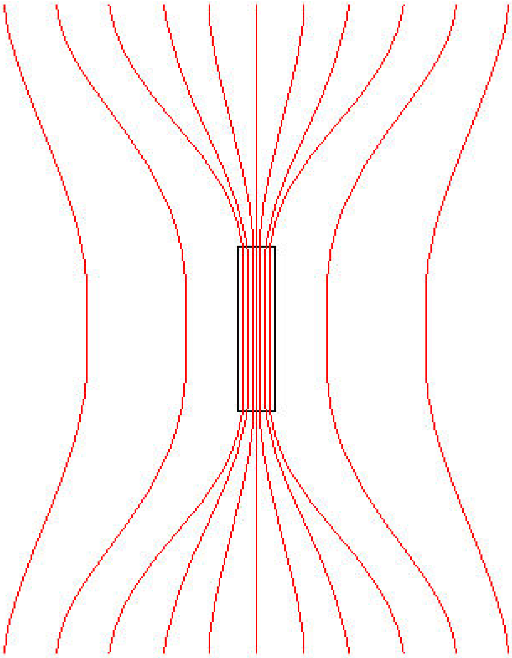

Figure L.3: Illustration of fringing of magnetic flux density due to presence of magnetic material

L.2.3 Characteristics of applied magnetic material

Two types of magnetic material can be applied in the attitude control system of the Delfi-C3 spacecraft. Hysteresis material is used to dampen out the rotational motion of the spacecraft around its x- and y-axes. For this reason, two small pieces of hysteresis material are placed along the x- and y-axes of the spacecraft. In longitudinal direction of the spacecraft, i.e. along its z-axis, two design options are present for the choice of magnetic material. One option is the application of hysteresis material, i.e. soft magnetic material, as has been done in case of the other two axes in the satellite fixed reference frame. As a second option, hard magnetic material can be used. At the time of writing of this document, the latter option of using a permanent magnets is being preferred.
For the implementation of the hysteresis material, PermeNorm 5000H2 will be used. Various important characteristics of this type of hysteresis material are summed in table L.1.

Table L.1: Important characteristics of PermeNorm 5000H2 hysteresis material

Parameter	Variable	Value	
Coercive force	H_c	5	$\mathrm{A.m^{-1}}$
Remnant flux density	B_r	1.2	T
Saturation flux density	B_s	1.55	T

The quantities mentioned in table L.1 relate to points on the BH-curve of the hysteresis material. The coercive force H_c equals the absolute value of the magnetic field strength, for which the flux in the material is equal to zero. On the other hand, the remnant flux density B_r is the absolute value of the flux density in the material when the magnetic field strength is equal to zero. Because the material is only able to conduct a finite amount of flux, the maximum absolute value of flux density in the material is given by the saturation flux density B_s.

One problem arises, when one wants to model the behaviour of the hysteresis material. Although it was mentioned in equation L.6 that the magnetic flux density and magnetic field strength are related by means of the magnetic permeability, it has to be noted that this permeability is far from constant when hysteresis material is considered. This leads to a highly non-linear relation between the magnetic field strength and the magnetic flux density, which in turn would mean a very tedious modeling process if one wants to have an extremely accurate model. However, a good approximation can be made by linearizing the behaviour of the material, which will lead to a simplification of the so-called BH-curve. This is done by defining both the pathway of increasing field strength and the pathway of decreasing field strength as a straight line in the BH-plane.

It is assumed that the simplified BH-curve crosses the H-axis at $-H_c$ for increasing field strengths (i.e. positive $\frac{\mathrm{d}H}{\mathrm{d}t}$) and at H_c for decreasing field strengths (i.e. negative $\frac{\mathrm{d}H}{\mathrm{d}t}$). Furthermore, it is stated that the BH-curve crosses the B-axis at $\frac{1}{2}B_s$ for increasing field strengths, and at $-\frac{1}{2}B_s$ for decreasing field strengths. With these assumptions, it is possible to generate the following equations describing the magnetic behaviour of the hysteresis material.

For positive $\frac{\mathrm{d}H}{\mathrm{d}t}$:

$$B = \frac{1}{2} \cdot B_s + \left(\frac{B_s}{2 \cdot H_c} \right) \cdot H \tag{L.17}$$

and for negative $\frac{\mathrm{d}H}{\mathrm{d}t}$

$$B = -\frac{1}{2} \cdot B_s + \left(\frac{B_s}{2 \cdot H_c} \right) \cdot H \tag{L.18}$$

Moreover, it is known that the flux density in the material cannot exceed B_s. Therefore, the magnitude of the flux density is limited to values between B_s and $-B_s$. The result of introducing these simplifications to the BH-curve of PermeNorm 5000H2 can be seen in figure L.4.

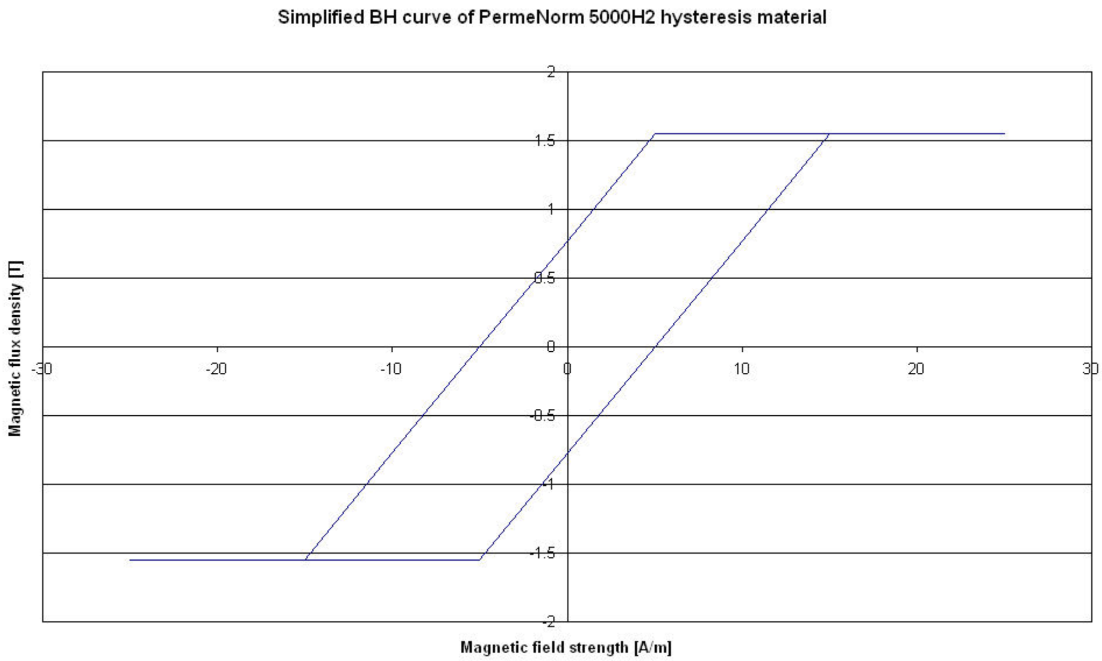

Figure L.4: Simplified BH-curve of PermeNorm 5000H2 hysteresis material

In case of the hard magnetic material, AlNiCo 5 cast magnetic material has been chosen to be applied. In table L.2, several important characteristics are shown.

In contrast to the soft magnetic hysteresis material, hard magnetic material is highly linear in its behaviour. Therefore, its BH-curve is defined by a straight line, which can be dictated by using two points on this curve. As the coercive force and the remnant flux density are known, its BH-curve can be produced. This curve is defined as:

Table L.2: Important characteristics of AlNiCo 5 cast hard magnetic material

Parameter	Variable	Value	
Coercive force	H_c	$5.09 \cdot 10^4$	$\mathrm{A.m^{-1}}$
Remnant flux density	B_r	1.28	T

$$B = B_r + \left(\frac{B_r}{H_c}\right) \cdot H \tag{L.19}$$

In figure L.5, a plot is given of the BH-curve of AlNiCo 5 cast magnetic material.

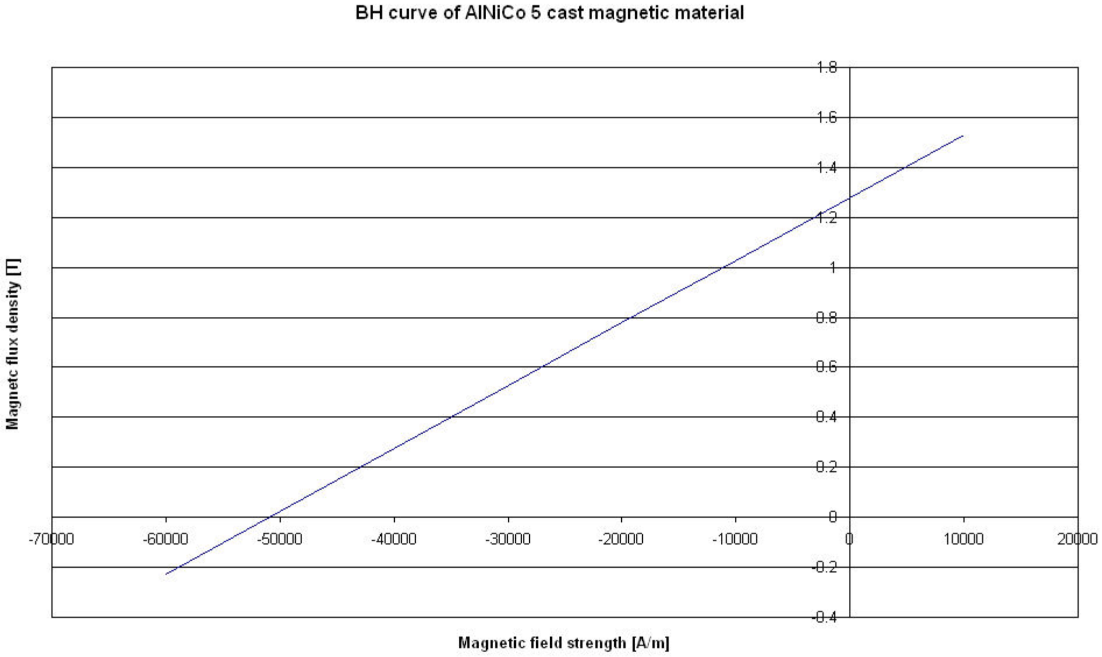

Figure L.5: BH-curve of AlNiCo 5 cast magnetic material

L.2.4 Calculation of magnetic control torque

As the characteristics of the various magnetic materials in the spacecraft are known, the magnetic dipole caused by the material at a particular moment can be calculated. It is known that the relation between magnetic field strength and magnetic flux density can also be written as [4]:

$$\vec{B} = \mu_0 \cdot (1 + \chi_m) \cdot \vec{H} = \mu_0 \cdot \left(\vec{H} + \vec{M}\right) \tag{L.20}$$

In this equation, χ_m is called the magnetic susceptibility of the magnetic material, and $\vec{M}$ is known as the magnetization. Rewriting this equation to solve for the magnetization results in:

$$\vec{M} = \frac{\vec{B}}{\mu_0} - \vec{H} \tag{L.21}$$

It is known that the magnetic dipole moment, which is formed by a particular piece of magnetic material, can be written as:

$$\vec{m} = \int \vec{M} \cdot \mathrm{d}V = \iiint \vec{M} \cdot \mathrm{d}x\mathrm{d}y\mathrm{d}z \tag{L.22}$$

which in fact simply denotes an integration of the magnetization of the material over its volume. Assuming that the magnetization of the material is homogeneous over the complete volume, this expression can be simplified to:

$$\vec{m} = \vec{M} \cdot V \tag{L.23}$$

where V is the volume of the magnetic material.

A torque will then be generated, because the dipole moment of the magnetic material will try to align itself with the Earth magnetic field. This reaction of the magnetic material is therefore expressed by:

$$\vec{T}_{mag} = \vec{m} \times \vec{B}_{ext} \tag{L.24}$$

An estimation of the produced magnetic control torques can be obtained by assuming that the rod of magnetic material is rotating in a stationary magnetic field. This motion effectively coincides with a rotation of the magnetic flux density in case of a stationary rod of magnetic material. A situational sketch of the rotation of the magnetic material is shown in figure L.6.

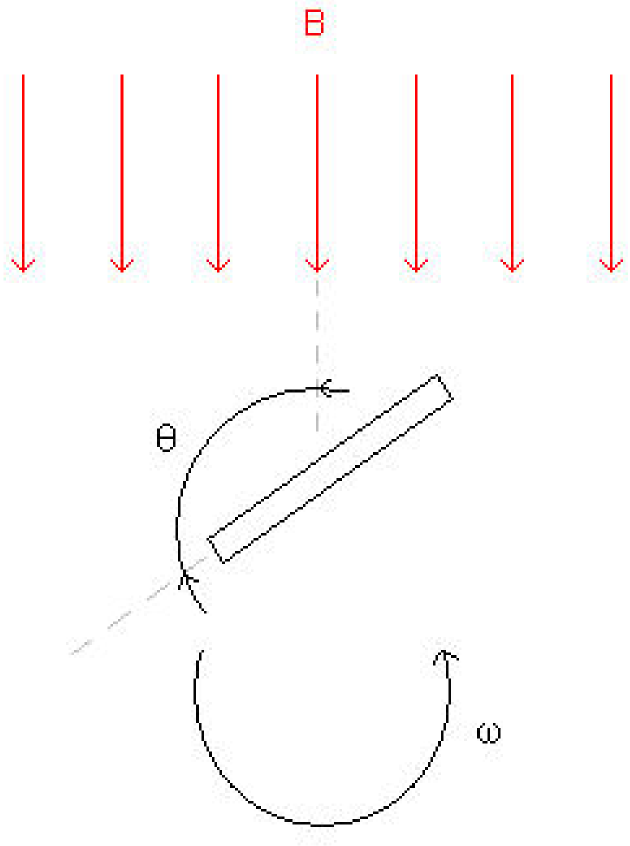

Figure L.6: Situational sketch of a rotating rod of magnetic material in a stationary magnetic field

It is assumed that the problem is two-dimensional, which means that the piece of material rotates in the plane of the magnetic flux density. Therefore, all vector quantities in the governing equations can be simplified to corresponding scalar quantities. Implementing this simplification, the rotating magnetic flux density as sensed by the magnetic material is expressed by:

$$B = \hat{B} \cdot \cos\theta = \hat{B} \cdot \cos\left(\omega\left(t - t_0\right)\right) \tag{L.25}$$

where $\hat{B}$ is the amplitude of the magnetic flux density, θ is the incidence angle of the rod of magnetic material with the magnetic flux vector, ω is the rotational rate of the rod of magnetic material, and t_0 denotes the last moment, at which the incidence angle is equal to zero.

To determine the magnitude of the Earth magnetic field, a worst case scenario is assumed. This scenario is obtained if the trigonometric term in equation L.5 is set equal to 1. This coincides with the situation, in which the spacecraft is directly above one of the magnetic poles of the Earth. Equation L.5 is then rewritten as:

$$\hat{B} = \left|\vec{B}\right| = 2 \cdot \frac{M}{r^3} \tag{L.26}$$

With the value of M being equal to $8.05 \cdot 10^{15}$ T.m^3 and the value of r being equal to $6378137 + 635000$ m, this magnitude can be evaluated to be equal to:

$$\hat{B} = 2 \cdot \frac{8.05 \cdot 10^{15}}{(6378137 + 635000)^3} = 4.667 \cdot 10^{-5} \text{ T} \tag{L.27}$$

With the expression for magnetic flux density known, the magnetic field strength can be determined using equation L.7. By using equations L.17, L.18, L.19, L.21, and L.23, the magnetic dipole moment of the rod of magnetic material can be found as a function of incidence angle θ. Finally, using equation L.24, the magnetic control torque generated by a rod of magnetic material is calculated.

Evaluating the magnetic control torque for a permanent magnet yields the values given in the graph in figure L.7. Note that the volume of the permanent magnet is taken to be equal to $250 \cdot 10^{-9}$ m^3.

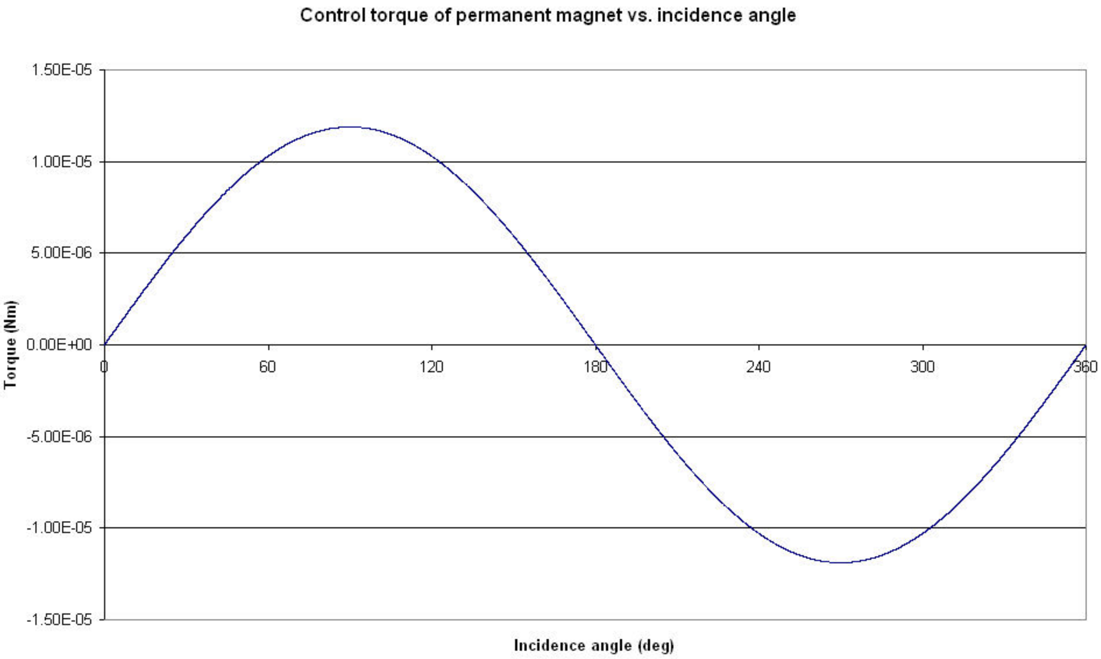

Figure L.7: Magnetic control torque generated by a permanent magnet as function of incidence angle

Performing an evaluation of the magnetic control torque for a hysteresis material rod yields the results in figure L.8. Note that the volume of a single hysteresis material rod is taken to be equal to $500 \cdot 10^{-9}$ m^3. Recall that the integral of this torque over the complete range of angles is negative, which is to be expected. After all, the hysteresis material has to dampen out the rotational rate of the spacecraft, which means that the net torque has to be in opposite direction of the rotation.

Investigating figures L.7 and L.8, the maximum and minimum values of the magnetic torques are found to be equal to the values mentioned in table L.3.

Table L.3: Maximum and minimum values of magnetic control torques

Type of magnetic material	Maximum torque (N.m)	Minimum torque (N.m)
Permanent magnet	$1.189 \cdot 10^{-5}$	$-1.189 \cdot 10^{-5}$
Hysteresis material	$2.632 \cdot 10^{-5}$	$-2.852 \cdot 10^{-5}$

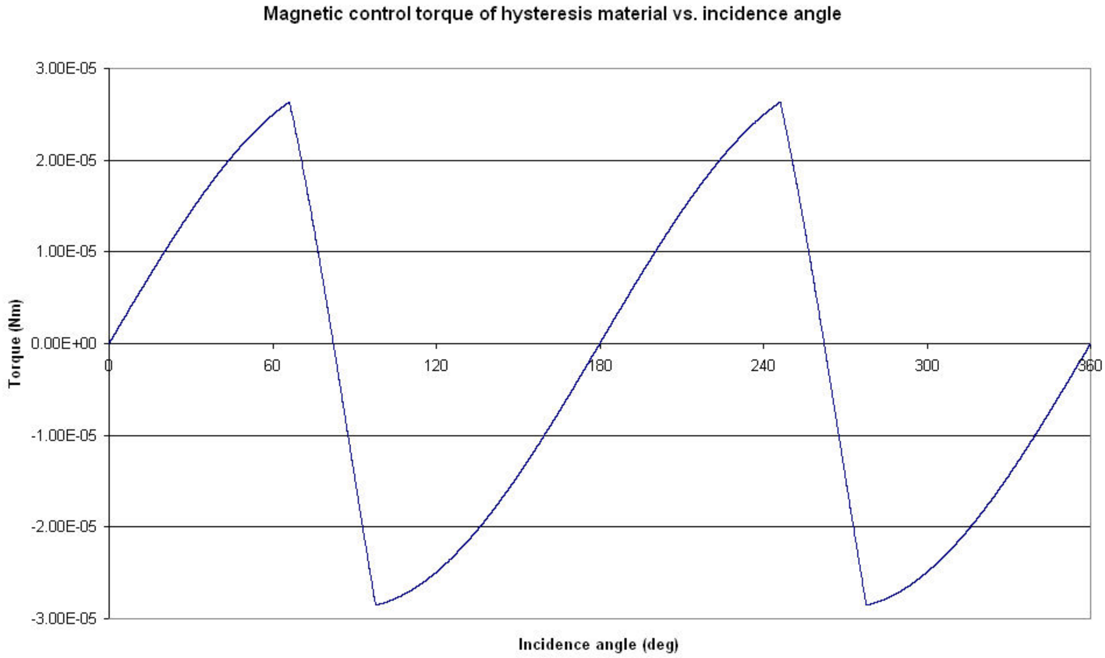

Figure L.8: Magnetic control torque generated by a hysteresis material rod as function of incidence angle

Please note that after integration of the spacecraft a possible remnant magnetic dipole can be present on the spacecraft, which is independent from the permanent magnet and the hysteresis material rods. This dipole will create a distubrance torque to the magnetic field as given in equation L.24. An estimation of this torque is given in appendix R.

L.3 Conclusions and recommendations

In the previous section, the magnetic control torques acting on the Delfi-C3 spacecraft is determined. The maximum and minimum values of the magnetic torque caused by both the hysteresis material and permanent magnet are calculated. For the permanent magnet with a volume of $250 \cdot 10^{-9}$ m^3, the amplitude of the torque was found to be $1.189 \cdot 10^{-5}$ N.m, while the amplitude of the torque generated by a single rod of hysteresis material with a volume of $500 \cdot 10^{-9}$ m^3 is equal to $2.852 \cdot 10^{-5}$ N.m.

Appendix M

DC3-TN-609-063 EuroSim - Determination of gravity gradient torque

M.1 Introduction

EuroSim is a simulation platform, in which the orbit of the Delfi-C3 spacecraft will be simulated. Interesting quantities, which can be determined from this simulation, are power generation and attitude reconstruction. For attitude reconstruction, it is important to determine the various disturbance torques acting on the spacecraft. One of these disturbance torques is the gravity gradient torque. The gravity gradient torque exists, because the gravity field in space is not homogeneous, but varies with altitude. Therefore, if the spacecraft is not exactly perpendicular or parallel to the gravity field, a small torque will be produced, which will cause a rotation of the spacecraft.
In this report, the gravity gradient torque acting on the Delfi-C3 spacecraft in orbit will be calculated. In section M.2.1, the equations required for deriving the gravity graident torque are presented. The rotational matrix, which relates the gravitional torque to the satellite attitude is calculated in section M.2.2. A first approximation of the magnitude of the gravity gradient torque is shown in section M.2.3.

M.2 Determination of gravity gradient disturbance torque

When a body is in a uniform gravitational field, its centre of mass becomes the centre of gravity and the gravitational torque about its centre of mass is zero. The gravitational field is not uniform over a body in space, however, and a gravitational torque exists about the body's centre of mass. In this section, the equations describing the gravitational torque are derived [17].

M.2.1 Derivation of governing equations

Consider a rigid body in a circular orbit. A local vertical and local horizontal (LVLH) reference frame A (also known as orbit reference frame) with its origin at the centre of mass of an orbiting spacecraft has a set of unit vectors $(\vec{a}_1, \vec{a}_2, \vec{a}_3)$, with $\vec{a}_1$ along the orbit direction, $\vec{a}_2$ perpendicular to the orbit plane, and $\vec{a}_3$ toward the Earth, as illustrated in figure M.1. Note that the positive direction of the vector $\vec{a}_2$ is chosen such that A is a right-handed Cartesian coordinate system.
The angular velocity of A with respect to the Earth inertial reference frame N is:

$$\vec{\omega}^{A/N} = -n \cdot \vec{a}_2 \tag{M.1}$$

where n is the constant orbital rate.
The gravitational force acting on a small mass element dm is given by:

$$\mathrm{d}\vec{f} = -\frac{\mu \cdot \vec{R}}{\left|\vec{R}\right|^3} \cdot \mathrm{d}m = -\frac{\mu \cdot \left(\vec{R}_c + \vec{\rho}\right)}{\left|\vec{R}_c + \vec{\rho}\right|^3} \cdot \mathrm{d}m \tag{M.2}$$

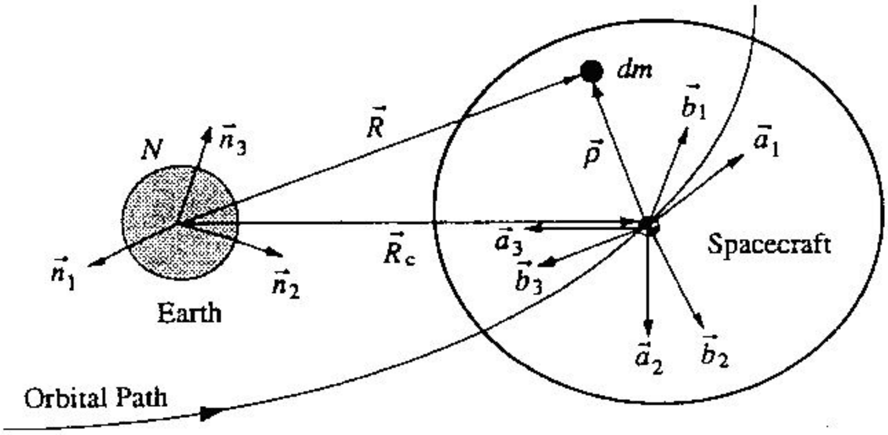

Figure M.1: Rigid body in a circular orbit

where μ is the gravitational parameter of the Earth, $\vec{R}$ and $\vec{\rho}$ are the position vectors of $\mathrm{d}m$ from the Earth's centre and the spacecraft's mass centre, respectively, and $\vec{R}_c$ is the position vector of the spacecraft's mass centre from the Earth's centre.

The gravity gradient torque about the spacecraft's mass centre is then expressed as:

$$\vec{M} = \int \vec{\rho} \times \mathrm{d}\vec{f} = -\mu \cdot \int \frac{\vec{\rho} \times \vec{R}_c}{\left|\vec{R}_c + \vec{\rho}\right|^3} \cdot \mathrm{d}m \tag{M.3}$$

and we have the following approximation:

$$\begin{aligned} \left|\vec{R}_c + \vec{\rho}\right|^{-3} = {R_c}^{-3} \cdot \left(1 + \frac{2 \cdot \left(\vec{R}_c + \vec{\rho}\right)}{{R_c}^2} + \frac{\rho^2}{{R_c}^2}\right)^{-\frac{3}{2}} = \\ {R_c}^{-3} \cdot \left(1 - \frac{2 \cdot \left(\vec{R}_c + \vec{\rho}\right)}{{R_c}^2} + \text{higher-order terms}\right) \end{aligned} \tag{M.4}$$

where $R_c = \left|\vec{R}_c\right|$ and $\rho = |\vec{\rho}|$. Because $\int \vec{\rho} \cdot \mathrm{d}m = 0$, the gravity-gradient torque neglecting the higher-order torque can be written as:

$$\vec{M} = -\frac{3\mu}{{R_c}^5} \cdot \int \left(\vec{R}_c \cdot \vec{\rho}\right) \cdot \left(\vec{\rho} \times \vec{R}_c\right) \cdot \mathrm{d}m \tag{M.5}$$

This equation is further manipulated as follows:

$$\begin{aligned} \vec{M} = -\frac{3\mu}{{R_c}^5} \cdot \vec{R}_c \times \int \vec{\rho} \cdot \left(\vec{\rho} \times \vec{R}_c\right) \cdot \mathrm{d}m = -\frac{3\mu}{{R_c}^5} \cdot \vec{R}_c \times \int \vec{\rho} \cdot \vec{\rho} \cdot \mathrm{d}m \cdot \vec{R}_c = \\ -\frac{3\mu}{{R_c}^5} \cdot \vec{R}_c \times \left(\int \rho^2 \hat{I} \cdot \mathrm{d}m - \hat{J}\right) \cdot \vec{R}_c = -\frac{3\mu}{{R_c}^5} \cdot \vec{R}_c \times \int \rho^2 \hat{I} \cdot \mathrm{d}m \cdot \vec{R}_c + \frac{3\mu}{{R_c}^5} \cdot \vec{R}_c \times \hat{J} \cdot \vec{R}_c = \\ \frac{3\mu}{{R_c}^5} \cdot \vec{R}_c \times \hat{J} \cdot \vec{R}_c \end{aligned} \tag{M.6}$$

because $\hat{J} = \int \left(\rho^2 \hat{I} - \vec{\rho}\vec{\rho}\right) \cdot \mathrm{d}m$ and $\vec{R}_c \times \hat{I} \cdot \vec{R}_c = \vec{R}_c \times \vec{R}_c = 0$.

Finally, the gravity gradient torque with respect to a satellite fixed reference frame is expressed in vector/dyadic form as:

$$\vec{M} = 3n^2 \cdot \vec{a}_3 \times \hat{J} \cdot \hat{a}_3 \tag{M.7}$$

where $n = \sqrt{\frac{\mu}{{R_c}^3}}$ is the orbital rate and $\vec{a}_3 \equiv -\frac{\vec{R}_c}{R_c}$.
Because $\vec{a}_3$ can be expressed in terms of basis vectors of the body-fixed reference frame B as:

$$\vec{a}_3 = C_{13}\vec{b}_1 + C_{23}\vec{b}_2 + C_{33}\vec{b}_3 \tag{M.8}$$

where C_{13}, C_{23}, and C_{33} denote coefficients used to transform the b-vector to $\vec{a}_3$. Now the gravity gradient torque can be rewritten in matrix form to:

$$\begin{pmatrix} M_1 \\ M_2 \\ M_3 \end{pmatrix} = 3n^2 \begin{pmatrix} 0 & -C_{33} & C_{23} \\ C_{33} & 0 & -C_{13} \\ -C_{23} & C_{13} & 0 \end{pmatrix} \begin{pmatrix} J_{11} & J_{12} & J_{13} \\ J_{21} & J_{22} & J_{23} \\ J_{31} & J_{32} & J_{33} \end{pmatrix} \begin{pmatrix} C_{13} \\ C_{23} \\ C_{33} \end{pmatrix} \tag{M.9}$$

M.2.2 Construction of rotational matrix

Consider a reference frame A with a right-hand set of three orthogonal unit vectors $(\vec{a}_1, \vec{a}_2, \vec{a}_3)$ and a reference frame B with another right-hand set of three orthogonal unit vectors $\left(\vec{b}_1, \vec{b}_2, \vec{b}_3\right)$. Basis vectors $\left(\vec{b}_1, \vec{b}_2, \vec{b}_3\right)$ of B are expressed in terms of basis vectors $(\vec{a}_1, \vec{a}_2, \vec{a}_3)$ of A as follows:

$$\vec{b}_1 = C_{11}\vec{a}_1 + C_{12}\vec{a}_2 + C_{13}\vec{a}_3 \tag{M.10}$$

$$\vec{b}_2 = C_{21}\vec{a}_1 + C_{22}\vec{a}_2 + C_{23}\vec{a}_3 \tag{M.11}$$

$$\vec{b}_3 = C_{31}\vec{a}_1 + C_{32}\vec{a}_2 + C_{33}\vec{a}_3 \tag{M.12}$$

where $C_{ij} \equiv \vec{b}_i \cdot \vec{a}_j$ is the cosine of the angle between $\vec{b}_i$ and $\vec{a}_j$, and C_{ij} is simply called the direction cosine.
For convenience, equations M.10 to M.12 can be written in matrix notation as follows:

$$\begin{pmatrix} \vec{b}_1 \\ \vec{b}_2 \\ \vec{b}_3 \end{pmatrix} = \begin{pmatrix} C_{11} & C_{12} & C_{13} \\ C_{21} & C_{22} & C_{23} \\ C_{31} & C_{32} & C_{33} \end{pmatrix} \begin{pmatrix} \vec{a}_1 \\ \vec{a}_2 \\ \vec{a}_3 \end{pmatrix} = \mathbf{C}^{B/A} \begin{pmatrix} \vec{a}_1 \\ \vec{a}_2 \\ \vec{a}_3 \end{pmatrix} \tag{M.13}$$

where $\mathbf{C}^{B/A} \equiv [C_{ij}]$ is called the direction cosine matrix, which describes the orientation of B relative to A and which can be written as:

$$\mathbf{C}^{B/A} \equiv \begin{pmatrix} \vec{b}_1 \cdot \vec{a}_1 & \vec{b}_1 \cdot \vec{a}_2 & \vec{b}_1 \cdot \vec{a}_3 \\ \vec{b}_2 \cdot \vec{a}_1 & \vec{b}_2 \cdot \vec{a}_2 & \vec{b}_2 \cdot \vec{a}_3 \\ \vec{b}_3 \cdot \vec{a}_1 & \vec{b}_3 \cdot \vec{a}_2 & \vec{b}_3 \cdot \vec{a}_3 \end{pmatrix} = \begin{pmatrix} \vec{b}_1 \\ \vec{b}_2 \\ \vec{b}_3 \end{pmatrix} \cdot \begin{pmatrix} \vec{a}_1 & \vec{a}_2 & \vec{a}_3 \end{pmatrix} \tag{M.14}$$

Consider three successive body-axis rotations that describe the orientation of a reference frame B relative to a reference frame A. For determining $\mathbf{C}^{B/A}$, the applied rotation sequence has to be known. EuroSim operates with a 312 rotation sequence, which is symbolically represented as:

$$\mathbf{C}_3\left(\theta_3\right) : A' \longleftarrow A \tag{M.15}$$

$$\mathbf{C}_1\left(\theta_1\right) : A'' \longleftarrow A' \tag{M.16}$$

$$\mathbf{C}_2\left(\theta_2\right) : B \longleftarrow A'' \tag{M.17}$$

where each rotation is described as:

$$\begin{pmatrix} \vec{a}'_1 \\ \vec{a}'_2 \\ \vec{a}'_3 \end{pmatrix} = \begin{pmatrix} \cos\theta_3 & \sin\theta_3 & 0 \\ -\sin\theta_3 & \cos\theta_3 & 0 \\ 0 & 0 & 1 \end{pmatrix} \begin{pmatrix} \vec{a}_1 \\ \vec{a}_2 \\ \vec{a}_3 \end{pmatrix} = \mathbf{C}_3\left(\theta_3\right) \begin{pmatrix} \vec{a}_1 \\ \vec{a}_2 \\ \vec{a}_3 \end{pmatrix} \tag{M.18}$$

$$\begin{pmatrix} \vec{a}''_1 \\ \vec{a}''_2 \\ \vec{a}''_3 \end{pmatrix} = \begin{pmatrix} 1 & 0 & 0 \\ 0 & \cos\theta_1 & \sin\theta_1 \\ 0 & -\sin\theta_1 & \cos\theta_1 \end{pmatrix} \begin{pmatrix} \vec{a}'_1 \\ \vec{a}'_2 \\ \vec{a}'_3 \end{pmatrix} = \mathbf{C}_1\left(\theta_1\right) \begin{pmatrix} \vec{a}'_1 \\ \vec{a}'_2 \\ \vec{a}'_3 \end{pmatrix} \tag{M.19}$$

$$\begin{pmatrix} \vec{b}_1 \\ \vec{b}_2 \\ \vec{b}_3 \end{pmatrix} = \begin{pmatrix} \cos\theta_2 & 0 & -\sin\theta_2 \\ 0 & 1 & 0 \\ \sin\theta_2 & 0 & \cos\theta_2 \end{pmatrix} \begin{pmatrix} \vec{a}''_1 \\ \vec{a}''_2 \\ \vec{a}''_3 \end{pmatrix} = \mathbf{C}_2\left(\theta_2\right) \begin{pmatrix} \vec{a}''_1 \\ \vec{a}''_2 \\ \vec{a}''_3 \end{pmatrix} \tag{M.20}$$

where $\mathbf{C}_i\left(\theta_i\right)$ denotes the direction cosine matrix $\mathbf{C}$ of an elementary rotation about the i-th axis of A with angle θ_i. A' and A'' are two intermediate reference frames with basis vectors $(\vec{a}'_1, \vec{a}'_2, \vec{a}'_3)$ and $(\vec{a}''_1, \vec{a}''_2, \vec{a}''_3)$, respectively. The three angles θ_1, θ_2, and θ_3 are called Euler angles.
By combining the preceding sequence of rotations, we obtain:

$$\begin{pmatrix} \vec{b}_1 \\ \vec{b}_2 \\ \vec{b}_3 \end{pmatrix} = \mathbf{C}_2\left(\theta_2\right) \begin{pmatrix} \vec{a}''_1 \\ \vec{a}''_2 \\ \vec{a}''_3 \end{pmatrix} = \mathbf{C}_2\left(\theta_2\right)\mathbf{C}_1\left(\theta_1\right) \begin{pmatrix} \vec{a}'_1 \\ \vec{a}'_2 \\ \vec{a}'_3 \end{pmatrix} = \mathbf{C}_2\left(\theta_2\right)\mathbf{C}_1\left(\theta_1\right)\mathbf{C}_3\left(\theta_3\right) \begin{pmatrix} \vec{a}_1 \\ \vec{a}_2 \\ \vec{a}_3 \end{pmatrix} \tag{M.21}$$

The rotation matrix to B from A, or the direction cosine matrix of B relative to A, is then defined as:

$$\mathbf{C}^{B/A} = \mathbf{C}_2\left(\theta_2\right)\mathbf{C}_1\left(\theta_1\right)\mathbf{C}_3\left(\theta_3\right) \tag{M.22}$$

or after expansion of the matrices:

$$\mathbf{C}^{B/A} = \begin{pmatrix} c_2c_3 - s_1s_2s_3 & c_2s_3 + s_1s_2c_3 & -c_1s_2 \\ -c_1s_3 & c_1c_3 & s_1 \\ s_2c_3 - s_1c_2s_3 & s_2s_3 + s_1c_2c_3 & c_1c_2 \end{pmatrix} \tag{M.23}$$

where $s_i \equiv \sin\theta_i$, and $c_i \equiv \cos\theta_i$.

M.2.3 Analytical evaluation of gravity gradient torque

As all required expressions are now derived, it is possible to construct the expression for the gravity gradient torque.

$$\begin{aligned} \begin{pmatrix} M_x \\ M_y \\ M_z \end{pmatrix} &= 3n^2 \begin{pmatrix} 0 & -c_1c_2 & s_1 \\ c_1c_2 & 0 & c_1s_2 \\ -s_1 & -c_1s_2 & 0 \end{pmatrix} \begin{pmatrix} J_{xx} & 0 & 0 \\ 0 & J_{yy} & 0 \\ 0 & 0 & J_{zz} \end{pmatrix} = \\ &-3n^2 \begin{pmatrix} (J_{yy} - J_{zz})\sin\theta_1\cos\theta_1\cos\theta_2 \\ (J_{xx} - J_{zz})\cos^2\theta_1\cos\theta_2\sin\theta_2 \\ (J_{yy} - J_{xx})\sin\theta_1\cos\theta_1\sin\theta_2 \end{pmatrix} = -\frac{3}{2}n^2 \begin{pmatrix} (J_{yy} - J_{zz})\sin 2\theta_1\cos\theta_2 \\ (J_{xx} - J_{zz})\cos^2\theta_1\sin 2\theta_2 \\ (J_{yy} - J_{xx})\sin 2\theta_1\sin\theta_2 \end{pmatrix} \end{aligned} \tag{M.24}$$

The values for the moments of inertia J_{xx}, J_{yy}, and J_{zz} are found in appendix K. The mean angular motion for a circular orbit is found to be:

$$n = \sqrt{\frac{\mu}{a^3}} \tag{M.25}$$

where μ is the gravitational parameter of the Earth, and a is the semi-major axis of the spacecraft orbit. Using an orbital altitude of 635 km, and substituting numerical values into equation M.25 leads to:

$$n = \sqrt{\frac{398600.44 \cdot 10^9}{(6378137.0 + 635000)^3}} = 1.07498 \cdot 10^{-3} \text{ rad.s}^{-1} \tag{M.26}$$

The maximum gravitational torque with respect to satellite fixed reference frame can now be found by inserting the values for n, J_{xx}, J_{yy}, and J_{zz}. Having the goniometrical terms equal unity leads to the maximum gravity gradient torque. This leads to:

$$\begin{pmatrix} (M_x)_{max} \\ (M_y)_{max} \\ (M_z)_{max} \end{pmatrix} = \left| -\frac{3}{2}n^2 \begin{pmatrix} 1.989 \cdot 10^{-2} \\ 1.989 \cdot 10^{-2} \\ 0 \end{pmatrix} \right| = \begin{pmatrix} 3.448 \cdot 10^{-8} \\ 3.448 \cdot 10^{-8} \\ 0 \end{pmatrix} \text{ N.m} \tag{M.27}$$

It has to be mentioned that the maximum gravity gradient torques around the various axes cannot be attained simultaneously, as $\sin\theta_i = 1$ and $\cos\theta_i = 1$ cannot occur at the same time.

M.3 Conclusions and recommendations

In the previous section, the gravity gradient torque acting on the Delfi-C3 spacecraft is determined. The magnitude of the torque is in the order 10^{-8}, with a maximum value of $3.448 \cdot 10^{-8}$ N.m.

Appendix N

DC3-TN-610-076 EuroSim - Determination of aerodynamic torque

N.1 Introduction

EuroSim is a simulation platform, in which the orbit of the Delfi-C3 spacecraft will be simulated. Interesting quantities, which can be determined from this simulation, are power generation and attitude reconstruction. For accurate attitude reconstruction, it is important to determine the aerodynamic torques acting on the Delfi-C3 spacecraft.
Aerodynamic torques are a result of the motion of the spacecraft through the Earth atmosphere. Although this atmosphere is every thin at the orbital altitude of the Delfi-C3 spacecraft it will resist the motion of Delfi-C3 resulting in the generation of aerodynamic drag forces. In case the working line of a drag force does not run through the center of mass of the spacecraft, an aerodynamic torque will be generated.
In this document, an expression for aerodynamic torque will be developed. Furthermore, an example calculation is shown for the torque on a single deployed solar panel. In subsection N.2.1, the physical nature of aerodynamic drag forces is clarified. As a result of these forces, aerodynamic torques will be generated, which are treated in subsection N.2.2. An example calculation of aerodynamic torque for a single deployed solar panel is shown in subsection N.2.3.

N.2 Determination of aerodynamic torque

N.2.1 Nature of aerodynamic forces

Aerodynamic torques are generated due to the various aerodynamic drag forces on the surface panels of the Delfi-C3 spacecraft. The projections of these drag forces through the centers of pressure corresponding to the respective forces in general do not intersect the center of mass of the satellite. Therefore, a torque will be created due to these aerodynamic drag forces [7].
With help of figure N.1, this torque can be expressed as:

$$\vec{T_a} = \vec{D} \times \vec{l} \tag{N.1}$$

where $\vec{D}$ equals the component of the drag force vector perpendicular to the body plate, and $\vec{l}$ equals the distance vector between the working line of the drag force, which passes the so-called center of pressure of the plate, and the center of mass of the satellite.
The magnitude of the drag force can be modeled by the generic aerodynamic drag equation:

$$D = \frac{1}{2} \cdot C_D \cdot \rho \cdot V^2 \cdot S \tag{N.2}$$

where C_D denotes the aerodynamic drag coefficient of the satellite, ρ equals the air mass density at the satellite's position, V equals the relative velocity of the satellite with respect to the surrounding air, and S is the surface area of the body panel.

In case of a general satellite, the drag coefficient CD lies in a range from 2.2 to 2.6. However, as a first approximation, the aerodynamic drag is assumed to consist only out of a transfer of momentum

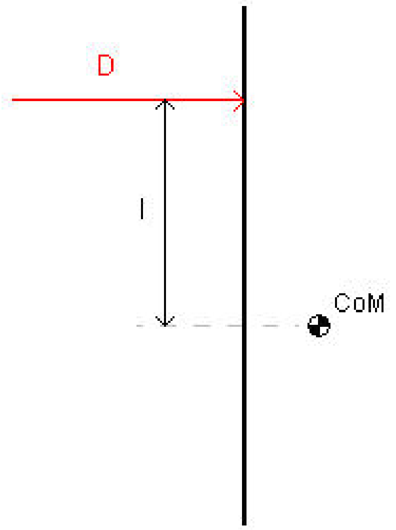

Figure N.1: Illustration of the generation of aerodynamic torques

from the colliding air particles to the satellite. This situation can be expressed by the well-known formula:

$$F \cdot \Delta t = m \cdot \Delta V \tag{N.3}$$

The mass flow of air particles m equals the volumetric flow of the particles times the air mass density. Moreover, the volumetric flow equals the velocity times the body panel surface. So the total mass which has collided with the satellite is written as:

$$m = \rho \cdot V \cdot S \cdot \Delta t \tag{N.4}$$

Now, it is assumed that the collision is completely elastic, i.e. the velocity of the air particles reduces after impact to zero. This equals:

$$\Delta V = V - 0 = V \tag{N.5}$$

which yields:

$$F \cdot \Delta t = \rho \cdot V \cdot S \cdot \Delta t \cdot V \tag{N.6}$$

$$F = D = \rho \cdot V^2 \cdot S \tag{N.7}$$

This expression has to be equal to the general formulation of an aerodynamic drag force. Therefore, the equation can be solved for C_D:

$$\rho \cdot V^2 \cdot S = \frac{1}{2} \cdot C_D \cdot \rho \cdot V^2 \cdot S \tag{N.8}$$

$$C_D = 2 \tag{N.9}$$

Therefore, as a first approximation C_D is taken as being equal to 2.
The air mass density ρ can be found with help of the general expression for air pressure:

$$\mathrm{d}p = -\rho \cdot g \cdot \mathrm{d}h \tag{N.10}$$

where p is the air pressure, g is the gravitational acceleration at the point of consideration, and h equals the altitude above sea level.
The gravitational acceleration g in its turn exhibits a reciprocal quadratic relation with altitude and can therefore be written as:

$$g = g_0 \cdot \left(\frac{R_e}{r}\right)^2 = g_0 \cdot \left(\frac{R_e}{R_e + h}\right)^2 \tag{N.11}$$

where g_0 equals the gravitational acceleration at sea level, and R_e denotes the radius of the Earth.
Introducing the ideal gas law yields a relation between the air pressure p and the air density ρ. This relation follows from the following expression:

$$p = \rho \cdot R \cdot T \tag{N.12}$$

where T denotes the temperature, and R is the specific gas constant of the medium under consideration.
Rewriting yields:

$$\rho = \frac{p}{R \cdot T} \tag{N.13}$$

leading to:

$$\mathrm{d}p = -\frac{p}{R \cdot T} \cdot g_0 \cdot \left(\frac{R_e}{R_e + h}\right)^2 \cdot \mathrm{d}h \tag{N.14}$$

$$\frac{R \cdot T}{p} \cdot \mathrm{d}p = -g_0 \cdot \left(\frac{R_e}{R_e + h}\right)^2 \cdot \mathrm{d}h \tag{N.15}$$

Integration of this equation yields the following expression:

$$R \cdot T \cdot (\ln p - \ln p_{ref}) = g_0 \cdot \left(\frac{{R_e}^2}{R_e + h} - \frac{{R_e}^2}{R_e + h_{ref}}\right) \tag{N.16}$$

$$\frac{p}{p_{ref}} = \exp\left(\frac{g_0}{R \cdot T} \cdot \left(\frac{{R_e}^2}{R_e + h} - \frac{{R_e}^2}{R_e + h_{ref}}\right)\right) \tag{N.17}$$

Reintroducing the ideal gas law finally yields the equation for the air mass density.

$$\frac{\rho}{\rho_{ref}} = \frac{T_{ref}}{T} \cdot \exp\left(\frac{g_0}{R \cdot T} \cdot \left(\frac{{R_e}^2}{R_e + h} - \frac{{R_e}^2}{R_e + h_{ref}}\right)\right) \tag{N.18}$$

By taking sea level as the reference altitude, the reference quantities in equation N.18 become the values of those quantities at sea level. Therefore:

$$h_{ref} = h_0 = 0 \text{ m} \tag{N.19}$$

$$T_{ref} = T_0 = 288.15 \text{ K} \tag{N.20}$$

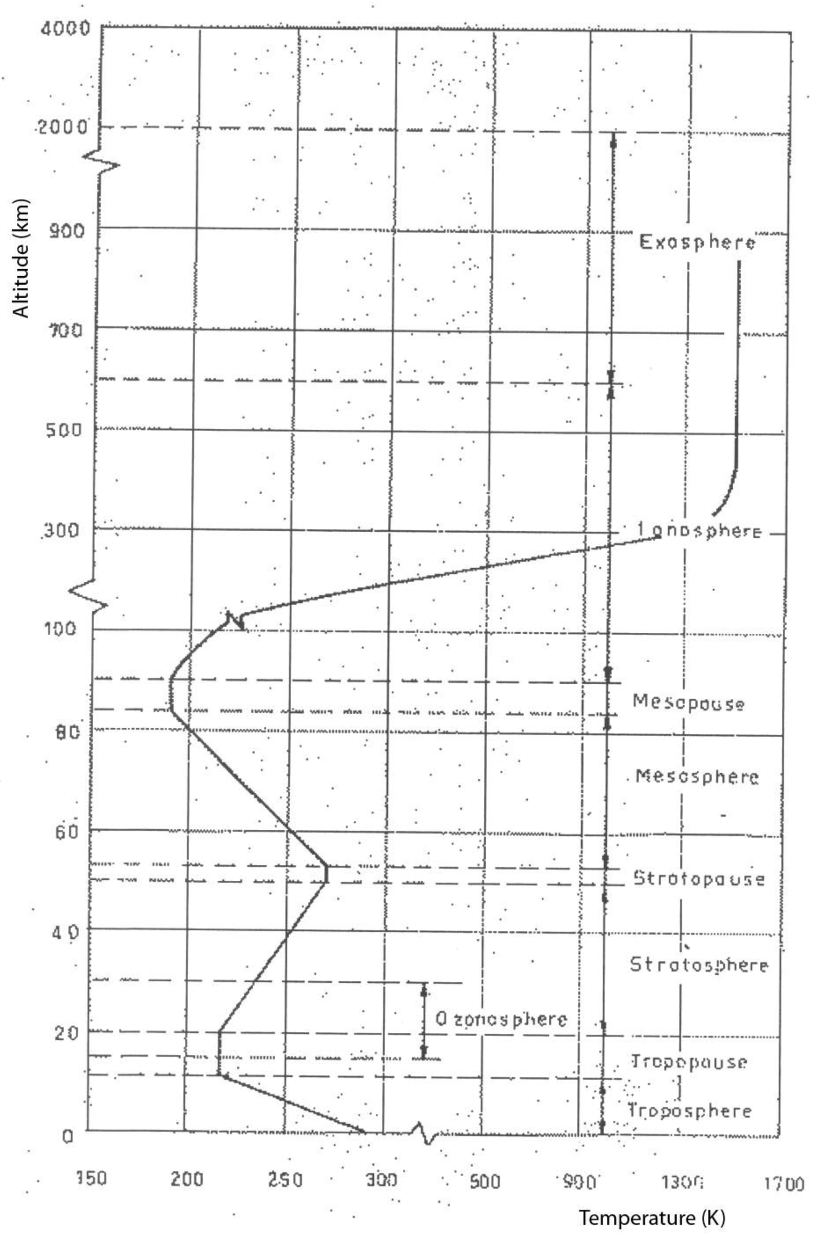

Figure N.2: Atmospheric temperature as a function of altitude [13]

$$\rho_{ref} = \rho_0 = 1.225 \text{ kg.m}^{-3} \tag{N.21}$$

The ambient temperature of the satellite is slightly more difficult to determine, as no unambiguous relation can be defined between the temperature and altitude. For the determination of the local temperature T, a look-up method in the known vertical temperature profile of the temperature can therefore be used. In figure N.2, the atmospheric temperature as a function of altitude is shown.
However, the temperature of the exosphere, i.e. the layer of the atmosphere, in which the Delfi-C3 spacecraft orbits the Earth, is highly dependent on the level of solar activity. As air mass density is directly related to atmospheric temperature, the dependency on solar activity is also valid for this quantity. Therefore, two cases will be defined:

- Nominal case with average solar activity level
- Worst case with maximum solar activity level

For both cases, a look-up table will be used for determining the actual air mass density at the altitude of Delfi-C3's position.

The relative velocity V of the satellite with respect to the surrounding air is equal to the difference between the velocity of the satellite in the Earth inertial reference frame and the velocity of the air particles. It is assumed that at the relevant altitudes no wind is present, so this velocity is only caused by the rotation of the Earth.

However, caution must be taken, because in general the satellite's velocity and the velocity of the air are not directed along the same vector. To have a valid equation, the two velocities have to be vectorially subtracted. Therefore, the relative velocity can be written as:

$$\vec{V}_{rel} = \vec{V}_{inertial} - \vec{V}_{air} = \vec{V}_{inertial} - \vec{\omega} \times \vec{r} \tag{N.22}$$

The calculated velocity relates to the center of mass of the satellite. The velocity to be used in the aerodynamic drag expression is the component of the complete velocity perpendicular to the body panel. Therefore, for every individual body panel the relevant velocity component has to be calculated. Recalling that vector $\vec{n}_i$ is the outward directed normal vector of body panel i yields a solution for the calculation of the perpendicular velocity component. After all, this is expressed as:

$$\vec{V}_i = V_{rel} \cdot \cos\psi_i \cdot \vec{n}_i = -\left(\vec{V}_{rel} \cdot \vec{n}_i\right) \cdot \vec{n}_i \tag{N.23}$$

The most difficult variable in the aerodynamic drag force expression to determine is the exposed body panel surface area. As the evaluation of this variable involves several complex calculations to take into account shadowing effects, the area calculation will be treated in a separate technical note. In appendix P, a full explanation of the applied algorithm for determining the shadowed surface area of the various panels is given.

N.2.2 Generation of aerodynamic torques

As the drag force on a particular panel is now completely defined, the torque resulting from this force can be calculated. For this calculation, it is necessary to know the position of the center of pressure on this panel. As this position is directly dependent on the shape and size of the exposed area, a rather complex calculation has to be performed in case of a shadowed panel. The determination of the position of the center of pressure in case of a shadowed panel is also treated in appendix P. As all torques are measured in a satellite fixed reference frame, the scalar expression for the aerodynamic torque as shown in equation N.1 has to be rewritten to a vector expression:

$$\left(\vec{T}_a\right)_i = \begin{pmatrix} (T_a)_x \\ (T_a)_y \\ (T_a)_z \end{pmatrix}_i = D_i \cdot \frac{\vec{V}_i}{|V_i|} \times \left(\vec{x}_{CoP/CoM}\right)_i \tag{N.24}$$

where D_i is the scalar value of the drag force acting on panel i, $\vec{V}_i$ is the vector representation of the perpendicular velocity component on panel i in a satellite fixed reference frame, and $\left(\vec{x}_{CoP/CoM}\right)_i$ is the distance vector between the center of pressure of panel i and the center of mass of the spacecraft.

In addition to the torques generated on the surface panels, also the induced torques on the antennae have to be taken into account. In appendix O, an explanation of the algorithm for determining the torques on the antennae is given.

The total aerodynamic torque acting on the spacecraft is then simply calculated by vectorially adding all individual contributions. This leads to:

$$\vec{T}_a = \sum_{i=0}^{13} \left(\vec{T}_a\right)_i + \sum_{j=0}^{7} \left(\vec{T}_a\right)_j \tag{N.25}$$

where $\left(\vec{T}_a\right)_i$ is the aerodynamic torque produced by panel i, and $\left(\vec{T}_a\right)_j$ is the aerodynamic torque produced by antenna j.

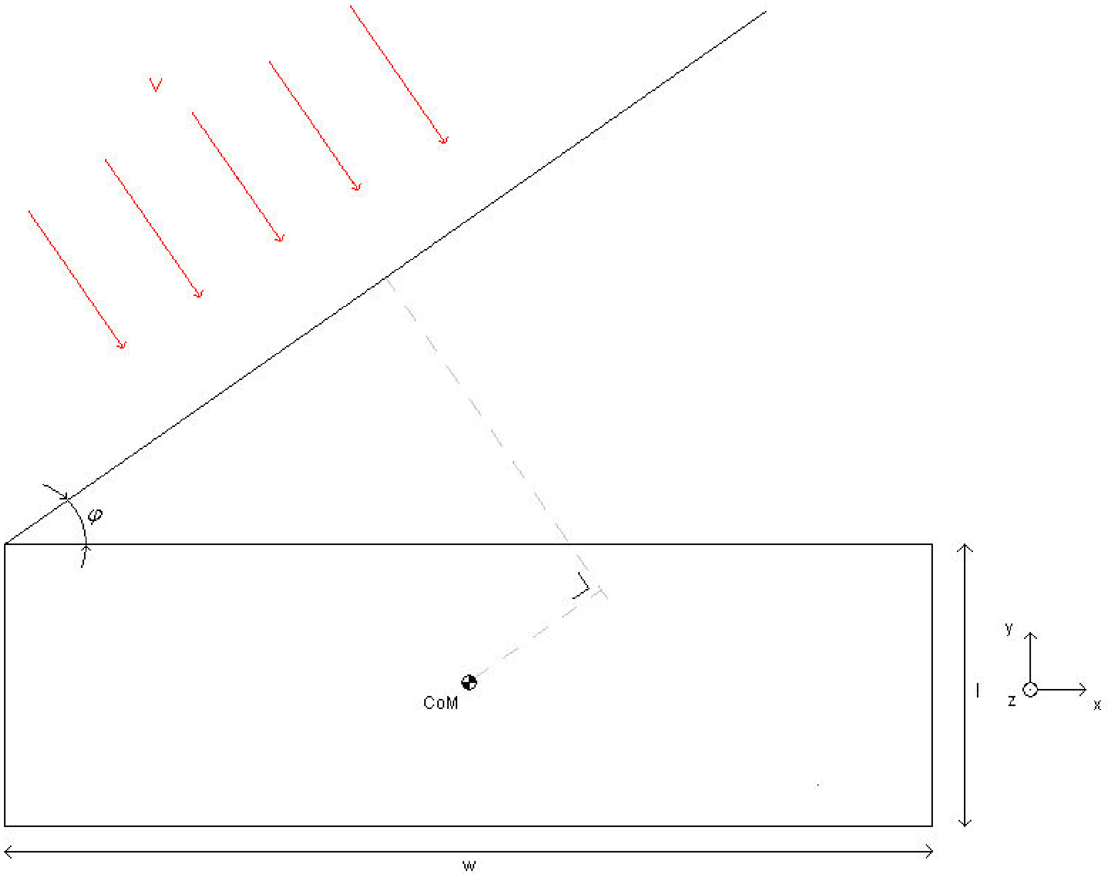

Figure N.3: Situational sketch for determining aerodynamic torque on a deployed solar panel

N.2.3 Calculation of aerodynamic torque due to a single deployed solar panel

To estimate the magnitude of the aerodynamic torque, the torque on a single deployed solar array is calculated. This is done with the assuming of a worst-case scenario. This implies that the velocity vector is perpendicular to the solar panel. This situation is shown in figure N.3.

Firstly, determine the velocity of the spacecraft relative to the Earth atmosphere. For this, use is made of the rotational velocity of the spacecraft. For a circular orbit, the mean angular motion can be expressed by:

$$n = \sqrt{\frac{\mu}{a^3}} \tag{N.26}$$

where μ is the gravitational parameter of the Earth, and a is the semi-major axis of the spacecraft orbit.

Substituting all relevant parameters into equation N.26 yields:

$$n = \sqrt{\frac{398600.44 \cdot 10^9}{(6378137.0 + 635000)^3}} = 1.07498 \cdot 10^{-3}\ \text{rad.s}^{-1} \tag{N.27}$$

Next, an Earth inertial reference frame is defined. In this reference frame, the xy-plan is perpendicular to the orbital plane of the spacecraft. The positive x-axis is directly over the equator, and the positive y-axis is in the direction of the North Pole. Having the positive z-axis point perpendicular to the paper towards the reader completes the right-handed Cartesian reference frame. An illustration of this reference frame is shown in figure N.4.

With the reference frame defined, it is now possible to construct the velocity vector of the spacecraft at any particular point in its orbit. Assuming the spacecraft is at its descending node, i.e. it crosses the equatorial plane in southward direction, the following expression can be written:

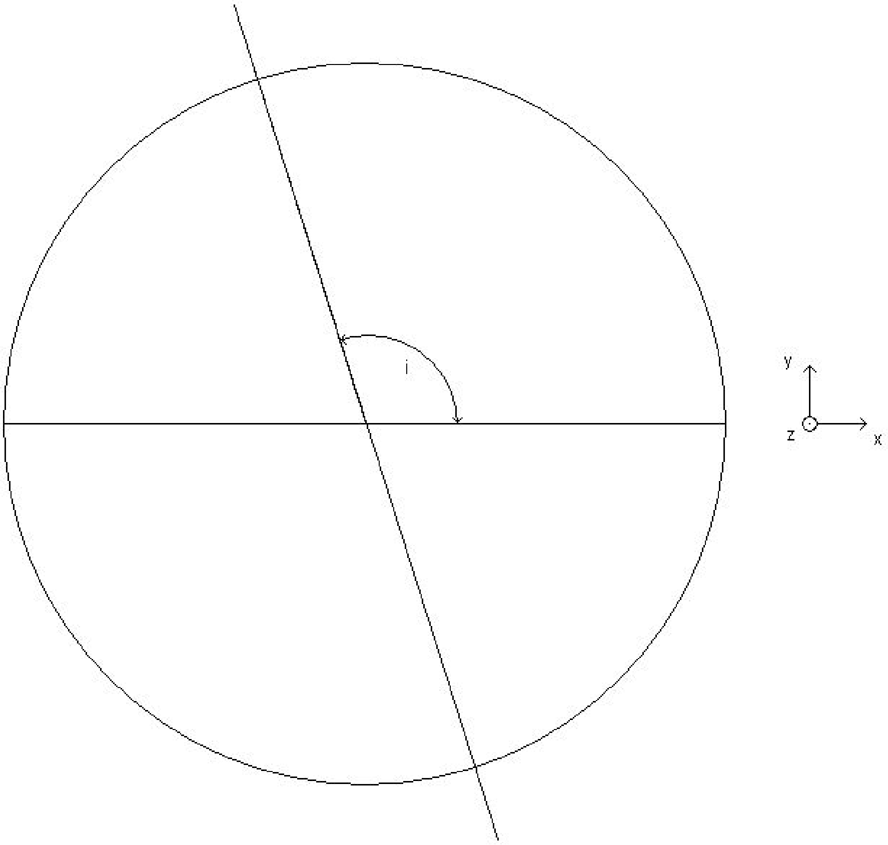

Figure N.4: Illustration of Earth Inertial reference frame

$$\vec{V}_{in} = \vec{n} \times \vec{r} = \begin{pmatrix} -n \cdot r \cdot \cos i \\ -n \cdot r \cdot \sin i \\ 0 \end{pmatrix} =$$

$$\begin{pmatrix} -1.07498 \cdot 10^{-3} \cdot (6378137.0 + 635000) \cdot \cos 97.91\,^{\circ} \\ -1.07498 \cdot 10^{-3} \cdot (6378137.0 + 635000) \cdot \sin 97.91\,^{\circ} \\ 0 \end{pmatrix} = \begin{pmatrix} 1035.5 \\ -7467.3 \\ 0 \end{pmatrix} \text{ m.s}^{-1} \tag{N.28}$$

In order to determine the velocity of the atmosphere at the orbital altitude of the Delfi-C3 spacecraft, it has to be recalled that the Earth rotates 2π radians in one sidereal day. Furthermore, the rotational axis of the Earth runs through the poles and therefore:

$$\vec{V}_{air} = \vec{\omega}_{Earth} \times \vec{r} = \begin{pmatrix} \omega_{Earth} \cdot r \\ 0 \\ 0 \end{pmatrix} =$$

$$\begin{pmatrix} \frac{2\pi}{23\frac{33641}{36000} \cdot 3600} \cdot (6378137.0 + 635000) \\ 0 \\ 0 \end{pmatrix} = \begin{pmatrix} 511.4 \\ 0 \\ 0 \end{pmatrix} \text{ m.s}^{-1} \tag{N.29}$$

Summing the inertial velocity of the spacecraft and the velocity of the atmosphere yields the relative velocity of the spacecraft with respect to the Earth atmosphere. Therefore, the magnitude of the relative velocity is determined with:

$$\left|\vec{V}_{rel}\right| = \sqrt{(1035.5 + 511.4)^2 + 7467.3^2} = 7626.2 \text{ m.s}^{-1} \tag{N.30}$$

By consulting literature, the maximum atmospheric density is found to be equal to:

$$\rho = 4.89 \cdot 10^{-13} \text{ kg.m}^{-3} \tag{N.31}$$

For determining the surface area of a single solar panel, it is assumed that a solar panel has the same dimensions as the underlying body panel. Hence:

$$S = l \cdot w = 0.3265 \cdot 0.1 = 3.265 \cdot 10^{-2} \text{ m}^2 \tag{N.32}$$

Recalling that the drag coefficient C_D is taken equal to 2.0, and denoting that the drag force is perpendicular to the solar panel, the drag force is calculated with:

$$D = \frac{1}{2} \cdot C_D \cdot \rho \cdot V^2 \cdot S = \frac{1}{2} \cdot 2.0 \cdot 4.89 \cdot 10^{-13} \cdot 7626.2^2 \cdot 3.265 \cdot 10^{-2} = 9.286 \cdot 10^{-7} \text{ N} \tag{N.33}$$

In order to determine the perpendicular distance between the working line of the drag force and the center of mass of the spacecraft, it is noticed that the center of pressure of the solar panel coincides with its geometrical center. Moreover, it is assumed that the center of mass of the spacecraft coincides with the geometrical center of the main body. Then the perpendicular distance is calculated to be:

$$d_{\perp} = \left(\frac{l}{2} \cdot \sin\theta + \frac{w}{2} \right) \cdot \sin\theta = 8.24 \cdot 10^{-2} \text{ m} \tag{N.34}$$

Multiplying the perpendicular distance with the magnitude of the drag force yields the produced aerodynamic torque, which equals:

$$|T_A| = 7.651 \cdot 10^{-8} \text{ N.m} \tag{N.35}$$

Please keep in mind that this value is only the contribution of a single solar panel. Additional contributions are found by the other solar panels, the antennae, and various body panels. Note however, that the front and back body panel, i.e. the square panels to which the antennae are attached, do not yield an aerodynamic torque in any situation.

As additional contributions will be involved, the total aerodynamic torque will likely be in the order of 10^{-7}.

N.3 Conclusions and recommendations

In the previous sections, a derivation of aerodynamic drag forces and aerodynamic torques is given. Furthermore, an example calculation for a single deployed solar array is shown. The magnitude of this torque is in the order of 10^{-7} N.m. This magnitude is non-negligible, and has therefore consequences for the attitude behaviour of the Delfi-C3 spacecraft.

Appendix O

DC3-TN-610-074 EuroSim - Determination of antennae induced torques

O.1 Introduction

EuroSim is a simulation platform, in which the orbit of the Delfi-C3 spacecraft will be simulated. Interesting quantities, which can be determined from this simulation, are power generation and attitude reconstruction. For attitude reconstruction, it is important to determine the various disturbance torques acting on the spacecraft.

Both the aerodynamic and the solar radiation torques are treated as disturbance torques. However, evaluating these disturbance torques for only the main body will not yield a satisfactory estimation. After all, the uplink and downlink antennae also contribute to these torques, and have to be taken into account.

In this report, a derivation for the calculation of antennae induced torques will be given. In subsection O.2.1 several general remarks concerning this derivation will be given. Antenna induced disturbance torques about the y-axis will be treated in subsection O.2.2. In subsection O.2.3, a treatise of antennae induced disturbance torque about the x-axis will be given, while the same will be doe for torques about the z-axis in subsection O.2.4. Next, in subsection O.2.5 an estimation of the magnitude of the torques, which are generated due to the antennas will be made. Finally, several shortcomings of the derived model will be given in subsection O.2.6.

O.2 Determination of antennae induced torques

O.2.1 General remarks

For a complete analysis of disturbance torques on the Delfi-C3 spacecraft, the downlink and uplink antennae have to be taken into account as well. Although in general the forces, which are produced on the antennae, are relatively small in magnitude, the accompanying torques cannot be neglected as the corresponding arm is relatively large in magnitude.

In order to develop expressions for the torques, which are generated by the antennae, it has to be noted that these torques are produced due to a difference in angle of incidence of two associated antennae with respect to the spacecraft velocity. Furthermore, it is assumed that every antenna is a two dimensional are, i.e. their thicknesses are infinitesimally small. Therefore, the analysis can be done by considering the behaviour of the antennae in three perpendicular planes: xy-plane, xz-plane, and yz-plane. For a successful analysis, it is necessary to consider the in-plane components of the spacecraft velocity; the out-of-plane component does not contribute to the considered torque.

O.2.2 Disturbance torque about y-axis

Firstly, the analysis is performed for the downlink antennae, which results in the situation sketched in figure O.1. Investigating figure O.1, it is noted that the vector $\vec{V}$ does not refer to the complete velocity component of the Delfi-C3 spacecraft, but that it denotes the velocity component in the plane of the drawing, i.e. the xz-plane. Two downlink antennae are drawn, which are referenced as I and II in figure

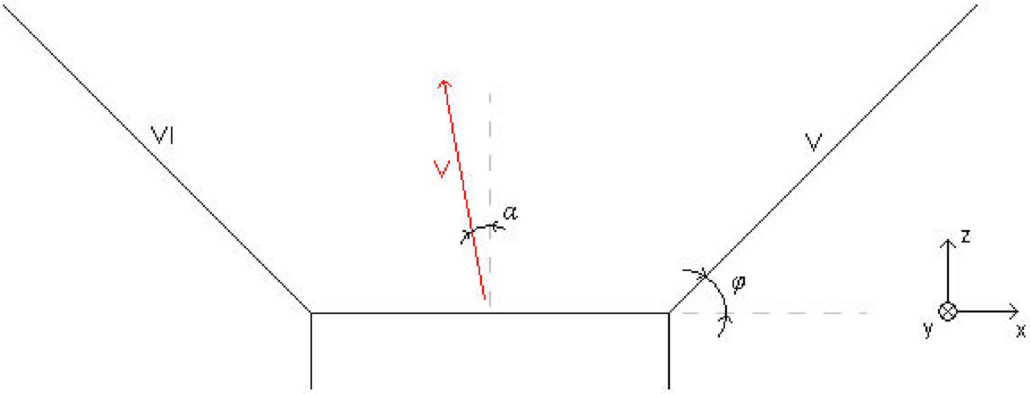

Figure O.1: Illustrational sketch for calculation of downlink antennae induced torques about y-axis

O.1. A careful observer may have noted that in reality, two additional antennae are present. However, the projections of these antennae are parallel to the normal vector of the connecting body panel (i.e. parallel to the z-axis). Evaluating the torques produced by these two downlink antennae about the y-axis, it can be easily seen that they cancel each other out, yielding an resultant torque of zero.
An additional variable sketched in figure O.1 is the angle α, which is the angle of the normal vector of the corresponding body panel (i.e. front panel) with the in-plane velocity component $\vec{V}$. Furthermore, ϕ is the angle between the plane of the connecting body panel and the downlink antennae I and II. In nominal conditions, ϕ is equal to 40 °.
Now, the view factors of antennae I and II can be determined. Thereafter, it is possible to extract the magnitude of the force acting on these antennae. In figure O.2, a sketch is given for determining the antenna view factors.

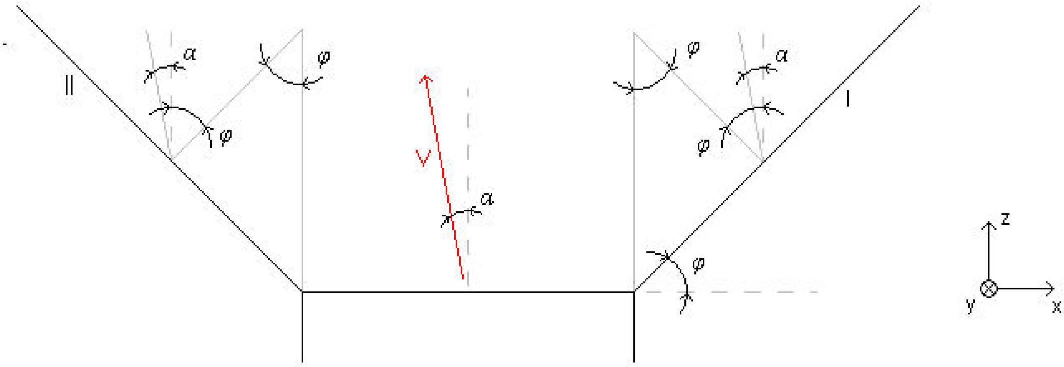

Figure O.2: Illustrational sketch for antenna view factor determination

Making use of figure O.2, it can be shown that the magnitude of the forces acting on antenna I and II can be written as:

$$F_I = k \cdot |\cos(\phi - \alpha)| \tag{O.1}$$

$$F_{II} = k \cdot |\cos(\phi + \alpha)| \tag{O.2}$$

where k is a scaling variable denoting the magnitude of the force in case the incidence angle would be equal to 90 °; this value is dependent on the nature of the disturbance. For determining the torque caused by these forces, it is convenient to write the force as two perpendicular contributions parallel to the local x- and z-axes (see figure O.2). Then, the following expressions can be written:

$$(F_I)_x = k \cdot |\cos(\phi - \alpha)| \cdot \sin\alpha \tag{O.3}$$

$$(F_I)_z = -k \cdot |\cos(\phi - \alpha)| \cdot \cos\alpha \tag{O.4}$$

$$(F_{II})_x = k \cdot |\cos(\phi + \alpha)| \cdot \sin\alpha \tag{O.5}$$

$$(F_{II})_z = -k \cdot |\cos(\phi + \alpha)| \cdot \cos\alpha \tag{O.6}$$

With the values for the forces known, the torque caused by these forces can be calculated. Firstly, the center of mass has to be determined, because a general equation for torque is written as:

$$T = F \cdot s \tag{O.7}$$

where s is the distance between the point, on which the force is acting, and the center of mass of the body. For the determination of this distance (or arm), use has to be made of the general geometry of the Delfi-C3 spacecraft. In the sketch in figure O.3, the projection of this geometry onto the xz-plane is shown.

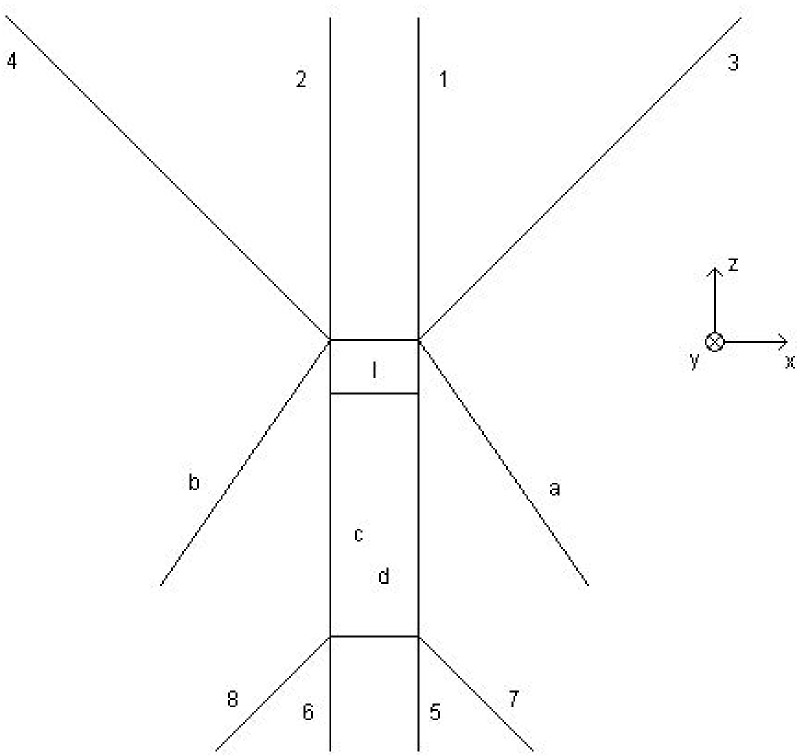

Figure O.3: Sketch of Delfi-C3 spacecraft model in xz-plane of satellite fixed reference frame

In appendix K, it has been determined that the position of the center of mass with respect to the origin of the satellite fixed reference frame, which is located at the geometrical center of the front body panel, is written as:

$$\vec{x}_{CoM} = \begin{pmatrix} x_{CoM} \\ y_{CoM} \\ z_{CoM} \end{pmatrix} = \begin{pmatrix} 0 \\ 0 \\ -162.2 \end{pmatrix} \text{mm} \tag{O.8}$$

With respect to the antennae, the point on which the resultant induced force is acting, which is known as the center of pressure, is located in the center of the antennae, due to geometrical symmetry of every antenna.
First, consider antenna I in figure O.2, which is equal to antenna 3 in figure O.3. Writing expressions for the arms corresponding with the decomposed forces $\left(F_I\right)_x$ and $\left(F_I\right)_z$ results in:

$$\left(s_I\right)_x = \frac{1}{2} \cdot l_{DLA} \cdot \sin\phi - z_{CoM} \tag{O.9}$$

$$\left(s_I\right)_z = \frac{1}{2} \cdot l_{DLA} \cdot \cos\phi + \frac{1}{2} \cdot w \tag{O.10}$$

where $\left(s_I\right)_i$ is the arm corresponding with $\left(F_I\right)_i$, with $i \in x, z$. Furthermore, w is the width of the spacecraft's body, l_{DLA} is the length of a downlink antenna, and z_{CoM} is the distance from the center of the panel to the center of mass of the spacecraft.
Subsequently, the magnitudes of the corresponding torques, which are formed about the y-axis of the satellite fixed reference frame, can be written as:

$$\left(\left(T_I\right)_x\right)_y = \left(F_I\right)_x \cdot \left(s_I\right)_x = k \cdot \left|\cos\left(\phi - \alpha\right)\right| \cdot \sin\alpha \cdot \left(\frac{1}{2} \cdot l_{DLA} \cdot \sin\phi - z_{CoM}\right) \tag{O.11}$$

$$\left(\left(T_I\right)_z\right)_y = \left(F_I\right)_z \cdot \left(s_I\right)_z = k \cdot \left|\cos\left(\phi - \alpha\right)\right| \cdot \cos\alpha \cdot \left(\frac{1}{2} \cdot l_{DLA} \cdot \cos\phi + \frac{1}{2} \cdot w\right) \tag{O.12}$$

Note that with this last calculation, the right-hand rule for determining torque sign has to be applied. In these calculations the nomenclature $\left(\left(T\right)_i\right)_j$ refers to a torque induced by a force parallel to the i-axis about the j-axis, with $i, j \in x, y, z$ and $i \neq j$.
Likewise, the torques generated about the y-axis by antenna II in figure O.2, which corresponds to antenna 4 in figure O.3, are expressed as:

$$\left(\left(T_I I\right)_x\right)_y = k \cdot \left|\cos\left(\phi + \alpha\right)\right| \cdot \sin\alpha \cdot \left(\frac{1}{2} \cdot l_{DLA} \cdot \sin\phi - z_{CoM}\right) \tag{O.13}$$

$$\left(\left(T_I I\right)_z\right)_y = -k \cdot \left|\cos\left(\phi + \alpha\right)\right| \cdot \cos\alpha \cdot \left(\frac{1}{2} \cdot l_{DLA} \cdot \cos\phi + \frac{1}{2} \cdot w\right) \tag{O.14}$$

Next, consider the uplink antennae. Producing a similar situational sketch for the uplink as has been done for the downlink antennae in figure O.1 leads to figure O.4:

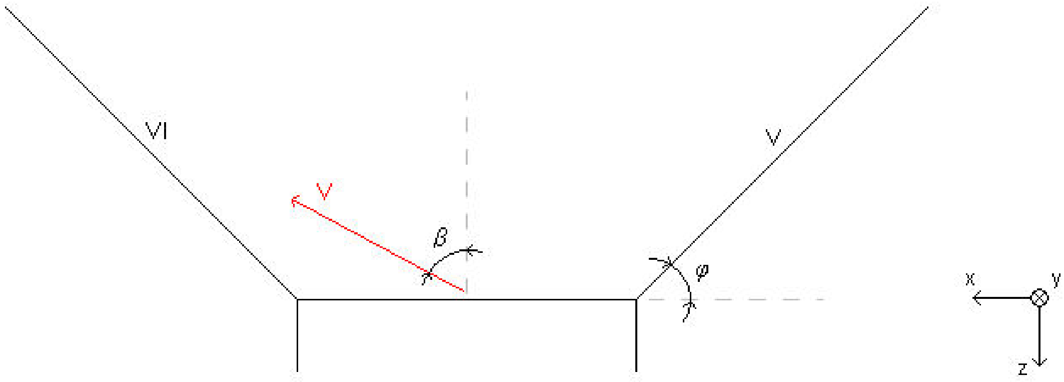

Figure O.4: Illustrational sketch for calculation of uplink antennae induced torques about y-axis

As was the case with the analysis of the downlink antennae induced forces, the velocity $\vec{V}$ in figure O.4 refers to the velocity component in the plane of drawing, so the velocity component out of this plane is not taken into account. Furthermore, only two antennae are drawn, which are referenced as antennae V

and VI, which are equal to antenna 7 and 8 in figure O.3. Note that the other two antennae connected to the corresponding body panel produce torques, which will cancel each other out.

Angle ϕ is the angle between the antennae and the corresponding body panel, which is equal to 40 ° in the nominal case. Angle β is replacing angle α, because β is referring to the angle between the in-plane velocity vector $\vec{V}$ and the normal vector of the corresponding body panel, which is equal to the back panel in case of considering uplink antennae. However, because $\vec{V}$ is a constant vector in every point in space, β can be related to α. After all, the normal vectors of the back panel and the front panel have equal working lines, but are shifted 180 ° in phase. Therefore, the following relation holds:

$$\beta = \alpha + \frac{\pi}{2} \tag{O.15}$$

Similarly to the analysis of the downlink antennae induced torques, the forces on the uplink antennae can be evaluated.

$$(F_V)_x = -k \cdot |\cos(\phi - \beta)| \cdot \sin\beta = k \cdot |\cos(\phi - \alpha)| \cdot \sin\alpha \tag{O.16}$$

$$(F_V)_z = k \cdot |\cos(\phi - \beta)| \cdot \cos\beta = -k \cdot |\cos(\phi - \alpha)| \cdot \cos\alpha \tag{O.17}$$

$$(F_{VI})_x = -k \cdot |\cos(\phi + \beta)| \cdot \sin\beta = k \cdot |\cos(\phi + \alpha)| \cdot \sin\alpha \tag{O.18}$$

$$(F_{VI})_z = k \cdot |\cos(\phi + \beta)| \cdot \cos\beta = -k \cdot |\cos(\phi + \alpha)| \cdot \cos\alpha \tag{O.19}$$

For determination of the torques, which are generated by these forces it is necessary to calculate the corresponding arms. As the position of the center of mass is given by equation O.8, and the center of pressure of a particular antenna corresponds with its geometrical center, the following expressions can be written for the arms of the forces acting on antenna V:

$$(s_V)_x = \frac{1}{2} \cdot l_{ULA} \cdot \sin\phi + l + z_{CoM} \tag{O.20}$$

$$(s_V)_z = \frac{1}{2} \cdot l_{ULA} \cdot \cos\phi + \frac{1}{2} \cdot w \tag{O.21}$$

where the newly introduced variable l_{ULA} is equal to the length of a uplink antenna. Similar equations can be written for antenna VI.

Then the torques induced by the uplink antennae can be simply calculated. The calculated torque is acting about the y-axis of the satellite fixed reference frame. Take note of the right-hand rule when determining the direction of these torques.

$$((T_V)_x)_y = -k \cdot |\cos(\phi - \alpha)| \cdot \sin\alpha \cdot \left(\frac{1}{2} \cdot l_{ULA} \cdot \sin\phi + l + z_{CoM}\right) \tag{O.22}$$

$$((T_V)_z)_y = k \cdot |\cos(\phi - \alpha)| \cdot \cos\alpha \cdot \left(\frac{1}{2} \cdot l_{ULA} \cdot \cos\phi + \frac{1}{2} \cdot w\right) \tag{O.23}$$

$$((T_{VI})_x)_y = -k \cdot |\cos(\phi + \alpha)| \cdot \sin\alpha \cdot \left(\frac{1}{2} \cdot l_{ULA} \cdot \sin\phi + l + z_{CoM}\right) \tag{O.24}$$

$$((T_{VI})_z)_y = -k \cdot |\cos(\phi + \alpha)| \cdot \cos\alpha \cdot \left(\frac{1}{2} \cdot l_{ULA} \cdot \cos\phi + \frac{1}{2} \cdot w\right) \tag{O.25}$$

The total disturbance torque about the y-axis induced by the antennae is then calculated by:

$$T_y = \sum_{i=I}^{VIII} \left(((T_i)_x)_y + ((T_i)_z)_y \right) \tag{O.26}$$

Recall that the force factor k is a linear function of the exposed area:

$$k = k(S) = l \cdot S \tag{O.27}$$

In case the torque generated by the downlink antennae is considered, k can then be written as:

$$k = k_{DLA} = c \cdot w_{DLA} \cdot l_{DLA} \tag{O.28}$$

where c is a constant factor, which is a measure for the pressure caused by the considered disturbance, w_{DLA} is the width of a downlink antenna, and l_{DLA} is the length of a downlink antenna. However, in case the uplink antennae are considered, k is expressed as:

$$k = k_{ULA} = c \cdot w_{ULA} \cdot l_{ULA} \tag{O.29}$$

where c is equal to the aforementioned pressure factor, w_{ULA} is the width of an uplink antenna, and l_{ULA} is the length of an uplink antenna. Note that w_{ULA} is equal to w_{DLA}, and will therefore be written as w_A.

Table O.1: Relevant characteristics of the Delfi-C3 spacecraft model

Parameter	Variable	Value		Remark
Length	l	326.5	mm	z-dimension SF
Width	w	100.0	mm	x-dimension SF
Depth	d	100.0	mm	y-dimension SF
Downlink antenna length	l_{DLA}	500.0	mm	
Uplink antenna length	l_{ULA}	180.0	mm	
Antenna width	w_A	6.0	mm	
Nominal solar panel angle	θ	35.0	°	w.r.t. underlying body panel
Nominal antenna angle	ϕ	40.0	°	w.r.t. xy-plane SF

In table O.1, several relevant characteristics of the Delfi-C3 spacecraft are given. With these quantities it is possible to write the antennae induced disturbance torque only as a function of c and α. After substitution of the values in table O.1 in the various torque equations and after performing the summation given in equation O.26, a plot of the torque as a function of c and α can be produced. This plot is given in figure O.5.

O.2.3 Disturbance torque about x-axis

As a next step, consider the disturbance torque about the x-axis of the satellite. In principle, the analysis of the disturbance torque follows exactly the same procedure as for the one of the torque about the y-axis. A situational sketch for determining the antennae induced disturbance torque about the x-axis is shown in figure O.6.

Investigating figure O.6, it is striking that the situation appears very similar to the one in figure O.1. Note however, that the velocity vector $\vec{V}$ refers to the velocity component in the lane of the drawing, i.e. in the yz-plane. Furthermore, the incidence angle γ denotes the angle between the normal vector of the connecting body panel, which is in this case the front panel, and the in-plane velocity vector.

Despite several minor differences between the disturbance torque analysis about the x-axis and the one about the y-axis, both analyses are very alike. Note however, that in case the torque about the x-axis is considered, the y-axis takes the place of the positive x-axis, and the x-axis takes the place of the negative y-axis. Therefore, the induced torque about the x-axis follows the same profile as shown in figure O.5 with an angular shift of 180°. The result is shown in figure O.7.

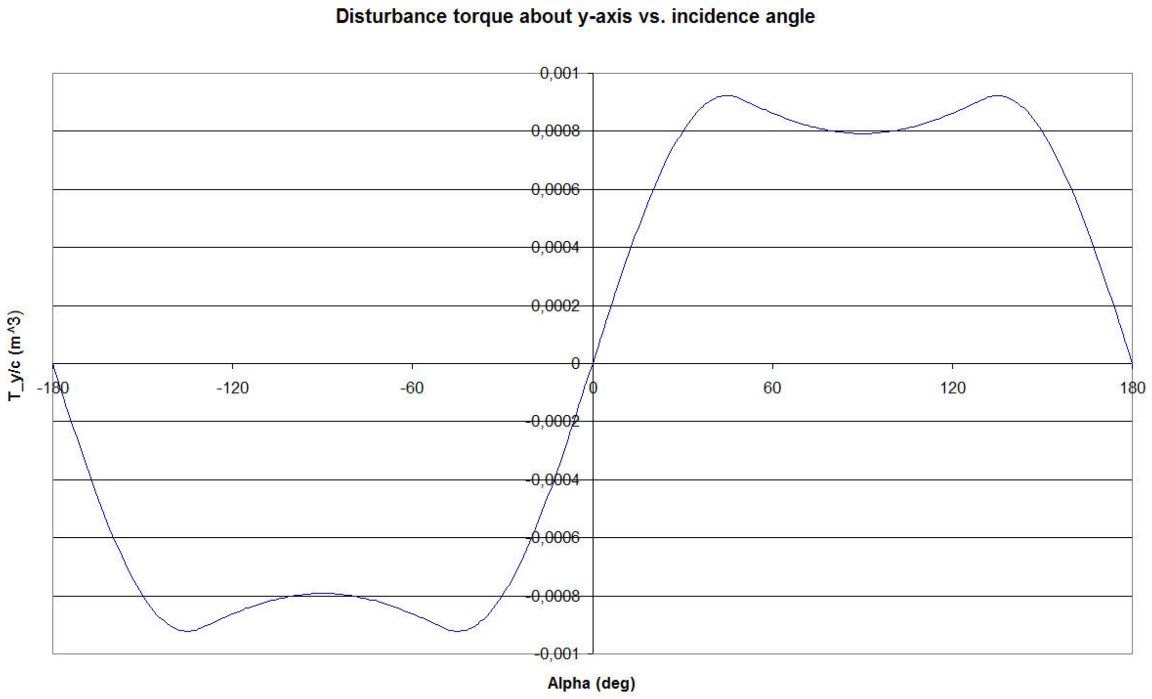

Figure O.5: Analysis of normalized disturbance torque about y-axis as a function of incidence angle

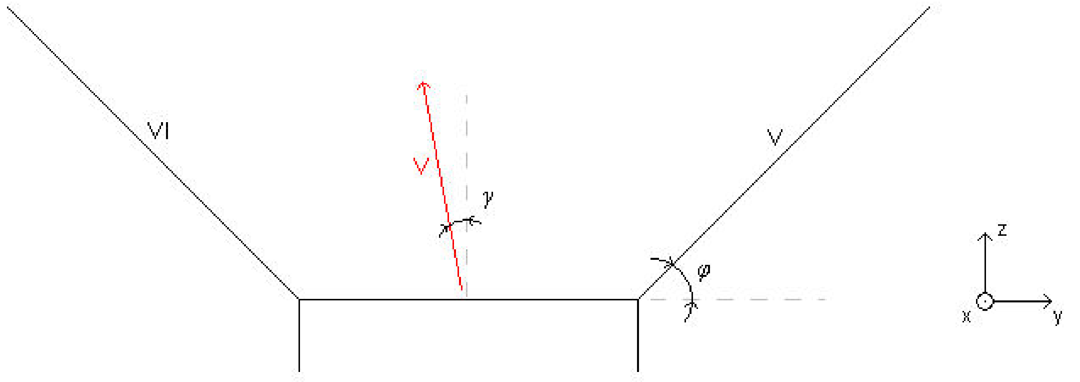

Figure O.6: Illustrational sketch for calculation of downlink antennae induced torques about x-axis

O.2.4 Disturbance torque about z-axis

Next, the disturbance torque about the z-axis will be determined. In figure O.8, the projection of the Delfi-C3 spacecraft onto the xy-plane is shown. All forces on the antennae in this plane, which can induce a torque about the z-axis are calculated at an earlier stage, so no additional forces need to be considered. It is assumed that the antennae are infinitesimally thin, so the antennae only produce a force parallel to their longitudinal direction. For example, antennae 3 and 4 in figure O.8 only generate a force in x-direction, while antennae 1 and 2 only produce a force in y-direction. In this configuration, the arm corresponding to every force parallel to the x-axis is the distance between an antenna with its longitudinal axis in x-direction and the center of mass. As the center of mass is positioned in the center of the square body panel, this distance is simply equal to:

$$s = \frac{d}{2} \tag{O.30}$$

In a similar way, the magnitude of an arm corresponding to a force parallel to the y-axis can be written as:

$$s = \frac{w}{2} \tag{O.31}$$

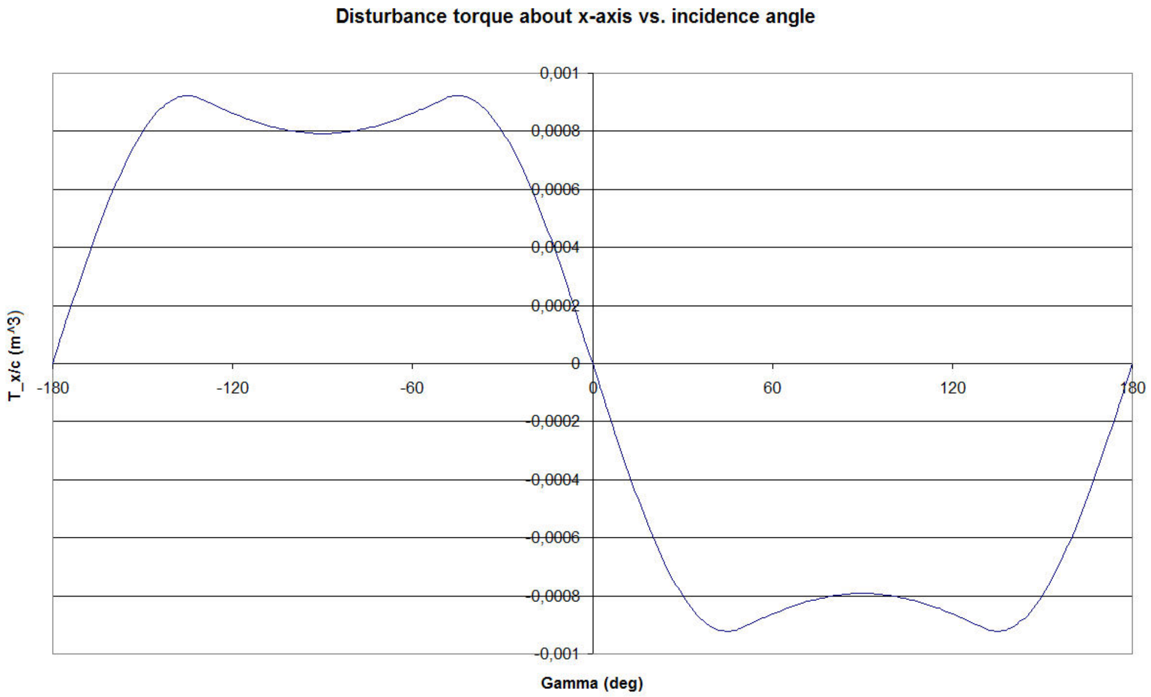

Figure O.7: Analysis of normalized disturbance torque about x-axis as a function of incidence angle

Noting that w is equal in magnitude to d, either one of the abovementioned equations can be omitted as equation O.30 is exactly equal to equation O.31.

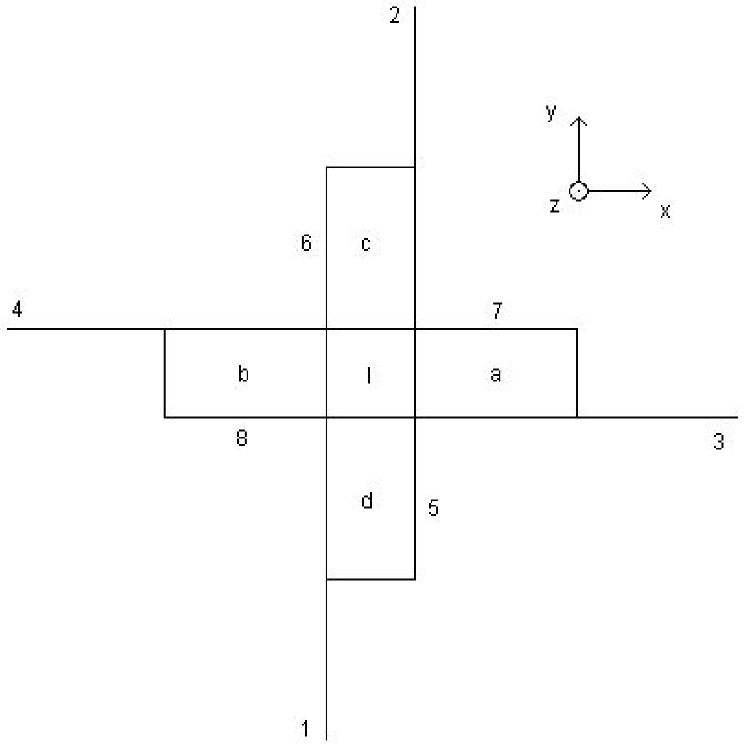

Figure O.8: Sketch of Delfi-C3 spacecraft model in xy-plane of satellite fixed reference frame

In figure O.9, a plot is shown of the induced torque by a single antenna. In fact, this function is only dependent on a single angle, either α or γ, dependent on the antennae under consideration. After all, the other angle of incidence does not influence the torque produced by the considered antenna, as it only influences a velocity component parallel to the antenna surface.

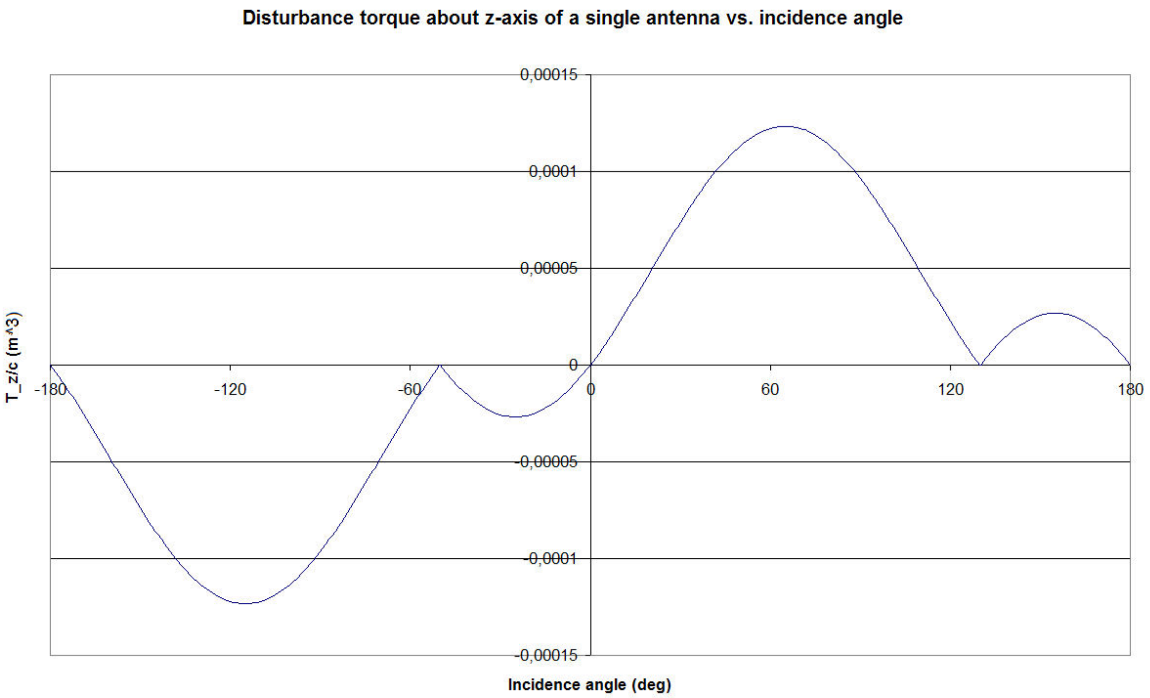

Figure O.9: Analysis of normalized disturbance torque due to a single antenna about z-axis as a function of incidence angle

Subsequently, the torque about the z-axis can be evaluated. This quantity is governed by the following expression:

$$T_z = \sum_{i=I}^{VIII} \Big(\big((T_i)_x \big)_z + \big((T_i)_y \big)_z \Big) = \frac{w}{2} \cdot \sum_{i=I}^{VIII} \left(\pm (F_i)_x \pm (F_i)_z \right) \tag{O.32}$$

After substituting the equations for the induced forces on the antennae, it is found that the resulting expression is a function of pressure c, angle α, and angle γ.
In figure 10, a plot is shown, which depicts the disturbance torque about the z-axis as a function of two incidence angles, α and γ. In this plot, α is set along the x-axis, while γ is set as a parameter. Consequently, multiple curves are shown, with every single curve corresponding to a particular value of γ. Note that switching α and γ will yield exactly the same plot.
Therefore, it is possible to determine, for which incidence angles the torque is at its extreme value. Torque maximums are created in case $\alpha = \pm 45\,°$, $\gamma = \pm 45\,°$ and minimums are produced in case $\alpha = \pm 135\,°$, $\gamma = \pm 135\,°$.

O.2.5 Torque magnitude estimation

To have an indication of the actual magnitude of the disturbance torques acting on the Delfi-C3 spacecraft, it is necessary to determine the pressure factor c. Two kinds of disturbance torques can be induced by the antennae: aerodynamic and solar radiation.
Firstly, the aerodynamic pressure is considered. This quantity can be written as:

$$c_{aero} = \frac{1}{2} \cdot C_D \cdot \rho \cdot V^2 \tag{O.33}$$

In a following discussion concerning aerodynamic torque calculation i.e. in appendix N, the value of every involved variable will be deduced with an explanation. In this discussion, the value of c_{aero} will be given:

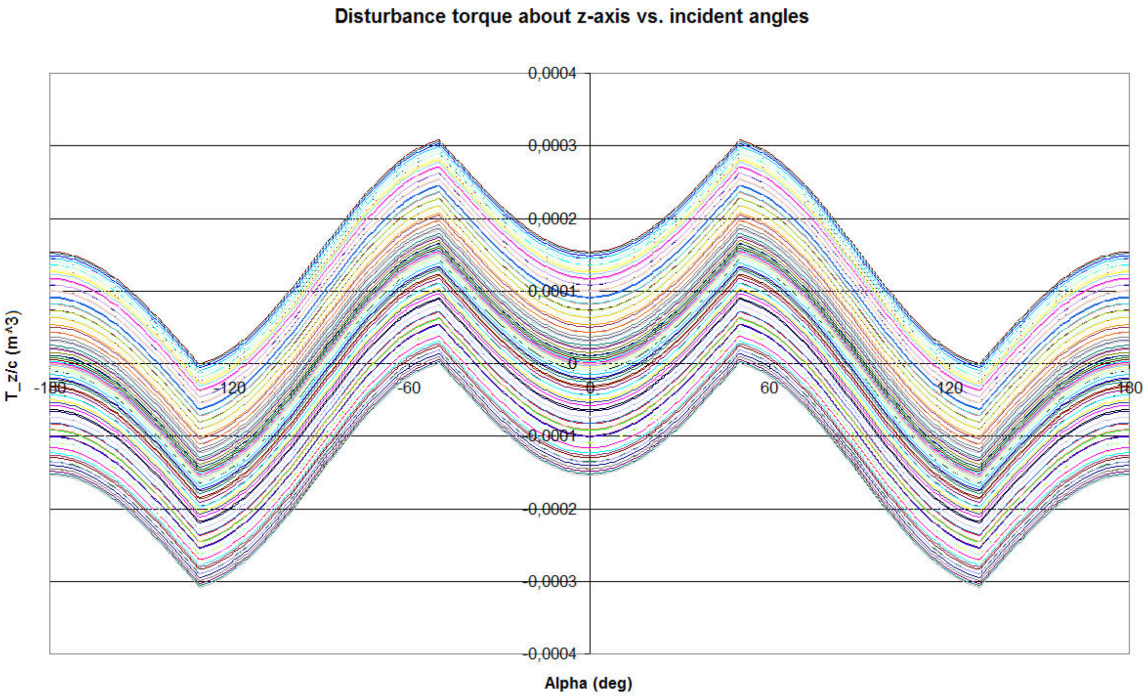

Figure O.10: Analysis of normalized disturbance torque about z-axis as a function of two incidence angles

$$c_{aero} = 2.7793 \cdot 10^{-5} \text{ N.m}^{-2} \tag{O.34}$$

Secondly, consider the solar radiation pressure, which can be expressed by:

$$c_{solar} = \frac{F}{c} \tag{O.35}$$

This expression will be further elaborated on in a following discussion concerning solar radiation torque calculation, i.e. in appendix Q. For now, the value is given to be:

$$c_{solar} = 4.5364 \cdot 10^{-6} \text{ N.m}^{-2} \tag{O.36}$$

In table O.2, a summary of the maximum magnitudes of both kinds of torques about the various axes of the Delfi-C3 spacecraft is given. Note that these values denote the magnitude of the torque prodcued by the sum of all uplink and downlink antennae.

Table O.2: Summary of maximum estimated induced antenna torques

	$\|\max T_x\|$ (N.m)	$\|\max T_y\|$ (N.m)	$\|\max T_z\|$ (N.m)
Aerodynamic torque	$2.56 \cdot 10^{-8}$	$2.56 \cdot 10^{-8}$	$8.55 \cdot 10^{-9}$
Solar radiation torque	$4.19 \cdot 10^{-9}$	$4.19 \cdot 10^{-9}$	$1.39 \cdot 10^{-9}$

O.2.6 Shortcomings

In the previous sections, the torques about the x-, y-, and z-axes were calculated. However, several issues are not addressed in this discussion, which will play a role on the induced torques in reality.

Firstly, it is possible for antennae to become shadowed by the body or solar panels. This means that in the homogeneous velocity vector field, a particular antenna will not be influenced by this velocity and will not generate any torque. However, this effect is difficult to model and it is assumed that it will not affect the calculation in a major way.

Secondly, the antennae are not infinitesimally small in reality, but will have a finite thickness. Therefore, additional forces will be created. However, these will be very small and therefore will not contribute to the calculation in a major sense.

Thirdly, torquing or bending of the antennae is possible to occur in reality. These phenomena will generate additional contributions to the torque calculation. Nevertheless, any bending or torquing of the antennae will remain very small, as the forces acting on these antennae are very small in magnitude.

O.3 Conclusions and recommendations

In the previous sections, the torques induced by the uplink and downlink antennae of the Delfi-C3 spacecraft were calculated. With the assumption that the antennae are two dimensional areas, a simple derivation can be made for the torque calculation.

Performing all involved calculations yields for the magnitudes of the antennae induced torques the values given in the following table:

	$\lvert\max T_x\rvert$ (N.m)	$\lvert\max T_y\rvert$ (N.m)	$\lvert\max T_z\rvert$ (N.m)
Aerodynamic torque	$2.56 \cdot 10^{-8}$	$2.56 \cdot 10^{-8}$	$8.55 \cdot 10^{-9}$
Solar radiation torque	$4.19 \cdot 10^{-10}$	$4.19 \cdot 10^{-10}$	$1.39 \cdot 10^{-10}$

Appendix P

DC3-TN-610-075 EuroSim - Area shadowing algorithm

P.1 Introduction

EuroSim is a simulation platform, in which the orbit of the Delfi-C3 spacecraft will be simulated. Interesting quantities, which can be determined from this simulation, are power generation and attitude reconstruction. For attitude reconstruction, it is important to determine the various disturbance torques acting on the spacecraft.
Both the aerodynamic and the solar radiation torques are treated as disturbance torques. Both types of torque are dependent on the amount of surface area of the satellite exposed to the vector quantity causing the disturbance. However, when evaluating these two types of torque, it is noticed that some parts of the spacecraft are not exposed to the vector quantity due to shadowing of spacecraft appendages. Accurate determination of the magnitude of this shadowed area is of utmost importance in order to calculate the various disturbance torques.
In this report, an algorithm for determining the magnitude of shadowed surface area on the spacecraft will be developed. In subsection P.2.1, several general remarks with respect to surface area shadowing will be given. Longitudinal shadowing will be treated in subsection P.2.2, while a treatise of lateral exposure will be given in subsection P.2.3. In subsection P.2.4, the centers of pressure corresponding with the remaining exposed surface area will be calculated. Finally, several shortcomings of the derived algorithm will be given in subsection P.2.5.

P.2 Determination of area shadowing algorithm

P.2.1 General remarks

In nominal conditions, the Delfi-C3 spacecraft makes use of deployable solar panels. These panels are at a distinct angle with the underlying body panel. Due to the fact that this angle is not equal to $90\,^{\circ}$, the solar panels will shadow parts of the underlying body panel. This phenomenon is mainly relevant for determining aerodynamic torque and solar radiation torque, as these two types of torque are dependent on the exposed surface area of the spacecraft. A small two-dimensional situation sketch of the shadowing principle is given in figure P.1.
Investigating figure P.1, it is seen that the shadowing of the body due to a single solar panel under influence of a vector $\vec{V}$ is shown. It is assumed that $\vec{V}$ is in the plane of the sketch and has the same magnitude and direction in the complete sketch, which means it is a homogeneous vector field. Then it is noticed that $\vec{V}$ is unable to reach part of the body, because $\vec{V}$ is blocked by the solar panel before it is able to arrive at this respective part. Such a situation is indicated in the sketch by drawing a shadow part, which refers to the part not reached by $\vec{V}$, and a light part, which is fully exposed to $\vec{V}$.
In the following sections, an algorithm will be derived, which calculates the surface area of the body, which is shadowed by the solar panels under influence of a randomly chosen vector V.

P.2.2 Longitudinal shadowing

The first step in generating an effective shadowing algorithm is deriving the shadowed area in longitudinal direction. For this reason, a situational sketch is used, which is shown in figure P.2.

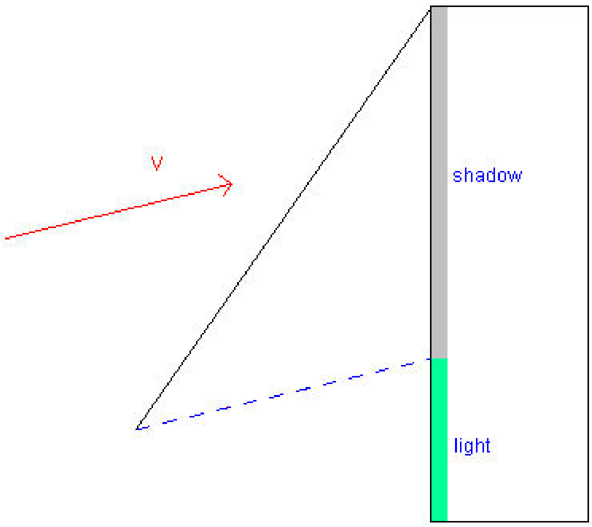

Figure P.1: Sketch of shadowing principle

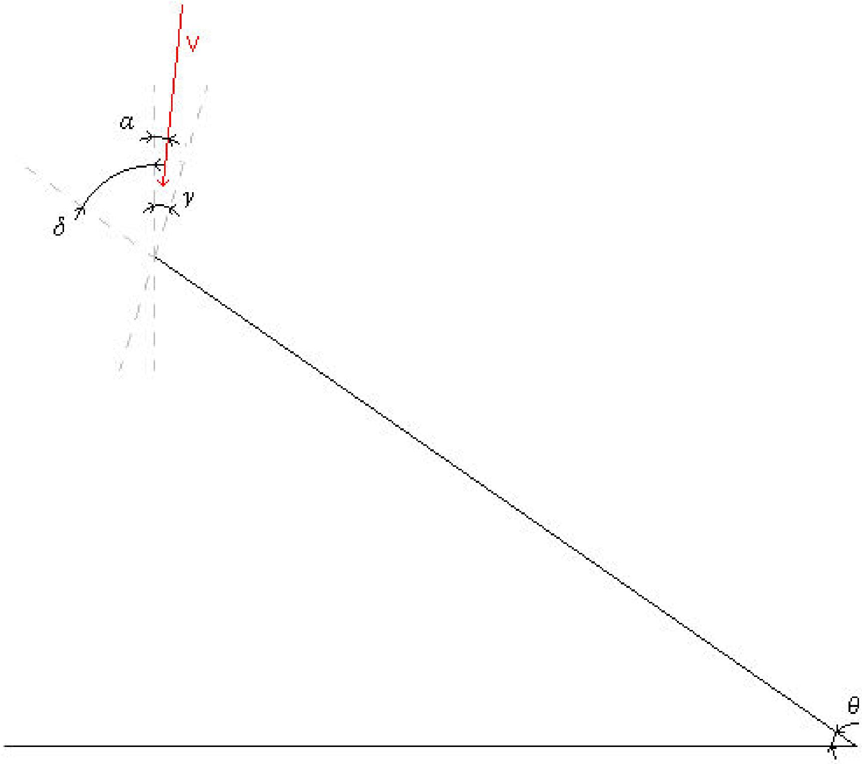

Figure P.2: Sketch of shadowing principle

Investigating figure P.2, it has to be mentioned that the drawn $\vec{V}$ vector is not equal to the complete three-dimensional $\vec{V}$ vector in the situation, but is only equal to the contribution of $\vec{V}$ in the plane of the drawing, which is the xz-plane or yz-plane. Therefore, only two of the three elements in the complete $\vec{V}$ vector are taken into account when determining shadowing in a longitudinal direction.

Furthermore, several relevant angles are shown in the sketch. Angle α is the angle between the 2 dimensional $\vec{V}$ vector and the normal vector of the underlying body panel. In the present situation, i.e. the panel hinge is located at the right-hand side of the sketch, and starting out from the body panel normal vector, α is positive in a clockwise sense. The angle between the solar panel and the underlying body panel in the actual situation is known as θ. Both angles γ and δ denote boundary conditions and are measured with respect to the normal vector of the corresponding body panel. In case α is exceeding either angle, the exposed area is equal in value to the exposed area in case α equals the exceeded angle. Angle γ is expressed as:

$$\gamma = \arctan\left(\frac{1-\cos\theta}{\sin\theta}\right) \tag{P.1}$$

Boundary angle δ can be written as:

$$\delta = \theta - \frac{\pi}{2} \tag{P.2}$$

For determining the exposed surface area, three cases can be distinguished. The choice of case is dependent on the value of angle α. In the following, the three cases are given together with their corresponding exposed areas.

- Case #1: $\alpha < \delta$

  $$A_{long} = l \cdot w \tag{P.3}$$

- Case #2: $\alpha > \delta$

  $$A_{long} = 0 \tag{P.4}$$

- Case #3: $\delta < \alpha < \gamma$

  $$A_{long} = l \cdot (1-\cos\theta) \cdot w + l \cdot \sin\theta \cdot \tan\alpha \cdot w \tag{P.5}$$

In these equations, l is the dimension of the satellite in longitudinal direction (z-direction), i.e. the length of the spacecraft, and w is the dimension in lateral direction (y-dimension), i.e. the width (or depth) of the spacecraft.

P.2.3 Lateral exposure

In addition to the longitudinal shadowing, it is possible that lateral exposure is taking place, which refers to the situation, in which surface area is "deshadowed" due to a lateral component of the velocity vector $\vec{V}$. A situational sketch showing the principle of lateral shadowing is given in figure P.3.
Looking at figure P.3, it firstly has to be mentioned that the shown situation is perpendicular to the z-axis of the spacecraft. Furthermore, vector $\vec{V}$ in the sketch is not equal to the total velocity vector, but is referring to the contribution of $\vec{V}$ in the plane of the drawing. Angle β is the angle between the vector V and the normal vector of the corresponding body panel. Angle ϵ describes a boundary condition, denoting the exact angle at which in case of complete longitudinal shadowing of the body panel, half of the panel will still subject to lateral exposure. This means that the exposed area is a perfect triangle, with every corner of the exposed triangle at a corner of the body panel. Angle ϵ can be expressed by:

$$\epsilon = \arctan\left(\frac{w \cdot \cos\theta}{l \cdot \sin\theta}\right) = \arctan\left(\frac{w}{l \cdot \tan\theta}\right) \tag{P.6}$$

Now, the exposed area of the underlying body panel can be calculated. Note that this area is depicted as a triangle, as the hypotenuse is a projection of the straight side of the solar panel onto the underlying body panel. In general, the value of the exposed area is dependent on both the value of α and β. Therefore, it is necessary to distinguish several cases.

- $\underline{\beta < \epsilon}$

  If β is smaller than ϵ, this means that in case of lateral exposure, the shadow does not extend beyond the sides of the body panel. The resulting situation is shown in figure P.4.

  For determining the area, which is laterally exposed to the $\vec{V}$ vector, use is made of a scale-down method from the exposed area in case of lateral coverage of the panel from front to end. In this latter case, the sides of the triangle can be written as:

  $$x' = l \tag{P.7}$$

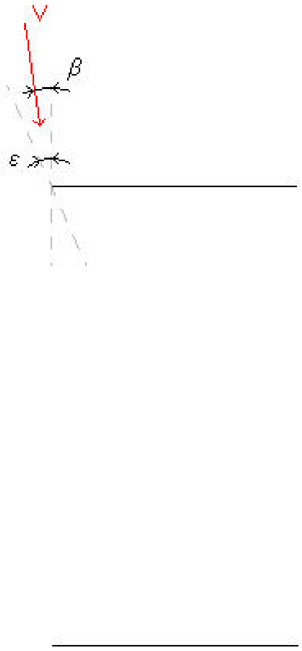

Figure P.3: Situational sketch of exposure principle in lateral direction

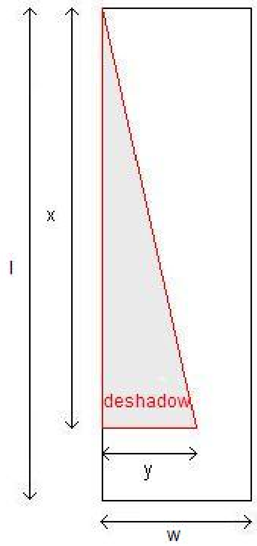

Figure P.4: Illustration of lateral exposure in case $\beta < \epsilon$

$$y' = l \cdot \tan\theta \cdot \tan\beta \tag{P.8}$$

The scaling factor can be written as:

$$k = \cos\theta + \sin\theta \cdot \tan\alpha \tag{P.9}$$

Then, the sides of the triangle are equal to:

$$x = k \cdot x' \tag{P.10}$$

$$y = k \cdot y' \tag{P.11}$$

And the general expression for the exposed area becomes:

$$A_{lat} = \frac{1}{2} \cdot x \cdot y = \frac{1}{2} \cdot l^2 \cdot \tan\theta \cdot \tan\beta \cdot (\cos\theta + \sin\theta \cdot \tan\alpha)^2 \tag{P.12}$$

- $\underline{\beta > \epsilon}$

  In case β is larger than ϵ, two different cases can be distinguished. The difference between these two cases can be made in the value of the lower side of the triangle. After all, if the lower side is larger than the width of the panel, the exposed area will not equal the triangular area, but will be limited by the area of the panel. The course of action taken to determine the exposed area is equal to the case, in which $\beta < \epsilon$. Therefore, a scale-down method with respect to the case, in which the total panel experiences lateral exposure, is applied. Hence:

$$x' = l \tag{P.13}$$

$$y' = l \cdot \tan\theta \cdot \tan\beta \tag{P.14}$$

$$k = \cos\theta + \sin\theta \cdot \tan\alpha \tag{P.15}$$

$$x = k \cdot x' \tag{P.16}$$

$$y = k \cdot y' \tag{P.17}$$

A distinction can be made between the following cases:

  - $\underline{y < w}$

    In case the complete triangle is within the boundaries of the body panel, the situation is equal to the sketch shown in figure P.5.

    In this case, there is no exposed area outside the body panel, so the total lateral exposed area equals the triangle area:

$$A_{lat} = \frac{1}{2} \cdot x \cdot y = \frac{1}{2} \cdot l^2 \cdot \tan\theta \cdot \tan\beta \cdot (\cos\theta + \sin\theta \cdot \tan\alpha)^2 \tag{P.18}$$

  - $\underline{y > w}$

    In case the shadow exceeds the boundaries of the body panel, the triangular area has to be decreased in order to arrive at the exposed area. As the sides of the triangle x and y are not representative to the exposed area, a simple multiplication with a scaling factor will not suffice to yield the correct value. Therefore, an additional scaling factor will be introduced, which will denote the scaling value of the superfluous triangle with respect to the complete triangle. The situation, in which the triangle is exceeding the boundaries of the body panel is shown in figure P.6.

    The newly introduced scaling factor, which is labeled m, is written as:

$$m = \frac{y - w}{y} \tag{P.19}$$

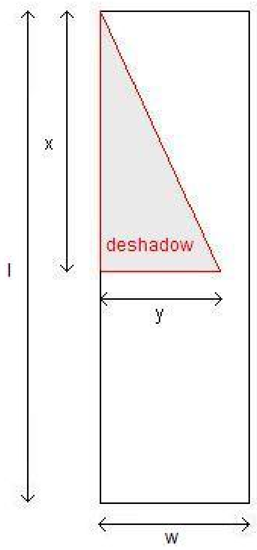

Figure P.5: Illustration of lateral exposure in case $\beta > \epsilon$, $y < w$

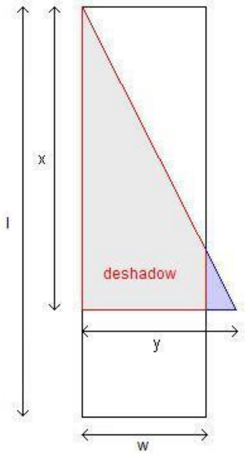

Figure P.6: Illustration of lateral exposure in case $\beta > \epsilon$, $y > w$

which will lead to the following expressions for the sides of the superfluous triangle:

$$y'' = m \cdot y \tag{P.20}$$

$$x'' = m \cdot x \tag{P.21}$$

As the exposed area equals the area of the superfluous triangle subtracted from the area of the complete triangle, this value can be expressed as:

$$A_{lat} = \frac{1}{2} \cdot x \cdot y - \frac{1}{2} \cdot x'' \cdot y'' = \frac{1}{2} \cdot \left(1 - \left(\frac{y - w}{y}\right)^2\right) \cdot x \cdot y \tag{P.22}$$

where x and y are given by equations P.16 and P.17.

Note that the exposed area can be divided into a triangular part with sides w and $(1 - m)\,x$ and a rectangular part with sides w and mx.

P.2.4 Centers of pressure

As the value of the exposed surface area is dependent on the values of α and β, also the corresponding centers of pressure are dependent on α and β. In general, the coordinates of the center of pressure can be written as:

$$q_{CoP} = \frac{\sum_{i=1}^{n}\left(\left(q_{CoP}\right)_i \cdot A_i\right)}{\sum_{i=1}^{n} A_i} \tag{P.23}$$

where $\left(q_{CoP}\right)_i$ is the q-coordinate of the center of pressure of the i-th area component, with $q \in x, y, z$, and A_i is the exposed surface area of the i-th area component.
In case of a purely triangular exposed surface area, n is equal to 1, and the center of pressure of the exposed area is found to equal the center of pressure of the triangle. Expressing the coordinates of the center of pressure relative to the geometrical center of the panel yields:

$$x_{CoP} = \frac{2}{3} \cdot x - \frac{1}{2} \cdot l \tag{P.24}$$

$$y_{CoP} = \pm\left(\frac{1}{2} \cdot w - \frac{1}{3} \cdot y\right) \tag{P.25}$$

where x-coordinate denotes the coordinate in the direction of the panel hinge, i.e. parallel to the longer side of the panel, and the y-coordinate is parallel to the shorter side of the panel.
When the triangle exceeds the boundaries of the body panel, n is equal to 2 as the exposed area is made up out of a triangular area and a rectangular area. Therefore, after evaluation of the expression governing the center of pressure, the coordinates of the center of pressure relative to the geometrical center of the panel can be written as:

$$x_{CoP} = \frac{\frac{1}{3}\left(1-m\right)^2 \cdot x^2 \cdot w + w \cdot x^2 \cdot m \cdot \left(1 - \frac{1}{2}m\right)}{\frac{1}{2}\left(1+m\right)^2 \cdot x \cdot w} - \frac{1}{2} \cdot l \tag{P.26}$$

$$y_{CoP} = \pm\frac{\frac{1}{2}w - \frac{1}{3}y}{\frac{1}{2}\left(1+m\right)^2 \cdot x \cdot w} \tag{P.27}$$

Note that these equations also hold for a purely triangular area with m equal to zero.
In a satellite fixed reference frame, the coordinates of the center of pressure can be found by vectorially adding the coordinates of center of pressure with respect to the geometrical center (or center of area) of the panel, and the coordinates of center of area of the panel with respect to the origin of the reference system.

$$\left(\vec{x}_{CoP/CoM}\right)_i = \left(\vec{x}_{CoA/CoM}\right)_i \pm \left(\vec{x}_{CoP/CoA}\right)_i \tag{P.28}$$

where $\left(\vec{x}_{CoP/CoM}\right)_i$ is the coordinate vector of the center of pressure on panel i in satellite fixed reference frame with respect to the center of mass of the spacecraft, $\left(\vec{x}_{Coa/CoM}\right)_i$ is the coordinate vector of the geometrical center of panel i with respect to the center of mass of the satellite, and $\left(\vec{x}_{CoP/CoA}\right)_i$ is the coordinate vector of the center of pressure of panel i with respect to the geometrical center of panel i. When evaluating this last expression, care has to be taken of the signs.

P.2.5 Shortcomings

Unfortunately, the previously described shadowing algorithm does not embrace all physically possible shadowing phenomena. Two situations, which are covered by the developed algorithm, are the shadowing of a body panel by its corresponding solar panel and the shadowing of the back side of a solar panel by the main body, or more accurately, the underlying body panel.
However, the shadowing of a back side of a solar panel by another solar panel is physically possible to occur, but cannot be described by the current algorithm. Furthermore, the shadowing of the main body and solar panels by the uplink and downlink antennae, and vice versa, will also play a role. These situations were deemed not worthwhile to model, because these algorithms are very complex to develop, while the accuracy of the model experiences only a minor diminishment.

P.3 Conclusions and recommendations

In the previous sections, an algorithm has been derived for the calculation of the surface area, which is shadowed under influence of a random vector $\vec{V}$. Shadowing in longitudinal direction and additional exposure due to a lateral velocity component have been determined. This has been done by introducing two incidence angles with which the exposed surface area can be calculated.
Furthermore, a calculation procedure of the center of pressure corresponding to the exposed surface area has been developed.

Appendix Q

DC3-TN-610-077 EuroSim - Determination of solar radiation torque

Q.1 Introduction

EuroSim is a simulation platform, in which the orbit of the Delfi-C3 spacecraft will be simulated. Interesting quantities, which can be determined from this simulation, are power generation and attitude reconstruction. For accurate attitude reconstruction, it is important to determine the solar radiation torque acting on the Delfi-C3 spacecraft.

Solar radiation torques are disturbance torques acting on the Delfi-C3 spacecraft generated due to the pressure of solar radiation. This pressure exerts on the exposed surface area of the spacecraft and will therefore generate a force and a accompanying torque. For an accurate analysis of the attitude behaviour of Delfi-C3 in the EuroSim orbit simulator, it is necessary to perform an evaluation of the solar radiation torque.

In this document, the principle of solar radiation torque generation will be investigated. In subsection Q.2.1, a derivation of the force generated by solar radiation is given. An explanation of the creation of a torque due to solar radiation is shown in Q.2.2. In subsection Q.2.3, a calculation of the solar radiation torque acting on a single deployed solar panel is given.

Q.2 Determination of solar radiation torques

Q.2.1 Derivation of solar radiation force

As a result of solar radiation pressure, solar radiation torques will be generated on the Delfi-C3 spacecraft. Solar radiation pressure is generated due to collisions of photons in the solar radiation with the surface area of the spacecraft. Although photons do not possess any mass, they possess momentum. Therefore, a momentum exchange will take place during the collisions, which leads to a production of a force [7].

A physical representation of this phenomenon is given in the following paragraphs. Firstly, the general expression of kinetic energy of a particular system is given by:

$$E = \int V \cdot \mathrm{d}p \tag{Q.1}$$

where V is the magnitude of the velocity of the system, and $\mathrm{d}p$ is a differential amount of momentum contained by the system.

Applying this expression to a stream of photons, it is found that a photon always travels with the speed of light. Therefore, in case the medium, through which the photons travel, is vacuum, this relation is rewritten to:

$$E = \int c \cdot \mathrm{d}p \tag{Q.2}$$

where c is the speed of light in vacuum, which is a constant parameter. After integration of the right-hand side of the equal sign, this becomes:

$$E = c \cdot p \tag{Q.3}$$

Furthermore, the amount of energy of a photon is expressed by Planck's law, which is written as:

$$E = h \cdot \nu \tag{Q.4}$$

where h is Planck's constant, and ν is the frequency of the photon in the electromagnetic spectrum. Equating the previous relations and solving for the momentum p yields:

$$p = \frac{h \cdot \nu}{c} \tag{Q.5}$$

Investigating equation Q.5, it is noticed that the numerator of the right-hand side term equals the amount of energy contained in a single photon. However, for a stream of photons at various frequencies, this equation has to be rewritten as:

$$P = \sum_{i=1}^{\infty} \frac{h \cdot \nu_i}{c} \tag{Q.6}$$

where ν_i denotes the frequency of individual photon i.
Next, the spectral density Φ is introduced, which is defined as the number of photons in a particular stream, which are at a defined frequency ν, or:

$$\Phi\left(\nu\right) = \sum n\Big|_{\nu} \tag{Q.7}$$

After substitution of this spectral density, equation Q.6 becomes:

$$P = \int \frac{h \cdot \Phi\left(\nu\right)}{c} \cdot \mathrm{d}\nu \tag{Q.8}$$

Recall that integration of the numerator of the quotient in the right-hand side of the equation multiplied with the differential operator on yields the total amount of energy contained by the stream of photons. In general, a change in momentum is equal to the product of a generated force and the time, during which this force acts. This is written as:

$$\Delta P = \int F \cdot \mathrm{d}t \tag{Q.9}$$

As the force is acting on a surface, it is possible to write the force as a product of pressure and exposed area. Hence, the following expression can be formulated:

$$\Delta P = \int p_s \cdot A \cdot \mathrm{d}t \tag{Q.10}$$

In an instantaneous timeframe, this equation can be rewritten to:

$$\mathrm{d}P = p_s \cdot A \cdot \mathrm{d}t \tag{Q.11}$$

Rewriting this equation yields the observation that the pressure exerted coincides with the momentum exchange per unit area and unit time. Returning to equation Q.8, it is noticed that the magnitude of momentum is equal to total amount of kinetic energy of the photons divided by the speed of light. Subsequently, it is identified that the total amount of energy of the photons in the system per unit time and per unit area is equal to the solar flux. Incorporating this observation finally yields:

$$p_s = \frac{S}{c} \tag{Q.12}$$

where S is the solar flux at the position of the spacecraft, and c is the speed of light in vacuum.
The magnitude of the force generated by the solar radiation pressure ps is dependent on the characteristics of the material, out of which the spacecraft body panel is composed. After all, these characteristics

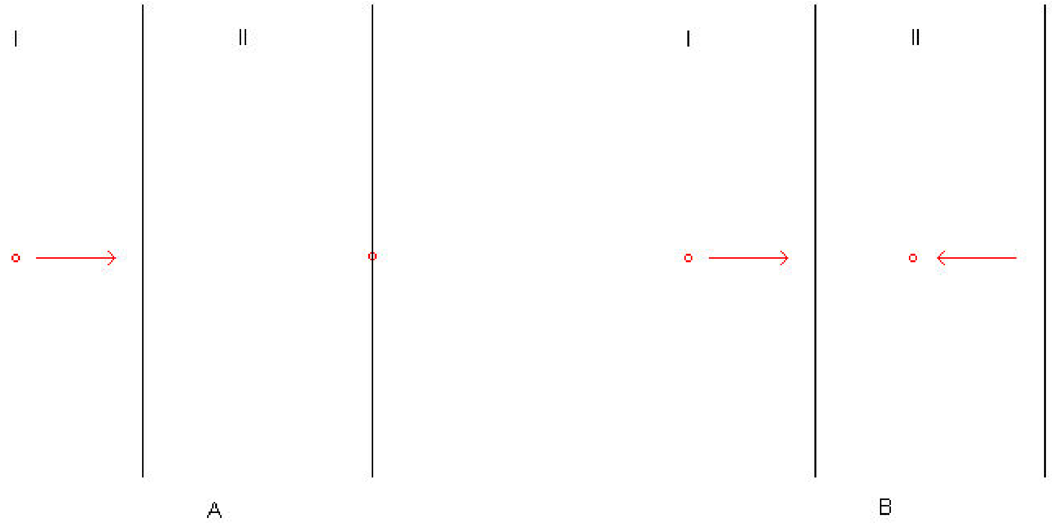

Figure Q.1: Illustration of exchange of momentum between incident photon and spacecraft; A. Complete absorption; B. Complete reflection

determine whether incident photons are absorbed by the body panel or reflected from the body panel. A difference exists between these two situations, as the law of conservation of momentum has to hold. An illustration of this phenomenon is shown in figure Q.1.

In figure Q.1, two distinct situations are depicted. In situation A, an arriving incident photon is absorbed by the subject body panel. However, in situation B, an arriving incident photon is reflected. In both situations, the law of conservation of momentum has to hold, which can be written as:

$$P_I = (P_{ph})_I + (P_S)_I = (P_{ph})_{II} + (P_S)_{II} = P_{II} \tag{Q.13}$$

where $(P_{ph})_I$ is the momentum of the photon in situation I, $(P_{ph})_{II}$ is the momentum of the photon in situation II, $(P_S)_I$ is the momentum of the spacecraft in situation I, and $(P_S)_{II}$ denotes the momentum of the spacecraft in situation II.

Evaluating this expression for situation A making use of equation Q.5 yields:

$$\frac{h \cdot \nu}{c} + P_S = 0 + P_S + \Delta P_S \tag{Q.14}$$

This expression denotes that the complete momentum of the photon is absorbed by the spacecraft, and is used to raise the value of the momentum of the spacecraft. However, in situation B the law of conservation of momentum becomes:

$$\frac{h \cdot \nu}{c} + P_S = -\frac{h \cdot \nu}{c} + P_S + \Delta P_S \tag{Q.15}$$

Investigating this expression reveals that in case of reflection of a photon, the momentum of the spacecraft is raised by a double amount than in case the photon is absorbed.

In general, an expression can be written, which relates the various optical parameters of any material:

$$\alpha + \rho + \tau = 1 \tag{Q.16}$$

where α is the absorptivity of the material, ρ is the reflectivity of the material, and τ is the transmissivity of the material. These characteristics are interpreted as the absorptivity being the ratio of the absorbed incident radiation to the total amount of incident radiation, the reflectivity being the ratio of the reflected incident radiation to the total amount of incident radiation, and the transmittivity being the ratio of the transmitted incident radiation to the total amount of incident radiation.

In figure Q.2, the optical properties of an illuminated body panel are illustrated.

In principle, the effects of these optical parameters can be interpreted as follows. For the absorbed incident radiation, the radiation pressure is equal to nominal pressure. However, the reflected incident

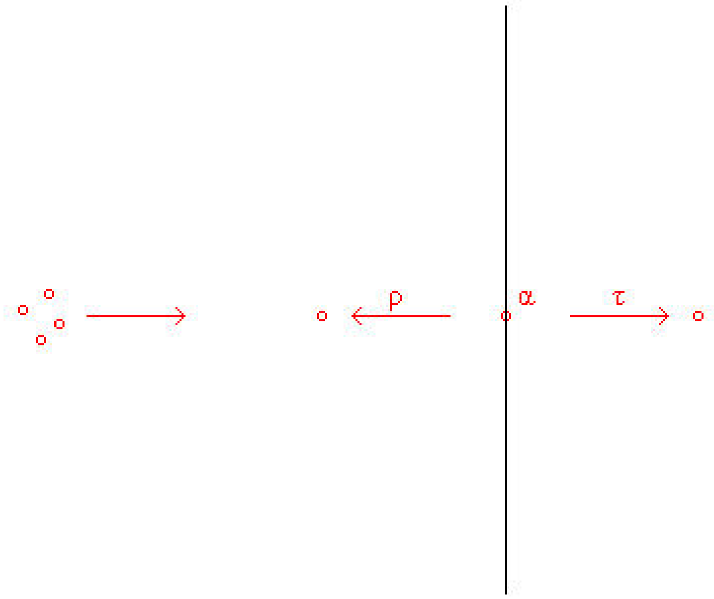

Figure Q.2: Illustration of optical properties of an illuminated body panel

radiation exerts effectively double pressure, while the transmitted part exerts none at all. With these observations, a force due to solar radiation can be written as:

$$F_s = (\alpha + 2 \cdot \rho) \cdot p_s \cdot A \tag{Q.17}$$

where A is the exposed surface area, on which the pressure is acting.
As all panels on the Delfi-C3 spacecraft are completely non-transparent, the transmittivity will always be equal to zero. After substituting and rewriting equation Q.16, this expression becomes:

$$F_s = (1 + \rho) \cdot p_s \cdot A \tag{Q.18}$$

Q.2.2 Generation of solar radiation torque

As the solar pressure force on a particular panel is now completely defined, the torque resulting from this force can be calculated. For this calculation, it is necessary to know the position of the center of pressure on this panel. As this position is directly dependent on the shape and size of the exposed area, a rather complex calculation has to be performed in case of a shadowed panel. The determination of the position of the center of pressure in case of a shadowed panel is also treated in appendix P. As in general, a torque can be calculated by taking the vector product of a force times the distance from center of pressure to center of mass, the following vector expression can be written:

$$\left(\vec{T}_s\right)_i = \begin{pmatrix} (T_s)_x \\ (T_s)_y \\ (T_s)_z \end{pmatrix}_i = (F_s)_i \cdot \frac{\vec{S}_i}{\left|\vec{S}_i\right|} \times \left(\vec{x}_{CoP/CoM}\right)_i \tag{Q.19}$$

where $(F_s)_i$ is the scalar value of the solar radiation force acting on panel i, $\vec{S}_i$ is the vector representation of the perpendicular solar flux component on panel i in a satellite fixed reference frame, and $\left(\vec{x}_{CoP/CoM}\right)_i$ is the distance vector between the center of pressure of panel i and the center of mass of the spacecraft.
In addition to the torques generated on the surface panels, also the induced torques on the antennae have to be taken into account. In appendix O, an explanation of the algorithm for determining the torques on the antennae is given.
The total solar radiation torque acting on the spacecraft is then simply calculated by vectorially adding all individual contributions. This leads to:

$$\vec{T}_s = \sum_{i=0}^{13} \left(\vec{T}_s\right)_i + \sum_{j=0}^{7} \left(\vec{T}_s\right)_j \tag{Q.20}$$

where $\left(\vec{T}_s\right)_i$ is the solar radiation torque produced by panel i, and $\left(\vec{T}_s\right)_j$ is the solar radiation torque produced by antenna j.

Q.2.3 Calculation of solar radiation torque due to a single deployed solar panel

In order to determine the order of magnitude of the solar radiation torque acting on the Delfi-C3 spacecraft, a calculation of the solar radiation torque acting on a single deployed solar panel is performed. This evaluation is done assuming a worst-case scenario. This situation is attained in case the solar flux vector is perpendicular to the solar panel. A situational sketch is shown in figure Q.3.

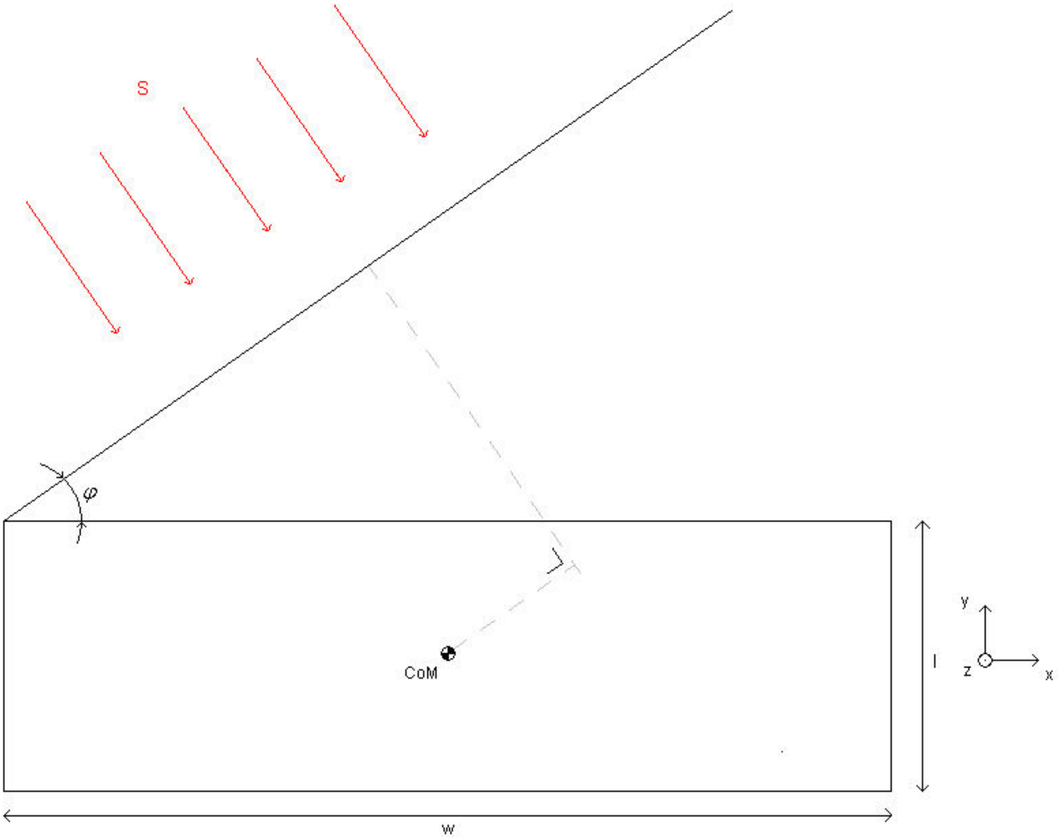

Figure Q.3: Situational sketch for determining solar radiation torque on a deployed solar panel

As a first indication of the solar radiation torque, it is assumed that the complete surface area is covered by the TEC cells used for main power generation. Investigating the characteristics of the TEC cells, it is found that the absorptivity of these cells is equal to 0.89. As the transmissivity of the cells is equal to zero, the reflectivity has to be equal to:

$$\rho = 1 - \alpha = 1 - 0.89 = 0.11 \tag{Q.21}$$

For determining the surface area of a single solar panel, it is assumed that a solar panel has the same dimensions as the underlying body panel. Hence:

$$A = l \cdot w = 0.3265 \cdot 0.1 = 3.265 \cdot 10^{-2}\ \text{m}^2 \tag{Q.22}$$

Furthermore, the solar flux is taken to be at its highest value, which is in case of winter solstice. After all, at this time the Earth is at perihelion, i.e. the position in the Earth's orbit closest to the Sun. Assuming that the Sun is a perfect spherical radiator, the solar flux at winter solstice can then be calculated with:

$$S = \frac{P_{Sun}}{4 \cdot \pi \cdot r^2} = \frac{P_{Sun}}{4 \cdot \pi \cdot (a \cdot (1-e))^2} \tag{Q.23}$$

where P_{Sun} is the total amount of power radiated by the Sun, a is the semi-major axis of the orbit of the Earth, and e is the eccentricity of the orbit of the Earth. Values for these parameters are given in table Q.1.

Table Q.1: Relevant parameters for solar flux calculation

Parameter	Variable	Value	
Total solar radiated power	P_{Sun}	$3.83 \cdot 10^{26}$	W.m^{-2}
Semi-major axis of orbit of the Earth	a	$1.49597870 \cdot 10^{11}$	m
Eccentricity of orbit of the Earth	e	0.016726	

Substituting these parameters yields the following result:

$$S = \frac{3.83 \cdot 10^{26}}{4 \cdot \pi \cdot (1.49597870 \cdot 10^{11} \cdot (1 - 0.016726))^2} \approx 1408.6 \text{ W.m}^{-2} \tag{Q.24}$$

The force due to solar radiation on the solar panel is then equal to:

$$F_s = (1+\rho) \cdot \frac{S}{c} \cdot A = (1 + 0.11) \cdot \frac{1408.6}{299792458} \cdot 3.265 \cdot 10^{-2} \approx 1.7028 \cdot 10^{-7} \text{ N} \tag{Q.25}$$

In order to determine the perpendicular distance between the working line of the drag force and the center of mass of the spacecraft, it is noticed that the center of pressure of the solar panel coincides with its geometrical center. Moreover, it is assumed that the center of mass of the spacecraft coincides with the geometrical center of the main body. Then the perpendicular distance is calculated to be:

$$d_{\perp} = \left(\frac{l}{2} \cdot \sin 35^\circ + \frac{w}{2}\right) \cdot \sin 35^\circ \approx 8.24 \cdot 10^{-2} \text{ m}^2 \tag{Q.26}$$

Multiplying the perpendicular distance with the magnitude of the drag force yields the produced aerodynamic torque, which equals:

$$T_s = F_s \cdot d_{\perp} = 1.403 \cdot 10^{-8} \text{ N.m} \tag{Q.27}$$

Note that the calculated value only denotes the solar radiation torque produced by a single deployed solar panel. Additional contributions are found by the other solar panels, the antennae, and various body panels. Note however, that the front and back body panel, i.e. the square panels to which the antennae are attached, do not yield a solar radiation torque in any situation.

Q.3 Conclusions and recommendations

In the previous sections, a derivation for the solar radiation torque acting on the Delfi-C3 spacecraft is given. Furthermore, an example calculation for a single deployed solar array is shown. The magnitude of this torque is in the order of 10^{-8} N.m. This magnitude is non-negligible, and has therefore consequences for the attitude behaviour of the Delfi-C3 spacecraft

Appendix R

DC3-TN-612-083 EuroSim - Assessment of magnetic disturbance torques

R.1 Introduction

EuroSim is a simulation platform, in which the orbit of the Delfi-C3 spacecraft will be simulated. Interesting quantities, which can be determined from this simulation, are power generation and attitude reconstruction. For accurate attitude reconstruction, it is important to determine the magnetic disturbance torques acting on the spacecraft.
Two sources of magnetic disturbance torques have been identified for the Delfi-C3 spacecraft. Lorentz torques are caused by Lorentz forces acting on current carrying wires. These forces are produced due to an interaction of the magnetic field with the flowing current. Induction torques are caused by a periodically changing magnetic field, which is a result of the rotation of the spacecraft. As a consequence of this rotation, a voltage will be induced leading to the flow of current. As these torques will yield effects on the rotational rate of the spacecraft, and therefore also on its attitude behaviour, an evaluation of these torques is necessary.
In this report, expressions for both induction torques and Lorentz torques will be derived, and the magnitude of these torques will be evaluated. In subsection R.2.1, the expression for the Lorentz torque will be derived. An evaluation of the produced Lorentz torques in a representative situation is given in subsection R.2.2. A derivation for the induction torque is shown in subsection R.2.3, while in subsection R.2.4 the magnitude of this induction torque will be evaluated and assessed.

R.2 Assessment of magnetic disturbance torques

R.2.1 Derivation of Lorentz torque

Lorentz torques are generated due to Lorentz forces acting on current carrying wires. These Lorentz forces are generated due to an interaction between the current in the respective wire and an external magnetic field. As in general, the working lines of these forces are at an offset with respect to the center of mass of the spacecraft, a torque will be created. A Lorentz force acting on a current carrying wire is written as [7]:

$$\vec{F}_L = \vec{B} \times \vec{I} \cdot l \tag{R.1}$$

where $\vec{B}$ is the field vector denoting Earth magnetic field, $\vec{I}$ is the electrical current vector flowing through the wire, and l is the length of the wire.
Therefore, the resultant of the Lorentz torques on the complete spacecraft caused by the produced Lorentz forces is expressed as:

$$\vec{T}_L = \sum_{i=1}^{n} \left(\vec{F}_L\right)_i \times \vec{d}_i = \sum_{i=1}^{n} \left(\vec{B} \times \vec{I}_i \cdot l_i\right) \times \vec{d}_i \tag{R.2}$$

where $\vec{I}_i$ is the electrical current vector flowing through wire i, and l_i is the length of wire i, and $\vec{d}_i$ is the distance vector from the working point of the Lorentz force on wire i to the center of mass of the spacecraft. By using the characteristic of the cross product:

$$\left(\vec{A} \times \vec{B}\right) \times \vec{C} = \left(\vec{A} \cdot \vec{C}\right) \vec{B} - \left(\vec{B} \cdot \vec{C}\right) \vec{A} \tag{R.3}$$

this latter identity can be rewritten to:

$$\vec{T}_L = \sum_{i=1}^{n} l_i \cdot \left(\left(\vec{B} \cdot \vec{d}_i\right) \vec{I}_i - \left(\vec{I}_i \cdot \vec{d}_i\right) \vec{B}\right) \tag{R.4}$$

R.2.2 Evaluation of Lorentz torque

In order to get an impression of the magnitude of the Lorentz torque, an evaluation of Lorentz torque on a single solar array is performed. In figure R.1, a sketch is shown of the current loop in the solar array.

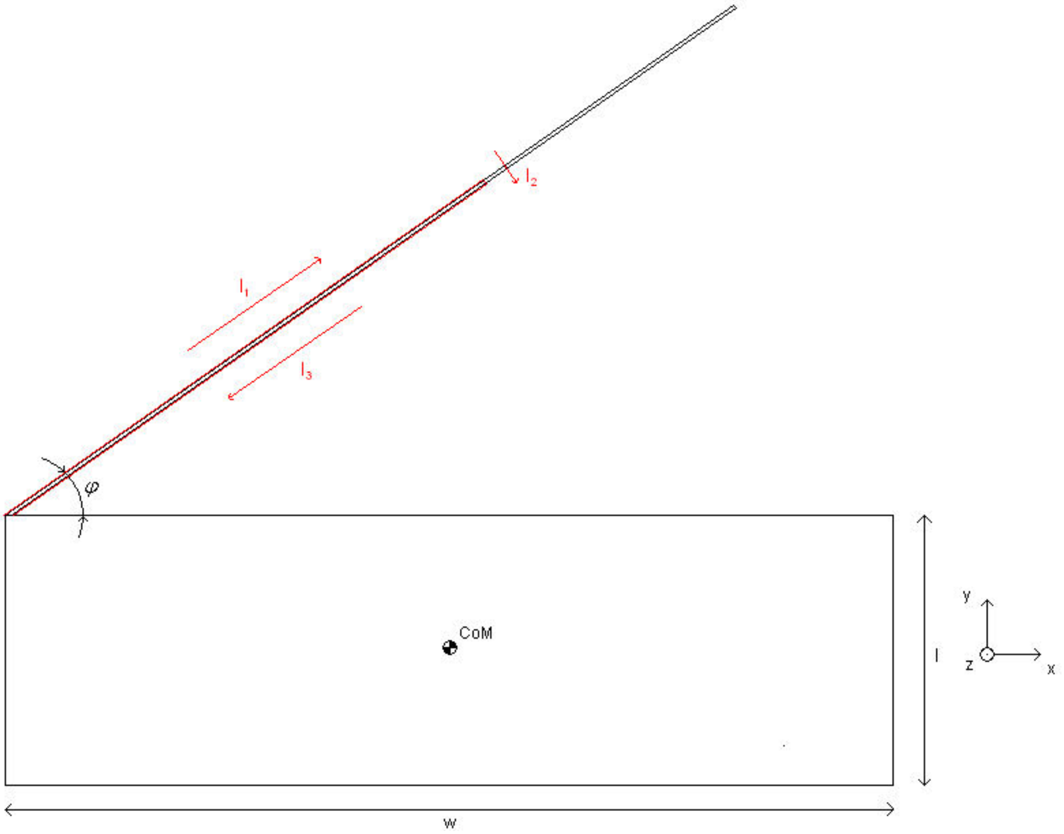

Figure R.1: Situational sketch of current loop in a solar array

As can be seen in figure R.1, the current loop is divided into three parts. Note that the loop is not closed. After all, the final part of the loop is functionally made up by the system bus. For now however, this part is neglected. The first part of the loop, which is referenced as part 1, is the go-line through the solar array, which in practice goes through the solar cells. Its counterpart, the return line, is referenced as part 3, and runs on the back of the solar array. The connection between part 1 and part 3 is referenced as part 2, and is assumed to run perpendicular to part 1 and part 3.
Furthermore, it is assumed that the complete current loop runs on the middle line of the solar array with respect to the dimension perpendicular to the plane of drawing.
To determine the magnitude of the Earth magnetic field, a worst case scenario is assumed. It is known that the magnitude of the Earth magnetic field is expressed by:

$$B = \frac{M}{r^3} \cdot \left(1 + 3 \cdot \sin^2\left(\Phi\right)\right)^{1/2} \tag{R.5}$$

where M is the moment of the Earth magnetic dipole, r is the distance from the center of the Earth to the spacecraft, and Φ is the latitude coordinate of the spacecraft on a sphere with radius r.

Assuming worst case conditions in equation R.5 will lead to setting the trigonometric term equal to 1, which corresponds to the position of the spacecraft directly above either one of the poles:

$$\hat{B} = \left|\vec{B}\right| = 2 \cdot \frac{M}{r^3} \tag{R.6}$$

This condition corresponds with a position of the spacecraft directly above one of the Earth poles.
With the value of M being equal to $8.05 \cdot 10^{15}$ T.m^3 and the value of r being equal to $6378137 + 635000$ m, this magnitude can be evaluated to be equal to:

$$\hat{B} = 2 \cdot \frac{8.05 \cdot 10^{15}}{(6378137 + 635000)^3} = 4.667 \cdot 10^{-5}\ \mathrm{T} \tag{R.7}$$

The magnitude of the current flowing through the wires is set to be equal to the short circuit current of the solar cells. This value is found to be equal to 0.3624 A. However, this situation denotes an absolute maximum in current flow. After all, the effective current flow will be smaller in magnitude, because the solar array has to provide power to the electrical power subsystem.
Note that in this situation the solar illumination vector coincides with the normal vector of the solar array, and that the temperature of the cells is equal to 28 °C.
With respect to geometry of the spacecraft, it is assumed that the center of mass of the spacecraft is in the geometrical center of the main body. Additional parameters needed for a successful analysis of the Lorentz torque caused by a single solar array are found in table R.1.

Table R.1: Geometrical parameters relevant for solar array Lorentz torque analysis

Parameter	Variable	Value	
Length of current path 1	l_1	214.5	mm
Length of current path 2	l_2	1.5	mm
Length of current path 3	l_3	214.5	mm
Solar panel angle	ϕ	35	°
Spacecraft body length	l	326.5	mm
Spacecraft body width	w	100	mm

In the analysis, it is furthermore assumed that the coordinate system used to determine the various vectors is a right-handed Cartesian system, with the positive x-axis going horizontally to the right, the positive y-axis going vertically upwards, and the positive z-axis going perpendicular to the paper in the direction of the reader. In this situation, the following vectors can be generated:

$$\vec{I_1} = \hat{I} \cdot \begin{pmatrix} \cos\phi \\ \sin\phi \\ 0 \end{pmatrix} \approx \begin{pmatrix} 0.29686 \\ 0.20786 \\ 0 \end{pmatrix}\ \mathrm{A} \tag{R.8}$$

$$\vec{I_2} = \hat{I} \cdot \begin{pmatrix} \sin\phi \\ -\cos\phi \\ 0 \end{pmatrix} \approx \begin{pmatrix} 0.20786 \\ -0.29686 \\ 0 \end{pmatrix}\ \mathrm{A} \tag{R.9}$$

$$\vec{I_3} = \hat{I} \cdot \begin{pmatrix} -\cos\phi \\ -\sin\phi \\ 0 \end{pmatrix} \approx \begin{pmatrix} -0.29686 \\ -0.20786 \\ 0 \end{pmatrix}\ \mathrm{A} \tag{R.10}$$

And:

$$\vec{d_1} = \begin{pmatrix} \frac{1}{2} \cdot l - \frac{1}{2} \cdot l_1 \cdot \cos\phi \\ -\frac{1}{2} \cdot w - \frac{1}{2} \cdot l_1 \cdot \sin\phi \\ 0 \end{pmatrix} \approx \begin{pmatrix} 75.4 \\ -111.5 \\ 0 \end{pmatrix}\ \mathrm{mm} \tag{R.11}$$

$$\vec{d_2} = \begin{pmatrix} \frac{1}{2} \cdot l + \frac{1}{2} \cdot l_2 \cdot \sin\phi - l_1 \cdot \cos\phi \\ -\frac{1}{2} \cdot w + \frac{1}{2} \cdot l_2 \cdot \cos\phi - l_1 \cdot \sin\phi \\ 0 \end{pmatrix} \approx \begin{pmatrix} -12.0 \\ -172.4 \\ 0 \end{pmatrix}\ \mathrm{mm} \tag{R.12}$$

$$\vec{d}_3 = \begin{pmatrix} \frac{1}{2} \cdot l - \frac{1}{2} \cdot l_1 \cdot \cos\phi + l_2 \cdot \sin\phi \\ -\frac{1}{2} \cdot w - \frac{1}{2} \cdot l_1 \cdot \sin\phi + l_2 \cdot \cos\phi \\ 0 \end{pmatrix} \approx \begin{pmatrix} 76.3 \\ -110.3 \\ 0 \end{pmatrix} \text{mm} \tag{R.13}$$

The only unknown vector is the Earth magnetic field $\vec{B}$. It is not known beforehand however, which field vector yields the largest Lorentz torque. Therefore, the calculation in equation R.4 is performed for three different Earth magnetic field vectors. In table R.2, the corresponding results for the total Lorentz torque acting on the spacecraft due a single solar array are given.

Table R.2: Generated Lorentz torques due to response of a single solar array to various magnetic field vectors

	$B_x = \hat{B}; B_y = 0; B_z = 0$	$B_x = 0; B_y = \hat{B}; B_z = 0$	$B_x = 0; B_y = 0; B_z = \hat{B}$
$(T_L)_x$ (N.m)	$-1.0858 \cdot 10^{-9}$	$-6.0748 \cdot 10^{-9}$	0
$(T_L)_y$ (N.m)	$-1.6234 \cdot 10^{-9}$	$2.8492 \cdot 10^{-9}$	0
$(T_L)_z$ (N.m)	0	0	$1.7634 \cdot 10^{-9}$

Comparing the values in table R.2 with the control torques generated by the magnetic material, it is noticed that the Lorentz torque is at least a factor 1000 smaller than the control torque. Therefore, it can be safely assumed that it may be neglected in the analysis of the attitude behaviour of the Delfi-C3 spacecraft.

R.2.3 Derivation of induction torque

Another magnetic torque, which will be generated in the Delfi-C3 spacecraft, is induction torque. Induction torques are in nature the same as the torque induced in an induction machine. Hence, they are caused by the reaction of induced currents to an external magnetic field. These induced currents are in turn caused by the rotation of an electrically conductive and magnetically susceptible material in an external magnetic field [5].
For the evaluation of this induction torque, a hypothetical situation, in which a short-circuited coil is placed in the Earth magnetic field, is used. A sketch of this situation is shown in figure R.2.

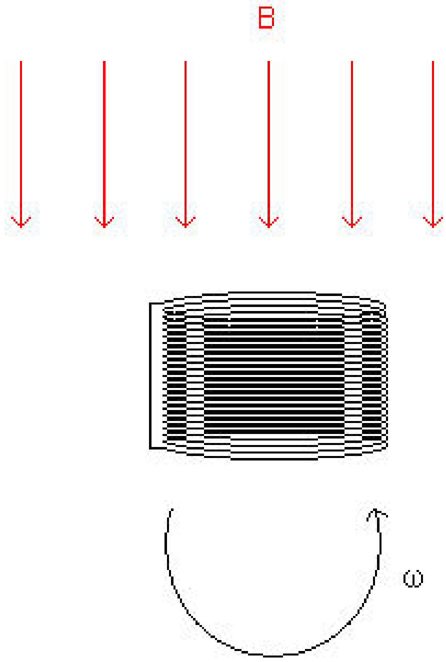

Figure R.2: Situational sketch of rotating short-circuited coil in an external magnetic field

In order to perform a successful analysis, several relevant parameters of the coil are calculated. Firstly, the self inductance of the coil is calculated. For this reason, the magnetic reluctance of the coil is determined with:

$$R_m = \frac{l_{coil}}{\mu \cdot A_{coil}} \tag{R.14}$$

where l_{coil} is the longitudinal length of the coil, A_{coil} is the cross-sectional area of the coil, and μ is the magnetic permeability of the medium enclosed by the coil. The magnetic permeability is also written as:

$$\mu = \mu_r \cdot \mu_0 \tag{R.15}$$

Furthermore, the cross-sectional area of the coil is assumed to be purely circular, which can therefore be expressed by:

$$A_{coil} = \frac{\pi}{4} \cdot d_{coil}^2 \tag{R.16}$$

where d_{coil} is the diameter of the coil.
It is assumed that the coil windings are wound in an extreme tight fashion, which means that no free space is present between the windings. Therefore, the length of the coil can be written as:

$$l_{coil} = N \cdot d_{wire} \tag{R.17}$$

where N denotes the number of windings in the coil, and d_{wire} is the diameter of a single coil winding. Then the magnetic reluctance of the coil can be rewritten to:

$$R_m = \frac{4 \cdot N \cdot d_{wire}}{\mu_r \cdot \mu_0 \cdot \pi \cdot d_{coil}^2} \tag{R.18}$$

The inductance of the coil is directly related to its magnetic reluctance using the following expression:

$$L = \frac{N^2}{R_m} = \frac{N \cdot \mu_r \cdot \mu_0 \cdot \pi \cdot d_{coil}^2}{4 \cdot d_{wire}} \tag{R.19}$$

A second important characteristic of the short-circuited coil is the resistance. In order to estimate the resistance, use is made of the following expression:

$$R = \frac{\rho \cdot l_{wire}}{A_{wire}} \tag{R.20}$$

where ρ is the specific resistivity of the wiring material, l_{wire} is total length of the wire, and A_{wire} is the cross-sectional area of the wire.
Because the wiring is assumed to be circular in geometry, the cross-sectional area of the current carrying wire is written as:

$$A_{wire} = \frac{\pi}{4} \cdot d_{wire}^2 \tag{R.21}$$

where d_{wire} is the diameter of the wire.
Due to the circular cross-sectional area of the coil, the total length of the wire is expressed as:

$$l_{wire} = N \cdot \pi \cdot d_{coil} + N \cdot d_{wire} \tag{R.22}$$

Substituting equations R.21 and R.22 into equation R.20 yields:

$$R = \frac{4 \cdot \rho \cdot N \cdot (\pi \cdot d_{coil} + d_{wire})}{\pi \cdot d_{wire}^2} \tag{R.23}$$

Because the coil is freely rotating in a stationary magnetic field, the magnetic flux density that would be sensed by the coil can be written as:

$$B = \hat{B} \cdot \sin\theta = \hat{B} \cdot \sin\omega t \tag{R.24}$$

where$\hat{B}$ is the absolute value of the magnetic flux density at the position of the coil, θ is the angle between the symmetry axis of the coil and the magnetic flux density vector, and ω is the rotational rate of the coil in the plane of the magnetic flux density.
The complete magnetic flux sensed by the coil is expressed by:

$$\phi = B \cdot A_{coil} = \hat{B} \cdot A_{coil} \cdot \sin\omega t \tag{R.25}$$

As the magnetic field is not constant in time, Faraday's law of induction has to be written. This expresses the induced voltage as a function of rotational rate and magnetic flux density with:

$$e = \frac{\mathrm{d}\lambda}{\mathrm{d}t} = N \cdot \frac{\mathrm{d}\phi}{\mathrm{d}t} \tag{R.26}$$

where λ is the so-called flux linkage of the coil, which is the product of the number of windings of the coil N and the magnetic flux ϕ.
Substituting equation R.25 into equation R.26 and performing the differentiation yields:

$$e = N \cdot \hat{B} \cdot A_{coil} \cdot \omega \cdot \cos\omega t \tag{R.27}$$

As the coil is short-circuited, an equivalent circuit of the coil can now be drawn. After all, only three elements are present in this circuit:

- Induced electro-motive force e, governed by equation R.27;
- Self-inductance of the coil L, governed by equation R.19;
- Ohmic resistance of the coil R, governed by equation R.23.

A schematic of the equivalent circuit of the short-circuited coil is shown in figure R.3.

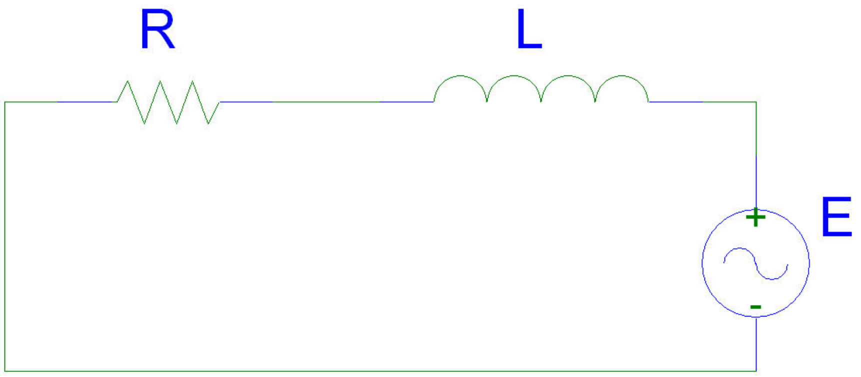

Figure R.3: Equivalent circuit of a short-circuited coil rotating in a stationary magnetic field

In order to develop an expression for the current flowing through the circuit, a phasor diagram has to be generated. For this reason, the inductive reactance of the coil has to be calculated, which is expressed by:

$$X_L = \omega \cdot L \tag{R.28}$$

The corresponding phasor diagram is shown in figure R.4.
Now the magnitude of the complex impedance of the circuit can be calculated with:

$$|Z| = \sqrt{R^2 + X_L^2} \tag{R.29}$$

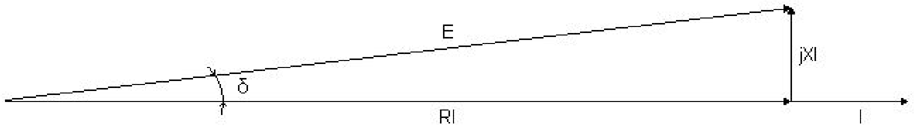

Figure R.4: Phasor diagram of a short-circuited coil rotating in a stationary magnetic field

And the current and electro-motive force are related by:

$$E = I \cdot |Z| \tag{R.30}$$

where E is the effective or root-mean-square value of the electromotive force, and I is the effective value of the current.
For a sinusoidal quantity, the effective value is directly related to the maximum value with:

$$\hat{A} = A \cdot \sqrt{2} \tag{R.31}$$

where A is the effective value of a random sinusoidal quantity, and $\hat{A}$ is the amplitude of this sinusoidal quantity. Therefore, equation R.30 can be rewritten to:

$$\hat{I} = \frac{\hat{E}}{|Z|} \tag{R.32}$$

The phase angle δ ("lasthoek") between the current i and the electromotive force e is written as:

$$\delta = \tan^{-1}\left(\frac{X_L}{R}\right) \tag{R.33}$$

Now, an expression for the current can be written:

$$i = \frac{N \cdot \hat{B} \cdot A_{coil}}{Z} \cdot \omega \cdot \cos(\omega t - \delta) \tag{R.34}$$

For the calculation of the generated torque, use is made of the energy balance:

$$p_{out} = p_{in} \tag{R.35}$$

which dictates that the input of energy into a system leads to a manifestation of this energy in this system in a certain form.
In case of the rotating coil, this balance is equivalent to:

$$p_{elec} + p_{mech} = p_{magn} \tag{R.36}$$

where p_{elec} is the dissipated electrical power of the system, p_{mech} is the mechanical power supplied by the system, and p_{magn} is the increase in magnetic energy stored in the system.
The contributions to the energy balance are written as:

$$p_{elec} = i^2 \cdot R \tag{R.37}$$

$$p_{magn} = L \cdot i \cdot \frac{\mathrm{d}i}{\mathrm{d}t} \tag{R.38}$$

$$p_{mech} = T \cdot \omega \tag{R.39}$$

Substituting equations R.37 to R.39 into equation R.36, and solving for the torque T finally yields:

$$T = \frac{L \cdot i \cdot \frac{\mathrm{d}i}{\mathrm{d}t} - i^2 \cdot R}{\omega} \tag{R.40}$$

R.2.4 Evaluation of induction torque

For the evaluation of the induction torque, the effects produced by a single current producing solar array will be investigated. It is assumed that the solar array is capable to freely rotate in space. The relevant parameters used in this analysis are shown in table R.3.

Table R.3: Relevant parameters for induction torque analysis on single solar array

Parameter	Variable	Value	
Length of copper wiring	l_{wire}	432	mm
Diameter of copper wiring (AWG28)	d_{wire}	0.32004	mm
Area of coil	A_{coil}	321.75	mm^2
Relative permeability	μ_r	1	
Specific resistivity (annealed copper)	ρ	1.68ů10-8	Ω.m
Rotational velocity	ω	10	$^\circ$.s^{-1}

The corresponding results are given in figure R.5.

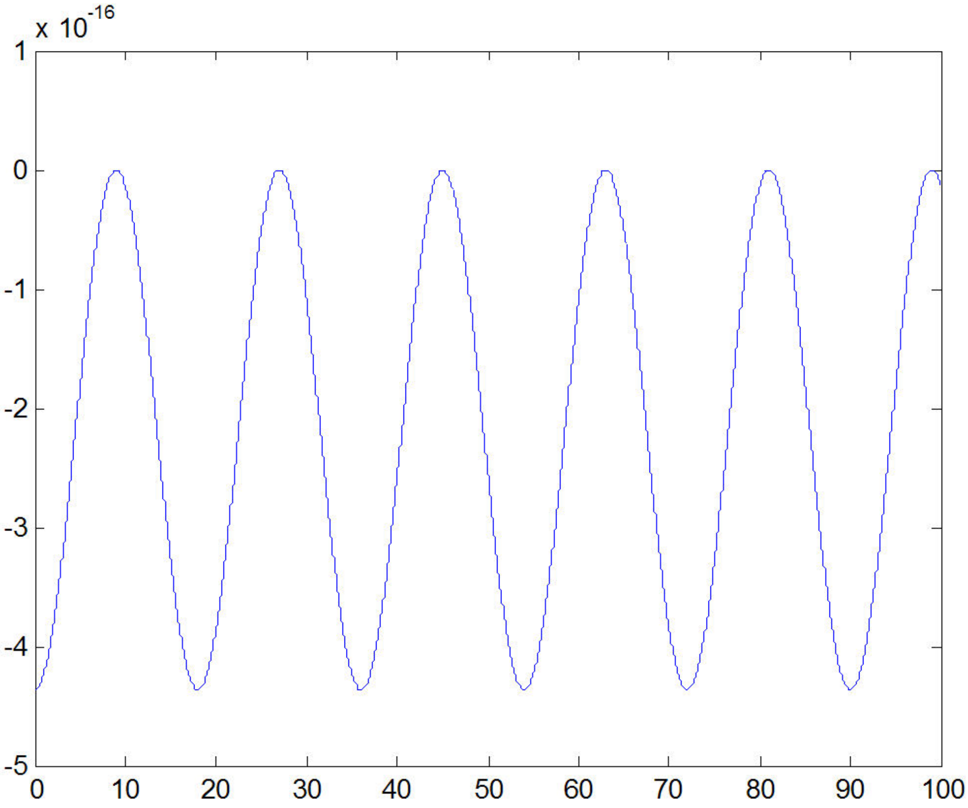

Figure R.5: Induction torque generated on single solar array

Comparing the results given in figure R.5 with the magnetic control torque, it can be safely concluded that induction torques can be neglected in the determination of the attitude behaviour of the Delfi-C3 spacecraft. After all, the magnetic control torque is a factor 10^{11} larger than the induction torque on a solar array. Therefore, induction torques will be completely neglected.

R.3 Conclusions and recommendations

In the previous sections, a derivation of the expressions for the magnetic disturbance torques acting on the Delfi-C3 spacecraft is given. Moreover, the magnitude of these magnetic disturbance torques is evaluated. Both Lorentz and induction torques have been considered. However, as the magnitudes of these torques are respectively a factor 10^3 and 10^{11} smaller than the magnitude of the magnetic control torque, they will be neglected in the determination of the attitude behaviour of the Delfi-C3 spacecraft.

Appendix S

DC3-TN-704-105
Thermal inputs for solar array performance simulation

S.1 Introduction

For successful operation of the Delfi-C3 spacecraft, sufficient electrical power has to be generated on the solar panels to supply the various systems in the spacecraft with power. As the power budget, which is required for designing the various systems, is dependent on the minimum value of generated power in orbit, the worst case scenario with respect to power generation has to be identified.

As the performance of the solar panels is heavily dependent on their temperature, the thermal behaviour of the solar panels has to be evaluated. After all, cold solar panels will yield a higher performance than hot solar panels. Therefore, a thermal analysis has to be performed of the Delfi-C3 solar panels.

In this document, a thermal analysis is performed of a single Delfi-C3 solar panel. In section S.2.1, the influence of temperature on the performance of solar cells is explained. A brief recapitulation of performing a thermal analysis is shown in section S.2.2. A description of the thermal model construction is given in section S.2.3. In section S.2.4, the addition of radiation dynamics to the thermal model is described. The influence of the spacecraft body on the thermal behaviour of the solar panel is highlighted in section S.2.5. In section S.2.6, a description of the modeling procedure of the various involved illumination sources is shown, while the effect of power flow from the solar cells to the spacecraft systems is given in section S.2.7. In section S.2.8, the results of several performed simulations of the thermal behaviour of the solar panel are shown, which will be compared to the results of the thermal analysis of the complete spacecraft in section S.2.9.

S.2 Delfi-C3 solar panel thermal analysis

S.2.1 Influence of temperature on solar cell characteristics

In order to determine the exact behaviour of the solar arrays in the situation, in which the Delfi-C3 spacecraft is in orbit, a careful analysis of the thermal conduct of these arrays has to be performed. This is an absolute necessity, because temperature is a factor with a large impact on the performance of solar cells. After all, an increase in temperature will mean a drop in open cell voltage and maximum power point voltage of a single solar cell. On the other side, a small increase in short circuit current and maximum power point current is achieved. However in general, a conclusion can be drawn that an increase in temperature is accompanied with a drop in electrical power.

As the electrical power subsystem of Delfi-C3 is designed to handle the minimum amount of power available in orbit, the maximum temperature of the photovoltaic cells has to be determined. In principle, the temperature of the cells will be different from the temperature of the substrate.

In figure S.1, the effects of solar cell temperature on the IV characteristic are shown. For three different temperatures, the IV characteristic is plotted.

S.2.2 Brief recapitulation of thermal analysis

For evaluating the temperature of the photovoltaic cells in orbit, a thermal analysis will be performed. This will be done by dividing the solar array into five discrete nodes. Every node is connected to every

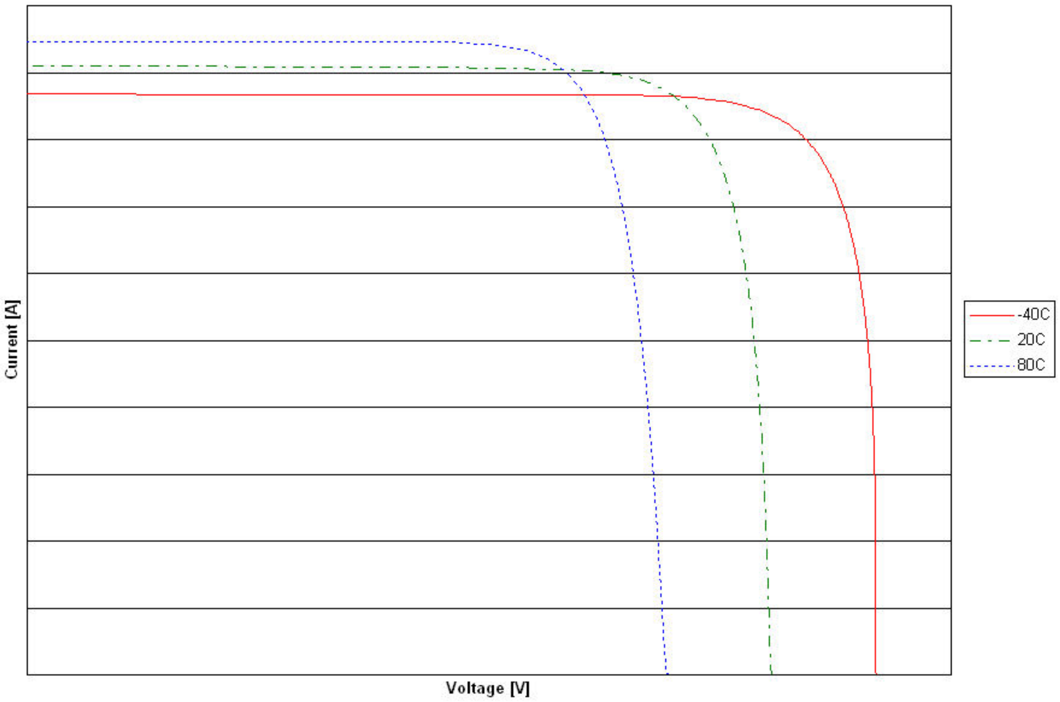

Figure S.1: Example solar cell IV characteristics for three different temperatures

other node by a thermal resistance. Furthermore, every node has a distinct thermal capacity.
In general, a similarity between electrical analysis and thermal analysis can be identified. This is done by using an analogy between electrical quantities and thermal quantities. The electrical quantity voltage is analogous to the thermal quantity temperature. Furthermore, the electrical quantity current is analogous to the thermal quantity heat flow. Thermal resistance and thermal capacitance are analogous to their respective electrical counterparts.
For performing the thermal analysis, use is made of the PSpice electrical network modelling programme. This computer programme is a widely used simulation environment for electrical network, and can be conveniently used for thermal modelling due to the analogy between thermal and electrical systems.
In principle, every thermal node is modelled by equipping it with a thermal capacitance. The value of this capacitance is equal to the total capacitance of the object, which the node is representing. Furthermore, thermal resistances are inserted between every set of two nodes. This resistance is taken to be equal to the thermal resistance between the center of the object, which the first node representing, to the center of the object, which the second node is representing. In figure S.2, the modelling of a single thermal node is depicted.

S.2.3 Construction of a complete stratic thermal model

Division of solar panel into thermal nodes

In order to perform thermal analysis, a real-life geometrical body, which is continuous in its geometrical dimensions, has to be reduced to a set of nodes, which each have infinitely small geometrical dimensions. In this collection of nodes, lumped thermal parameters are present, which are derived from the thermal characteristics of the original body. In case of a solar array, performing this division results in five nodes positioned at the following places:

- TEC array front structure - body side
- TEC array front structure - TFSC side
- TEC photovoltaic cells
- TEC array back structure
- TFSC photovoltaic cells + structure

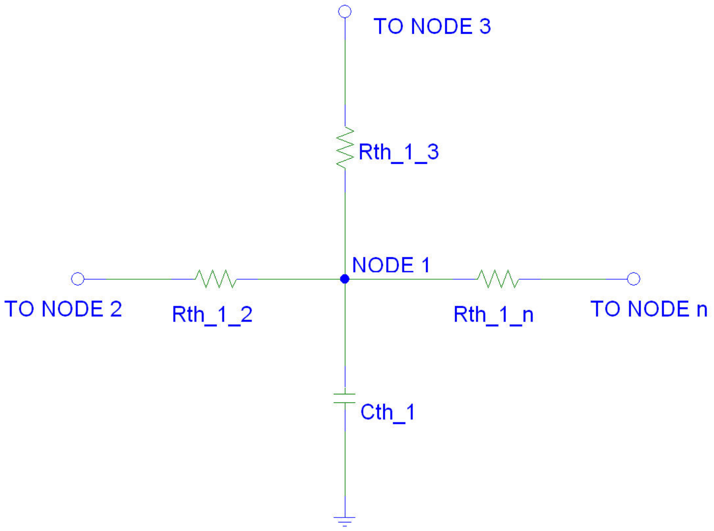

Figure S.2: Example solar cell IV characteristics for three different temperatures

An elaboration of the division of the solar panel into thermal nodes is shown in figure S.3, figure S.4, and table S.1. In figures S.3 and S.4, the front and back side of the panel are respectively depicted. The sections, which are contracted into nodes, are given distinct colours. A summary of these sections with the corresponding colours in the figures is given in table S.1.

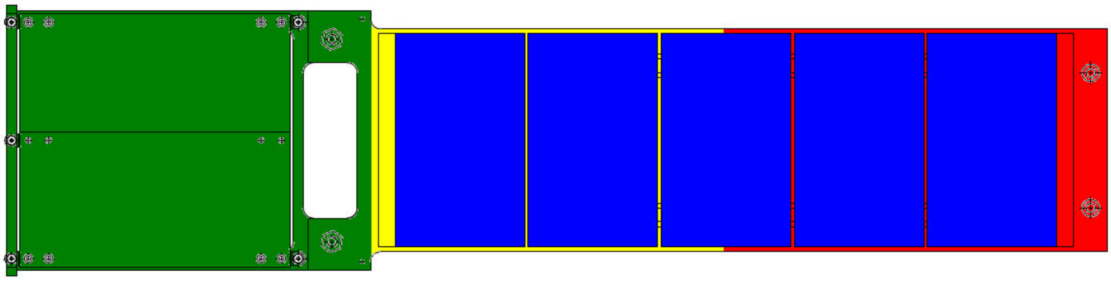

Figure S.3: Representation of thermal nodes on solar panel front side

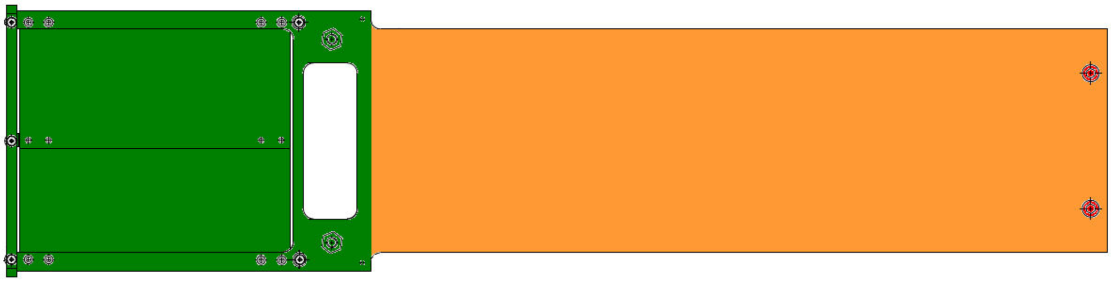

Figure S.4: Representation of thermal nodes on solar panel back side

Table S.1: Summary of thermal node representation of solar panel

Node	Position	Colour
1	TEC array front structure - body side	Red
2	TEC array front structure - TFSC side	Yellow
3	TEC photovoltaic cells	Blue
4	TEC array back structure	Orange
5	TFSC photovoltaic cells + structure	Green

Following the procedure of constructing a thermal model for a solar array will result in the complete thermal model shown in figure S.5. This model implements the five thermal nodes listed in table S.1 with relevant thermal resistances and thermal capacities inserted. Note that in this model no external stimuli are present.

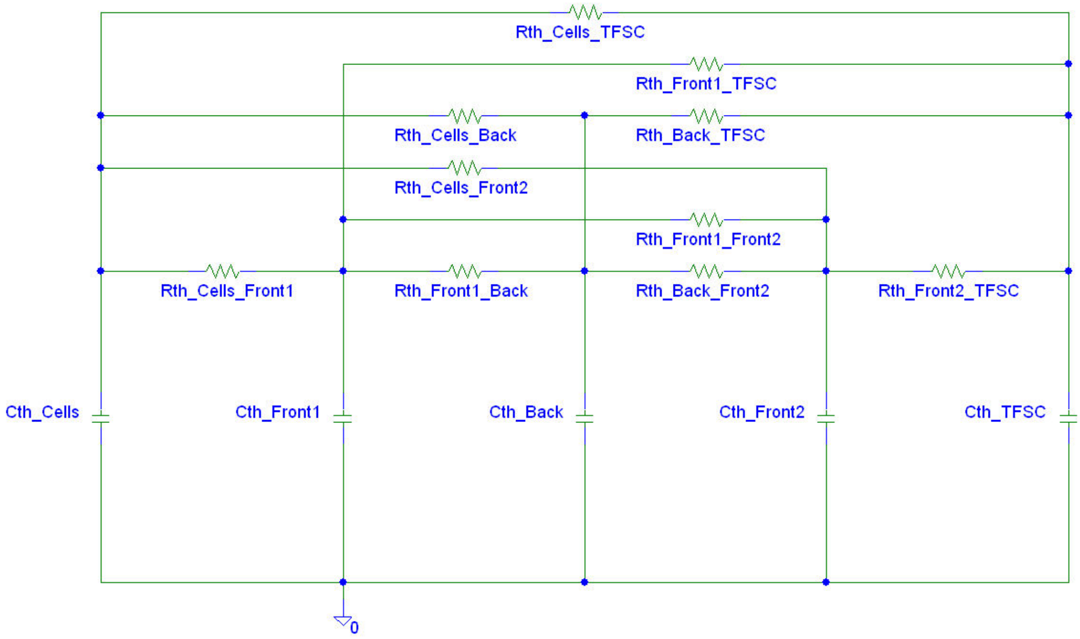

Figure S.5: Complete static thermal model of solar panel

Determination of geometrical properties

In order to complete the static thermal model of the solar panel, values have to be assigned to the various electrical components in the model. However, for assessing the values of the various thermal capacitances and thermal resistances, the materials used to construct the components on the solar panel have to be identified. Furthermore, the specific thermal capacities of these materials have to be collected. When these values are known, the values of the thermal capacities in the model can be calculated.

For the substrate of the TEC photovoltaic cells, carbon fiber reinforced plastic is used. More accurately, unidirectional M55J is applied as material for the substrate making use of 20 0.06 mm carbon fibers as reinforcement. The TEC photovoltaic cells themselves are composed out of gallium arsenide (GaAs). Furthermore, the TFSC photovoltaic cells are manufactured out of copper indium gallium diselenide (CuInGaSe2 or CIGS), while the supporting structure of the TFSC cells is produced out of a titanium alloy, Ti-6Al-4V.

A next point of interest in constructing the thermal model is the total set of geometrical dimensions of the various components in the solar panel. After all, the values of the thermal resistances and the thermal capacitances are largely defined by these geometrical dimensions. In order to extract values for the dimensions, the production drawings of the TEC structure and the TFSC structure have to be investigated. For reference, these are shown in Appendix A.1 and A.2 respectively.

In table S.2, the geometrical characteristics of the TEC photovoltaic cells are listed. Note that the mentioned geometrical dimensions are for a single cell. The complete array is composed of multiple cells, so the geometrical dimensions have to be derived.

Table S.2: Geometrical characteristics of TEC photovoltaic cells

Parameter	Value	
Length of single TEC photovoltaic cell	63.22	mm
Width of single TEC photovoltaic cell	38.46	mm
Thickness of TEC photovoltaic cell	0.1547	mm
Amount of TEC photovoltaic cells in array	5	

The geometrical characteristics of the TEC support structure are shown in table S.3.

Table S.3: Geometrical characteristics of TEC support structure

Parameter	Value
Length of TEC support structure	222.5 mm
Width of TEC support structure	66 mm
Thickness TEC support structure	1.25 mm

In table S.4, the geometrical characteristics of the TFSC support structure are summarized. Note that in the TTFSC structure a gap is situated. During calculation of the thermal capacity of the TFSC cells, this gap has to be taken into account. Therefore, Geometrical dimensions of this hiatus have to be known.

Table S.4: Geometrical characteristics of TFSC support structure

Parameter	Value
Length of TFSC support structure	110.5 mm
Width of TFSC support structure	77 mm
Thickness TFSC support structure	1.5 mm
Length of gap in TFSC support structure	46 mm
Width of gap in TFSC support structure	16 mm

With respect to the TFSC photovoltaic cells, the geometrical properties are listed in table S.5. Note that the mentioned geometrical dimensions relate to the complete array of TFSC cells.

Table S.5: Geometrical characteristics of TFSC photovoltaic cells

Parameter	Value
Length of TFSC photovoltaic array	85.5 mm
Width of TFSC photovoltaic array	66 mm
Thickness TFSC photovoltaic array	50 μm

With the geometrical dimensions known of all involved components, the volumes and exposed surface areas of the components can be calculated. Investigating figures S.3 and S.4, it has to be mentioned that the exposed surface area is represented by the area in the plane of the figures.
Therefore, the volume and surface area of the TEC photovoltaic cells become:

$$V_{TEC\_cells} = n \cdot l_{cell} \cdot w_{cell} \cdot t_{cell} = 5 \cdot 0.06322 \cdot 0.03846 \cdot 0.0001547 = 1.8807 \cdot 10^{-6} \text{ m}^3 \tag{S.1}$$

$$V_{TEC\_cells} = n \cdot l_{cell} \cdot w_{cell} = 5 \cdot 0.06322 \cdot 0.03846 = 1.2157 \cdot 10^{-2} \text{ m}^2 \tag{S.2}$$

where $_{cell}$ is the length of a single TEC photovoltaic cell, w_{cell} is the width of a single TEC photovoltaic cell, t_{cell} is the thickness of a single TEC photovoltaic cell, and n is the amount of cells positioned in a complete array.
Furthermore, the volume and surface area of the TEC support structure can be calculated:

$$V_{TEC\_struc} = l_{struc} \cdot w_{struc} \cdot t_{struc} = 0.2225 \cdot 0.066 \cdot 0.00125 = 1.8356 \cdot 10^{-5} \text{ m}^3 \tag{S.3}$$

$$V_{TEC\_struc} = l_{struc} \cdot w_{struc} = 0.2225 \cdot 0.066 = 1.4685 \cdot 10^{-2} \text{ m}^2 \tag{S.4}$$

where l_{struc} is the length of the TEC support structure, w_{struc} is the width of the TEC support structure, and t_{struc} is the thickness of the TEC support structure.
Calculating the volume and surface of the TFSC photovoltaic cells leads to:

$$V_{TFSC\_cells} = l_{T\_cell} \cdot w_{T\_cell} \cdot t_{T\_cell} = 0.0855 \cdot 0.066 \cdot 0.00005 = 2.8217 \cdot 10^{-7} \text{ m}^3 \tag{S.5}$$

$$V_{TFSC\_cells} = l_{T\_cell} \cdot w_{T\_cell} = 0.0855 \cdot 0.066 = 5.643 \cdot 10^{-3} \text{ m}^2 \tag{S.6}$$

where l_{T_cell} is the length of the TFSC photovoltaic array, w_{T_cell} is the width of the TFSC photovoltaic array, and t_{T_cell} is the thickness of a TFSC photovoltaic cell.
Performing the calculations for the volume and surface area of the TFSC support structure:

$$\begin{aligned} V_{TFSC\_struc} &= \left(l_{T\_str} \cdot w_{T\_str} - l_{gap} \cdot w_{gap} - A_{TFSC\_cells}\right) \cdot t_{T\_str} = \\ &= \left(0.1105 \cdot 0.077 - 0.046 \cdot 0.016 - 5.643 \cdot 10^{-3}\right) \cdot 0.0015 = 3.194 \cdot 10^{-6} \text{ m}^3 \end{aligned} \tag{S.7}$$

$$\begin{aligned} A_{TFSC\_struc} &= \left(l_{T\_str} \cdot w_{T\_str} - l_{gap} \cdot w_{gap} - A_{TFSC\_cells}\right) = \\ &0.1105 \cdot 0.077 - 0.046 \cdot 0.016 - 5.643 \cdot 10^{-3} = 2.1295 \cdot 10^{-3} \text{ m}^2 \end{aligned} \tag{S.8}$$

where l_{T_str} is the length of the TFSC support structure, w_{T_str} is the width of the TFSC support structure, t_{T_str} is the thickness of the TFSC support structure, l_{gap} is the length of gap in the TFSC support structure, and w_{gap} is the width of the gap in the TFSC support structure.
In table S.6, a summary is shown of the values of the volume and surface area of the various components applied on the solar panel.

Table S.6: Summary of volumes and surface areas of the various components on solar panel

Component	Volume (m^3)	Surface area (m^2)
TEC photovoltaic cells	$1.8807 \cdot 10^{-6}$	$1.2157 \cdot 10^{-2}$
TEC support structure	$1.8356 \cdot 10^{-5}$	$1.4685 \cdot 10^{-2}$
TFSC photovoltaic cells	$2.8215 \cdot 10^{-7}$	$5.643 \cdot 10^{-3}$
TFSC photovoltaic cells	$3.194 \cdot 10^{-6}$	$2.1295 \cdot 10^{-3}$

Generation of node thermal capacities

With the geometrical dimensions known, it is possible to determine the various thermal capacities in the thermal model of the solar panel. The value of a thermal capacitance is calculated with:

$$C_{th} = c_{th} \cdot l \cdot w \cdot t = c_{th} \cdot A \cdot t = c_{th} \cdot V \tag{S.9}$$

where c_{th} is the specific thermal capacity of the material represented by the respective node, l is the length of the object represented by the node, w is the width of this object, and t is the thickness of this object, A is the surface area of the object represented by the node, and V is the volume of the object represented by the node.
In table S.7, a summary of the materials used in the manufacturing of the solar panel and their corresponding specific heat capacities is shown [14] [1] [3] [8].

Table S.7: Summary of applied solar panel materials with corresponding specific thermal capacities

Material	Component	Specific heat capacity (J.m^{-3}.K^{-1})
Carbon fibre reinforced plastic M55J	TEC structure	1302000
Gallium arsenide	TEC photovoltaic cells	1739000
Copper indium gallium diselenide	TFSC photovoltaic cells	???
Titanium alloy Ti-6Al-4V	TFSC structure	2317000

Using the values shown in tables S.6 and S.7, the thermal capacitances of the various nodes can be determined.
Calculating the thermal capacity for the TEC photovoltaic cells results in:

$$(C_{th})_{TEC\_cells} = (c_{th})_{GaAs} \cdot V_{TEC\_cells} = 1739000 \cdot 1.8807 \cdot 10^{-6} = 3.2705 \text{ J.K}^{-1} \tag{S.10}$$

With respect to the node on the front of TEC support structure at the side of the spacecraft body, its thermal capacity is calculated to be:

$$(C_{th})_{TEC\_body} = (c_{th})_{CFRP} \cdot \frac{V_{TEC\_struc}}{4} = 1302000 \cdot \frac{1.8356 \cdot 10^{-5}}{4} = 5.9750 \text{ J.K}^{-1} \tag{S.11}$$

A similar calculation can be performed for the node on the front of the TEC support structure at the side of the TFSC payload:

$$(C_{th})_{TEC\_TFSC} = (c_{th})_{CFRP} \cdot \frac{V_{TEC\_struc}}{4} = 1302000 \cdot \frac{1.8356 \cdot 10^{-5}}{4} = 5.9750 \text{ J.K}^{-1} \tag{S.12}$$

Applying the equation for calculating the thermal capacity to the node at the back of the TEC support structure yields:

$$(C_{th})_{TEC\_back} = (c_{th})_{CFRP} \cdot \frac{V_{TEC\_struc}}{2} = 1302000 \cdot \frac{1.8356 \cdot 10^{-5}}{2} = 11.9499 \text{ J.K}^{-1} \tag{S.13}$$

For determining the thermal capacity of the TFSC node, it has to be noticed that this node comprises in fact two components. After all, both the TFSC structure and TFSC cells are represented by the TFSC thermal node. For the calculation of the thermal capacity, this has to consequence that the capacities of the two involved components have to be added. However, the specific heat capacity of the TFSC photovoltaic cells is unknown making calculation of the thermal capacity impossible. However, the volume of this component is far smaller than the volume of the support structure. Therefore, assuming the specific thermal capacity of the cells in equal order to the specific thermal capacity of the support structure, the contribution of the cells can be neglected. This lead to:

$$(C_{th})_{TSFC} = (c_{th})_{Ti} \cdot V_{TFSC\_struc} = 2317000 \cdot 3.194 \cdot 10^{-6} = 7.4005 \text{ J.K}^{-1} \tag{S.14}$$

Note that the introduced simplification will not yield large problems in the analysis. After all, the objective is to calculate the thermal behaviour of the TEC photovoltaic cells. Any simplification in the TFSC payload is therefore allowed if the consequences are not dire.
In table S.8, a summary of the thermal capacities of the various involved node sin the thermal model of the solar panel is shown.

Table S.8: Summary of thermal capacities of various thermal nodes

Node	Thermal capacity (J.K^{-1})
TEC array front structure - body side	5.9750
TEC array front structure - TFSC side	5.9750
TEC photovoltaic cells	3.2705
TEC array back structure	11.9499
TFSC photovoltaic cells + structure	7.4005

Generation of node thermal resistances

Next, the thermal resistances between the various have to be determined. A first step in performing this analysis is creating a diagram showing the connections between the various nodes. Investigating figures S.3 and S.4, and relating these to figure S.5, the diagram shown in figure S.6 can be created. The drawn connections will be represented by a finite thermal resistance. On the other hand, any non-drawn connection will possess an infinitely large finite thermal resistance.
The value of a thermal resistance can be determined by using the following expression:

$$R_{th} = \frac{1}{G_{th}} = \frac{\Delta x}{k \cdot A} \tag{S.15}$$

where Δx is the distance between thermal node 1 and thermal node 2, with node 1 and node 2 at the terminals of the respective thermal resistance R_{th}, k is the thermal conductivity coefficient of the material of constituting the thermal resistance, and A is the cross-sectional area of the geometry constituting the thermal resistance.

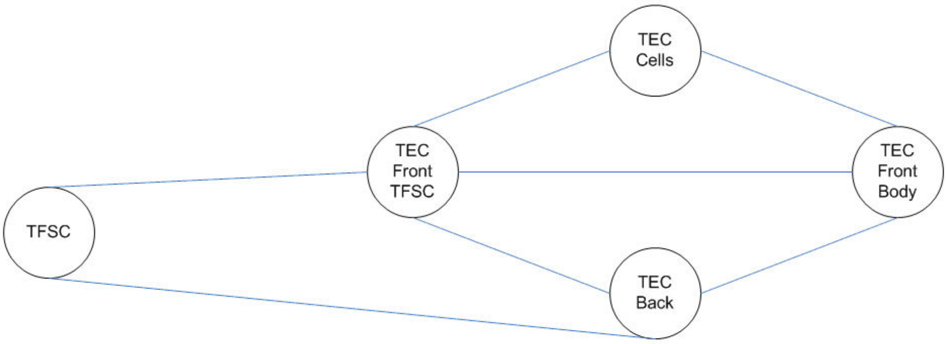

Figure S.6: Complete static thermal model of solar panel

For geometrical positioning of the nodes, it is assumed that every node is lumped in the center of mass of the component it represents. For the four nodes representing the complete TEC panel, this poses no problem as all are rectangular components. Therefore, the position of the node is in the geometrical center of its corresponding component.
However, positioning of the TFSC node is slightly more difficult due to its uncommon geometry. Nevertheless, the general formula for determining the center of mass of a geometrical object can be applied. This formula is expressed by:

$$x_{CoM} = \frac{M_x}{m} \tag{S.16}$$

where x_{CoM} is the coordinate on the x-axis of the projection of the center of mass onto the x-axis, m is the mass of the respective spacecraft, and M_x is the so-called first moment of mass around the x-axis.
Applying this expression, a definition has to be given for the x-axis. Investigating appendix T.2, it is however seen that the only coordinate of interest is in the longitudinal direction of the solar panel, i.e. from the connection of the TFSC frame to the TEC panel to the TFSC photovoltaic cells. Setting the connection to the TEC panel as baseline, the following first moment of mass can be calculated:

$$\bar{M}_x = 25 \cdot 77 \cdot 12.5 - 46 \cdot 16 \cdot 14 + 2 \cdot 85.5 \cdot 5.5 \cdot 67.75 = 77477.375 \text{ mm}^3 \tag{S.17}$$

Note that it is assumed that every part of the TFSC frame has equal mass density. Therefore, the first moment of mass can be normalized by taking out the mass density in its expression.
Performing a similar normalization procedure for determining the mass of the complete TFSC frame leads to:

$$\bar{M}_x = 25 \cdot 77 - 46 \cdot 16 + 2 \cdot 85.5 \cdot 5.5 = 2129.5 \text{ mm}^2 \tag{S.18}$$

With the two variables known, the center of mass can be evaluated:

$$x_{CoM} = \frac{77477.375}{2129.5} = 36.38 \text{ mm} \tag{S.19}$$

This coordinate is taken with respect to the connection of the TFSC frame to the TEC support structure.
In table S.9, a summary of the materials used for manufacturing the components on the solar panel is given and their corresponding thermal conductivities are shown [1] [3] [2].

Table S.9: Summary of applied solar panel materials with corresponding thermal conductivities

Material	Component	Thermal conductivity (W.m^{-1}.K^{-1})
Carbon fibre reinforced plastic M55J	TEC structure	7.0 // fiber; 0.8 ⊥ fiber
Gallium arsenide	TEC photovoltaic cells	55.0
Copper indium gallium diselenide	TFSC photovoltaic cells	???
Titanium alloy Ti-6Al-4V	TFSC structure	15.6

Using the data given in tables S.6 and S.9, it is possible to calculate the values of the various thermal resistances in the model by applying equation S.15 to the various connections in the thermal node model. A simplification in these calculations can be made, by observing in tables S.2, S.3, S.4, and S.5 that for every component integrated in the solar panel, the geometrical thickness is much smaller in magnitude than the geometrical width and the geometrical length. In expression form this results in:

$$t \ll l \tag{S.20}$$

$$t \ll w \tag{S.21}$$

Calculating the thermal resistance for the connection between the front side of the TEC support structure at the body side to the front side of the TEC support structure at the TFSC side leads to:

$$(R_{th})_{front_1\_front_2} = \frac{1}{2} \cdot l_{TEC\_struc} \cdot \frac{1}{k_{CFRP//} \cdot w_{TEC\_struc} \cdot \frac{1}{2} \cdot t_{TEC\_struc}} = \frac{222.5 \cdot 10^{-3}}{7 \cdot 66 \cdot 10^{-3} \cdot 1.25 \cdot 10^{-3}} = 385.28 \text{ K.W}^{-1} \tag{S.22}$$

Determining the thermal resistance for the connection between the front side of the TEC support structure at the body side and the TEC photovoltaic cells results in:

$$(R_{th})_{front_1\_cells} = \frac{1}{4} \cdot l_{TEC\_struc} \cdot \frac{1}{k_{CFRP//} \cdot w_{TEC\_struc} \cdot \frac{1}{2} \cdot t_{TEC\_struc}} = \frac{1}{2} \cdot \frac{222.5 \cdot 10^{-3}}{7 \cdot 66 \cdot 10^{-3} \cdot 1.25 \cdot 10^{-3}} = 192.64 \text{ K.W}^{-1} \tag{S.23}$$

Note that effects of thickness in this calculation have been neglected as has been postulated previously (inclusion would lead to an additional resistance of 0.23 K.W^{-1} $\longrightarrow$ thickness neglect seems justified). Performing a similar calculation for the thermal resistance for the connection between the front side of the TEC support structure at the TFSC and the TEC photovoltaic cells yields:

$$(R_{th})_{front_2\_TFSC} = \frac{1}{4} \cdot l_{TEC\_struc} \cdot \frac{1}{k_{CFRP//} \cdot w_{TEC\_struc} \cdot \frac{1}{2} \cdot t_{TEC\_struc}} = \frac{1}{2} \cdot \frac{222.5 \cdot 10^{-3}}{7 \cdot 66 \cdot 10^{-3} \cdot 1.25 \cdot 10^{-3}} = 192.64 \text{ K.W}^{-1} \tag{S.24}$$

Calculating the thermal resistance for the connection between the between the front side of the TEC support structure at the body side and the back side of the TEC support structure gives as result:

$$(R_{th})_{front_1\_back} = \frac{1}{4} \cdot l_{TEC\_struc} \cdot \frac{1}{k_{CFRP//} \cdot w_{TEC\_struc} \cdot \frac{1}{2} \cdot t_{TEC\_struc}} = \frac{1}{2} \cdot \frac{222.5 \cdot 10^{-3}}{7 \cdot 66 \cdot 10^{-3} \cdot 1.25 \cdot 10^{-3}} = 192.64 \text{ K.W}^{-1} \tag{S.25}$$

Furthermore, performing a similar calculation for between the between the front side of the TEC support structure at the TFSC side and the back side of the TEC support structure yields:

$$(R_{th})_{front_2\_back} = \frac{1}{4} \cdot l_{TEC\_struc} \cdot \frac{1}{k_{CFRP//} \cdot w_{TEC\_struc} \cdot \frac{1}{2} \cdot t_{TEC\_struc}} = \frac{1}{2} \cdot \frac{222.5 \cdot 10^{-3}}{7 \cdot 66 \cdot 10^{-3} \cdot 1.25 \cdot 10^{-3}} = 192.64 \text{ K.W}^{-1} \tag{S.26}$$

With respect to the TFSC photovoltaic array, it has to be mentioned that the TFSC photovoltaic cells do not contribute to the thermal resistance. After all, they do not possess any thermal capacity. Furthermore, its very small thickness can justify an assumption that the resistance is very high and the TFSC cells are in open.

Subsequently, the thermal resistance for the connection between the TFSC structure and the backside of the TEC support structure is evaluated to be equal to:

$$
\begin{aligned}
&(R_{th})_{TFSC\_back} = \frac{1}{2} \cdot l_{TEC\_struc} \cdot \frac{1}{k_{CFRP//} \cdot w_{TEC\_struc} \cdot \frac{1}{2} \cdot t_{TEC\_struc}} + \\
&\frac{1}{k_{Ti} \cdot t_{TFSC\_struc}} \cdot \left(\frac{1}{2} \cdot \frac{2 \cdot l_{gap}}{w_{TFSC} - w_{gap}} + \frac{l_{TFSC\_body} - lgap}{w_{TFSC}} + \frac{1}{2} \cdot \frac{l_{TFSC\_CoM} - l_{TFSC\_body}}{w_{TFCS\_leg}} \right) = \\
&\frac{222.5 \cdot 10^{-3}}{7 \cdot 66 \cdot 10^{-3} \cdot 1.25 \cdot 10^{-3}} + \frac{1}{15.6 \cdot 1.5 \cdot 10^{-3}} \cdot \left(\frac{1}{2} \cdot \frac{14 \cdot 10^{-3}}{15.5 \cdot 10^{-3}} + \frac{11 \cdot 10^{-3}}{77 \cdot 10^{-3}} + \frac{1}{2} \cdot \frac{13.38 \cdot 10^{-3}}{5.5 \cdot 10^{-3}} \right) = \\
&462.67 \text{ K.W}^{-1} \qquad \text{(S.27)}
\end{aligned}
$$

Performing a similar calculation for the thermal resistance for the connection between the TFSC structure and the front side of the TEC support structure at the TFSC side results in:

$$
\begin{aligned}
&(R_{th})_{TFSC\_front_2} = \frac{1}{4} \cdot l_{TEC\_struc} \cdot \frac{1}{k_{CFRP//} \cdot w_{TEC\_struc} \cdot \frac{1}{2} \cdot t_{TEC\_struc}} + \\
&\frac{1}{k_{Ti} \cdot t_{TFSC\_struc}} \cdot \left(\frac{1}{2} \cdot \frac{2 \cdot l_{gap}}{w_{TFSC} - w_{gap}} + \frac{l_{TFSC\_body} - lgap}{w_{TFSC}} + \frac{1}{2} \cdot \frac{l_{TFSC\_CoM} - l_{TFSC\_body}}{w_{TFCS\_leg}} \right) = \\
&\frac{1}{2} \cdot \frac{222.5 \cdot 10^{-3}}{7 \cdot 66 \cdot 10^{-3} \cdot 1.25 \cdot 10^{-3}} + \frac{1}{15.6 \cdot 1.5 \cdot 10^{-3}} \cdot \left(\frac{1}{2} \cdot \frac{14 \cdot 10^{-3}}{15.5 \cdot 10^{-3}} + \frac{11 \cdot 10^{-3}}{77 \cdot 10^{-3}} + \frac{1}{2} \cdot \frac{13.38 \cdot 10^{-3}}{5.5 \cdot 10^{-3}} \right) = \\
&270.03 \text{ K.W}^{-1} \qquad \text{(S.28)}
\end{aligned}
$$

In table S.10, a summarizing matrix of the thermal resistances between the various applied thermal nodes in the thermal model of the solar panel is shown.

Table S.10: Summary of thermal resistances between involved nodes in solar panel thermal model

R_{th} (K.W^{-1})	TEC cells	TEC front-body	TEC front-TFSC	TEC back	TFSC
TEC cells	0	192.64	192.64	∞	∞
TEC front-body	192.64	0	385.28	192.64	∞
TEC front-TFSC	192.64	385.28	0	192.64	270.03
TEC back	∞	192.64	192.64	0	462.67
TFSC	∞	∞	270.03	462.67	0

S.2.4 Addition of solar radiation dynamics

In addition to the static modeling of the solar panel, several dynamic characteristics have to be included in the thermal model. Thermal dynamic behaviour is governed by absorption and emission of the energy transferred by electromagnetic waves. In the following paragraphs, the various contributions to the radiation dynamics are explained [10].

For a spacecraft in orbit, the largest source of incoming energy is solar radiation. This energy is transferred to the solar panel due to absorption of the radiation by exposed surface area. Absorption of solar radiation by a particular object is expressed by:

$$P_{abs} = \alpha \cdot A \cdot S \qquad \text{(S.29)}$$

where A is the exposed surface area of the component, S is the solar flux at the position of the spacecraft, and α is the so-called absorptivity of the object, which relates to the ratio of radiation absorbed by the object to the total amount of incoming radiation.

Furthermore, the components on the solar panel emit energy in the infrared spectral band. Emission of radiation by a particular object is written as:

$$P_{em} = \epsilon \cdot \sigma \cdot A \left(T^4 - {T_s}^4 \right) \qquad \text{(S.30)}$$

where ϵ is the so-called emissivity of the object, σ is the Stefan-Boltzmann constant, A is the exposed surface area of the component, and T is the temperature of the object, and T_s is the temperature of cold space.

Furthermore, albedo has to be taken into account. Albedo is in fact solar radiation reflected by the Earth's atmosphere. Therefore, the expression governing the absorption of albedo radiation closely resembles the expression relating to the absorption of solar radiation. However, not all radiation illuminating the Earth's atmosphere is reflected, so a scaling factor has to be introduced. This yields the following expression:

$$P_{alb} = \alpha \cdot a \cdot A \cdot S \cdot (\sin \rho)^2 \tag{S.31}$$

where a is the albedo factor, and ρ is Earth angular radius.

Furthermore, due to the fact that the spacecraft is in a low Earth orbit, the components on the solar panel will receive infrared radiation emitted by the Earth. This radiation is largely governed by the expression relating to emission of electromagnetic radiation. Therefore, the following expression can be written:

$$P_{ir} = \epsilon \cdot \sigma \cdot A \cdot \left(T^4 - {T_E}^4\right) \cdot (\sin \rho)^2 \tag{S.32}$$

where T_E is the mean temperature of the Earth.

As previously mentioned, the dynamic behaviour of components in a thermal model is largely defined by the optical characteristics of the various involved nodes. Therefore, the optical parameters of the materials used in manufacturing of the solar panel have to be determined.

For optical purposes, the materials mentioned in table S.11 can be used for representation of the various nodes. However, the front side of the TEC support structure is equipped with a thin layer of Kapton, which will influence the optical characteristics. In table 11, a summary of the optical characteristics of the various involved nodes in the thermal model of the solar panel is shown.

Table S.11: Summary of optical characteristics of various nodes in solar panel thermal model

Node	Material	Absorptivity	Emissivity
TEC photovoltaic cells	Gallium arsenide	0.89	0.88
TEC array front structure-body	Kapton	0.93	0.84
TEC array front structure-TFSC	Kapton	0.93	0.84
TEC array back structure	Carbon fiber reinforced plastic	0.89	0.84
TFSC support structure	Titanium (Ti-6Al-4V)	0.12	0.181

As a definition of the Earth angular radius, the following expression is written:

$$\rho = \arcsin\left(\frac{R_E}{R_E + h}\right) \tag{S.33}$$

where R_E is the mean equatorial radius of the Earth, and h is the orbital altitude of the spacecraft.

In table S.12, additional parameters needed for determining the dynamic thermal behaviour of the solar panel thermal model are summarized.

Table S.12: Summary of additional parameters for determining dynamic behaviour of solar panel thermal model

Parameter	Variable	Value	
Mean equatorial radius of Earth	R_E	6378137	m
Spacecraft orbital altitude	h	635000	m
Earth angular radius	ρ	1.141973	rad
Stefan-Boltzmann constant	σ	$5.67051 \cdot 10^{-8}$	$\mathrm{W.m^{-2}.K^{-4}}$
Albedo factor	a	0.34	
Temperature of cold space	T_s	4	K
Mean temperature of the Earth	T_E	288	K

S.2.5 Influence of spacecraft body

In the thermal analysis of the solar panel, an additional component besides the solar panel has to be taken into account in the form of the spacecraft body. After all, the solar panel is connected to the body by means of a hinging mechanism, which will cause conductive heat transfer between the panel and the body. Moreover, radiative emission of the back side of the TEC structure and the TFSC frame is constrained due to the fact that the body limits the exposure to cold space. Therefore, a view factor has to be introduced, which takes into account mutual coupling of heat transfer mechanisms between the body and the back side of the solar panel.

The hinge between the solar panel and the spacecraft body is manufactured out of bronze. In order to determine the thermal resistance, which is constituted by the hinge, several characteristics of the hinge have to be known. Investigating the technical drawings of the hinge yields the parameters shown in table S.13.

Table S.13: Summary of characteristics of solar panel hinge

Parameter	Variable	Value	
Thermal conductivity bronze	k_{bronze}	26.0	W.m^{-1}.K^{-1}
Length hinge	l_{hinge}	24.0	mm
Width hinge	w_{hinge}	60.0	mm
Thickness hinge	t_{hinge}	2.0	mm

Using these parameters to calculate the thermal resistance of the hinge leads to:

$$(R_{th})_{hinge} = l_{hinge} \cdot \frac{1}{k_{bronze} \cdot w_{hinge} \cdot t_{hinge}} = 24.0 \cdot 10^{-3} \cdot \frac{1}{26.0 \cdot 60.0 \cdot 10^{-3} \cdot 2.0 \cdot 10^{-3}} = 7.69 \text{ K.W}^{-1} \tag{S.34}$$

In addition to the thermal resistance of the hinge, the resistance between the node at the front side of the TEC structure at the body side and the solar panel hinge has to be taken in to account. Relating to the parameters in tables S.3, S.9, and S.13, the following calculation is performed to evaluate this thermal resistance:

$$(R_{th})_{front_1\_hinge} = \frac{1}{2} \cdot \left(l_{TEC\_struc} - l_{hinge}\right) \cdot \frac{1}{k_{CFRP//} \cdot w_{TEC\_struc} \cdot \frac{1}{2} \cdot t_{TEC\_struc}} =$$
$$\left(225.0 \cdot 10^{-3} - 24.0 \cdot 10^{-3}\right) \cdot \frac{1}{7 \cdot 6.0 \cdot 10^{-3} \cdot 1.25 \cdot 10^{-3}} = 348.05 \text{ K.W}^{-1} \tag{S.35}$$

Next to the conductive heat flow through the solar panel hinge, the radiative heat emission to the body via the back side of the TFSC frame and the TEC structure has to be taken into account. To construct these thermal connections between the node at the back side of the TEC structure and the body, and the node at the TFSC frame and the body, the thermal resistance has to be known. Equation S.15 cannot be used in this situation, because this expression is only valid for conductive heat transfer.

Therefore, additional expressions have to be found to take mutual heat exchange between the solar panel and the spacecraft body into account. Consulting literature, it is found that heat transfer can be described by:

$$P_{rad} = \sigma \cdot G_R \cdot \left({T_1}^4 - {T_2}^4\right) \tag{S.36}$$

where σ equals the Stefan-Boltzmann constant, G_R is the thermal conductivity between node 1 and node 2, T_1 is the temperature of node 1, and T_2 is the temperature of node 2.

For the thermal conductivity between two nodes in the situation the heat transfer mechanism is equal to radiation, the following expression is used:

$$G_R = \epsilon_1 \cdot \epsilon_2 \cdot A_1 \cdot F_{12} \tag{S.37}$$

where ϵ_1 is the emissivity of node 1, ϵ_2 is the emissivity of node 2, A_1 is the exposed surface area of node 1, and F_{12} is the so-called view factor between node 1 and node 2.

A view factor between two nodes is defined as the ratio of the amount of emitted radiation by node 1 received by node 2 to the total amount of emitted radiation of node 1. In order to assess these values it is assumed that every infinitely small part of exposed surface on the back side of the solar panel radiates parallel to its normal vector. This situation is sketched in figure S.7.

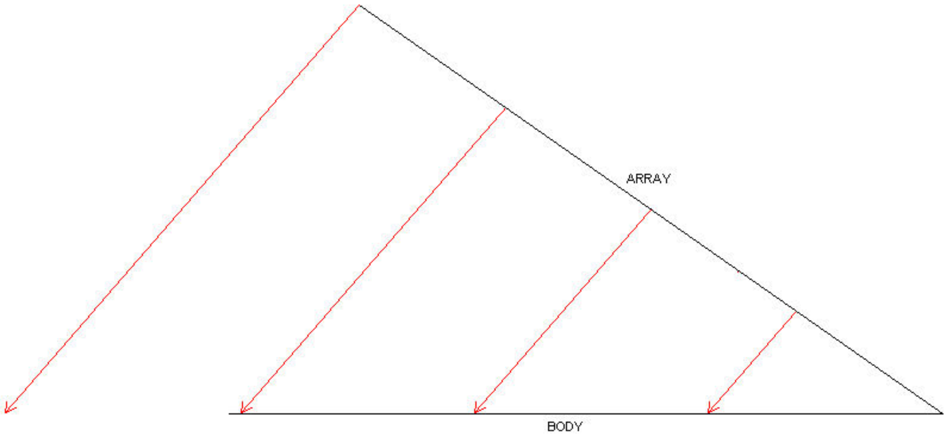

Figure S.7: Sketch of mutual heat exchange between back side of solar panel and spacecraft body

An evaluation of the amount of surface area of the back solar panel radiating onto the spacecraft body can be made by using trigonometric rules. After performing a geometric analysis of figure S.7, it is found that the panel area needed to irradiate the complete spacecraft body is equal to:

$$s_{proj} = l \cdot \cos\theta \tag{S.38}$$

where l is the length of the spacecraft body, and θ is the angle between the body and the solar panel.
As the width of the spacecraft body is larger than the width of the solar panel, the dimension perpendicular to the drawing plane in figure S.7 does not contribute to assessment of the view factor.
In table S.14, several relevant parameters are listed for evaluation of the view factor of the back of the solar panel.

Table S.14: Relevant geometrical parameters of spacecraft body

Parameter	Variable	Value	
Length of spacecraft body	l	326.5	mm
Nominal solar panel angle	θ	35.0	$\circ$
Emissivity of spacecraft body	ϵ	0.29	

Substitution of the parameters in table S.14 into equation S.38 yields:

$$s_{proj} = 326.5 \cdot \cos 35^\circ = 267.45 \text{ mm} \tag{S.39}$$

Next, a comparison of this result with the geometrical dimensions of the involved thermal nodes, which are shown in figures S.3 and S.4, has to be performed.
A first observation is that the complete back side of the TEC solar panel is emitting to the spacecraft body, because the length of the projecting body shown in equation S.39 is larger than the length of the back side panel. Therefore, it can be concluded that the view factor of the back side of the TEC panel is equal to unity. In order to incorporate this observation, emission to cold space has to be deleted from the model. After all, all emission of this particular node is taking place to the spacecraft body.
Then, the thermal conductivity between the spacecraft body and the back side of the TEC panel can be calculated using table S.11:

$$(G_R)_{TEC\_body} = 0.84 \cdot 0.29 \cdot 1.4685 \cdot 10^{-2} \cdot 1 = 3.577 \cdot 10^{-3} \text{ m}^2 \tag{S.40}$$

Secondly with respect to the TFSC thermal node, it is noticed that the length of the projecting body corresponding with the TFSC node has to be equal to:

$$(s_{proj})_{TFSC} = s_{proj} - l_{TEC} = 267.45 - 222.5 = 44.95 \text{ mm} \tag{S.41}$$

Determination of the view factor of the TFSC to the spacecraft body involves slightly more calculations than determination of the view factor of the TEC back side panel to the body. Then, the area under influence of emission to the spacecraft body is equal to:

$$(A_{proj})_{TFSC} = 25 \cdot 10^{-3} \cdot 77 \cdot 10^{-3} - 14 \cdot 10^{-3} \cdot 46 \cdot 10^{-3} + \\ 2 \cdot \left(44.95 \cdot 10^{-3} - 25 \cdot 10^{-3}\right) \cdot 5.5 \cdot 10^{-3} = 1.50045 \cdot 10^{-3} \text{ m}^2 \tag{S.42}$$

This result implies that the view factor of the complete TFSC node is calculated by dividing the projected surface area by the total surface area of the TFSC node. Performing this calculation leads to:

$$F_{TFSC\_body} = \frac{(A_{proj})_{TFSC}}{A_{TFSC}} = \frac{1.50045 \cdot 10^{-3}}{2.1295 \cdot 10^{-3}} = 0.7046 \tag{S.43}$$

This result enables the calculation of the thermal conductivity between the TFSC node and the spacecraft body. Accomplishing this calculation leads to:

$$(G_R)_{TFSC\_body} = 0.181 \cdot 0.29 \cdot 2.1295 \cdot 10^{-3} \cdot 0.7046 = 7.8758 \cdot 10^{-5} \text{ m}^2 \tag{S.44}$$

In the complete thermal model of the solar panel, the spacecraft body is implemented as an infinitely large heat capacitance. Therefore, it will have a constant temperature during the thermal analysis.

S.2.6 Modeling of illumination sources

For modeling the illumination sources, which are needed to provide external input to the model, current sources are applied. However, it has to be taken into account that the spacecraft is rotating. Therefore, the solar flux and albedo flux are represented as a sinusoidal current source. Note that only positive values are valid in this case. After all, no radiation will flow from the solar panel to the solar radiation source or the albedo radiation source. Consequently, both solar and albedo radiation will be represented by a capped sinusoidal current source in PSpice. Note that these sources are in anti phase with respect to each other.

Furthermore, it is assumed that the spacecraft is rotating solely about its x-axis, i.e. no rotational velocity is present about its y- or z-axis. It is assumed that Delfi-C3 is directly in the field of view of the Sun to the Earth. Hence, this situation can be sketched as is shown in figure S.8.

In case the Delfi-C3 spacecraft is rotating about its x-axis as previously described, the radiative flux on one of its solar panels will be equal to the profile shown in figure S.9.

In case of the solar flux waveform, its maximum value will be equal to the nominal value of the solar flux in orbit around the Earth. A similar consideration is made for the albedo flux; its maximum value equals the nominal value of albedo flux at the orbital altitude of Delfi-C3.

It has to be noticed that the solar flux is dependent on the season. After all, the orbit of the Earth is slightly elliptic, and therefore possesses a distinct perihelion and aphelion. In winter solstice, the Earth is closest to the Sun, i.e. in perihelion, while in summer solstice, the Earth is farthest from the Sun, i.e. in aphelion.

In the vicinity of the Earth, the solar flux is expressed by:

$$S = \frac{P}{4\pi \cdot {r_E}^2} \tag{S.45}$$

where P is the total energy produced in the Sun, and r_E is the distance between the center of the Sun and the center of the Earth.

The distance between the Sun and the Earth can be described by a general Kepler orbit. Implementing the equation for a Kepler orbit leads to the distance between the Sun and the Earth in aphelion is written as:

$$(r_E)_a = \bar{r}_E \cdot (1 + e) \tag{S.46}$$

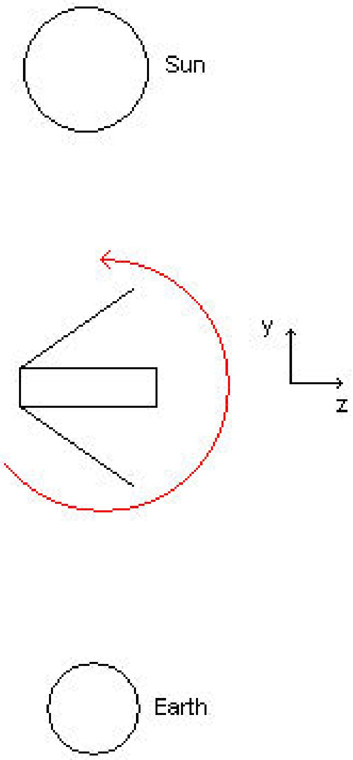

Figure S.8: Sketch of Delfi-C3 attitude in Sun Earth system

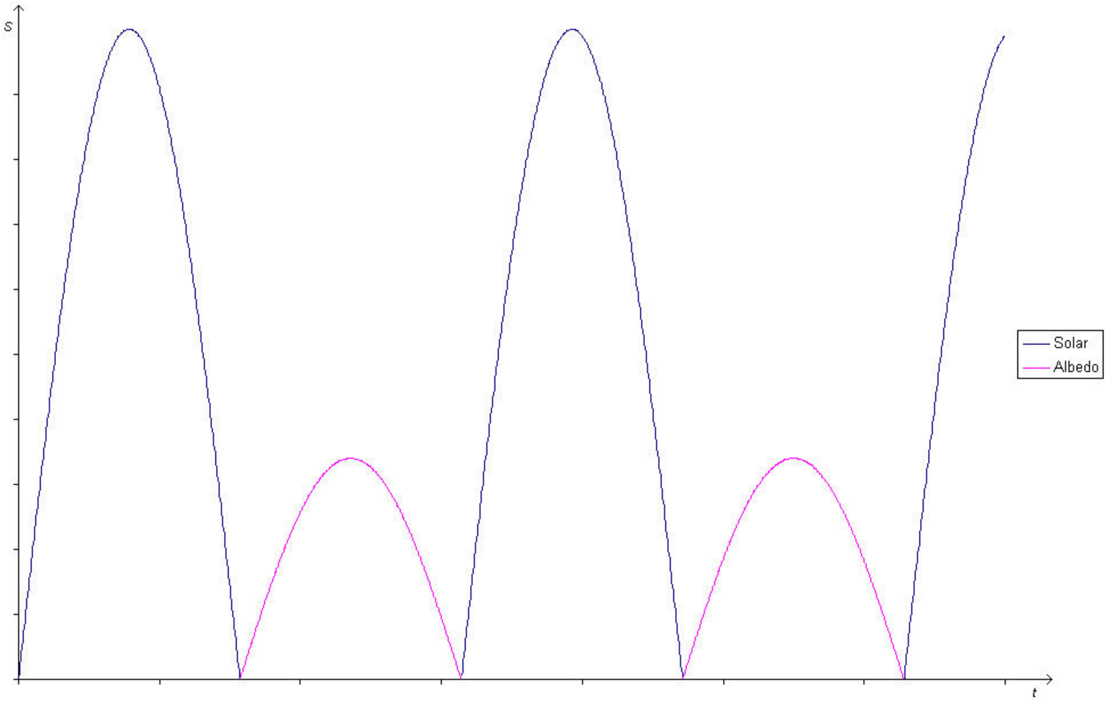

Figure S.9: Sketch of Delfi-C3 attitude in Sun Earth system

where $\bar{r}_E$ is the mean distance between the Earth and the Sun, and e is the eccentricity of the orbit of the Earth around the Sun.

Similarly, the distance between the Sun and the Earth in aphelion is expressed as:

$$(r_E)_p = \bar{r}_E \cdot (1 - e) \tag{S.47}$$

Investigating equations S.45 to S.47, it is noticed that the solar flux attains a maximum value when the Earth is in perihelion. As the hot case is most interesting in the thermal analysis, it will be assumed that the Earth is in perihelion during the thermal analysis.

In table S.15, the parameters needed for determining the solar flux incident to the solar panel are summarized [15].

Table S.15: Summary of parameters for determination of solar flux

Parameter	Variable	Value	
Mean distance Earth - Sun	$\bar{r}_E$	$149598 \cdot 10^6$	m
Eccentricity Earth orbit	e	0.0167	
Perihelion distance Earth - Sun	$(r_E)_p$	$1.470997 \cdot 10^{11}$	m
Total generated solar energy	P	$383 \cdot 10^{24}$	W
Solar flux in perihelion	S_p	1408.5	W.m^{-2}

S.2.7 Flow of electrical power

In addition to thermal and optical properties of the solar array, the electrical properties play a role as well. After all, the energy balance in the various nodes of the thermal model has to hold. Most nodes only have energy components consisting of thermal conductive and thermal radiative energy. However, the TEC cells will generate electrical power, which will flow to the various subsystems in the spacecraft body. This flow of electrical power has to be incorporated in the model, and will therefore result in an additional energy component on the TEC cells.

An exact value for the generated electrical energy is difficult to determine, because the electrical power subsystem implements a switching regulator system. Therefore, the instantaneous power flow experiences changes in its magnitude at a high frequency. However, for modeling purposes the average amount of electrical power can be used.

A valid estimation can be found by investigating the behaviour of the electrical power subsystem and the IV characteristic of the TEC cells. It is known that the electrical power system switches between a solar array voltage of 8V and 5V. In this specific range, the solar array current remains more-or-less constant, and is set at 0.375 A. Then the electrical power generated on the solar array will be equal to:

$$P = \frac{V_{high} + V_{low}}{2} \cdot I = \frac{8 + 5}{2} \cdot 0.375 = 2.4375 \text{ W} \tag{S.48}$$

This value is linearly related to the amount of incident solar radiation. Therefore, it has to be recalled that the calculated value is obtained in case of a perpendicular incidence angle of the radiation vector with respect to the cells. Changes in radiation will directly affect the magnitude of generated electrical power.

Note that the minimum value of required electrical power has been chosen such that the solar arrays are capable of generating this amount in every operating condition. As the worst-case condition for generation of electrical power is in the hot case, thermal effects do not influence this power flow. After all, this flow is constant due to the operation method of the electrical power system. Any remaining potential electrical energy on the solar panel will be converted into thermal energy.

S.2.8 Simulation results

As the thermal model is completely defined, it is now possible to perform simulations of the thermal behaviour of the solar panel. For performing these simulations, two distinct scenarios will be investigated. These are deviating from each other with respect to their rotational velocity. After all, the rotational velocity of the spacecraft has the requirement to be in the range from 0.2 deg.s^{-1} to 10 deg.$^{-1}$. These two extreme values will be investigated.

For the simulations, the initial temperature of all involved thermal nodes is set equal to the constant temperature of the spacecraft body. This temperature is set to be equal to 24 °C.

Simulation time is equal to 6000 seconds, which coincides with 100 minutes. This time is slightly larger than a single orbit time. Note however that in orbit the spacecraft will spend part of this orbital period in eclipse. This eclipse period is not incorporated in the model.

In the first simulation, the thermal behaviour is evaluated in case the Delfi-C3 spacecraft is rotation with 0.2 deg.s^{-1} about its x-axis. In figure S.10, the waveform of temperature of the TEC photovoltaic cells is shown.

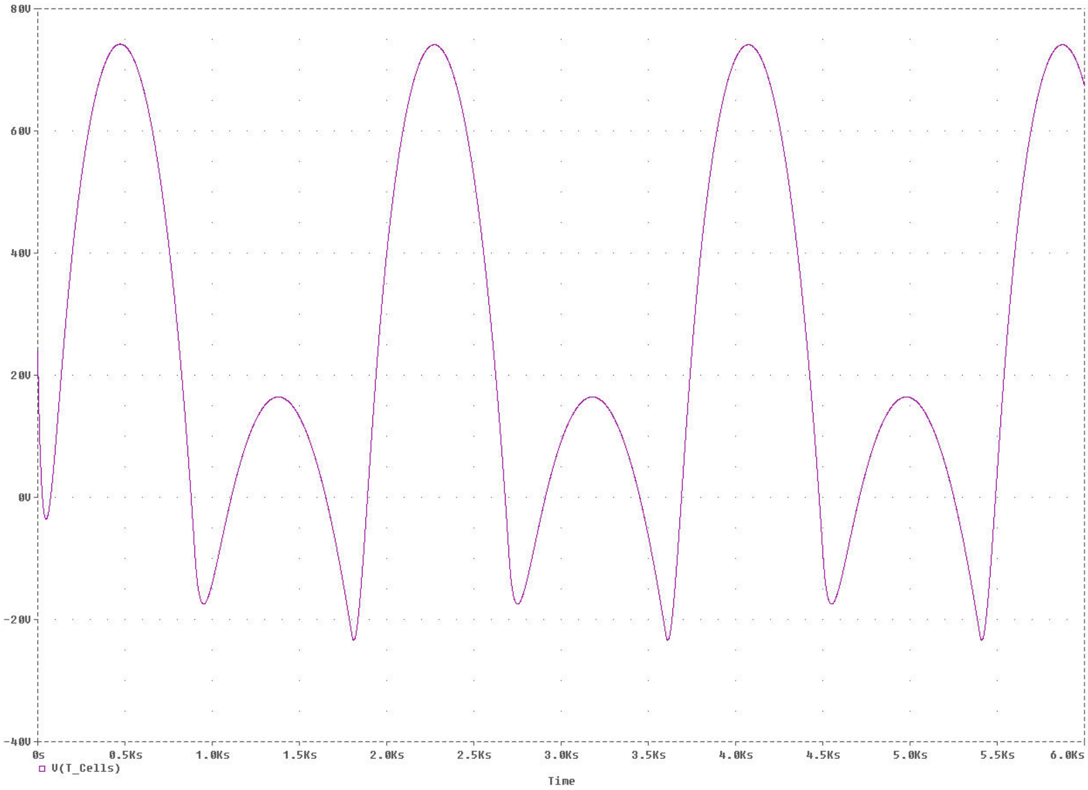

Figure S.10: Thermal profile of TEC photovoltaic cells - rotational velocity 0.2 deg.s^{-1}

Investigating figure S.10, it is noticed that the steady-state behaviour is comprised of two superimposed oscillations. This is to be expected as the solar flux and the albedo flux are modeled as a sinusoidal input source to the model. Therefore, the oscillation in the TEC cell temperature with large amplitude is attributed to the solar flux and the oscillation with small amplitude to the albedo flux.

By examining figure S.10, the extreme values of the temperature can be extracted. These values are listed in table S.16.

Table S.16: Extreme values of TEC photovoltaic cell temperature - rotational velocity 0.2 deg.s^{-1}

Parameter	Value	
Maximum value of TEC cell temperature	74.1	°C
Minimum value of TEC cell temperature	-23.3	°C
Amplitude of TEC cell temperature	97.4	°C

In the second simulation, the rotational velocity of the Delfi-C3 spacecraft is equal to 10 deg.s^{-1}. In figure S.11, the thermal behaviour of the TEC photovoltaic cells is shown.

For purposes of clarity, a close-up of the waveform is shown in figure S.11, because the period of the oscillation is small compared to the complete simulation time. This zoomed in part of the thermal profile is shown in figure S.12.

As can be noticed in figure S.12, the thermal profile consists of two superimposed oscillations. In contrast to the profile for a rotational velocity of 0.2 deg.s^{-1}, these oscillations cannot be distinguished individually. Due to the finite thermal capacitance of the TEC cells, the fall period of the first oscillation is not completed at the time the rise of the second oscillation initiated. Therefore, the thermal behaviour resembles a single distorted oscillation.

In table S.17, the extreme values of the temperature of the TEC cells are listed.

In order to evaluate the absolute maximum temperature the TEC cells are able to reach in orbit, a simulation is performed with a constant illumination source. This source replaces the sinusoidal source

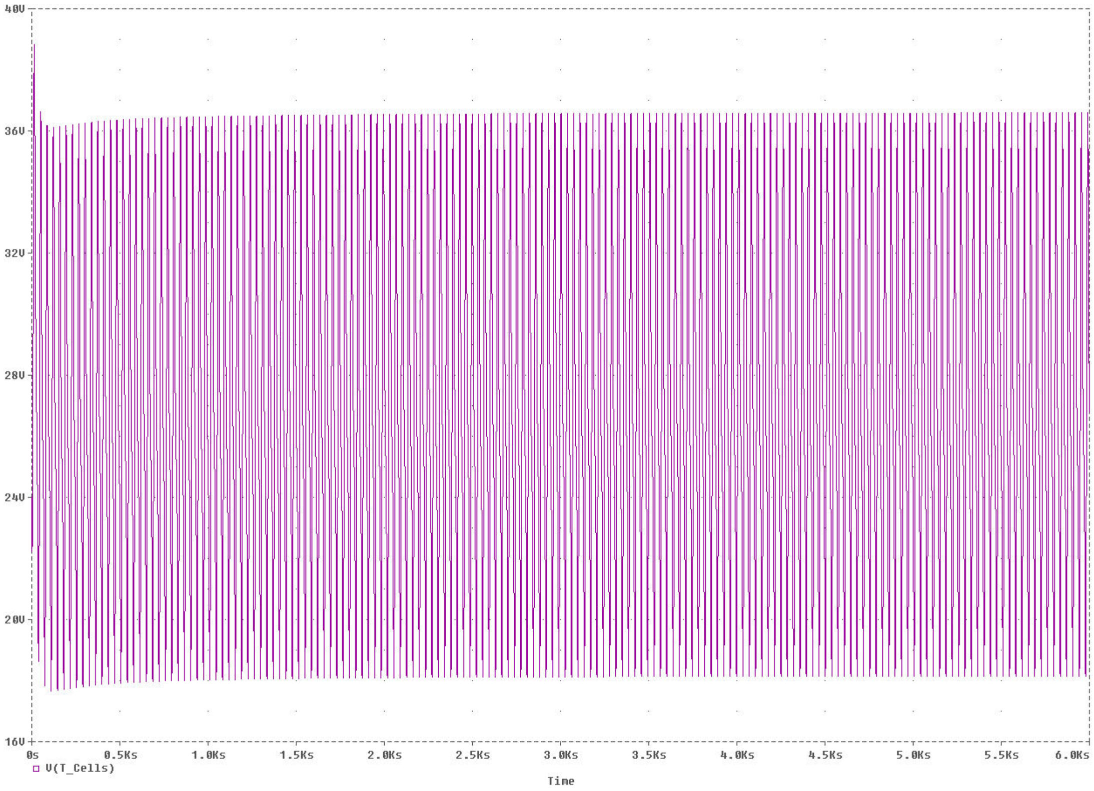

Figure S.11: Thermal profile of TEC photovoltaic cells - rotational velocity 10 deg.s^{-1}

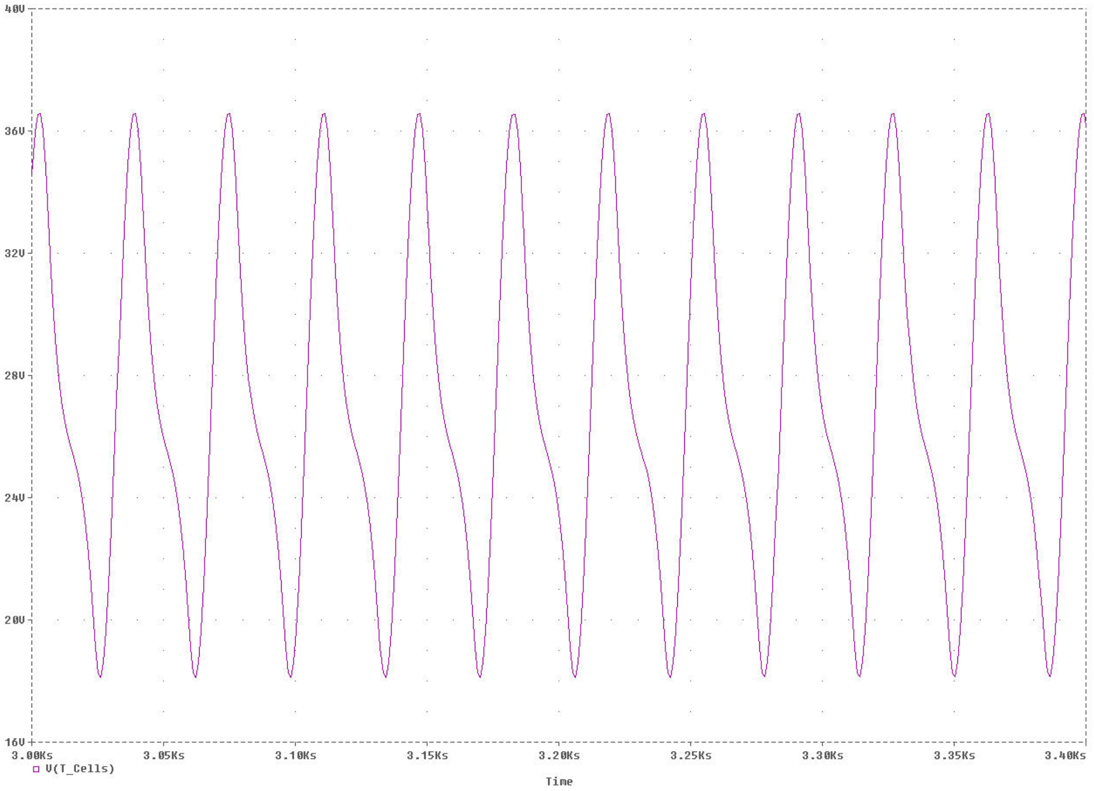

Figure S.12: Close-up of thermal profile of TEC photovoltaic cells - rotational velocity 10 deg.s^{-1}

used to test the behaviour of the TEC cells under influence of a rotational velocity. Note that the constant illumination source represents continuous illumination by solar flux. In figure S.13, the results of the analysis using a constant illumination source are shown.

Investigating figure S.13, it is noticed that the temperature is approaching the maximum temperature

Table S.17: Extreme values of TEC photovoltaic cell temperature - rotational velocity 10 deg.s^{-1}

Parameter	Value
Maximum value of TEC cell temperature	36.6 °C
Minimum value of TEC cell temperature	18.2 °C
Amplitude of TEC cell temperature	18.4 °C

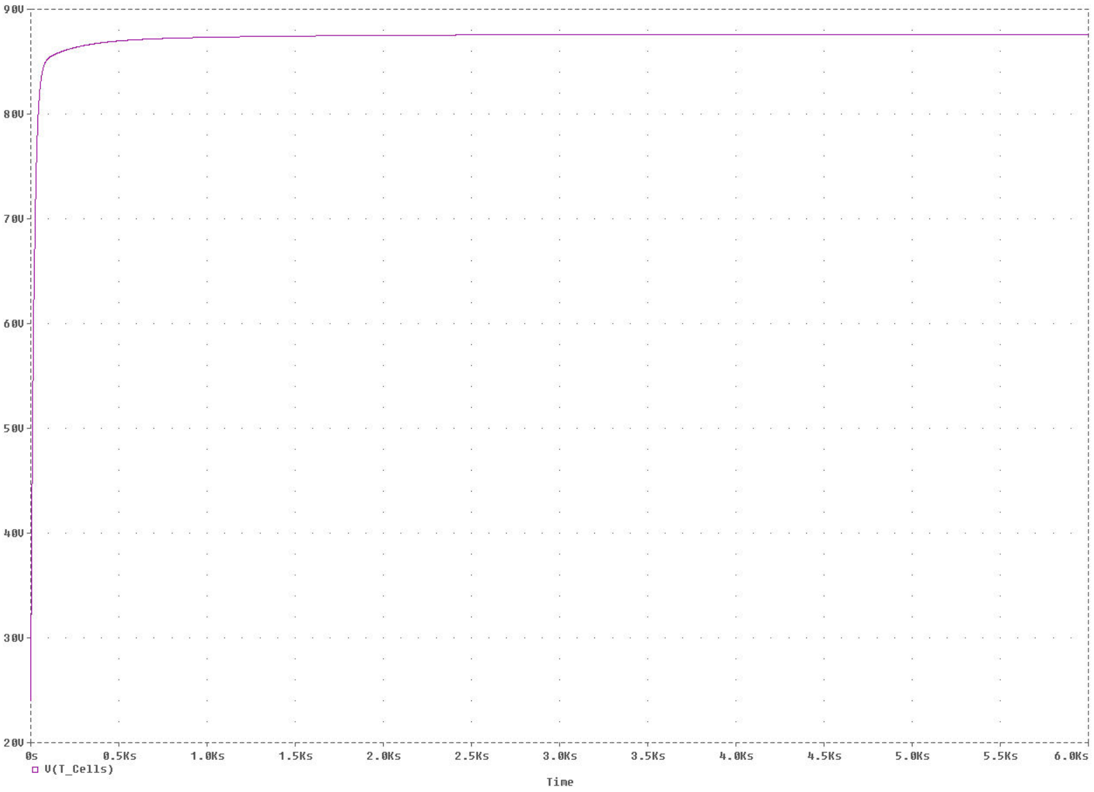

Figure S.13: Thermal profile of TEC photovoltaic cells - constant maximum solar flux

asymptotically. After evaluating this absolute maximum temperature of the TEC cells, it is found to be equal to 87.6 °C.

A similar analysis can be performed for the absolute minimum temperature of the solar array. This situation is modeled by removing the solar flux from the model and implementing a constant albedo source. This represents the situation, in which the solar panel faces the Earth and is completely shadowed by the spacecraft body from solar illumination. In figure S.14, the results of this simulation are shown. By investigating figure S.14, it is noticed that the temperature approaches its absolute minimum value in an asymptotic way. Reading the value of the absolute minimum temperature yields −35.2 °C.

S.2.9 Compliance with complete spacecraft thermal model results

In order to assess the reliability of the results of the thermal analysis, they will be compared to the results of the thermal analysis performed for the complete spacecraft. This latter analysis is performed for various operational scenarios. For reliability purposes, the hottest temperature found in the solar panel simulations will be compared with the hot case temperature of the spacecraft analysis. A similar observation will be done for the coldest temperature in the solar panel analysis and the cold case temperature of the spacecraft analysis.

In table S.18, the cold and hot extremes of both the solar panel analysis and the spacecraft analysis are listed.

Table S.18: Extreme values of TEC photovoltaic cell temperature - rotational velocity 10 deg.s^{-1}

Parameter	Result solar panel analysis	Result spacecraft analysis
Cold case temperature	-35.2 °C	-98.3 °C
Hot case temperature	87.6 °C	83.7 °C

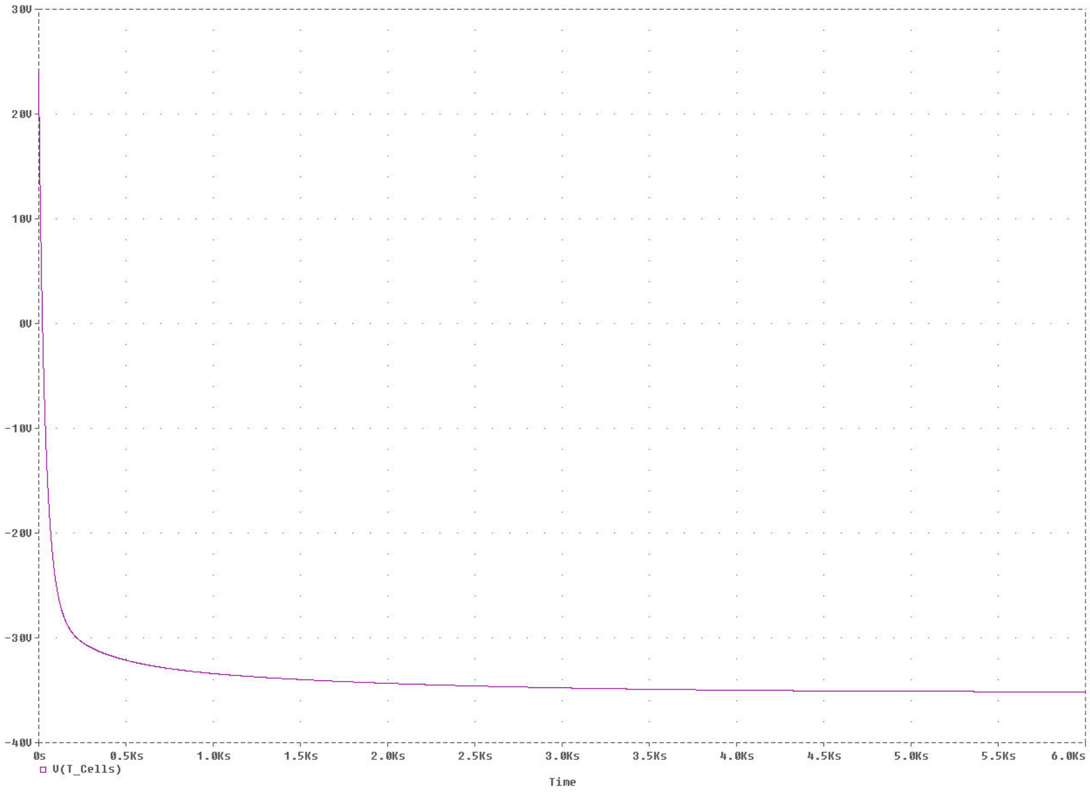

Figure S.14: Thermal profile of TEC photovoltaic cells - no solar flux

Investigating table S.18, it is found that the cold case temperatures in solar panel analysis and spacecraft analysis deviate heftily. On the other hand, the hot case temperatures show reasonably good compatibility.

S.3 Conclusions and recommendations

In this document, the thermal model representing a single Delfi-C3 solar panel is described. An explanation is given of the modeling of the solar panel into thermal nodes. Furthermore, the calculation of the thermal capacitances and thermal resistances in the model is shown. Both solar flux and albedo flux are incorporated in the model as external stimulation sources. Fine tuning of the model is achieved by introducing the influence of the spacecraft body and power flow from the photovoltaic cells.
Several simulations have been performed using this model. These simulations deviate form each other by varying the rotational speed influencing the input waveforms of the solar flux and albedo flux.
In case the rotational velocity of the Delfi-C3 spacecraft is equal to 0.2 deg.s^{-1}, the maximum temperature of the TEC cells will reach 74.1 °C, while the minimum temperature will be equal to -23.3 °C.
In the situation that the rotational velocity equals 10 deg.s^{-1}, the maximum temperature of the TEC cells is equal to 36.6 °C and the minimum temperature equals to 18.2 °C.
Evaluation of the absolute maximum temperature of the TEC cells yields 87.6 °C. For the absolute minimum temperature, the value of -35.2 °C is found.

Appendix T

Production drawings of solar panel components

T.1 TEC Structure

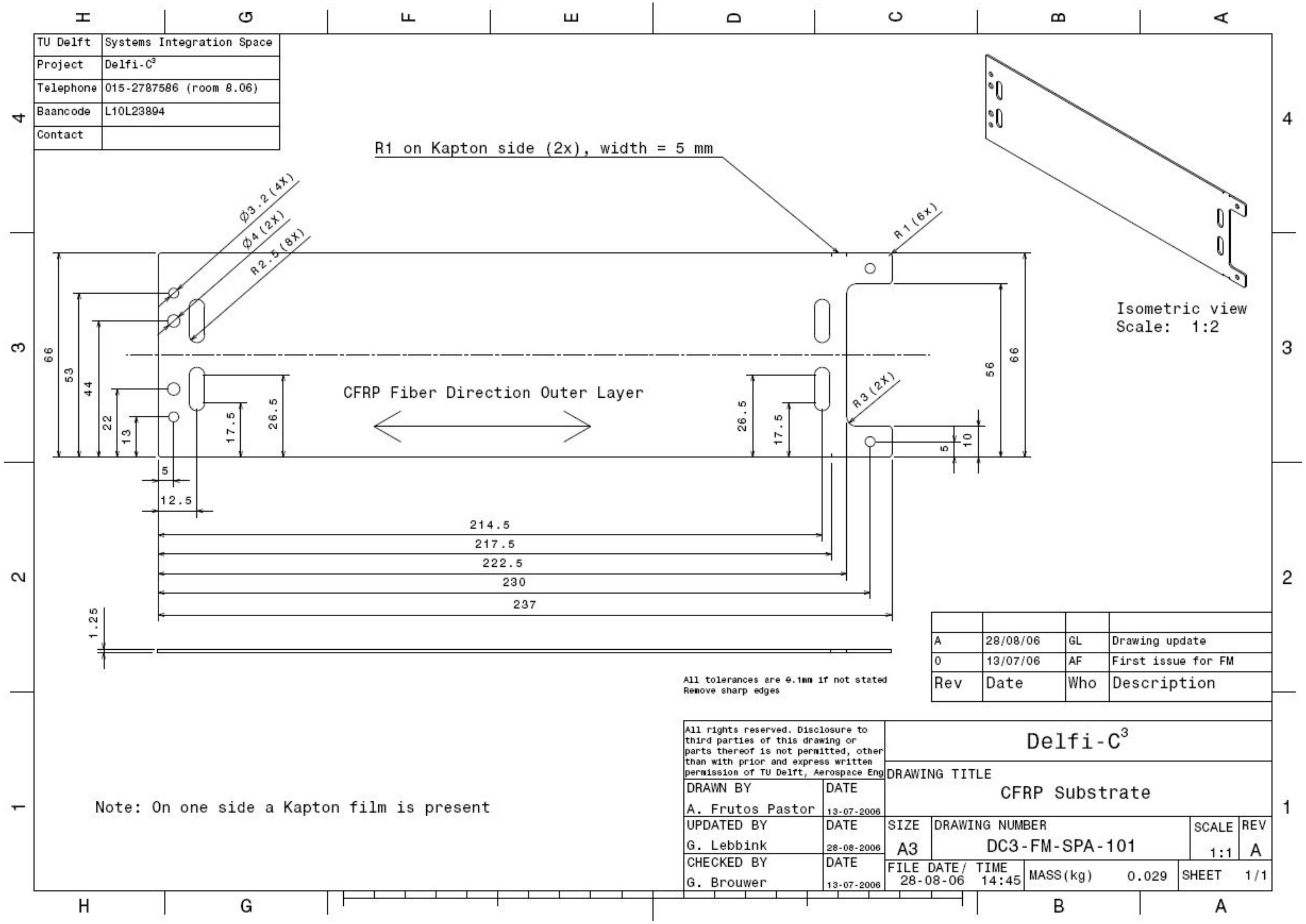
TU Delft
Systems Integration Space
Project
Delfi-C^3
Telephone
015-2787586 (room 8.06)
Baancode
L10L23894
Contact
R1 on Kapton side (2x), width = 5 mm
Ø3.2(4X)
Ø4(2X)
R2.5(8X)
R1(6x)
R3(2X)
Isometric view
Scale: 1:2
CFRP Fiber Direction Outer Layer
66
53
44
22
13
17.5
26.5
26.5
17.5
56
66
5
10
5
12.5
214.5
217.5
222.5
230
237
1.25
All tolerances are 0.1mm if not stated
Remove sharp edges
A
28/08/06
GL
Drawing update
0
13/07/06
AF
First issue for FM
Rev
Date
Who
Description
Note: On one side a Kapton film is present
All rights reserved. Disclosure to third parties of this drawing or parts thereof is not permitted, other than with prior and express written permission of TU Delft, Aerospace Eng
Delfi-C^3
DRAWING TITLE
CFRP Substrate
DRAWN BY
DATE
A. Frutos Pastor
13-07-2006
UPDATED BY
DATE
G. Lebbink
28-08-2006
CHECKED BY
DATE
G. Brouwer
13-07-2006
SIZE
A3
DRAWING NUMBER
DC3-FM-SPA-101
SCALE
1:1
REV
A
FILE DATE/ TIME
28-08-06 14:45
MASS(kg)
0.029
SHEET
1/1
H
G
F
E
D
C
B
A
1
2
3
4

T.2 TFSC Structure

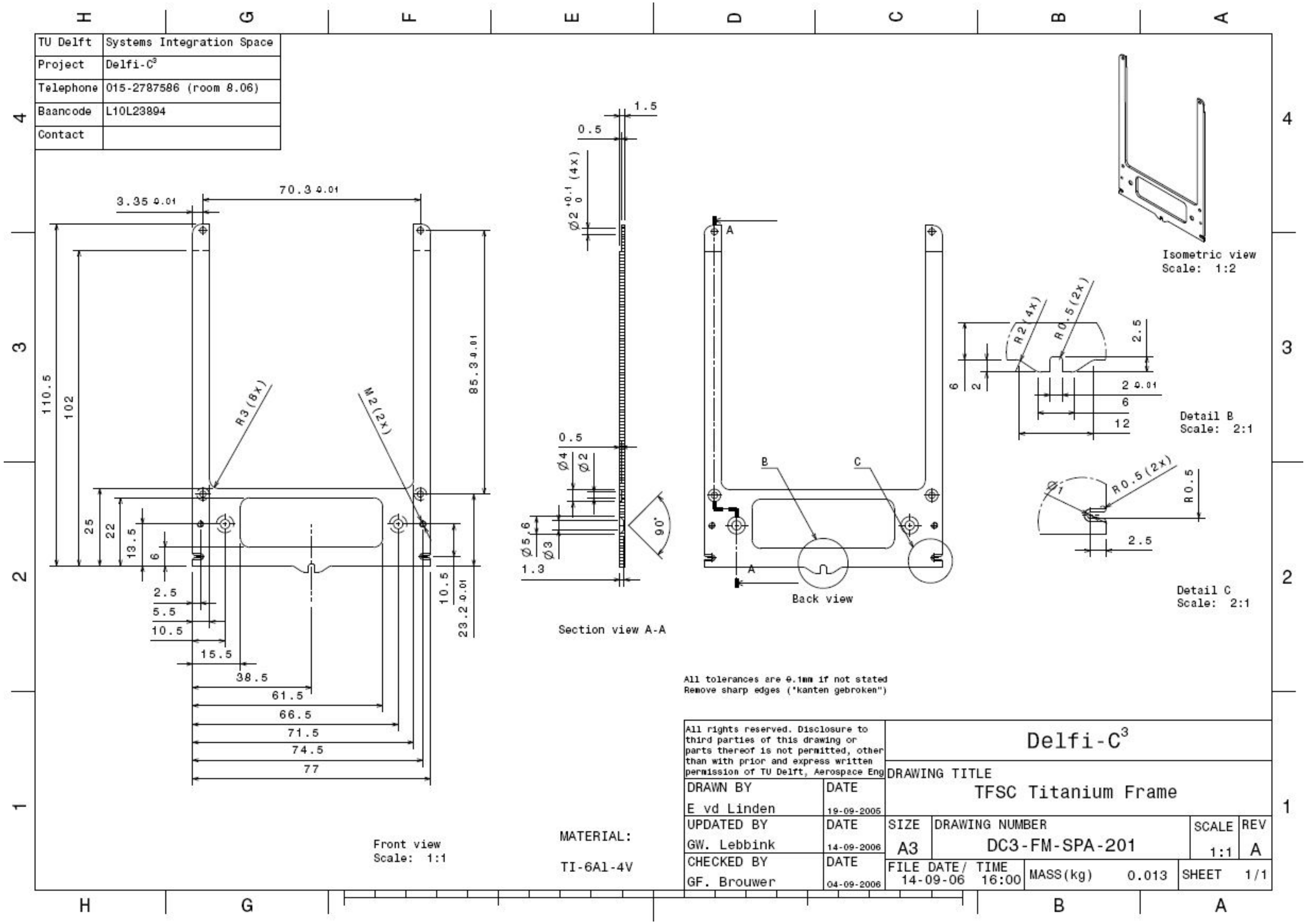
TU Delft
Systems Integration Space
Project
Delfi-C³
Telephone
015-2787586 (room 8.06)
Baancode
L10L23894
Contact
3.35 ±0.01
70.3 ±0.01
110.5
102
25
22
13.5
6
R3 (8x)
M2 (2x)
85.3 ±0.01
10.5
23.2 ±0.01
2.5
5.5
10.5
15.5
38.5
61.5
66.5
71.5
74.5
77
Front view
Scale: 1:1
1.5
0.5
Ø2 +0.1 0 (4x)
0.5
Ø4
Ø2
Ø5.6
Ø3
1.3
90°
Section view A-A
A
B
C
Back view
Isometric view
Scale: 1:2
R2 (4x)
R0.5 (2x)
6
2
2.5
2 ±0.01
6
12
Detail B
Scale: 2:1
Ø1
R0.5 (2x)
R0.5
2.5
Detail C
Scale: 2:1
All tolerances are ±0.1mm if not stated
Remove sharp edges ("kanten gebroken")
MATERIAL:
TI-6Al-4V
All rights reserved. Disclosure to third parties of this drawing or parts thereof is not permitted, other than with prior and express written permission of TU Delft, Aerospace Eng
Delfi-C³
DRAWING TITLE
TFSC Titanium Frame
DRAWN BY
E vd Linden
DATE
19-09-2006
UPDATED BY
GW. Lebbink
DATE
14-09-2006
CHECKED BY
GF. Brouwer
DATE
04-09-2006
SIZE
A3
DRAWING NUMBER
DC3-FM-SPA-201
SCALE
1:1
REV
A
FILE DATE / TIME
14-09-06 16:00
MASS(kg)
0.013
SHEET
1/1
H
G
F
E
D
C
B
A
1
2
3
4

Appendix U

Initial operations timeline

U.1 Scenario #1: Successful deployment - No initial rotational rate

U.1.1 Array power

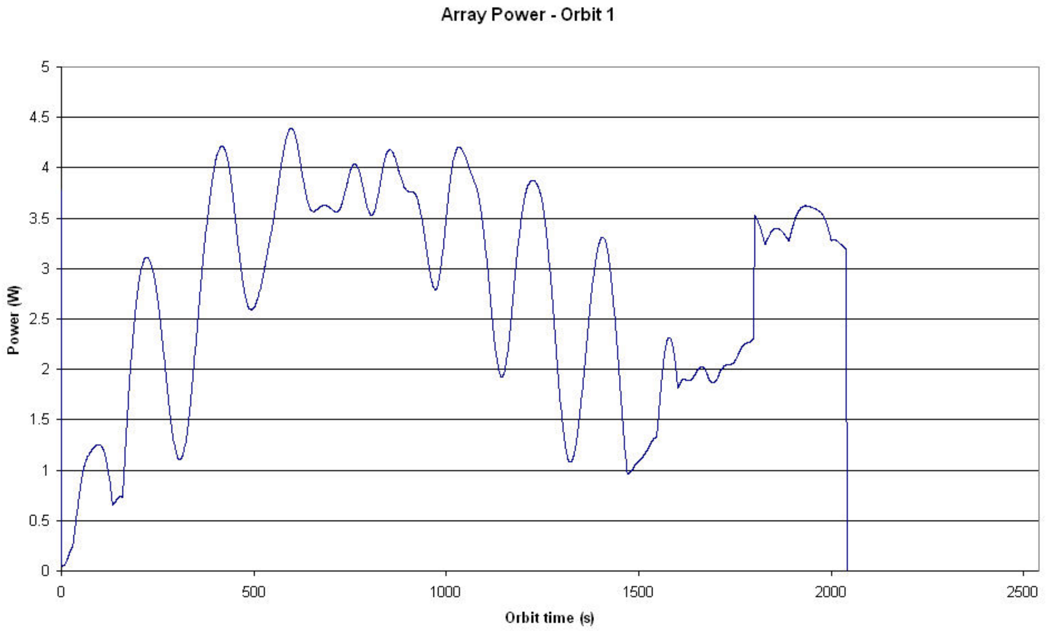

Figure U.1: Scenario 1 - Orbit 1 - Array power

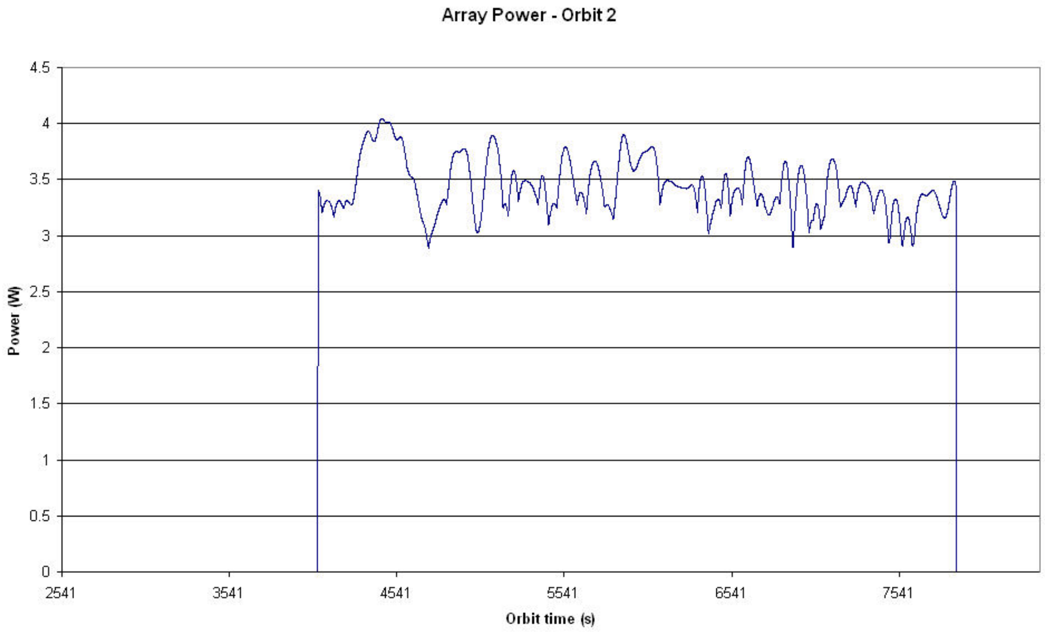

Figure U.2: Scenario 1 - Orbit 2 - Array power

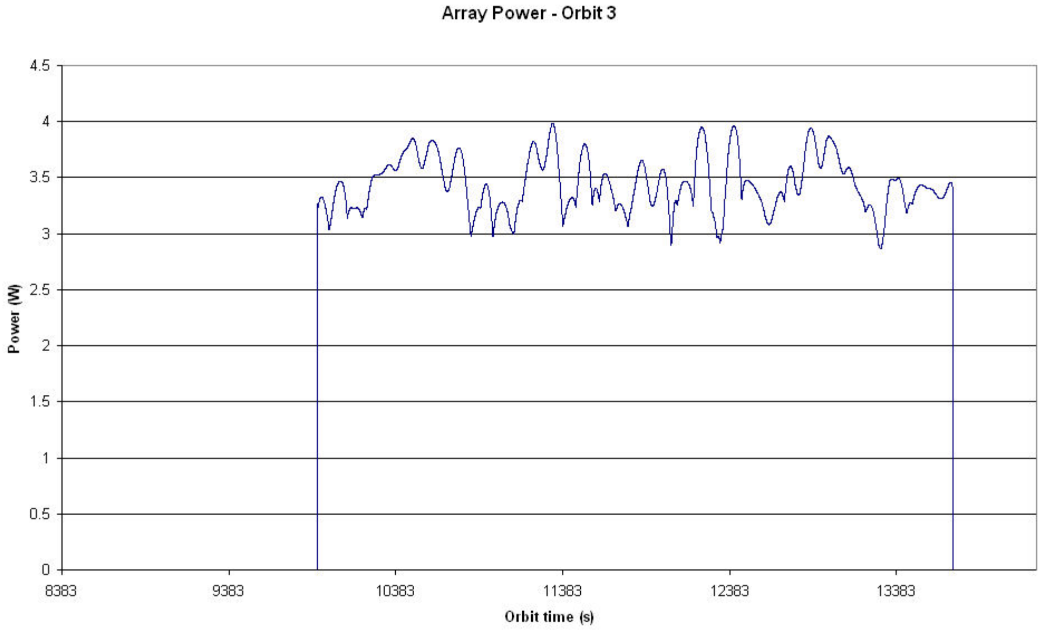

Figure U.3: Scenario 1 - Orbit 3 - Array power

U.1.2 Rotational velocity

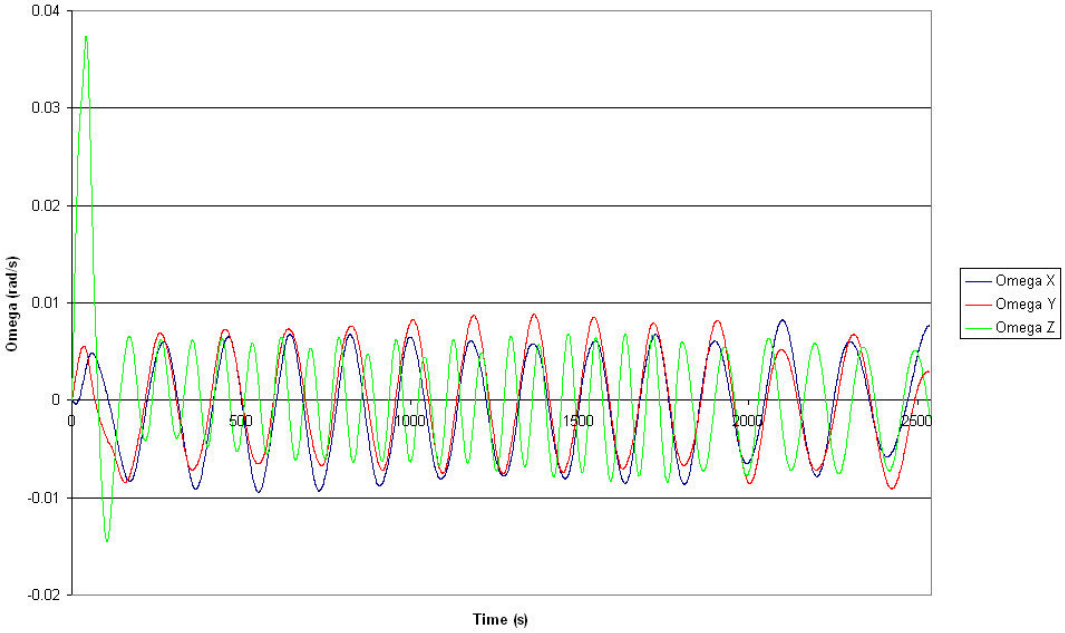

Figure U.4: Scenario 1 - Orbit 1 - Rotational velocity

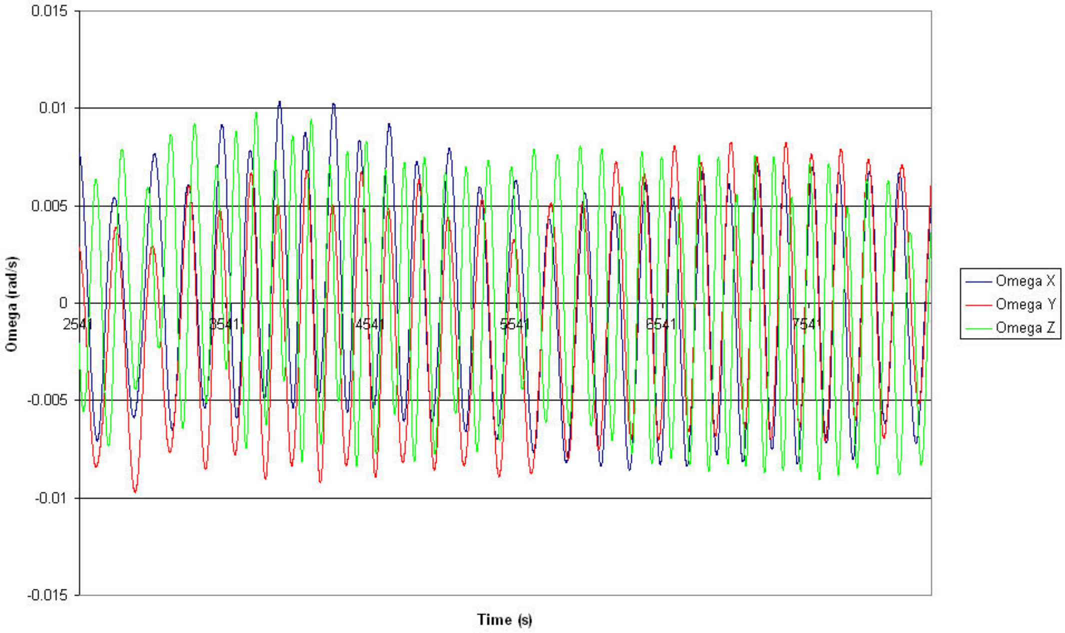

Figure U.5: Scenario 1 - Orbit 2 - Rotational velocity

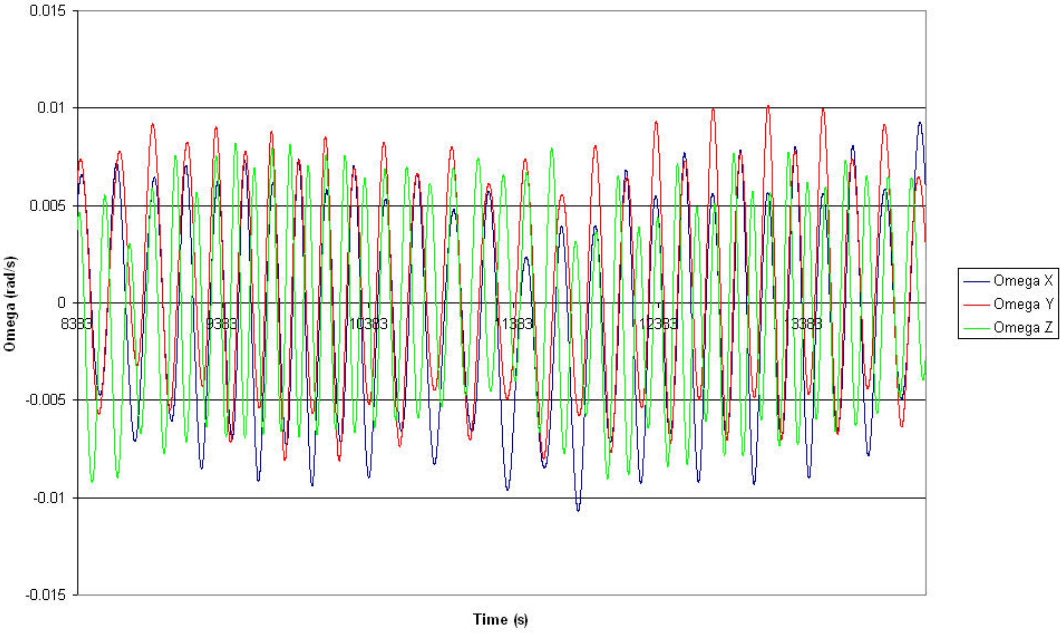

Figure U.6: Scenario 1 - Orbit 3 - Rotational velocity

U.1.3 Rotational speed

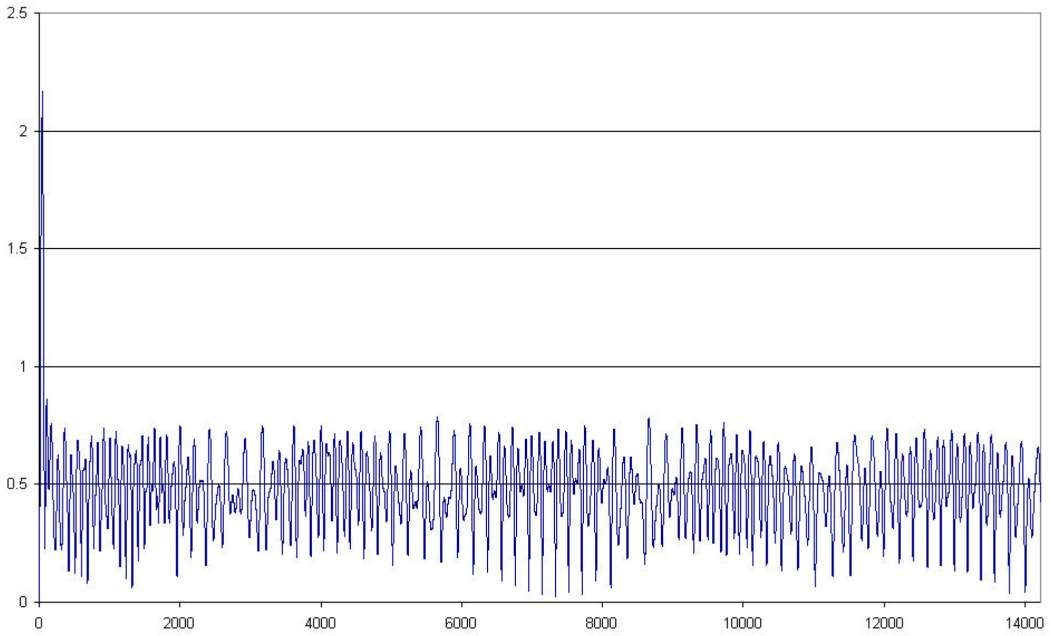

Figure U.7: Scenario 1 - Rotational speed

U.2 Scenario #2: Successful deployment - Maximal initial rotational rate

U.2.1 Array power

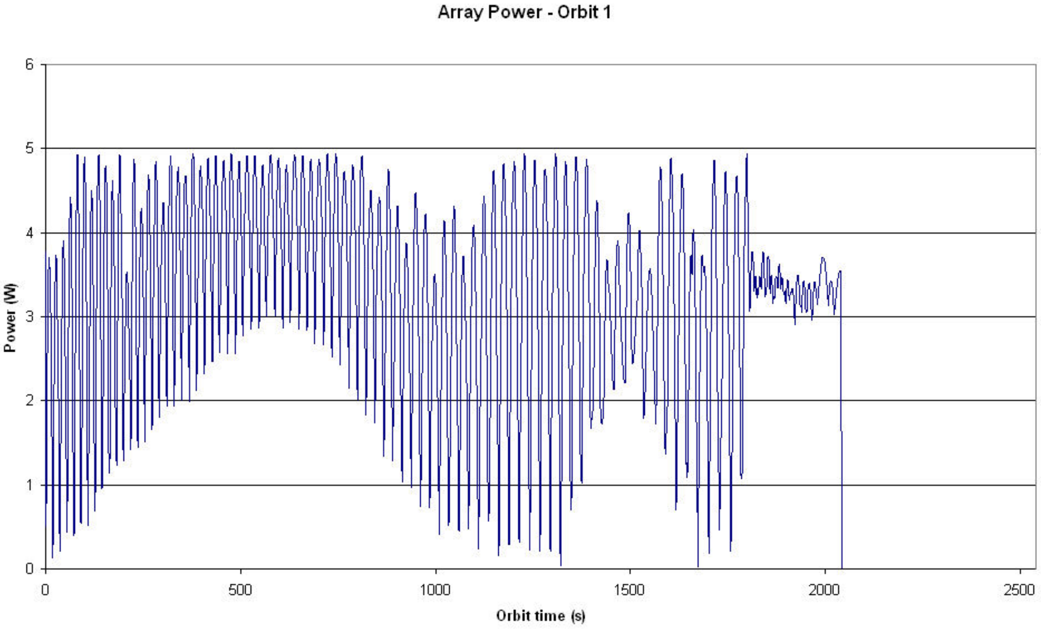

Figure U.8: Scenario 2 - Orbit 1 - Array power

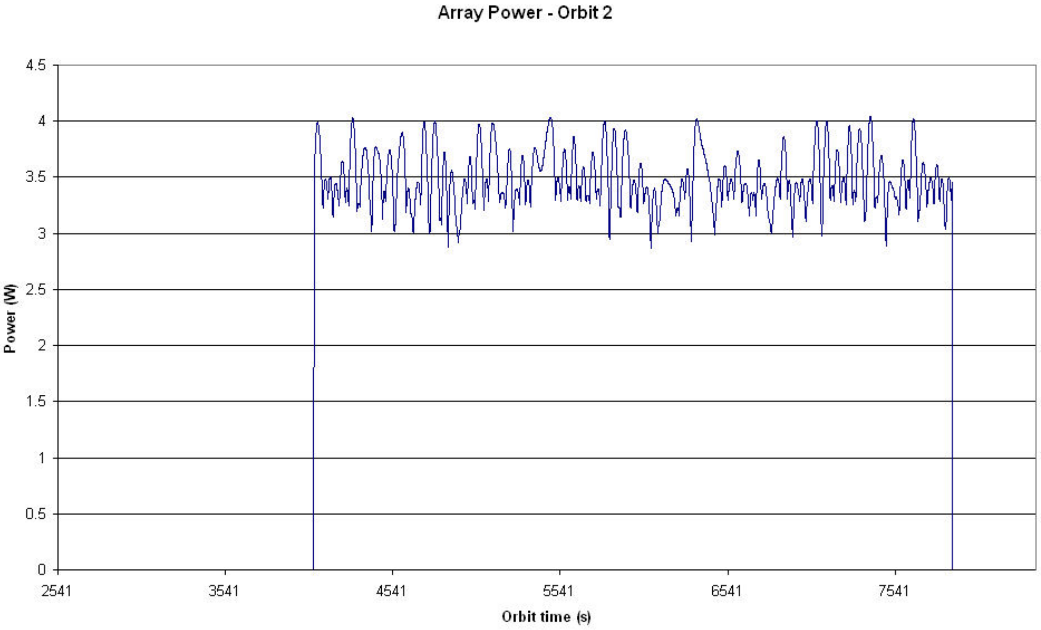

Figure U.9: Scenario 2 - Orbit 2 - Array power

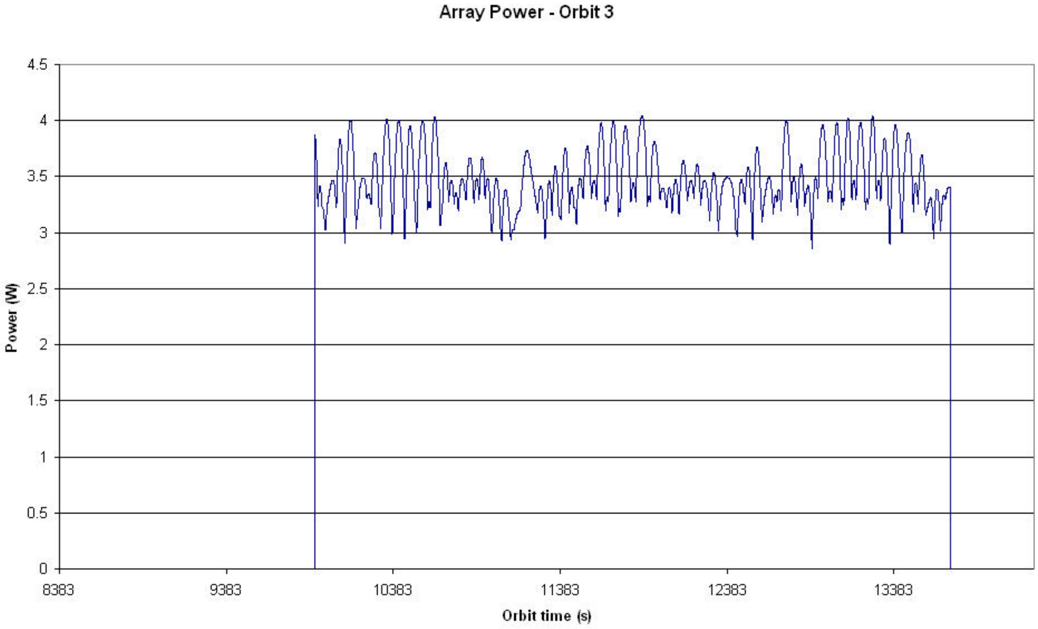

Figure U.10: Scenario 2 - Orbit 3 - Array power

U.2.2 Rotational velocity

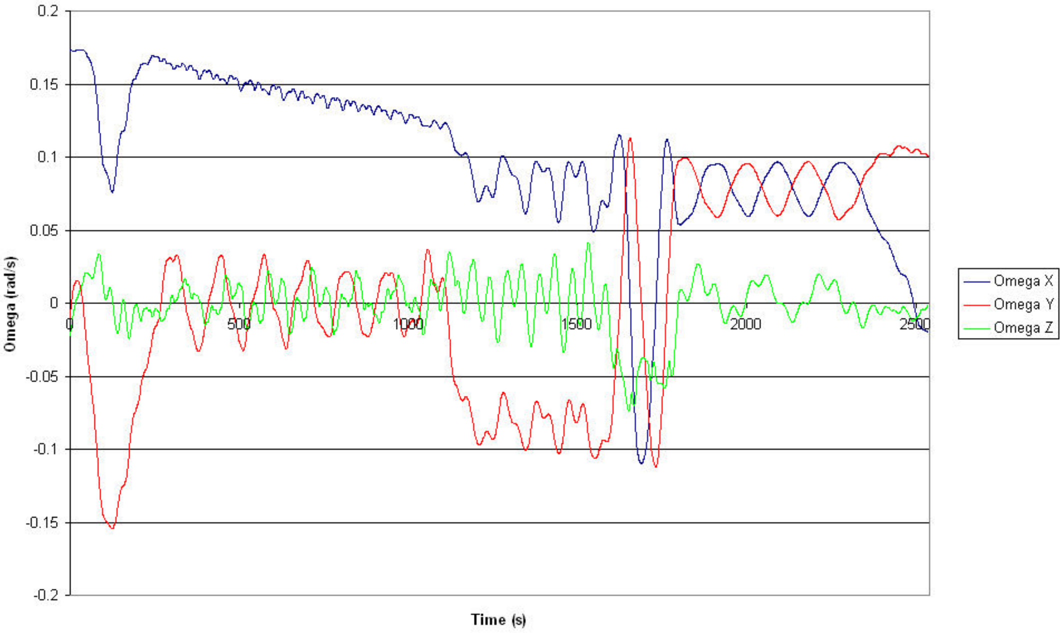

Figure U.11: Scenario 2 - Orbit 1 - Rotational velocity

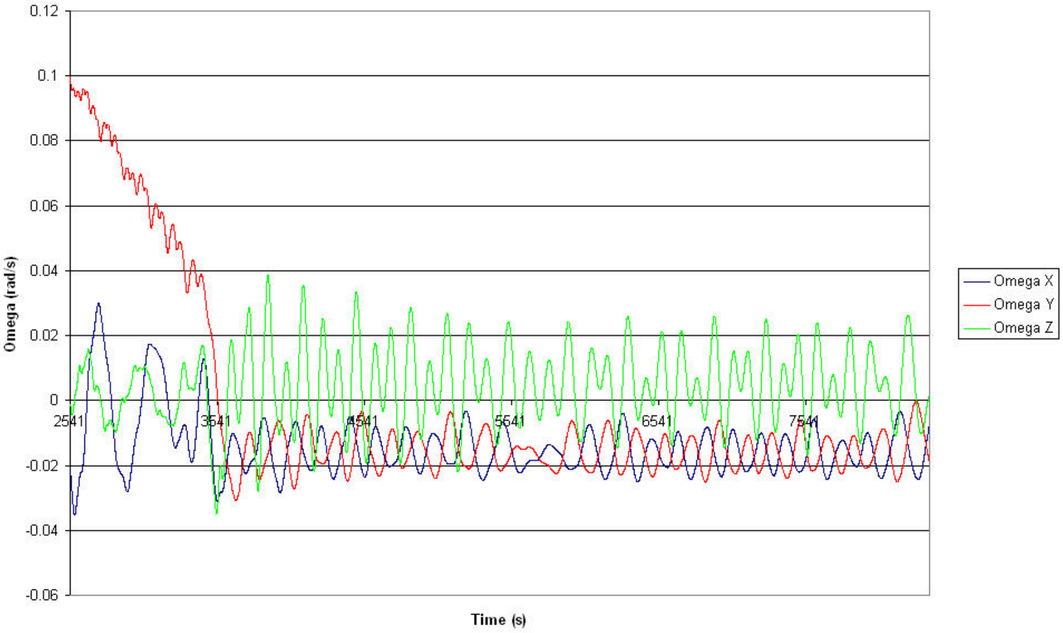

Figure U.12: Scenario 2 - Orbit 2 - Rotational velocity

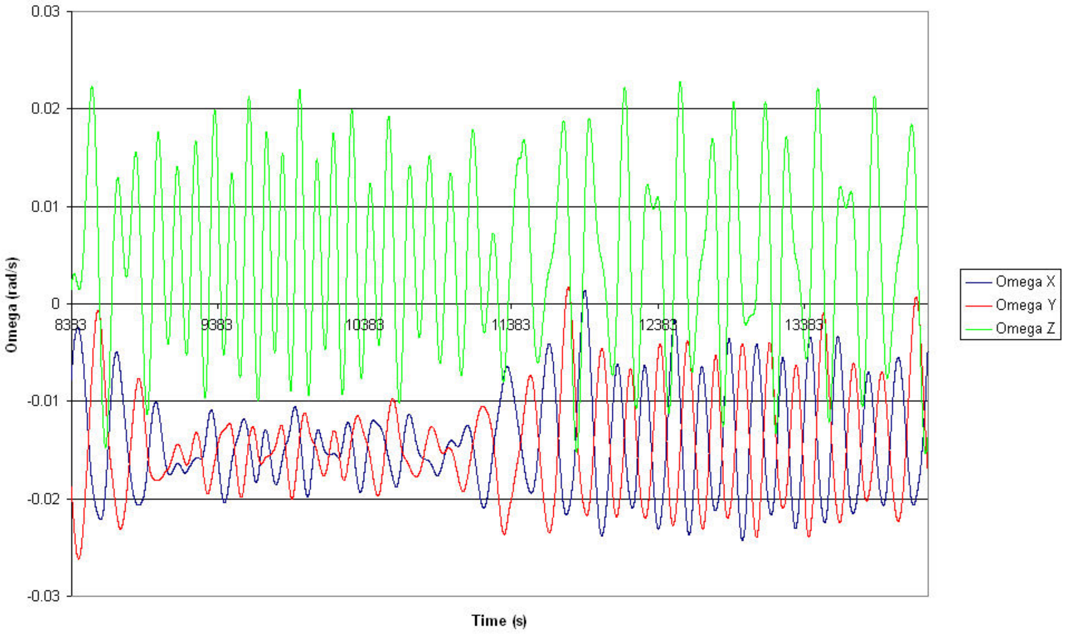

Figure U.13: Scenario 2 - Orbit 3 - Rotational velocity

U.2.3 Rotational speed

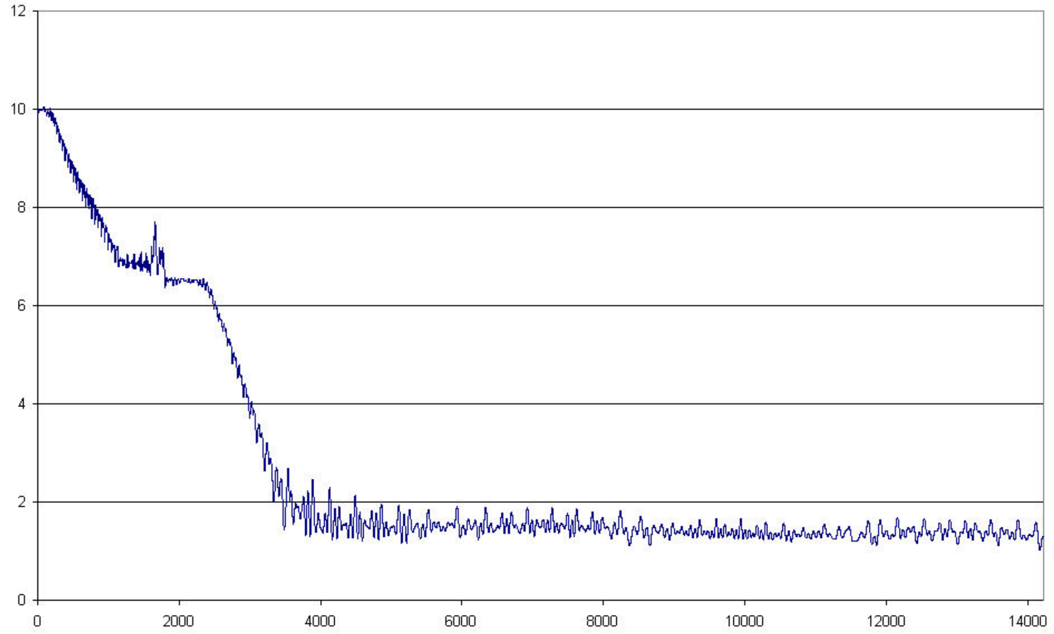

Figure U.14: Scenario 2 - Rotational speed

U.3 Scenario #3: Single deployment failure - No initial rotational rate

U.3.1 Array power

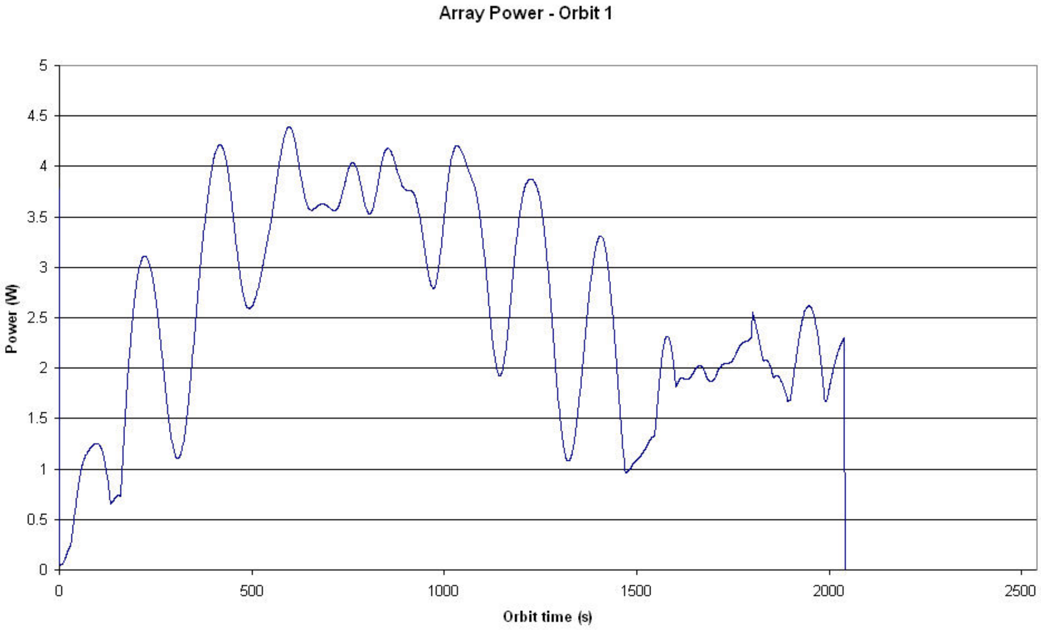

Figure U.15: Scenario 3 - Orbit 1 - Array power

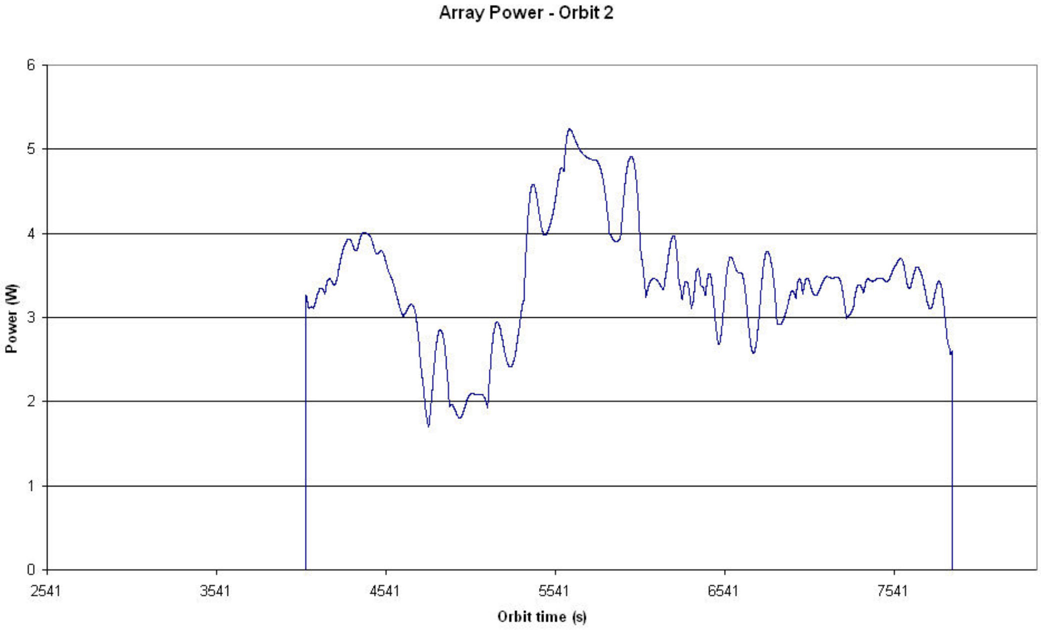

Figure U.16: Scenario 3 - Orbit 2 - Array power

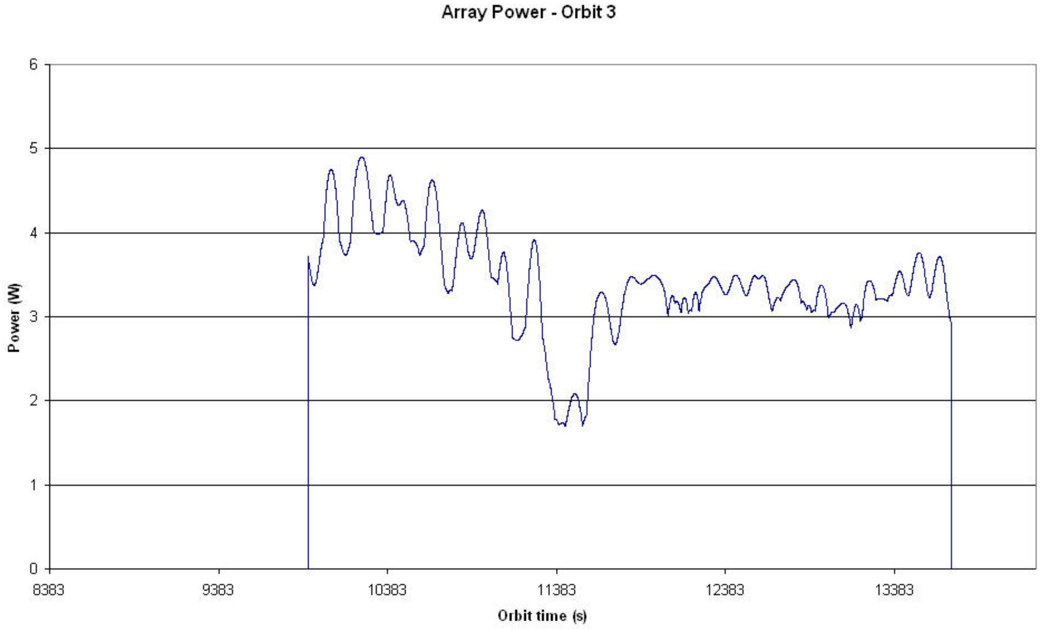

Figure U.17: Scenario 3 - Orbit 3 - Array power

U.3.2 Rotational velocity

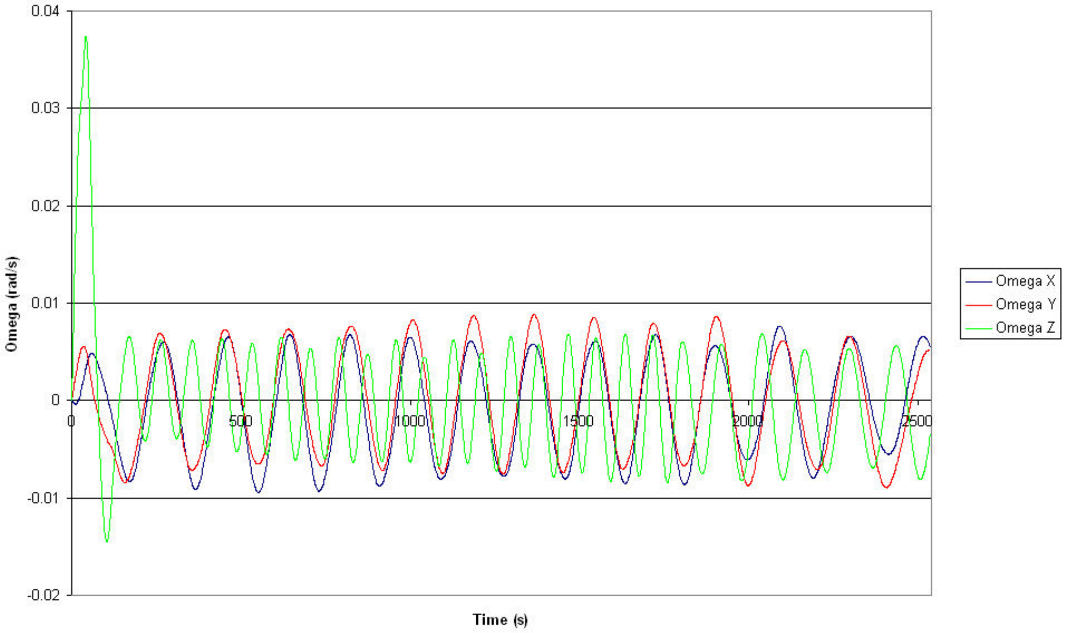

Figure U.18: Scenario 3 - Orbit 1 - Rotational velocity

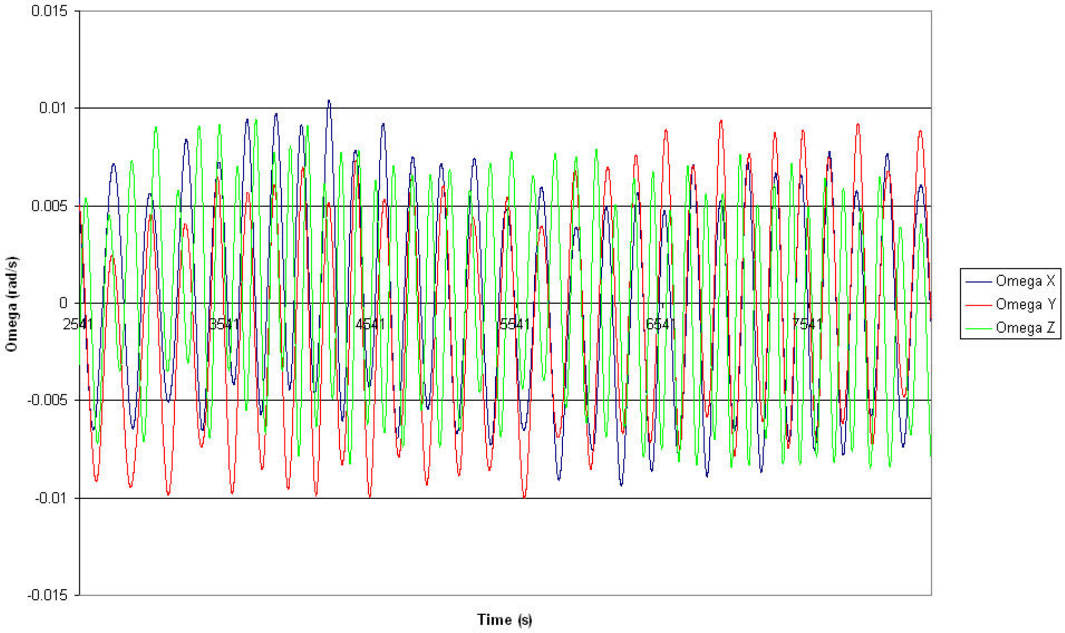

Figure U.19: Scenario 3 - Orbit 2 - Rotational velocity

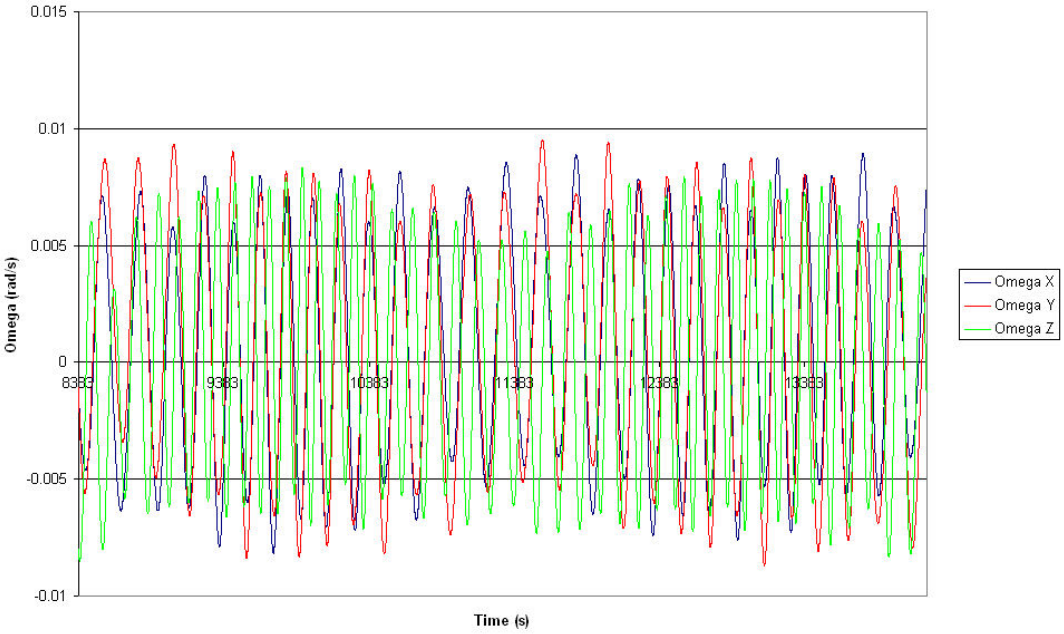

Figure U.20: Scenario 3 - Orbit 3 - Rotational velocity

U.3.3 Rotational speed

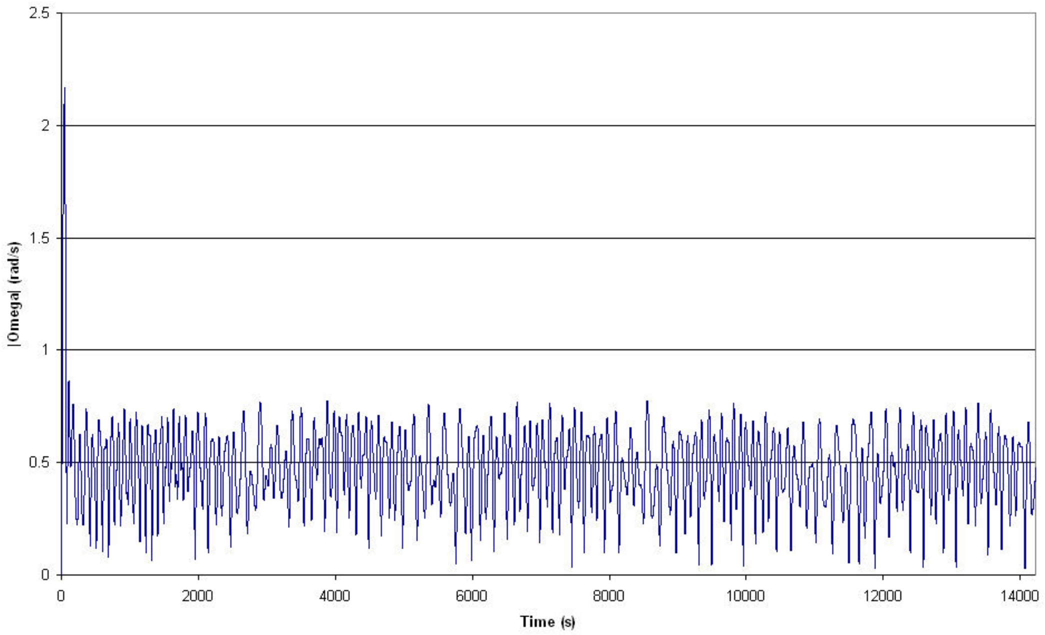

Figure U.21: Scenario 3 - Rotational speed

U.4 Scenario #4: Single deployment failure - Maximal initial rotational rate

U.4.1 Array power

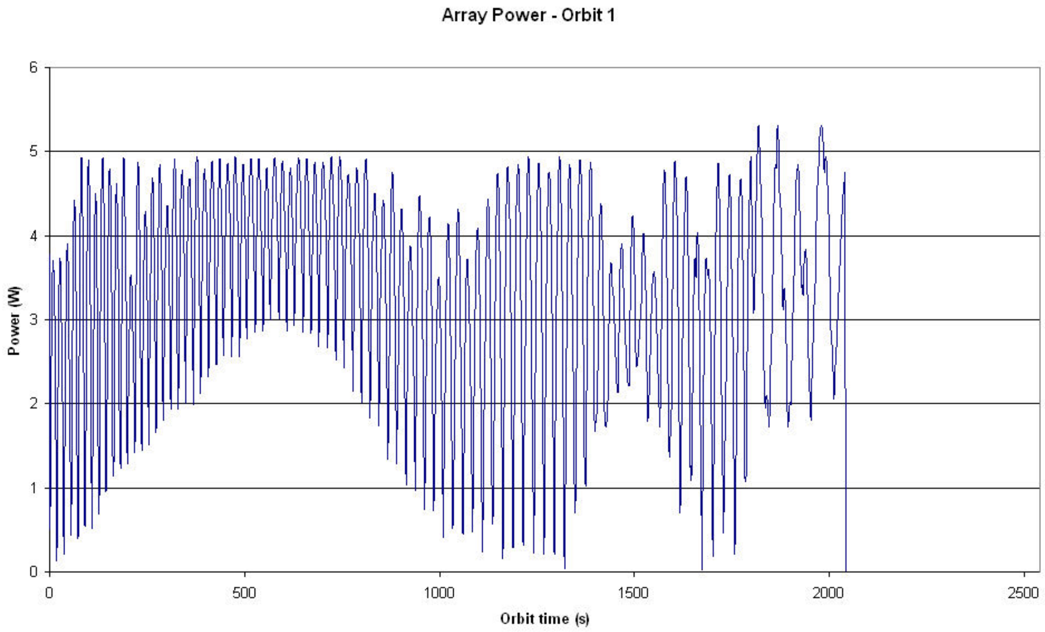

Figure U.22: Scenario 4 - Orbit 1 - Array power

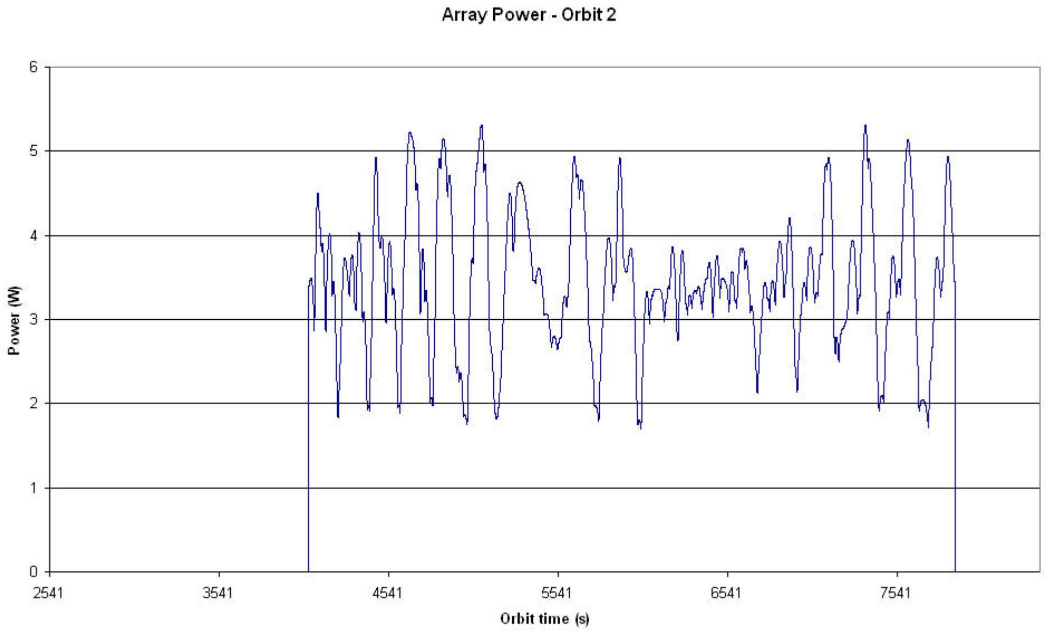

Figure U.23: Scenario 4 - Orbit 2 - Array power

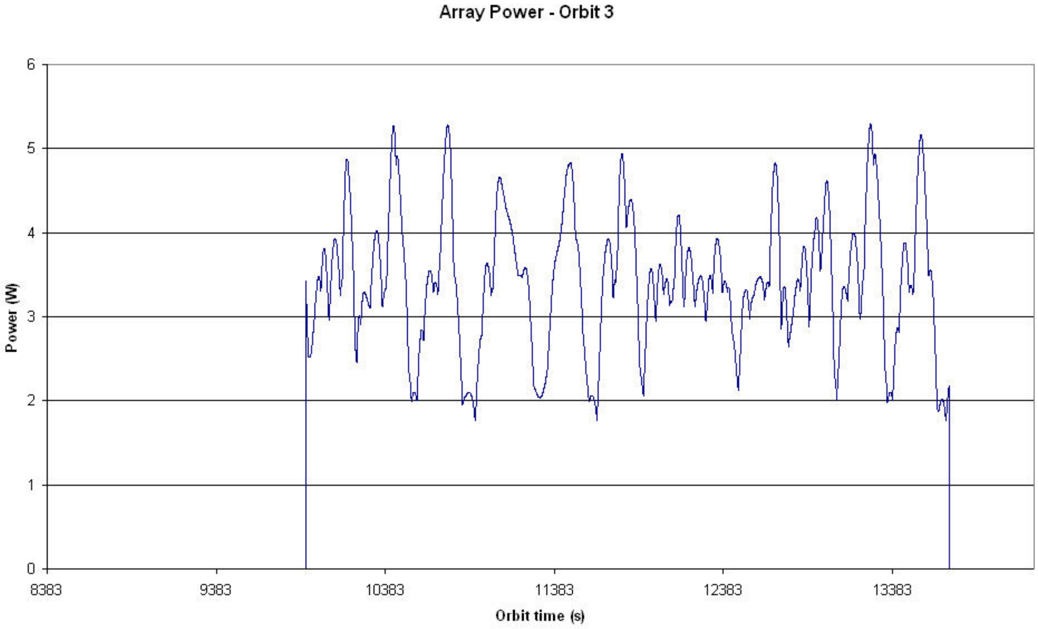

Figure U.24: Scenario 4 - Orbit 3 - Array power

U.4.2 Rotational velocity

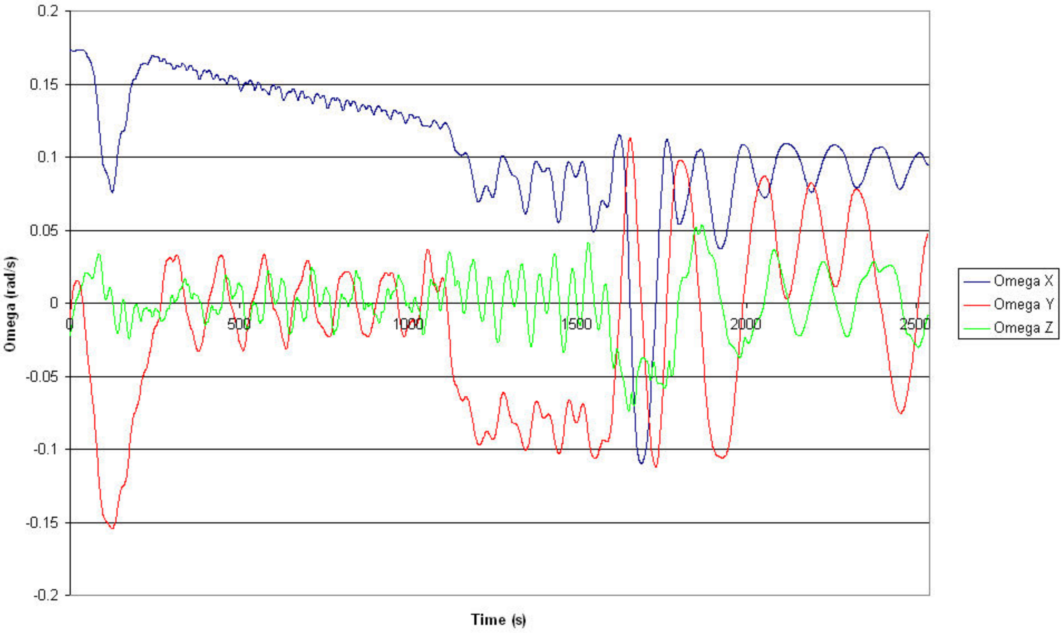

Figure U.25: Scenario 4 - Orbit 1 - Rotational velocity

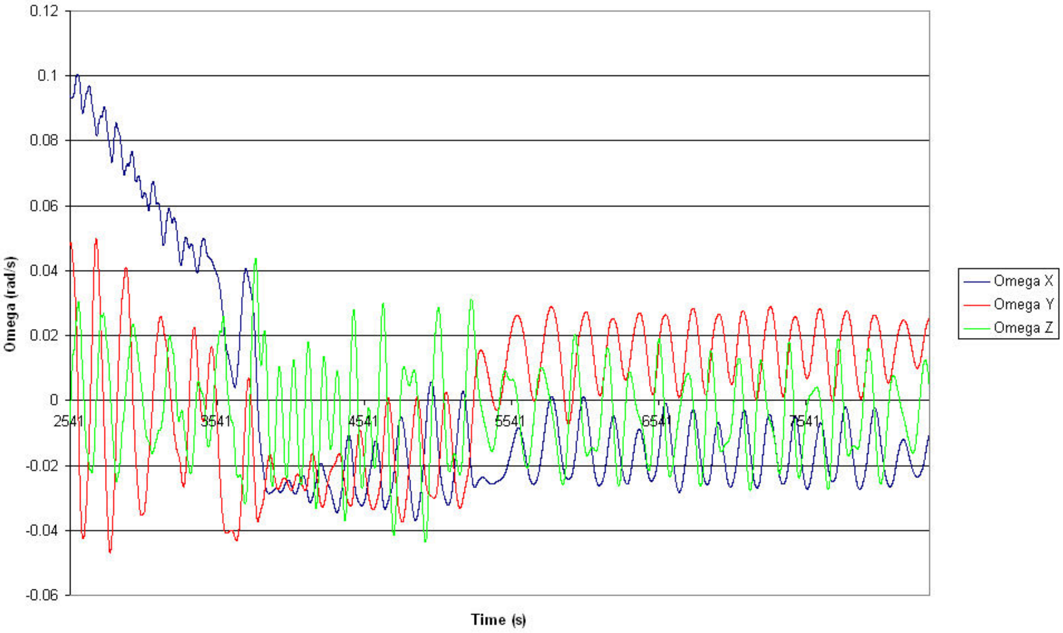

Figure U.26: Scenario 4 - Orbit 2 - Rotational velocity

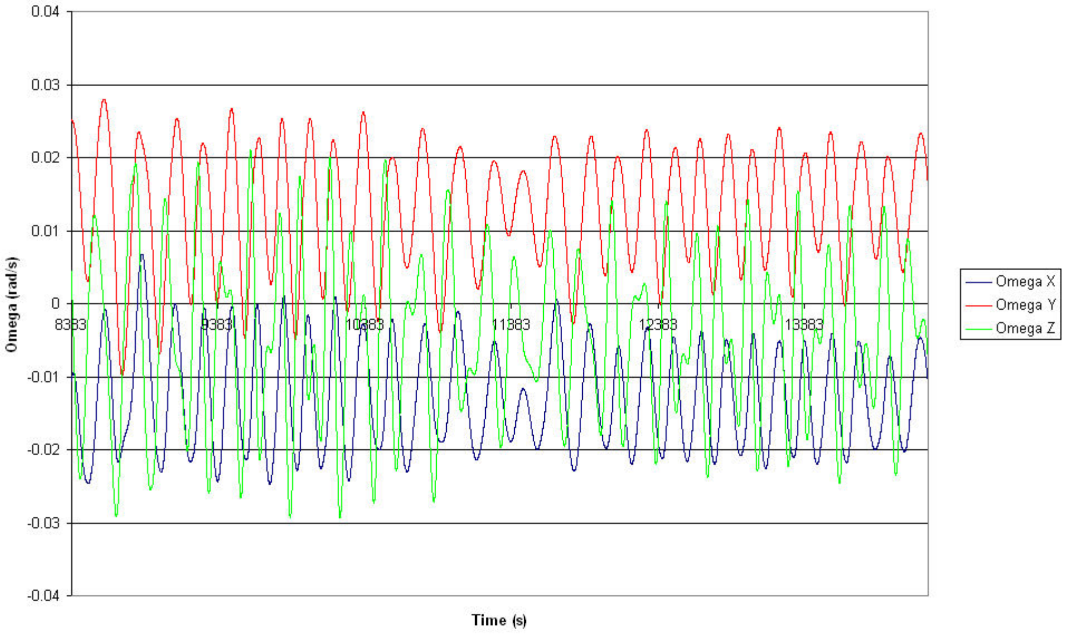

Figure U.27: Scenario 4 - Orbit 3 - Rotational velocity

U.4.3 Rotational speed

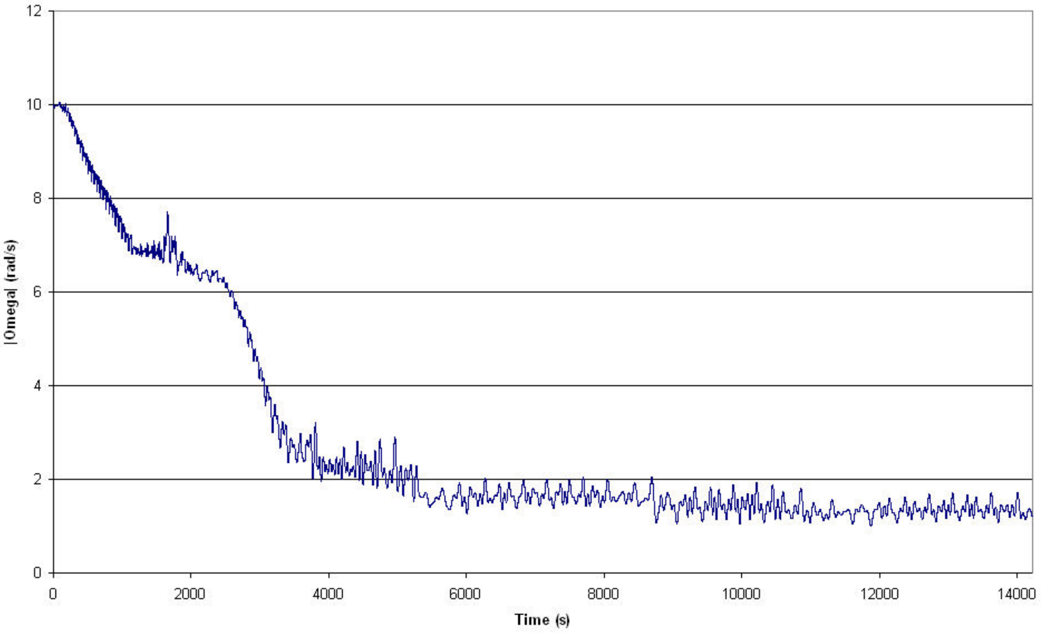

Figure U.28: Scenario 4 - Rotational speed

Appendix V

DC3-TR-703-008
Dummy load board verification

V.1 Introduction

In order to perform a successful verification of the electrical power subsystem board, the output of the converter array on the EPS board has to be connected to a representative load. This load has to be switchable, because it has to be able to simulate a varying electrical load during the start-up sequence. Therefore, use is made of a dummy load board, which imitates the resistive and capacitive impedances of the various loads in the spacecraft. Connecting this board to the electrical power subsystem board would result in a representative setup for verification.

In this document, the verification results of the dummy load board are shown. A comparison will be made of the required impedances of the various load batches and the measured impedances.

V.2 Dummy load board verification

For verification of the electrical power subsystem board, a dummy load board is applied. This board is capable of simulating the various loads in the Delfi-C3 spacecraft. In the current situation, the dummy load board consists of five switchable loads, which each represent a particular batch of loads during the start-up sequence of the spacecraft. In case the Delfi-C3 spacecraft is in orbit, these batches will be switched on sequentially. Simulation by having switchable loads mimics this behaviour in a convenient way.

During design of the dummy load board, the values of the various representative load impedances could be easily found. For the resistances, the values were calculated by:

$$R_{load} = \frac{V_{bus}^2}{P_{load}} \tag{V.1}$$

In this expression, P_{load} is determined with help of the power budget (version 4.2). The input capacitance of the various loads is directly determined by investigating the various schematics corresponding to the design of the printed circuit boards. Summarizing, the input impedances of all load batches in the spacecraft are shown in table V.1

Manufacturing of the dummy load board is performed with thick film resistors with 5% tolerance and tantalum capacitors with 20% tolerance.

In order to use the dummy load board for simulating the spacecraft loads for testing of the electrical power subsystem, the dummy load board will have to be verified.

For additional use, the allocation of the various batches to the switches has to be mentioned. After all, the switches are not sorted in ascending order with respect to switch-on time. In table V.2, a list is shown, in which the allocation of the various switches is depicted. Note that switch #1 is the switch at the left hand side end of the switch box.

For the verification of the resistance, two small tests have been performed. Test one involved measurement of the resistance by using the resistance measurement option on the Tenma 72-7770 digital multimeter. Test two involved connection of the various loads to a 12V bus, and measurement of the steady-state current flowing through this load. Application of Ohm's law will yield the effective resistance of the load. In table V.3, the measured and calculated values of the various resistances are shown.

Table V.1: Impedance values of various load batches

Subsystem	Resistance (Ω)	Capacitance (μF)
Batch 1		
Misc. PIC (#10)	5270	6
OBC	1250	10
RAP Rx	1210	10
ATRX Rx	1210	10
Batch 2		
RAP Tx	76.3	10
Batch 3		
ComBo	1830	10
Batch 4		
MeBo #1	1460	10
Batch 5		
MeBo #2	1460	10

Table V.2: Load batch allocation to the various switches on the dummy load board

Switch	Wire colour	Batch	Subsystems
#1	Brown	#3	ComBo
#2	Red	#2	Rap Tx
#3	Pink	#4	MeBo 1
#4	Yellow	#5	MeBo 2
#5	Green	#1	Misc. PICs, RAP Rx, ATRX Rx, OBC

Table V.3: Measured and calculated resistance of the various dummy load batches

Batch	Switch	Required R (Ω)	Measured R (Ω)	Measured I (mA)	Calculated R (Ω)
#1	#5	378.4	390	30.74	390.4
#2	#2	76.3	75.2	156.0	76.9
#3	#1	1830	1743	6.90	1739
#4	#3	1460	1495	8.04	1494
#5	#4	1460	1495	8.04	1494

Verification of the applied capacitances cannot be easily achieved by a simple measurement, as this would require uncommon capacitance meters. However, a less accurate but easier option of determining the capacitance is the inspection of the used components during manufacturing of the dummy load board. The results of this inspection are listed in table V.4.

Note: During measurements, it was noticed that results would vary if different multimeters were used for determining resistance and current. Therefore, it is advised to check the accuracy of the digital multimeters.

Table V.4: Inspected capacitance of the various dummy load batches

Batch	Switch	Required C (μF)	Inspected C (μF)
#1	#5	36	36.8
#2	#2	10	10
#3	#1	10	10
#4	#3	10	10
#5	#4	10	10

Comparing the required values of the resistances with the measured values in the dummy load board, it is noticed that these coincide fairly well. Furthermore, a comparison between the inspected values and required values of the capacitances results in a very good match.

V.3 Conclusions and recommendations

In this document, the results of the verification of the dummy load board are described. The resistance and capacitance values of the various dummy load batches on the dummy load board are measured. Furthermore, they are compared to the required values. Concluding, the matching between required and measured values was in general rather good.

Appendix W

Electrical power subsystem requirements

Appendix X

Test procedure for the centralized electrical power system

Appendix Y

Example test procedure for the decentralized electrical power system

1 Electrical Power Subsystem Requirements

1.1 General Requirements and Constraints

1.1.01 Characteristic Units

<Deleted>

1.1.02 EPS Components

The EPS shall consist of 4 strings of GaAs solar cells (1 string per panel) and the necessary control electronics and wiring harness.

1.1.03 EPS Electronics Mass

The EPS electronics mass shall not exceed 150g.

1.1.04 Solar Panel Mass

The accumulated solar panel mass shall not exceed 370g including margins and TFSCs subsystem.

1.1.05 Solar Panel Envelope

The solar panels shall fit within a dynamic envelope of 340x87.7x8.7 mm (LxWxT) including margins and TFSCs subsystem, as specified in the P-POD specifications.

1.1.06 Solar Panel Thermal Envelope

<Moved to TCS> (-55 C < T < 55 C)

1.1.07 Solar Cells Area

<Deleted>

1.1.08 Solar Cells Thermal Envelope

<Moved to TCS> (-55 C < T < 55 C)

1.1.09 EPS Electronics Volume

<Deleted>

1.1.10 EPS Electronics Thermal Envelope

<Moved to TCS> (-25 C < T < 40 C)

1.1.11 Wiring Harness Loops

The EPS wiring harness loops shall have a minimized enclosed area.

1.2 Functional Requirements

1.2.01 Power Distribution

The EPS shall be able to provide power to subsystems when not in eclipse/off mode.

1.2.02 Power Switching

The EPS shall be able to switch power supplied to all subsystems, except for the RAP and ATRX receivers, the OBC and the Watchdog.

1.2.03 **Power Dissipation**

The EPS shall be able to dissipate excess power.

1.2.04 **Power Storage**

The EPS shall not include primary batteries.

1.2.05 **Bus Voltage Regulation**

The EPS shall be able to regulate bus voltages.

1.2.06 **Bus Voltage Monitoring**

The EPS shall be able to monitor bus voltages and supply this data to the CDHS.

1.2.07 **Current Monitoring**

The EPS shall be able to monitor currents from each individual solar panel.

1.2.08 **Overcurrent Protection**

The EPS shall include overcurrent protection on all independent power supply lines within the satellite.

1.2.09 **Undervoltage Protection**

<Deleted>

1.2.10 **EMI/RFI Suppression**

The EPS shall include EMI/RFI suppression for all subsystems.

1.2.11 **Transient Suppression**

The EPS shall include transient suppression for all subsystems.

1.2.12 **Fault Tolerance**

<Deleted>

1.2.13 **GaAs Solar Cell Reversed Power Protection**

<Deleted>

1.2.14 **GaAs Solar Cell Failure**

A solar cell string shall be capable of providing power in case of failure of one cell.

1.3 Performance Requirements

1.3.01 **Minimum Power**

The EPS shall deliver a minimum of 2.6 W in normal operations.

1.3.02 **Bus Voltage**

The EPS shall regulate the bus voltage to a standard of 12.0 V +/- 0.48 V.

1.3.03 **COMMS Bus Voltage**

<Deleted>

1.3.04 **Bus Voltage Measurement Accuracy**

The bus voltage shall be determined with an accuracy better than 50 mV.

1.3.05 **Current Measurement Accuracy**

The current delivered by each individual solar panel shall be determined with an accuracy of at least 10 mA.

1.3.06 **Mechanical loads**

<Moved to System Requirements>

1.4 RAMS Requirements

<Moved to System RAMS Requirements>

1.5 Operational Requirements

1.5.01 **Autonomous Operations**

The EPS shall operate autonomously.

1.5.02 **Autonomous Wake-up**

The EPS shall wake up autonomously after power interruption through the use of POR circuitry.

1.5.03 **Operational Modes**

The EPS shall deliver power in all operational modes of the satellite.

1.6 Interface Requirements

1.6.01 **Detachable panels**

The solar panels shall be detachable from the satellite structure.

1.6.02 **Subsystems Interface**

The EPS shall interface with other subsystems as specified in the ICD.

1.6.03 **Triple Junction Cells Mounting**

The GaAs solar cells shall be mounted on a deployable panel

1.6.04 **Solar Panel Mounting**

<Moved to STS requirements>

1.6.05 **TFSC Structure Support**

<Moved to STS requirements>

1.7 Testing Requirements

1.7.01 **Operational Modes Testing**

The EPS shall be tested for all operational modes as specified in the AIV Plan.

1.7.02 **GaAs Power Cell Testing**

Each string of power cells shall be functionally tested before and after integration.

1 Introduction

In order to check the operation of the Electrical Power Subsystem (EPS) board, several tests have to be performed. After all, it has to be made sure that the EPS board is capable of providing sufficient power to the spacecraft systems under all realistic circumstances. The variety in in-orbit circumstances will be caused by differences in illumination conditions, thermal conditions, and connected impedance. Therefore, functional, performance and environmental tests have to be accomplished. Furthermore, several general characteristics of the board have to be practically determined to ensure compliance with the various system budgets.

In this document, an outline will be given of the test procedure for the EPS board. The various test resources needed to perform the test successfully are summed and briefly described. Furthermore, the various tests to be accomplished are extensively illustrated. A test procedure is given to ensure a correct order of the performed tests, and to identify possibilities of performing multiple tests simultaneously.

After this introduction, the various test resources required for the testing of the EPS board are described in chapter 2. In chapter 3, a description of the various tests of the EPS board is given. A test matrix, which illustrates the order of testing is given in chapter 4. A description of the test criteria is shown in chapter 5. Finally, in chapter 6, several conclusions and recommendations accompanying the test procedure of the EPS board are mentioned.

2 Test resources

In this chapter, a brief description will be given of all resources involved in the testing of the Electrical Power Subsystem board. These resources can be divided into three categories: locations, equipment, and personnel.

2.1 Locations

At a basic level, only two locations will be used for performing the subsystem level tests of the Electrical Power Subsystem board. These are:

- EEMCS
  Delft University of Technology, Faculty of Electrical Engineering, Mathematics, and Computer Sciences, 18th floor, room …..
- AE
  Delft University of Technology, Faculty of Aerospace Engineering, 8th floor, room 8.01

In general, due to the abundance of test equipment present, performance testing will be accomplished at EEMCS. However, the presence of a thermal vacuum chamber dictates that functional and environmental testing will be done at AE.

2.2 Equipment

In order to successfully perform tests on the Electrical Power Subsystem board, various measuring and stimulating equipment has to be used. These are briefly described in the following sections.

2.2.1 Mechanical equipment

- Ruler
  This device is a commonly available simple ruler, which can be used for determining dimensions of geometrical bodies. It is available at both EEMCS and AE.

- Scales
  This device is a commonly available set of digital scales, which can be used for determining the mass of a geometrical body. It is available at both EEMCS and AE.

2.2.2 Environmental control equipment

- Thermal vacuum oven
  This facility is a confined environment, which can be pumped vacuum on demand. Furthermore, the temperature of this environment can be raised above nominal room temperature. For these reasons, it can be applied to test the Electrical Power Subsystem board for functional operation in vacuum and high temperature conditions. This facility is available at AE.

- Transverse electromagnetic cell
  This facility is a confined environment, which is electromagnetically isolated from its surroundings. It can be used to separate the electromagnetic radiation generated by an individual electrical part from the surrounding radiation. Moreover, adding an external source to the chamber will lead to a determinable reaction of the primary part to this specific source. This facility is available at EEMCS.

- Solar cannon

This facility consists of a large lamp, which is capable of producing illumination comparable to solar illumination. This comparability exists in both electromagnetic spectrum and power density. It can be used to illuminate solar panels in order to encourage them to produce electrical power. This action can be used for testing the response of the Electrical Power Subsystem board to realistic power inputs from the solar panels. This facility is available at AE.

2.2.3 Electrical measuring equipment

- Digital multimeter
  This device is a commonly available simple digital multimeter, which can be used for measuring DC voltages and currents. It is restricted to measuring only a single quantity at a time, but can be flexibly applied for quick checks of voltages and currents. It is available at both EEMCS and AE.

- Oscilloscope
  This device is a commonly used oscilloscope, which can be used to visualize voltages and currents in the time domain. An available oscilloscope is the Fluke PM3082, which has four channels. This means it is able to measure and visualize four signals at a time. It is available at both EEMCS and AE.

- Spectral analyzer
  This device is a commonly used spectral analyzer, which can be used to visualize voltages and currents in the frequency domain. It is capable of performing a Fourier analysis on a signal and splitting it into signals in a frequency range of 50Hz to 1800MHz. It is available at EEMCS.

2.2.4 Electrical stimulating equipment

- 12V DC Power supply
  This device is a generic direct current power supply. It can be set to generate a 12V DC supply for powering electronic equipment. However, the delivered current is limited by a maximum. It is available both at EEMCS and AE.

- Signal generator
  This device is a commonly used signal generator, which can be used to create an AC voltage signal in any common shape (sine, triangle, sawtooth, block). Furthermore, the frequency and amplitude of the signal can also be set. It is available at EEMCS. XXX

- Solar cell simulator
  This device is an electronic apparatus capable of simulating a solar array. Using a diode to simulate the IV characteristics of a solar array, it can be used to achieve a valid coupling between terminal voltage and delivered current. Having four channels, it can be used to simulate the IV characteristics of four arrays simultaneously. Attaching the simulator to a personal computer enables a software interface, which can be used for adjusting the power input to the simulated arrays. This adjustment can be done statically, which means inserting fixed values for the presented power, and dynamically, which means insertion of time variant values for the presented power. Note that although it is capable of simulating time-varying behaviour of solar cells, it does not simulate the capacitance of these cells. Custom made for the EPS board tests, it is available at EEMCS.

- Solar cell simulator (2)
  This device is functionally a copy of the previous device, with the exception that it is limited to static simulations only. It is available at EEMCS.

- Dummy load board
  This device is a circuit board consisting of resistors and capacitances mimicking the impedances of the various subsystems on board of the spacecraft. Making use of mechanical or solid-state switches, it is possible to connect the various systems to the EPS board output in a timed sequence. Custom made for the EPS board tests, it is available at EEMCS.

- Solar array
  This device is an exact copy of a single solar array implemented in the Delfi-C3 spacecraft. Its electrical characteristics are the same as the solar arrays, which are applied in-orbit. Therefore, it can be used to test the behaviour of the EPS board with accurate impedance at the input. It is available at AE.

- I2C checkout equipment board (ICE)
  This device mimics the behaviour of the I2C data bus. In fact it is a PIC microcontroller programmed to simulate the commanding behaviour of the on-board computer. It has to be powered by a 12V DC power supply and hooked up to a personal computer to send commands. Furthermore, it can be set to master or slave mode for flexible checkout of the data interface of the various printed circuit boards. This device is available at AE.

2.3 Personnel

In Table 1, a summary is given of all personnel involved in testing of the Electrical Power Subsystem Board. In the description of every test, the acronyms corresponding to the relevant personnel will be mentioned. These personnel have to be present in order to perform a valid test of the EPS board.

Table 1: Summary of personnel associated with EPS tests

Acronym	Full name	Affiliation	Function
AD	Adil Bahrouch	SystematIC Design BV	EPS Design Engineer
BM	Bert Monna	SystematIC Design BV	Supervisor of EPS Design
CW	Chris Werkmeester	TU Delft – AE – SIS	ICE Design Engineer
FH	Frank te Hennepe	TU Delft – AE – SIS	EPS Systems Engineer
GB	Geert Brouwer	TU Delft – AE – SIS	Head of Testing
RB	Remco Boom	TU Delft – AE – SIS	EPS PIC Programmer

3 Test description

In this chapter, the various tests for the EPS board are briefly described. The complete test procedure involves several tests, which can be divided into four general categories:

- General tests
- Functional tests
- Performance tests
- Environmental tests

Every test has to be accomplished with the intention as if the hardware subject to the test is used as flight hardware.

All requirements mentioned relate to the latest version of the SPEC file:
SPEC version 4.1, December 2005

General remark

In case of connection to a system bus connector, application of pin saving cables is obligatory.

Caution!

During handling and testing of the subsystem board, make sure to take precautions against electrostatic discharge. Testing personnel are obliged to attach themselves to electrical ground.

3.1 General tests

3.1.1 Mass measurement

Purpose: Determining mass of EPS board
Corresponding requirement: 6.1.02
Personnel: FH, GB
Location: AE
Equipment: EPS board, accurate scales
Action:

1. Turn on scales;
2. Put EPS board on scales;
3. Read the value for its mass from the scales;
4. Write down mass value;
5. Turn off scales.

Notes:

3.1.2 EPS board envelope determination

Purpose: Determining geometrical dimensions of EPS board
Corresponding requirement: 6.1.08
Personnel: FH, GB
Location: AE
Equipment: EPS board, ruler
Action:

1. Place ruler alongside X-dimension of the EPS board;
2. Read the value for its X-dimension from the ruler;

3. Write down the value for the X-dimension;
4. Repeat steps 1 to 3 for the Y-dimension of the EPS board;
5. Repeat steps 1 to 3 for the Z-dimension of the EPS board.

Notes:

3.1.3 EPS board workmanship check

Purpose: Check quality of workmanship performed on EPS board
Corresponding requirement:
Personnel: FH, GB
Location: AE
Equipment: EPS board, microscope
Action:

1. Place EPS board under microscope;
2. Check position of component on board by crosschecking with layout drawing;
3. Check electrical and mechanical connection of component with printed circuit board;
4. Repeat steps 2 and 3 for every component on board.

Notes:

3.2 Performance tests

3.2.1 Virtual EPS board static conversion efficiency test <OBSOLETE>

Purpose: Check whether the EPS board is capable of producing the minimum electrical bus power under various realistic static solar illumination conditions using a power simulator as power source at the EPS input terminals
Corresponding requirement: 6.2.01, 6.2.05, 6.3.01, 6.3.02
Personnel: AD, FH
Location: EEMCS
Equipment: EPS board, 12V DC power supply, solar cell simulator, oscilloscope, multimeter, dummy load board, live solar array
Action:

1. Connect 12V DC power supply to the power input of the solar cell simulator;
2. Connect solar cell simulator outputs to EPS board inputs;
3. Connect dummy load board to EPS converter output;
4. Connect positive terminal of solar array #1 to pin 6 of system bus connector;
5. Connect negative terminal of solar array #1 to pin 5 of system bus connector;
6. Connect positive terminal of solar array #2 to pin 7 of system bus connector;
7. Connect negative terminal of solar array #2 to pin 8 of system bus connector;
8. Ensure shadowing of both solar arrays;
9. Switch on 12 V DC power supply;
10. Find the relevant test in Appendix C.1;
11. Connect the oscilloscope probes to the relevant connection points on the EPS board;
12. Insert multimeter in current measurement mode in relevant branch;
13. Set dummy load board to represent only minimum electrical load (only batch 1);
14. Switch on solar cell simulator;
15. Switch on oscilloscope;
16. Set power level of solar array input 1 to the prescribed value using the solar cell simulator;
17. Repeat step 16 for solar array inputs 2, 3, and 4;
18. Set oscilloscope to correct settings;
19. Extract voltage waveforms from oscilloscope;
20. Connect next batch of loads on dummy load board to EPS board output;

21. Repeat steps 19 and 20 until dummy load board represents full load;
22. Turn off solar cell simulator;
23. Turn off oscilloscope;
24. Repeat steps 10 to 23 for every entry in Appendix C.1;
25. Turn off 12V DC power supply.

Notes: Test is performed in ambient (± 20 °C)

3.2.2 Live EPS board static conversion efficiency test

Purpose: Check whether the EPS board is capable of producing the minimum electrical bus power under various realistic static solar illumination conditions using illuminated genuine solar arrays as power source at the EPS input terminals

Corresponding requirement: 6.2.01, 6.2.05, 6.3.01, 6.3.02

Personnel: AD, BM, FH

Location: AE

Equipment: EPS board, 12V DC power supply, solar cell simulator, oscilloscope, multimeter, dummy load board, live solar array, solar cannon

Action:

1. Perform steps 3 to 8 of test 3.2.1;
2. Remove cover of solar arrays;
3. Place solar arrays in test rig;
4. Find the relevant test in Appendix C.2;
5. Connect the oscilloscope probes to the relevant connection points on the EPS board;
6. Insert multimeter in current measurement mode in relevant branch;
7. Set dummy load board to represent only minimum electrical load (only batch 1);
8. Position test rig at prescribed angle with respect to incident solar illumination;
9. Switch on oscilloscope;
10. Switch off artificial lighting;
11. Switch on solar cannon;
12. Set oscilloscope to correct settings;
13. Extract voltage waveforms from oscilloscope;
14. Connect next batch of loads on dummy load board to EPS board output;
15. Repeat steps 13 and 14 until dummy load board represents full load;
16. Switch off solar cannon;
17. Switch on artificial lighting;
18. Turn off oscilloscope;
19. Repeat steps 4 to 17 for every entry in Appendix C.2;

Notes: Test is performed in ambient (± 20 °C)

3.2.3 Live EPS board start up behaviour test

Purpose: Determine the start up behaviour of the EPS board by monitoring the relevant electrical quantities directly after sudden illumination of the solar arrays

Corresponding requirement: 6.2.01, 6.2.05, 6.3.01, 6.3.02

Personnel: AD, BM, FH

Location: AE

Equipment: EPS board, 12V DC power supply, solar cell simulator, oscilloscope, multimeter, dummy load board, live solar array, solar cannon

Action:

1. Perform steps 3 to 8 of test 3.2.1;
2. Remove cover of solar arrays;
3. Place solar arrays in test rig;
4. Find the relevant test in Appendix C.3;

5. Connect the oscilloscope probes to the relevant connection points on the EPS board;
6. Insert multimeter in current measurement mode in relevant branch;
7. Set dummy load board to represent only minimum electrical load (only batch 1);
8. Position test rig at prescribed angle with respect to incident solar illumination;
9. Switch on oscilloscope;
10. Switch off artificial lighting;
11. Switch on solar cannon;
12. Set oscilloscope to correct settings;
13. Extract voltage waveforms from oscilloscope;
14. Connect next batch of loads on dummy load board to EPS board output;
15. Repeat steps 13 and 14 until dummy load board represents full load;
16. Switch off solar cannon;
17. Switch on artificial lighting;
18. Turn off oscilloscope;
19. Repeat steps 4 to 17 for every entry in Appendix C.3;

Notes: Test is performed in ambient (± 20 °C)

3.2.4 Virtual EPS board dynamic conversion efficiency test <OBSOLETE>

Purpose: Check whether the EPS board is capable of producing the minimum electrical bus power during various realistic solar illumination transient simulations
Corresponding requirement: 6.2.01, 6.2.05, 6.3.01, 6.3.02
Personnel: AD, FH
Location: EEMCS
Equipment: EPS board, 12V DC power supply, solar cell simulator, oscilloscope, multimeter, dummy load board, live solar array
Action:

1. Connect 12V DC power supply to the power input of the solar cell simulator;
2. Connect solar cell simulator outputs to EPS board inputs;
3. Connect dummy load board to EPS converter output;
4. Connect positive terminal of solar array #1 to pin 6 of system bus connector;
5. Connect negative terminal of solar array #1 to pin 5 of system bus connector;
6. Connect positive terminal of solar array #2 to pin 7 of system bus connector;
7. Connect negative terminal of solar array #2 to pin 8 of system bus connector;
8. Set dummy load board to full load representation, i.e. connect full load to EPS board;
9. Switch on 12 V DC power supply;
10. Find relevant test in Appendix C.4;
11. Connect the oscilloscope probes to the relevant connection points on the EPS board;
12. Insert multimeter in current measurement mode in relevant branch;
13. Switch on solar cell simulator;
14. Switch on oscilloscope;
15. Set power level of solar array input 1 to the prescribed value using the solar cell simulator;
16. Repeat step 13 for solar array inputs 2, 3, and 4;
17. Set oscilloscope to correct settings;
18. Set the solar cell simulator to start of simulation;
19. Wait for simulation to be fully performed;
20. Extract voltage waveforms from oscilloscope;
21. Turn off solar cell simulator;
22. Turn off oscilloscope;
23. Repeat steps 10 to 22 for every entry in Appendix C.4;
24. Turn off 12V DC power supply.

Notes: Test is performed in ambient (± 20 °C)

3.3 Functional tests

3.3.1 PIC supply voltage test

Purpose: Check whether the PIC supply circuitry is effective in converting the 12V bus voltage down to the 3V3 PIC supply voltage
Corresponding requirement: 6.2.05
Personnel: FH
Location: EEMCS
Equipment: EPS board, 12 V DC power supply, oscilloscope, multimeter
Action:

1. Connect the positive terminal of the 12V DC power supply to the *V_bus_high_ABF_SYS_C* bus, i.e. pins 16 and 17 of the system bus connector;
2. Connect the negative terminal of the 12V DC power supply to electrical ground, i.e. pins 11 and 12 of the system bus connector;
3. Connect an oscilloscope probe to the PIC power input measurement point (VM2) on the EPS board;
4. Find relevant test in Appendix C.5;
5. Switch on 12V DC power supply;
6. Set voltage settings of 12 V DC power supply to prescribed value;
7. Turn off 12V DC power supply;
8. Switch on oscilloscope;
9. Set oscilloscope to take measurement on voltage trigger;
10. Switch on 12V DC power supply;
11. Wait for voltage waveform to assume steady state behaviour;
12. Extract voltage waveform from oscilloscope;
13. Switch off 12V DC power supply;
14. Switch off oscilloscope;
15. Repeat steps 4 to 14 for every entry in Appendix C.5.

Notes: Test is performed in ambient (± 20 °C)

3.3.2 PIC current measurement test

Purpose: Check whether the MAX4172 circuit is capable of providing an accurate measurement of the solar array output currents
Corresponding requirement: 6.2.07, 6.3.05
Personnel: FH, RB
Location: AE
Equipment: EPS board, 12 V DC power supply, solar cell simulator, oscilloscope, multimeter, dummy load board
Action:

1. Connect 12V DC power supply to the power input of the solar cell simulator;
2. Connect solar cell simulator outputs to EPS board inputs;
3. Connect dummy load board to EPS converter output;
4. Find relevant test in Appendix C.6;
5. Connect the oscilloscope probes to the relevant current sense amplifier output measurement point on the EPS board;
6. Insert multimeter in current measurement mode in relevant branch;
7. Set dummy load board to full load representation, i.e. connect full load to EPS board;
8. Switch on 12 V DC power supply;
9. Switch on solar cell simulator;
10. Switch on oscilloscope;

11. Set power level of relevant solar array to the prescribed value using the solar cell simulator;
12. Set oscilloscope to correct settings;
13. Extract voltage waveforms from oscilloscope;
14. Read value of current magnitude from multimeter;
15. Turn off solar cell simulator;
16. Turn off 12V DC power supply;
17. Repeat steps 4 to 17 for every entry in Appendix C.6;
18. Turn off oscilloscope.

Notes: Test is performed in ambient (± 20 °C)

3.3.3 PIC I2C interface test

Purpose: Check whether the MAX4172 circuit is capable of providing an accurate measurement of the solar array output currents

Corresponding requirement: 6.2.07, 6.3.05

Personnel: FH, RB, CW

Location: AE

Equipment: EPS board, 12 V DC power supply, solar cell simulator, oscilloscope, multimeter, I2C checkout equipment board

Action:

1. Connect 12V DC power supply to the power input of the solar cell simulator;
2. Connect I2C checkout equipment board to the system bus connector;
3. Connect I2C checkout equipment board to 12V DC power supply;
4. Connect I2C checkout equipment board to USB port on personal computer;
5. Connect solar cell simulator outputs to EPS board inputs;
6. Connect dummy load board to EPS converter output;
7. Find relevant test in Appendix C.6;
8. Connect the oscilloscope probes to the relevant current sense amplifier output measurement point on the EPS board;
9. Insert multimeter in current measurement mode in relevant branch;
10. Set dummy load board to full load representation, i.e. connect full load to EPS board;
11. Switch on 12V DC power supply;
12. Switch on solar cell simulator;
13. Switch on oscilloscope;
14. Enable master mode on I2C checkout equipment board;
15. Set power level of relevant solar array to the prescribed value using the solar cell simulator;
16. Set oscilloscope to correct settings;
17. Extract voltage waveforms from oscilloscope;
18. Acquisition current measurement data from PIC using I2C checkout equipment board;
19. Read value of current magnitude from multimeter;
20. Turn off solar cell simulator;
21. Turn off 12V DC power supply;
22. Repeat steps 7 to 21 for every entry in Appendix C.6;
23. Turn off oscilloscope.

Notes: Test is performed in ambient (± 20 °C)

3.4 Environmental tests

3.4.1 Elevated temperature test <DELETED>

Purpose: Check whether the EPS board is capable of producing the minimum electrical bus power under various realistic static solar illumination conditions at elevated temperatures
Corresponding requirement: 6.1.09, 6.2.01, 6.2.05, 6.3.01, 6.3.02
Personnel: AD, FH
Location: AE
Equipment: EPS board, 12 V DC power supply, solar cell simulator, oscilloscope, multimeter, dummy load board, thermal vacuum oven, solar array
Action:

1. Place EPS board in thermal vacuum chamber;
2. Route measurement and power wiring through cabling slot in thermal vacuum chamber;
3. Perform steps 1 to 8 of test 3.2.1;
4. Perform step 10 to 23 of test 3.2.1;
5. Remove all air in thermal vacuum oven by pumping oven vacuum;
6. Extract voltage waveforms from oscilloscope;
7. Fire up the thermal vacuum oven;
8. Extract voltage waveforms from oscilloscope;
9. Find relevant test in Appendix C.5;
10. Perform steps 10 to 23 of test 3.2.1;
11. Repeat steps 9 and 10 for every entry in Appendix C.5;
12. Turn off 12V DC power supply;
13. Shut down thermal vacuum chamber.

Notes: Steps 5 to 8 are inserted to ensure proper operation during vacuum pumping and heating of thermal vacuum oven. In case of failure during preparatory operations of the oven, the exact circumstances at time of failure can be easily determined.

3.4.2 Reduced temperature test <DELETED>

Purpose: Check whether the EPS board is capable of producing the minimum electrical bus power under various realistic static solar illumination conditions at reduced temperatures
Corresponding requirement: 6.1.09, 6.2.01, 6.2.05, 6.3.01, 6.3.02
Personnel: AD, FH
Location: AE
Equipment: EPS board, 12 V DC power supply, solar cell simulator, oscilloscope, multimeter, dummy load board, XXX
Action:

XXX

1. Switch on 12 V DC power supply;
2. Switch on solar cell simulator;
3. Switch on oscilloscope;
4. Set power level of solar array 1 to the prescribed value using the solar cell simulator;
5. Repeat step 8 for solar array 2, 3, and 4;
6. Set oscilloscope to correct settings;
7. Perform conversion simulation;
8. Extract voltage waveforms from oscilloscope;
9. Repeat steps 7 to 11 for every entry in the conversion table;
10. Turn off solar cell simulator;
11. Turn off 12V DC power supply;
12. Turn off oscilloscope.

XXX

Notes:

3.4.3 Electromagnetic radiation test <DELETED>

Purpose: Determine radiated electromagnetic interference caused by nominal operation of the EPS board
Corresponding requirement: 6.2.10, 6.2.11
Personnel: AD, FH
Location: EEMCS
Equipment: EPS board, 12 V DC power supply, solar cell simulator, oscilloscope, multimeter, dummy load board, spectral analyzer, TEM cell
Action:

1. Place EPS board in TEM cell;
2. Place field probe in TEM cell
3. Route measurement and power wiring through cabling slot in TEM cell;
4. Connect 12V DC power supply to the power input of the solar cell simulator;
5. Connect solar cell simulator outputs to EPS board inputs;
6. Connect dummy load board to EPS converter output;
7. Connect field probe output to spectral analyzer;
8. Set dummy load board to full load representation, i.e. connect full load to EPS board;
9. Find relevant test in Appendix C.7;
10. Switch on 12 V DC power supply;
11. Switch on solar cell simulator;
12. Set power level of relevant solar array to the prescribed value using the solar cell simulator;
13. Extract frequency waveforms from spectral analyzer;
14. Repeat steps 9 to 13 for every entry in Appendix C.7;
15. Turn off solar cell simulator;
16. Turn off 12V DC power supply;
17. Turn off spectral analyzer.

Notes: Test is performed to determine the amount of electromagnetic radiation caused by the EPS board. After all, too much radiation could lead to interference with other systems if the frequencies of this radiation match the operation frequencies of these systems.

3.4.4 Electromagnetic susceptibility test <DELETED>

Purpose: Determine electromagnetic susceptibility by checking spectral response of the EPS board
Corresponding requirement: 6.2.10, 6.2.11
Personnel: AD, FH
Location: EEMCS
Equipment: EPS board, 12 V DC power supply, solar cell simulator, oscilloscope, multimeter, dummy load board, signal generator, TEM cell
Action:

4 Test matrix

In this chapter, the test procedure of the EPS board is given. In Table 2, the details of this procedure are given.

Table 2: Outline of EPS board test procedure

Date	Test #	Test description	Corresponding section
	1	Mass measurement	3.1.1
	2	EPS board envelope determining	3.1.2
	3	Live EPS board static conversion efficiency test	3.2.1
	4	Live EPS board start up behaviour test	3.2.3
	5	PIC supply voltage test	3.3.1
	6	PIC current measurement test	3.3.2
	7	PIC – I2C interface test	3.3.3
	8	EPS board workmanship check	3.1.3

In Figure 1, a flow diagram of the EPS board test procedure is shown.

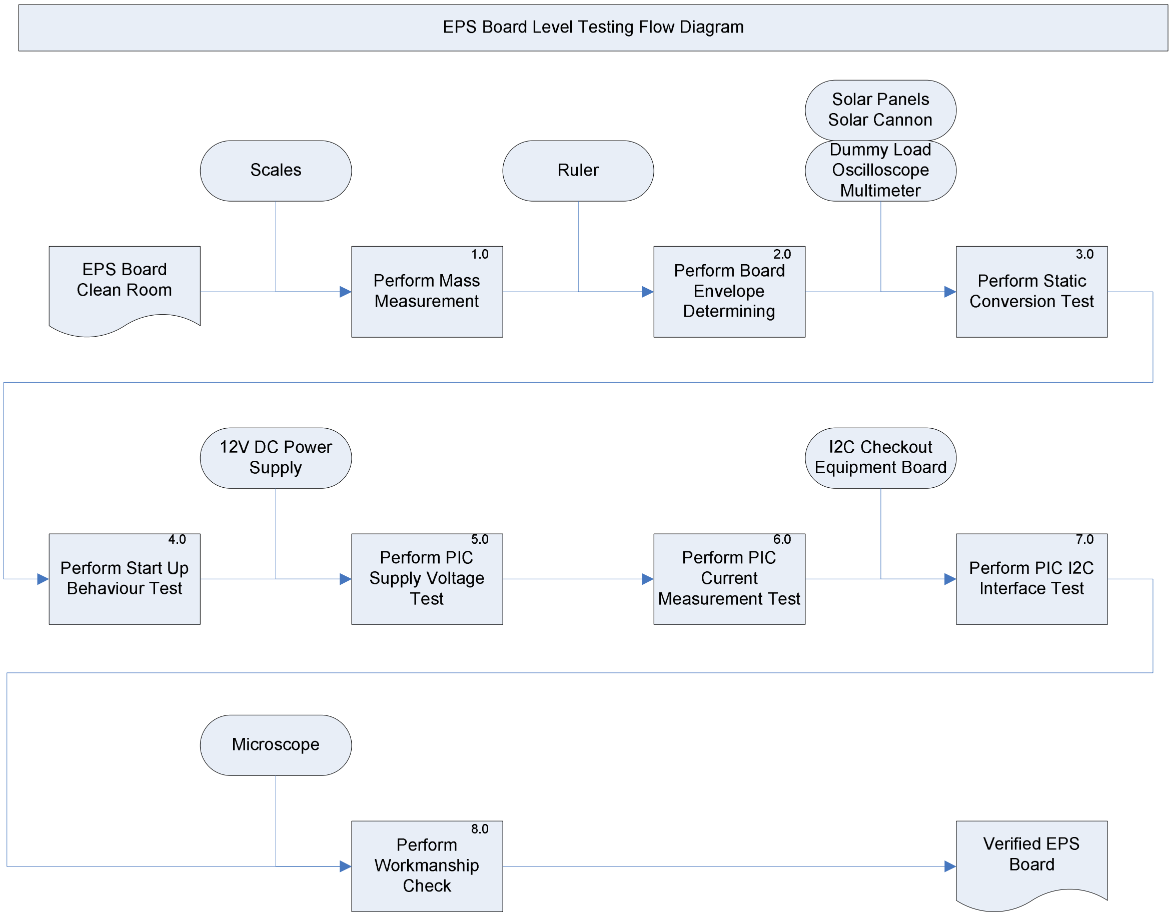
EPS Board Level Testing Flow Diagram
Scales
Ruler
Solar Panels
Solar Cannon
Dummy Load
Oscilloscope
Multimeter
EPS Board
Clean Room
1.0
Perform Mass Measurement
2.0
Perform Board Envelope Determining
3.0
Perform Static Conversion Test
12V DC Power Supply
I2C Checkout Equipment Board
4.0
Perform Start Up Behaviour Test
5.0
Perform PIC Supply Voltage Test
6.0
Perform PIC Current Measurement Test
7.0
Perform PIC I2C Interface Test
Microscope
8.0
Perform Workmanship Check
Verified EPS Board

Figure 1: Flow diagram of EPS Board Level test procedure

5 Pass / fail criteria

5.1 General tests

5.1.1 Mass measurement

Corresponding test: 3.1.1
Corresponding requirement:
6.1.02 **Subsystem mass**
The EPS total mass shall not exceed 150g
Criterion assessment:
A mass budget is generated for the complete Delfi-C3 spacecraft. Every subsystem is allotted a particular amount of mass in order to prevent the complete spacecraft from obtaining too much mass. This test is to check whether the mass of the EPS board is smaller than or equal to the allotted amount.
Pass criterion: Mass of EPS board is smaller than or equal to 150 g
Fail criterion: Mass of EPS board is larger than 150 g

5.1.2 EPS board envelope determining

Corresponding test: 3.1.2
Corresponding requirement:
6.1.08 **EPS electronics volume**
The EPS board shall fit within a dynamic envelope of 90 × 96 × 16 mm (L × W × T) including margins
Criterion assessment:
In order to fit in the printed circuit board stack of the Delfi-C3 spacecraft, the EPS board has to fit in a particular dynamic envelope. This envelope is equal to the circumferential envelope of the printed circuit board used for accommodation of the EPS.
Pass criterion: Compliance to all three of the following criteria:

- Length of EPS board is smaller than or equal to 90 mm;
- Width of EPS board is smaller than or equal to 96 mm;
- Height of EPS board is smaller than or equal to 16 mm.

Fail criterion: Compliance to one or more of the following criteria:

- Length of EPS board is larger than 90 mm;
- Width of EPS board is larger than 96 mm;
- Height of EPS board is larger than 16 mm.

5.1.3 EPS board workmanship check

Corresponding test: 3.1.3
Corresponding requirement:
Criterion assessment:
Creation of a fully operational printed circuit board requires manufacturing of the board and population of the various components on the board. However, this procedure remains a human process, and errors are likely to occur. Misplacement of components and inferior connections are common errors. In order to identify these errors a workmanship check has to be made by inspecting the position of every component and its connections to the printed circuit board.
Pass criterion: Every component on the EPS board is positioned in the correct place and is settled in a mechanically and electrically correct way
Fail criterion: One or multiple components on the EPS board are positioned in a wrong place or have inferior connections to the printed circuit board

5.2 Performance tests

5.2.1 Virtual EPS board static conversion efficiency test <OBSOLETE>

Corresponding test: 3.2.1
Corresponding requirement:
6.2.01 **Power distribution**
The EPS shall be able to provide power to subsystems when not in eclipse/off mode
6.2.05 **Bus voltage regulation**
The EPS shall be able to regulate bus voltages
6.3.01 **Minimum power**
The EPS shall deliver a minimum of 2.6 W in nominal operations
6.3.02 **Bus voltage**
The EPS shall regulate the bus voltage to a standard of 12V +/- 0.48V for all subsystems
Criterion assessment: When the Delfi-C3 spacecraft is in orbit, the EPS board has to be able to provide sufficient power to the bus under various conditions. These conditions vary in the amount of illumination on every solar array of Delfi-C3. In every condition, the EPS has to sufficiently energize the bus in order to supply power to all loads. This test is performed to check for capability of EPS board to deliver sufficient power to the system bus under various illumination conditions. Furthermore, the test is accomplished to yield transient start-up behaviour of the EPS board by having the load impedance change due to switching on of loads. During this test, constant illumination inputs (greater than or equal to zero) for all four simulates arrays are used. Successful operation is attained in case the bus voltage is stably maintained at its nominal value of 12V during full supply to all loads in the spacecraft.
Pass criterion: Bus voltage remains stable at 12V in case all loads are connected to the bus for all possible illumination conditions
Fail criterion: Bus voltage collapses or remains stable at a value lower than 12V in case all loads are connected to the bus for any of the possible illumination conditions

5.2.2 Live EPS board static conversion efficiency test

Corresponding test: 3.2.2
Corresponding requirement:
6.2.02 **Power distribution**
The EPS shall be able to provide power to subsystems when not in eclipse/off mode
6.2.06 **Bus voltage regulation**
The EPS shall be able to regulate bus voltages
6.3.02 **Minimum power**
The EPS shall deliver a minimum of 2.6 W in nominal operations
6.3.02 **Bus voltage**
The EPS shall regulate the bus voltage to a standard of 12V +/- 0.48V for all subsystems
Criterion assessment: Idem to 5.2.1
Pass criterion: Idem to 5.2.1
Fail criterion: Idem to 5.2.1

5.2.3 Live EPS board start up behaviour test

Corresponding test: 3.2.3
Corresponding requirement:
6.2.03 **Power distribution**
The EPS shall be able to provide power to subsystems when not in eclipse/off mode
6.2.07 **Bus voltage regulation**
The EPS shall be able to regulate bus voltages
6.3.03 **Minimum power**

The EPS shall deliver a minimum of 2.6 W in nominal operations

6.3.02 **Bus voltage**

The EPS shall regulate the bus voltage to a standard of 12V +/- 0.48V for all subsystems

Criterion assessment: Idem to 5.2.1

Pass criterion: Transient start-up behaviour of the EPS board after supplying power at its input is settled down after XXX ms

Fail criterion: Transient start-up behaviour of the EPS board after supplying power at its input is not settled down after XXX ms

5.2.4 Virtual EPS board dynamic conversion efficiency test <OBSOLETE>

Corresponding test: 3.2.4

Corresponding requirement:

6.2.01 **Power distribution**

The EPS shall be able to provide power to subsystems when not in eclipse/off mode

6.2.05 **Bus voltage regulation**

The EPS shall be able to regulate bus voltages

6.3.01 **Minimum power**

The EPS shall deliver a minimum of 2.6 W in nominal operations

6.3.02 **Bus voltage**

The EPS shall regulate the bus voltage to a standard of 12V +/- 0.48V for all subsystems

Criterion assessment:

When the Delfi-C3 spacecraft is in orbit, the EPS board has to be able to provide sufficient power to the bus under various conditions. These conditions vary in the amount of illumination on every solar array of Delfi-C3. In every condition, the EPS has to sufficiently energize the bus in order to supply power to all loads. This test is performed to check for capability of EPS board to deliver sufficient power to the system bus during various solar illumination transient simulations. During this test, variable illumination inputs (greater than or equal to zero) for all four simulates arrays are used. These inputs are dependent of the rotational rate of the satellite. Therefore, the illumination inputs are generated by the Delfi-C3 simulation in EuroSim. A personal computer is used to transfer these illumination inputs to the solar cell simulator. Successful operation is attained in case the bus voltage is stably maintained at its nominal value of 12V during full supply to all loads in the spacecraft.

Pass criterion: Bus voltage remains stable at 12V in case all loads are connected to the bus for all possible illumination scenarios

Fail criterion: Bus voltage collapses or remains stable at a value lower than 12V in case all loads are connected to the bus for any of the possible illumination scenarios

5.3 Functional tests

5.3.1 PIC supply voltage test

Corresponding test: 3.3.1

Corresponding requirement:

6.2.05 **Bus voltage regulation**

The EPS shall be able to regulate bus voltages

Criterion assessment:

The PIC microcontroller situated on board of the EPS board functions at 3.3V in nominal operations. This 3.3V is generated on board by decreasing the bus voltage to the PIC input voltage. For this purpose, a circuit is used, which reacts in a non-linear fashion to the bus voltage. This circuit is designed to be able to generate 3.3V as the PIC input voltage in case the bus voltage is 12V. However, the bus voltage can deviate from its nominal value, which will affect the value of the PIC input voltage. This test is performed in order to check whether the PIC input voltage remains at an acceptable level by changing the bus voltage between realistic levels. In order to protect the PIC microcontroller, the PIC incorporates a brown-out voltage, which is set at 2.6V. Therefore, the PIC input voltage has to be larger than 2.6V to prevent the PIC from shutting down. No functionality test is performed to test the operational characteristics of the PIC.

Pass criterion: PIC input voltage should remain larger than 2.6V for every realistic value of the bus voltage

Fail criterion: PIC input voltage drops beneath 2.6V for any realistic value of the bus voltage

5.3.2 PIC current measurement test

Corresponding test: 3.3.2

Corresponding requirement:

6.2.07 **Current monitoring**

The EPS shall be able to monitor currents from each individual solar panel

6.3.05 **Current measurement accuracy**

The current delivered by each individual solar panel shall be determined with an accuracy of at least 10 mA

Criterion assessment:

Every board in the printed circuit board stack has a current measurement circuit. This circuit consists of a sensing resistor, a current-sense amplifier, and a shunt resistor. In general, a voltage is generated at the output of the current-sense amplifier, which is directly related to the current flowing through the main branch. For post operation purposes a coefficient is calculated which relates the voltage to the current. However, due to tolerances in the component values this coefficient can deviate in reality from the calculated value. Therefore, a test is performed to determine the coefficient. The processing capabilities of the PIC will not be tested, because software is needed to implement this feature.

Pass criterion: No pass criteria are present. Test results are applied to calibrate microcontroller in order to conform to requirement and/or improve measurement accuracy.

Fail criterion: No output voltage is generated by the MAX4172 component

5.3.3 PIC – I2C interface test

Corresponding test: 3.3.3

Corresponding requirement:

6.6.02 **Subsystems interface**

The EPS board shall interface with other subsystems as specified in the ICD

Criterion assessment:

In order to transmit measurement data from the spacecraft to the ground station, the data acquisitioned by the PIC microcontrollers has to be sent via the I2C data bus to the on-board computer. It is critical that this data is sent by the microcontroller and received by the on-board computer in a correct way. Furthermore, application of the I2C protocol may not have any influence on the actual data package. Therefore, a test will be performed to check whether the output of the MAX4172 current measurement circuitry is equal to the value of the measurement taken by the PIC and sent over the I2C bus to its master. Application of the I2C checkout equipment is a necessity in order to simulate the behaviour of the master on the I2C bus.

Pass criterion: Measurement value transmitted to ICE is equal to corresponding output voltage of MAX4172 current measurement circuitry within a tolerance of ± 3 bits

Fail criterion: Measurement value transmitted to ICE deviates from corresponding output voltage of MAX4172 current measurement circuitry by more than 3 bits accuracy

5.4 Environmental tests

5.4.1 Elevated temperature test <DELETED>

Corresponding test: 3.4.1
Corresponding requirement:
6.1.09 **EPS electronic thermal envelope**
The EPS has to be able to operate within a temperature range of 253 K < T < 318 K
6.2.01 **Power distribution**
The EPS shall be able to provide power to subsystems when not in eclipse/off mode
6.2.05 **Bus voltage regulation**
The EPS shall be able to regulate bus voltages
6.3.01 **Minimum power**
The EPS shall deliver a minimum of 2.6 W in nominal operations
6.3.02 **Bus voltage**
The EPS shall regulate the bus voltage to a standard of 12V +/- 0.48V for all subsystems
Criterion assessment: In orbit, the temperature of the Delfi-C3 spacecraft will differ for a large part. However, in every possible condition the EPS board has to be able to supply sufficient power to the bus. This means that at thermally hot and vacuum conditions, the EPS board has to be able to conform to the criteria postulated in section 5.2.1 and section 5.2.2. During preliminary thermal analyses the maximum temperature, at which the EPS board will operate, is estimated at 40 °C. Therefore, this test is performed to check whether the EPS board is capable of generating sufficient bus power in case of an elevated board temperature.
Pass criterion: Bus voltage remains stable at 12V in case all loads are connected to the bus for all possible illumination conditions during steady-state and transient conditions, where vacuum and elevated temperatures are enforced.
Fail criterion: Bus voltage collapses or remains stable at a value lower than 12V in case all loads are connected to the bus for any of the possible illumination conditions during steady-state and transient conditions, where vacuum and elevated temperatures are enforced.

5.4.2 Reduced temperature test <DELETED>

Corresponding test: 3.4.2
Corresponding requirement:
6.1.10 **EPS electronic thermal envelope**
The EPS has to be able to operate within a temperature range of 253 K < T < 318 K
6.2.02 **Power distribution**
The EPS shall be able to provide power to subsystems when not in eclipse/off mode
6.2.06 **Bus voltage regulation**
The EPS shall be able to regulate bus voltages
6.3.02 **Minimum power**
The EPS shall deliver a minimum of 2.6 W in nominal operations
6.3.02 **Bus voltage**
The EPS shall regulate the bus voltage to a standard of 12V +/- 0.48V for all subsystems
Criterion assessment: In orbit, the temperature of the Delfi-C3 spacecraft will differ for a large part. However, in every possible condition the EPS board has to be able to supply sufficient power to the bus. This means that at thermally cold and vacuum conditions, the EPS board has to be able to conform to the criteria postulated in section 5.2.1 and section 5.2.2. During preliminary thermal analyses the minimum temperature, at which the EPS board will operate, is estimated at -20 °C. Therefore, this test is performed to check whether the EPS board is capable of generating sufficient bus power in case of a reduced board temperature.
Pass criterion: Bus voltage remains stable at 12V in case all loads are connected to the bus for all possible illumination conditions during steady-state and transient conditions, where vacuum and reduced temperatures are enforced.

Fail criterion: Bus voltage collapses or remains stable at a value lower than 12V in case all loads are connected to the bus for any of the possible illumination conditions during steady-state and transient conditions, where vacuum and reduced temperatures are enforced.

5.4.3 Electromagnetic radiation test <DELETED>

Corresponding test: 3.4.3
Corresponding requirement:
6.2.10 **EMI/RFI suppression**
The EPS shall include EMI/RFI suppression for all subsystems
6.2.11 **Transient suppression**
The EPS shall include transient suppression for all subsystems
Criterion assessment: Electromagnetic interference is produced by every current carrying line, which is subject to transients in voltage or current. These transients will produce electromagnetic waves, which can be picked up by other electronic circuits. Due to the interaction of these waves with the subject circuit, a distorting signal can be created in this latter electrical network, which can lead to unwanted response of electronic components. Moreover, electromagnetic interference can be created at a particular frequency, which is used for communications. This will lead to a noisy communication signal. For this reason, the produced transients and accompanying electromagnetic interference has to be suppressed as much as possible.
Pass criterion: Minimal production of EM waves
Fail criterion: Excessive production of EM waves in spectra, to which components in Delfi-C3 are sensitive

5.4.4 Electromagnetic susceptibility test <DELETED>

Corresponding test: 3.4.4
Corresponding requirement:
6.2.10 **EMI/RFI suppression**
The EPS shall include EMI/RFI suppression for all subsystems
6.2.11 **Transient suppression**
The EPS shall include transient suppression for all subsystems
Criterion assessment: Electromagnetic interference is produced by every current carrying line, which is subject to transients in voltage or current. These transients will produce electromagnetic waves, which can be picked up by other electronic circuits. Due to the interaction of these waves with the subject circuit, a distorting signal can be created in this latter electrical network, which can lead to unwanted response of electronic components. For this reason, the response of an electronic circuit to electromagnetic interference has to be minimal to avoid unwanted responses.
Pass criterion: Minimal response to signals in spectra of communication signals
Fail criterion: Excessive response to signals in spectra of communication signals

6 Conclusions and recommendations

In this document, the various tests needed to validate the Electrical Power Subsystem board are described. Besides descriptions of the various tests, a description of the required test resources is given. Furthermore, an outline of the test procedure is shown in this document. Pass and fail criteria of the various tests are listed.

Test description

In this chapter, the various tests for the combination board are briefly described. The complete test procedure involves several tests, which can be divided into four general categories:

- General tests
- Functional tests
- Performance tests
- Environmental tests

Every test has to be accomplished with the intention as if the hardware subject to the test is used as flight hardware.

All requirements mentioned relate to the latest version of the SPEC file:
SPEC version 4.1, December 2005

General remark

In case of connection to a system bus connector, application of pin saving cables is obligatory.

Caution!

During handling and testing of the subsystem board, make sure to take precautions against electrostatic discharge. Testing personnel are obliged to attach themselves to electrical ground.

Remark

No test points are present on the combination board. In order to measure the voltage at a particular node, two options are present:

- Measure voltage at a connected pin on a electronic component or connector
- Pierce through the soldering mask and measure voltage on relevant connection line
- Measure voltage at transconduction holes present on the relevant connection line

1.1 General tests

1.1.1 Mass measurement

Purpose: Determining mass of combination board
Corresponding requirement:
Personnel: BV, GB
Location: AE
Equipment: Combination board, accurate scales
Action:

1. Turn on scales;
2. Put combination board on scales;
3. Read the value for its mass from the scales;
4. Write down mass value;
5. Turn off scales.

Notes:

1.1.2 Combination board envelope determination

Purpose: Determining geometrical dimensions of combination board
Corresponding requirement:
Personnel: BV, GB
Location: AE
Equipment: Combination board, ruler
Action:

1. Place ruler alongside X-dimension of the combination board;
2. Read the value for its X-dimension from the ruler;
3. Write down the value for the X-dimension;
4. Repeat steps 1 to 3 for the Y-dimension of the combination board;
5. Repeat steps 1 to 3 for the Z-dimension of the combination board.

Notes:

1.2 Performance tests

1.2.1 On-board FM/430 5V conversion test

Purpose: Check whether the MAX1836 step down converter is successful in converting the 12V bus voltage down to the 5V input voltage for the FM/430 flight board
Corresponding requirement: 6.2.05
Personnel: TH, FH
Location: AE
Equipment: Combination board, 12 V DC power supply, oscilloscope, multimeter
Action:

1. Connect the positive terminal of the 12V DC power supply to the *V_bus_high_ABF_SYS_C* bus, i.e. pins 16 and 17 of the system bus connector;
2. Connect the negative terminal of the 12V DC power supply to electrical ground, i.e. pins 11 and 12 of the system bus connector;
3. Connect an oscilloscope probe to the output measurement point of 5V step down converter on the combination board for the FM/430 supply;
4. Switch on oscilloscope;
5. Find relevant test in Appendix C.2;
6. Switch on 12V DC power supply;
7. Set output voltage of 12V DC power supply to prescribed value;
8. Wait for voltage waveform to assume steady state behaviour;
9. Extract voltage waveform from oscilloscope;
10. Switch off 12V DC power supply;
11. Repeat steps 6 to 11 for every entry in Appendix C.2;
12. Switch off oscilloscope.

Notes: Test is performed in ambient (± 20 °C)

1.2.2 On-board AWSS 3V3 conversion test

Purpose: Check whether the MAX1836 step down converter is successful in converting the 12V bus voltage down to the 3V3 input voltage for the autonomous wireless sun sensor
Corresponding requirement: 6.2.05
Personnel: TH, FH
Location: AE
Equipment: Combination board, 12 V DC power supply, oscilloscope, multimeter
Action:

1. Connect the positive terminal of the 12V DC power supply to the *V_bus_high_ABF_SYS_C* bus, i.e. pins 16 and 17 of the system bus connector;
2. Connect the negative terminal of the 12V DC power supply to electrical ground, i.e. pins 11 and 12 of the system bus connector;
3. Connect an oscilloscope probe to the output measurement point of 3V3 step down converter on the combination board for the AWSS supply;
4. Ensure the local EPS PIC is programmed for OBM mode;
5. Switch on oscilloscope;
6. Find relevant test in Appendix C.3;
7. Switch on 12V DC power supply;
8. Set output voltage of 12V DC power supply to prescribed value;
9. Wait for voltage waveform to assume steady state behaviour;
10. Extract voltage waveform from oscilloscope;
11. Switch off 12V DC power supply;
12. Repeat steps 6 to 11 for every entry in Appendix C.3;
13. Switch off oscilloscope.

Notes: Test is performed in ambient (± 20 °C); OBM mode is enabled in local EPS PIC

1.3 Functional tests

1.3.1 Local EPS PIC supply voltage test

Purpose: Check whether the local EPS PIC supply circuitry is effective in converting the 12V bus voltage down to the 3V3 local EPS PIC supply voltage
Corresponding requirement: 6.2.05
Personnel: TH, FH
Location: AE
Equipment: Combination board, 12 V DC power supply, oscilloscope, multimeter
Action:

1. Connect the positive terminal of the 12V DC power supply to the *V_bus_high_ABF_SYS_C* bus, i.e. pins 16 and 17 of the system bus connector;
2. Connect the negative terminal of the 12V DC power supply to electrical ground, i.e. pins 11 and 12 of the system bus connector;
3. Connect an oscilloscope probe to the local EPS PIC power input measurement point on the combination board;
4. Switch on oscilloscope;
5. Find relevant test in Appendix C.4;
6. Switch on 12V DC power supply;
7. Set output voltage of 12V DC power supply to prescribed value;
8. Wait for voltage waveform to assume steady state behaviour;
9. Extract voltage waveform from oscilloscope;
10. Switch off 12V DC power supply;
11. Repeat steps 6 to 11 for every entry in Appendix C.4;
12. Switch off oscilloscope.

Notes: Test is performed in ambient (± 20 °C)

1.3.2 FM/430 current measurement test

Purpose: Check whether the MAX4172 circuit is capable of providing an accurate measurement of the current flow into the supply of the FM/430 flight board
Corresponding requirement: 6.2.07, 6.3.05
Personnel: TH, FH
Location: AE

Equipment: Combination board, 12 V DC power supply, oscilloscope, multimeter
Action:

1. Connect the positive terminal of the 12V DC power supply to the positive terminal of the multimeter in current measurement mode;
2. Connect the negative terminal of the multimeter to the *V_bus_high_ABF_SYS_C* bus, i.e. pins 16 and 17 of the system bus connector
3. Connect the negative terminal of the 12V DC power supply to electrical ground, i.e. pins 11 and 12 of the system bus connector;
4. Connect the oscilloscope probes to the FM/430 current sense amplifier output measurement point on the combination board;
5. Switch on oscilloscope;
6. Find relevant test in Appendix C.5;
7. Switch on 12V DC power supply;
8. Set output voltage of 12V DC power supply to prescribed value;
9. Wait for voltage waveform to assume steady state behaviour;
10. Extract voltage waveform from oscilloscope;
11. Read value of current magnitude from multimeter;
12. Switch off 12V DC power supply;
13. Repeat steps 7 to 13 for every entry in Appendix C.5;
14. Switch off oscilloscope.

Notes: Test is performed in ambient (± 20 °C)

1.3.3 AWSS current measurement test

Purpose: Check whether the MAX4172 circuit is capable of providing an accurate measurement of current flow into the supply of the autonomous wireless sun sensor
Corresponding requirement: 6.2.07, 6.3.05
Personnel: TH, FH
Location: AE
Equipment: Combination board, 12 V DC power supply, oscilloscope, multimeter
Action:

1. Connect the positive terminal of the 12V DC power supply to the receiving end of the positive terminal of the multimeter in current measurement mode;
2. Connect the negative terminal of the multimeter to the *V_bus_high_ABF_SYS_C* bus, i.e. pins 16 and 17 of the system bus connector
3. Connect the negative terminal of the 12V DC power supply to electrical ground, i.e. pins 11 and 12 of the system bus connector;
4. Connect the oscilloscope probes to the FM/430 current sense amplifier output measurement point on the combination board;
5. Ensure local EPS PIC is programmed for OBM mode;
6. Switch on oscilloscope;
7. Find relevant test in Appendix C.6;
8. Switch on 12V DC power supply;
9. Set output voltage of 12V DC power supply to prescribed value;
10. Wait for voltage waveform to assume steady state behaviour;
11. Extract voltage waveform from oscilloscope;
12. Read value of current magnitude from multimeter;
13. Switch off 12V DC power supply;
14. Repeat steps 7 to 13 for every entry in Appendix C.6;
15. Switch off oscilloscope.

Notes: Test is performed in ambient (± 20 °C); OBM mode is enabled in local EPS PIC